THE AXIAL BEHAVIOUR OF DISPLACEMENT PILES IN CHALK

A thesis submitted to Imperial College London in partial fulfilment of the requirements for the degree of Doctor of Philosophy and for the Diploma of Imperial College

by

Róisín Buckley

Department of Civil and Environmental Engineering

Imperial College London

London SW7 2AZ

FEBRUARY 2018

DECLARATION

The work presented in this thesis was undertaken in the Department of Civil and Environmental Engineering at Imperial College London and at a test site close to the village of St. Nicholas-at-Wade, UK. This thesis is the result of my own work and any quotation from, or description of, the work of others has been appropriately referenced, whether published or unpublished. This thesis is not the same as any that I have submitted for any degree, diploma or other qualification at any other university. No part of this thesis has been or being concurrently submitted for any such degree, diploma or other qualification.

The copyright of this thesis rests with the Author and is made available under a Creative Commons Attribution Non-Commercial No Derivatives licence. Researchers are free to copy, distribute or transmit the thesis on the condition that they attribute it, that they do not use it for commercial purposes and that they do not alter, transform or build upon it. For any reuse or redistribution, researchers must make clear to others the licence terms of this work.

Róisín Buckley

London, February 2018

ABSTRACT

Current axial capacity design methods for piles driven in chalk are known to be unreliable, in particular where low-medium density material is encountered. The primary complexities associated with using driven pre-formed displacement piles to withstand predominantly axial loading include (i) determining their installation resistance (ii) assessing pile static load behaviour after allowing for set-up and (iii) the effects of axial cyclic loading on the behaviour. The development of improved design methods has been impeded by a lack of both instrumented pile test data and the understanding they can bring regarding the fundamental underlying effective stress mechanisms.

The work described in this thesis was motivated by an Innovate-UK joint industry project related to the Wikinger offshore windfarm in the German Baltic Sea. The Author's investigations included analysis of full-scale offshore static and dynamic pile tests on open-ended steel tubular piles founded in glacial till and chalk at Wikinger. The tests were supplemented by further experiments on reduced-scale open-ended driven piles and heavily instrumented closed-ended Imperial College Piles at an analogous onshore test site, in Kent, UK. The onshore test site facilitated a systematic investigation of how ageing and cyclic loading affects driven piles over an eight-month period. Shaft capacity was shown to increase significantly with time and the cyclic tests indicated that one-way axial cyclic loading is not as detrimental to aged capacity as previously feared.

The understanding drawn from the Author's work was used to map out a route towards better rules for predicting the axial capacity of open and closed-ended displacement piles in chalk. A new effective stress-based approach to predict radial effective stresses is proposed, based on the key phenomena identified, namely (i) the use of CPT cone resistance to allow for local variations in properties (ii) the marked effect of the relative distance from the pile tip below any given chalk horizon (iii) the interface effective stress shear failure characteristics and (iv) addressing the significant capacity gains which occur with time. The new approach is shown to lead to far better predictions of both soil resistance to driving and long-term capacity than the current industry design methods.

ACKNOWLEDGEMENTS

Foremost, I wish to thank my supervisors, Prof. Richard Jardine and Dr. Stavroula Kontoe for their support and guidance over the last three and a half years and for helping me to develop many of the ideas in this thesis.

The research project was part of a Joint Industry Project between Imperial College, Iberdrola and the Geotechnical Consulting Group, supported by Innovate UK. The funding from Innovate UK is gratefully acknowledged, as are Dr. Felix Schroeder and Pedro Barbosa for their invaluable technical input and advice. I also wish to thank Atkins for the funding they provided during the final phase of field testing.

I am heavily indebted to Dr. Emil Ushev and Tingfa Liu who helped with the field testing and kept everything going when I had an unavoidable accident. I also wish to thank all of the other Researchers and Academic Staff who gave up their time to take part; Dr. James Lawrence, Dr. Tom Shire, Dr. Sarah Tallett-Williams and Dr. Vasia Tsaparli.

I am grateful to Prof. Mark Randolph who kindly allowed me to use his software program IMPACT to analyse the dynamic data and who provided invaluable advice. I am grateful to Peter Middendorp and Allnamics who provided access to their software and carried out development work. I also wish to thank Brian McKenzie, Michel Maron and Zine Labidine Delimi from Fugro France for allowing me to work with them on CAPWAP in Paris.

I thank the technical staff, in particular Mr. Duncan Parker, who made an excellent contribution to the research and was always great company during long days on site. I also wish to thank Dr. Sunday Popo-olo and Leslie Clark from the Structures department as well as Steve Ackerley and Graham Keefe from the Geotechnics Section.

The ICP tests were possible with the support of Prof. Barry Lehane and Tom Pine, who came from UWA to help with the testing. Dr. Jit Kheng Lim is also gratefully acknowledged for his technical help and work to prepare the pile in UWA. I also thank Cambridge In Situ Ltd., in particular Robert Whittle and Clive Dalton, for their help with the equipment and for giving up their time to help in times of crisis.

I thank the MSc students whose hard work supported the research; Derek Chan, Lauren Doughty, Ignacio Ebensperger, Sarah Esper and Christopher Norrie. I also thank those who contributed data or other valuable input; Dr. John Carey, Dr. Francesca Ciavaglia, Dr. Andrea Diambra, Dr. Mike Long, Chris Hartley, Julian Osborne, Dr. Elisabeth Palix, Sebastien Burlon, Wolf Eckhart-Semme, Dr. Philip Smith and Colin Spinley.

Ar ndóigh, táim buíoch do mo theaghlach agus mo chairde in Éirinn, i Londain, i Meiriceá, agus san Astráil, as a dtacaíocht agus a ngrá.

TABLE OF CONTENTS

DECLARATION I

ABSTRACT II

ACKNOWLEDGEMENTS III

TABLE OF CONTENTS IV

LIST OF SYMBOLS X

CHAPTER 1 INTRODUCTION 1

1.1 Research background 1
1.2 Research scope and methodology 4
1.3 Contents of the thesis 8

CHAPTER 2 CHALK AS AN ENGINEERING MATERIAL 10

2.1 Introduction 10
2.2 Deposition & diagenesis 11
2.3 Composition 14
2.4 Discontinuities & weathering 15
2.5 Index properties 15
2.6 Engineering classification of chalk 21
2.7 Permeability 25
2.8 In situ testing 25
2.8.1 Cone penetration tests 25
2.8.2 Pressuremeter tests 27
2.8.3 Geophysical testing 28
2.9 Features of the mechanical behaviour of chalk 31
2.9.1 Pre-yield behaviour & small strain stiffness 31
2.9.2 Critical state soil mechanics and the state parameter for granular soils 32
2.9.3 Behaviour of bonded soils and weak rocks 34
2.10 Behaviour of intact chalk 39
2.10.1 Pre-yield behaviour 39
2.10.2 Yielding in compression 41
2.10.3 Behaviour under shear and effective strength parameters 41
2.11 Behaviour of remoulded chalk 45
2.11.1 Formation & Occurrence 45
2.11.2 Behaviour of unaged chalk slurry 46
2.11.3 Gains in strength with time 46

2.12 Interface shear behaviour 49
2.13 Summary of chalk behaviour 53

CHAPTER 3 EVALUATING THE AXIAL CAPACITY OF DISPLACEMENT PILES IN CHALK 55

3.1 Introduction 55
3.2 Axial behaviour of piled foundations 55
3.2.1 Axial pile testing & interpretation 55
3.2.2 Pile shaft & base resistance 57
3.2.3 Considerations for open-ended tubular piles 57
3.2.4 Time effects on capacity 59
3.2.5 Axial cyclic loading 59
3.3 Axial capacity of driven piles in clays and sands 63
3.3.1 Stress changes during installation, equalisation and load testing of piles in clay 63
3.3.2 Axial capacity design methods for clay 64
3.3.3 Stress changes during installation, equalisation and load testing of piles in sand 69
3.3.4 Axial capacity design methods for sand 71
3.4 Axial capacity of driven piles in chalk 77
3.4.1 Stress changes during installation, equalisation and load testing 77
3.4.2 Axial capacity design methods in chalk 78
3.5 Published and unpublished pile test data in chalk 86
3.5.1 Tests on partial displacement open-ended piles and H piles 87
3.5.2 Tests on large displacement closed-ended piles 102
3.6 Observations from the extended database of tests 119
3.7 Summary and concluding remarks 129

CHAPTER 4 DYNAMIC METHODS TO DETERMINE AXIAL PILE CAPACITY 131

4.1 Introduction 131
4.2 Wave equation theory & background 132
4.3 Numerical methods for the solution of the one dimensional wave equation 133
4.4 Dynamic pile testing in practice 136
4.5 The use of soil resistance models 140
4.6 Shaft and base models after Smith (1962) 141
4.6.1 Original model formulation 141
4.6.2 Modifications to the original model 143
4.7 Soil resistance models after Simons and Randolph (1985) and Deeks and Randolph (1995) 146
4.7.1 Sensitivity of model parameters 149
4.7.2 Limitations of existing models 153
4.8 Wave equation implementation in software 159
4.8.1 Commercial & research codes 159
4.8.2 Comparison between numerical methods 160

4.9 Signal matching methodology 161
4.9.1 Data quality assessment 162
4.9.2 Parameter selection 163
4.9.3 Assessment of soil resistance to driving (SRD) 164
4.9.4 Signal matching of individual signals 167
4.9.5 Qualitative assessment of match quality 168
4.10 Accuracy of dynamic pile testing 171
4.10.1 Dependency of the solution on the operator 171
4.10.2 Comparison with static load tests 172
4.11 Concluding remarks 175

CHAPTER 5 STATIC AND DYNAMIC PILE TESTS AT THE WIKINGER OFFSHORE WINDFARM 176

5.1 Introduction 176
5.2 Study objectives and methodology 177
5.2.1 Motivation for experimental investigation 177
5.2.2 Testing campaigns at Wikinger 179
5.2.3 Experimental aims 179
5.3 Geology and stratigraphy at the windfarm 180
5.4 Description of test sites 181
5.5 Glacial till deposits encountered at the test sites 184
5.5.1 Description & occurrence 184
5.5.2 In-situ testing 184
5.5.3 Index testing 185
5.5.4 Undrained shear strength and critical state parameters 185
5.5.5 Stress state and yield stress ratio 186
5.5.6 Interface shear behaviour 187
5.5.7 Sensitivity 189
5.6 Maastrichtian chalk encountered at the test sites 196
5.6.1 Description & occurrence 196
5.6.2 In situ testing 196
5.6.3 Index testing 198
5.6.4 Intact chalk strength & stiffness 199
5.6.5 Putty chalk strength, stiffness & time effects 200
5.6.6 Interface shear behaviour 202
5.7 Pre-construction pile test campaign 214
5.7.1 Pile configurations & installation 214
5.7.2 Static and dynamic testing system 216
5.7.3 Static load test procedure 217
5.7.4 Testing programme 217
5.8 Production piling dynamic test campaign 218
5.8.1 Production pile installation 219
5.8.2 Testing programme 219
5.9 Results & interpretation 225

5.9.1 Adopted dynamic parameters for signal matching 225
5.9.2 Base resistance from dynamic tests 227
5.9.3 Pile resistance at the end of installation 228
5.9.4 Effect of penetration depth on shaft resistance during driving 229
5.9.5 Long-term load displacement behaviour 230
5.9.6 Time effects on shaft resistance from dynamic tests 234
5.9.7 Quantification of set-up trends 235
5.9.8 Predictions of shaft capacity at the till dominated site 237
5.10 Summary and concluding remarks 251

CHAPTER 6 STATIC AND CYCLIC DRIVEN PILE TESTS AT ST. NICHOLAS-AT-WADE 253

6.1 Introduction 253
6.2 Experimental aims 253
6.3 Test site at St Nicholas-at-Wade 254
6.4 Ground conditions 257
6.4.1 Geology & stratigraphy 257
6.4.2 In-situ testing 258
6.4.3 Index testing 261
6.4.4 One-dimensional compression 261
6.4.5 Triaxial stress paths 262
6.4.6 Interface shear behaviour 263
6.5 Pile and driving details 279
6.5.1 Pile details 279
6.5.2 Pile resistance at the end of driving 279
6.5.3 Drainage characteristics during driving 280
6.5.4 The effects of pile installation on the surrounding chalk mass 281
6.6 Testing programme 286
6.7 Experimental procedures 287
6.8 Ageing Observations 292
6.9 Cyclic test results & interpretation 296
6.9.1 Axial cyclic stiffness 297
6.9.2 Impact on tension capacity 297
6.9.3 Cyclic stability criteria 298
6.9.4 Permanent accumulated displacements 298
6.10 Summary & concluding remarks 307

CHAPTER 7 INSTRUMENTED PILE TESTS AT ST. NICHOLAS-AT-WADE310

7.1 Introduction 310
7.2 Experimental aims 311
7.3 The Imperial College instrumented pile 312
7.3.1 Background 312
7.3.2 Pile configuration 313

7.3.3 Instruments & calibrations 313
7.3.4 Instrument performance 317
7.3.5 Data acquisition 318
7.4 Experimental procedures 324
7.4.1 Test preparation 324
7.4.2 Pile Installation 324
7.4.3 Equalisation and long-term monitoring 325
7.4.4 Load testing 325
7.5 Testing programme 325
7.6 Results & Interpretation 329
7.6.1 Installation resistance 329
7.6.2 Penetration pore pressures 330
7.6.3 Base resistance measurements 330
7.6.4 Shaft effective stresses close to pile tips 331
7.6.5 Local shaft effective stresses 332
7.6.6 Long-term equalisation 333
7.6.7 Static Load testing 334
7.6.8 Change in static capacity with time 336
7.6.9 Stress changes during installation, equalisation and load testing 337
7.6.10 Cyclic load testing 342
7.7 Summary & Concluding remarks 360

CHAPTER 8 TOWARDS A NEW DESIGN APPROACH FOR DISPLACEMENT PILES IN LOW-MEDIUM DENSITY CHALK 362

8.1 Introduction 362
8.2 Current understanding of displacement piles in chalk 365
8.3 Data sources and comparison of the chalk encountered at the test sites 366
8.4 Base capacity of open and closed-ended piles 373
8.5 Contributions to capacity due to interface dilation 375
8.5.1 Effect of relative interface roughness 375
8.5.2 Magnitude of dilation 377
8.5.3 Prediction of interface dilation during pile loading 380
8.6 Stress changes during pile installation, equalisation and loading 385
8.7 Adopted approach to estimate shaft resistance 391
8.8 Increases in axial shaft capacity with time 392
8.9 Short-term (driving) radial effective stress 395
8.9.1 Relationship between radial effective stress and cone resistance 395
8.9.2 Interface shear behaviour 395
8.9.3 Reductions in stress with distance from the pile tip 396
8.9.4 Preliminary correlation for soil resistance to driving 397
8.10 Equalised radial effective stress 406
8.10.1 Choice of equalisation period 406
8.10.2 Preliminary correlations for equalised radial effective stresses 407

8.11 Predictions of shaft capacity using existing methods 411
8.12 Reliability of the new approach to estimate shaft capacity 412
8.12.1 Comparison with tests on open-ended piles 412
8.12.2 Comparison with tests on closed-ended piles 413
8.13 Other design considerations 417
8.13.1 Axial cyclic loading 417
8.13.2 Effect of loading sense 418
8.13.3 Interactions with lateral loading 419
8.14 Summary and concluding remarks 420

CHAPTER 9 CONCLUSIONS AND RECOMMENDATIONS FOR FUTURE RESEARCH 422

9.1 Introduction 422
9.2 Primary experimental results 423
9.2.1 Offshore static and dynamic tests at the Wikinger offshore windfarm 423
9.2.2 Onshore static, dynamic and cyclic tests at St. Nicholas-at-Wade 424
9.2.3 Onshore jacked ICP tests at St. Nicholas-at-Wade 426
9.3 Towards a new effective stress based design approach for displacement piles in chalk . 427
9.4 Recommendations for future work 428

REFERENCES 430

LIST OF FIGURES 450

LIST OF TABLES 462

APPENDIX A-1 SUPPLEMENTARY PILE TEST DATA 464

APPENDIX A-2 PILE TEST EXTRAPOLATION METHODS 505

APPENDIX A-3 CONSULTANT'S ORIGINAL PILE DESIGN 508

APPENDIX A-4 SHAFT CAPACITY PREDICTIONS 512

APPENDIX A-5 PILE EXHUMATION INSPECTIONS 520

APPENDIX A-6 ICP INSTRUMENT PERFORMANCE 526

LIST OF SYMBOLS

Roman alphabet

A	Cross-sectional area
A_{ann}	Cross-sectional area of the open-ended pile annulus
A_b	Cross-sectional area of the pile base
A_{gross}	Gross enclosed cross-sectional area of the pile
A_r	Pile base effective area ratio
A_s	Area of pile shaft
A_1	Load at which $k_c = 0$ (pile test extrapolation method)
a_c	Cone area ratio
a_t	Parameter applied to reduce capacity of open-ended piles in sand tested in tension
a_0	Dimensionless frequency factor
b	Bishop parameter
b_t	Parameter to reduce radial effective stresses under tension loading (tension = 0.8)
C	Multiplier for cyclic displacement power law trend
C_b	Base dashpot constant (dynamic soil resistance models)
C_c	Compression index
C_s	Shaft dashpot constant (dynamic soil resistance models)
C_1	Parameter pile test extrapolation method
C_2	Parameter pile test extrapolation method
c	Compressional wave speed in an unconfined rod
c'	Effective cohesion intercept
c_b	Base dashpot constant per unit area (dynamic soil resistance models)
c_h	Coefficient of horizontal consolidation
$c_{h,nc}$	Normally consolidated coefficient of horizontal consolidation (oedometer)
$c_{h,oc}$	Overconsoliated consolidation coefficient of horizontal consolidation
$c_{h,piezo}$	Coefficient of horizontal consolidation from PCPT dissipation tests
c_{ij}	SST calibration coefficients
c_s	Shaft dashpot constant per unit area (dynamic soil resistance models)
c_v	Coefficient of vertical consolidation
c_1	Supplementary radiation dashpot (Deeks and Randolph (1995) model)
D	Pile diameter
D_{cpt}	CPT diameter
D_{eq}	Equivalent diameter of a circular pile
D_i	Internal pile diameter

D_r	Sand relative density
D_{50}	Median particle size (50% of mass is smaller than/larger than)
E	Young's modulus
E_{intact}	Intact small strain stiffness (laboratory)
E_{mass}	Rock mass small strain stiffness (in the field)
E_{sec}	Secant stiffness from triaxial test
E_u	Undrained Young's modulus
$E_{0.001}$	Small strain Young's modulus on laboratory samples at 0.001% strain
E_1	Initial Young's modulus
e	Void ratio
e_{cs}	Void ratio at critical state
e_{max}	Maximum possible void ratio (loosest packing)
e_{min}	Minimum possible void ratio (densest packing)
e_0	Initial void ratio
F	Force in the pile
F_c	Calculated upward wave value (match quality definition)
F_d^i	Downward incident wave
F_d^t	Downward transmitted wave
F_m	Measured upward wave value (match quality definition)
F_{max}	Maximum measured upward wave value (match quality definition)
F_r (or R_f)	CPT friction ratio (= f_s/q_c)
F_{up}^r	Upward reflected wave
F_{up}	Upward travelling component of force
f	Function
f_s	CPT sleeve friction
G	Shear modulus[1]
G_s	Specific gravity
G_{max}	Maximum small strain shear stiffness
G_1	Secant shear stiffness
g	Function
H_p	Height of the internal soil plug
h	Distance from the pile tip
h_{ALC1}	Height of the bottom-most load cell (ALC1) above the tip
I_L	Liquidity index
I_p	Plasticity index
I_r	Rigidity index = G/s_u
i	Square root of minus 1
i_{end}	End index of the interval (match quality definition)

i_{start}	Start index of the interval (match quality definition)
J_b	Smith damping constant (base)
J'_b	Smith damping constant (base) allowing for viscous effects
J_s	Smith damping constant (shaft)
J'_s	Smith damping constant (shaft) allowing for viscous effects
j	Rock mass factor ($=E_{mass}/E_{intact}$)
K	Coefficient of lateral pressure (CIRIA PG6 design method)
K_b	Base spring constant (dynamic soil resistance models)
K_c	Coefficient of radial effective stress (shaft) after full equalisation = $\sigma'_{rc}/\sigma'_{vo}$
K_f	Coefficient of radial effective stress (shaft) at failure = $\sigma'_{rf}/\sigma'_{vo}$
K_s	Shaft spring constant (dynamic soil resistance models)
K_0	Coefficient of earth pressure at rest (*in-situ*) = σ'_h/σ'_{vo}
k_b	Base spring constant per unit area (dynamic soil resistance models)
k_c	Semi-logarithmic creep rate
k_l	Cyclic loading stiffness
k_s	Shaft spring constant per unit area (dynamic soil resistance models)
$k_{s,ref}$	Reference static stiffness
$k_{s,ul}$	Unloading shaft spring constant per unit area (dynamic resistance models)
k_{stat}	Static loading stiffness
k_u	Cyclic unloading stiffness
L	Pile length
L_{meas}	Measuring length below PDA sensors in dynamic tests
L_p	Length of pile penetration
$L_{p,chlk}$	Length of pile penetration in chalk
$L_{p,cpt}$	Length of penetration of CPT or PCPT
$L_{p,fgt}$	Length of pile penetration in fluvioglacial till deposits
$L_{p,gt}$	Length of pile penetration in glacial till deposits
$L_{p,hc}$	Length of pile penetration in holocene deposits
M	Empirical parameter used to assess set up factor in Skov and Denver (1988) equation
M_q	Signal match quality in % over interval
$M_{q,overall}$	Overall signal match quality
M_{tc}	Stress ratio at critical state in triaxial stress space
m	Empirical parameter used to assess set up factor in Tan *et al.* (2004) equation
m_0	Supplementary lumped mass connected through pile base node
m_1	Supplementary lumped mass connected through pile radiation dashpot c_1
N	Number of axial cycles applied
N_c	Bearing capacity factor (total stress)
N_{cum}	Cumulative number of axial cycles applied

N_f	Number of cycles to failure
N_{kt}	Empirical cone factor
N_p	Number of elements in the internal soil plug
N_q	Bearing capacity factor (effective stress)
N_s	Number of elements along the pile shaft
n	Porosity
P_L	Pressuremeter limit pressure
p'	Mean effective stress
p_a	Atmospheric pressure (absolute)
p'_{cs}	Mean effective stress at critical state
Q_{ALC1}	Load at the bottom-most ICP load cell (ALC1)
Q_b	Pile base axial load resistance (capacity)
$Q_{b,0.1D}$	Pile base axial load resistance at a displacement of 10% the pile diameter
$Q_{ba,0.1D}$	Pile base axial load resistance under annulus at a displacement of 10% D
Q_c	Calculated pile shaft design capacity
Q_{cpt}	Total load (from top load cell) to advance CPT or PCPT
Q_{cyc}	Axial cyclic load amplitude
Q_m	Measured pile shaft capacity
Q_{max}	Maximum axial cyclic load
Q_{mean}	Mean axial cyclic load
Q_{min}	Minimum axial cyclic load
Q_{net}	Current net (less pile and soil weight) static tension shaft capacity
Q_{pc}	Tension capacity post cyclic loading test
Q_{ref}	Reference axial static pile capacity
Q_s	Pile shaft axial load resistance (capacity)
$Q_{s,ref}$	Reference load for static stiffness k_{stat}
Q_t	Current static tension shaft capacity
Q_{tip}	Load from CPT q_c measurement
Q_{tot}	Pile total axial load resistance (capacity) or total CPT/ICP installation load
q	Deviatoric stress
q_b	Pile end-bearing unit resistance
q_{ba}	Pile end-bearing resistance under annulus
$q_{b,lim}$	Limit base unit resistance
$q_{b,res}$	Residual base resistance
$q_{b,stat}$	Limit base stress plastic slider (dynamic soil resistance model)
$q_{b,0.1D}$	Pile end-bearing unit resistance at a displacement of 10% the pile diameter
$q_{ba,0.1D}$	Pile end-bearing resistance under annulus at a displacement of 10% D
q_c	CPT tip resistance

$q_{c,1.5D}$	Average CPT tip resistance ±1.5D around pile base
$q_{k,b}$	Base loading quake (dynamic soil resistance model)
$q_{k,s}$	Shaft loading quake (dynamic soil resistance model)
$q_{ku,b}$	Base unloading quake (dynamic soil resistance model)
$q_{ku,s}$	Shaft unloading quake (dynamic soil resistance model)
q_t	Net (corrected) cone resistance
$q_{t,ref}$	Reference net (corrected) cone resistance for variable rate test
$q_{t,1.5D}$	Average net CPT tip resistance ±1.5D around pile base
q_u	Unconfined compressive strength
R	Pile radius
R_a	Average centre line roughness
R_{cpt}	Radius of the CPT
R_{crit}	Critical relative roughness
R_f (or F_r)	CPT friction ratio (= f_s/q_c)
R_{max}	Maximum interface roughness
R_n	Relative roughness = R_{max}/D_{50}
$R_{n,max}$	Maximum relative roughness = R_a/D_{50}
$R_{t,c}$	Designer's characteristic tensile capacity
R*	Equivalent radius for open-ended piles
r	Radial distance from the pile centre
S_r	Degree of saturation
S_t	Sensitivity
$S_{\omega 1}$	Function of the dimensionless frequency factor a_0
$S_{\omega 2}$	Function of the dimensionless frequency factor a_0
s	Pile head displacement
s_a	Pile head displacement at time t_a
s_{acc}	Accumulated cyclic displacement
s_b	Pile head displacement at time t_b
s_u	Undrained shear strength
$\bar{s}_u$	Mean undrained shear strength
s_{ult}	Ultimate pile head displacement
T	Cyclic period
$T_b^{S \text{ or } D}$	Static or dynamic base resistance at a given node
T_s	Shaft resistance at a given node (dynamic soil resistance model)
$T_s^{S \text{ or } D}$	Static or dynamic shaft resistance at a given node
T_t	Total soil resistance at a given node (dynamic soil resistance model)
T_{50}	Time to achieve 50% of ultimate pile set-up
t	time

t_a	Time t_a for assessing creep rate k_c
t_b	Time t_b for assessing creep rate k_c
t_{ref}	Reference time to assess pile set up
t_w	Pile wall thickness
t_{zone}	Thickness of the zone observed around the pile shaft
t_0	Start of force application (dynamic test)
$t_{0+2L/c}$	Time for return of wave from bottom of the pile to instrument level
t_{50}	Time for 50% pore water pressure dissipation in a dynamic test
U_n	Unloading factor (dynamic soil resistance model)
u_{ann}	Excess pore water pressure over the annular area
u_1	PCPT excess pore water pressures measured at the tip position
u_2	PCPT excess pore water pressures measured at the shoulder position
V	Normalised velocity
V_{cpt}	Normalised velocity of the CPT
V_i	Input voltage for SST transducers
V_p	Elastic compression wave velocity
V_{pile}	Normalised velocity of the pile
V_s	Elastic shear wave velocity[1]
V_0	Output voltage for SST transducers
v	Specific volume (=1+e)
v_{cpt}	Velocity during a cone penetration test
v_d	Downward travelling component of velocity
v_p	Velocity of the pile
v_{up}	Upward travelling component of velocity
w	Displacement
w_c	Water content
w_f	Water content after consolidation of chalk putty around driven pile
w_l	Liquid limit
w_p	Pile displacement
w_{pl}	Plastic limit
w_s	Displacement of the soil
w_{sat}	Saturation moisture content
Z	Pile impedance
z	Depth

Can be used with the following further subscripts:

1. hv - propagating horizontally and polarised vertically;, hh - propagating horizontally and polarised horizontally, vh - propagating vertically and polarised horizontally

Greek alphabet

α	α–type driven pile design method factor
α_b (=J′$_b$)	Base viscosity parameter (soil resistance model)
$\alpha_{b,cpt}$	Base reduction factor CPT type pile design method
$\alpha_{s,cpt}$	Shaft reduction factor CPT type pile design method
α_s (=J′$_s$)	Shaft viscosity parameter (soil resistance model)
α_t	Empirical factor for base resistance which depends on penetrate rate and tip geometry
α_0	Deeks and Randolph (1995) base model parameter
α_1	Deeks and Randolph (1995) base model parameter
β	β –type driven pile design method factor
β_b	Base viscosity parameter (soil resistance model)
β_s	Shaft viscosity parameter (soil resistance model)
β_0	Deeks and Randolph (1995) base model parameter
β_1	Deeks and Randolph (1995) base model parameter
Γ	Specific volume on the critical state line at p′ = 1kPa
γ_{bulk}	Bulk density
γ_{dry}	Dry density
Δ	Change in sample height
Δl	Element length
Δr	Average movement of the soil grains due to dilation
Δv	Relative velocity between the pile and soil
$\Delta\sigma'_{rd}$	change of radial effective stress during shearing due to dilation
δ'	Interface angle of shearing resistance
δ'_{cpt}	Interface angle of shearing resistance along CPT friction sleeve
δ'_f	Failure interface angle of shearing resistance
δ'_{peak}	Peak interface angle of shearing resistance
δ'_{ult}	Ultimate interface angle of shearing resistance
ε	Strain
ζ	Multiplier for radial effective stress expression
η	Exponent for radial effective stress expression
θ_i	Angle of sliding for a small particle against a rough steel interface
θ_j	Angle of sliding for a large particle against a rough steel interface
κ	Exponent for radial effective stress expression
Λ	Set-up factor on shaft capacity
Λ_{ult}	Ultimate set-up factor on shaft capacity

λ	Slope of the isotropic compression line
λ_f	Non-dimensional friction coefficient
μ	Mean
N	Specific volume on the NCL at p′=1kPa
π	Mathematical constant
ρ	Pile mass density
ρ_{bulk}	Bulk density
ρ_s	Soil mass density
σ	Axial stress in the pile = $E\varepsilon$
σ_r	Radial total stress[2,3]
σ'_r	Radial effective stress[2,3]
σ'_{vy}	Vertical effective yield stress
σ'_{vy}*	Vertical effective yield stress of the reconstituted material at the same v as σ'_{vy}
σ'_v or σ'_{v0}	Vertical effective stress
$\overline{\sigma}'_{vo}$	Mean undrained shear strength along pile shaft
σ_z	Vertical effective stress[2]
σ'_z	Average vertical effective stress[2]
$\sigma'_{1,2,3}$	Effective principal stresses
σ'_θ	Effective circumferential (hoop) stress[2]
τ_{avg}	Average shaft shear stress at failure from static or dynamic test = Q_s/A_s
$\tau_{avg}(t)$	Average shaft shear stress at failure from static or dynamic test at time t
τ_{cpt}	Overall shaft stress along the advancing CPT cone and steel rods
τ_f	Calculated long-term local shear stress at static failure from design methods[4]
τ_{fi}	Calculated local shear stress during driving (SRD)
$\tau_{f,lim}$	Limit local shear stress at failure
τ_i	Initial shear stress - Alm and Hamre (2002) method
$\tau_{install}$	Average shaft shear stress at failure during installation of ICP
τ_{inter}	Limit shaft shear stress at low strain rates (dynamic soil resistance model)
τ_{res}	Residual shear stress
τ_{rz}	Local shear stress measured by SSTs on the ICP
$\tau_{s,d}$	Local shear stress at failure interpreted from dynamic tests
$\tau_{s.m}$	Measured local shear stress at failure averaged between strain gauges from static tests
$\tau_{s,p}$	Local shear stress calculated using soil disp and pile velocity (soil resist models)
τ_{stat}	Limit shear stress plastic slider (dynamic soil resistance model)
υ	Poisson's ratio
φ'	Angle of shearing resistance

φ'_{cs}	Angle of shearing resistance at critical state
χ	Exponent for cyclic displacement power law trend
ψ	State parameter
ω	Angular frequency

Can be used with the following further subscripts:

1. a/ax – axial; c – cavity; h – horizontal; s – shear; v – vertical; vol – volumetric; θ – circumferential
2. m – moving; max – maximum; min – minimum; s – stationary
3. c – end of primary consolidation; d – dilation; f – failure; i – during driving; 0 – initial
4. int – internal; ext – external

Acronyms & Abbreviations

ALC	Axial load cell
ALPACA	Axial-Lateral Chalk Analysis for Piles Applying multi-scale field and laboratory testing
API	American petroleum institute
BoP	Beginning of driving pause
BoR	Beginning of restrike
BSH	Bundesamt für Seeschifffahrt und Hydrographie
$CaCO_3$	Calcium carbonate
CAPWAP	Case Pile Wave Analysis Program
CAU	Consolidated anistropically undrained triaxial test
CD	Consolidated drained triaxial test
CFA	Continuous flight auger
CIRIA	Construction industry research and information association
CNS	Constant normal stiffness
CoV	Coefficient of variation
CPT	Cone penetration resistance
CRP	Constant rate of penetration
CSL	Critical state line
CSSM	Critical state soil mechanics
C574	CIRIA C574 design method (Lord *et al.*, 2002)
D	Pile diameter
DPT	Dynamic pile test
DS	Direct shear test
EC7	Eurocode 7
EoD	End of driving
EoP	End of driving pause
EURIPIDES	European Initiative on Piles in Dense Sand

FoS	Factor of Safety
FSA	Fleury-sur-Andelle
GCG	Geotechnical consulting group
HIT	Humber international terminal
HPD	High pressure dilatometer
HST	Humber sea terminal
IAC	Intact ageing characteristic
IC	Imperial College
ICP	Imperial College Pile
ICP-05	Imperial College Pile design method
IDD	Intact dry density
IFR	Incremental filling ratio
IST	Interface shear tester
ISO	International standards organisation
JIP	Joint industry project
LCC	Limiting compression curve
LVDT	Linear variable differential transducers
ML	Maintained load
MQ	CAPWAP match quality
MS	Metastable axial cyclic loading condition
MSt	Mild steel
NC	Normally consolidated
NCL	Normal compression line
NGI	Norwegian geotechnical institute
NMC	Natural moisture content
OCR	Overconsolidation ratio
OSS	Offshore substation
OWF	Offshore windfarm
PC	Pre-construction pile test campaign at Wikinger
PCC	Precast concrete pile
PCPT	Cone penetration test with pore pressure measurement
PDA	Pile driving analyser
PFC	UK Parallel Flange Channel
PG6	CIRIA PG6 design method (Hobbs and Healy, 1979)
PIV	Particle image velocimetry
PLI	Point load index
PP	Production piling test campaign at Wikinger
PPT	Pore Pressure transducers

P-wave	Elastic compression wave
RGH	Enhanced interface roughness
S	Stable axial cyclic loading condition
SBP	Self-boring pressuremeter
SCPT	Seismic cone penetration test
SEM	Scanning electron microscope
SH	Steel H pile
SHS	Square Hollow Section
SLT	Static load test
SMT	Smooth interface roughness
SNW	St. Nicholas-at-Wade
SPT	Standard penetration test
SRD	Soil resistance to driving
SS	Stainless steel
SST	Surface stress transducer
STD	Standard interface roughness
Stdev	Standard deviation
SW	Self weight
S-wave	Elastic shear wave
SX	Steel cruciform pile
TB	Steel tube pile
TNO	Netherlands Organisation for Applied Scientific Research
TPC	Post-cyclic tension
UCS	Unconfined compressive strength
UR	Utilisation ratio ($=Q_{max}/Q_{ref}$)
US	Unstable axial cyclic loading condition
UU	Unconsolidated undrained triaxial test
UWA	University of Western Australia
WSD	Working stress design
WTG	Wind turbine generator
YSR	Yield stress ratio or apparent overconsolidation ratio
Zv	Velocity times impedance

CHAPTER 1 Introduction

1.1 Research background

The focus of this thesis is the behaviour of axially loaded displacement piles driven in low-medium density chalk, which are deployed to support major offshore and near-shore structures as well as more modest domestic and industrial building projects. Chalk, a highly variable soft biomicrite composed of mainly silt-sized crushable calcium carbonate particles, is found widespread across Northern Europe and under the North Sea, where thicknesses can exceed 1200m; Clayton *et al.* (2002), Mortimore (2012). The extent of chalk across North-west Europe is shown on Figure 1-1.

Piles have been used by mankind to support structures since pre-historic times, to transfer loads from structures to deeper, more competent soil. Globally, the civil engineering piling market is roughly equally subdivided between displacement piles, which are driven, jacked or screwed into place and non-displacement piles such as bored and continuous flight auger (CFA) piles (Mandolini *et al.*, 2005). Driven displacement piles are well suited for offshore, marine and other over-water applications since they do not require any special casings or reinforcement and they can be used immediately, with no delays after driving to allow for concrete to cure. Driven piles facilitate top-down construction as they can be relatively easily integrated into a bridge pier, wind turbine or other structure post-installation. Offshore pile foundations are generally dominated by open-ended, large-diameter driven steel tubular sections. Multi-piles, used to support wind turbine jacket structures, are often 2 to 3m in diameter with penetration lengths of approximately 30m (e.g. Barbosa *et al.*, 2017), while wind turbine monopile foundation diameters are now typically between 6 and 8m with penetration depths of 25 to 45m (Hamre, 2018). Similar, high capacity large-scale open-ended driven steel piles are used for near-shore, bridge and harbour foundations such as those driven in chalk at the Port of Dover (D=1.2m) and the Port of Felixstowe (D=1.6m).

Driven pile lengths depend on the required axial load carrying capacity of the pile-founding material system, which for a single pile in compression, is a sum of the shaft (Q_s) and base (Q_b) resistances provided by the soil or rock. The load carrying capacity of a pile is verified by either static or dynamic pile testing with static load tests being the most accurate means of determining axial pile capacity. Load carrying capacity is predicted by designers using axial capacity design methods. Research conducted over the last two decades has greatly improved the understanding of the fundamental effective stress processes governing the axial capacity of displacement piles in sands and clays (e.g. Bond and Jardine, 1991, Lehane and Jardine, 1994a, Lehane *et al.*, 1993, Randolph *et al.*, 1994, Chow, 1997). This in turn has led to the development of new axial capacity design methods and the collation of pile test databases (e.g. Jardine *et al.*, 2005a, Lehane *et al.*, 2005a, Lehane *et al.*, 2012b).

The design and installation of displacement piles can be problematic when chalk is encountered within the founding stratum, with both pile "runs" (free falls under self-weight) and refusals reported. The understanding of the behaviour of displacement piles in chalk has failed to keep pace with the developments seen in sands and clays and is becoming a significant area of research interest, with the dual expansion of offshore windfarms in Northern Europe and the advancement of several onshore infrastructure projects which will be founded in chalk. The primary complexities associated with utilising driven pre-formed displacement piles in low-medium density chalk to withstand predominantly axial loading can be broadly separated into three key issues, namely (i) determining their installation resistance (ii) assessing pile static load behaviour after allowing for set-up and (iii) the effects of axial cyclic loading on the pile behaviour.

Installation resistance: Few static load tests have been reported to prove or predict the ability of displacement piles in chalk to carry axial loads. While refusals have been reported in high density chalk, low shaft driving resistances (between 0 and 20kPa) are often observed in low-medium density chalk that suggest very low static service capacities (Lord *et al.*, 2002, Vijayvergiya *et al.*, 1977). The construction industry research and information association (CIRIA) offer design guidelines based on six tests at four sites that indicate widely different ultimate unit shaft resistances of 20 to 120kPa for low-medium and high density chalks respectively (Lord *et al.*, 2002). These values appear remarkably low, given the strength and stiffness of intact chalk, which is a soft rock. The low static shaft capacities recommended by Lord *et al.* (2002) are based on a small database of tests and imply that only low shaft stresses

are available for service use. Stark choices have to be made when selecting design parameters that can impact significantly on axial pile design.

Ageing effects: Dynamic monitoring often shows capacity growth over driving pauses. Long-term beneficial time effects on static shaft resistance have been reported in sands (see Jardine *et al*. (2006), Rimoy *et al.* (2015) or Gavin *et al.* (2015)) and clays, e.g. Karlsrud *et al.* (2014). Lord *et al.* (2002) suggest that field set-up also takes place with low-medium density chalk, due to pore pressure dissipation and/or internal re-cementing of the putty annulus around the pile. The limited studies on pile ageing in chalk are complicated by the quality of the tests and the piles' previous loading histories (e.g. Lahrs and Kallias, 2013, Ciavaglia *et al.*, 2017a). Re-testing pre-failed piles can be misleading; pre-failed piles often show far less set-up than equivalent "virgin" piles in sands and clays; Jardine *et al.* (2006), Jardine and Standing (2012), Karlsrud *et al.* (2014). Capacity changes are best observed when static or dynamic pile tests are conducted on previously untested piles at different times after driving. Beneficial effects on capacity are not considered in the current (CIRIA) design method, which may lead to conservative estimates of capacity.

Axial cyclic loading: Over their life cycle, most foundations are subjected to cyclic loading, which may apply under a wide range of loading rates. Offshore piles sustain wind and wave loading cycles during storms, while wind-turbines impose millions of rotating blade cycles (Jardine *et al.*, 2012). The effects of axial cyclic loading has been investigated in field and model tests in sands and clays (e.g. Karlsrud *et al.*, 1986, Jardine and Standing, 2012, Tsuha *et al.*, 2012). The tests in sand by Jardine and Standing (2012) showed that axial cycling affects pile stiffness as well as the load carrying capacity of full-scale piles. The effect of axial cyclic loading on the aged capacity of displacement piles in chalk remains a significant unknown with a very limited number of available case studies (e.g. Burland and French, 1990). It is sometimes argued that any advantageous time effects on capacity might be negated by a perceived high susceptibility of chalk to axial cyclic loading that may reduce the axial capacity to levels as low as those seen during installation. There is currently no available guidance to allow for axial cyclic or lateral cyclic effects in design, which poses significant difficulties for offshore pile foundation design.

The primary research questions identified by the Author can be summarised as:

1. What is the primary mechanism causing low axial resistance during and after driving of steel pre-formed piles in low-medium density chalk;

2. What is the mechanism behind any increases in capacity with time: when does ageing begin, how does it affect the stiffness trends, does an upper limit to the trend exist and is there a scale effect;
3. What is the effect of axial cyclic loading on piles whose capacity has increased with time.

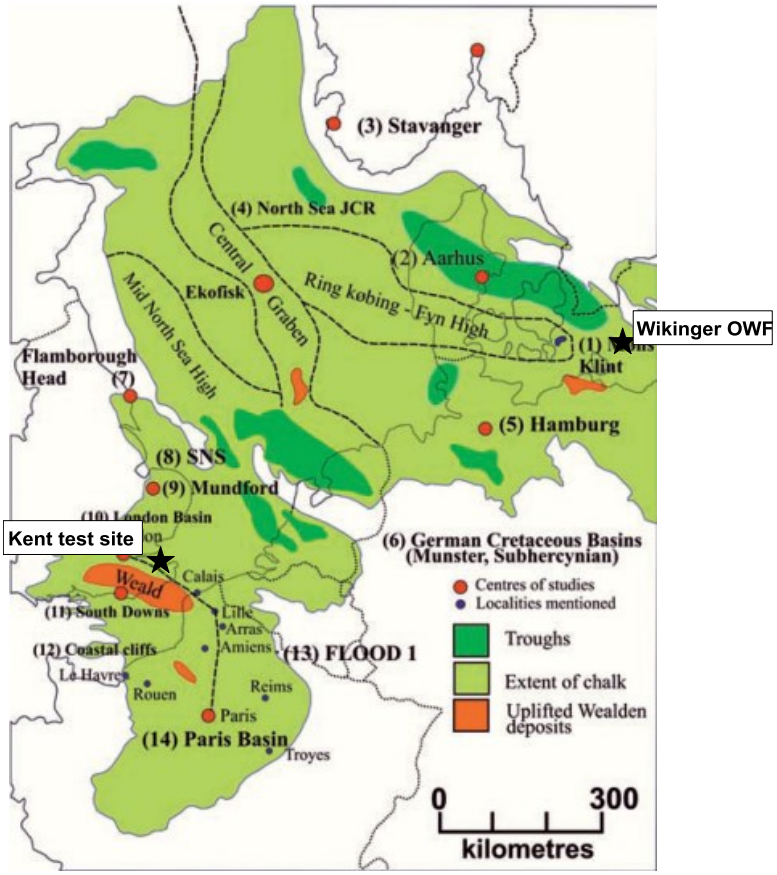


Figure 1-1 The extent of the Chalk in north west Europe (Mortimore, 2012)

1.2 Research scope and methodology

The design guidance shortcomings discussed above pose significant risks in particular for the potentially thousands of offshore wind-turbines planned for installation in chalk and indicates the scale of the urgent requirement for further investigation. There is a clear need for reliable static and cyclic pile tests at chalk sites, supported by high quality site characterisation, to provide benchmarks against which potential predictive procedures may be developed, assessed and calibrated. The objective of this PhD study was to use carefully timed and planned field experiments to investigate the above research questions, advance understanding of displacement piles in chalk and investigate a potential route for development of a new method to predict axial capacity.

The Author's research was initially motivated by the Wikinger offshore windfarm, currently under construction by Iberdrola in the German Baltic Sea (shown previously on Figure 1-1). The windfarm includes seventy wind turbine generators (WTGs) and one offshore substation, installed in water depths up to 42m, supported by open-ended tubular steel piles (2.7m to 3.67m in diameter) which will carry their environmental loads by predominantly axial push-pull loading, plus associated lateral loads. The piles are founded in 50% Weichsellian glacial till and 50% low-medium density Maastrichtian chalk. Wikinger is located in German waters, where there are strict regulatory requirements on proving pile capacity. Uncertainty over installed load-carrying capacity led Iberdrola to investigate other means of proving the piles' capacity which resulted in the execution of novel offshore axial static and dynamic tests on 1.37m to 3.7m diameter piles at the site.

The Author's main supervisor, Prof. Richard Jardine, was initially involved in the Wikinger offshore testing as a consultant, engaged by Iberdrola to advise on the static and dynamic testing as well as the technical proposals submitted by various contractors. He was supported by Drs. Felix Schroeder and Andrew Merritt of the Geotechnical Consulting Group (GCG). The offshore experiments conducted at Wikinger were designed to investigate;

1. Dynamic pile resistances during driving in glacial till and chalk, employing PDA instrumentation fitted near the pile head;
2. The effects on driving resistance of any pauses in driving;
3. The long-term capacity and stiffness available in the glacial till and chalk, working with both static and dynamic re-strikes on separate 'virgin' piles conducted 3.5 months after installation.

The Wikinger consultancy assignment led to a joint application in March 2014 by Iberdrola, Imperial College and GCG to the funding body Innovate-UK to carry out a full analysis of the site investigation and pile test results, integrate these with all other publicly available data and use the new information to develop new methods for assessing driveability and axial capacity for piles driven in chalk as well as develop and demonstrate new methods for conducting offshore pile testing in difficult ground conditions. The application was successful and the resulting JIP was led by Pedro Barbosa of Iberdrola, with Prof. Richard Jardine and Dr. Stavroula Kontoe providing the academic leadership along with input from Dr. Felix Schroeder. The Author was employed as a research assistant to work on all aspects of the project from its 1st October 2015 start until its October 2017 completion. The Author's first

tasks were to interpret the extensive site investigation dataset acquired by Iberdrola, undertake a literature review and then conduct specialist laboratory testing at Imperial College on Wikinger samples.

The main pre-construction Wikinger fieldwork programme comprised dynamically instrumented test pile driving, followed by ageing and then static and dynamic offshore tests at three locations. The work was undertaken by Bilfinger Marine and Offshore Systems GmbH between October 2014 and January 2015, liaising closely with the JIP team members who had helped to design the field work proposals and methodologies. The field test results were passed immediately to the research team and the Author for analysis. Iberdrola were able then to revise their foundation designs, and achieve considerable economies, based on the Author's analysis and recommendations from their independent designer. Full-scale production piling proceeded at Wikinger between March and December 2016. Dynamic tests were conducted at 10% of locations to satisfy local regulatory requirements and analysed by the Author in conjunction with GCG and the Author's academic supervisors.

The Wikinger tests provided the first seafloor offshore pile loading experiments and instrumented aged re-strike tests on chalk of which the Author is aware. The novel techniques employed in tests on six offshore scale piles gave both fresh insights and invaluable benchmarks regarding driven offshore pile behaviour in chalk that were integrated fully into the Authors' research. The academic team decided to expand the scope of the study to help deliver as fully as possible the JIP aims by conducting two supplementary programmes of onshore field testing at an analogous onshore test site, located close to the village of St. Nicholas-at-Wade, Kent, Southern UK (see also Figure 1-1) between October 2015 and July 2016. The Author took the primary responsibility for setting up, conducting and analysing these experiments, along with additional site investigations and laboratory testing conducted at Imperial College. Further funding was secured for the new tests from Atkins, Iberdrola and GCG.

The St. Nicholas at Wade test programme comprised tests on seven reduced-scale driven open-ended steel piles (139mm diameter) along with two experiments on 102mm diameter closed-ended jacked highly instrumented Imperial College Piles (ICPs). Professor Barry Lehane's team from the University of Western Australia (UWA) provided technical support with the 'ICP' programme of tests, returning to the UK equipment that had been loaned to UWA. The pile testing could be more easily controlled at the onshore test site than in the

offshore environment, and the multiple piles driven at the same location facilitated a more comprehensive investigation of how ageing and cyclic loading affected driven steel piles over an eight-month period. The driven pile research tests were planned to investigate:

1. Dynamic resistances during and at the end of pile driving, using PDA instrumentation fitted near the pile head;
2. How pile installation and subsequent static and cyclic testing affected the chalk surrounding the pile shaft;
3. Tension (shaft) capacity-ageing trends for virgin piles over 8 months after installation through static tests;
4. The impact of re-testing piles which had been previously subjected to static tension failure; and
5. How multiple 'virgin' piles respond to large numbers of one-way axial load cycles after 8 months of ageing after driving.

Knowledge of the radial effective stresses acting over the pile shaft is a fundamental requirement of any effective stress-based pile design method. The testing methodology for the jacked instrumented piles focused on investigating the fundamental effective stress behaviour of displacement piles in chalk, considering:

1. Installation local shaft effective stresses (σ_r and τ_{rz}) and base stresses (q_b) mobilised during installation and their relationship to; pile installation rate, chalk properties and in particular CPT cone resistance and increasing penetration or relative tip depth (h/R);
2. The effect of extended monitoring periods following installation on the load displacement behaviour and local shaft effective stresses; and
3. The effective stress paths followed at points along the pile shaft during static and cyclic pile tests and their relationship to the behaviour seen in laboratory tests.

Ancillary MSc projects were undertaken to add information to the JIP project. The Author played a supporting role in five such projects, which investigated;

- The behaviour of remoulded or puttified chalk samples from Wikinger in the laboratory completed by Lauren Doughty in 2016 (Section 5.6.5);
- Laboratory interface shear behaviour of chalk on samples from the St. Nicholas-at-wade site, completed by Derek Chan in 2017 (Section 6.4.6); and

- Pile driveability in chalk with studies by Christopher Norrie, Ignacio Ebensperger and Sarah Esper between 2015 and 2017 (Section 8.9.3).

1.3 Contents of the thesis

The thesis is organised into nine chapters; the first being the current ***Chapter 1*** which provides the introduction and sets out the research scope.

Chapter 2 provides an overview of the engineering behaviour of chalk including deposition, diagenesis, structure and weathering, the engineering classification of chalk and *in-situ* testing. Overviews of the mechanical behaviour of both intact chalk and remoulded chalk, that forms around the shaft of driven piles, are also provided covering the factors that influence most significantly the analysis of the Author's pile test data.

Chapter 3 reviews the advances made in understanding the behaviour of displacement piles in sands and clays and the axial capacity design methods available in those materials. The current position regarding displacement piles in chalk is then evaluated, drawing on a critical review of published and unpublished pile test data. The outcomes highlight the areas requiring significant further research and frame the experimental aims of the Author's research.

Chapter 4 gives an overview of dynamic methods used to determine axial resistance in piles. The theoretical background of one-dimensional stress wave theory is reviewed along with some soil resistance models currently in use and the numerical methods used for solution of the one dimensional wave equation. A methodology for the analysis of the dynamic data is outlined, which was adopted to carry out the analyses described in subsequent chapters.

Chapter 5 describes the results of the static and dynamic Wikinger offshore pile test experiments. A brief overview of the geology and stratigraphy at the windfarm and test sites is given. The pile test campaigns are described followed by discussion and interpretation of the results obtained.

Chapter 6 describes the driven pile tests conducted at the St. Nicholas-at-Wade test site. The pile details, testing programme and experimental procedures are described before the main observations, interpretation and the primary conclusions of the testing programme are outlined. Elements of the work described have been published by Buckley *et al.* (2018a).

Chapter 7 describes the jacked ICP tests conducted at the St. Nicholas-at-Wade test site. The ICP pile, its instruments and their calibration are described in full. The experimental procedures

are then described and are followed by the main results, interpretation and the conclusions from this component of the field testing. Elements of the work set out have been published by Buckley *et al.* (2018b).

Chapter 8 maps out a route towards better rules for predicting the axial capacity of open-ended and closed-ended displacement piles in chalk. A new approach to predict both during driving and long-term equalised radial effective stresses is proposed, based on the key phenomena identified in earlier chapters. Preliminary recommendations for shaft capacity predictions are tested against the available small database of high quality static tests. Parallel recommendations are discussed regarding base capacity, as are the effect of loading direction, axial cyclic loading and possible interactions with lateral loading components.

Chapter 9 summarises the conclusions from the main aspects of the work and provides recommendations for future research.

CHAPTER 2

Chalk as an engineering material

2.1 Introduction

The Author's research included analysis of full-scale offshore static and dynamic pile tests at the Wikinger site in the German Baltic Sea and at an onshore test site in Kent, Southern UK. The experiments involved piles driven either partially or entirely in low-medium density, structured white chalk. This chapter outlines the various depositional and post-depositional processes which led to the formation of the Chalk and affect the properties of the material encountered. The engineering classification of chalk and the relevant *in-situ* tests are outlined, which are implemented and discussed further in subsequent chapters. A summary of the mechanical behaviour of both intact and remoulded putty chalk, that forms around the shaft of driven piles, is also provided covering the factors that influence most significantly the analysis of the Author's pile test data.

The Chalk of Northern Europe (shown previously on Figure 1-1) extends from Germany and Denmark to the United Kingdom where it is seen in outcrop in England, Ireland and parts of Scotland. Extensive deposits can be found in Belgium, Denmark, England, France, Germany and Holland and across the Baltic and North Sea where thickness can exceed 200m (Bell *et al.*, 1999, Clayton *et al.*, 2002). The Chalk outcrop in England (Figure 2-1) extends from the East Riding of Yorkshire, through East Anglia to the Devon coast, covers almost 15% of the surface area of the country (Razoaki, 2000) and is the main aquifer for potable groundwater (Mortimore *et al.*, 2001). Upper Cretaceous to Oligocene (younger) chalks can also be found exposed on the islands of Paxi and Antipaxi in the Ionian sea in Greece, in the North African region in Libya and Algeria and the Middle East e.g. the Eocene chalk of Israel (Mortimore, 1990, Talesnick and Brafman, 1998). Cretaceous chalk is also widespread across

North America with the Selma Chalk found in Alabama, Mississippi and Tennessee (Mortimore, 1990).

Several large engineering projects have been constructed in the Chalk of Northwest Europe, including the Channel Tunnel and the Channel Tunnel Rail Link, motorways such as the M25 in the UK, the TGV railway from Paris to Lille in France and numerous offshore wind energy projects including the Sheringham Shoal and Thanet Offshore windfarms. The Chalk is also a major oil reservoir in the North Sea with the Ekofisk oil field expected to continue production until at least 2028 (Mortimore *et al.*, 2001). Ongoing engineering projects involving chalk include the Dover harbour expansion, the High Speed 2 backbone rail network in the UK as well as numerous offshore hydrocarbon and renewable energy projects.

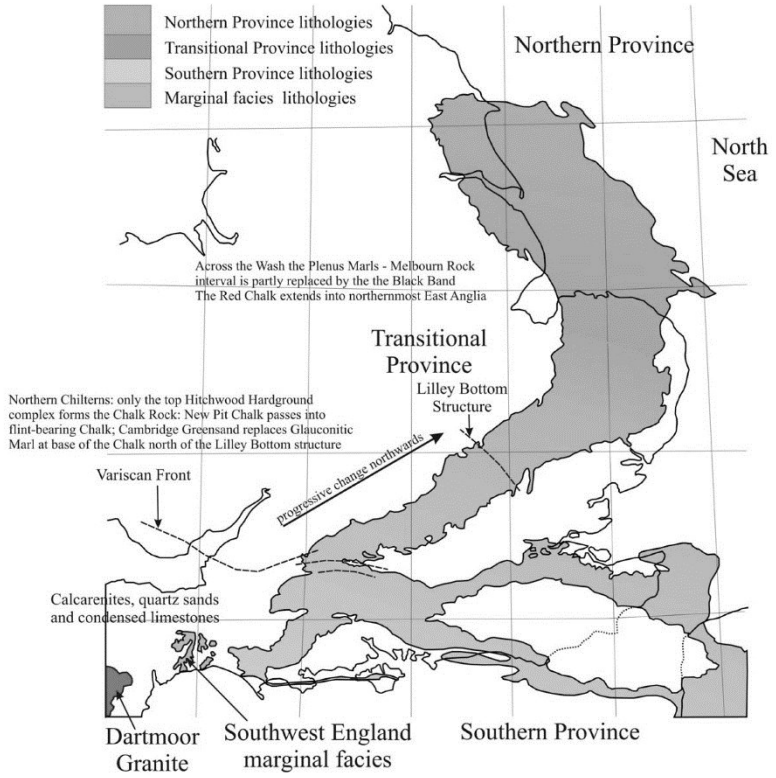


Figure 2-1 Distribution of Upper Cretaceous chalk lithologies in England (Mortimore, 2011)

2.2 Deposition & diagenesis

Chalk is a generally soft, white, pure biomicrite limestone comprised almost entirely of calcium carbonate ($CaCO_3$) derived from the remains of plant and animal life. Deposition occurred mainly during the Cretaceous period (100-65 million years ago) when sea levels rose and covered a large portion of Northern Europe (Hancock, 1975). The depth of the basin is

thought to lie between 50 and 500m, with a minimum water depth for deposition of between 200 and 300m (Clayton, 1983). The Cretaceous period takes its name from the deposit (*creta* = chalk) with the term introduced by the Belgian geologist, Omalius d'Halloy in 1882 (Mortimore *et al.*, 2001). The Chalk used as a proper noun (with a capital first letter) is equivalent to the Upper Cretaceous series.

During the Cretaceous, favourable temperature and nutrient conditions caused calcareous marine algae to bloom on the surface. Chalk was deposited as the skeletal remains of the sub-microscopic algae along with that of foraminifera and less commonly, benthos such as echinoids and bivalves. These provided the biochemical means to precipitate calcium carbonate and formed a fine grained, pure, low magnesium calcite ooze on the ocean floor, which lithified to form chalk (Clayton, 1983, Mortimore *et al.*, 2001, Clayton *et al.*, 2002). The algal coccolithophoridae consist of coccospheres on to which are mounted a number of coccoliths (Figure 2-2). During decomposition, the coccospheres were destroyed and the coccoliths provide the finest fraction of chalk which dominates the behaviour, particularly in high porosity deposits (Clayton and Matthews, 1987, Clayton *et al.*, 2002).

The chalk's high porosity and low density is an unusual feature which typifies the deposit. Deposition was initially as a granular material with up to 80% porosity (Scholle, 1974). Diagenesis began soon after when some consolidation of the calcite ooze occurred. The chalk's grading and particle shape controlled its depositional porosity, along with any biological reworking that occurred after deposition. The maximum porosity found under present conditions for the English chalk is approximately 50%; later diagenetic processes can reduce this porosity to less than 5% (Clayton and Matthews, 1987).

Unlike sedimentary rocks, which lithify gradually in parallel with consolidation, lithification of chalk occurred by early cementation at grain contact points that allowed it to support high overburden pressures without further large strain consolidation. As a result, porosity does not tend to reduce systematically with burial depth. Increases in vertical effective stresses have little effect on porosity, until stress levels rise sufficiently to overcome cementing and particle interlocking and cause grain crushing (Clayton and Matthews, 1987).

Although deposition and cementation occurred pene-contemporaneously, chalk profiles are often non-uniform and well cemented layers may overlie poorly cemented ones (Matthews, 1993, Bell *et al.*, 1999). The engineering behaviour of chalk is distinct from other carbonate rocks such as Limestone partly due to its composition of stable low magnesium calcite.

Limestone was deposited in warm shallow water with its initial form rich in aragonite, a metastable polymorph of calcium carbonate, which provided cement that bonded particles together and filled pore spaces, resulting in a significantly lower porosity material (Clayton, 1983).

Chalk is also typified by a rhythmic stratification which is thought to be due to climatic fluctuations, organic productivity and input of clastic material (Hart, 1987, Clayton *et al.*, 2002). Episodic marl seams are frequently found that were formed by the deposition of volcanic ash (Mortimore *et al.*, 2001, Lord *et al.*, 2002). European Chalks also include rhythmic layers of black flint, which is a very hard (Unconfined Compressive Strength (UCS) up to 800MPa for 300-400mm thick nodules), brittle, microcrystalline, siliceous rock. Flint forms in the remains of animal burrow structures with inclusions often in the shapes of these structures (Bromley, 1967). Sheet flints infill horizontal or inclined fractures by a similar chemical process to burrow structures, and are a focus of groundwater flow (Lord *et al.*, 2002, Mortimore, 2014a). Omission surfaces occur occasionally, caused by bio-turbation induced hardening of the seabed sediment during breaks in deposition, which form nodular chalks and hard-grounds, a form of intrinsic diagenesis. Where sedimentation halted for extended periods, hard grounds coalesced to form 'Chalkstone' e.g. the Chalk Rock of Wiltshire.

Non-intrinsic diagenesis of chalk occurred by external processes. An example is hardening of chalk by pressure, due to tectonic activities or late-stage solution, which causes $CaCO_3$ at the grain contacts to weaken, dissolve and precipitate as overgrowth on coccolith plates. It is thought that the hardness of the chalks in the northern province of England are a result of this pressure solution and re-deposition of calcite (Hancock, 1975, Clayton *et al.*, 2002). A widely held view is that the typically high porosity chalks in Southern England were affected in well-defined areas by tectonic activity, causing the de-structuration and pore collapse structure that is characteristic of the low porosity, high density chalks seen in south Dorset, the Hog's back (Surrey) and the Isle of Wight. Dipping strata are indicative of tectonic activity; porosity was shown to reduce significantly with increasing dip by Clayton and Matthews (1987).

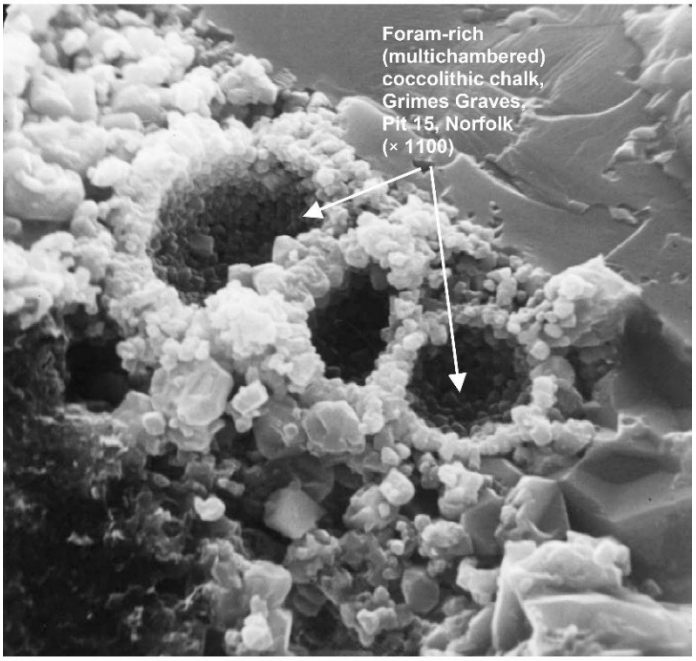


Figure 2-2 Coccolithic chalk with foraminifera from Grimes Graves, Norfolk (Lord *et al.*, 2002)

2.3 Composition

Chalk is essentially a granular assembly of silt to clay sized grains that is weakly cemented, with some of the grains bonded together as part of the coccoliths themselves. The quantities of cement are likely to be very small, since bonds between grains are difficult to see on scanning electron micrographs even at high magnification (Clayton, 1983). Throughout the vast majority of the Chalk, the $CaCO_3$ content is greater than 98%. Clay minerals are rare and tend to occur only at the base of the deposit. Within the grey (formerly Lower) chalk calcium carbonate content can fall as low as 55% due to substantial clay contents e.g. the Anglo-Paris basin (Clayton *et al.*, 2002).

The fine fractions (approximately 0.5-10μm), which form the bulk of the deposit and dominate the behaviour of soft white chalks, are made up of coccoliths (Clayton, 1983, Razoaki, 2000). The coarser fraction, between 10 and 100 μm is composed of foraminifera (Figure 2-2) and other fragments of bi-valve shells and constitutes (Razoaki, 2000). Less commonly, chalks can be found with dispersed silica contents greater than 40% by weight (Clayton, 1990). The chalk normally has no organic content.

2.4 Discontinuities & weathering

The mechanical behaviour and mass permeability of *in-situ* chalk is controlled by discontinuities, the most important characteristics of which are style of fracture, frequency and discontinuity aperture, with the latter controlling the mass compressibility of the chalk mass (Lord *et al.*, 2002). The discontinuities may cause a reduction in mass strength of an order of magnitude compared with the strength of the intact chalk (Holloway-Strong *et al.*, 2007).

Remote from areas affected by complex geological movements, the discontinuity pattern of the English Chalk can be characterised by a set of sub-horizontal bedding discontinuities and several sets of steeply dipping often sub-vertical joints. The frequency of discontinuities can be quite variable across the deposit and often increases significantly near the ground surface (Matthews, 1993).

Weathering mechanisms e.g. stress relief close to a cliff or valley side, frost or freeze/thaw action and dissolution close to the ground surface add further fractures to the existing sets which may result in a very close fracture spacing. In some cases, weathering causes a complete lack of structure resulting in gradation into a soil with intact chalk fragments suspended within a matrix of remoulded material, so called "structureless" chalk (Matthews, 1993, Clayton *et al.*, 2002). The general trend for English chalk is for structureless chalk to overlie structured material, for discontinuity spacing to increase with depth and for aperture and infill amount to decrease with depth.

Intact chalk lies close to full saturation *in-situ*, due to its fine grained nature and the temperate climate in which it occurs. Open or partly open discontinuities within the intact chalk will be air filled onshore above the water table (Clayton *et al.*, 2002) and water filled below the water table and offshore which may have important implications when comparing behaviour at onshore and offshore sites.

2.5 Index properties

Studies of index properties have primarily focused on the chalk of Southern England, where the hardness, density, porosity and strength are shown to vary both regionally and stratigraphically (Mortimore and Fielding, 1990, Bloomfield *et al.*, 1995, Clayton, 1983). Typical values of index properties for English chalk are given in Table 2-1. An indication of the geographical spread of dry density as interpreted by Clayton (1983) is shown on Figure 2-3. While uniform in terms of composition, chalk is highly non-uniform in terms of porosity,

as a result of the wide range of depositional, diagenetic and tectonic processes described in the previous sections. Away from areas where these processes occurred, e.g. in areas of Kent and Norfolk (Southern Province, see Figure 2-1), the chalk remains a soft, white, weak material with porosities which can be greater than 50% (Bell *et al.*, 1999). The densities of the Chalk from Yorkshire (Northern Province) are appreciably higher, with chalk from East Anglia (Transitional Province) exhibiting intermediate values.

Table 2-1: Typical range of index properties for chalk (Lord *et al.*, 2002)

Property	**Units**
Dry density (Mg/m^3)	1.29 – 2.46
Porosity, n (%)	9 – 52
Void ratio, e	0.1 – 1.1
Saturated moisture content, w_{sat} (%)	4 – 40
Calcium carbonate content, $CaCO_3$ (%)	55 – 99
Specific gravity, G_s (-)	2.69 – 2.71
Liquid limit, w_l (%)	18 – 53
Plasticity index, I_p (%)	4 – 30
Liquidity index, I_L	-2.25 – +2.5
Point load index (MPa)	0.01 – 1.15
Unconfined compressive strength, q_u (MPa)	0.7 – 40

Mechanical action on samples of intact chalk causes crushing which leads to an increase in fines content. Bundy (2013) showed that the median grain size, D_{50} for samples of Culver and Newhaven chalk can range from 1 to 10 μm depending on the sample preparation method and grinding time in a Tema mill machine. His tests indicated the predominant minimum particle size was between 2 and 4μm and was consistent with the largest dimension of the individual coccolith laths. Grain size distributions for a range of crushed chalks determined by Clayton (1978) are shown on Figure 2-4. The material is known to dry very rapidly when exposed to the air.

Intact Dry Density (IDD) is the most widely reported index parameter for chalk, since it is one of the easiest to determine, and has been shown to be most representative of the mass behaviour beneath foundations and in earthworks (Clayton, 1990, Matthews and Clayton, 1993). Intact dry density is determined by displacement of water in a gas jar by the method given in BS1377:2 BSI (1990b). A range of IDD of 1.29 to 2.46 Mg/m^3 was reported by Clayton (1983) for English chalk with an average of 1.71 Mg/m^3 and a standard deviation of 0.27 Mg/m^3. The specific gravity, G_s has been widely reported as close to 2.7; Clayton (1983)

found, for a wide range of chalk samples, that G_s varied from 2.69 to 2.71. Saturated moisture contents, w_{sat} are also often reported as an index parameter for chalk. The void ratio, porosity, saturated water content and IDD are related (Figure 2-5) and can be calculated from each other when one is known, because of the limited range of specific gravity (Clayton *et al.*, 2002).

For the majority of chalk, which is almost pure calcium carbonate, plasticity is constant and lies within a narrow range. The liquid limit of crushed white chalk generally lies between 18 and 32% and the plasticity index between 4 and 9%, indicating low plasticity. The clay content in the lower chalk however is sufficient to alter its plasticity to give a range of plasticity between low and intermediate. Liquid limit increases with increasing porosity since it defines the point at which the voids become filled with water and the particles lose contact (Clayton, 1978). High porosity, low strength chalks have liquid limits close to the saturation water content and tend to break down into their parent coccoliths when crushed, giving a uniform material with particle sizes of less than 10μm. In contrast, lower porosity chalks with stronger bonding break down into a well graded material (Clayton, 1983).

Unconfined compressive strength test results depend on the size of the sample, the method of the test and the platen friction and therefore should be considered as an index test as opposed to a measure of strength. Their use in chalk is also limited since UCS testing requires samples with height to diameter ratios of generally between 2 and 3 and chalk cores are often unsuitable due to disturbance caused during drilling. Point load index (PLI) tests are too insensitive to adequately characterise high porosity/low density chalks (Lord *et al.*, 2002). However UCS has been found to correlate well with index properties such as IDD and w_{sat} (Mortimore and Fielding, 1990). A number of UCS tests were conducted on a wide range of chalks by Matthews and Clayton (1993) on 38mm diameter samples with a height to diameter ratio H:D of approximately 2:1. The results correlated with IDD and thus porosity with the strength increasing with increasing density (Figure 2-6).

Also evident from Figure 2-6 is the sensitivity of unconfined compressive strength to initial moisture content, with a ratio of dry to saturated strength of 2:1. The unconfined stiffness was shown to be less susceptible to initial moisture content with a ratio of 1.2:1. Water-saturated chalk is known to be significantly weaker than oil-saturated or dry chalk, a phenomenon known in the study of hydrocarbon reservoirs as “water weakening” (Risnes, 2001). The relationship between UCS and IDD is approximately linear for the dry samples only. Bell *et al.* (1999) showed that the weaker the rock the higher the loss of strength on

saturation. Capillary tension decrease, pore pressure increase, reduction in friction and chemical and physical deterioration have been suggested as explanations of this phenomenon (Matthews and Clayton, 1993).

Thixotropy is the ability of remoulded materials to regain strength with time under constant volume or water content (Seng and Tanaka, 2012). A thixotropic material can change from a gel (a state in which flow will occur after applied shear force reaches a given value) to a sol (where the material will flow under any applied shear force); Boswell (1948). The degree of thixotropy of Senonian (Cretaceous) chalk was investigated by Boswell (1948) who found it to be moderately thixotropic with an 'N' value between 1.5 and 2.3 (the N value defines the void ratio that the material behaves thixotropically in an inverted test tube when a finger tap is applied to the side of the test tube). Bundy (2013) investigated the thixotropic properties of remoulded samples formed from various English chalks and found N values of 2.1 to 2.3, making the chalk of similar (moderate) thixotropy to silt and clay soils.

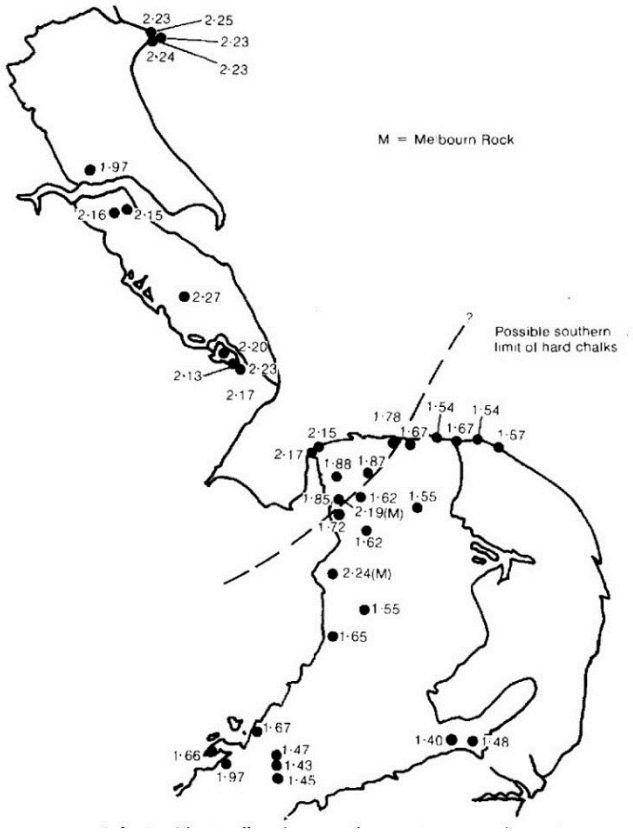


Figure 2-3 Geographical variation in intact dry density for a study in English chalk by Clayton (1983)

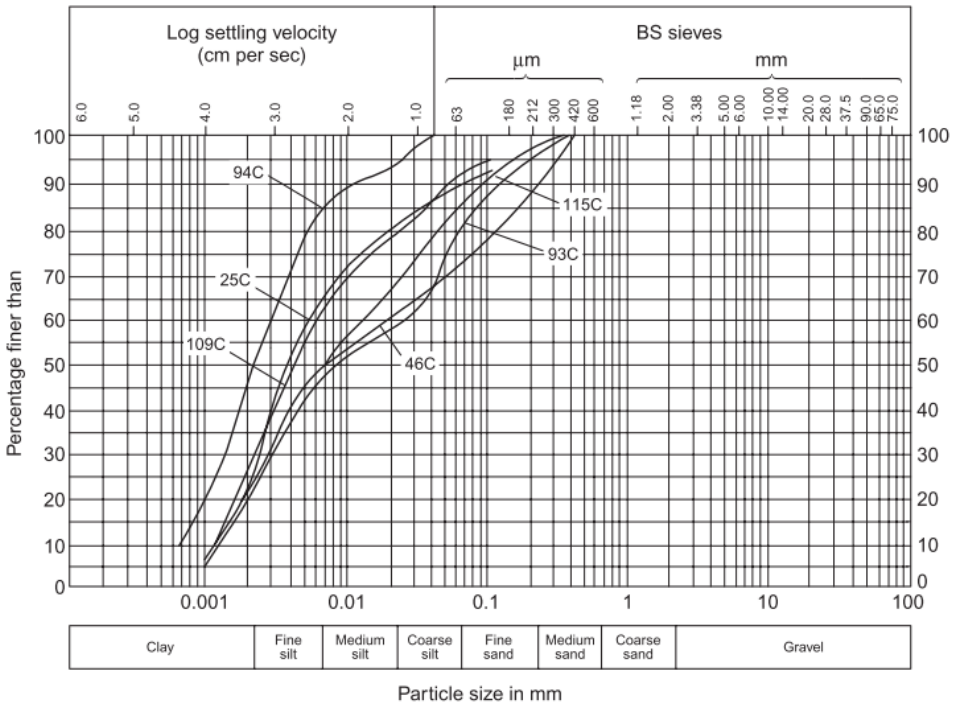


Figure 2-4: Grain sizes for a range of crushed chalks by wet sieving (Clayton, 1978, Lord et al., 2002)

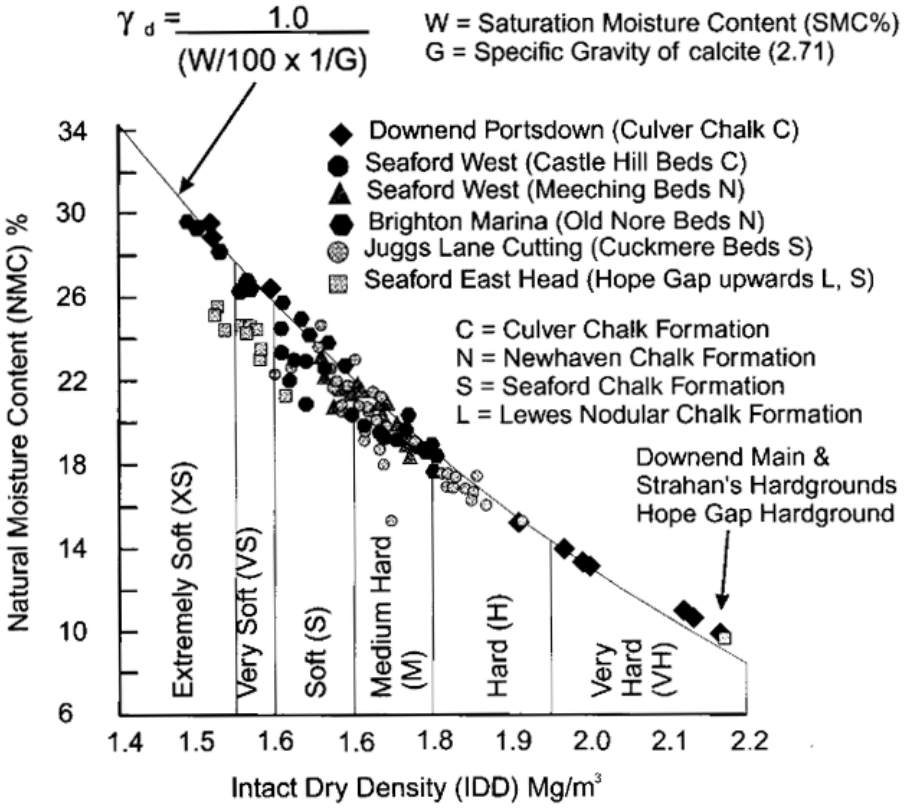


Figure 2-5 Moisture contents of natural occurring chalks from cliffs and quarry faces and Intact Dry Density – saturated moisture content line (Mortimore and Fielding, 1990, Mortimore *et al.*, 2004)

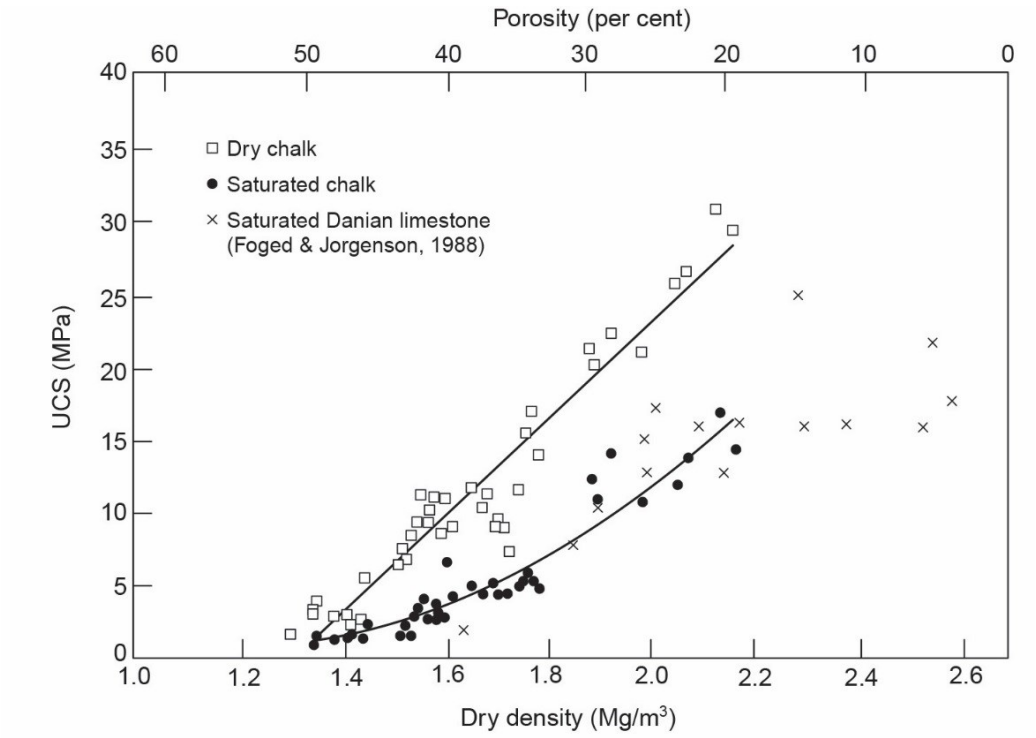


Figure 2-6 Variation of UCS strength with IDD and porosity (Matthews and Clayton, 1993)

2.6 Engineering classification of chalk

In the UK, rocks are generally described in accordance with BS 5930: 2015 (BSI, 2015) with descriptions based on colour, grain size, texture, weathering, structure, rock name and strength. It is difficult to distinguish the engineering performance of different chalks using this system since (i) colour is generally white when un-weathered, with some exceptions e.g. the Red Chalk formation of northern England and the North Sea (ii) grain size is predominantly extremely fine and (iii) texture can only be assessed accurately using an electron microscope (Mortimore and Fielding, 1990). A modified approach to classification is required to avoid overly complex field descriptions and ensure a consistent approach to classification.

Ward *et al.* (1968) provided the first engineering classification scheme for the Chalk based on weathered grades observed at a site in Mundford, Norfolk, shown on Table 2-2. The method was based on fracture frequency and aperture with five different grades, determined from visual observations, ranging from a structureless melange (Grade VI/V) to a completely unweathered material (Grade I), The classification was developed in order to enable the results of a tank loading test to be extrapolated over a large (25 km^2) site and was not intended to be used for classification at other sites. A tentative correlation between SPT and chalk grade was proposed by Wakeling (1970) which was widely adopted despite significant criticisms of the practice (see Hobbs and Healy, 1979, Burland, 1990). Despite warnings from Ward *et al.* (1968), that the Mundford classification system was site specific, it was applied widely throughout the deposit until a revised grading scheme was proposed.

CIRIA PR11 (Lord *et al.*, 1994) identified chalk hardness, discontinuity spacing and pattern and discontinuity aperture as the most important factors influencing the behaviour of the intact mass. The authors used those factors as the basis of a new classification scheme, shown on Figure 2-7, intended to capture the behaviour of all chalk formations:

- The chalk is first split into categories of either structured (Grade A/B/C) or structureless (Grade D) chalk;
- Structured chalk is classified as low, medium or high density based on field and/or laboratory determinations of intact dry density (Table 2-3);
- Structured chalk is then subdivided by discontinuity aperture (Grade A to C) and by discontinuity spacing (subscript 1 to 5);

- Structureless Grade D material is subdivided further based on the amount of comminuted (broken down into its fine constituents) chalk in the matrix;
- Where the coarse fragments are less than 65% the matrix dominates (Grade Dm) and where the coarse fragments exceed 65% the coarse fragments dominate (Grade Dc);
- Chalk putty or remoulded chalk, discussed later, is often associated with Mundford Grade V/VI or CIRIA grade D.

Table 2-2: Classification of chalk at the Mundford site (Ward *et al.*, 1968, Wakeling, 1970, Power, 1982)

Grade	General description	q_c (MPa)[1]	F_r (%)[1]
VI	Extremely soft, structureless chalk containing small lumps of intact chalk	<5	-
V	Structureless remoulded chalk containing small lumps of intact chalk	5-15	0.75 - 1
IV	Rubbly, partly weathered chalk with bedding and jointing. Joints 10–60 mm apart, open to 20 mm, and often infilled with soft, remoulded chalk and fragments	5-15	1.0 - 1.25
III	Rubbly to blocky unweathered chalk. Joints 60–200 mm apart, open to 3 mm, and sometimes infilled with fragments	15-20	1.25 - 1.5
II	Blocky medium-hard chalk. Joints more than 200 mm apart and closed	>20	1.5 - 20
I	As for Grade II, but hard and brittle	No penetration	

1. Ranges of q_c and F_r from Power (1982)

Table 2-3: Intact dry density scales of chalk; Mortimore *et al.* (1990), Matthews *et al.* (1993)

Density scale	IDD (Mg/m^3)	Porosity, n[1] (-)	w_{sat}[1] (%)
Low density	< 1.55	>0.43	> 27.5
Medium density	1.55 – 1.70	0.43 – 0.37	27.5 – 21.8
High density	1.70 – 1.95	0.37 – 0.28	21.8 – 14.3
Very high density	> 1.95	< 0.28	< 14.3

1. Based on a specific gravity of calcite $G_s = 2.70$

Since its introduction, the CIRIA classification scheme been widely adopted to classify chalk in onshore and offshore engineering projects and was unchanged when the updated CIRIA C574 recommendations were published in 2002. Clayton *et al.* (2002) argue that the tightness of the individual blocks has the most significant effect on mass compressibility and

that the CIRIA scheme places too much importance on discontinuity aperture and insufficient emphasis on fracture spacing. Much of the literature on chalk properties, behaviour and pile testing pre-dates the CIRIA scheme and uses the Mundford scheme for classification, which can introduce contradictions in interpretation of historical information. Spink (2002) provides a tentative means of converting the broad Mundford grades to CIRIA grades, shown in Table 2-4 which is used by the Author in reviewing some of the historical case studies described in Chapter 3.

Table 2-4: Structured chalk grading and comparison between Mundford and CIRIA grading schemes (Spink, 2002)

Typical discontinuity spacing & BS5930 term	**Typical discontinuity aperture/infill thickness**			**Grade**
	Open or infilled >3mm	**Open or infilled <=3mm**	**Closed or clean**	
<20mm	IV	NA	NA	Mundford
Extremely close	C5	(B5)	(A5)	CIRIA
20-60mm	IV	III/IV*	NA	Mundford
Very close	C4	B4	(A4)	CIRIA
60-200mm	III/IV*	III	II/III*	Mundford
Close	C3	B3	A3	CIRIA
200-600mm	NA	[II/III*] or {NA}	[II] or {1}	Mundford
Medium	(C2)	B2	A2	CIRIA
>4=600mm	NA	NA	[II] or {1}	Mundford
Wide	(C1)	(B1)	A1	CIRIA

*=Mundford undefined extended grading
NA=Mundford grade not applicable
( )= not common [ ]= low, medium and high density { }=high and very high density

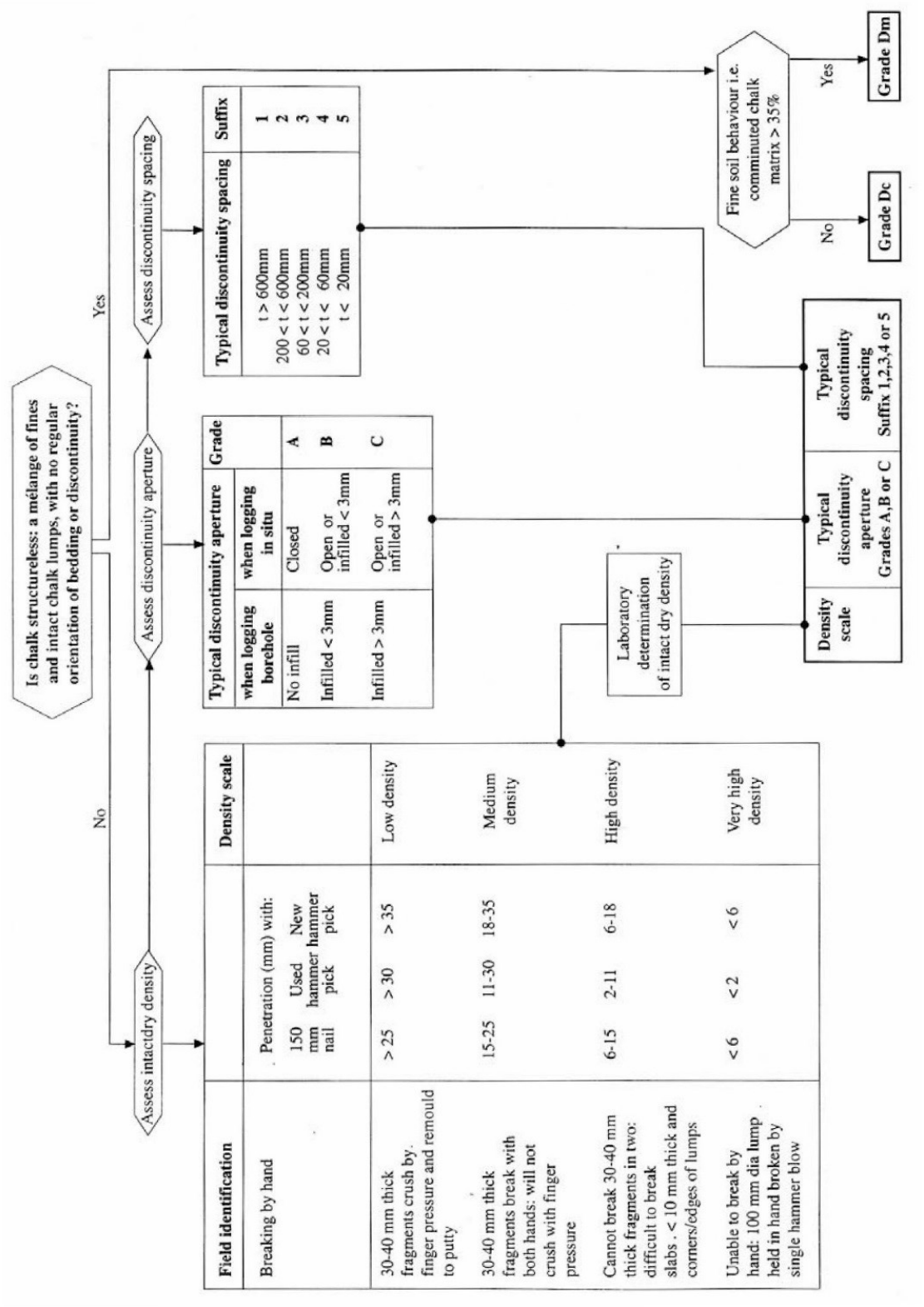


Figure 2-7 CIRIA chalk grading scheme proposed by Lord *et al.* (1994), Lord *et al.* (2002)

2.7 Permeability

The Chalk is thought to be the most important aquifer in Europe and yields over 50% of the potable groundwater used in the UK (Downing, 1993). For example, the town of Brighton obtains 98% of its water supply from local chalk (Mortimore *et al.*, 2001). Chalk is distinguished from other soils and rocks in that it has a high porosity micro-fabric combined with a network of discontinuities which leads to dually porous behaviour; Burland (1990). Permeability is controlled fundamentally by discontinuity pattern, frequency and properties and to a lesser extent by the matrix permeability (Price *et al.*, 1993, Bell *et al.*, 1999). Bell *et al*. (1999) compared porosity with inter-granular permeability and found low correlation, probably due to the size of the interconnections between the pores, indicating that permeability is not governed by inter-granular flow.

Intact chalk's field permeability is high enough for it to be considered as a free draining material (Lord *et al.*, 2002). Piezocone dissipation tests carried out in the field on low-medium density fractured Grade B2/B3 chalk (Diambra *et al.*, 2014) indicate times for 50% dissipation of penetration generated excess pore water pressures of less than 10 seconds. The tendency for permeability measured from pumping tests to increase with improving chalk grade was highlighted by Roberts and Preene (1990) and Mortimore (1996). In structureless Grade Dm/Dc chalk, permeability ranges from 10^{-7} to 10^{-9} m/s, increasing to between 10^{-3} and 10^{-5} m/s in Grade B/C chalk.

2.8 In situ testing

2.8.1 Cone penetration tests

To date, a consistent method has not been developed that links the CIRIA chalk grades described in the previous section to *in-situ* testing results. The limitations of the standard penetration test (SPT) and the need for various corrections are well documented, see for example Skempton (1986) for SPT tests in sands. Chalk can completely de-structure under high compressive stresses and Lord *et al.* (2002) note that SPT N values are "largely a function of the progressive dynamic bearing capacity failure ahead of the SPT shoe". The tentative correlation between Mundford chalk grade and SPT N value proposed by Wakeling (1970) was criticised by several authors, including Burland (1990), for attempting to relate blow count to a visual weathering grade. As such, SPTs are only useful as a broad indicator of where the chalk lies on the density scale. Cone Penetration Tests (CPT) or Cone Penetration tests with

pore pressure measurement (PCPT) appear to be a better tool for investigation of chalk strata, providing reliable and repeatable data which can be correlated with site specific descriptions. Bracegirdle *et al.* (1990) found cone penetration resistance a particularly useful parameter to help identify the extent of cavities and zones of disturbed material at depth within the Upper Chalk at a site near Costessey, Norfolk.

Cone resistance, q_c in chalk tends to be higher than is seen in most clays and closer to that developed in medium dense sands. Friction ratios fall between 1 and 5%, within the ranges seen in both sands and clays. Structured chalk is identifiable by the nature of the q_c profile signatures, which frequently include a sequence of sharp peaks over small (<0.5m) intervals. These peaks are thought to be related to the presence of flints as well as the manner in which penetration resistance "builds up and is then followed by grain crushing and closure of discontinuities" (Power, 1982) in a pattern similar to stick-slip friction. An example of this behaviour at the Mundford site is shown in Figure 2-8. Variations in the CPT profile are likely to relate to changes in density, degree of cementation and jointing and fissuring, since the dry density of chalk can vary by as much 0.1 Mg/m^3 over 0.1m depth (Lord *et al.*, 1994). The spiky nature of cone penetration profiles in chalk has led previous researchers to recommend averaging the resistance over some interval of penetration to give more representative results. While Power (1982) recommended averaging over 1m penetrations, Smith (2001) concluded that an averaging interval of 0.3m penetration was more reasonable in relation to the dimensions of the cone.

Ambiguities in differentiating chalk from other materials in PCPT tests are most conclusively resolved by consideration of the excess pore water pressures. Very little excess pore water pressure is induced in sands due to the free draining nature of the material. Excess pore water pressures in chalk are generally remarkably high, greater than those seen in clay strata, although they tend to dissipate rapidly when penetration is paused. High excess pore water pressures may also develop in clays, but their dissipation will usually be far slower. As described above excess pore water pressures measured at the shoulder (u_2) position by Diambra *et al.* (2014) reached 2MPa and dissipated in less than 10 seconds for most tests; similar trends were reported offshore at the Amethyst gas field by Power *et al.* (1990). The generation of high pore pressures may be surprising, considering the chalk's silt-size particles and regular discontinuities, which lead to high permeabilities. The high penetration pore pressures close to the cone tip are probably caused by the collapse of the chalk's structure around the cone. Local

grain crushing and the closing of discontinuities is likely as penetration occurs, which are all relieved when pushing is halted (Power *et al.*, 1990).

Searle (1979) proposed relationships between cone resistance, q_c friction ratio, F_r (or R_f) and chalk density in English chalk based on results obtained using a mechanical CPT. He plotted the relationships in the form of a chart which attempted to delineate the results in terms of the degree of cementation and the site-specific Mundford grades. Power (1982) describes a research programme which aimed to relate cone parameters for the electric CPT to Mundford chalk grade and Young's modulus, E as found from field tank loading tests. He found that both q_c and F_r increased with increasing chalk grade and E, and gave the broad ranges for q_c and F_r for each grade given in Table 2-2 (previously). In Mundford equivalent CIRIA Grade A/B structured chalk q_c tends to range from 15 to 20MPa with F_r between 1.25 and 1.5 %. Power (1982) notes that cone penetration may not be possible in high density Grade A chalk. Lunne *et al.* (1997) cite an unpublished BRE report by Powell and Quarterman (1994) which examined CPT tests at five sites including the Mundford site. While they found that q_c and F_r generally increased with increasing chalk grade (V to II), as observed by Power (1982), the ranges varied between sites. It is also worth noting that the majority of the Powell and Quarterman (1994) data would fall outside of the Power classification ranges, even for the Mundford site (Figure 2-9). Smith (2001) discusses CPT test results at 11 locations at sites within the grey (formerly lower), Southern Province, Transitional Province, and Northern Province chalks. He also observed general trends of increasing q_c and F_r with improving chalk grade, but significant overlap between parameters encountered at different sites. These studies, when taken together, as shown on Figure 2-9, suggest that delineation of chalk grades may not be possible using only q_c and F_r.

2.8.2 Pressuremeter tests

Pressuremeter tests, which expand a hydraulic or gas inflated flexible rubber membrane in a long cylindrical cavity and in a theoretically undisturbed soil mass can be interpreted to determine strength and stiffness properties. The quality of the test depends on how the "cavity" is formed and how the radial displacements are measured. Self-boring pressuremeters (SBP) provide the highest quality test since they cause less installation disturbance, however their penetration may be impeded by flint bands within the chalk. Pre-bored high pressure dilatometer tests placed in boreholes and pushed-in devices may also be used, although these are more affected by installation effects.

Pressuremeter tests are routinely used to design foundations in France (Bustamante *et al.*, 1980, Frank, 2009) where they are also assumed to provide representative *in-situ* engineering strength and stiffness in chalk. Whittle *et al.* (2017) describe a programme of pressuremeter tests in highly weathered chalk located offshore Northern France, where pre-bored, self-boring and pushed-in pressuremeters were considered. The tests indicated chalk behaves in a drained manner, even at relatively rapid rates of strain change, confirming observations made in the PCPT dissipation tests described previously.

2.8.3 Geophysical testing

Several studies have shown that ultrasonic shear and compression wave velocities increase with increasing density and reducing porosity (Urmos and Wilkens, 1993, Pedersen and Rhett, 1998, Gommesen and Fabricius, 2001). Ultrasonic velocities are calculated from the transit time it takes an ultrasonic P- or S- wave pulse to travel the length of a sample. An example of measurements taken on intact samples from the North Sea is shown on Figure 2-10. The results indicate that compression (P-wave) velocity for low-medium density chalk (porosity = 37% to greater than 43%) ranges from 1.9 to 2.9km/s, and for high to very high density chalk (porosity 28 to 37%) is between 2.9 and 3.7km/s. Shear (S-wave) velocity for low-medium density ranges from approximately 1 to 1.8km/s and for high-very high density lies between 1.8 and 2.2 km/s.

Clayton *et al.* (1994) present a comparison between shear stiffness inferred from surface Raleigh wave geophysical tests conducted in the field and small strain unconfined compressive stiffness measured using local instrumentation in the laboratory. As illustrated on Figure 2-11, discontinuities dominated the stiffness of the rock mass, leading to lower measurements of chalk mass shear stiffness than intact shear stiffness The average rock mass factor, j ($=E_{mass}/E_{intact}$) interpreted by comparing the results of plate loading tests at the sites (E_{mass}) with laboratory measurements (E_{intact}) ranged from 0.03 for the high density site (A) to 0.2 for the low density site (C), illustrating the influence of discontinuities on the compressibility *in-situ*. The effect was more pronounced in the high density material, since the brittle behaviour of the intact rock leads to a loose fracture system and the intact stiffness has little effect on that of the chalk mass (Matthews and Clayton, 1993). In contrast, low density chalks are less brittle and tend to have relatively tight fractures, therefore the mass strength and stiffness tend towards the intact strength and stiffness as the porosity increases (Clayton *et al.*, 2002).

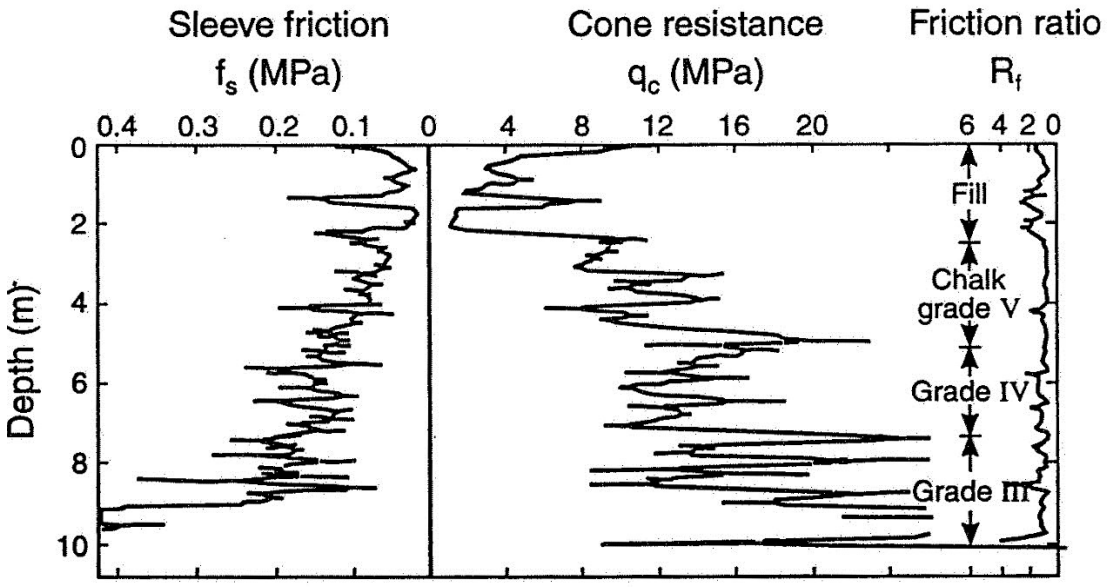


Figure 2-8 Typical cone penetration test profile in chalk at the Mundford site (Power, 1982)

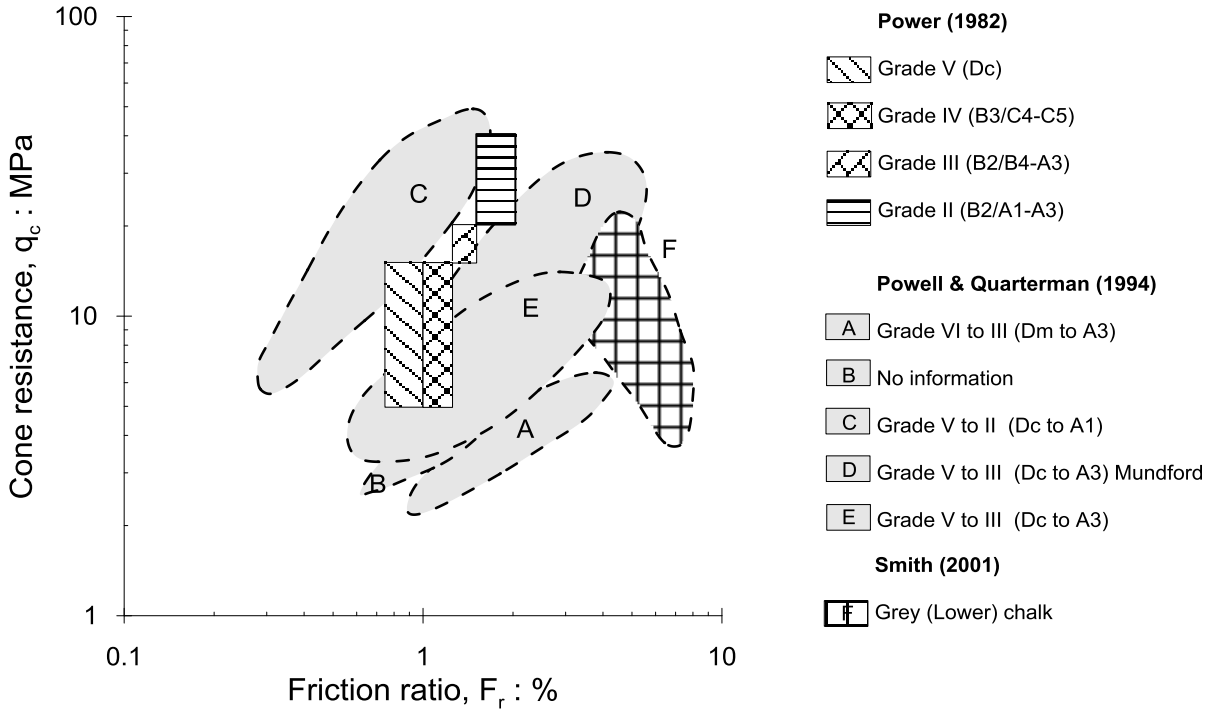


Figure 2-9 Classification of chalk grade using CPT tests from results available in the literature (data from Power, 1982, Powell and Quarterman, 1994, Smith, 2001)

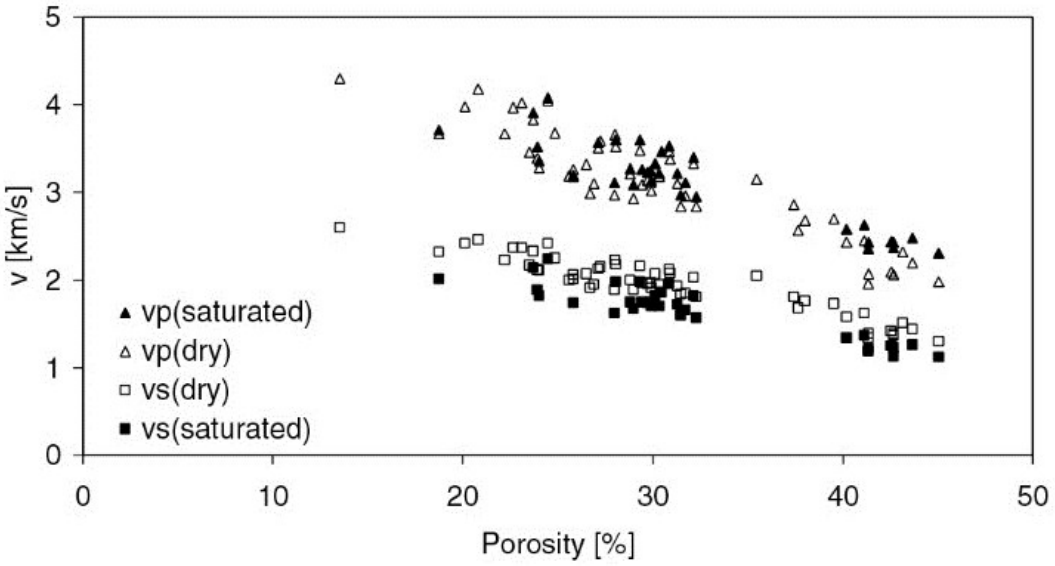


Figure 2-10 Relationship between ultrasonic velocity and porosity (adapted from Røgen *et al.*, 2005)

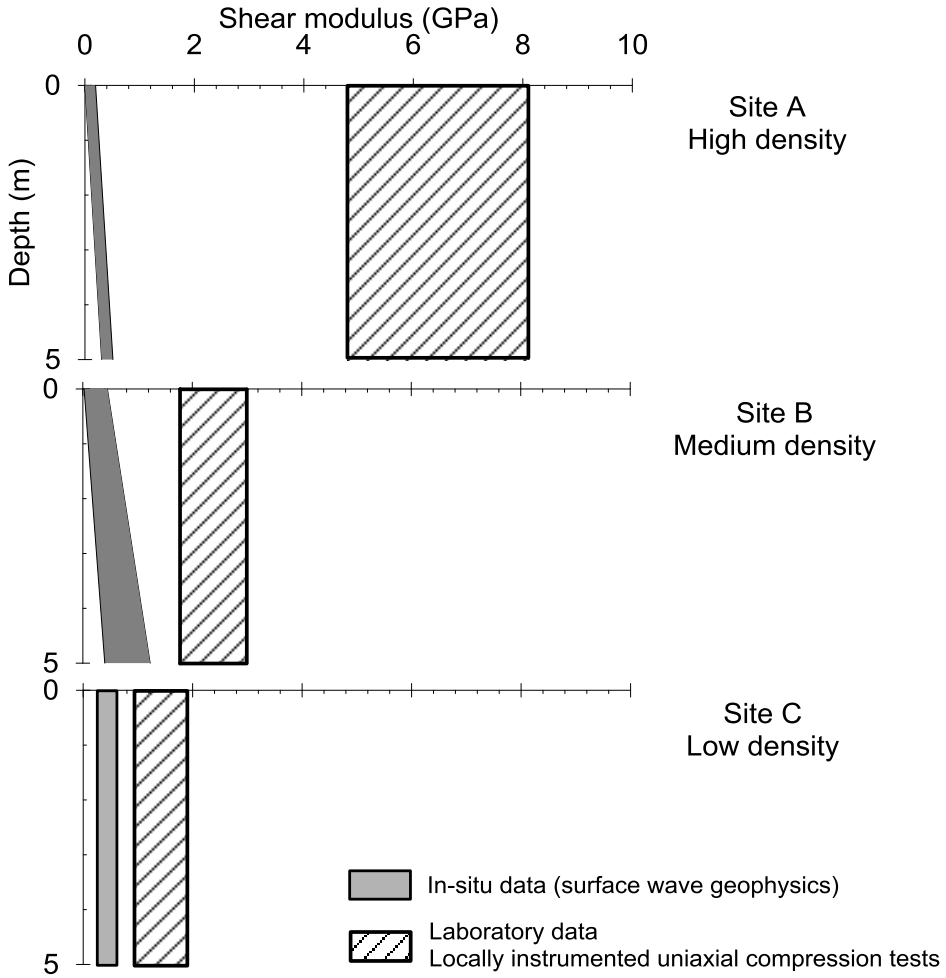


Figure 2-11: Comparison of initial shear modulus measured in surface geophysics and laboratory tests (adapted from Clayton *et al.*, 1994, Clayton *et al.*, 2002)

2.9 Features of the mechanical behaviour of chalk

Intact chalk lies between a hard soil, where the stress-strain behaviour is non-linear even at very small strains, and a soft rock where the behaviour may appear as linearly elastic over a far wider strain range (Matthews and Clayton, 1993). Bonding, cementation or structure, typical of cemented soils and soft rocks, dominate the behaviour of intact chalk and play a smaller role in the behaviour of aged remoulded material. Remoulded "putty" chalk and chalk which has had its bonding partially or completely destroyed can be shown to behave in a similar manner to granular soils, where behaviour is governed by initial state and intrinsic properties. The latter can be characterised within the critical state framework. The following sections give a brief review of the general aspects of both behaviours.

2.9.1 Pre-yield behaviour & small strain stiffness

The term "yielding" was traditionally used to refer to the onset of plastic behaviour and a change from linear to non-linear stiffness behaviour. Yielding in soils is now well known to be non-linear even at small strains and can be a gradual process. Several constitutive models have been developed which describe the yielding of soil using kinematic surfaces for each yielding phase (e.g. Al-Tabbaa and Wood, 1989, Stallebrass and Taylor, 1997). Jardine (1992) used high resolution laboratory tests on clays to propose a multiple kinematic surface framework. Later work showed that the framework could be applied to sands (Kuwano and Jardine, 1998, Kuwano, 1999, Kuwano and Jardine, 2007). The primary features of the framework, which includes two kinematic yield surfaces (Y_1 and Y_2) within the conventional Y_3 yield surface, are illustrated on Figure 2-12.

Within the limited kinematic hardening surface (Y_1), the behaviour is elastic although potentially effective stress-level dependent and anisotropic (Kuwano and Jardine, 1998). Once engaged, the Y_1 surface is dragged with the effective stress point, changing shape and scale with p' and with proximity to the outer large-scale (Y_3) surface. The Y_3 surface corresponds to the yield surface recognised in classical critical state soil mechanics (Jardine, 1992) and is associated with significant loss of stiffness, contraction, dilation and sudden failure.

Plastic straining is initiated when the stress point engages the Y_1 yield surface. The intermediary Y_2 yield surface marks the point (i) where strain increment directions can change (ii) where strain rate or time dependency begins and (iii) beyond which permanent strains (or reductions in p' for undrained tests) accumulate significantly in cyclic tests (Jardine, 2014). The Y_2 surface was identified by Kuwano and Jardine (2007) in drained tests primarily as the

point where their sands' strain increment directions ($d\varepsilon_s/d\varepsilon_v$) changed from following an elastic pattern to be dominated by the soils' plastic response.

In a material such as intact chalk, which has significant degrees of structure and bonding, the Y_1 surface is likely to be more extensive and related to the chalk's porosity or degree of cementation. The size of the yield locus may be expected to increase with the degree of bonding or cementation, separate from any effects of stress history.

2.9.2 Critical state soil mechanics and the state parameter for granular soils

Soils are distinct from many other engineering materials in that they undergo volume change; when soils are sheared under drained conditions they change in volume as a consequence of the soil's initial state. The inclusion of density as a state variable rather than a soil property was addressed in the critical state soil mechanics (CSSM) framework introduced by Schofield and Wroth (1968). The CSSM framework is used extensively to predict volumetric changes of clays, and has been applied by several authors to interpret the behaviour of sands, including Been and Jefferies (1985), and used as a basis of several proposed numerical constitutive models (e.g. Manzari and Dafalias, 1997, Taborda *et al.*, 2014).

Roscoe *et al.* (1958) defined critical state as the state in which a soil continues to deform at constant stress and constant void ratio. The volumetric behaviour of a sand at large strains will reach a steady state where the deviatoric stress, q, the volumetric strains (drained tests) and the pore water pressures (undrained tests) all become constant. Critical states are assumed to be independent of the soil's initial density and structure. In specific volume, v (=1+e) and mean effective stress space (v:lnp′) the locus of these critical state points forms a critical state line (CSL) traditionally represented as a straight line parallel to the normal compression line (NCL):

$$\textbf{NCL}: v = N - \lambda \ln(p') \qquad 2\text{-}1$$

$$\textbf{CSL:}\ v = \Gamma - \lambda \ln(p') \qquad 2\text{-}2$$

where N, Γ and λ are intrinsic soil parameters; N and Γ are equal to the specific volume at a mean effective stress, p′ of 1kPa and λ is the slope of the line in v:lnp′ space. In compression, loose soils will show a reduction in pore volume due to particle rearrangement. Loosely packed samples can define a unique state at a given stress level before converging onto the NCL. For granular materials, which can exist at different void ratios at the same stress level, different samples can have different non-coincident NCLs which will approach a unique Limiting

Compression Curve (LCC) for the material when sand particles begin to crush at high stress levels (Pestana and Whittle, 1995). As shown on Figure 2-13, compression paths at low stresses are therefore almost flat and can be parallel in v:lnp′ space for samples placed at different initial void ratios. The stress at which the LCC is reached depends on the strength of the individual particles. A curved CSL for sands is suggested by the results of high pressure triaxial tests which initiate grain crushing at high stresses e.g. Been *et al.* (1991), Altuhafi and Jardine (2011). A power law relationship for the critical state locus can be used in place of Eq. 2-2 as suggested by Li and Wang (1998).

The stress ratio at critical state is given in triaxial stress space by:

$$M_{tc} = \frac{q}{p'} \qquad 2\text{-}3$$

with M_{tc} related to the angle of shearing resistance, φ' in compression by:

$$M_{tc} = \frac{6\sin\varphi'}{3 - \sin\varphi'} \qquad 2\text{-}4$$

During compression and shear, the behaviour of granular soils depends on their initial "state", which comprises both the current porosity and effective stress level. The initial state of a sand can be used to predict its volumetric behaviour during shearing. The state parameter, ψ proposed by Been and Jefferies (1985) is a measure of the deviation of the current state of a granular soil from the CSL which is fixed for a given soil (Figure 2-14). Where e is the current void ratio and e_{cs} is the void ratio at critical state at the same mean effective stress:

$$\psi = e - e_{cs} \qquad 2\text{-}5$$

The state parameter, ψ can be used to explain and predict the behaviour of granular soils during shear, as was shown by Been and Jefferies (1986). As illustrated on Figure 2-15, tests with similar ψ values show similar normalised behaviour during shearing. During drained shearing, denser-than-critical samples will first contract until the stress state reaches a "characteristic point" where dilation is initiated, which then continues to critical state. In undrained shearing, the behaviour is essentially similar except that the volume remains constant and the path in v:lnp′ space is horizontal. Looser-than-critical samples generally reach critical state with no dilation or softening.

2.9.3 Behaviour of bonded soils and weak rocks

The state parameter and critical state framework do not fully capture the effects of pre-existing fabric or structure due to bonding. Leroueil and Vaughan (1990) showed that a large number of natural soils have a bonded structure similar to a weak rock and that their behaviour cannot be interpreted using void ratio and stress history alone. Comparison of the oedometer compression curves of the same material in a structured and completely de-structured state (Figure 2-16) gives an indication of "structure permitted space" which defines the state in which the material can only exist due to the effects of its bonding, natural void structure or cementation.

The microstructure of "structured" materials remains intact at low stresses and the impact of small stress perturbations may be practically reversible. The effective stress paths developed under one dimensional K_0 compression may resemble those of an elastic material with low values of Poisson's ratio. When Y_3 yielding occurs, the structure begins to progressively break down and at large strains the stress path follows the K_0 stress path of the same soil in its de-structured state. Typical yield curves for structured soils and weak rocks are shown on Figure 2-17.

Leroueil and Vaughan (1990) also showed that shearing behaviour of structured and bonded materials depends on their initial conditions. Stress-strain behaviour depends on the position of the initial state relative to the bonded Y_3 yield locus. Shearing samples which have undergone Y_3 yielding results in behaviour similar to that seen in an un-cemented material. Samples sheared at low confining stresses can be expected to fail in a brittle manner. Shearing can involve apparent double-yield points with the initial yield associated with destruction of cementation or structure and the onset of plastic straining, or engagement of the Y_1 surface. The work of Leroueil and Vaughan (1990) was confirmed by tests on cemented carbonate sand by Coop *et al.* (1995) and in work conducted on intact chalk, discussed within the next section.

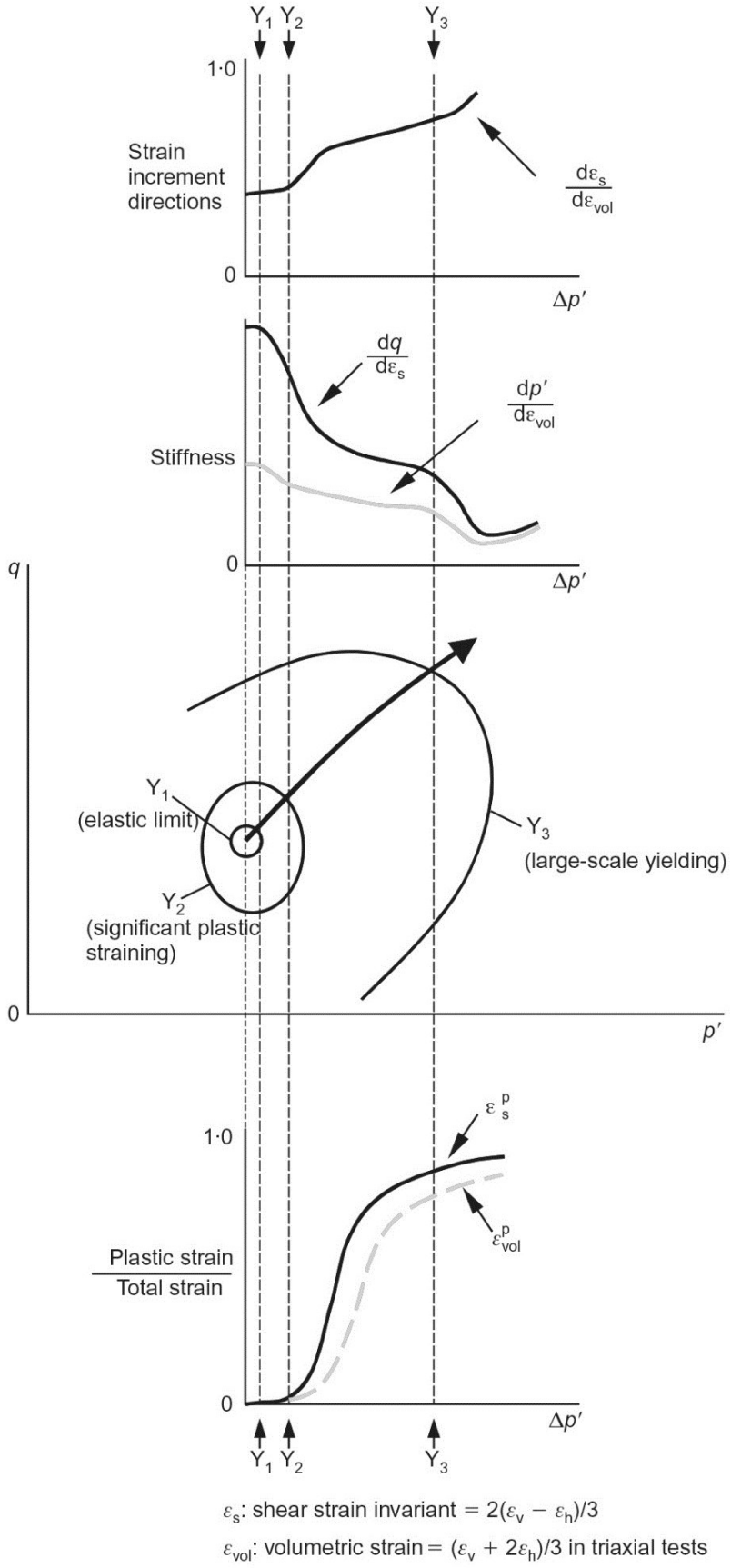


Figure 2-12 Scheme for multiple yielding surface framework (Kuwano and Jardine, 2007)

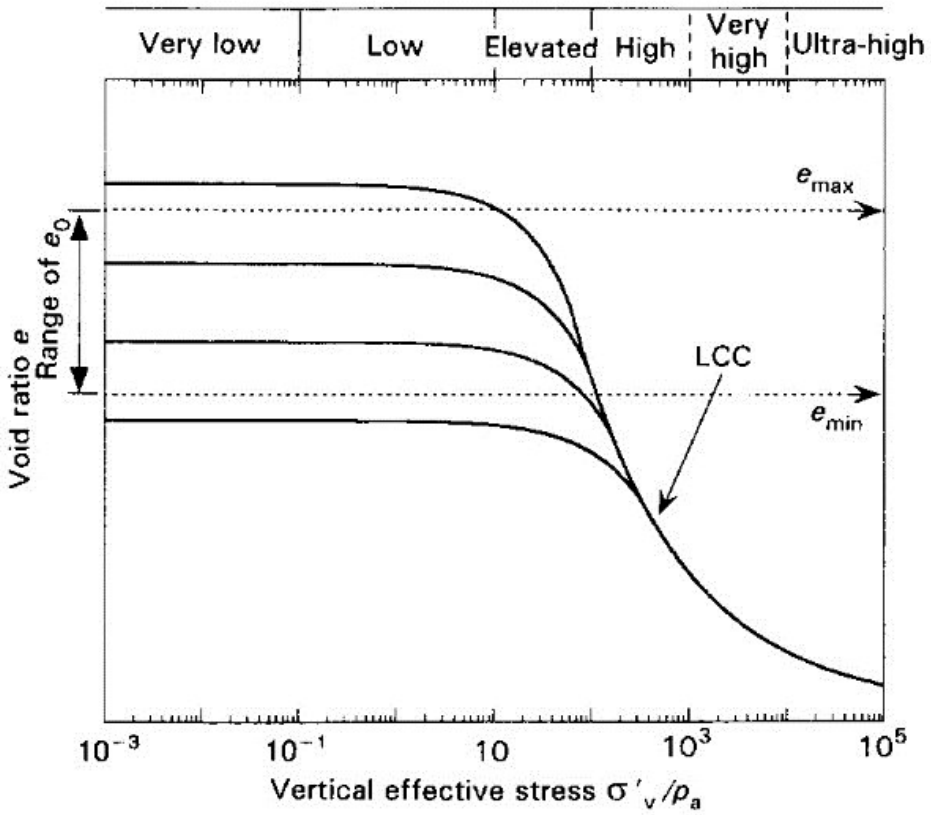


Figure 2-13 One dimensional compression for cohesionless soils showing the Limiting Compression Curve (Pestana and Whittle, 1995)

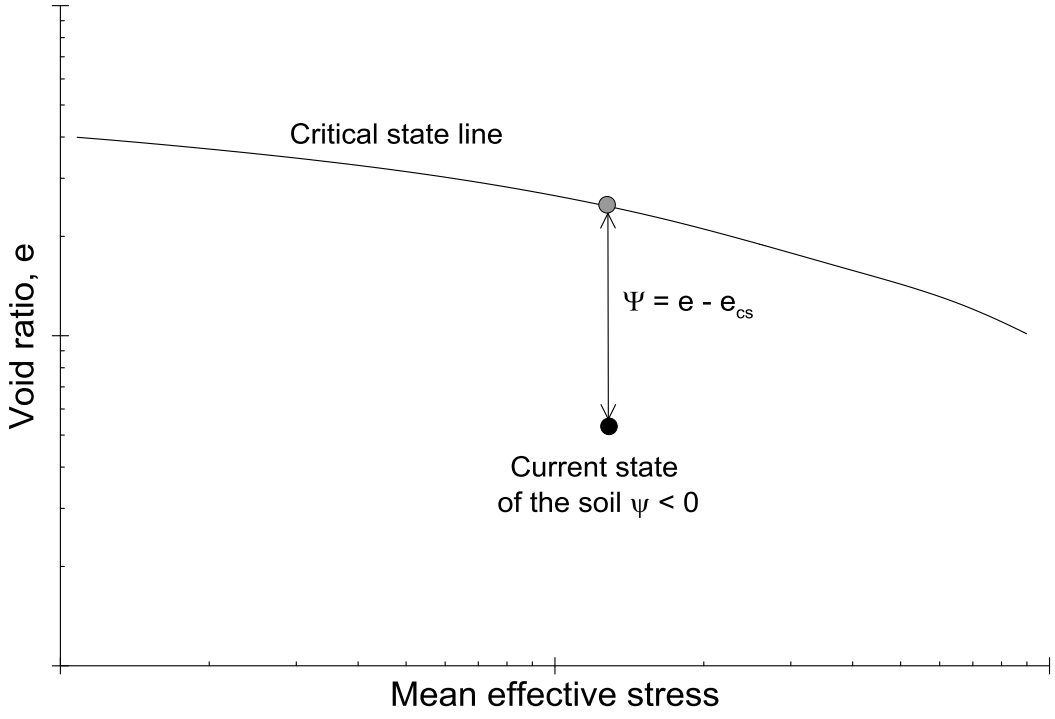


Figure 2-14 Definition of the state parameter

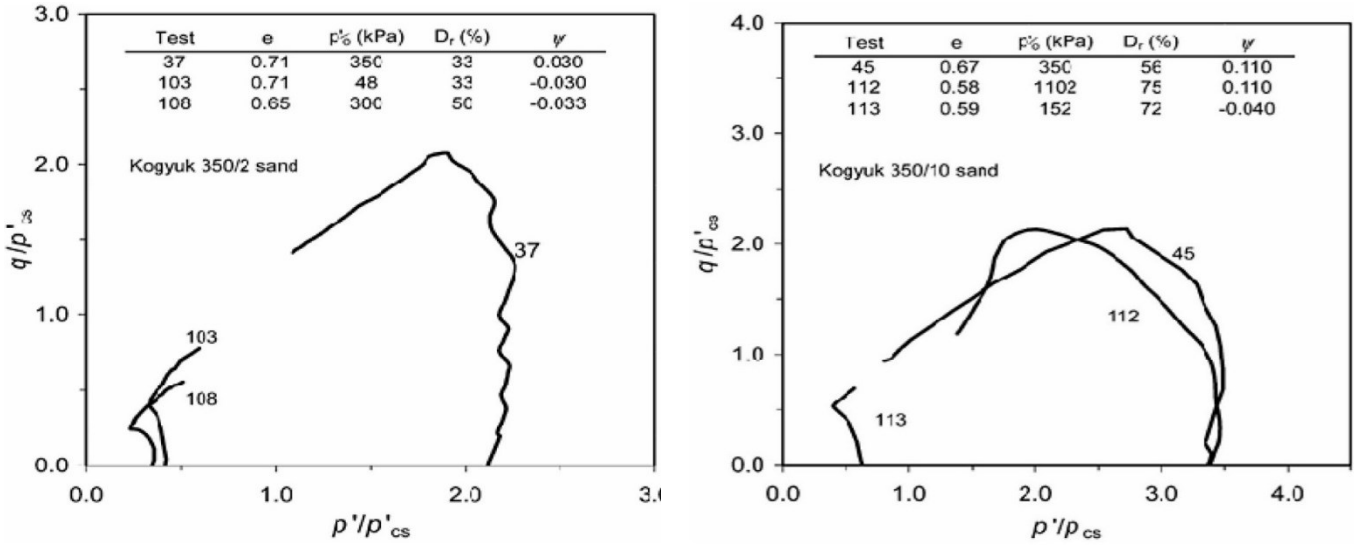


Figure 2-15 Comparison of behaviour of sand as a function of relative density and the state parameter (Been and Jefferies, 2006)

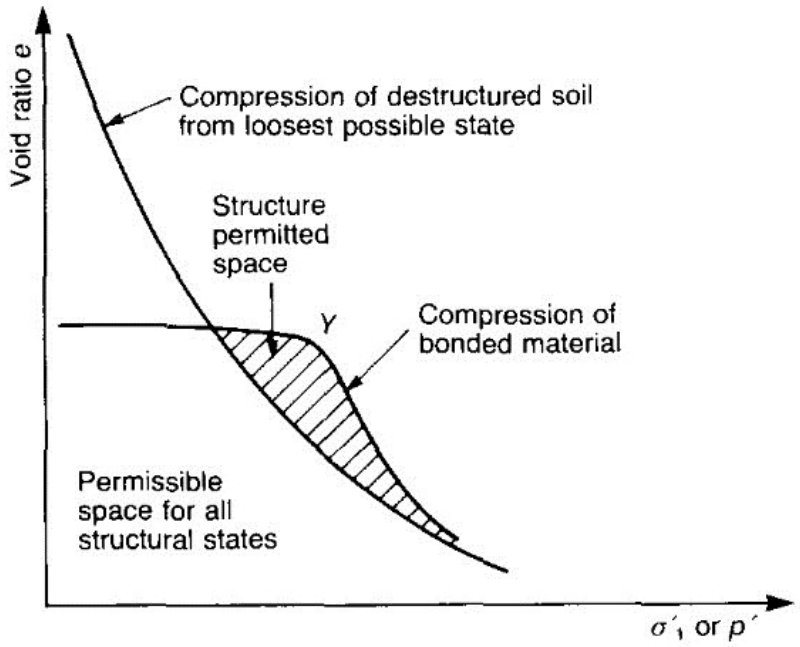


Figure 2-16 De-structured and structured oedometer compression curves and structure permitted space (Leroueil and Vaughan, 1990)

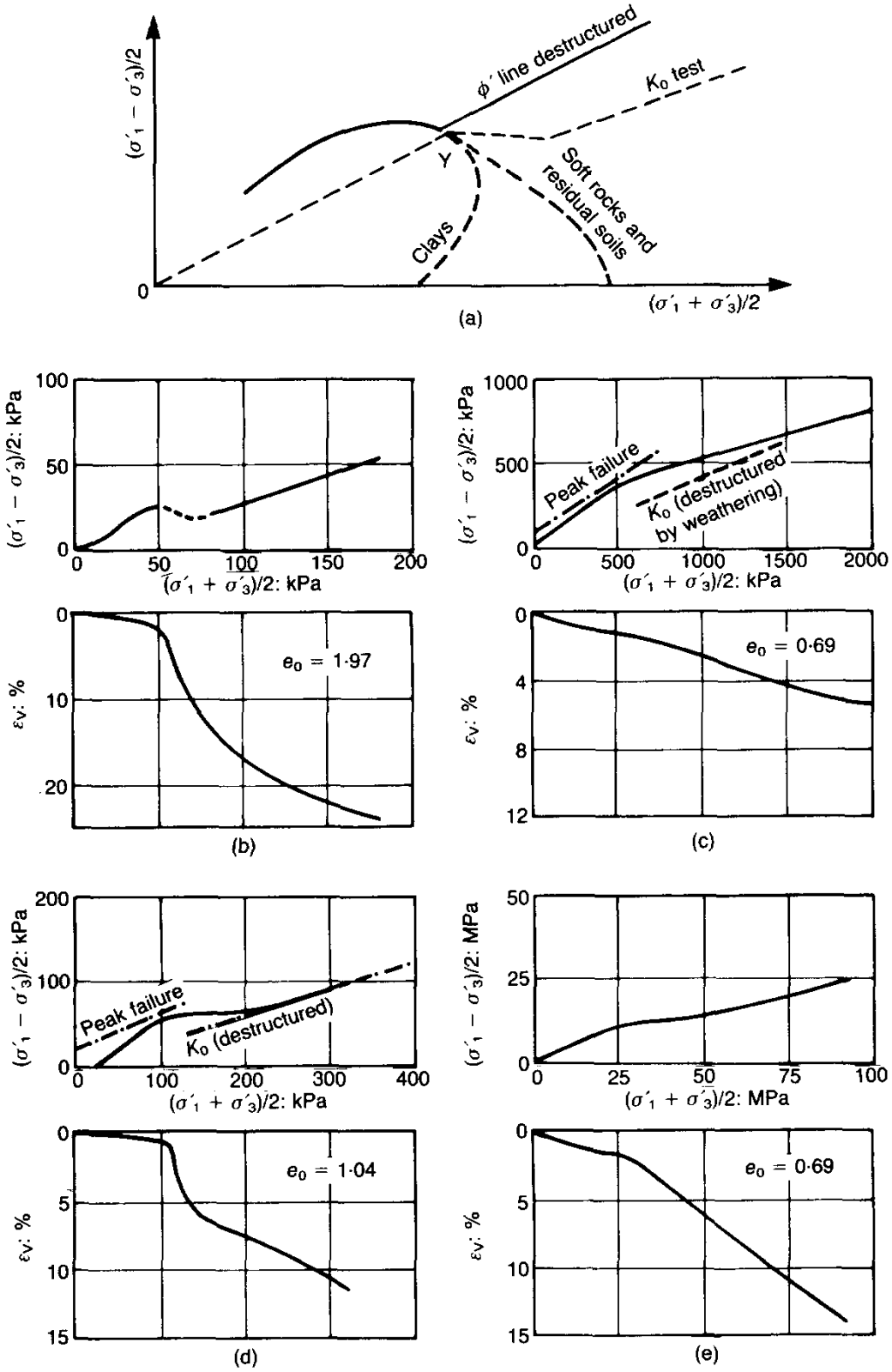


Figure 2-17 One dimensional K_0 compression tests on four different structured materials (a) schematic stress paths (b) sensitive Canadian clay (c) unweathered Keuper Marl (Mercia Mudstone) (d) artificially bonded soil (e) chalk (Leroueil and Vaughan, 1990)

2.10 Behaviour of intact chalk

Matthews and Clayton (1993) showed that the rock mass factor, j increases with decreasing intact dry density, for chalk sites with similar discontinuity characteristics. Therefore as porosity increases, the intact strength and stiffness describe the strength and stiffness of the chalk mass. The behaviour of intact chalk is therefore important for deep foundations installed in chalk where discontinuities are tight and widely spaced and the chalk mass strength and stiffness tend towards the intact strength and stiffness.

Since the late 1970s, research into aspects of the mechanical behaviour of intact chalk has been driven by subsidence problems associated with the use of low-density chalks in hydrocarbon production (Addis and Jones, 1990, Talesnick *et al.*, 2001). Research efforts have focused on two streams; i) attempting to describe the mechanical behaviour of chalk using a soil mechanics approach in triaxial experiments conducted at Imperial College and University College London in the late 1980s and early 1990s (Addis and Jones, 1990, Leddra and Jones, 1990, Leddra *et al.*, 1993, Petley *et al.*, 1993, Kågeson-Loe *et al.*, 1993) and ii) so called "water weakening" or consideration of well subsidence as a coupled hydro-mechanical problem involving multi-phase reactions of oil and water as pore fluids (e.g. Risnes *et al.*, 1996, Risnes and Flaageng, 1999, Risnes, 2001, Collin *et al.*, 2002, Delage *et al.*, 2008). Further experimental studies have aimed to quantify other aspects of material behaviour such as intact stiffness and material anisotropy (e.g. Jardine *et al.*, 1985, Matthews and Clayton, 1993, Talesnick *et al.*, 2001, Holloway-Strong *et al.*, 2007, Korsnes *et al.*, 2008). The following sections give a brief overview of the behaviour of intact chalk samples in laboratory testing.

2.10.1 Pre-yield behaviour

Studies have shown that intact chalk exhibits a high initial stiffness and appears to behave elastically practically until its yield stress is reached (Jardine *et al.*, 1985, Addis and Jones, 1990, Leddra *et al.*, 1993). Jardine *et al.* (1985) carried out undrained locally instrumented triaxial tests on saturated chalk from Northfleet, Kent, which showed that the undrained Young's modulus, E_u fell gradually from the beginning of the test from an initial value of 6GPa to approximately 4GPa, over 0.07% strain. A bi-linear stress path was observed and the pre-yield straining was found to be non-linear and recoverable. Matthews and Clayton (1993)'s locally instrumented uniaxial compressive strength tests on dry English chalk of

varying porosities showed elastic behaviour over the majority of the strain range tested and failure at low to medium strains (<0.15%), with some deviation for the higher porosity sample.

Chalk formation by sedimentation and compaction may be expected to lead to transverse isotropy in planes parallel to bedding planes (Hickman, 2004). Papamichos *et al.* (1997) indicate significant elastic anisotropy for a high porosity chalk sampled at Pietra Leccese, Italy. The results reported by Talesnick *et al.* (2001) on a high porosity air dried Eocene chalk from Israel show stress-strain transverse elastic anisotropy with the plane of isotropy defined by the bedding plane. The modulus of deformation was found to be 60% higher when measured parallel to bedding than when measured perpendicular. The compressive strength was also found to be 50% higher in the direction parallel to bedding. Similar results were obtained by Korsnes *et al.* (2008) for mutually perpendicular samples drilled from blocks of medium density chalk from Liège, Belgium and low density chalk from Stevns Klint, Denmark.

Results from undrained triaxial tests conducted by Heymann (1998) are shown on Figure 2-18. The small strain stiffness of the structured samples at 0.001% strain, $E_{0.001}$ ranged from 4100 to 4900kPa, which is an order of magnitude greater than that observed for tests on the London Clay by Clayton and Heymann (2001). Notably, the values of $E_{0.001}$ were 3 to 4 times greater than the seismic stiffness from surface wave geophysics methods at the same site, reported by Clayton *et al.* (1994), thought to be due to the highly fractured nature of the chalk and the larger volume of chalk that is tested by geophysical methods.

Decreases in porosity or increases in cementation can be expected to lead to increases in the initial stiffness of chalk and expansion of the Y_1 yield surface. The elastic compressional (P-wave) velocity was shown previously to increase with increasing density. Locally instrumented uniaxial compression tests on English chalk by Matthews and Clayton (1993), shown on Figure 2-19, confirm this trend; the initial secant stiffness for the high density sample (n = 29%) was 25GPa reducing to 10GPa for the medium density (n = 40%) sample and 6GPa for the low density (n = 45%) sample. Leddra *et al.* (1993) compared the response of three chalks of low (n = 4-8%), medium (n = 38%) and high (n = 28%) porosity during K_0 loading in the triaxial cell and also showed that the yield stress increases with decreasing porosity.

Initial stiffness depends on the initial moisture content in a similar manner to strength. Matthews and Clayton (1993) found the initial stiffness of saturated samples was approximately 80% of that of dry samples in locally instrumented unconfined strength tests on

English chalk. Talesnick *et al.* (2001) showed that the modulus of deformation reduced with increasing water content and observed a dramatic (≈50%) reduction in stiffness when a sample tested at an initial water content of 5.65% was compared to that of an air dried sample (water content = 1.4%).

2.10.2 Yielding in compression

In q-p′ stress space, the shape of the elastic yield surface can be traced by plotting the yield points in compression tests found at different confining stress conditions. The yield stress marks the onset of significant volumetric strain due to permanent plastic deformations. Collin *et al.* (2002) compared the stress points where yielding occurred in hydrostatic, triaxial and K_0 compression tests on high porosity Lixhe chalk from Liège, Belgium and showed that the yield points trace an approximate elliptical surface.

After exhibiting very high stiffness at small strains, standard drained triaxial tests manifest significant volumetric strains after the onset of yield that is related to breakdown of structure within the intact material. This is termed "pore collapse" by several researchers, e.g. Collin *et al.* (2002) and can be considered analogous to de-structuration within the framework of Leroueil and Vaughan (1990). The vertical effective stress where yielding occurs is usually expected to be greater than the past maximum *in-situ* vertical effective stress level, assuming that weathering and recent processes have not affected bonding in the material (Clayton and Matthews, 1987).

Addis and Jones (1990) describe one dimensional (K_0) stress paths on high porosity chalk which led to yield at approximately 7MPa, followed by a progressive de-structuring until the stress path reaches the K_0 stress path for a de-structured material. Heymann (1998) investigated a high porosity chalk from Suffolk and identified a dramatic reduction in volumetric stiffness after yielding under isotropic loading. The average yield stress was 2.9MPa and the reduction in volume was approximately 10%.

2.10.3 Behaviour under shear and effective strength parameters

Undrained triaxial tests by Kågeson-Loe *et al.* (1993) on low-medium density intact chalk from Butser Hill, Hampshire are shown on Figure 2-20 and illustrate the dependence of shearing behaviour on initial confining stress. Samples consolidated to relatively low effective confining stresses of 1.5MPa (test a) manifested brittle failure after an axial strain of <0.1%, with a sudden drop in deviator stress. Similar behaviour was observed by Jardine *et al.* (1985)

in tests on intact chalk from Northfleet, Kent. Consolidation to higher confining stresses (tests b and c) causes isotropic yielding and leads to a contractive phase during shear. The behaviour is similar to an un-cemented granular material, with post-peak strain softening. At confining stresses well above the yield isotropic stress (test d), loss of bonding occurs during consolidation and the material strain hardens during shearing towards ultimate failure.

The results of several studies indicate that isotropic stresses well in excess of the yield stress are required to cause widespread bond breakage in chalk. Strain localisation has been observed in high porosity samples in the form of numerous randomly orientated failure planes, even at a confining stress of 10MPa, with parts of the coccolith fabric remaining intact in some cases. Isotropic stresses in excess of 30MPa, i.e. test d, were required before the specimens deformed in a continuous fashion and barrelling was observed (Leddra and Jones, 1990, Petley *et al.*, 1993, Heymann, 1998, Clayton *et al.*, 2002).

Very little information is available in the literature which describes the change in stiffness during shear for intact samples. Figure 2-18 shows stiffness generally reducing with axial strain in undrained triaxial tests, with the exception of CH1 and CH4, conducted at low stress levels, where an increase of stiffness with strain was shown initially, associated with the closure of micro-cracks (Clayton and Heymann, 2001). As seen previously, structure increases stiffness; comparison of the structured sample CH5 (consolidated to a stress level far below the isotropic yield stress) and the pre-yielded specimen CH14 (whose initial p' was well in excess of the isotropic yield stress) indicates a five-fold reduction in stiffness. Samples with low levels of bonding, post de-structuration, were shown by Clayton and Heymann (2001) to be influenced by the mean effective stress while intact samples were less sensitive to changes in p'.

Lord *et al.* (2002) indicate that, for massive chalks, cohesion, c' can vary from 100kPa to greater than 2MPa, while φ' can range from 36° to 42° with a mean of 39°. For low-medium density material, φ' varies from 38 to 42° with c' ranging from 75 to 130kPa. The critical state strength obtained by Leddra and Jones (1990) for samples de-structured prior to shearing fell well below this with $c'=0$ and $\varphi'=30.5°$.

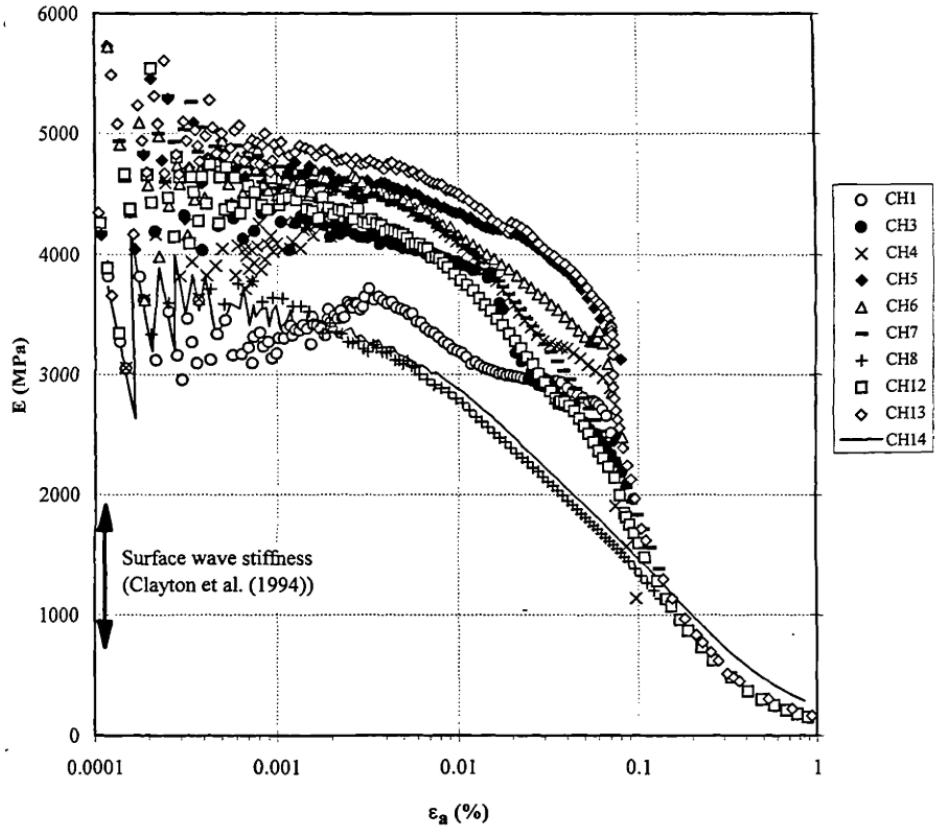


Figure 2-18 Stiffness of chalk during undrained shearing in triaxial and surface wave from field testing methods (E=3G assumed for geophysical data) (Heymann, 1998)

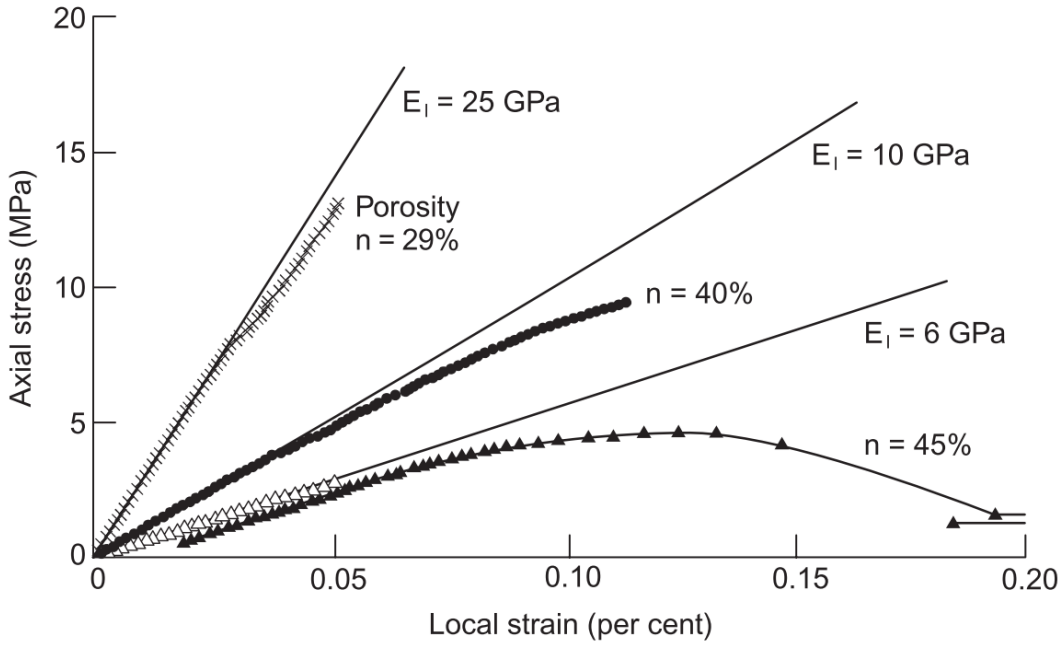
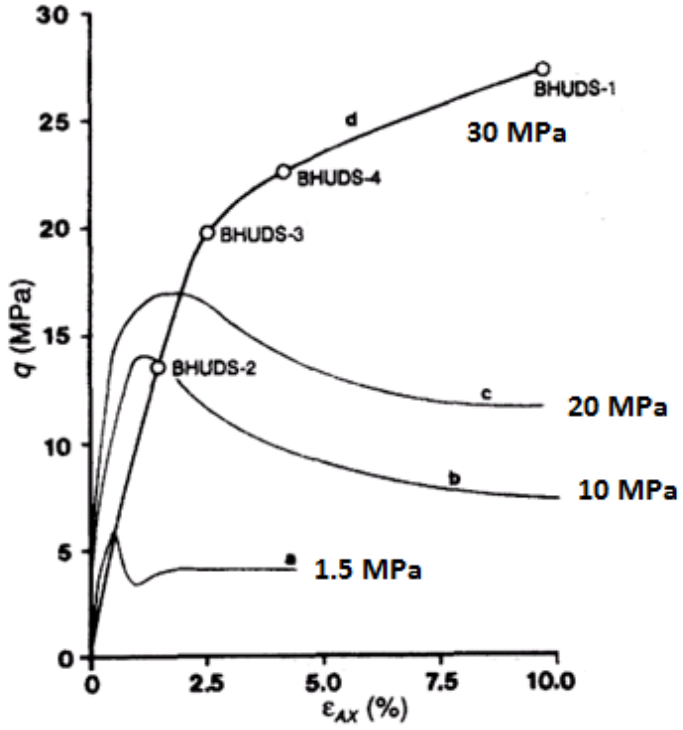
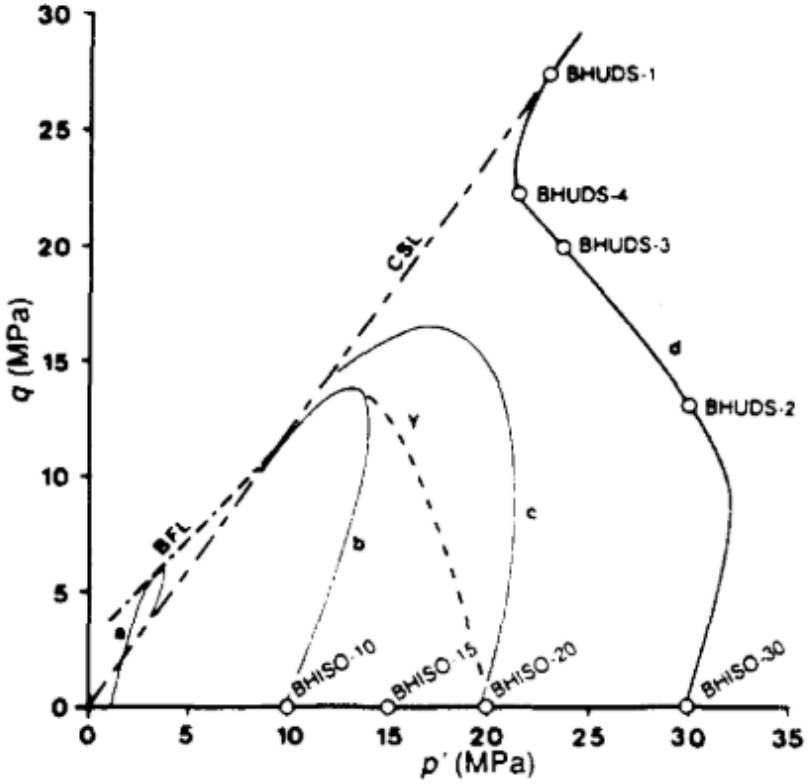


Figure 2-19 Stress-strain curves for low, intermediate and high density chalks in uniaxial compression (Matthews and Clayton, 1993)



(a)



(b)

Figure 2-20 Undrained triaxial tests adapted from Kågeson-Loe et al. (1993) on high porosity Butser Hill chalk consolidated to different mean effective stresses a) stress-strain behaviour b) stress paths Note: numbers indicate initial confining stress in MPa

2.11 Behaviour of remoulded chalk

2.11.1 Formation & Occurrence

The high porosity of low-medium density chalk leads to it manifesting liquidity indices, when saturated, close to unity. As expected, chalk has low remoulded shear strength and becomes a "slurry" or "putty" when subjected to high energy from shearing, vibration or crushing. The susceptibility of chalk to crushing was shown by Clayton (1990) to be directly related to its porosity and density; at its maximum porosity it can be crushed with finger pressure becoming a paste, as interstitial water is released (Clayton *et al.*, 2002). Figure 2-4 showed that when crushed, chalk comprises predominantly silt and clay sized particles, with a minimum particle size similar to the size of the constituent coccoliths.

Chalk putty can form naturally in discontinuities within the chalk mass, in areas which have undergone shear stress, tectonic stress or landslides. Freeze/thaw action can also cause a disaggregation of massive chalk into cobbles and boulders within a putty matrix. Putty is commonly formed in the course of engineering operations, such as foundations and tunnelling. Major earthworks projects involve vibration, grinding and crushing leading to putty formation and issues with trafficability, handling and placing. Chalk has also been known to mobilise into a slurry around reservoir wells, leading to a lack of support for the cased well. Dynamic percussion damage during pile driving causes de-structuration and crushing of hollow $CaCO_3$ particles beneath pile tips, forming a low strength putty that spreads along the pile and limits drastically the radial effective stresses and shear resistances that can act on the pile shaft; Hobbs and Atkinson (1993), Lord *et al.* (2002). If not anticipated and controlled, chalk putty formation can have a dramatic effect on an engineering project (Addis and Jones, 1990).

Although it is a problematic engineering material, the behaviour of remoulded or putty chalk has been investigated in only a limited number of studies (Clayton, 1978, Razoaki, 2000, Bundy, 2013, Borges, 2014). Each of the studies reported in the literature employed a different method of sample preparation. In this thesis, "putty chalk" refers to chalk broken down into its finer constituents by compaction, either in the field or in the laboratory. The term "slurry" chalk is used to refer to dry chalk ground to a finer particle size and mixed with water until the liquid limit or desired moisture content is reached. As discussed in Section 2.5, high porosity chalks tend to break down to a uniform material with particle sizes which range from 0.5 to 10 μm, with the resulting grain size distribution affected by the method of preparation.

2.11.2 Behaviour of unaged chalk slurry

Oedometer tests conducted by Clayton and Matthews (1987) on chalk slurry are shown in Figure 2-21, where the labels show the initial intact water content/porosity prior to grinding and slurry formation. Similar to sands, for low stress levels, void ratio at any given stress level is a function of the initial void ratio of the material and a series of non-coincident NCLs results. A unique LCC, such as was shown on Figure 2-13 and is associated with crushing of the particles, was not approached, even for high porosity samples at stress levels of almost 1MPa.

The effective angle of shearing resistance, φ' for remoulded material from triaxial tests is generally thought to lie between 29 and 34° with cohesion, c' in the range of 0 to 10kPa (de Raguenel, 1973, Lake, 1975, Clayton, 1977, Clayton, 1978, Bundy, 2013). The most comprehensive study of chalk slurry reported to date was by Razoaki (2000). After preparation, samples of medium density Newhaven chalk from East Sussex were placed in a specially made oedometer for four hours under a normal stress of 87kPa. The subsequent isotropic compression tests show a relatively straight NCL for stresses up to 600kPa (Figure 2-22). Razoaki's tests indicated that the behaviour of unaged chalk slurry during shear is similar to that of a medium dense granular material or a low plasticity silt (e.g. Hyde *et al.*, 2006). During drained tests, samples contracted initially prior to reaching the characteristic point where dilation is initiated and increases until a peak stress ratio is attained. The peak strength ratios attained correspond to a φ' of 31.2°. At critical state the value of M_{tc} was equal to 1.22 equivalent to φ' of 30.5°. Figure 2-23 shows typical behaviour during undrained triaxial compression tests from Razoaki (2000). The undrained tests all contracted initially prior to showing a tendency to dilate at the phase transformation point. A higher critical state stress ratio was achieved in the undrained tests than observed during drained tests suggesting the paths are defining a Hvorslev-like surface on the dry side of critical state and would have reached the same ratio with further shearing.

2.11.3 Gains in strength with time

Lord *et al.* (2002) report that compacted chalk in the field can stabilise and increase in strength with time. Stabilisation and increase in the strength of putty chalk has also been used to explain the strong pile set-up, or increase in capacity with time, observed in tests on driven piles. Lord *et al.* (2002) attributed time-dependent gains in strength to i) consolidation following dissipation of excess pore water pressures and/or ii) the release of calcium carbonate during compaction which can grow over the grain contacts and provide additional cement.

Clayton and Matthews (1987) compared SEM images of compacted Senonian chalk fill before and after compaction and noted the presence of aragonite crystals in the compacted fill, presumably re-deposited from the solution of calcite particles in the remoulding process. The authors note surprise at the results particularly as aragonite, a high temperature polymorph, would be expected to break down rapidly to calcite before it could be seen in an SEM image. As discussed in Section 2.5, chalk is only moderately thixotropic. Investigations of strength increases in remoulded chalk are discussed further below.

Dissipation of pore water pressures

The permeability of intact chalk is sufficiently high for it to be considered as practically free draining in most engineering applications (Section 2.7). However, compaction and puttification can produce fines and close discontinuities which could reduce the permeability. Despite issues with handling and placing of chalk putty, Clayton (1978) reports that the rate of consolidation of re-compacted crushed chalk is relatively rapid with c_v values of 10-70 m^2/year, far higher than those observed in most clays. Bundy (2013) gave permeability values from laboratory tests on chalk slurry in the range 2.5-13 x 10^{-9} m/s at confining pressures up to 400kPa, consistent with the ranges for structureless chalk given in Section 2.7.

Changes in compressibility characteristics

Razoaki (2000) investigated time dependent shearing behaviour by subjecting samples to drained and undrained ageing. Drained ageing involved the chalk being "kept under constant load for the entire ageing period. During undrained ageing the chalk was "compressed for a few hours, sealed, waxed and aged" under zero load. The effect of *drained* ageing on the compression paths of three samples aged for 0, 28 and 120 days is shown on Figure 2-22. Ageing increases pre-yield stiffness and allows the state to move to the right of the un-aged compression line and stretch out the "structure permitted space" as defined by Leroueil and Vaughan (1990) (Figure 2-16). Both the pre-yield stiffness and the yield stress increased with age, with ageing also increasing the slope of the post-yield compression path. Both aged specimen paths collapsed back on the normal compression lines after yield.

Changes in stiffness

The drained triaxial tests by Razoaki (2000) showed a similar qualitative stress-strain response to the unaged samples. An increase in small strain stiffness was observed on the order of 20% after 28 days and 35% after 56 days, attributed to the increase in density obtained during

drained ageing. The undrained triaxial compression tests on samples subjected to drained ageing, shown in Figure 2-24, indicate further the effect of age on the initial stiffness and the undrained stress path. The initial, almost vertical, portion of the stress path of the 120 day test is credited to higher small strain stiffness, leading to expansion of the Y_1 yield surface with time. When the structure collapses, the material contracts and then phase transforms in a similar manner to the unaged sample. The behaviour shown is typical of bonded soils and intact chalk which are characterised by the presence of "double-yield" points (e.g. Figure 2-17 (d)). Post initial yield, the stress path behaved in a similar manner to the unaged sample. This suggests the effect of increased stiffness is related to increased structure and cementation within the sample, which is destroyed with continued shearing.

No increase in structure permitted space and little difference was observed between the unaged and aged tests which were subjected to undrained ageing. This indicates that the development of structure is a creep related phenomenon that occurs during consolidation and/or drained ageing and is not wholly related to internal re-cementing of chalk. The results presented by Razoaki form a comprehensive and interesting study of chalk slurries. However, the sample preparation method, of forming the samples in the consolidometer, resulted in over-consolidation of the reconstituted samples used to different degrees and may have led to some unintended early age re-stabilisation of the properties.

Bialowas *et al.* (2016) also report increases in shear stiffness with time, measured using bender elements incorporated within a triaxial cell, for air dried, crushed and reconstituted chalk from the Author's test site at St. Nicholas-at-Wade, Kent described in Chapter 6. Under maintained load tests, a time dependent increase in small strain stiffness was observed which reached a maximum of 20% over 20 days.

Changes in shear strength

Early work by Clayton (1977) investigated the change in effective strength of triaxial samples with time at constant water content and suggested some slight recovery of cohesion with time (Figure 2-25). The effective cohesion at peak strength of the reconstituted chalk increased from 3 to 10kPa over a period of approximately 80 days, reaching a stable value thereafter up to a time period of almost a year. The change in c' was interpreted by assuming that φ' does not increase with age. This may not be a valid assumption considering research by e.g. Lade and Overton (1989) which has shown that cement content causes an increase in both the cohesive and frictional components of strength. At large strains, Razoaki (2000) showed

that the shearing behaviour of the aged and unaged samples reached the same q/p′ ratio at critical state. Further tests are required to investigate these trends using a range of consolidation stresses and sample ages.

2.12 Interface shear behaviour

Interface roughness is known to have a significant effect on the frictional resistance available between sand and steel and the magnitude of dilation developed during interface failure. The interface shear strength between sand and different construction materials is usually thought to be lower than the soil-soil shear strength and to reduce with the roughness of the interface; Potyondy (1961).

Few interface shear tests on samples of chalk are reported in the literature. Ziogos *et al.* (2016) carried out a range of chalk-steel interface tests using a torsional interface shear tester (IST) device on samples of high density Flamborough chalk, using interfaces with average centre-line roughness values, R_a which varied from 0.4 to 34μm and stress levels which reached up to 1MPa. The values of δ'_{peak} and δ'_{ult} increased linearly with R_a, and did not appear to reach a plateau, as was observed in comparison tests on sandstone and has been seen in other studies on sands (e.g. Jardine *et al.*, 1993, Barmpopoulos *et al.*, 2010). In the tests reported by Ziogos *et al.* (2016), both δ'_{peak} and δ'_{ult} are affected by increasing normal stress level. At normal stress levels less than about 300Pa, δ'_{ult} was equal to approximately 30.5°, confirming results obtained by Le et al. (2014), and falling towards the lower end of the critical state φ' range for remoulded chalk discussed previously, of between 29 and 34°.

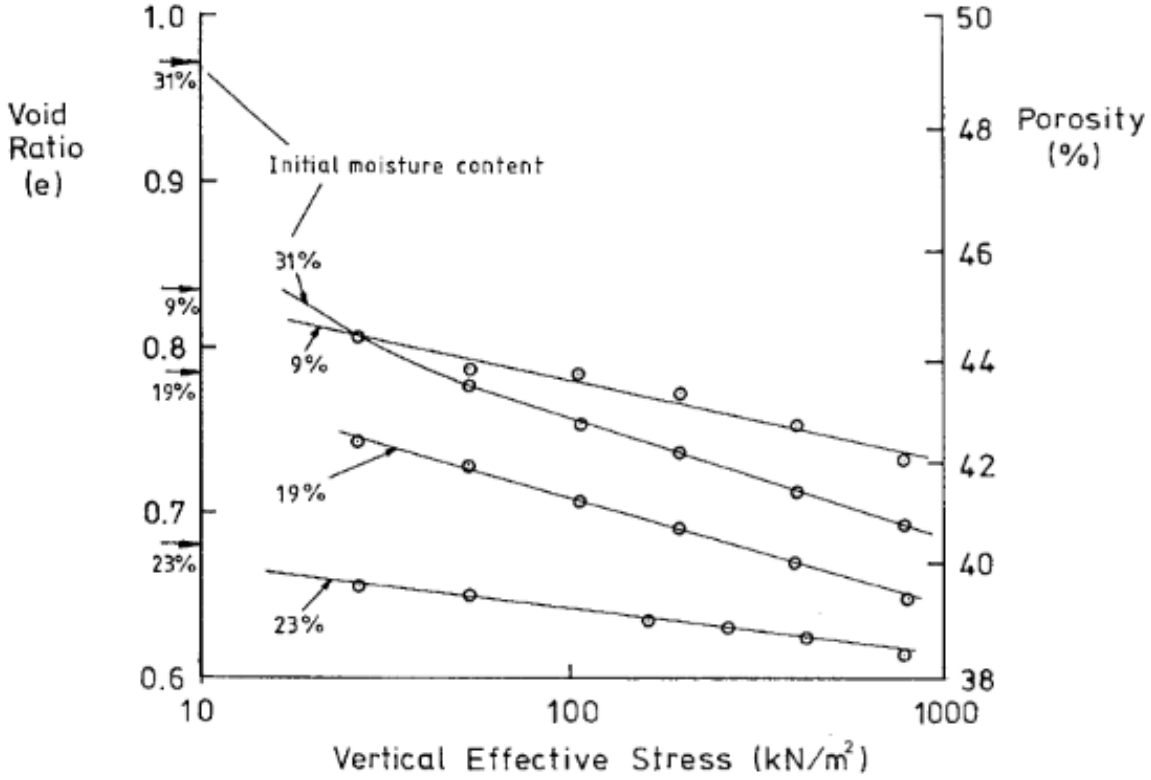


Figure 2-21 Compression of chalk slurry in the oedometer test (Clayton and Matthews, 1987)

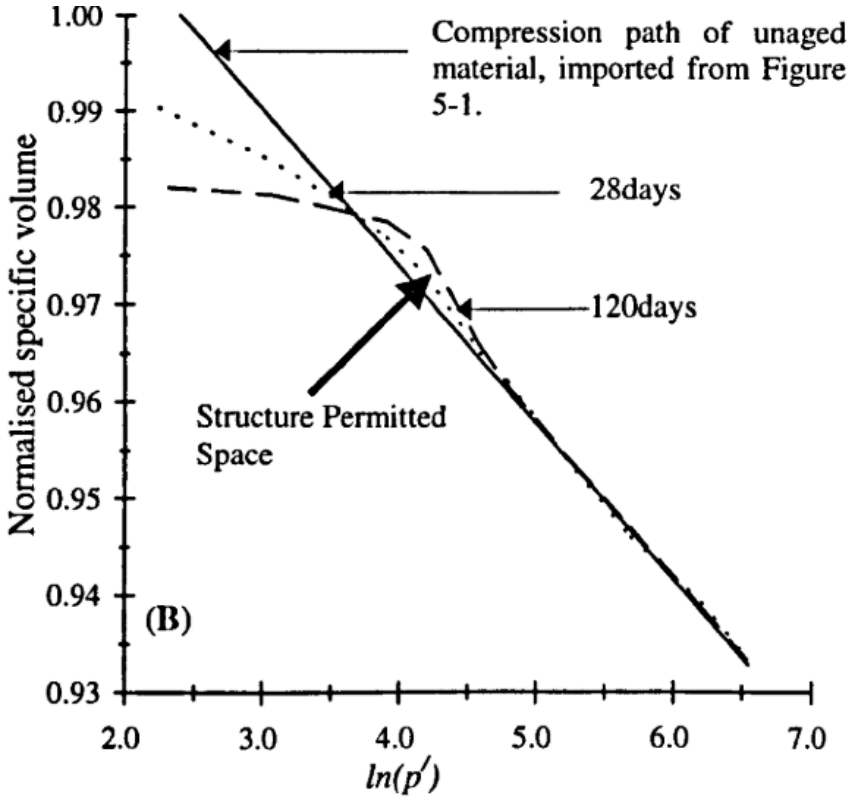


Figure 2-22 Compression paths for aged and unaged chalk slurry (Razoaki, 2000)

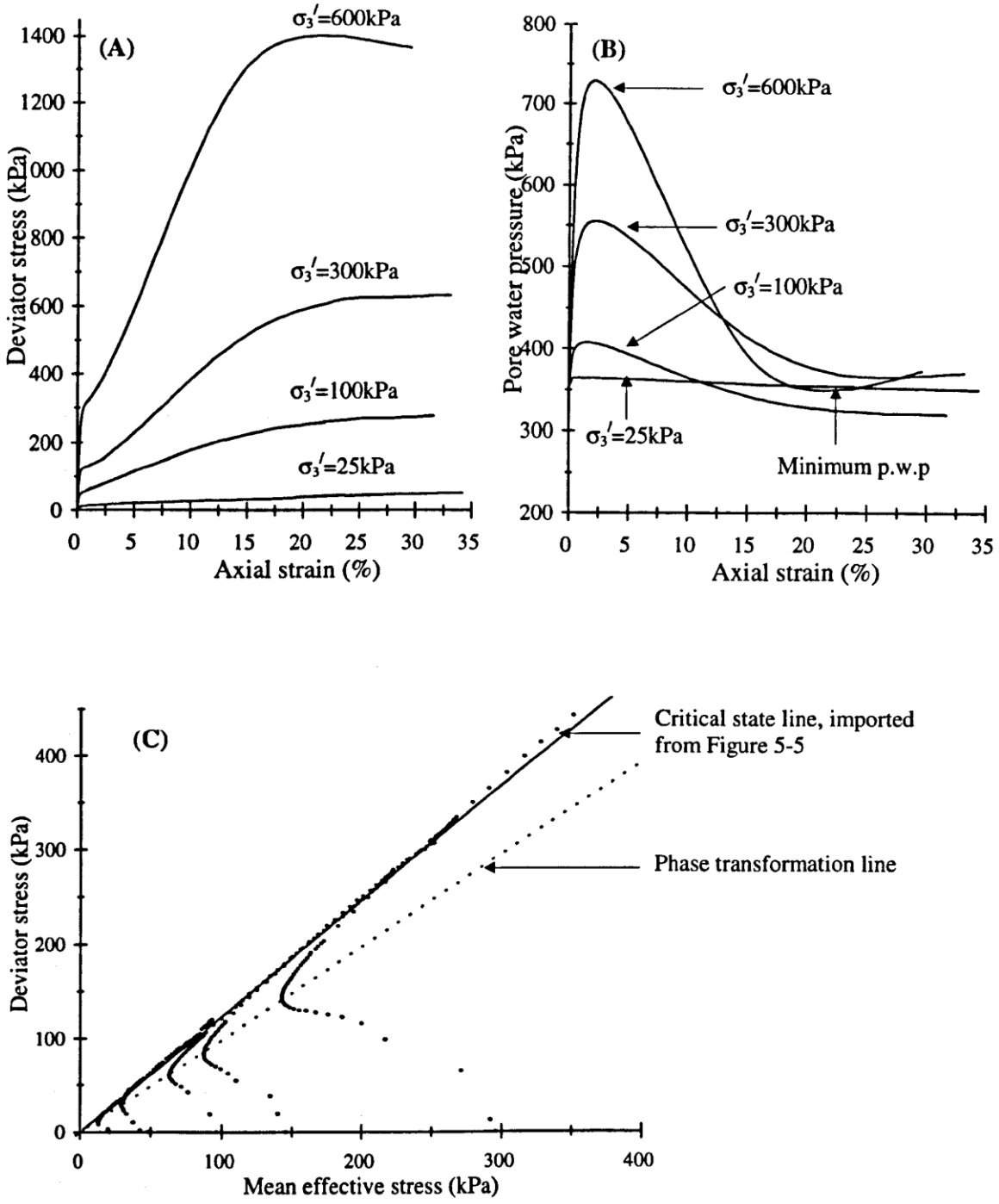


Figure 2-23 Undrained triaxial compression tests on chalk slurry (Razoaki, 2000)

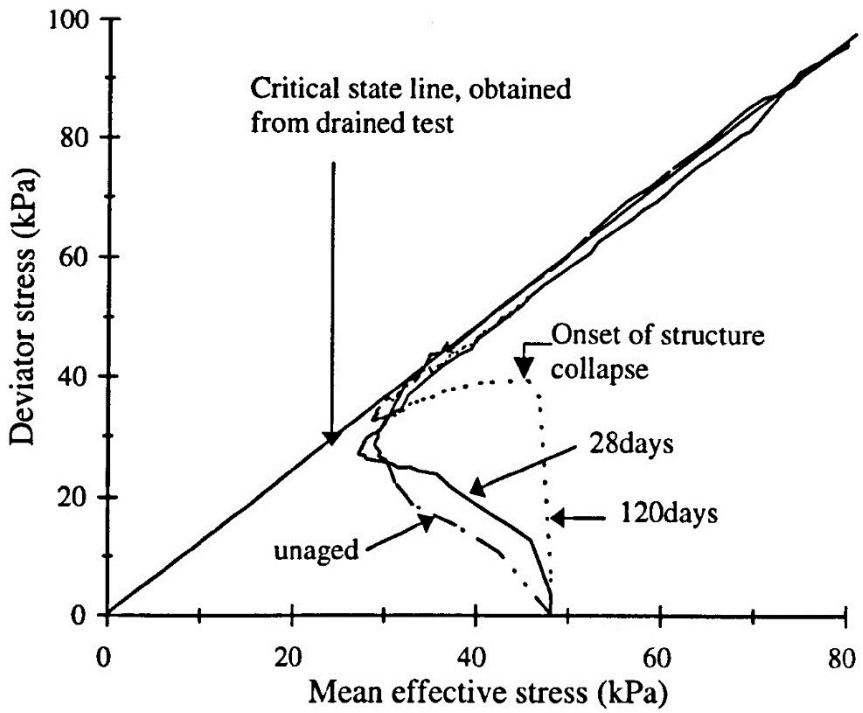


Figure 2-24 Undrained triaxial compression stress paths showing the effect of ageing on undrained stress path for chalk slurry (Razoaki, 2000)

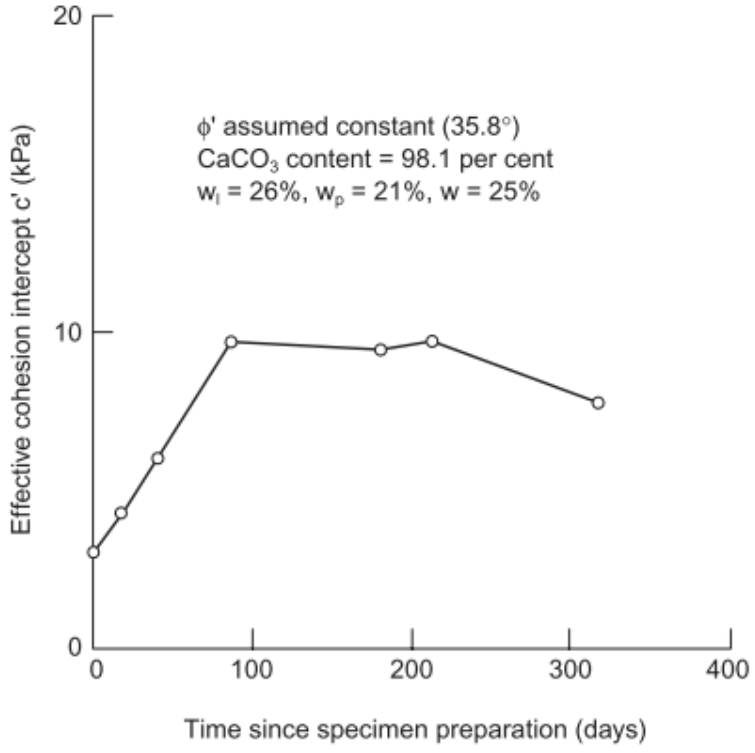


Figure 2-25 Change in effective stress at constant water content for remoulded white chalk (Figure taken from Lord et al., 2002)

2.13 Summary of chalk behaviour

This chapter has presented an overview of the occurrence, properties and behaviour of intact and remoulded chalk which is encountered at both of the Author's chalk study sites, described in subsequent chapters. The following summary points are noted:

- Chalk is widespread across Northern Europe and is the focus of several ongoing infrastructure and renewable energy projects;
- The Chalk is predominantly a soft, white, pure, low-medium density material composed almost entirely of calcium carbonate. A number of depositional and post depositional processes have resulted in a material with properties which can vary widely geographically and stratigraphically;
- The fracture style, frequency and discontinuity aperture control the mechanical behaviour, mass permeability and mass compressibility of the *in-situ* chalk mass. *In-situ*, chalk lies close to full saturation. Open or partly open discontinuities are air-filled above the water table and water filled below the water table;
- Engineering classification is complicated by the apparent uniformity of the material. The current classification system classifies chalk by intact dry density and assigns chalk grades based on discontinuity spacing, pattern and aperture;
- Chalk is a dually porous material due to the high porosity micro-fabric combined with a network of discontinuities. In the field, permeability is sufficiently high for it to be considered as a free draining material. Cone penetration test profiles are typified by relatively high cone resistance and friction sleeve values combined with the build-up of significant pore water pressures (in excess of 2MPa) which dissipate almost immediately when penetration is halted;
- The behaviour of intact chalk lies between a hard soil and a soft rock. Bonding, cementation or structure, typical of cemented soils and soft rocks, dominates the behaviour of intact chalk and plays a smaller role in the behaviour of aged remoulded material;
- The high porosity which typifies white chalk, combined with its high natural moisture content, close to the liquid limit, and high degree of saturation allows it to degrade rapidly under compressive stresses to a "slurry" or "putty" material. Particles tend to break down to sizes similar to the size of the individual coccolith plates;

- Remoulded slurry chalk and chalk which has had bonding partially or completely destroyed at high confining pressures behaves in a similar manner to a granular soil or a low plasticity silt, where behaviour is governed by initial state and intrinsic properties. The latter can be defined by the state parameter within the critical state framework;
- Samples of chalk slurry aged under load in the triaxial cell and subjected to triaxial compression tests showed increases in "structure permitted" space and initial stiffness, associated with drained creep and the development of structure and possibly cementation within the sample, which is subsequently destroyed with further shearing.

CHAPTER 3

Evaluating the axial capacity of displacement piles in chalk

3.1 Introduction

The understanding of the behaviour of displacement piles in sands and clays has developed in several research centres following a number of experimental test programmes, in the late 1980s and early 1990s, which highlighted the scientific weaknesses of the standard industry methods. The understanding of the behaviour of displacement piles in chalk has lagged behind the developments made in sands and clays and is becoming a significant area of research interest with the dual expansion of offshore windfarms in Northern Europe and the advancement of several onshore infrastructure projects which will be founded in chalk.

This chapter first reviews the advances made in understanding of the behaviour of displacement piles in sands and clays and the axial design methods available in those materials. The current position regarding displacement piles in chalk is then evaluated, drawing on a critical review of published and unpublished pile test data. The outcomes highlight the areas requiring significant further research and frame the experimental aims of the Author's research, which is presented in subsequent chapters. Section 3.4.1 was published previously (in part) by Buckley *et al.* (2018a).

3.2 Axial behaviour of piled foundations

3.2.1 Axial pile testing & interpretation

Static load tests to failure are the most accurate means of determining pile capacity. Loading is applied in tension or compression, using either the Maintained Load (ML) or

Constant Rate of Penetration (CRP) procedures, until sufficient displacement has been generated to mobilise the ultimate capacity. The capacities developed depend on the displacement rate at which the pile fails; slow ML tests give lower resistances than fast CRP tests. The ultimate axial capacity of a pile foundation, Q_{tot} or the load at the pile head which will cause it to fail, is the sum of the total ultimate shaft resistance, Q_s, and the ultimate base resistance, Q_b.

$$Q_{tot} = Q_s + Q_b \quad 3\text{-}1$$

Pile capacity is traditionally defined at a pile displacement equivalent to 10% of the pile diameter (Vijayvergiya, 1977, Yang *et al.*, 2016). During a static pile load test, Q_{tot} is measured at the pile head. In a tension test, Q_{tot} is equal to the shaft load, Q_s, less the weight of the pile itself and any internal soil and any contribution from reverse end bearing. In a compression test, Q_{tot} includes contributions from both the base and shaft, which can only be separated using strain gauges or load cell instrumentation along the shaft. Studies which include tests on fully instrumented displacement piles are rare and in practice most piles do not have full instrumentation (Fellenius, 2002). Standard electrical resistance bonded and welded strain gauges are prone to damage during installation and may require protective channels which affect the pile shape and the bending stiffness. Recent pile testing programmes have used fibre Bragg grating sensors as an alternative, which do not require protective channels (Doherty *et al.*, 2015, Byrne *et al.*, 2017).

The interpretation of ultimate base resistance of driven piles during a static load test can be affected by residual axial compression loads generated during driving. As shown schematically on Figure 3-1, any residual loads remaining after driving are balanced by residual shaft stresses close to the pile tip. The effect of residual loads is greatest where large base resistances are generated during driving, as in sands. Ignoring residual loads in test interpretation, e.g. by zeroing strain gauges after installation, can lead to under-estimation of base loads and over estimation of shaft resistance and distorted profiles of shear stress (Chow, 1997). Methods to estimate residual stresses in the field were suggested by Hunter and Davisson (1969) and Briaud and Tucker (1984). Residual stresses can also have a substantial effect on the pile response under dynamic conditions (Simons, 1985) and methods to account for residual stresses have been incorporated into pile driving analyses; e.g. Rausche *et al.* (1996), Randolph (2008).

3.2.2 Pile shaft & base resistance

As outlined in later sections, the local shaft capacities of piles driven in sands and clays are governed by an effective stress Coulomb interface shaft failure criterion, where the ultimate unit shaft shear stress, τ_f can be calculated from the product of the radial effective stress acting on the pile shaft at failure and the coefficient of friction, $\tan\delta'$, where δ' is the peak or ultimate effective stress angle of interface shearing resistance between the pile and soil. At each layer within a soil profile:

$$\tau_f = \sigma'_r \tan\delta' \qquad 3\text{-}2$$

The ultimate shaft resistance is calculated over the pile penetration length, L_p by summing the product of the unit shaft resistance in each layer, with depth, z, integrated over the surface of the pile:

$$Q_s = \pi D \int_0^{L_p} \tau_f \, dz = \pi D \int_0^{L_p} \sigma'_r \tan\delta' dz \qquad 3\text{-}3$$

For closed-ended piles, the ultimate base resistance is the maximum stress mobilised on the pile base, $q_{b,0.1D}$ multiplied by the gross or total area of the pile base, A_b:

$$Q_{b,0.1D} = A_b q_{b,0.1D} = \pi \frac{D^2}{4} q_{b,0.1D} \qquad 3\text{-}4$$

Where $Q_{b,0.1D}$ is the base capacity achieved when the displacement is equal to 10% of the pile diameter.

3.2.3 Considerations for open-ended tubular piles

When an open-ended pile is driven, an internal soil column, or soil plug, forms inside the pile. The external forces acting on the pile during "unplugged" and "plugged" penetration are illustrated on Figure 3-2. Unplugged or "fully coring" pile penetration occurs when the soil column inside an open-ended pile remains stationary while the pile is moving. "Plugged" penetration occurs when the soil inside the pile moves downwards at the same rate as the pile. "Partially plugged" penetration occurs when the internal soil column moves downwards with, but at a slower rate than, the pile. The degree of plugging can be quantified by the Incremental Filling Ratio (Paikowsky *et al.*, 1989) defined as:

$$IFR = \frac{\Delta H_p}{\Delta z} \qquad 3\text{-}5$$

where ΔH_p is the change in height of the soil plug during an increment of penetration Δz. The IFR is equal to unity when the pile is fully coring, and zero when the pile is fully plugged. Values of IFR between 0 and 1 indicate partially plugged penetration. Large diameter piles generally penetrate in an unplugged manner during pile driving due to the inertia of the soil column, which contributes to the overall driving resistance; Rausche and Hussein (2000) however plugging can still occur during static loading.

For open-ended tubular steel piles the shaft capacity in compression can occur on both the internal and external areas and Q_s can be further described as the sum of the shaft capacity acting on the external and internal surface areas:

$$Q_s = \pi\left(D\int_0^{L_p}\tau_{f,ext}\,dz + D_i\int_0^{H_p}\tau_{f,int}\,dz\right) \quad 3\text{-}6$$

Where $\tau_{f,ext}$ and $\tau_{f,int}$ are the external and internal shaft shear resistance, H_p is the height of the internal soil plug, and D_i is the internal pile diameter. Unplugged piles are known to displace much lower volumes of soil than closed-ended piles and have lower base resistances (e.g. Randolph, 2003, Xu *et al.*, 2006, Gavin and Lehane, 2007). Field load tests were performed by Salgado *et al.* (2002) on both instrumented closed-ended and instrumented open-ended double-walled piles installed in sand at a test site on the Pigeon River, Indiana. The latter were used to separate the resistance contributions from the plug, annulus and the shaft. Their results indicate that, for sands, the plug contributes to the static base capacity, for piles which penetrate in both a plugged and an unplugged manner. They showed that the base resistance of an open-ended pile was 36% lower than the equivalent closed-ended pile and the plug resistance was 30% of the annular resistance. For open-ended steel piles, the base capacity mobilised under the annulus can be defined as:

$$Q_{ba,0.1D} = \pi\frac{D^2 - D_i^2}{4}q_{ba,0.1D} = A_{ann}q_{ba,0.1D} \quad 3\text{-}7$$

where $q_{ba,0.1D}$ is the end bearing under the annulus at a displacement of 10% of the pile diameter. However, it is difficult to separate contributions from the internal shaft resistance, plug resistance and annular resistance without further instrumentation, such as instrumented double-walled pile tests, analyses using finite elements (e.g. Joseph *et al.*, 2017) or other numerical means. In routine design, capacity prediction methods generally use simplifications to account for the different contributions to end bearing outlined above, which are discussed further in Section 3.3.

3.2.4 Time effects on capacity

As well as being affected by the rate of testing to failure, the capacities of displacement piles may be substantially different after extended periods following driving. Capacity changes can be best observed when static pile tests are conducted on previously untested "virgin" piles at different times after driving. Dynamic load tests (Chapter 4) conducted on the last driving blow are often utilised to provide a reference zero age capacity, as are early age static loading tests. Beneficial ageing effects have been observed previously in the field during tests on driven steel and concrete piles founded in sands and clays e.g. Karlsrud and Haugen (1986), Skov and Denver (1988), Jardine *et al.* (2006), Karlsrud *et al.* (2014).

3.2.5 Axial cyclic loading

Foundations are often subjected to repeated or cyclic loading under a wide range of loading rates. Wind and wave loading cycles are applied to offshore piles during storms, as well was millions of cycles from turbine blades (Jardine *et al.*, 2012). The effects of relatively slow wave load cycling can be investigated in field or model pile tests, or through numerical analysis developed from soil element test behaviour.

Regular cyclic loading is often characterised in terms of the average and cyclic components defined in Figure 3-3, normalised by the appropriate static pile capacity, Q_{ref}. Where one-way axial cyclic loading is applied, a shaft utilisation ratio can also be defined where $UR = Q_{max}/Q_{ref}$. Cyclic axial loading tests on piles driven in clays and sands show trends that have been classified as Stable, Metastable or Unstable (Karlsrud *et al.*, 1986, Poulos, 1988, Jardine and Standing, 2000, Tsuha *et al.*, 2012, Jardine *et al.*, 2012). Following earlier test programmes on clays by NGI, notably at the Haga site (Karlsrud *et al.*, 1986), Jardine & Standing (2012) and Rimoy *et al.* (2013) applied working definitions in their interpretation of open tube piles driven in dense sand at Dunkirk that referred to both possible numbers of cycles N and rates of permanent cyclic displacement accumulation, with:

- **Stable (S):** No failure within 1000 cycles. Pile displacements accumulate slowly over hundreds of cycles and tend to stabilise with cycling, remaining below 0.01D and showing rates of change of less than 1mm/1000 cycles and negligible loss of cyclic stiffness. Cycling in this range does not affect foundation serviceability or reduce operational shaft capacity;
- **Unstable (US):** pile displacements accumulate rapidly leading to cyclic failure at N<100 with either accumulated displacements greater than 0.1D or a rate of

accumulation of displacement greater than 1mm/10 cycles. The foundations may become unserviceable and potentially suffer marked reductions in operational shaft capacity;

- **Metastable (MS):** transitional behaviour where cyclic loading may lead to failure with $100 < N < 1000$ and pile displacements developing at moderate rates over tens to hundreds of cycles without stabilisation. Serviceability and operational shaft capacity losses depend on numbers of cycles applied. Displacements of 0.01D to 0.1D develop at rates between 1mm/1000 cycles and 1mm/10 cycles.

Cyclic stability interaction diagrams, such as the one shown in Figure 3-4, demonstrate how the number of cycles, N and the parameters Q_{cyc}/Q_{ref} and Q_{mean}/Q_{ref} interact in determining the response of a pile to uniform applied cyclic load. The top-left to right-bottom diagonal in this diagram represents the static failure conditions, where UR is equal to 1. Jardine & Standing (2012) checked their piles' post-cyclic operational tension capacities by carrying out static tension tests to failure soon after the cyclic loading test.

A range of procedures exist to address non-dynamic axial cycling for piles driven in sands and clays. Jardine *et al.* (2012) and Andersen *et al.* (2013) set out approaches involving empirical global methods, local (t-z) analyses based on soil element or instrumented pile tests and numerical techniques based on advanced constitutive models. Whilst the latter provide potentially the most powerful tools, difficulties arise in full implementation, see for example Buckley (2014). High quality cyclic load tests along with supporting site characterisation are required, as a first basis, on which potential predictive measures can be assessed and calibrated.

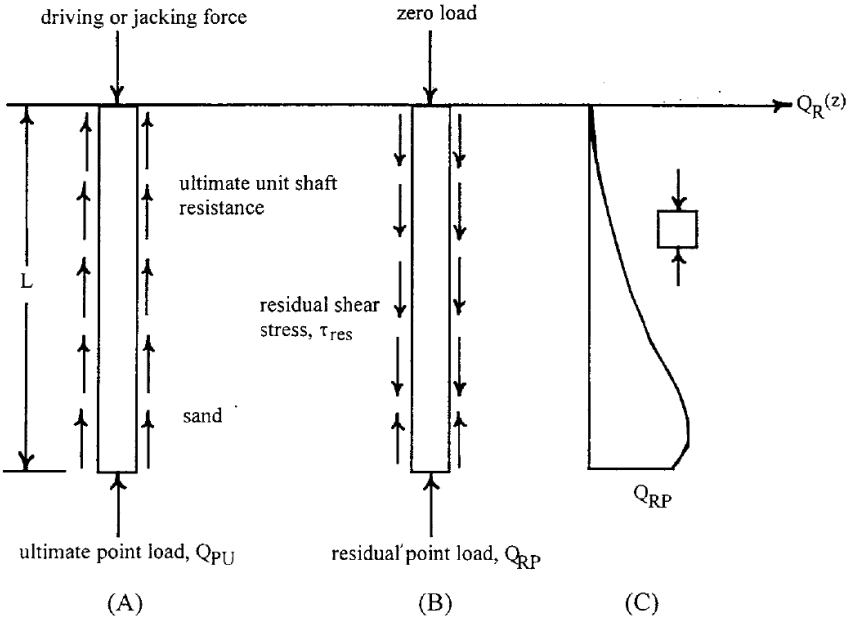


Figure 3-1: (a) A pile in sand under compression load (installation process) (b) residual stresses at the end of the compression test (c) variation of residual load with depth (Alawneh and Malkawi, 2000)

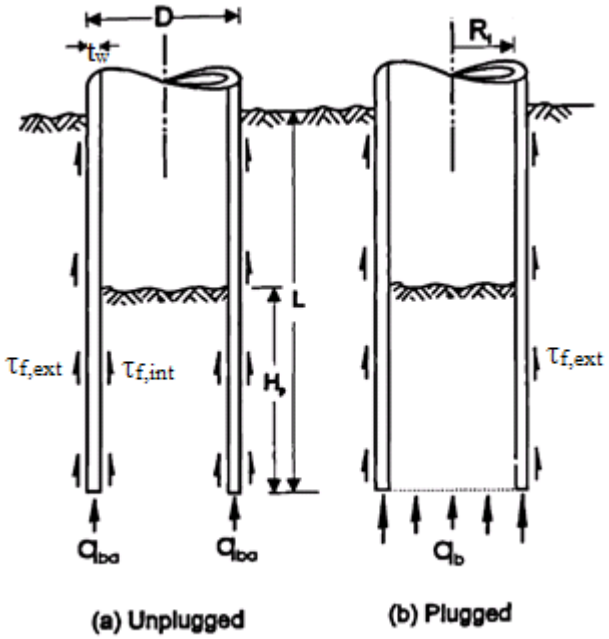


Figure 3-2: Shaft capacity components in open-ended piles (a) unplugged or fully coring mode (b) plugged mode (adapted from Chow, 1997)

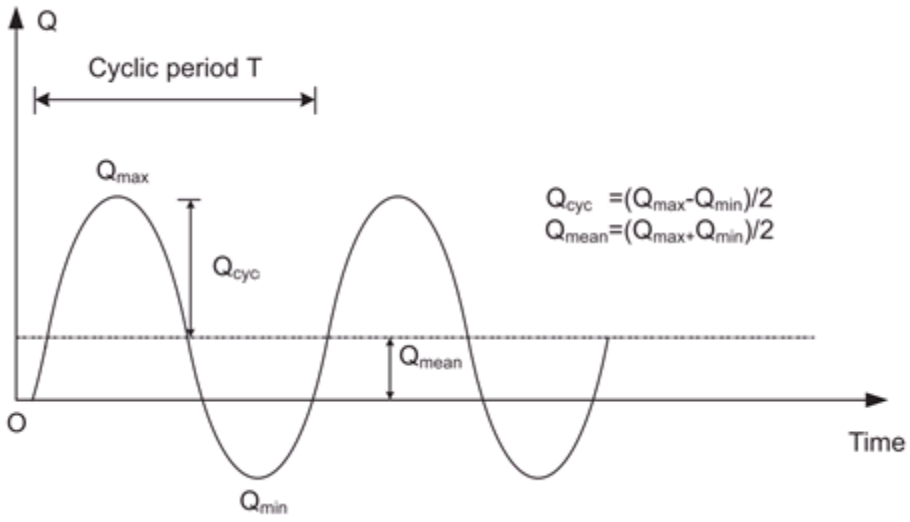


Figure 3-3: Schematic illustration of the definitions of Q_{mean} and Q_{cyc} (adapted from Jardine and Standing, 2012)

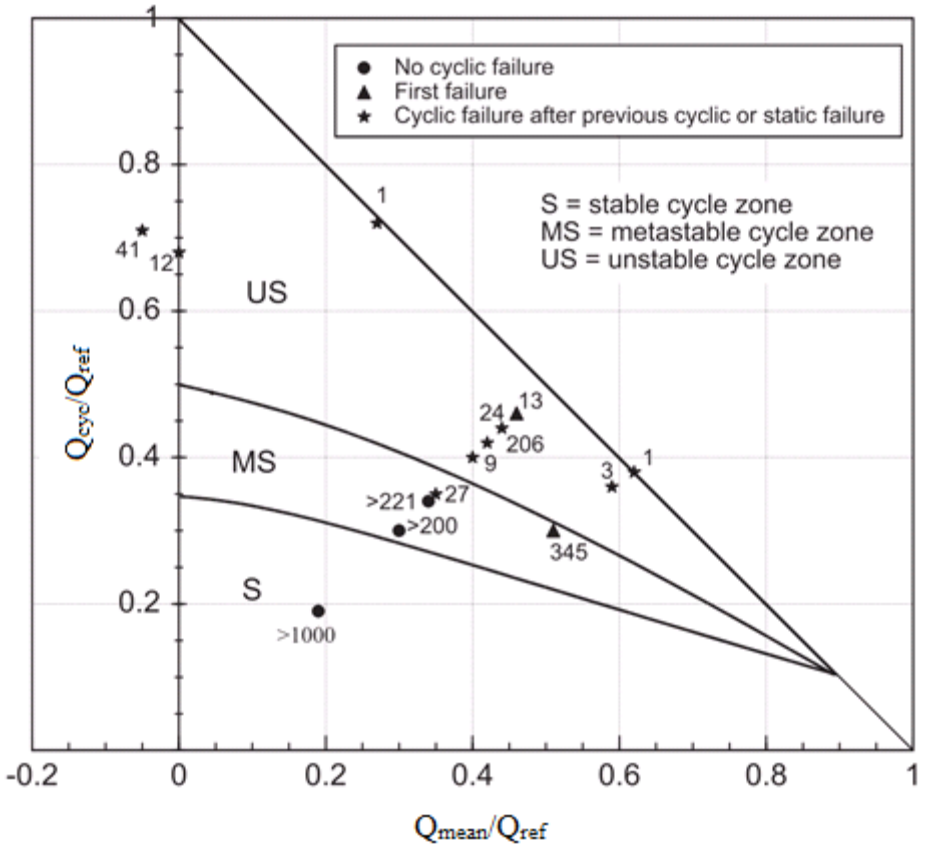


Figure 3-4: Interaction diagram showing the influence of number of cycles N and normalised loading parameters on cyclic response along with tentative stability zones (adapted from Jardine and Standing, 2012) Note: Q_{ref} taken as tension shaft capacity

3.3 Axial capacity of driven piles in clays and sands

3.3.1 Stress changes during installation, equalisation and load testing of piles in clay

The shaft stresses acting on a displacement pile in clay depend on the *in-situ* conditions and the changes that occur during long-term equalisation and subsequent loading. During fast installation in low permeability clays, soil elements along the shaft are subjected to high shear strains with zero volume change as the pile tip passes. Large positive pore water pressure increases are generated beneath the tip due to increases in mean total stresses. Pore water pressure changes are also generated during installation in response to shearing, with their sign depending on whether the material is dilatant or contractant. The latter components become more important at points well above the pile tip. Radial effective stresses, σ'_{ri} applying on the pile shaft immediately after driving depend on the initial stresses, σ'_{r0} and the magnitude and sign of the excess pore water pressures generated during installation.

The post-installation radial effective stresses on the pile shaft also tend to be lower at soil horizons well above the pile tip. This trend was recognised from pile installation records in clays and termed 'friction fatigue' by Heerema (1978). Marked reductions in σ'_{ri} at any particular soil horizon, as the pile tip passes, were observed directly in highly instrumented Imperial College Pile tests in Canon's Park in London Clay (Jardine, 1985, Bond, 1989, Bond and Jardine, 1991) and at various other clay sites (Lehane and Jardine, 1994a, Lehane and Jardine, 1994b, Chow, 1997). The dependence of radial effective stresses on relative tip depth, h is illustrated schematically on Figure 3-5 (a), while Figure 3-5 (b) shows results from measurements taken on the highly instrumented ICP in soft marine Bothkennar clay carried out by Lehane and Jardine (1994a); measurements taken at different h/R values as the pile penetrates illustrate the tendency for σ'_{ri} to reduce with increasing pile penetration.

Considerable increases in the axial capacity of piles in clay with time have been reported by e.g. Karlsrud and Haugen (1986), Fellenius *et al.* (1992), Karlsrud *et al.* (1993b), Karlsrud *et al.* (2014) and Afshin and Rayhani (2015). Three potential set-up patterns were suggested by Komurka *et al.* (2003) involving (i) capacity gain associated with radial effective stress changes linked to initial excess pore water pressure dissipation (ii) any longer term

changes in the pore water pressures surrounding the pile and (iii) an extended ageing period involving processes that are not associated with changes in pore pressures.

After installation, the excess pore water pressures generated during pile driving dissipate causing a change in the effective stress regimes surrounding the pile shaft. Depending on the stiffness and permeability of the clay, these stress changes can be completed shortly after driving or may take many months or even years to equalise fully. Dissipation of positive pore water pressures leads to changes in the shaft radial effective stress and water contents, which may contribute to pile set-up, or increase in capacity with time. Equalisation times have been modelled previously using consolidation theory and analytical solutions based on linear-elastic perfectly plastic cavity expansion theory (Randolph and Wroth, 1979), using critical state soil mechanics models or strain path approaches combined with more advanced models (Baligh, 1985). Where increases in pile capacity are fully attributable to excess pore water pressure dissipation, the above methods may be used to gauge the rate of progress.

It appears likely that loading to failure after ageing involves a similar local shaft failure mechanism to that set out in Eq. 3-2, where:

$$\tau_f = \sigma'_{rc} \tan\delta_f' \qquad 3\text{-}8$$

where δ'_f lies between the peak and ultimate value and σ'_{rc} is the local radial effective stress applying at the end of equalisation and ageing.

3.3.2 Axial capacity design methods for clay

The American Petroleum Institute (API) recommended practice (RP2A-WSD) for fixed structures (API, 2000), now also included in ISO 19902:2007 (ISO, 2007), is widely adopted to design offshore piles in clay. The guidance involves a total stress "alpha" methodology which relies on significant simplifications of the complex processes described previously. The value of τ_f, which is assumed to act on both the inside and the outside of open-ended piles loaded in compression ($\tau_f = \tau_{f,ext} = \tau_{f,int}$), is given as a function of the undrained shear strength, s_u and an adhesion factor, α:

$$\tau_f = \alpha s_u \qquad 3\text{-}9$$

The correlation, originally proposed by Randolph and Murphy (1985), between α and s_u is based on a database of axial pile load tests and takes the form:

$$\alpha = \left(\frac{s_u}{\sigma'_{vo}}\right)^{0.5}_{nc}\left(\frac{s_u}{\sigma'_{vo}}\right)^{-0.5} \text{ for } \frac{s_u}{\sigma'_{vo}} < 1.0 \quad 3\text{-}10$$

$$\alpha = \left(\frac{s_u}{\sigma'_{vo}}\right)^{0.5}_{nc}\left(\frac{s_u}{\sigma'_{vo}}\right)^{-0.25} \text{ for } \frac{s_u}{\sigma'_{vo}} > 1.0 \quad 3\text{-}11$$

The normally consolidated stress ratio, $(s_u/\sigma'_{vo})_{nc}$ is determined empirically with a first estimate of 0.25. The relationship between α and s_u is non-linear, with α reducing as s_u increases, as was first reported by Tomlinson (1957). The importance of several other factors in controlling α, such as overconsolidation ratio (OCR), pile length and soil sensitivity have since been realised (Focht and Vijayvergiya, 1972, McClelland, 1974, Kraft *et al.*, 1981, Randolph, 1983). Eq. 3-10 and 3-11 lead to higher α values (>0.33) in soft normally consolidated materials with low stress ratios than in stiff overconsolidated materials which tend to have s_u/σ'_{vo} ratios of 1 and higher.

Ultimate base resistance is calculated using traditional bearing capacity theory, with $q_{b,0.1D} = q_{ba,0.1D} = N_c s_u$. The empirical deep bearing capacity factor N_c of 9 given by Skempton (1951) is often adopted which is similar to the theoretical value obtained from cavity expansion solutions (Vesic, 1977, Randolph and Gourvenec, 2011). For unplugged piles, the bearing pressure is assumed to act under the annular area of the pile only. Plugged piles are assumed to develop end bearing under the total base area. In summary:

Unplugged penetration $Q_{ba,0.1D} = A_{ann} q_{ba,0.1D}$ 3-12

Plugged penetration $Q_{b,0.1D} = A_b q_{b,0.1D}$ 3-13

The API/ISO method does not consider "friction fatigue" or length effects explicitly which can lead to significantly lower values of shear stresses at a given horizon for long piles (e.g. Kolk and der Velde, 1996). The method also does not consider the low α values seen in some lean clays where the plasticity index is less than 20% (Karlsrud *et al.*, 1993a). Variations in interface friction angle between clay types is not addressed in the alpha method, which can cause a reduction in shaft resistance in clays that form low δ' angle residual surfaces during shearing. The installation of a pile in cohesive soil is controlled by the effective stress regime with complex changes occurring during pile driving which cannot be captured referring only to the s_u profile; Randolph and Murphy (1985). A review of pile test results in their databases and predictions using the API method by Chow (1997), Jardine *et al.* (2005a) and Lehane *et al.* (2017) indicated significant biases and skews in predictions with respect to pile length (or L_p/D) and yield stress ratio (YSR) or apparent OCR.

The observed limitations of the API method led to a campaign of field experiments using the highly instrumented Imperial College Pile (ICP), examples of which were cited earlier to illustrate stress changes during pile installation. Tests were conducted at four clay sites where the effective stresses developed on the pile shafts were monitored during installation, pore pressure equalisation and load testing (Jardine, 1985, Bond and Jardine, 1991, Lehane and Jardine, 1992a, b, Chow, 1997). The primary results and observations led to the development of the ICP-05 pile design method for clay described by Jardine *et al.* (2005a) which is outlined below.

The ICP experiments showed that the local radial effective stresses developed on the pile shaft following full pore pressure equalisation depend on the pre-installation *in-situ* stresses, the relative pile tip depth, h, YSR and soil sensitivity, S_t. Shaft failure was found to follow an effective stress Coulomb law involving the radial effective stresses applying at the end of equalisation. Lehane and Jardine (1992a, 1992b) illustrated that the radial effective stresses tended to reduce during loading to failure. Reductions during loading were captured using a loading factor K_f/K_c (where K_f is the coefficient of radial effective stress at failure and K_c is the coefficient of radial effective stress after full equalisation) equal to 0.8, which was kept constant regardless of direction of loading or drainage conditions. This modified Eq. 3-8 to:

$$\tau_f = \frac{K_f}{K_c}\sigma'_{rc}\tan\delta = \sigma'_{rf}\tan\delta' = 0.8K_c\sigma'_{vo}\tan\delta_f' \qquad 3\text{-}14$$

The value of δ'_f lies between peak and ultimate, with the operational value depending on the degree of progressive failure, the pile roughness, the type of clay and previous shearing. A wide range of peak and ultimate δ' values of between 10 and 40° was found possible in clays, which tend to correlate negatively (and rather unsatisfactorily) with the plasticity index. The interface shear parameter, δ' measured during the ICP tests was found to be best predicted by the large shear displacement residual strength behaviour seen in ring shear tests, carried out using interfaces with similar roughness characteristics to the piles and at effective normal stress levels similar to the expected *in-situ* pile shaft radial effective stresses. A correlation was proposed for the lateral earth pressure coefficient, K_c for both open and closed-ended piles which takes the form:

$$K_c = [2.2 + 0.016YSR - 0.87\log S_t]YSR^{0.42}\left(\frac{h}{R}\right)^{-0.2} \qquad 3\text{-}15$$

The correlations for radial effective stresses given in Eq. 3-14 and 3-15 were developed from the ICP test results, which had a closed-end condition. Chow (1997) considered different routes to link the closed-ended expressions to open-ended pile behaviour and eventually incorporated the equivalent radius of a solid pile R* for open-ended partial displacement piles in place of the pile radius, R in Eq. 3-15. Inclusion of R* leads to the radial effective stresses of open-ended piles reducing with the wall thickness, t_w since R* reduces with the ratio D/t_w, which is not included in other design methods such as the API (Jardine and Chow, 2007).

Chow (1997) found that the use of traditional bearing capacity theory to predict base resistance led to a wide scatter in results and a CPT based approach was favoured for ultimate base resistance. Methods to predict base resistance from CPT cone tip resistance have been in use since the 1970s; e.g. Schmertmann (1978), De Kuiter and Beringen (1979). For closed-ended piles, the ICP-05 method recommends $q_{b,01.D}$ equal to $0.8q_{c,1.5D}$ for undrained loading and equal to $1.3q_{c,1.5D}$ if drainage can occur during loading. Following Bustamante and Gianeselli (1982) $q_{c,1.5D}$ is equal to the arithmetic average of q_c over a length equivalent to ±1.5D from the pile base.

For open-ended piles, Jardine *et al.* (2005a) conclude that plugging is a function of pile diameter and cone resistance, with plugging occurring where:

$$\frac{D_i}{D_{cpt}} + 0.45\frac{q_c}{p_a} < 36 \qquad 3\text{-}16$$

The diameter of the CPT, D_{cpt} is equal to 36mm and atmospheric pressure p_a is equal to 100kPa. For piles which plug during loading, the ICP-05 method concludes that half of the end resistance of a closed-ended pile develops on the piles' total base area, with $q_{b,01.D}$ equal to $0.4q_{c,1.5D}$ for undrained conditions. Jardine *et al.* (2005a) considered, from the results of instrumented pile and pile plug resistance tests, that internal shaft resistance is small and concentrated near the bottom of the pile, effectively contributing to the overall base resistance. Unplugged piles are thought to develop end bearing on the annular steel area only, and no specific allowance is made for internal shear stresses:

Unplugged penetration $$Q_{ba,0.1D} = A_{ann}q_{ba,0.1D} = A_{ann}q_{c,1.5D} \qquad 3\text{-}17$$

Plugged penetration $$Q_{b,0.1D} = A_b q_{b,0.1D} = A_b 0.4 q_{c,1.5D} \qquad 3\text{-}18$$

A clear trend was observed for higher base resistances in tests to develop where loading was applied under effectively drained conditions and increases of 60% on Eq. 3-17 and 3-18 are advised if the loads are applied slowly enough to allow drainage to occur.

Application of the updated design procedures to a database of 55 high quality field tests led to significantly improved coefficients of variation when compared to predictions obtained using the API recommendations (Jardine *et al.*, 2005a). The ratio of calculated to measured capacities showed no skew with length or YSR. There was also no skew observed with plasticity index although a bias was observed in certain very low plasticity, low YSR Norwegian clay-silts (Karlsrud *et al.*, 1993b, Jardine *et al.*, 2005a).

Lehane *et al.* (2017) report work undertaken as part of a JIP to assess design methods in use for offshore piles. They evaluated the performance of the ICP-05 clay method using a newly assembled database of pile tests in clay. The method did not perform as well as previously reported which was recognised to be due to (i) the test selection criteria, which excluded all the ICP tests and many of the 55 pile tests used to calibrate the ICP-05 method reducing the number to 22 and (ii) inclusion of several tests from sites, including Lierstranda in Norway, where very low axial capacities had been measured in low YSR silty clay deposits showing very low cone resistance values. Potential problems had been raised by Chow (1997) and Jardine *et al.* (2005a) previously with several of the tests. Jardine *et al.* (2005a) state that ICP-05 clay method should not be applied to such clays.

A CPT based method, developed previously by Lehane *et al.* (2012b) following a similar database study, provided generally good predictions to the database selected by Lehane *et al.* (2017). The method relates shaft resistance to CPT cone resistance, retaining the ICP-05 h/R* term in Eq. 3-15 and reducing the lower limit on h/R* to 1. Two expressions are proposed;

$$\tau_f = \frac{0.23 q_t \left[\max\left(\frac{h}{R^*}, 1\right)\right]^{-0.2}}{(q_t/\sigma'_{v0})^{0.15}} \tan\delta'_f \qquad 3\text{-}19$$

$$\tau_f = 0.055 q_t \left[\max\left(\frac{h}{R^*}, 1\right)\right]^{-0.2} \qquad 3\text{-}20$$

Where q_t is the net cone resistance corrected for pore pressure effects on a cone of area ratio a_c:

$$q_t = q_c + u_2(1 - a_c) \qquad 3\text{-}21$$

Surprisingly, the alternative formulation (Eq. 3-20), which does not include the interface friction angle or the effective over-burden stress, led to lower CoVs when tested against field data and tests conducted in the centrifuge. The performance of the ICP-05 clay method, along with Eq. 3-19 and 3-20, is assessed further in Chapter 5, where they are used to predict the shaft capacity for piles installed primarily in clay till at an offshore test site.

3.3.3 Stress changes during installation, equalisation and load testing of piles in sand

The radial and shear shaft stresses applying on displacement pile shafts in sand depend similarly on the initial *in-situ* stresses as well as the changes that occur during installation, equalisation and load testing. Sand is often sufficiently free draining for any excess pore water pressures generated by pile driving to dissipate fully during installation. ICP experiments in sand performed by Lehane *et al.* (1993) and Chow (1997), similar to those described above for clay, showed that radial stresses and base resistance rose and fell within variable profiles in patterns that correlated well with the CPT q_c profiles, indicating that sand state or relative density is critical in defining pile capacity. The experiments also showed marked reductions, with relative tip depth, in radial effective stresses in both loose and dense sands, with a stronger dependency than that seen in clays (Figure 3-6). Similar to clays, shaft resistance during loading to failure was shown to follow an effective stress Coulomb law.

As with clays, static loading to failure in sands led to an initial small reduction in shaft radial effective stresses. However, after passing a phase transformation point, the local effective stress paths showed increases in radial effective stresses up to a local critical state point at which failure occurred. This feature contributed an extra component of radial effective stress, $\Delta\sigma'_{rd,}$ interpreted as kinematically constrained dilation at the interface between the pile and soil (Lehane *et al.*, 1993), giving:

$$\tau_f = (\sigma'_{rc} + \Delta\sigma'_{rd})\tan\delta'_{ult} = \sigma'_{rf}\tan\delta'_{ult} \qquad 3\text{-}22$$

Where δ'_{ult} is the constant volume angle of interface resistance which is less than δ'_{peak} and does not depend on sand density. Boulon and Foray (1986) argued that with sands, the magnitude of $\Delta\sigma'_{rd}$ can be estimated by a simple elastic cavity expansion expression which includes the average movement of the soil grains, Δr due to dilation:

$$\Delta\sigma'_{rd} = \frac{4G\Delta r}{D} \qquad 3\text{-}23$$

The component, $\Delta\sigma'_{rd}$, which increases with the inverse of the diameter could contribute, for example, up to 40% of the capacity of the small (101mm diameter) ICP piles, but the component is unlikely to add more than 5% of the capacity of a large 2m diameter pile (Jardine and Chow, 2007).

Increases in capacity with time in clean free draining sands tend to be associated with medium to long-term ageing processes as opposed to the dissipation of pore water pressures seen in clays. Field testing has shown significant gains in capacity with time e.g. Skov and Denver (1988), Chow *et al.* (1998), Axelsson (2000), Bullock *et al.* (2005b), Jardine *et al.* (2006), Karlsrud *et al.* (2014), Gavin *et al.* (2015) summarised recent field studies which indicated that open and closed-ended piles formed of steel, concrete and timber show significant capacity increases after driving which appear to tend to an equilibrium after approximately one year. Rimoy *et al.* (2015) categorise the alternative mechanisms to explain pile ageing in sands suggested by Schmertmann (1991), Åstedt *et al.* (1992), Chow *et al.* (1998), Bea *et al.* (1999), Axelsson (2000), Lim and Lehane (2014) and others into three hypotheses:

- **Radial stress re-distribution**: Extreme distributions of circumferential (hoop), σ'_{θ} and radial, σ'_{r} effective stresses are generated during pile installation which develop their maxima remote from the pile wall and are supported by arching around the pile shaft. Over time, creep leads to relaxation and re-distribution of these stresses and increases in radial effective stresses on the pile shaft;
- **Increases in shaft dilation:** Increases in the dilation component $\Delta\sigma'_{rd}$ during loading due to re-arrangements in the microstructure and increases in grain interlocking with time. Any increases in the radial dilation amount, Δr or the operational shear stiffness would lead to an increase in capacity via Eq. 3-22 and 3-23;
- **Physico-chemical processes:** Physico-chemical processes between the sand, groundwater and/or the pile material causing bonding between the sand and the pile, an increase in interface roughness or sand stiffness that causes failure to occur in the soil mass. The latter increases the pile's effective diameter, D and where Δr or G are increased also the dilational component $\Delta\sigma'_{rd}$. Shearing under soil-soil conditions would be dominated by the sand-sand φ', which is higher than δ'_{ult} (Kishida and Uesugi, 1987).

Pile ageing in sands appears to be independent of sand stiffness changes and to be more marked in larger diameter piles The above cavity expansion approach to estimating the

dilational component of capacity may not be able to capture some of the key ageing features seen in the field (Gavin *et al.*, 2015, Rimoy and Jardine, 2015).

3.3.4 Axial capacity design methods for sand

The API RP2A-WSD recommended practice (API, 2007), now incorporated in ISO 19902: 2007, includes an effective stress "beta" approach within the main text of the recommendations. The API/ISO beta approach calculates shaft resistance from:

$$\tau_f = \beta\sigma'_{vo} \leq \tau_{f,lim} \qquad 3\text{-}24$$

Values of β and the limiting shear stress, $\tau_{f,lim}$ vary with the type and density of the sand. Values quoted in API/ISO are for open-ended piles with an increase of 25% allowed for closed-ended piles. The method was calibrated using primarily un-instrumented piles whose average unit shaft resistance suggested that τ_f did not increase in proportion to depth and should be limited by $\tau_{f,lim}$, conflicting with recent understanding of the dependence of τ_f on relative tip depth. Ultimate base resistance is calculated from:

$$q_{b,0.1D} = q_{ba,0.1D} = N_q\sigma'_{vo} \leq q_{b,lim} \qquad 3\text{-}25$$

with $q_{b,lim}$ also varying with soil type and density and N_q is a dimensionless bearing capacity factor calculated from the angle of shearing resistance. The end bearing is applied in the same manner as that shown in Eq. 3-12 and 3-13.

The API/ISO method is clearly a simplification of the complex governing mechanisms described previously. Reviews of pile test results and predictions using the API method by Chow (1997), Jardine *et al.* (2005a), Lehane *et al.* (2005b), Yang *et al.* (2016) and Lehane *et al.* (2017) indicate generally poor reliability, and showed significant biases and skews in predictions with respect to pile length (or L_p/D) and relative density, being systematically non-conservative in loose sands and with high L_p/D piles and conservative in dense sands and with low L_p/D piles.

The ICP tests carried out in loose silica sand in Labenne (Lehane *et al.*, 1993) and dense marine sand at Dunkirk (Chow, 1997) led to considerable advancements in the understanding of the behaviour of displacement piles in sand and the development of the ICP-05 sand design methodology (Jardine *et al.*, 2005a). The equalised radial effective stresses, σ'_{rc}, measured by the ICP, normalised by the cone resistance, q_c, were found to follow a power law trend with

h/R in the Labenne and Dunkirk tests (Figure 3-7) and led to an expression for σ'_{rc} for closed-ended piles which takes the form:

$$\sigma'_{rf} = \zeta q_c \left(\frac{\sigma'_{vo}}{p_a}\right)^{\kappa} \left(\frac{h}{R}\right)^{-\eta} \quad 3\text{-}26$$

Parameter ζ is used to reflect the stress reduction from q_t to the radial effective stress immediately behind the pile tip. The second term and exponent κ account for a weak dependence on the effective overburden stress. The h/R term and exponent η account for the observed rapid attenuation of radial effective stress above the pile base. For an open-ended tubular steel pile R is equal to the equivalent radius, $R^*=(R^2 - R_i^2)^{0.5}$) giving:

$$\sigma'_{rf} = \zeta q_c \left(\frac{\sigma'_{vo}}{p_a}\right)^{\kappa} \left(\frac{h}{R^*}\right)^{-\eta} \quad 3\text{-}27$$

For both closed and open-ended piles, $\zeta = 0.029$, $\kappa = 0.13$ and $\eta = 0.38$. The h/R* term has a lower limit of 8. Eq. 3-27 is combined with Eq. 3-22 and Eq. 3-3 to predict the pile shaft capacity. The ultimate angle of interface friction is estimated from ring shear tests on samples from the site and does not depend on the sand density state.

The dilation component, $\Delta\sigma'_{rd}$, is estimated using Eq. 3-23 with the operational shear modulus obtained from the correlation with q_c given by Baldi *et al.* (1989). The G value in Eq. 3-23 should ideally be measured in the G_{hh} direction and may need to account for strain level and non-linearity. While the maximum dilation at the interface tends to increase with the median grain size, D_{50} and the pile roughness and is influenced by the stress and density of the sand and the stress state relative to that at critical state (Been and Jefferies, 1985), Chow (1997) and Jardine *et al.* (2005b) found a simple rule of Δr equal to twice the average roughness, R_a provided a good match to measurements of $\Delta\sigma'_{rd}$. The latter rule applies in cases where the interface's relative roughness, R_n ($R_n = R_a/D_{50}$ where D_{50} is the mean particle size) is less than the critical value, which for a perfectly rough response is approximately 0.1 (Kishida and Uesugi, 1987).

Based on a database of 81 high quality static load tests, the following correlation was developed for shaft resistance:

$$\tau_f = a_t(b_t\sigma'_{rc} + \Delta\sigma'_{rd})\tan\delta_{ult} \quad 3\text{-}28$$

Where a_t is a reduction factor (0.9) applied to the capacity of open-ended piles tested in tension and b_t reduces the radial effective stresses on the pile to account for reduced capacity

under tension loading (0.8 in tension, 1.0 in compression) due to principal stress rotation and elastic Poisson effects (Lehane *et al.*, 1993, De Nicola and Randolph, 1993).

As noted earlier, base capacity was found to correlate directly with CPT q_c reflecting the geometric similarity between the CPT and pile tip conditions. Database studies conducted by Chow (1997) indicated an unexpected scale effect for the base capacity of closed-ended piles with $q_{b,0.1D} \neq q_{c,1.5D}$ (with $q_{c,1.5D}$ equal to the cone resistance averaged 1.5 diameters above and below the pile tip). The ICP-05 sand method therefore recommends a relationship between $q_{b,0.1D}$ and $q_{c,1.5D}$ which varies with diameter for closed-ended piles:

$$q_{b,0.1D} = q_{c,1.5D}\left[\max\left(1 - 0.5\log\left(\frac{D}{D_{cpt}}\right), 0.3\right)\right] \qquad 3\text{-}29$$

where D_{cpt} is equal to 36mm. The closed-ended pile database was re-analysed by White and Bolton (2005) who argue that the apparent reduction in end resistance with diameter is attributable to partial embedment of the pile into the stratum and partial mobilisation of base resistance. After allowing for partial embedment effects by applying weighting to $q_{c,1.5D}$ to allow for weaker layers and allowing for mobilisation by defining failure using a large displacement plunging criterion, they found a mean ratio of $q_b/q_{c,1.5D}$ equal to 0.9 which they argue did not vary with pile diameter. Reduction in the ratio $q_b/q_{c,1.5D}$ due to progressive failure was not considered as it was argued that failure does not occur through the propagation of shear bands along slip planes. While the question of scale remains open to debate and field verification, it is generally acknowledged that $q_b/q_{c,1.5D}$ values must be far lower than 0.9 in practical design.

Jardine *et al.* (2005a) conclude that plugging in sands is related to the pile diameter, relative density and cone resistance. The results of studies into pile plugging and from the database of open-ended pile tests (Brucy *et al.*, 1991, Chow, 1997) led to the conclusion that plugging would occur if both:

$$D_i < 0.02(D_r - 30) \quad \text{and} \quad \frac{D_i}{D_{cpt}} < 0.083\frac{q_{c,1.5D}}{p_a} \qquad 3\text{-}30$$

where D_r is the relative density in %, D_i is in metres, $q_{c,1.5D}$ and p_a are in kPa.

For piles which plug during loading, the ICP-05 design method determines that half of the end resistance of closed-ended piles develops on the pile's total base area (i.e. Eq. 3-4), showing a similar scale effect with diameter with $q_{b,01.D}$ equal to:

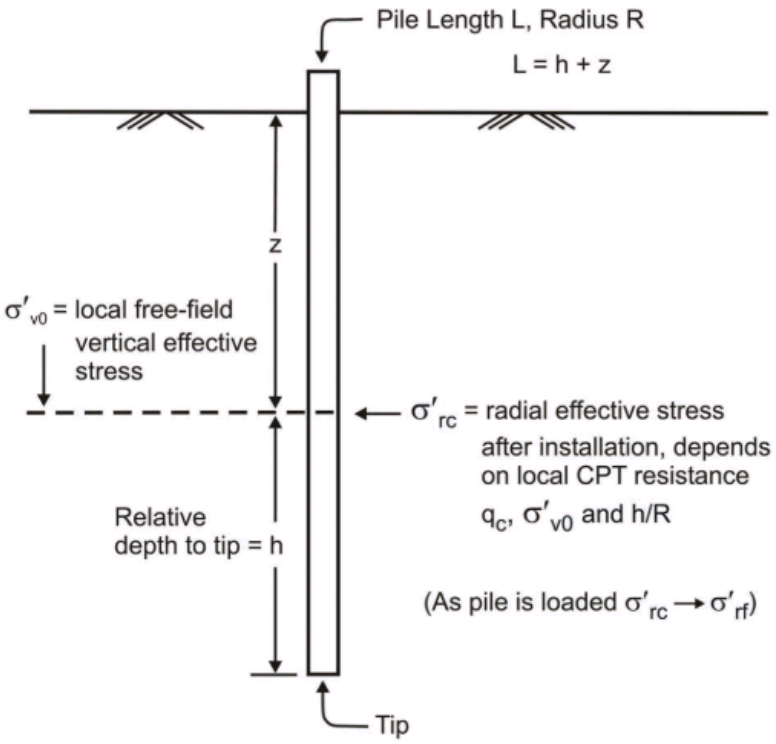
$$q_{b,0.1D} = q_{c,1.5D}\left[\max\left(0.5 - 0.25\log\left(\frac{D}{D_{cpt}}\right), 0.15, A_r\right)\right] \quad 3\text{-}31$$

Where A_r is the effective area ratio defined as:

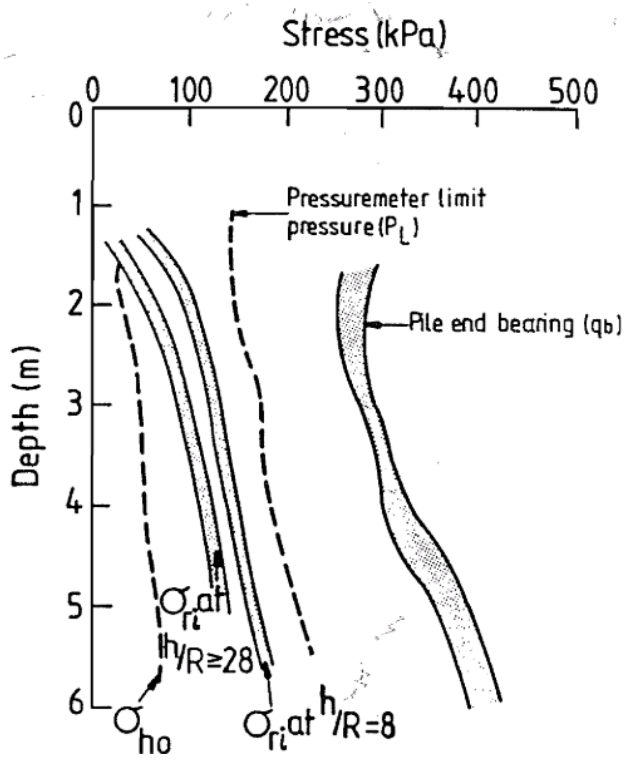
$$A_r = 1 - \left(\frac{D_i}{D}\right)^2 \quad 3\text{-}32$$

For open-ended fully coring piles, the end bearing, $q_{ba,0.1D}$ mobilised at failure is taken as equal to $q_{c,1.5D}$, despite the different shapes of the cone and pile annulus. The method indicates that the ratio of $q_{ba,0.1D}/q_{c,1.5D}$ is approximately 0.7, and the remaining $0.3q_{c,1.5D}$ is thought to offset acknowledged contributions to capacity from the internal soil plug, which are not considered explicitly.

The API/ISO recommendations also invite designers to consider a number of recently developed CPT-based design methods to predict axial capacity in sands, included in the commentary section, which are considered "preferable to the main text approach" where the designers are suitably experienced and high quality site investigation data are available. The methods included are simplified versions of the ICP-05 sand method (Jardine *et al.*, 2005a); the broadly similar UWA-05 (Lehane *et al.*, 2005a) and Fugro-05 (Kolk *et al.*, 2005) methods and the NGI-05 method (Clausen *et al.*, 2005). A summary of the methods was provided by Schneider *et al.* (2008). Comparisons between the predictions obtained with each of these methods are discussed by Lehane *et al.* (2005b), Jardine and Chow (2007), Yang *et al.* (2016) and Lehane *et al.* (2017).



(a)



(b)

Figure 3-5: Dependence of radial effective stresses after installation on relative tip depth (a) definition of relative tip depth (Jardine and Chow, 2007) (b) Installation radial effective stresses measured at instruments along the pile shaft with different h/R values in a soft marine clay (Lehane and Jardine, 1994a)

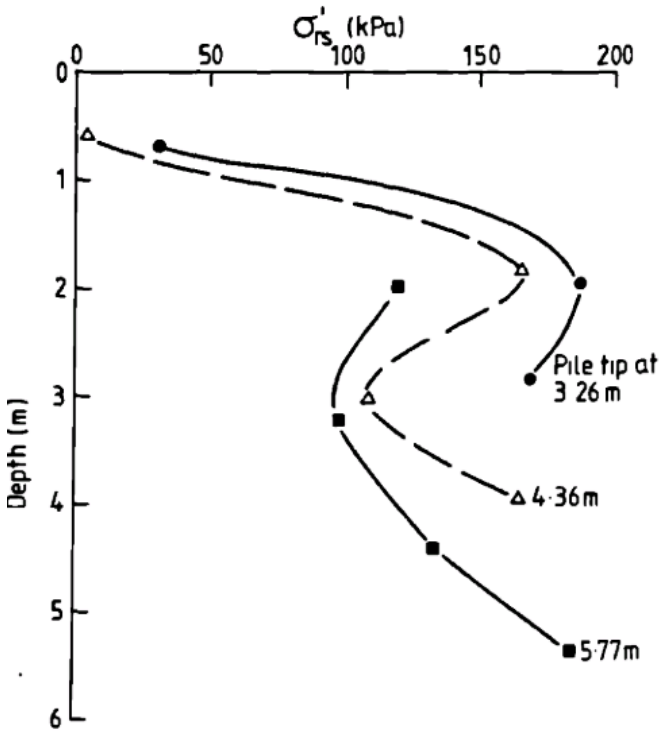


Figure 3-6: Stationary radial effective stresses measured in dense sand at Dunkirk at different instrumentation levels reflecting the importance of h/R (Chow, 1997)

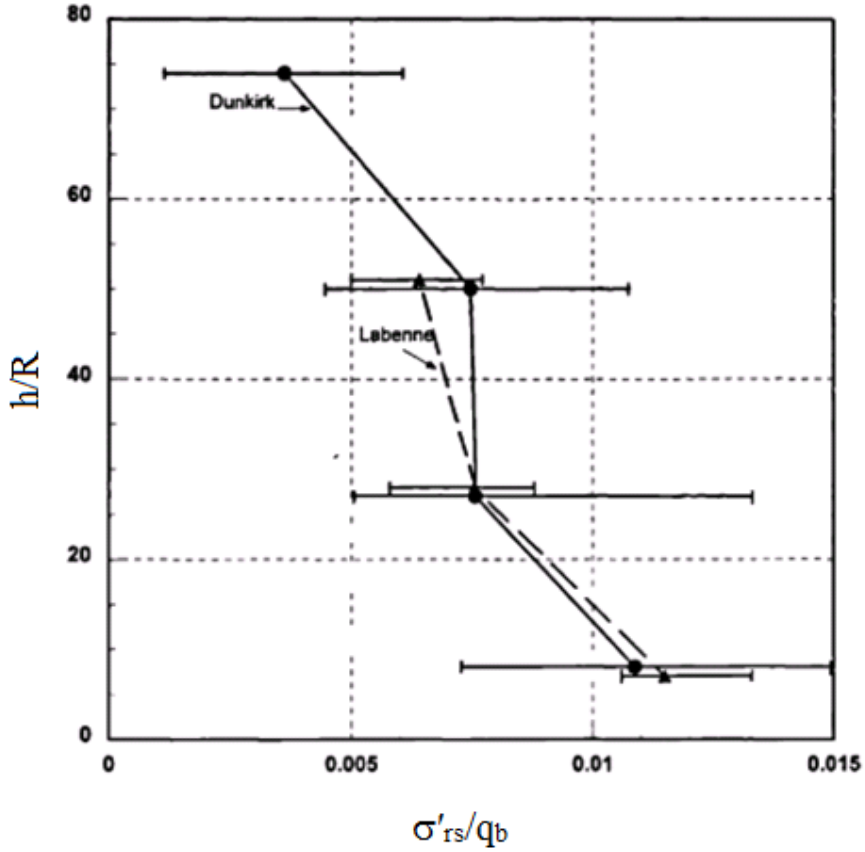


Figure 3-7: Variation in stationary radial stationary effective stresses (σ'_{rs}/q_b) normalised by base resistance with h/R during installation of piles in sand (Chow, 1997)

3.4 Axial capacity of driven piles in chalk

3.4.1 Stress changes during installation, equalisation and load testing

The previous sections highlighted the significant advances in understanding of displacement pile behaviour in clays and sands which have led to the development of new axial capacity design methods. Equivalent advancements have yet to be made into the understanding of the fundamental stress changes occurring when piles are driven in chalk and subjected to later static axial loading tests.

While few carefully stage-loaded static load tests have been reported to establish the ability of displacement piles to carry axial loads in chalk, low shaft driving resistances (between 0 and 20kPa) have been reported from dynamic driving analyses, that suggest low static service capacities (Vijayvergiya *et al.*, 1977, Lord *et al.*, 2002). The low installation capacities are reflected in the conservative current industry design guidelines, described further later, which recommend values for ultimate shaft resistance of 20kPa in low-medium density chalk and 120kPa in all other densities and grades. These values appear remarkably low, given the intact chalk's properties, described in Chapter 2, where Unconfined Compressive Strength (UCS) ranges from 1.25 to >12.5MPa (Bowden *et al.*, 2002) and q_c from 4 to > 50MPa (Power, 1982). Dynamic percussion damage during driving provides one explanation for low driving resistance. De-structuration and crushing of hollow calcium carbonate ($CaCO_3$) particles beneath the advancing pile tips produces low strength putty that spreads along the pile and limits drastically the radial effective stresses and shear resistances that can act on the shaft; Hobbs and Atkinson (1993), Lord *et al.* (2002).

The shaft shear stresses available at any depth appear to attenuate with increasing relative distance from the pile tip, h, as the pile penetrates (see Norrie, 2015), similar to the dependencies on "h/R" or "h/R*" observed in clays and sands as discussed in Section 3.3. High-level laboratory simple shear cyclic loading and cyclic cone penetration tests have also been found to reduce the shear stresses that intact chalk can carry to as low as 4kPa (Carrington *et al.*, 2011, Diambra *et al.*, 2014). Large diameter offshore piles have been known to free-fall considerable distances rapidly in chalk without any hammering (Norrie, 2015, Carotenuto *et al.*, 2018). Therefore cyclic loading is not essential for low installation resistance to develop.

Dynamic monitoring often shows capacity growth with time over driving pauses in chalk. While Lord *et al.* (2002) suggested that field set-up takes place with low-medium density

chalk, due to (i) pore pressure dissipation and/or (ii) internal re-cementing of the putty annulus around the pile thus changing its properties with time, redox chemical reactions may also play a role. Vijayvergiya *et al.* (1977) reported an 80% increase in dynamic driving resistance over a 60 day pause in an offshore project, while Skov and Denver (1988) interpreted a 383% increase over 13 days from static and dynamic load tests on two concrete piles driven in chalk. Lahrs and Kallias (2013) reported 50% to 60% increases in shaft resistance in chalk over four months from multiple offshore dynamic restrikes on 1.5m diameter piles, but found the shaft capacity of a single pile fell over time when subjected to multiple restrikes and a static test. However, re-testing pre-failed piles is often misleading as they often show far less set-up than equivalent "virgin" piles in sands and clays; Jardine *et al.* (2006), Jardine and Standing (2012), Karlsrud *et al.* (2014). Ciavaglia *et al.* (2017a) described the results of three tension tests conducted on the same 0.762m diameter 4m long steel piles, which showed static shaft resistances increasing by 700% in re-tests conducted over four months. Their strain gauge readings indicated four to six times higher shaft resistances applying over the lower halves of the piles, as well as a significant deleterious effect of previous lateral loading.

Any beneficial time effects on capacity may be negated by a perceived high susceptibility of chalk to axial cyclic loading, which may reduce the axial capacity to levels as low as those seen during installation. The effect of axial cyclic loading on the aged capacity of displacement piles remains a significant unknown with a very limited number of available case studies (e.g. Burland and French, 1990). There is currently no available guidance to allow for axial cyclic or lateral cyclic effects in design, which poses significant difficulties for offshore pile foundation design.

3.4.2 Axial capacity design methods in chalk

CIRIA design recommendations

The now superseded CIRIA PG6 *Piling in Chalk* guide (Hobbs and Healy, 1979) originally recommended an effective stress based Coulomb approach to calculate the shaft resistance applying on driven pre-formed piles based on available static pile test results. A traditional β-approach was adopted, where the radial stress acting on the pile was calculated by multiplying the *in situ* stress, σ'_{vo} by the coefficient of lateral pressure, K:

$$\tau_f = \sigma'_{vo} K \tan\delta' \qquad 3\text{-}33$$

The value of δ' was chosen based on laboratory testing and engineering judgement. Tentative correlations between SPT N number and K were provided along with correction

factors to account for the different pile dimensions and types. Due to remoulding of the chalk during a standard penetration test, the N value is more representative of dynamic bearing capacity failure ahead of the SPT shoe than of the lateral stresses applying on the sides of a steel pile. Any correlation between lateral earth pressure and SPT value should be treated with considerable caution (Lord *et al.*, 2002). Hobbs and Healy (1979) recommend K of approximately 0.8 and a relatively low δ' value of 20° giving τ_f equal to $\approx 0.291\sigma'_{vo}$. From the results of plate loading tests and static compression tests Hobbs and Healy (1979) suggested that ultimate base resistance can be calculated by empirical correlations with SPT N value.

$$q_{b,0.1D} = 225N \text{ (kPa)} \qquad 3\text{-}34$$

The next update to the recommendations for design of driven piles in chalk was the CIRIA PR11 guide, *Foundations in Chalk* (Lord *et al.*, 1994). The outcomes of load tests inspected by the authors caused them to move away from the PG6 effective stress method to calculate shaft capacity. From 20 available case studies, pile types were placed into two classes based on the likelihood of penetration into chalk of different densities and grades, as summarised in Table 3-1. *Type PS* piles included small displacement piles such as H-piles, open-ended steel tubes and box piles that are all unlikely to plug during installation. *Type PL* piles include closed-ended steel tubes and boxes and pre-cast concrete piles. The CIRIA current chalk grading classification system was shown on Figure 2-7.

From the available case studies, Lord *et al.* (2002) concluded that small displacement piles (*Type PS*) in low-medium density material of all grades will penetrate very easily, mobilising very low driving resistances which did not appear to increase to any extent with depth (Vijayvergiya *et al.*, 1977). Open-ended tubular steel piles were thought unlikely to plug during installation and will "tend to cut through chalk, by severe percussion crushing the chalk beneath the steel rim of the pile under repeated high energy blows" mobilising very little shaft stress during installation. In contrast, small displacement piles were thought to penetrate medium-high density grade A chalk with difficulty, due to the tightness of the chalk blocks, mobilising high shaft resistance. Penetration was thought possible in medium-high density Grade B/C/D chalk, where the chalk mass has a more open structure. Large displacement piles (*Type PL*) were classed as unlikely to penetrate into medium-high density Grade A chalk, but penetration was thought possible in low-medium density and medium-high density Grade A/B/C/D material but with higher overall shaft resistances than small displacement piles.

Table 3-1: Summary of pile categories and likelihood of pile penetration in chalk of different grade and density (Lord *et al.*, 1994, Lord *et al.*, 2002)

	Likelihood of penetration			
Density	**Low – medium**		**Medium-high**	
Grade	**Grade A**	**Grade B/C/D**	**Grade A**	**Grade B/C/D**
Type PS Small displacement piles (H-piles, open-ended steel tubes and boxes)	Easy	Easy	Difficult	Possible
Type PL Large displacement piles (Closed-ended steel tubes and boxes, precast concrete)	Possible	Possible	Unlikely	Possible

The CIRIA pile test database of *Type PS* and *Type PL* tests is shown on Figure 3-8 (a) where the average shaft resistance in chalk, τ_{avg} ($=Q_s/A_s$) is plotted against the average overburden stress as in the original document. All of the tests on *Type PL* piles were compression tests which required critical assumptions regarding shaft capacity in the overlying material and/or ultimate base capacity. Further detail on individual tests is provided later in Section 3.5 and in Appendix C2 of CIRIA PR11 (Lord *et al.*, 1994). The authors noted the following trends from their rather sparse database;

- Average shaft resistance did not appear to increase with depth or increasing vertical effective stress;
- Small displacement piles driven into low-medium density chalk (records PS1 and PS3) mobilised low τ_{avg} of between 8 and 42kPa with an average of 23kPa;
- Small displacement piles driven into medium-high density Grade A chalk (records PS2 and PS4) mobilised high τ_{avg} of 125 and 150kPa;
- Large displacement piles (*Type PL*) generally mobilise τ_{avg} of between 30 and 60kPa, which do not appear to increase with increasing effective overburden stress. The uniform nature of the results led the authors to conclude the chalk was of low-medium density at the tested sites.

The low installation resistances observed in the CIRIA database may also be attributable to "h/R" effects or "friction fatigue" processes; Figure 3-8 (b) re-plots the CIRIA database results as average shaft resistance against total penetration into chalk. Discounting records PS2 and PS4, which relate to high density Grade A chalk, a tendency for average shaft

resistance to reduce with increasing penetration into chalk is observed for the *Type PL* piles. The four records relating to Type PS piles show a relatively constant trend in τ_{avg} with depth of between 8 and 42kPa.

Figure 3-9 plots the measured ultimate base resistance from the CIRIA database tests against SPT N value and indicates a broad trend for $q_{b,0.1D}$ to increase with N from 13 tests on driven pre-formed piles. The three of these records (PS1 tests) that relate to small displacement piles follow a lower trend. Also shown are the upper and lower bound correlations between $q_{b,0.1D}$ and N suggested by Lord *et al.* (2002) based on the available results. For design, the lower bound estimate of $q_{b,0.1D}$=200N (kPa) was recommended to estimate base resistance which may lead to significant overestimation for small displacement piles based on the trend interpreted by the Author. A tentative correlation between $q_{b,0.1D}$ and q_c was also suggested by those authors which amounted to $q_{b,0.1D}$ equal to 0.75 to 1.0 times q_c.

Insufficient test results were available to Lord *et al.* (1994) to allow them to demonstrate any more precise relationships or develop further the original PG6 effective stress method to estimate shaft resistance. For large displacement (*Type PL*) piles, they suggest that penetration may not be possible in "tightly jointed" Grade A chalk. Where installation is in "open jointed" chalk (Grade B/C/D) an ultimate shaft resistance of 30kPa is recommended for large displacement piles.

For small displacement (*Type PS*) piles, based on six tests at four sites (shown on Figure 3-8), Lord *et al.* (1994) recommended adopting an ultimate shaft resistance of 120kPa in high density Grade A chalk, and 20kPa in all other densities and grades, reducing to 10kPa if there is a possibility that the pile may "whip" during installation as with flexible H piles.

The latter recommendations of ultimate shaft resistance equal to either 20 or 120kPa in low-medium density and medium-high density chalk respectively are widely different and appear remarkably low given the chalk's intact strength. The recommendations do not take into account any beneficial time effects on capacity, which they note may be significant, and imply low shaft radial effective stresses even after full equalisation. The guidelines are routinely adopted for axial capacity design in chalk and result in widely different values when selecting design parameters for driven pre-formed piles. The recommendations were not revisited when the updated CIRIA C574 *Engineering in chalk* guidelines were published in 2002.

Vijayvergiya *et al.* (1977)

Vijayvergiya *et al.* (1977) describe a method, based on 47 pile load test results, to predict axial pile capacity of open-ended steel piles driven in North Sea chalk. A quasi-effective stress method was used to relate τ_f to mean vertical effective stress along the embedded length, $\bar{\sigma}'_{vo}$ and mean undrained shear strength along the embedded length, $\bar{s}_u$, giving:

$$\tau_f = \lambda_f(\bar{\sigma}'_{vo} + 2\bar{s}_u) \quad 3\text{-}35$$

The method takes friction fatigue or length effects into account via λ_f, a non-dimensional friction coefficient that depends on the pile penetration, obtained from back analysis of data from 47 piles tests at various sites in chalk. The value of be λ_f can be approximated by a power law relationship with the length of penetration, L_p:

$$\lambda_f = 0.5054 L_p^{-0.349} \quad 3\text{-}36$$

Based on the results in the database, the end bearing was recommended as 50 tonnes per square foot (tsf) or 5.4MPa.

Bustamante and Gianeselli (1982)

Bustamante and Gianeselli (1982) calculated shaft resistance for a range of pile types, which were primarily bored piles, but also included driven precast concrete piles and driven steel piles. The piles were installed in "soft" (q_c < 5MPa) and "weathered to fragmented" chalk (q_c > 5MPa) and calculated τ_f as a proportion of CPT cone resistance, q_c;

$$\tau_f = \frac{q_c}{\alpha_{s,cpt}} \leq \tau_{f,lim} \quad 3\text{-}37$$

where q_c is in kPa, $\tau_{f,lim}$ is a limiting value of τ_f and $\alpha_{s,cpt}$ is a reduction factor which depends on pile type. For driven pre-cast piles in "soft" chalk $\alpha_{s,cpt}$ and $\tau_{f,lim}$ are equal to 100 and 35kPa, changing to 60 and 120kPa respectively in "weathered to fragmented chalk". For driven steel piles in soft chalk, $\alpha_{s,cpt}$ and $\tau_{f,lim}$ are equal to 120 and 35kPa respectively, changing to 80 and 120kPa respectively in weathered and fragmented material. End bearing was obtained from:

$$q_{b,0.1D} = q_c \alpha_{b,cpt} \quad 3\text{-}38$$

where, q_c is in MPa and $\alpha_{b,cpt}$ is a bearing capacity factor which for driven pre-formed piles equals 0.3 and 0.4 in soft and weathered to fragmented chalk respectively. The method suggested by Bustamante and Gianeselli (1982) has an advantage over the CIRIA recommendations in that is based on CPT cone resistance which involves a similar mechanism to pile penetration and accounts for changes in chalk properties with depth.

Carrington *et al.* (2011)

A method to predict ultimate shaft resistance based on laboratory testing has been suggested by Carrington *et al.* (2011) who derived values for τ_f applying on small displacement piles in low-medium density chalk from the results of high-level laboratory cyclic simple shear tests. Intact samples from the North Sea were consolidated to a normal stress equal to the estimated *in-situ* lateral stress and then subjected to strain controlled high level cyclic loading to simulate the effects of pile installation. The samples were then allowed to rest for 48 hours under constant volume prior to being sheared statically to failure to obtain a post-cyclic shear strength, τ_{res} taken as equivalent to the strength of the remoulded chalk after installation. The ultimate shaft resistance is then calculated as:

$$\tau_f = \tau_{res} \frac{\tan\delta'}{\tan\varphi'} \qquad 3\text{-}39$$

Where $\tan\delta'/\tan\varphi'$ is an adhesion factor (0.7 to 0.89), obtained from soil-soil and soil-steel direct shear box tests, used to reduce τ_{res} to account for shearing between the pile interface and the soil. The adopted approach led to τ_f values between 20 and 50kPa in the experiments reported by Carrington *et al.* (2011). While the latter values exceed the CIRIA recommendation value for low-medium density material, the implicit assumption is that low installation resistance applies over the whole pile shaft and is caused by load cycling during driving. As noted earlier, large diameter offshore piles have been known to free-fall considerable distances rapidly in chalk without any hammering, so cyclic loading cannot be the only factor controlling low installation resistance. In addition, only the benefits of ageing under constant volume for 48 hours are considered.

COWI/IMS (CIJV, 2014b)

A further method was proposed by the pile designers for the Wikinger offshore windfarm, discussed in Chapter 5, where shaft capacity was estimated using the results of CNS-DS soil-soil tests. The samples were remoulded to replicate the conditions next to the shaft and consolidated to an *in-situ* horizontal stress calculated using an assumed K_0 value of 0.4. The obtained shear stress at failure was plotted against σ'_{vo} to establish a trend with depth, which had a slope β similar to Eq. 3-24:

$$\tau_f = \beta\sigma'_{vo} \leq 100\text{kPa} \qquad 3\text{-}40$$

$$\beta = K\tan\delta'_{ult} \quad 3\text{-}41$$

An adhesion factor was used to reduce the values obtained from the soil-soil CNS tests to account for soil-steel conditions in the real (soil-steel) case resulting in a value of δ'_{ult} of 32°. Characteristic and lower bound shaft resistance were recommended for all chalk types as β = 0.21. Upper bound values of β were given for structureless (0.25), low density structured (0.29) and medium density structured chalk (0.33). The characteristic β=0.21 equates to a K=0.33, while the UB value for medium density structured gives K=0.53. An arbitrary limit of 100kPa was imposed on τ_f which limits the UB trend for structured chalk at σ'_{vo} values of between 300 and 345kPa and the characteristic trend at σ'_{vo} values to be greater than 475kPa.

The inherent assumption of the method is that τ_f is provided by a consistent annulus of remoulded chalk whose strength is related to the failure strength in a CNS-DS test, which has not been proven by back analysis using pile load tests. The effect of pile length is not considered, nor are any beneficial effects of time on capacity. For low density chalk, the method is essentially the same as the superseded CIRIA PG6 method (Eq. 3-33).

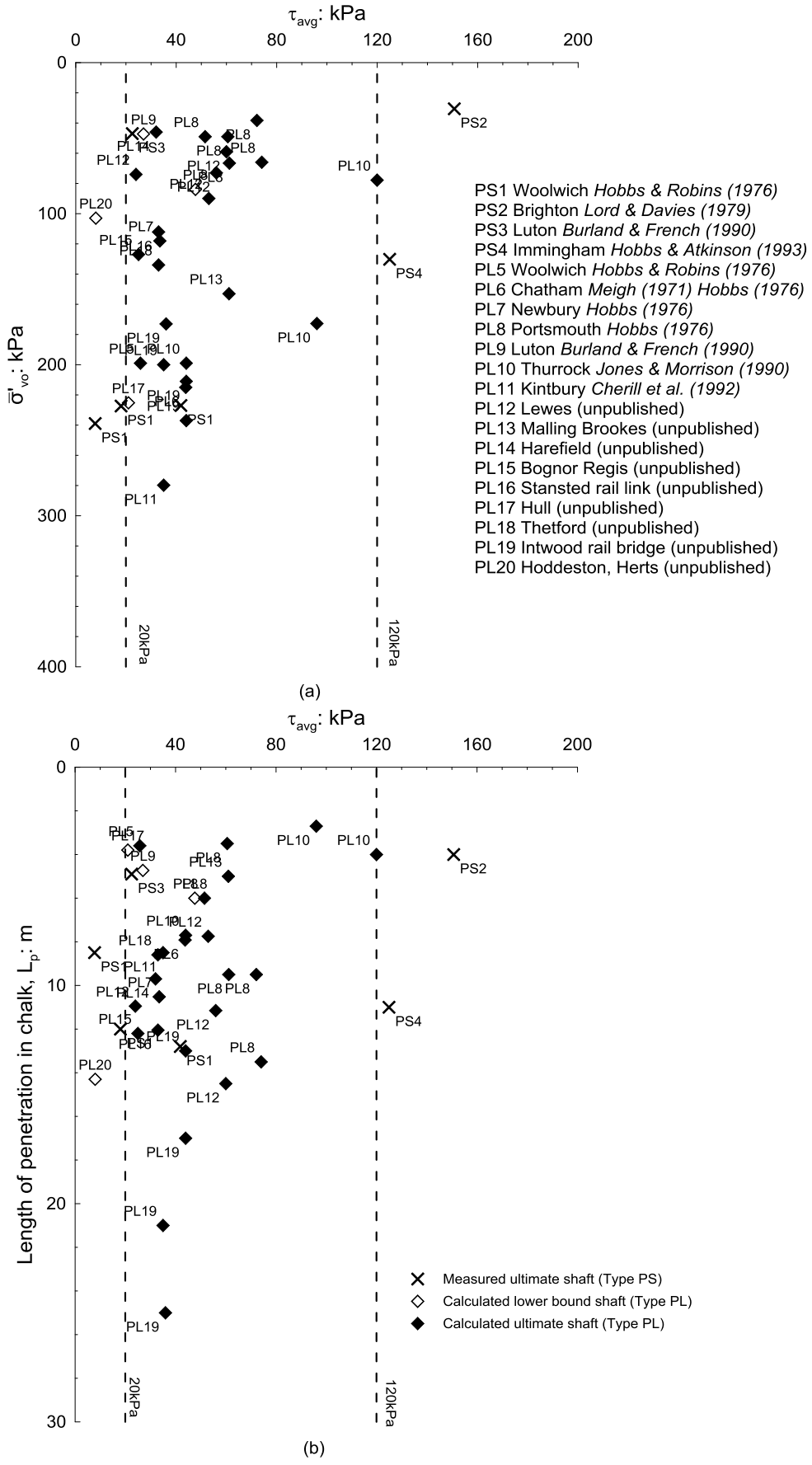


Figure 3-8: Average shaft resistance from CIRIA PR11/C574 database (a) versus average vertical effective stress (b) versus penetration of pile into chalk (adapted from Lord *et al.*, 2002)

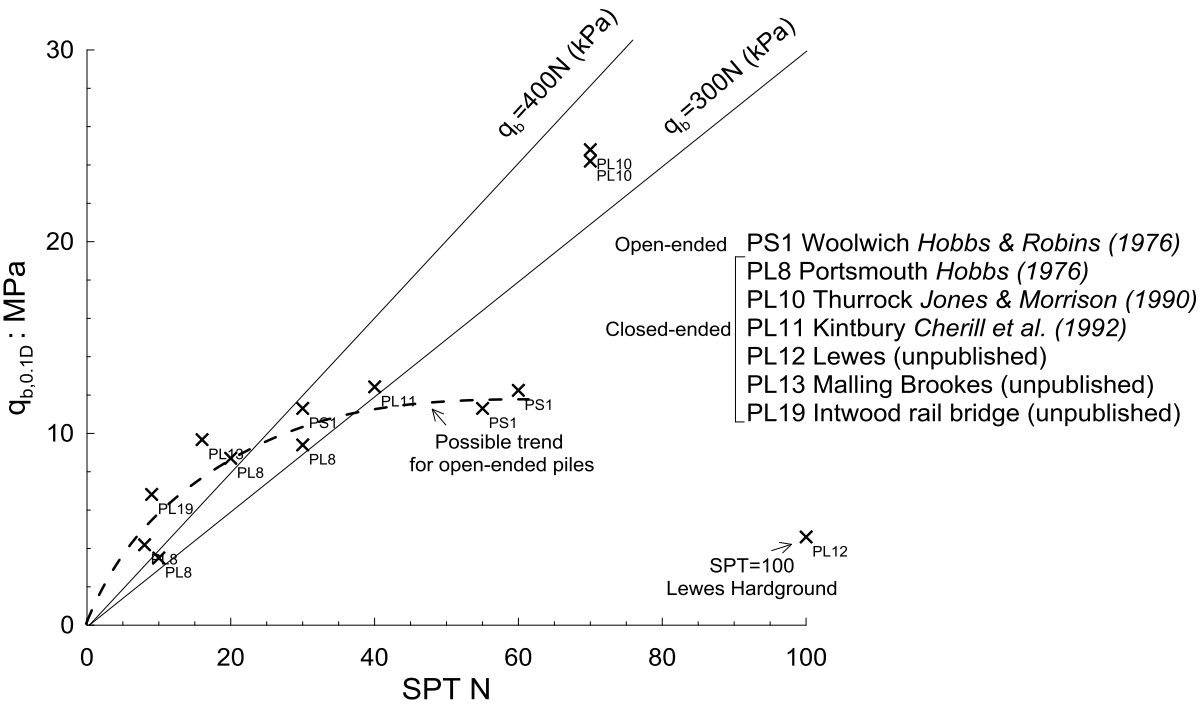


Figure 3-9: Ultimate base resistance versus SPT N value from CIRIA PR11/C574 test database (adapted from Lord *et al.*, 2002)

3.5 Published and unpublished pile test data in chalk

The potentially conservative current (CIRIA) design guidelines for pre-formed piles in chalk are based on a limited database of pile load tests of mixed quality. The design methods described do not consider the different effective stress conditions which may apply during installation, equalisation and load testing in chalk, including the effect of pile penetration on attenuation of stresses during driving or the potential beneficial effects of time on capacity. The effects of axial cyclic loading are only considered in one of the methods, where it is invoked as a mechanism to explain low driving resistances and not to address cyclic loading in service.

This section reviews the available database of static, dynamic and cyclic pile tests in chalk. Both published tests from the literature and unpublished tests provided to the Author are described. The database is summarised in Table 3-2. The results include and supplement the CIRIA (Lord *et al.*, 2002) dataset and tests identified from outside the original CIRIA database are indicated in parentheses. Tests on closed-ended full displacement piles and open-ended partial displacement piles are included in the following sections. Open-ended partial displacement piles are more relevant to the large diameter offshore piles described in Chapter 5 and the smaller diameter driven pile experiments described in Chapter 6. Closed-ended large displacement piles are relevant to the Imperial College highly instrumented jacked pile tests

described in Chapter 7. Both types of piles are discussed further in Chapter 8. The results are compared with the current design prediction methods and are used to demonstrate trends in the database and to highlight areas of further research. For all of the compression tests on open-ended piles considered, it is assumed for simplicity that all of the end bearing is sustained on the annular area only, i.e. $q_{ba,0.1D} = Q_b/A_{ann}$.

Table 3-2: Summary of piles in the chalk test database

Test site	Closed ended (PL) [1]	Open-ended (PS) [1]	All[1]
Number of sites	-	-	17 (7)
Number of piles	24 (8)	27 (20)	51 (28)
Sites with CPT data	1 (1)	2 (2)	3 (3)
Driven pre-formed steel	6 (1)	27 (20)	33 (21)
Jacked pre-formed steel	2 (2)	-	2 (2)
Driven precast	16 (6)	-	16 (6)
First time tension tests	7 (5)	5 (2)	12 (7)
Tension re-tests[2]	27 (21)	23 (9)	50 (30)
Compression tests[3]	12 (1)	1 (0)	13 (1)
Compression re-tests[3]	2 (2)	6 (6)	8 (8)
First time cyclic tests	0 (0)	0 (0)	0 (0)
Cyclic re-tests	2 (0)	9 (7)	11 (7)
Post cyclic failure tension tests	2 (0)	4 (2)	6 (2)
First time dynamic tests	4 (4)	15 (15)	19 (19)
Dynamic re-tests	2 (2)	17 (17)	19 (19)
Range diameters[4] (mm)	140 – 510	158 – 1500	140 – 1500
Average diameter[4] (mm)	357	865	626
Test time after installation (days)	0 - 693	0 – 726	0 - 726

1. Values in parenthesis indicate additional tests to the original CIRIA database
2. Tension or compression re-test on a pile previously subjected to static or dynamic loading post driving
3. Static compression tests included where the separation between base and shaft capacity is known
4. Diameter or equivalent diameter.: $D_{eq} = \sqrt{4A_{gross}/\pi}$ where A_{gross} is the gross enclosed area of the pile

3.5.1 Tests on partial displacement open-ended piles and H piles

North Woolwich (Hobbs and Robins, 1976)

Hobbs and Robins (1976) describe driven pile tests carried out as part of the Thames Flood Prevention Scheme at Gallions Point, North Woolwich. The ground conditions comprise Made Ground, Alluvium and gravel with chalk encountered between approximately 13 and 17mbgl. A borehole carried out at the nearby King George V Dock at Gallions Point Marina (BGS, 2016b) indicated predominantly Mundford Grade III to IV chalk, approximately equivalent to Grade B or C chalk within the CIRIA classification scheme (Spink, 2002). The chalk at the site is of low-medium density (Lord *et al.*, 2002).

The results of static tension and compression tests are reported on three driven 254 x 254mm (H section) Universal Bearing piles (Pile 4, 5 and 12). The un-instrumented piles were generally subjected to static compression tests approximately three weeks after driving followed by static tension tests to failure after further equalisation. The authors estimated the shaft resistance in the chalk by assuming distributions in the overlying layers which are inevitably open to uncertainty. The results are summarised as:

- Pile 4 was initially driven 3.3m into chalk and subjected to two axial compression tests to failure, both 23 days following driving. The pile was subsequently driven a further 5.2m and subjected to a compression test and then a tension test, 28 days and 54 days after re-driving respectively. The static tension test (4a) indicated τ_{avg} ($=Q_s/A_s$) of 42kPa in the chalk;
- Pile 5 was initially driven 7.8m into the chalk layer and subjected to two axial compression tests to failure, 21 days following driving. Pile 5 was subsequently re-driven a further 4.2m and subjected to three more axial compression tests over a 12 day period. A further axial compression test, which did not reach full failure, followed 40 days after re-driving. A tension test (5a) was then carried out 75 days after re-driving which gave a low τ_{avg} in chalk of 8kPa;
- Pile 12 was driven 12.8m into chalk and subjected to a static compression test 32 days after driving. A static tension test carried out 24 days later indicated τ_{avg} in the chalk of 19kPa.

The tension tests on the previously failed piles account for three of the six test results used to develop the current axial capacity design guidelines.

Brighton Marina (Lord and Davies, 1979)

Lord and Davies (1979) describe the installation and testing of a trial open-ended tubular steel pile at Brighton Marina. The 800mm OD pile, which had a 20mm wall thickness, was driven 4m into high density chalk (Lord *et al.*, 2002). The boreholes at the site indicated Mundford Grade II (≈ Grade A/B).

The test pile was subjected to rapid lateral loading and unloading tests up to maximum load of 1000kN, an unknown number of days after driving. A static axial tension test followed the lateral cyclic and static tests which did not reach full failure. The authors extrapolated the test curve and report τ_{avg} at failure of 175kPa (although a value of 150kPa is taken by Lord *et*

al. (2002)). The latter test result accounts for one of two tests on high density material, as shown on Figure 3-8.

Fleury-sur-Andelle, France (Bustamante *et al.*, 1980)

Bustamante *et al.* (1980) reported instrumented compression tests on driven H-piles at site in Fleury-sur-Andelle, France, as summarised on Table 3-3. The tests are not included in the CIRIA database, potentially because they were published only in French. Supplementary data on the tests was provided to the Author by Électricité de France, which is included in Appendix A-1. The ground conditions comprise clay and gravel with structureless chalk encountered between 2.9 and 9mbgl underlain by low density structured chalk (described as "weathered chalk with blocks"). The pile and *in-situ* test locations are shown on Figure 3-10. As shown on Figure 3-11 (a), cone resistance in the structureless chalk generally ranged between 2 and 6MPa, reaching 10MPa in the structured material below approximately 9m depth. The results of compression tests are reported on a H-section 360 x 330mm pile (P3) driven to penetrations of approximately 10.3m or 7.5m into the chalk. The instrumented pile was subjected to several compression tests after driving at various ages although the strain gauge measurements from only one of the re-tests is reported in the paper. Table 3-3 indicates a tendency for the total capacity to increase with time with a maximum set-up factor observed, for the H piles, of 1.6 between 86 and 546 days. Early age tests are not available to assess the overall capacity change since installation over this time period.

Table 3-3: Summary of compression tests at Fleury-sur-Andelle (Bustamante *et al.*, 1980)

Pile	L_p (m)	$L_{p,chlk}$ (m)	Age (days)	Q_{tot} (kN)	τ_{avg} (kPa)	Chalk τ_{avg} (kPa)
P1 Pre-cast Concrete *(PL)*	10.35	≈7.4	86	780	-	-
			104	900	-	-
			118	980	86	62
			130	980	-	-
			149	1020	-	-
P2 Closed Steel tube *(PL)*	10.3	≈7.4	387	1090	-	-
			92	590	-	-
			693	700	29	39
			701	680	-	-
P3 H pile *(PS)*	10.3	≈7.4	86	550	-	-
			394	800	74	111
			461	850	-	-
			546	860	-	-

The profile of shaft stress interpreted from the strain gauge measurements at failure, $\tau_{s,m}$ from the compression test are shown on Figure 3-11 (b). The test was conducted 394 days after driving. The shaft stress from the strain gauges at failure can be seen to broadly follow the trend of CPT cone resistance with depth. In the chalk, τ_{avg} at failure was equal to 111kPa with markedly higher values closer to the pile tip indicated by the strain gauges. Insufficient information is provided to assess end bearing for this pile. Further tests, on closed-ended piles, at the Fleury-sur-Andelle site are discussed in Section 3.5.2.

Leagrave, Luton (Burland and French, 1990)

Burland and French (1990) describe tests on two 6m long, 140x140mm open box section, "Wedge Piles" installed at a site in Luton. The chalk from surface consists of low-medium density structureless (Grade Dm) chalk with CPT q_c values of 2 to 4MPa and F_r ratios of 1 to 2%. The "Wedge Pile" comprises an outer shell which is initially driven to the required penetration depth and subsequently expanded along its length using an expanding inner section. Previously, trial tests on small model piles in the laboratory showed increases in shaft friction in sand by between 300 and 450% for expansions between 5 and 20% of the width of the piles.

The two piles were subjected to axial static tension testing as well as one-way axial cyclic loading tests. Post cyclic static failure tests were also carried out to check the effect of cycling on operational tension capacity. The tests are summarised on Table 3-4. Considering the unexpanded piles' behaviour first; Pile 1, tested in tension 6 days after driving without expansion, gave τ_{avg} of 24kPa (Test 1U.1/1.U.2). A tension retest 14 days later indicated a 5kPa increase in τ_{avg} (Test 1U.3). Test 1U.2 accounts for another of the six test results used to develop the current axial capacity design guidelines (Lord *et al.*, 2002). Tests 1U.1 and 2A.1 were carried out at similar times after driving with the latter test following expansion of the pile by 14.3% along its length immediately after driving. Comparison of these two tests indicates capacity increases of ≈400% when the pile was expanded and tested at the same age. Figure 3-12 compares the behaviour of an unexpanded box pile 20 days after driving (Test 1U.3) with piles expanded by between 14.3 and 21.4% at 5 days after driving, indicating that τ_{avg} increases with percentage expansion of the pile.

Test 1A.2 was an axial cyclic loading test consisting of 25 cycles at a utilisation ratio (UR see Section 3.2.5) of 0.5, in which no failure was observed. A post cyclic tension test indicated a 14.2% reduction in capacity following cyclic loading. Test 2B.2 was a cyclic test which comprised 50 cycles at a UR of 0.5. A subsequent tension test to failure indicated a

17.4% reduction in operational tension capacity when compared to the pre-failure static tension conducted on the previous day (2B.1).

Table 3-4: Static axial tension and one way cyclic tests using at Luton (Burland and French, 1990)

Pile	Type	Test	Age (days) [1]	Expansion (%)	UR	N (N_f)	τ_{avg} (kPa)	Capacity loss (%)
1	Box	1U.1	6	0			27[2]	
	(PS)	1U.2	6	0			24	
		IU.3	20	0			29	
		1A.1	5	14.3			141	
		1A.2[3]	5	14.3	0.49	25	121[4]	14.2
		1A.3	198	14.3			150	
2	Box	2A.1	5	14.3			107	
	(PS)	2A.2	19	14.3			115	
		2B.1	5	21.4			155	
		2B.2[3]	6	21.4	0.5	50	128[4]	17.4
		2B.3	20	21.4			142	
		2B.4	110	21.4			145	
		2B.5	203	21.4			125	
3	Crucif	3U.1	12	0			23	
	(PL)	3U.2[3]	12	0	0.45	50	23[4]	0
		3B.1	9	21.4			111	
		3B.2	126	21.4			114	
4	Crucif	4A.1	12	10.7			163	
	(PL)	4A.2[3]	24	10.7	0.48	(20)	66[4]	60
		4A.3	169	10.7			79	

1. Days between driving (or expansion) and tension test to failure
2. Load control system failed during this test
3. Axial cyclic test
4. Post cyclic static tension test

LPG jetty, Lincolnshire (Hobbs and Atkinson, 1993)

Hobbs and Atkinson (1993) describe static tension and compression tests on a 914 mm diameter open-ended tubular steel test pile, with a wall thickness of 19mm, installed at Immingham, Humberside. The pile was driven through 8m of alluvium and 11m into the underlying high density Grade A chalk and a static tension test was completed. Although the time between driving and load testing is unknown, it is assumed that the static tension test was completed soon after driving since both were conducted over-water. The tension test indicated an average shaft resistance of 125kPa. The latter test result is similar to the value of 175kPa reported at Brighton Marina (Lord and Davies, 1979), discussed above, and accounts for the second of two tests (PS4) on high density grade A chalk shown on Figure 3-8.

Humber International Terminal & Humber Sea Terminal (Moulds, 2001)

Moulds (2001) describes dynamic and static testing of nine 1067mm diameter tubular (t_w = 25mm) open-ended steel piles installed as part of two deep water berthing facilities at Immingham; the Humber International Terminal (HIT) and the Humber Sea Terminal (HST). The results were published at a similar time to the CIRIA C574 recommendations and were not included in the database. The chalk at HIT is of medium-high density Grade A/B. At HST high density chalk Grade A/B chalk was encountered. The piles generally penetrated 15m into chalk at HIT and 5 to 7m at HST. Back analyses of dynamic load tests carried out at HIT, between 0 and 24 days after driving, were reported by the authors. The resulting shaft capacity profiles are shown on Figure 3-13 (a). Little details were provided on the dynamic analysis. The profiles indicate a dependence of local dynamic shaft resistance, $\tau_{s,d}$ at end of driving and beginning of restrike on normalised distance from the pile tip, h, with values up to 400kPa interpreted near the base which reduce to values generally less than 10kPa further along the shaft. The results indicate set-up factors on dynamic shaft resistance in medium-high density chalk of between 1.2 and 1.8, 24 days after driving. A similar trend was observed for two of the piles at HST which showed set-up factors of between 1 and 1.7 at 61 days (Figure 3-13 (b)). The remaining two piles at HST (6F and 10F) showed higher set-up factors over the first 10 days of 2.5 and 2.8.

An axial static tension test was also conducted at HST, 30 days after the installation of a test pile, with similar dimensions to the working pile described above, driven to a similar depth of penetration in chalk (≈9m). The test did not reach full failure and was terminated at a maximum load of 4.5MN when the pile head displacement was 5.9% of the diameter. Assuming that the majority of the shaft friction mobilised was in the chalk layer, as in the dynamic tests shown in Figure 3-13, and assuming a 9m penetration into chalk, gives a (lower bound) τ_{avg} of 149kPa. No information is available on the installation resistance of this pile. The latter result is consistent with the results in similar high density chalk described previously at Brighton (Lord and Davies, 1979) and Immingham (Hobbs and Atkinson, 1993) although the pile age at the time of testing of the latter two tests is not known.

Hemmoor, Germany (Lahrs and Kallias, 2013)

Lahrs & Kahlias (2013) report dynamic test results from the Baltic 2 offshore windfarm, which the Author assumes involved low-medium density chalk, and further dynamic, static and cyclic results from an analogous onshore site in Hemmoor, Germany. Several details on the

testing have been omitted due to the confidential nature of the data. The tests were reported in German, and have been interpreted as accurately as possible by the Author.

Dynamic tests were carried out at the offshore site on 1.5m diameter piles at end of driving and one, two and four months later. Both the amount of penetration into the chalk of each pile and whether the same piles were re-struck on each occasion is unclear. These factors could explain the relatively modest set-up factors of 1.5 to 1.6 observed after four months.

The onshore programme consisted of dynamic tests on five 1.5m diameter piles undertaken at the end of driving and on three occasions following driving. Four of the piles (P01, P02, P03, P04) were installed to a total depth of 50m and sleeved in the overlying material to a depth of 26.5m, penetrating 23.5m into the chalk. Pile P05 was installed to a depth of 43m and sleeved to a depth of 26.5m, penetrating 16.5m into the chalk. After the dynamic tests, it appears that the same piles were re-tested; two in axial static tension (P01 & P03), two under axial cyclic loading followed by post cyclic static tension (P02 and P04), and one case in axial compression (P05). The results of the tests on P02 were not included in the paper.

The end of driving capacities from the dynamic tests suggest low average mobilised shaft resistances of between 0 and 12kPa (Table 3-5). The annular end-bearing, q_{ba} interpreted from the dynamic tests ranged from 3.9 to 30MPa. It has been assumed that the majority of the shaft friction mobilised in the dynamic test was mobilised on the outside of the pile, and that compressive dynamic shaft resistance is approximately equal to tensile shaft resistance during a static test. The set-up factors, Λ, determined in this way are shown graphically on Figure 3-14 versus number of tests, since only partial information on pile ages is available. Pile P01 gave τ_{avg} of 114kPa at the first restrike (BoR1) compared to a zero value at EoD, indicating remarkable set-up occurred over this unknown time period. Pile P03, P04 and P05 indicated equally remarkably high set-up factors at BoR1 of between 8.6 and 12.7 over their unknown pause durations between the end of installation and the first restrike. Further restrike tests on the same piles showed an unexpected but consistent trend of capacity decrease with time. The interval between BoR1 and BoR2 was 41 days, which allowed some capacity recovery, evident in the set-up trends, which seem to show a plateau and not reduce significantly. The time between BoR2 and BoR3 was just 7 days, leaving little time for capacity recovery, and a more marked reduction is seen. The static tension test on Pile P01, at an unknown age, showed 70% lower capacity (τ_{avg} =33kPa) than expected, when compared to the prior restrike test, which gave τ_{avg} =114kPa. The static test on Pile P03 showed a lower τ_{avg} of 23kPa, an unspecified

time following BoR3, equivalent to a reduction in capacity of 75%. The surprising trend of capacity decrease with time may be attributable to the application of multiple restrike blows to the same pile with dynamic re-testing, reducing the operational tension capacity. Earlier studies in sands and clays have shown that ageing trends are disrupted and even reversed when multiple tests are conducted on the same piles (Jardine *et al.*, 2006, Karlsrud *et al.*, 2014).

Axial cyclic loading was applied to Pile P02 and P04, however only the results of P04 are reported within the paper. Cycling was applied to P04 with Q_{cyc}=0.23MN and Q_{mean}=1.4MN for 1000 cycles, which is equivalent to Q_{cyc}/Q_{ref} of 0.03 and Q_{mean}/Q_{ref} of 0.19. The reference static capacity, Q_{ref} is taken here as the dynamic shaft resistance mobilised during the third restrike (7.24MN) test on pile P04. The latter results in a shaft resistance utilisation ratio (UR) of 0.31. The results are not reported in detail, however the authors report stable behaviour at these cyclic load levels.

While the experimental design of the tests at Hemmoor led to ambiguous results which are difficult to interpret with the limited available information, the case history indicates:

- Low installation τ_{avg} in low-medium density chalk from dynamic tests, which ranged from negligible to 12kPa;
- Significant increases in capacity between end of driving and the first restrike test, where τ_{avg} reached between 101 and 149kPa;
- Multiple dynamic restrike tests on the same pile may severely counteract beneficial time effects on capacity in chalk leading to a reduction in capacity with time and/or restrike blows.

Table 3-5: Dynamic & static shaft resistances (after Lahrs & Kahlias, 2013)

	Shaft resistance, f_s (kPa)					
Date	**EOD**	**1st Restrike**	**2nd Restrike**	**3rd Restrike**	**Static Test**	
Age	**Unknown**	**07/10/2011**	**17/11/2011**	**24/11/2011**	**Unknown**	**Testing Mode**
P01	0	114	-	-	33	Static tension
P03	12	110	106	60	23	Static tension
P04	12	149	109	65	16	Post-cyclic tension
P05	12	101	82	67	-	Compression test

Static tension tests at St Nicholas-at-Wade (Ciavaglia *et al.*, 2017a, b)

Ciavaglia *et al.* (2017a, 2017b) describe the "Wind Support" JIP, a programme of static tension and static and cyclic lateral tests on piles installed at a test site close to the village of St

Nicholas-at-Wade, Kent, UK. The site is a previous chalk quarry from which all overburden and weathered chalk has been removed, leaving low-medium density Grade B2/B3 chalk from surface which grades to Grade B2/A2 with depth. The test site was also utilised in the Author's research and further details are provided in Chapter 6. The raw data were kindly provided to the Author by Dr. John Carey of Wind Support Ltd.

The "Wind Support" piles were driven with a 7t hydraulic hammer and subjected to dynamic restrike between two and twelve hours following driving. A summary of the pile details relevant to this study (Pile 1, 2 and 4) is given in Table 3-6. Pile 3 and 5 were subjected to lateral loading tests only and are outside the scope of this thesis.

The piles had vibrating wire strain gauges installed in diametrically opposite pairs at intervals along the pile shaft. The gauges were protected inside angular steel channels welded to the pile wall that prevented damage during driving. The inertia of the piles was such that they were fully coring during installation with the steel displacing the chalk and the internal plug reaching as high as 1.5m above ground level. No end of driving dynamic analyses were conducted, however Table 3-6 includes the results of dynamic restrike tests carried out between two and twelve hours after driving, using CAPWAP which indicated τ_{avg} of between 21kPa 27kPa with one surprisingly high value of 43kPa, and annular end bearing, q_{ba} values of between 6.1 and 9.2MPa respectively or 0.43 to 0.62 times the cone resistance. The tests were carried out by a sub-contractor and the raw data was not available to the Author.

The axial pile tests, conducted between November 2011 and March 2012, consisted of static tension tests on Pile 1 and Pile 2 to investigate changes in capacity with time, along with static and cyclic lateral tests on Pile 2 and Pile 4. Pile 4 was exhumed after all testing was complete and a zone of remoulded chalk, 0.78 to 1.57 times the wall thickness, t_w was observed surrounding the pile. A wedged shaped failure thought to relate to previous lateral testing was observed, along with a zone of fractured chalk extending to 880mm (r/R = 2.31) from the pile centre (Muir Wood *et al.*, 2015, Ciavaglia *et al.*, 2017a). The angular steel channels and consequent irregular pile geometry were thought to have contributed to the remoulded zone thickness and affected the lateral response. Muir Wood *et al.* (2015) also studied the behaviour of driven steel plates which they thought could represent the installation effects induced by large diameter monopiles. They drove plates of varying thicknesses to depths of 2m, at the same site, and found a remoulded zone formed parallel to the plates with thicknesses of approximately $0.4t_w$.

The axial tension programme conducted on Pile 1, summarised in Table 3-7 and shown graphically on Figure 3-15, was preceded by a dynamic restrike test, two hours after driving. The same pile was re-tested statically in tension on three subsequent occasions timed at 6, 50 and 119 days after driving. In contrast to the tests at Hemmoor, the operational shaft capacity increased significantly with time in these tests, following the bi-linear set-up trend shown in Figure 3-16, where the net shaft load at failure is compared to the compressive shaft capacity from the dynamic test at restrike. A small increase in capacity (≈10%) was observed between the dynamic test and the first static test 6 days later. Shaft capacity doubled between 6 and 50 days and increased threefold over the 69 days between the final two tests. It is not known if the rate of capacity increase stabilised with time. Comparison between the static tests at 6 and 119 days indicates an overall set-up factor of 7.4. Comparison of the 119 day static test with the (+2hr) restrike test indicates a higher still set-up factor of 8.1.

Table 3-6: Summary of pile details and CAPWAP results for relevant historical tests at St. Nicholas at Wade (Wind-Support, 2012)

Test pile	D (mm)	t_w (mm)	L_p (m)	L_p/D	t (hours)	τ_{avg} (kPa)	$q_{b,a}$ (MPa)
1	762	44.5	4	5.3	2	21	6.5
2	762	44.5	4	5.3	12	43	9.2
4	762	25.4	10	13.1	12	27	6.1

Table 3-7: Axial tension testing programme on Pile 1 and Pile 2 during Phase 1 tests at St. Nicholas at Wade (Wind-Support, 2012, Ciavaglia *et al.*, 2017a, b)

Pile	Code	Age (days)	Mode	τ_{avg} (kPa)	Λ	Outcome
1	1_A6	6	Static tension	23	1.1	Failure
	1_A50	50	Static tension	57	2.7	Failure
	1_A119	119	Static tension	169	8.1	Failure
2	2_M6	6	Static lateral	-	-	Up to 9% lateral capacity
	2_A7	7	Static tension	22	0.5	Failure
	2_M51	51	Static lateral	-	-	Up to 8% lateral capacity
	2_A52	52	Static tension	60	1.4	Failure
	2_M120	120	Static lateral	-	-	Up to 50% lateral capacity
	2_A122	122	Static tension	75	1.7	Failure

The static axial tension tests conducted on Pile 2 are also summarised in Table 3-7 and shown on Figure 3-17. The previous static lateral tests conducted on the pile are also noted on Table 3-7 to illustrate the pile's loading history. A similar investigation of tension shaft capacity with time was conducted, with tests on Pile 2 conducted 7, 52 and 122 days after driving. Application of a lateral load equivalent to 9% of the lateral capacity six days after

driving may explain why the tension shaft capacity was only 50% of that interpreted from the restrike conducted 12 hours after driving (Figure 3-16). However, τ_{avg} indicated by the latter was particularly high (=47kPa), while the first static re-tests on Pile 1 and 2 indicated similar values of 23 and 22kPa at 6 and 7 days after driving, respectively. Application of further lateral loading in tests 2_M51 and 2_M120 led to an overall set-up trend which fell below that of Pile 1, which had not been subjected to any previous lateral loading, and resulted in a relatively modest set-up factor of 1.7 at 122 days. The results indicate that lateral loading has a significant deleterious effect on axial capacity leading to a reduction in the trend of capacity growth with time.

The global stiffness trends observed during the static axial tension tests are shown on Figure 3-18, where global stiffness is defined as the load change ΔQ from an initial load divided by the total displacement from the same reference point. All three tests on Pile 1 show similar initial (non-linear) stiffnesses which degraded more rapidly in earlier tests (1_A2 and 1_A50). Test 1_A119 showed a significantly higher stiffness at a range of loading levels. In the case of Pile 2 (Figure 3-18 (b)), global stiffness appears to increase marginally with time with the effects of intermittent lateral loading evident in the stiffness degradation trends. Test 2_A122, subjected to lateral loading equivalent to 50% of its lateral capacity, showed a higher stiffness than the other two piles initially, but degraded rapidly to share a similar stiffness to test 2_A52 over the majority of the loading range.

Finally, Figure 3-19 shows the load distribution along the pile length at tension failure from the strain gauge data for tests 2_A7, 2A_122 and 1_A119 as interpreted by Ciavaglia *et al.* (2017a). The results indicate four to six times higher shaft resistance applying on the lower parts of the piles, which does not follow the trends in chalk properties with depth, illustrating that as with sands and clays, the relative tip depth, h has an important impact on long-term local shaft resistance. Comparing Test 1_A119 and Test 2_A122 also demonstrates the significant deleterious effect of previous lateral loading on the shaft resistance from the strain gauges.

Axial cyclic tests St Nicholas at Wade (Iberdrola, 2013)

Iberdrola (2013) conducted further testing on the piles, tested previously by Ciavaglia *et al.* (2017a, 2017b), approximately 19 months after the end of the first phase of testing. Two-way axial cyclic tests were conducted on Pile 1 and Pile 4, followed in each case by a static compression test. The testing was carried out by Wind Support Ltd. The results were published in part by Dührkop *et al.* (2015) and the Author is grateful to Iberdrola for their permission to

discuss the outcomes here. The tests conducted on Pile 1 during the first phase were summarised previously in Table 3-7. The second phase of the testing programme on Pile 1 is summarised in Table 3-8 and Figure 3-20.

Table 3-8: Two way axial cyclic and compression tests on Pile 1 during second phase of testing at St Nicholas at Wade by Iberdrola (2013)

Test code[1]	Age (days)	Q_{tot} (kN)	Q_{max} (kN)	Q_{min} (kN)	N_{cum}[2]	Q_{cyc}/Q_{ref}	Q_{mean}/Q_{ref}	UR	Comment
-	692	-574	-	-	-	-	-	-	Check response
-		-	+50	-27	-	0.01	0.02	0.02	Log strain gauges
1_CY_692a		-	+50	-27	27	0.08	0.02	0.02	Two way cyclic
1_CY_692b		-	+170	-94	315	0.08	0.02	0.06	Two way cyclic
-		-	0	0	-	-	-	-	Load held at zero
1_CY_692c		-	+170	-94	325	0.08	0.02	0.06	Two way cyclic
1_CY_692d		-	+250	-174	329	0.13	0.02	0.11	System failure
-	694	-	+50	-27	-	0.01	0.02	0.02	Check response
1_CY_694a		-	+50	-27	334	0.01	0.02	0.02	Log strain gauges
1_CY_694b		-	+170	-94	566	0.08	0.02	0.06	Two way cyclic
1_CY_694c		-	+250	-174	900	0.13	0.02	0.11	Two way cyclic
1_AC_694a		+800	-	-	-	-	-	-	Max system load
1_AC_694b		+1600	-	-	-	-	-	-	Max system load

1. Test code nomenclature gives pile number, test type (CY – two way cyclic, AC compression), pile age and test stage (a = 1st test, b = 2nd test)
2. Cumulative cycles since the beginning of the test

The pile was first loaded statically in tension up to a net load of 574kN followed by an initial packet of two way cyclic loading (1_CY_692a) with peaks and troughs of 27kN (tension) and 50kN (compression) respectively. The purpose of these tests was to check the response of the system and log the strain gauges. The first planned cyclic tests (1_CY_692b/c) involved two-way cycling, at primarily 0.05Hz, for 298 cycles between a net tensile load of 94kN and a compressive load of 170kN. The only value of Q_{ref} available to normalise the results was the tension shaft capacity from test 1_A119 during Phase 1, ≈19 months prior and applying this indicates Q_{cyc}/Q_{ref} of 0.08 and Q_{mean}/Q_{ref} of 0.02, equivalent to a shaft UR of 0.06. The evolution of permanent accumulated cyclic displacement normalised by pile diameter s_{acc}/D with cycles is shown on Figure 3-21. The pile displaced downwards over this packet of cycling and only began to stabilise at N≈180 when the displacement under the peak compressive load reached ≈44mm (s_{acc}/D=5.8%). During the previous axial tension testing, a gap of approximately 44mm had opened beneath the pile between the bottom of the pile plug and the intact chalk (Iberdrola,

2013). Plastic displacement during the cyclic test therefore only began to occur when two-way cycling led to the closing of the space beneath the pile.

The next successful packet of planned cyclic tests (1_CY_694b) involved cycling at an increased frequency of 0.1Hz at the same loading levels as in the previous packet for 232 cycles. The s_{acc}/D-N trends, (Figure 3-21) indicate a slight reduction in the peak displacement under compressive load with cycling and an increase in the peak displacement under tensile load. The final packet of cycling (1_CY_694c) involved 334 cycles between a net tensile load of 174kN and a compressive load of 250kN (Q_{cyc}/Q_{ref} of 0.13 and Q_{mean}/Q_{ref} of 0.02, equivalent to a shaft UR of 0.11). The peak permanent displacements continued to accumulate rapidly during this phase with the peak-to-peak displacement increasing from 2.2%D to 13.1%D. The trend was for the peak displacement under tension loading to increase significantly, and the peak displacement under compression to reduce slightly, effectively due to the pile being pulled out of the ground.

The apparent cyclic damage indicated by the displacement accumulation trends is also reflected in the cyclic loading and unloading stiffness behaviour, plotted in Figure 3-22. A strong degradation in stiffness is observed initially, falling to 35% the reference value (taken at the beginning of test 1_CY692b), which as with the displacement trends, stabilised when N reached approximately 180 at a displacement of 44mm. Continued degradation to 20% of the reference value was observed over the next test (1_CY_694b). Degradation in stiffness was sharper over the final packet of cycling (1_CY_694c) resulting in just ≈2% of the initial stiffness remaining at the end of cycling. A post cyclic tension test to check the operational tension capacity was not carried out.

The static and cyclic lateral loading tests conducted previously on the "long" Pile 4 were summarised by Ciavaglia *et al.* (2017b) and included cyclic lateral loading up to 1500kN and static lateral loading up to 2000kN, up to 122 days after driving. The latter loads, which reached the maximum capacity of the testing rig, were insufficient to cause failure. The axial cyclic loading tests conducted on Pile 4 during the second phase are summarised on Table 3-9 and Figure 3-23. The first packet of axial cyclic loading on Pile 4 (4_CY_695a) involved two-way cycling, at primarily 0.1Hz, for 200 cycles between a net tensile load of 220kN and a compressive load of 360kN (Q_{cyc}/Q_{ref} of 0.07 and Q_{mean}/Q_{ref} of 0.02, equivalent to a shaft UR of 0.05). The value of Q_{ref} was assessed from test 1_A119, conducted approximately 19 months prior. The trend over 4_CY_695a was for the peak displacement under compression to increase

slightly and irrecoverably over 200 cycles (Figure 3-24). The second packet of cyclic loading (4_CY_695b) involved two way cycling, for 220 cycles between a net tensile load of 350kN and a compressive load of 490kN (Q_{cyc}/Q_{ref} of 0.1 and Q_{mean}/Q_{ref} of 0.02, equivalent to a shaft UR of 0.09). The peak displacement under tensile and compressive loading increased significantly at a constant rate leading to a peak to peak displacement at the end of cycling of 5.5%D (Figure 3-24). The final packet of cycles (4_CY_695c) applied at the same load levels as test Cyclic 2, led to continuing displacement accumulation. The test was halted after 55 cycles when the total peak to peak displacement had reached 8.7%D.

The cyclic loading and unloading stiffnesses offered by Pile 4 show gradual losses, with degradation amounting to 80% at the end of 4_CY_695a, reducing to 2% at the end of test 4_CY_695c (Figure 3-25). The post cyclic tensile static test (4_A695) failed at 320kN, equivalent to τ_{avg} of 11kPa. This represents a reduction in shaft capacity of 93% for Pile 4, based on the "last seen" value of τ_{avg}, during test 1_A119, 119 days after driving. It is clear that the multiple axial and lateral re-tests degraded Pile 4's load carrying capability dramatically.

Table 3-9: Two way axial cyclic and compression tests on Pile 4 during second phase of testing at St Nicholas at Wade by Iberdrola (2013)

Test code[1]	Age (days)	Q_{tot} (kN)	Q_{max} (kN)	Q_{min} (kN)	N_{cum}[2]	Q_{cyc}/Q_{ref}	Q_{mean}/Q_{ref}	UR	Comment
-	695	-	+360	-220	-	-	-	-	Check response
4_CY695a		-	+360	-220	200	0.07	0.02	0.09	Two way cyclic
-		-	+490	-490	-	-	-	-	Check response
4_CY695b		-	+490	-350	420	0.09	0.02	0.11	Two way cyclic
-		-	+490	-490	-	-	-	-	Check response
4_CY695c		-	+490	-350	475	0.09	0.02	0.11	Two way cyclic
4_A695		-260	-	-	-	-	-	-	Tension failure
4_AC695a		+2000	-	-	-	-	-	-	Max system load

1. Test code nomenclature gives pile number, test type (CY – two way cyclic, A axial, AC compression), pile age and test stage (a = 1st test, b = 2nd test)
2. Cumulative cycles since the beginning of the test

Pile 1 was subjected to two static compression tests at the end of its axial cyclic testing programme. The pile was first loaded to the maximum (800kN) that could be applied with the system deployed, without failure (1_AC_694a). The test system capacity was subsequently increased but only a displacement of 1.1% of the diameter developed under loading to 1600kN (1_AC_694a). Pile 4 was also subjected to a static compression test (4_AC_695) at the end of the axial cyclic testing programme. The tensile static test conducted immediately prior

(4_A695) led to failure at a shaft load of 260kN. The pile was loaded to the maximum system load of 2000kN and no failure was observed at a displacement of 4.7% of the diameter. Extrapolation of the test curve assuming a hyperbolic relationship between applied load and permanent displacement, to a displacement of 10% of the pile diameter, using two methods (Chin, 1970, Decourt, 1999) as detailed in Appendix A-2, suggests failure might have occurred under a total load of approximately 2.75MN. The end bearing interpreted depends on the assumptions made about the contributions from the annular area and the soil plug. Assuming the pile is plugged, and applying the base load on the gross base area during static failure (Eq. 3-4) leads to $q_{b,0.1D}$ approximately equal to 5MPa or $q_{ba,0.1D}/q_{c,1.5D}$ equal to $0.34q_{c,1.5D}$. Applying a ratio of $0.7q_{c,1.5D}$ to the annular area and subtracting from the total base capacity indicates that end bearing on the soil plug is equivalent to approximately $0.28q_{c,1.5D}$.

Port of Felixstowe

Multiple tubular steel piles have been installed in chalk for the Port of Felixstowe. Two instrumented pile tests were conducted as part of the design of the rear crane beam pile foundation of the Felixstowe South Reconfiguration Project. The results have not been published previously and the data were provided to the Author by Royal Haskoning DHV with the permission of Costain Ltd. The details of the tests were summarised by Hartley (2015) and supplementary information is provided in Appendix A-1. The ground conditions at the site consist of sand, gravel and clay to ≈26.5m depth, underlain by structured low-medium density Grade B/C chalk. Two 762mm diameter tubular steel piles with a wall thickness of 44.5mm were installed to penetrations of between 17.8 and 18.0m. Pile 2 was sleeved in the chalk to separate the resistance from that in the overlying sediments. The piles were instrumented with vibrating wire strain gauges welded on to the pile surface and protected by a U-channel steel section. The U-channels consisted of parallel flange channels of 200mm x 90mm with a cross sectional area of 37.9cm^2. After installation, 16 of the 30 strain gauges on Pile 1 were fully functional, while 25 out of the 27 gauges on Pile 2 were working after driving.

Dynamic load tests were carried out on both piles 2 days after installation and static compression load tests were carried out 43 days after installation. The dynamic test interpretation appears reasonable, although only the contractor's reports were provided to the Author. A second dynamic restrike test followed, 7 days after the static compression test. In the chalk, τ_{avg} had reached between 61 and 66kPa after 2 days, based on the first dynamic restrike test. No end of driving tests are available. The static compression test conducted 41 days after the dynamic test showed lower τ_{avg} in the chalk of between 47 and 58kPa,

considering the strain gauge measurements. The further restrike test 7 days later indicated slightly higher τ_{avg} between 62 and 67kPa. Very little increase in capacity occurred between the first dynamic test and the subsequent static and dynamic tests suggesting that either (i) set-up was negligible or largely complete at 2 days after installation or (ii) the restrike test had a significant deleterious effect on capacity.

Figure 3-26 plots the local shaft resistance, $\tau_{s,d}$ determined from the restrike tests (at 2 and 50 days after driving) and the strain gauges, $\tau_{s,m}$ at failure during the intermediate static test (43 days after driving). As shown on Figure 3-26, both the dynamic and static tests indicated higher local shaft resistances in the vicinity of the pile tip, confirming a strong dependence of shaft friction on relative tip depth, h, and negligible increases in capacity over time in chalk between the various re-tests. It is worth noting from Figure 3-26 that the strain gauge measurements indicated significant set-up (on the order of 400%) in the sand and gravel over the equalisation period. The set-up was not evident in the sand and gravel when the dynamic test was conducted 7 days later.

3.5.2 Tests on large displacement closed-ended piles

Chatham, Kent (Meigh, 1971)

A series of tests were described by Meigh (1971) on driven closed-ended steel cased piles driven in chalk at Chatham, Kent. The ground conditions at the site consisted of made ground of variable thicknesses, underlain by Alluvium and gravel to 18m and chalk. The chalk is described as weak to medium strong Mundford Grade IV to Grade III (Grade B/C). Borehole information available from a nearly residential development indicates low density Grade C3-C5 chalk between 12.3 and 25m (BGS, 2016a).

A 508mm diameter steel tube (TP12), was driven 7.9m into the chalk. The test pile was sleeved through the made ground and alluvium to allow the shaft friction in the chalk to be determined. The pile was tested in axial compression 14 days following driving. The piles were not instrumented and Hobbs (1977) interpreted, using unknown assumptions, τ_{avg} between 35 and 54kPa and an end bearing of 7 to 8MPa. Although not quantified, Meigh (1971) noted from analysis of the results of compression tests on TP12 and five other un-sleeved piles driven at the site, that shaft resistance in the Alluvium and chalk appeared to increase with time.

Drayton, Portsmouth (Hodges and Pink, 1971)

The results of steel closed-ended piles jacked and tested at a site in Drayton, near Portsmouth, were described by Hodges and Pink (1971). The ground conditions consisted of highly weathered, assumed low-medium density, Mundford Grade VI to IV (Grade Dm/Dc to C). Two piles of 170 and 220mm diameter with 60° apex conical tips were jacked at a rate of 0.33mm/s to depths up to 15m below ground level. Delays between 8 minutes and 18 days were imposed prior to static load testing in compression and tension.

The τ_{avg} determined from the tension tests was generally between 5 and 10kPa, which led to a correlation between calculated local shaft resistance at failure, τ_f in kPa, in weathered chalk and CPT cone resistance, q_c based on the results of jacked pile tests:

$$\tau_f = 0.0009 q_c \qquad 3\text{-}42$$

The CPT was advanced in 75mm intervals and the test was conducted manually, probably allowing at least partial pore pressure dissipation to occur. The authors also present a comparison between their CPT q_c values and ultimate toe resistance from the compression tests, as shown on Figure 3-27. The cone resistance was averaged over an interval 2.3D above and 1.5D below the pile toe, with a weighting applied to the resistance below the toe. The pile test was conducted in a similar manner to the mechanical CPT and the procedures adopted led to a good coincidence between the two measurements with $q_b \approx 0.9 q_c$.

North Woolwich (Hobbs and Robins, 1976)

Hobbs and Robins (1976) describe, for the North Woolwich site described in Section 3.5.1, the results of static tension and compression tests on a closed-ended 364mm diameter steel tube. Pile 6 was driven 3.6m into the chalk layer and after 21 days was subjected to two compression tests to failure. A static tension test carried out 50 days later indicated τ_{avg} as 26kPa (Record PL5 on Figure 3-8). It is unclear how the shaft and base resistance contributions were separated in these tests by the authors.

Newbury, Berkshire (Hobbs and Robins, 1976)

Hobbs and Robins (1976) and Hobbs (1977) report limited details of compression tests on a 510 mm diameter closed-ended steel cased pile at Newbury, Berkshire "driven easily" into chalk to 10.5m. A value of τ_{avg} of 33kPa, 5 days after driving, was interpreted from the pile test by unknown means by Hobbs (1977).

Portsmouth, UK (Lord, 1976)

Lord (1976) report the results of static compression tests on six pre-cast concrete shell piles, between 380 and 510mm in diameter, installed to total depths of between 7 and 17m. The piles penetrated between 3.5 and 13.5m into chalk, which was overlain by marine and alluvial deposits and peri-glacial clay. In the chalk, τ_{avg}, interpreted by Lord *et al.* (1994), varied between 48 and 72kPa and reduced with increasing penetration into the chalk. The base resistance interpreted by the authors ranged from 4.8 to 9.4MPa.

Fleury-sur-Andelle, France (Bustamante *et al.*, 1980)

Instrumented compression tests on closed-ended steel tubular piles and precast concrete piles conducted at the site in Fleury-sur-Andelle, described in Section 3.5.1 were also reported by Bustamante *et al.* (1980). Supplementary data on the tests were provided to the Author by Électricité de France, which is included in Appendix A-1. The pile and *in-situ* test locations were shown previously on Figure 3-10. The results of compression tests are reported on one 400 x 400mm square section pre-cast concrete pile (P1) and one closed-ended 445mm diameter steel tube (P2). Both piles were driven to penetrations of approximately 10.3m or 7.5m into the chalk. The instrumented piles were subjected, at various ages after driving, to several compression tests (Table 3-3, previously) although the authors only report the strain gauge measurements from only one of the re-tests. Table 3-3 indicates a tendency for the total capacity to increase with time, despite the multiple re-testing procedure. However, early age tests are not available to assess the overall capacity change since installation over this time period.

The profiles of shaft stress interpreted from the strain gauge measurements at failure for the compression tests on the closed ended piles are shown on Figure 3-11 (b). The tests were conducted between 118 and 693 days after driving. The shaft shear stress distribution given by the strain gauges at failure can be seen to broadly follow the trend of CPT cone resistance with depth. In the chalk τ_{avg} lay between 32 and 58kPa on the aged closed-ended piles and with markedly higher values closer to the pile tip indicated by the local strain gauge measurements. End bearing, $q_{b,0.1D}$ ranged from 1.8 to 2.5MPa.

Nykøbing Falster, Denmark (Skov and Denver, 1988)

Skov and Denver (1988) describe dynamic and static tests on five square section (300mm x 300mm) pre-cast concrete piles installed in chalk to 11m depth at Nykøbing Falster, Denmark. The piles' capacity changes with time were assessed through dynamic "first-time" tests on separate "virgin" piles at 1, 5, 8 and 11 days after driving and a static test on a

previously untested pile 14 days after driving (Pile PB2). After its static test, PB2 was subjected to further restrike tests 25 and 39 days after the end of driving. The set-up factors on *total* capacity obtained are summarised on Figure 3-28 where the capacity is normalised by the capacity obtained in the dynamic test conducted 1 day after driving. Capacity can be seen to increase significantly with time with a capacity gain of ≈383% observed in the static test conducted 14 days after installation. Subsequent restrike tests led to higher still capacity gains which reached 740%, 39 days after driving. It is not clear if the virgin "first-time" loading curve would have shown the same long-term trends.

Leagrave, Luton (Burland and French, 1990)

The "Wedge Pile" tests described by Burland and French (1990) at Leagrave Luton (3.5.1) also included tests on cruciform (closed-ended) sections assembled from four 6m long 70 x 70 x 10mm equal angle sections (Pile 3 and 4). The piles were subjected to axial static tension testing as well as one way axial cyclic loading tests. Post cyclic static failure tests were also carried out to check the effect of cycling on operational tension capacity. The tests were summarised previously on Table 3-4. Cruciform Pile 3, tested in tension 12 days after driving without expansion, gave τ_{avg}=23kPa (Test 3U.1). Test 3U.2 was a cyclic test which comprised 50 cycles at a UR of 0.45; a subsequent tension test indicated no change in operational tension capacity. Test 4A.2 reached cyclic failure after 20 cycles at UR ≈ 0.48, with a subsequent 60% reduction in capacity when compared to test 4A.1.

Thurrock, Essex (Jones and Morrison, 1990)

Static compression and dynamic tests were conducted on three square section (275mm x 275mm) pre-cast concrete piles installed into chalk in the Lakeside area of Thurrock, Essex as reported by Jones and Morrison (1990). The results were interpreted by Lord *et al.* (1994) who indicated τ_{avg} between 44 and 120kPa and decreased with increasing penetration into chalk (or relative tip depth, h). The age of the piles at the time of testing is not given and the interpreted end bearing pressures ranged from 12.4 to 24.8MPa.

Kintbury, Berkshire (Cherrill *et al.*, 1992)

Square section (275mm x 275mm) pre-cast concrete piles were installed through 12m of fill and 8.5m into intact chalk at a disused chalk quarry site in Kintbury, Berkshire. A static compression test conducted an unknown period of time after driving gave τ_{avg} of 35kPa and q_b of 12.4MPa as interpreted by the authors.

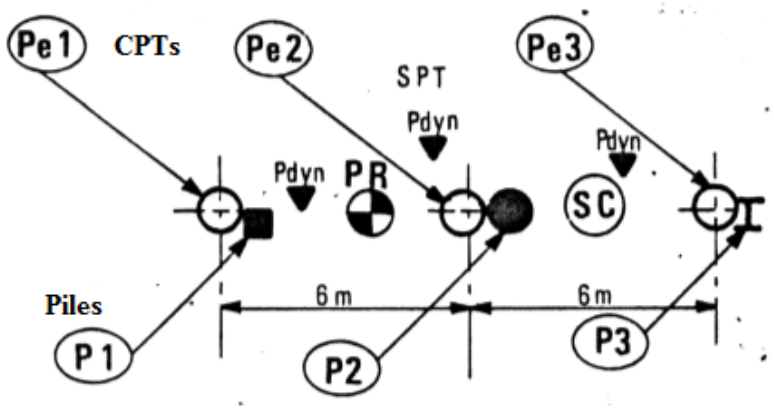


Figure 3-10: Piles and *in-situ* locations tests at Fleury-sur-Andelle; adapted from Bustamante *et al.* (1980)

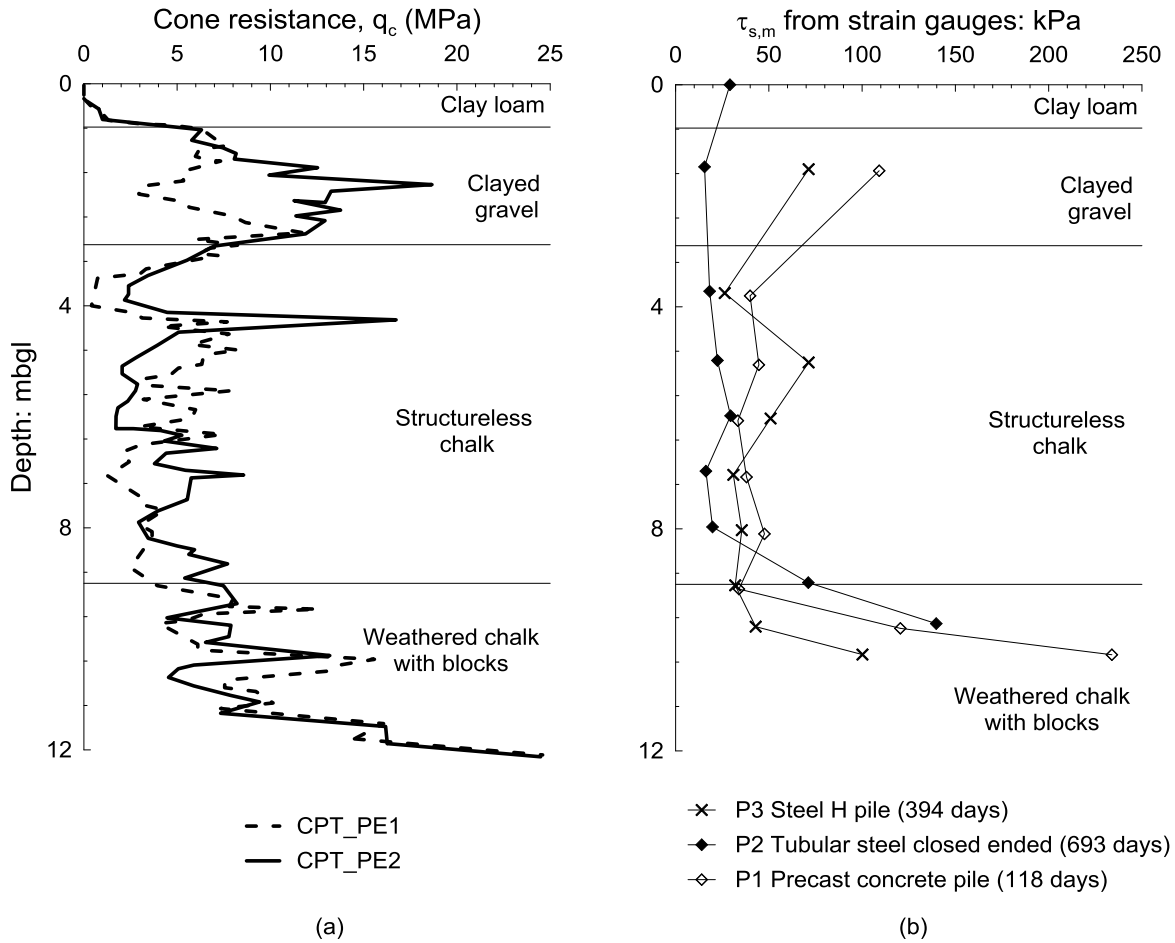
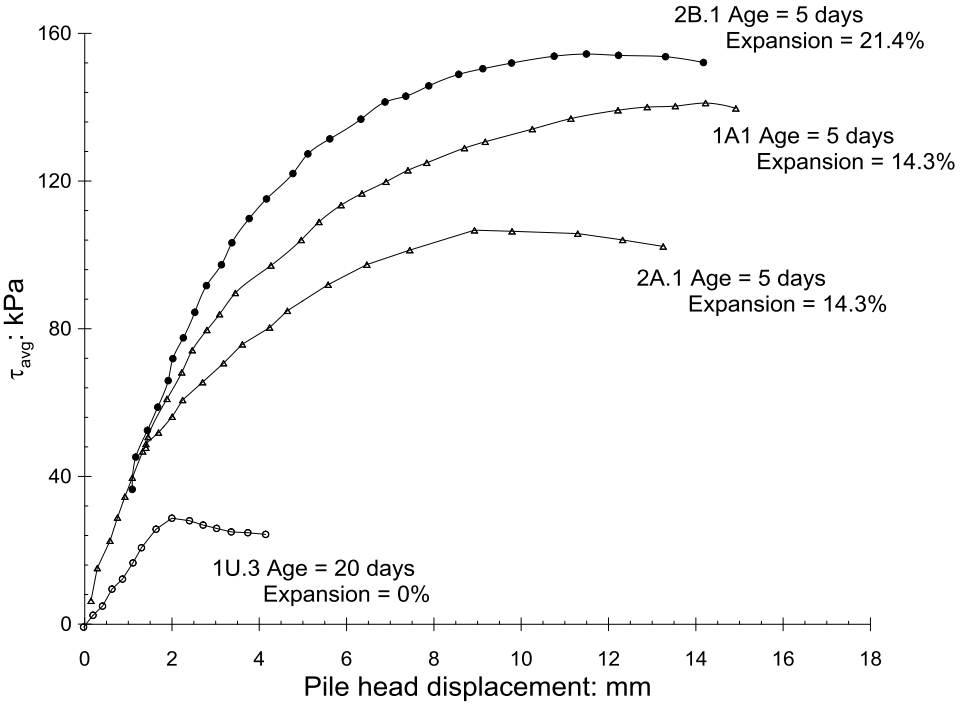


Figure 3-11: Pile tests Fleury-sur-Andelle (a) cone penetration profiles (b) shear stress from strain gauges at static failure during compression tests; adapted from Bustamante *et al.* (1980)



a

Figure 3-12: Load displacement behaviour of expanded and unexpanded box piles (Burland and French, 1990)

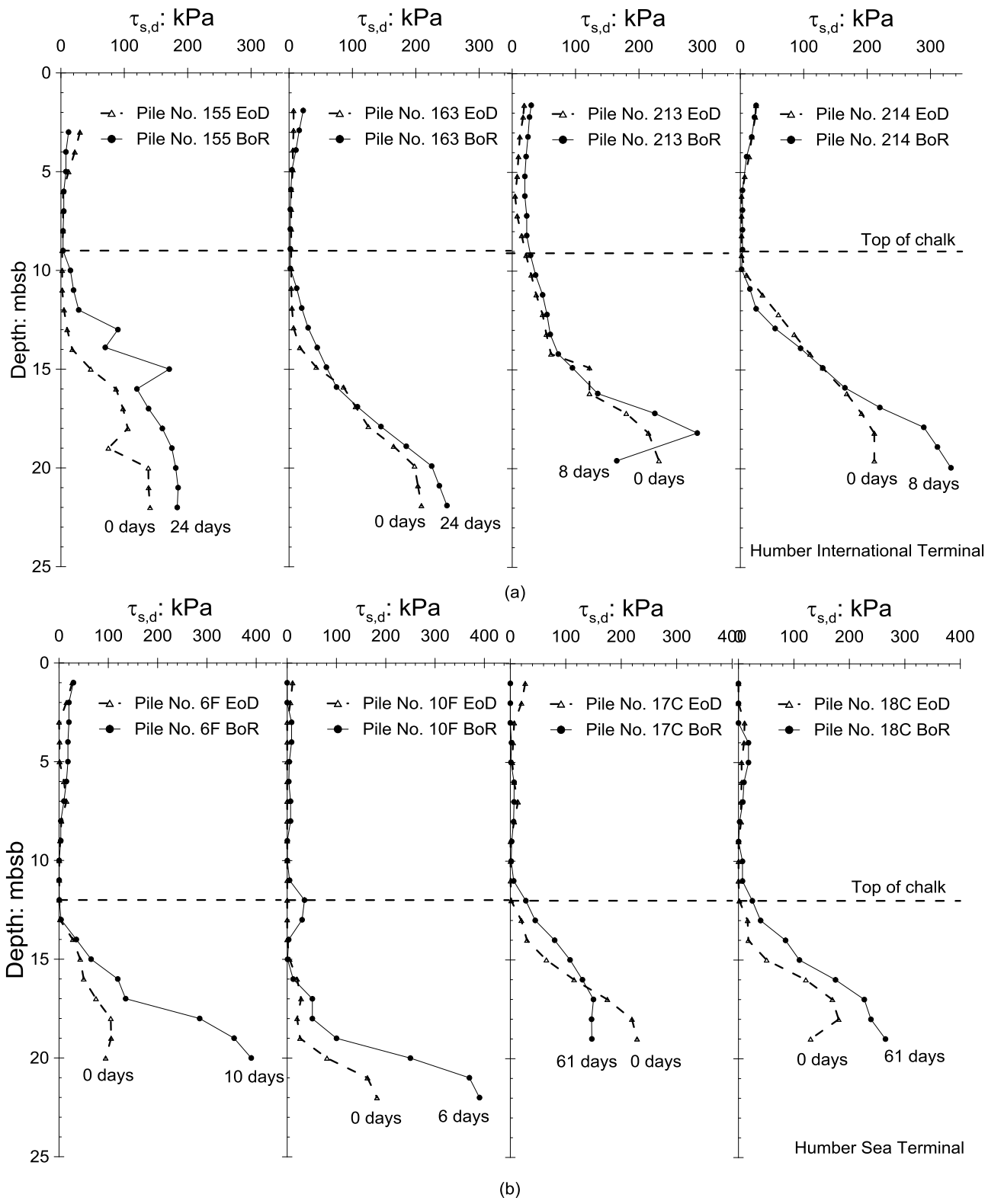


Figure 3-13: Results of signal matching at end of driving (EoD) and beginning of restrike (BoR) at a) Humber International Terminal and b) Humber Sea terminal (adapted from Moulds, 2001)

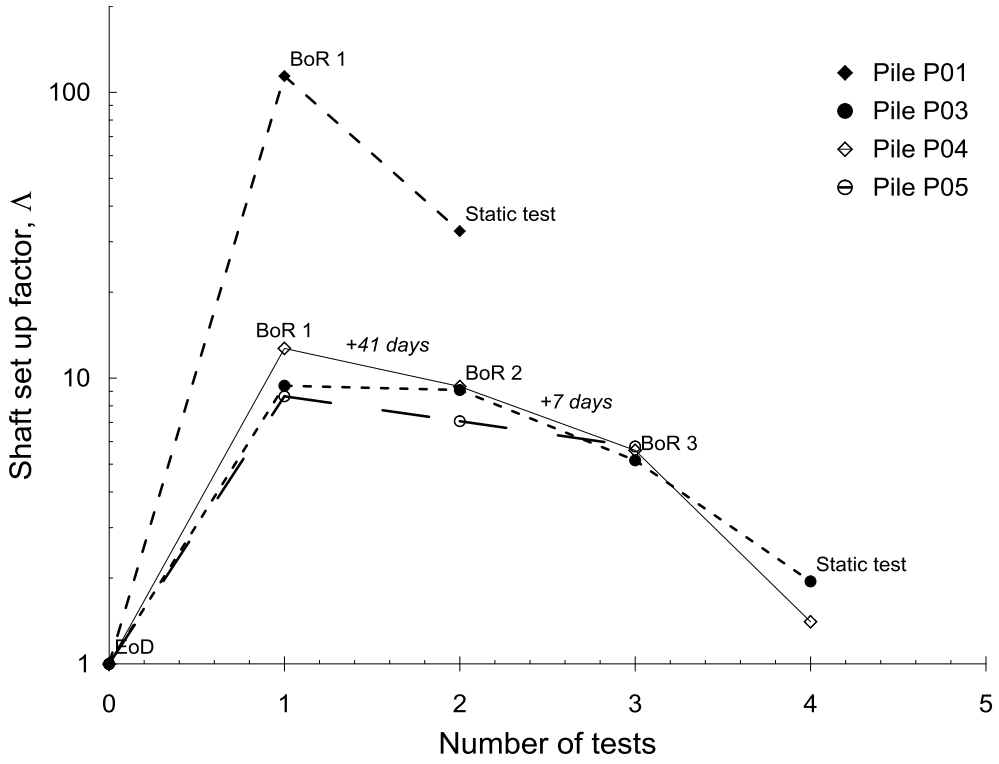


Figure 3-14: Dynamic and static set-up factors obtained from tests on four piles in Hemmoor Germany. (adapted from Lahrs and Kallias, 2013)

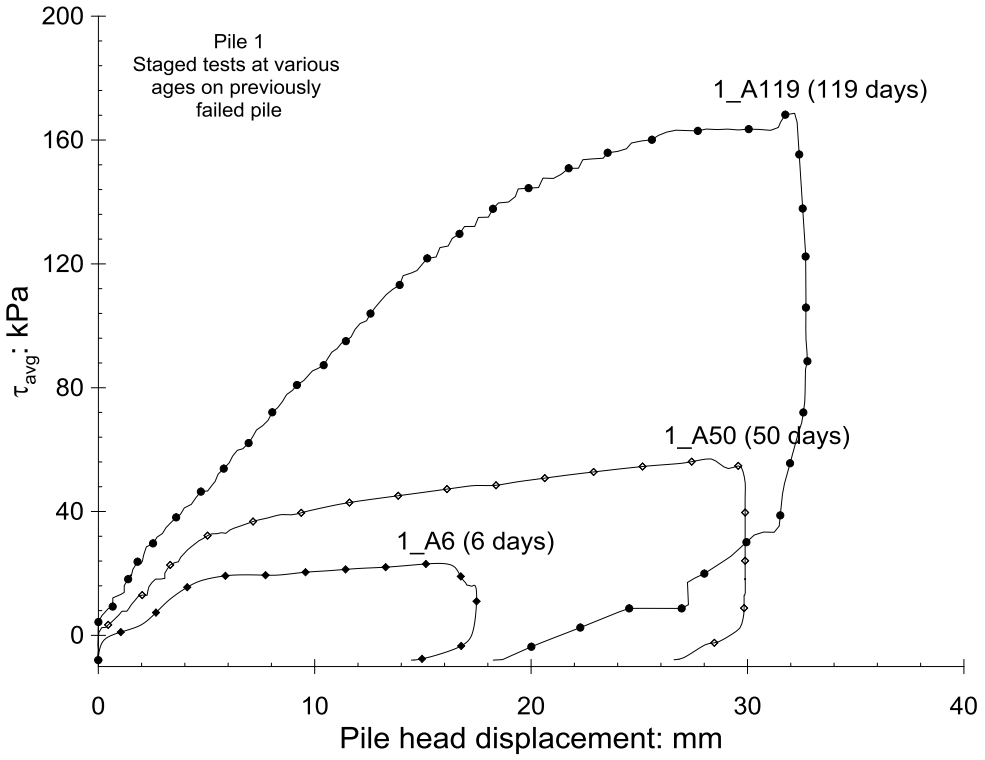


Figure 3-15: Staged axial static tension tests at various ages at St. Nicholas at Wade on Pile 1 (adapted from Ciavaglia *et al.*, 2017a)

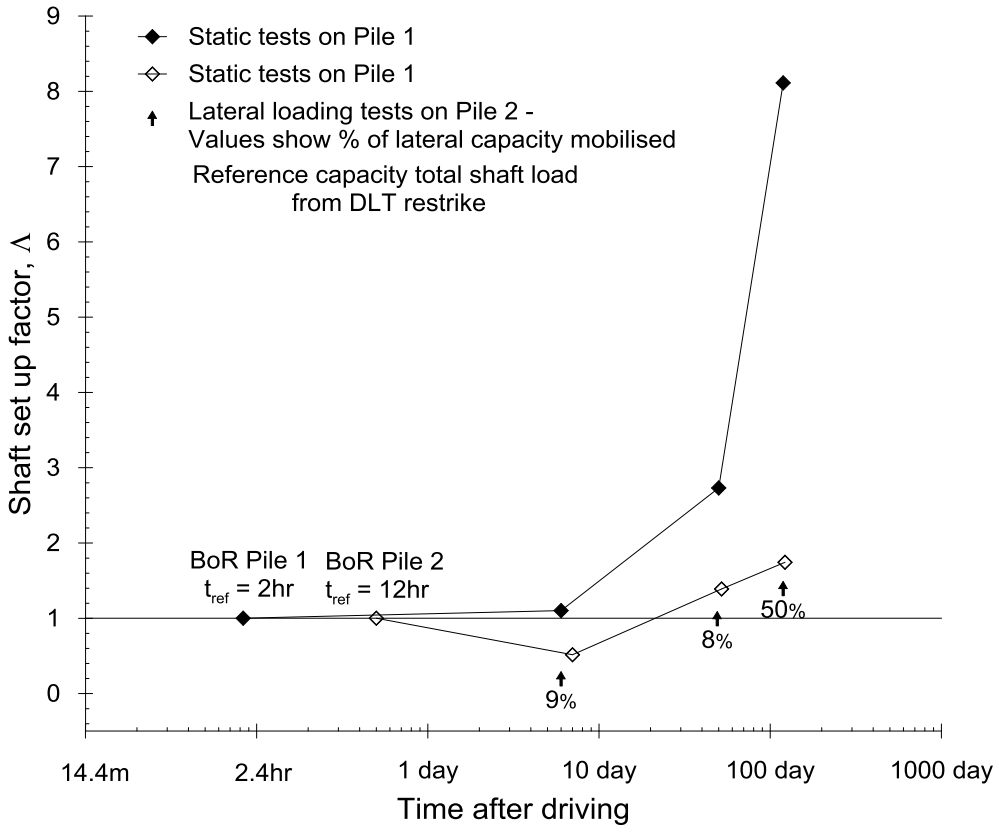


Figure 3-16: Normalised shaft load versus time after driving for static tension tests on Pile 1 and Pile 4 at St. Nicholas at Wade (Wind-Support, 2012, Ciavaglia *et al.*, 2017a, b)

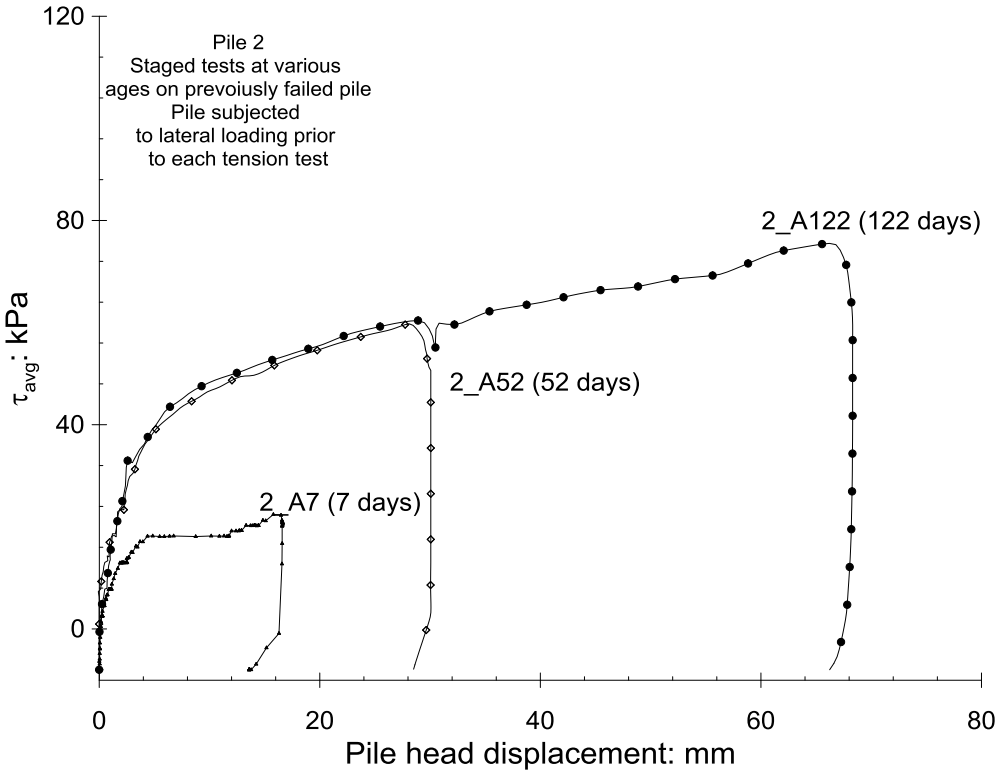
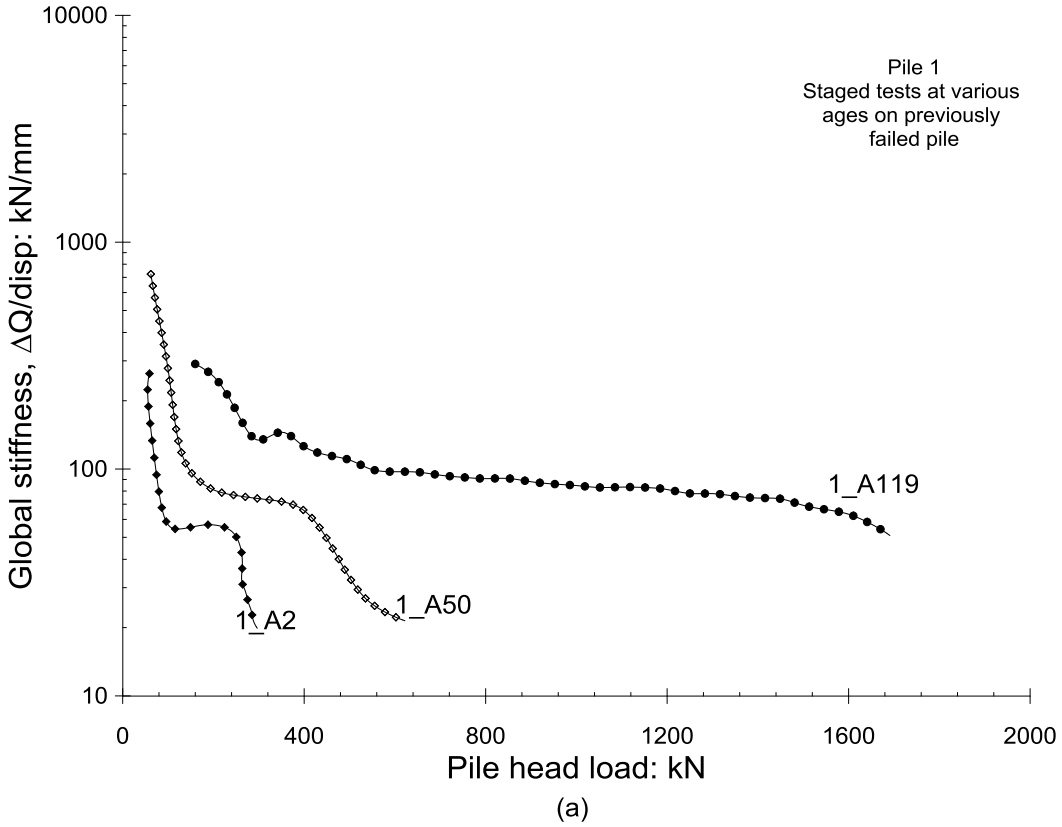


Figure 3-17: Staged axial static tension tests at various ages at St. Nicholas at Wade on Pile 2 (adapted from Ciavaglia *et al.*, 2017a)



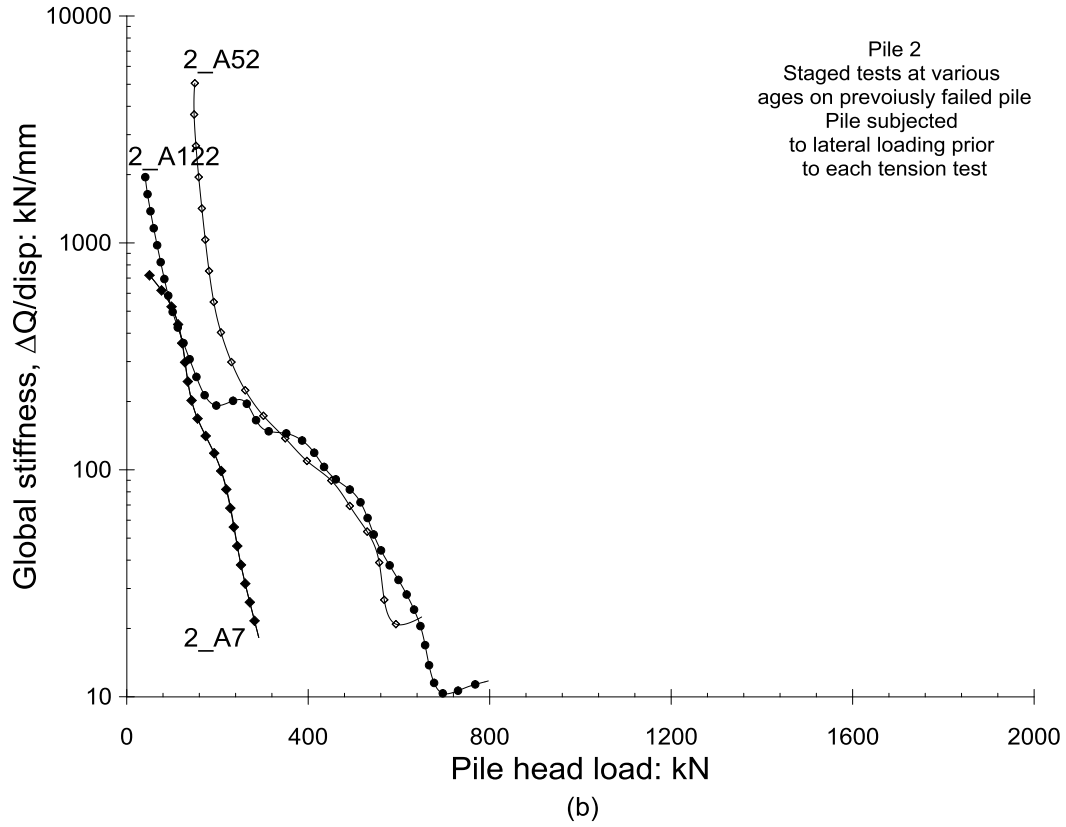


Figure 3-18: Pile global axial stiffness versus pile head displacement for static tension tests on a) Pile 1 b) Pile 2 (after Ciavaglia *et al.*, 2017a, Wind-Support, 2012)

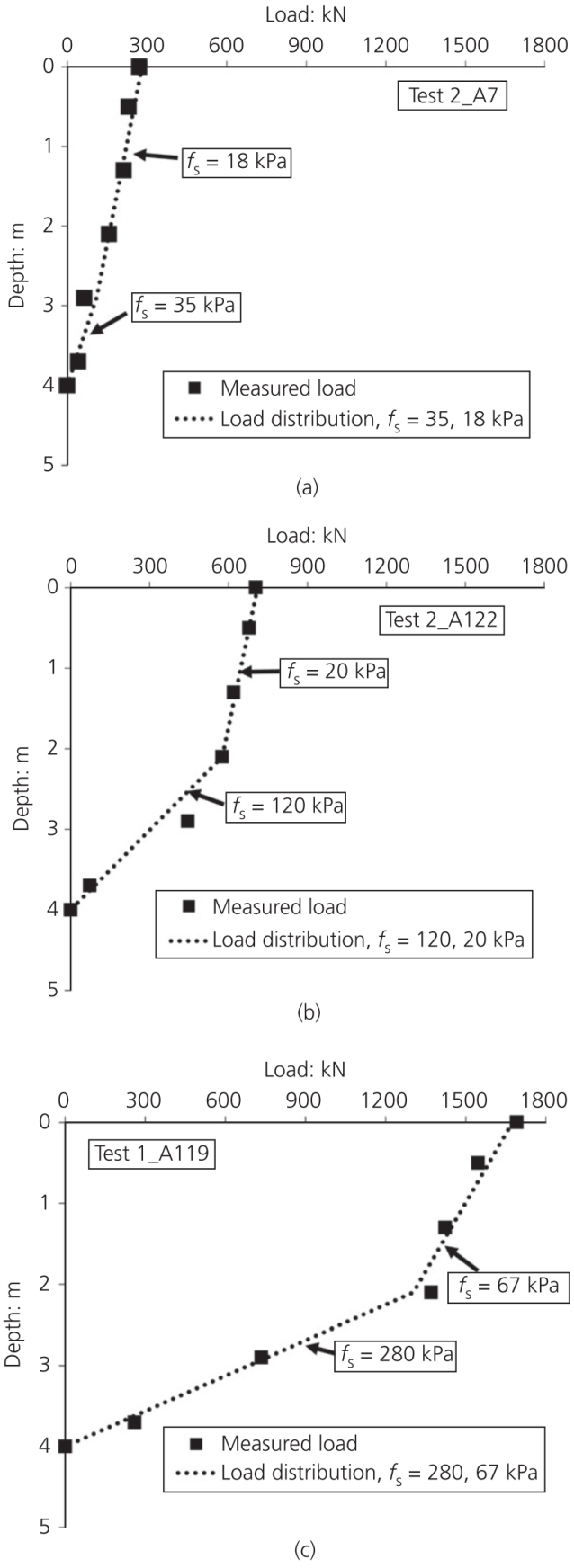


Figure 3-19: Load distribution along the pile length at tension failure for a) 2_A7, b) 2_A122 and c)1_A119 (Ciavaglia *et al.*, 2017a)

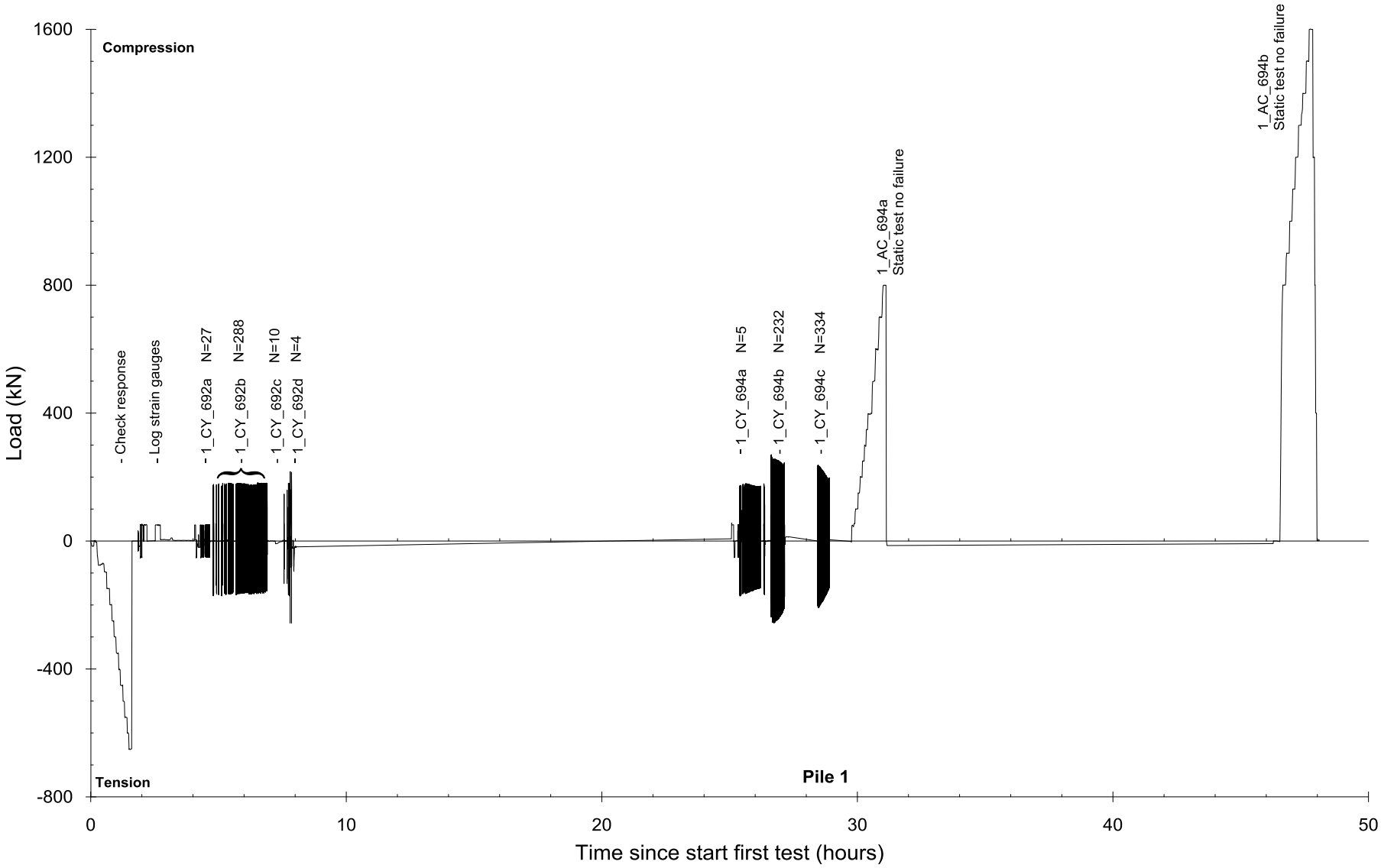


Figure 3-20: Applied load versus time for cyclic and static tests on Pile 1 during Phase 2 (Iberdrola, 2013)

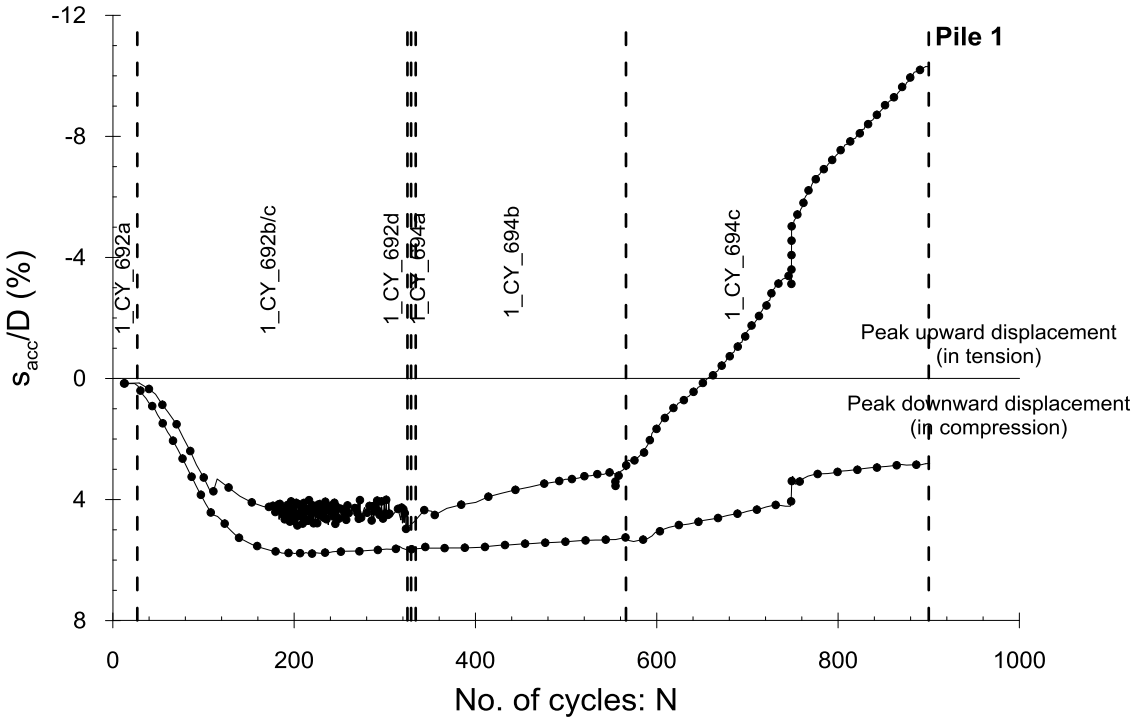


Figure 3-21: Permanent accumulated cyclic displacement normalised by pile diameter for cyclic tests on Pile 1 (Iberdrola, 2013)

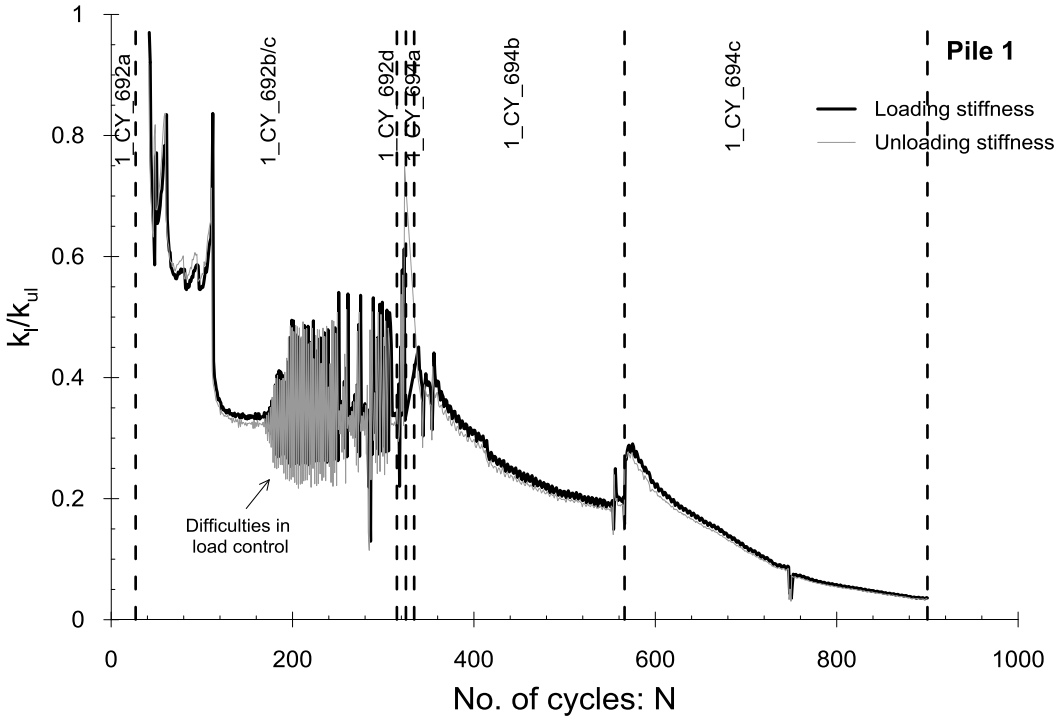


Figure 3-22: Cyclic loading and unloading stiffnesses for cyclic tests on Pile 1 (Iberdrola, 2013)

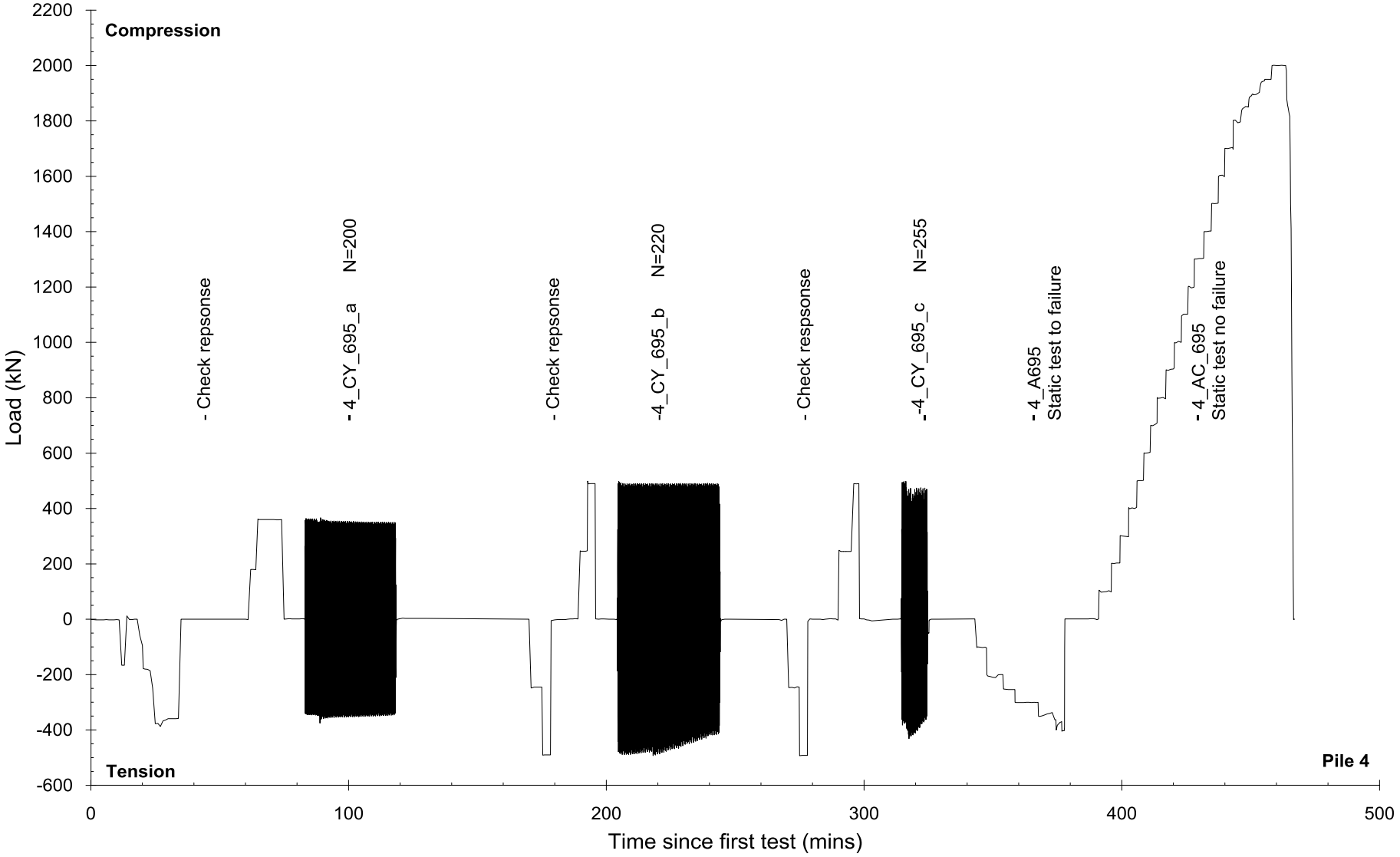


Figure 3-23: Applied load versus time for cyclic and static tests on Pile 4 during Phase 2 (Iberdrola, 2013)

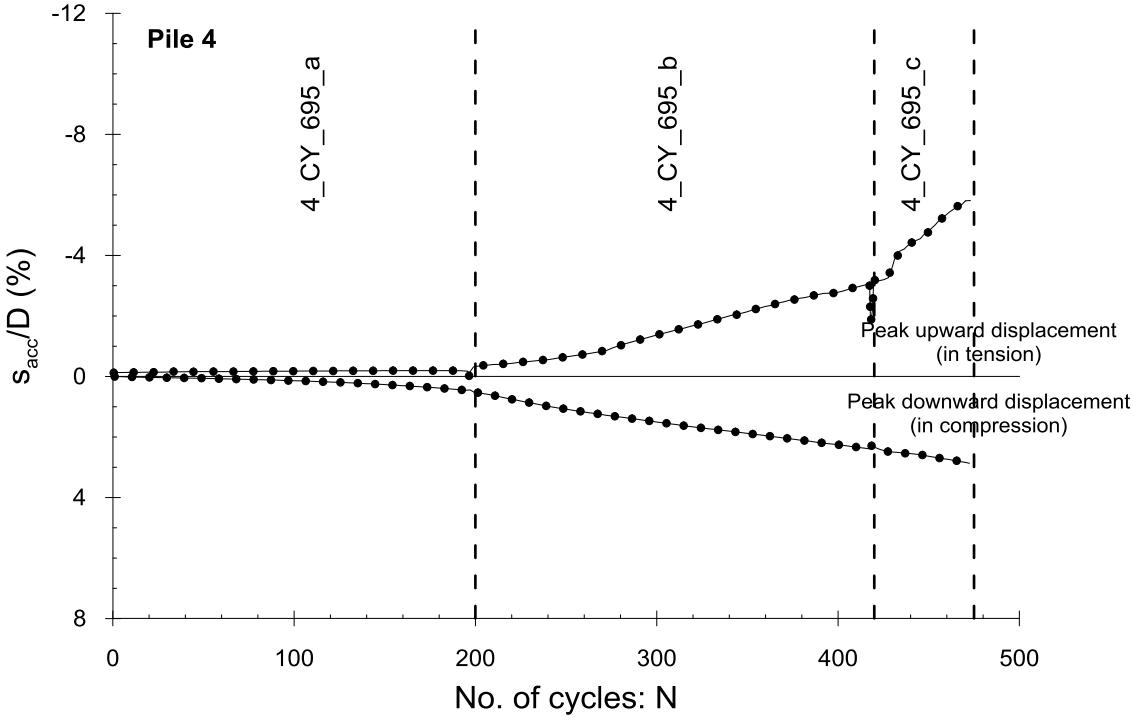


Figure 3-24: Permanent accumulated cyclic displacement normalised by pile diameter for cyclic tests on Pile 4 (Iberdrola, 2013)

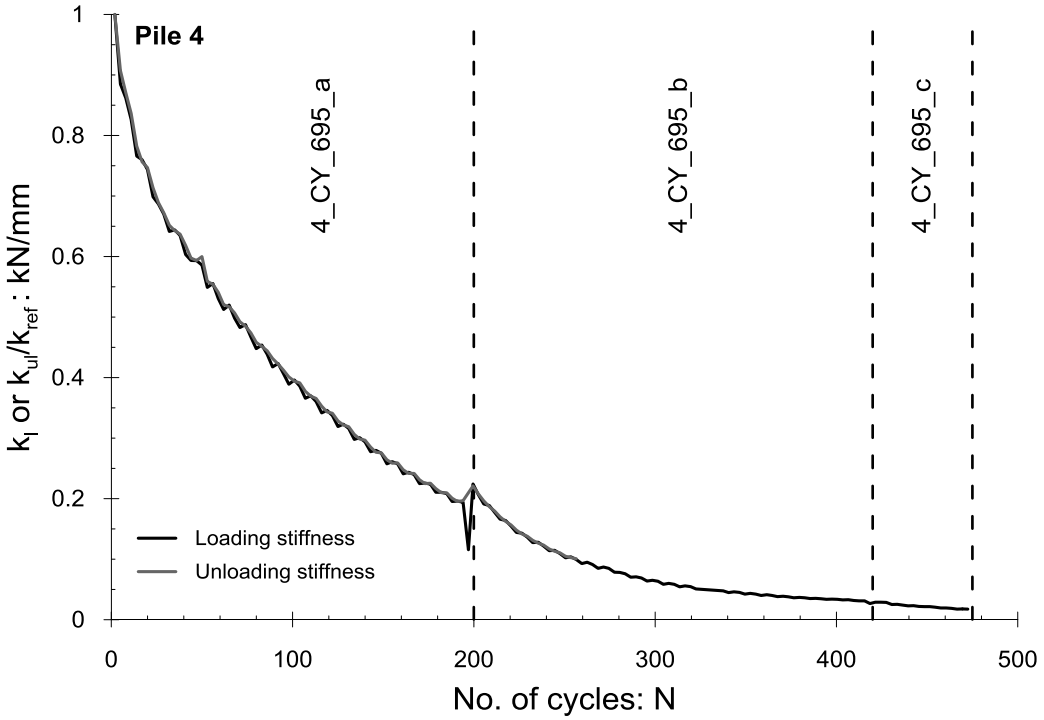


Figure 3-25: Cyclic loading and unloading stiffnesses for cyclic tests on Pile 4 (Iberdrola, 2013)

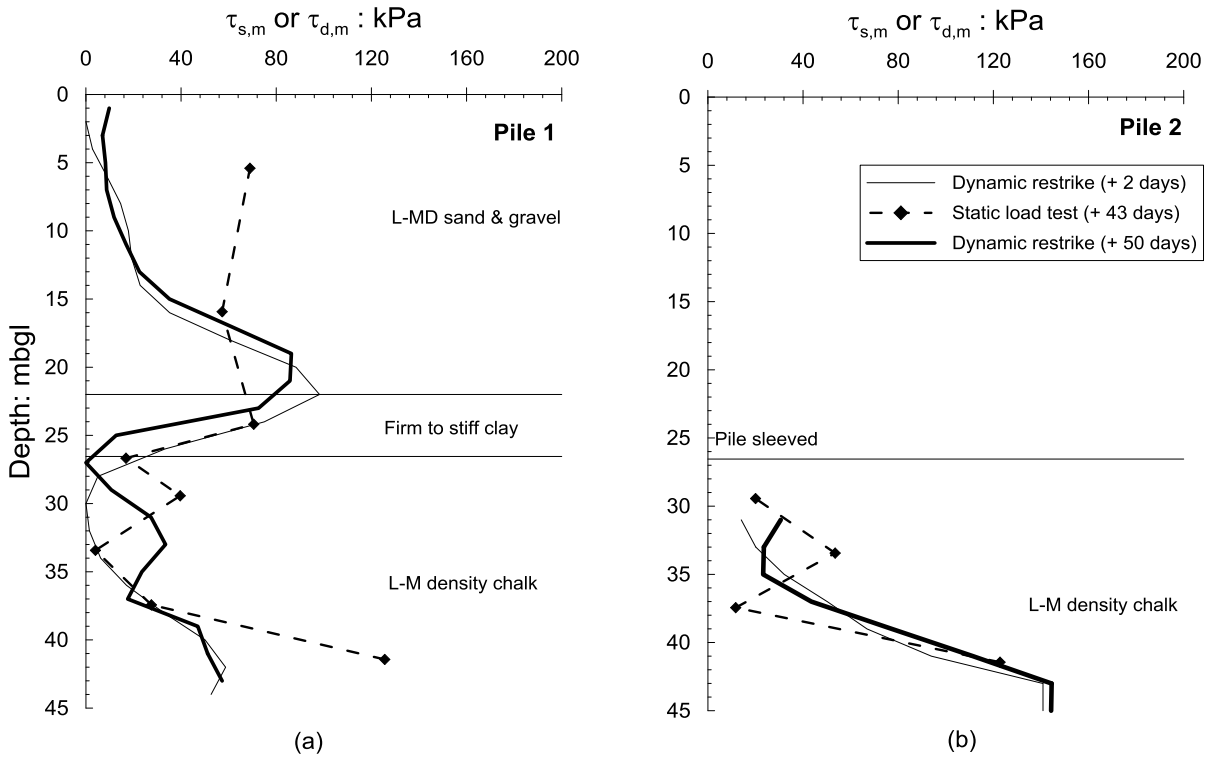


Figure 3-26: Local shaft resistance from dynamic and static pile tests at Port of Felixstowe; adapted from data provided by Hartley (2015)

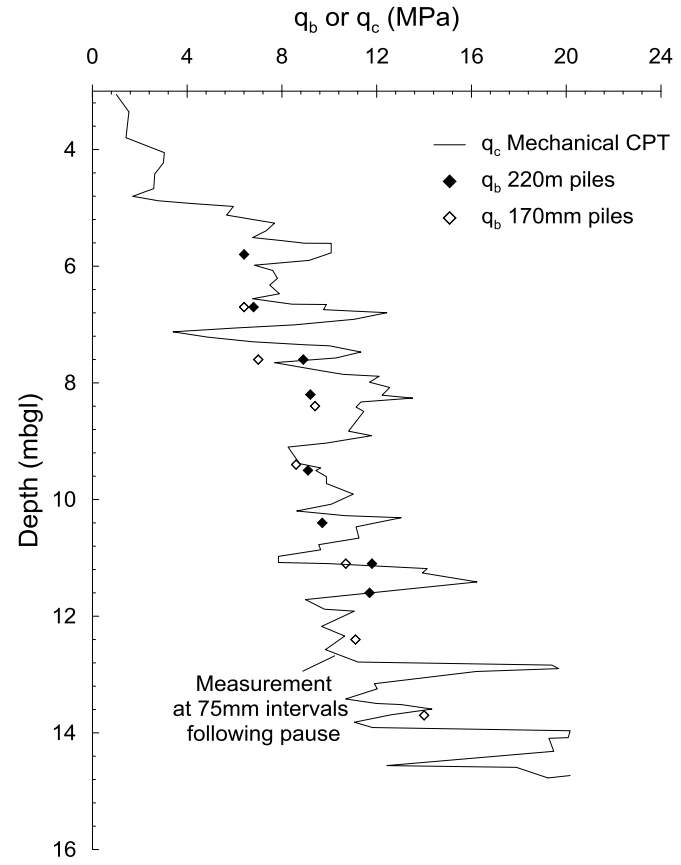


Figure 3-27: Cone resistance and base capacity from pile tests (after Hodges and Pink, 1971)

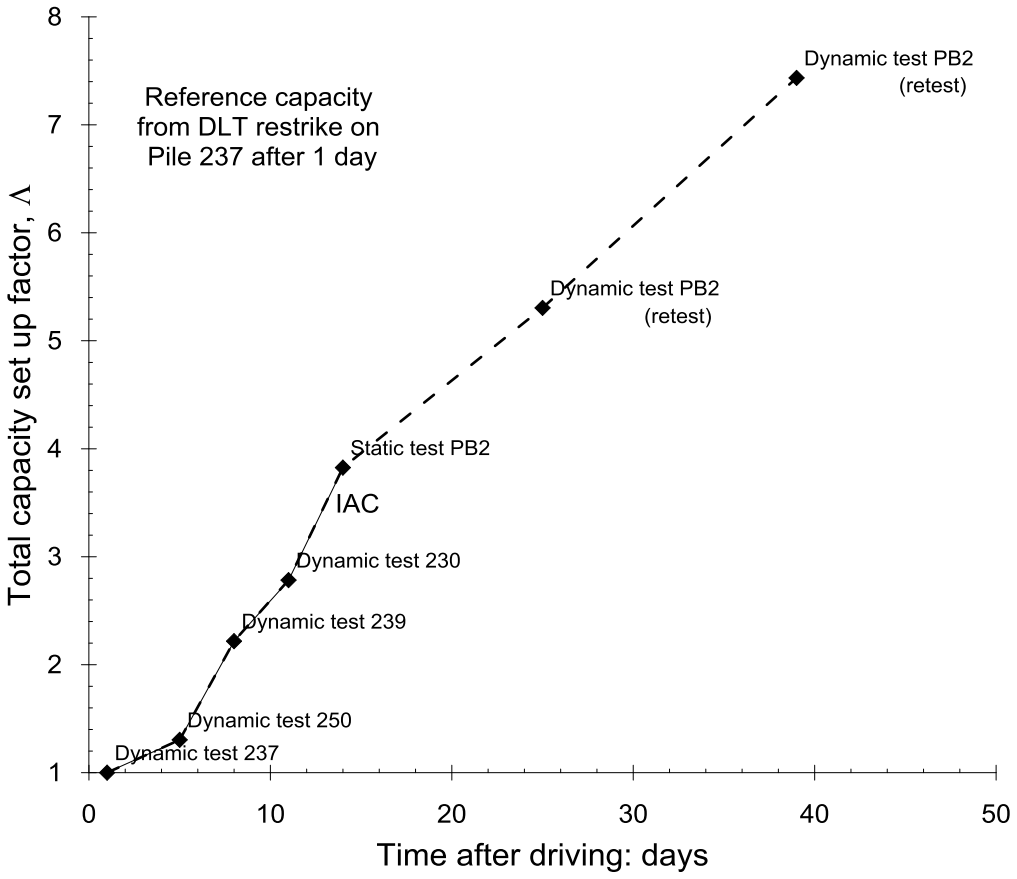


Figure 3-28: Set-up factor against time after driving for tests on pre-cast concrete piles driven at Nykøbing Falster; after Skov and Denver (1988)

3.6 Observations from the extended database of tests

The previous section described the published and unpublished load test data available for displacement piles driven in chalk. A summary of the results of static tests on closed-ended and open-ended piles is given in Table 3-10 and Table 3-11 respectively.

Base resistance mobilised during static loading on closed-ended piles appears to be a function of CPT cone resistance. The static compression tests conducted by Hodges and Pink (1971) indicated that q_b follows the tends of q_c (Figure 3-27) with q_b approximately equal to $0.9q_c$ when q_c was averaged over 2.3D above and 1.5D below the pile tip. The additional tests and site characterisation reported by Hodges and Pink (1971) and Bustamante *et al.* (1980) demonstrated that changes in chalk properties with depth and mobilisation of capacity for closed-ended piles are related to the trends in CPT cone resistance at relevant depths, although this warrants further investigation.

A remoulded annulus of putty chalk forms around the shafts of open-ended driven steel piles in low-medium density chalk during driving, which limits dramatically the radial effective stresses and shear resistances that can act on the shaft; Hobbs and Atkinson (1993), Lord *et al.* (2002). In one investigation, the annulus thickness amounted to ≈0.4 to 1.6 times the wall thickness.

Table 3-10 indicates that τ_{avg} mobilised by closed ended (*Type PL*) piles varies generally from 30 to 60kPa and reduces with increasing penetration into chalk (e.g. considering the piles at Portsmouth and Thurrock). Information on pile age at the time of testing is only available for approximately 30% of the cases considered.

Figure 3-29 plots τ_{avg} from the original CIRIA database of *Type PS* piles, along with the additional static tests on open-ended piles added to the database by the Author. For open-ended piles driven in chalk, the value of τ_{avg} varies within a very wide range of <20 to 170kPa. On closer inspection of the available results, τ_{avg} can be seen to vary with:

1. *Chalk density or grade*: e.g. comparing North Woolwich and Humber HST which were installed to similar penetrations in chalk and tested over broadly similar timeframes of 30 to 50 days (Table 3-11). Insufficient test data exists to make an assessment of the effect of chalk *grade* (i.e. fracture spacing and nature) on capacity, separate to chalk density;

2. *Increasing penetration or relative tip depth, h/R:* seen most clearly at Fleury-sur-Andelle (Figure 3-11), Humber HST and HIT (Figure 3-13), St. Nicholas-at-Wade (Figure 3-19) and the Port of Felixstowe (Figure 3-26);
3. *Time*: Shaft capacity increases significantly with time, achieving capacities up to 800% higher than the end of installation values over time periods of only four months after installation; Figure 3-30 (a).

Further, the above three factors appear to be interrelated based on the available results, with capacity increase with time also a function of:

1. *Chalk density or grade*: tests at St. Nicholas-at-Wade and Nyøkbing Falster in low-medium density chalk show marked increases in capacity which reached between 700 and 800% after 39 and 119 days (Figure 3-30 (a)). In contrast, tests conducted at HST and HIT in medium-high density chalk reached an equilibrium set-up factor of 2 over 10 days (Figure 3-30 (b));
2. *Capacity increase follows the trends in h/R*: for example, comparing test 2_A7 and test 1_A119 on Figure 3-19. Similar trends are seen in dynamic tests on open-ended piles (Figure 3-13) with locally higher values of $\tau_{s,d}$ close to the pile tip, and are also apparent for closed-ended piles (Figure 3-11).

The mechanisms which lead to these capacity increases are not fully understood and warrant further investigation. Traditionally, capacity increases in chalk are thought to relate to pore pressure dissipation/consolidaiton and/or re-cementing of chalk putty in the annulus around the pile thus changing its properties with time. However, Burland and French's (1990) tests on steel box piles, that could be expanded mechanically after driving (Figure 3-12), showed capacity increases when their cross-sectional areas were expanded. The latter suggests that set-up is related to changes in the lateral stress regime and is not solely to do with changing chalk putty properties. The significant increases in total capacity observed in static and dynamic tests on pre-cast concrete piles (Figure 3-28), also indicate that capacity increases are not limited to pre-formed steel piles.

Establishing "virgin" trends is key to tracking capacity increases with time accurately, using the end of driving as a reference point, since the set-up trends observed from the chalk database were also shown to depend on:

1. *The chosen reference time, t_{ref}:* Set-up can be masked when tests at extended periods after driving are used as a reference point. At the Port of Felixstowe, very little set-up

was seen in a static test at 41 days when compared to a 2 day dynamic restrike test. Equally, at St. Nicholas-at-Wade, the set-up trend may have been skewed by using reference tests from 2 and 12 hours after driving (Figure 3-30 (a));

2. *Previous loading history*; Set-up at Hemmoor (Figure 3-14) was severely impacted by previous (dynamic) restrike testing and showed set-down with time. At St. Nicholas-at-Wade, lateral loading tests significantly reduced the beneficial effect of time on capacity and the operational stiffness (Figure 3-17). However, for piles only subjected to axial testing, capacity regain did not appear adversely affected by previous loading to failure (Figure 3-15).

Table 3-10: Summary of static tests on closed-ended piles where ultimate shaft resistance is known

Location	Test No.	Section[1]	L_p (m)	$L_{p,\ chlk}$ (m)	D or D_{eq} (m)	Test type[2]	Re-test	Age (days)	CPT data	$q_{b,0.1D}$ (MPa)	τ_{avg} (kPa)[3]
Chatham, *Kent, UK* *Meigh (1971)*	12	TB	25.9	7.9	508	SC	N	14	N	7-8	35-54
North Woolwich, London *Hobbs and Robins (1976)*	6	TB	18.5	3.6	364	SC	N	21		3.2	26
Newbury, Berkshire *Hobbs and Robins (1976), Hobbs (1976)*	N1	TB	17	10.5	510	SC	N	5	N	7.5	33
Portsmouth, UK *Lord (1976)*	W1	PCC	17	13.5	510	SC	N	-	N	9.4	48
	W2	PCC	13	9.5	510	SC	N	-	N	6.5	61
	W3	PCC	9.5	6.0	510	SC	N	-	N	4.8	61
	W6	PCC	13	9.5	380	SC	N	-	N	8.7	74
	W7	PCC	9.5	6.0	380	SC	N	-	N	3.5	52
	W8	PCC	7	3.5	380	SC	N	-	N	4.2	72
Fleury sur Andelle *Bustamante et al. (1980)*	P1 (3)	PCC	10.5	7.5	204	SC	Y	118	Y	2.5	58
	P2 (2(	TB	10.5	7.5	445	SC	Y	693	Y	1.8	32
Thurrock Jones and Morrison *(1990)*	A	PCC	7.0	4.0	310	SC	N	-	N	12.4	120
	BPT12	PCC	13.5	7.7	310	SC	N	-	N	24.8	44
	BTP1	PCC	13.5	2.7	310	SC	N	-	N	24.2	96
Leagrave, Luton *Burland and French (1990)*	3U.1	SX[1]	4.9	4.9	140	ST	N	12	N	-	23
	3U.2	SX[1]	4.9	4.9	140	ST	N	12	N	-	23
Kintbury, Berkshire *Cherrill et al.* (1992)	K1	PCC	20.5	8.5	310	SC	N	-	N	12.4	35

1. TB = steel tube PCC= precast concrete SX = steel cruciform
2. SC = static compression ST = static tension
3. Average shaft resistance in chalk only from static testing

Table 3-11: Summary of static tests on open-ended piles where ultimate shaft resistance is known

Location	Test No.	Section[1]	L_p (m)	$L_{p,\,chlk}$ (m)	D or D_{eq} (m)	Test type[2]	Re-test	Age (days)	CPT data	$q_{ba,0.1D}$ (MPa)[3]	τ_{avg} (kPa)[4]
North Woolwich London *Hobbs and Robins (1976)*	4a	SH	23.3	8.5	287	SC	Y	54	N	8.3	42
	5a	SH	27.3	12.0	287	SC	Y	71	N	12.0	8
	12	SH	25.2	12.8	287	SC	Y	56	N	11.3	19
Brighton Marina, *Lord and Davies (1979)*	B1	TB	4.0	4.0	800	ST	Y	-	N	-	150
Fleury sur Andelle *Bustamante et al. (1980)*	2	SH	10.5	7.5	158	SC	Y	394	Y	-	111
Leagrave, Luton, *Burland and French (1990)*	1U.1	SB	4.7	4.7	158	ST	N	6	N	-	27
	1U.2	SB	4.7	4.7	158	ST	Y	6	N	-	24
	1U.3	SB	4.7	4.7	158	ST	Y	20	N	-	29
LPG jetty, Lincs *Hobbs and Atkinson (1993)*	U	TB	19.0	11.0	914	ST	N	-	N	-	125
Humber HST *Moulds (2001)*	TP	TB	22.0	9.0	1067	ST	N	30	N	-	149
Hemmoor, Germany *Lahrs and Kallias (2013)*	P01	TB	50.0	23.5	1500	ST	N	-	N	-	33
	P03	TB	50.0	23.5	1500	ST	Y	-	N	-	23
	P04	TB	43.0	16.5	1500	TPC	Y	-	N		16
	P05	TB	50.0	23.5	1500	SC	Y	-	N	36	-
St. Nicholas at Wade, Kent *(Ciavaglia et al., 2017a)*	1_A6	TB	4.0	4.0	762	ST	N	2	Y	-	23
	1_A50	TB	4.0	4.0	762	ST	Y	50	Y	-	57
	1_A119	TB	4.0	4.0	762	ST	Y	119	Y	-	169
	2_A7	TB	4.0	4.0	762	ST	Y	7	Y	-	22
	2_A52	TB	4.0	4.0	762	ST	Y	52	Y	-	60
	2_A122	TB	4.0	4.0	762	ST	Y	122	Y	-	75
Hemmoor, Germany *Lahrs and Kallias (2013)*	P01	TB	50.0	23.5	1500	ST	N	-	N	-	33
	P03	TB	50.0	23.5	1500	ST	Y	-	N	-	23
	P04	TB	43.0	16.5	1500	TPC	Y	-	N		16
	P05	TB	50.0	23.5	1500	SC	Y	-	N	36	-
Port of Felixstowe *Hartley (2015)*	TP1	TB	44.4	17.8	762	SC	Y	43	N	16	47
	TP2	TB	40.4	18.0	762	SC	Y	43	N	20	58

1. TB = steel tube SB = steel box pile SH = steel H pile
2. SC = static compression ST=static tension TPC=post static cyclic tension
3. All end bearing assumed to be under the annulus for open ended steel piles
4. Average shaft resistance in chalk only from static testing

Figure 3-31 illustrates the predictive reliability of shaft capacity values calculated for the tests in the database using the CIIRA PG6 and PR11/C574 methods. For tests (20) on open-ended piles, the ratios of calculated to measured shaft capacity, Q_c/Q_m are plotted against diameter, length of penetration into chalk and pile age. The pre-2002 effective stress PG6

method, which does not take length effects into account, shows generally poor performance with Q_c/Q_m ratios that are both conservative and non-conservative and tend to increase with L_p. Overall, the mean Q_c/Q_m value is 1.72 and the standard deviation is 2.56 (CoV = 1.49). The current CIRIA C574 rule for open-ended piles performs better for long piles in the short-term as it take length effects into account, to some extent, and indirectly by adopting a constant τ_f of 20kPa with depth. However the method is highly conservative in the long-term with the Q_c/Q_m ratios reducing significantly as the pile age increases with a minimum of 0.12 for the 119 day test on Pile 1 at St. Nicholas-at-Wade. Overall, the mean Q_c/Q_m value is 0.75 and the standard deviation is 0.52 (CoV= 0.7). The shaft resistance predicted by all six available methods for chalk, described in Section 3.4.2, is compared with the measured values from the test on Pile 1 on Figure 3-32. With the exception of the Vijayvergiya *et al.* (1977) method which predicts a constant value of 220kPa with depth, the prediction methods provide reasonable estimates (or slight over-estimates) of the +2hour dynamic test capacity, but significantly under-predict the long-term capacity and provide highly conservative estimates of the 119 day static capacity.

The effect of axial cyclic loading on aged capacity is difficult to ascertain due to the piles' previously loading histories. The cyclic loading tests' Q_{mean} and Q_{cyc} components from all available tests are plotted on Figure 3-33. The stable (S), metastable (M) and unstable (US) regions interpreted by Jardine and Standing (2012) for dense Dunkirk sand are also shown. All of the tests are on previously failed piles. Primary observations include:

- The Luton box pile test failed after 20 cycles presumably exhibiting US behaviour with a 60% reduction in operational tension capacity;
- Pile 1 and Pile 4 at St. Nicholas-at-Wade failed with N<1000, significant permanent displacement and post-cyclic reductions in capacity up to 93% (US behaviour);
- Pile P04 at Hemmoor reached 1000 cycles without failure (apparently stable) with uncertain influence on operational capacity.

All of the test outcomes, whether MS, US or S, obtained in the chalk tests fall within the stable region on the dense sand diagram, suggesting a strong and highly concerning susceptibility of chalk to axial cyclic loading. Relatively modest cyclic loading combinations appear to lead to severe reductions in shaft capacity and stiffness, which could reduce the operational shaft capacity values to as low as those noted during installation. Resolving whether these trends are due to pre-failing the piles in earlier, often arbitrary, testing sequences poses one of the main questions addressed by the Author in Chapter 6.

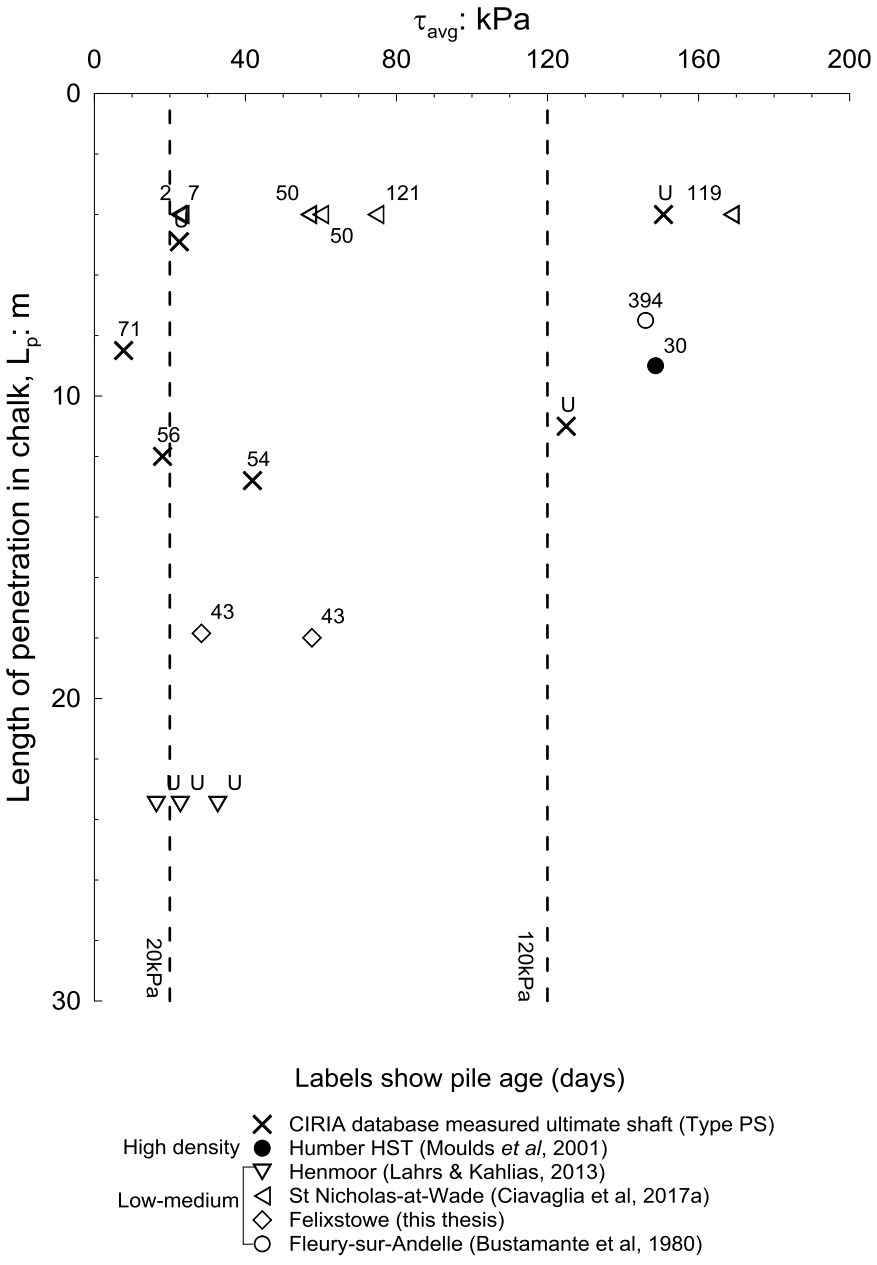
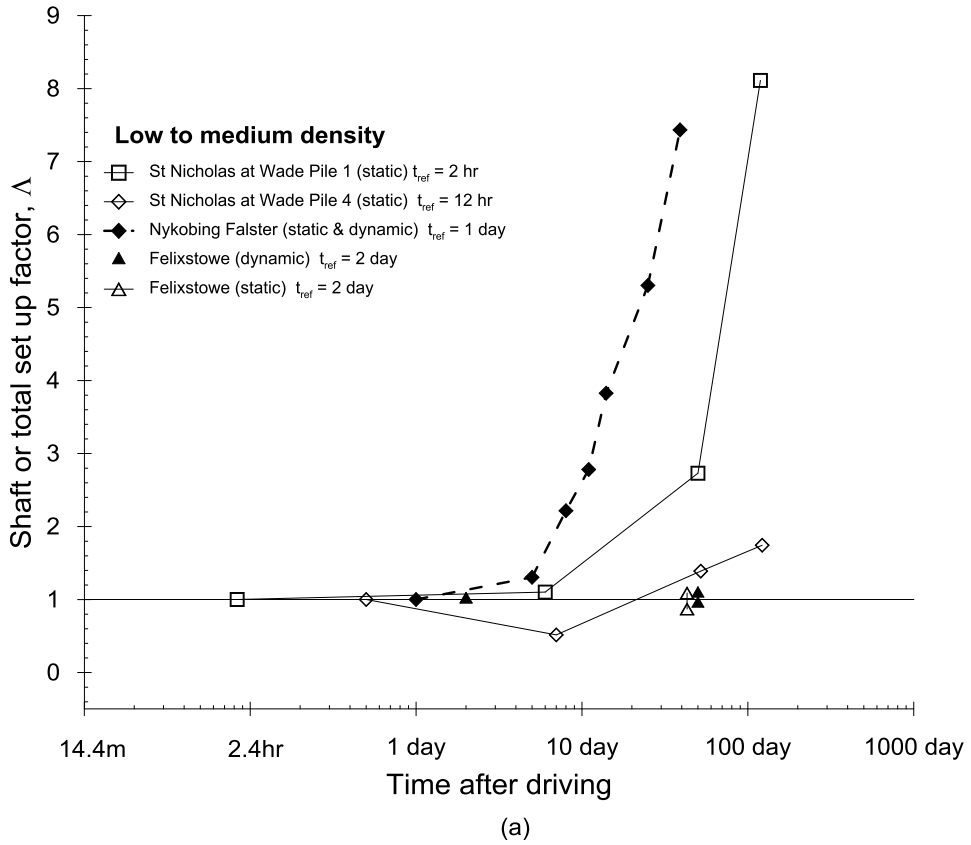
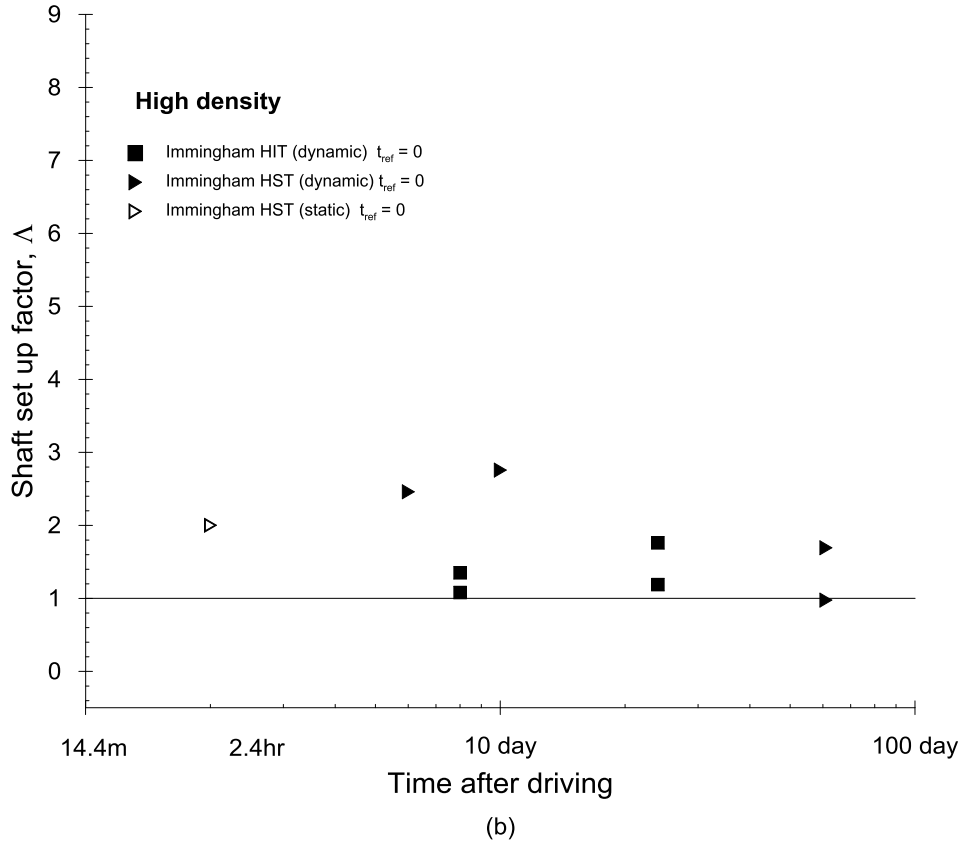


Figure 3-29: Additional test results on Type PS piles along with CIRIA database Type PS tests shown on Figure 3-8



(a)



(b)

Figure 3-30: Set-up factors with time for tests in the database (a) low-medium density chalk (b) high density chalk

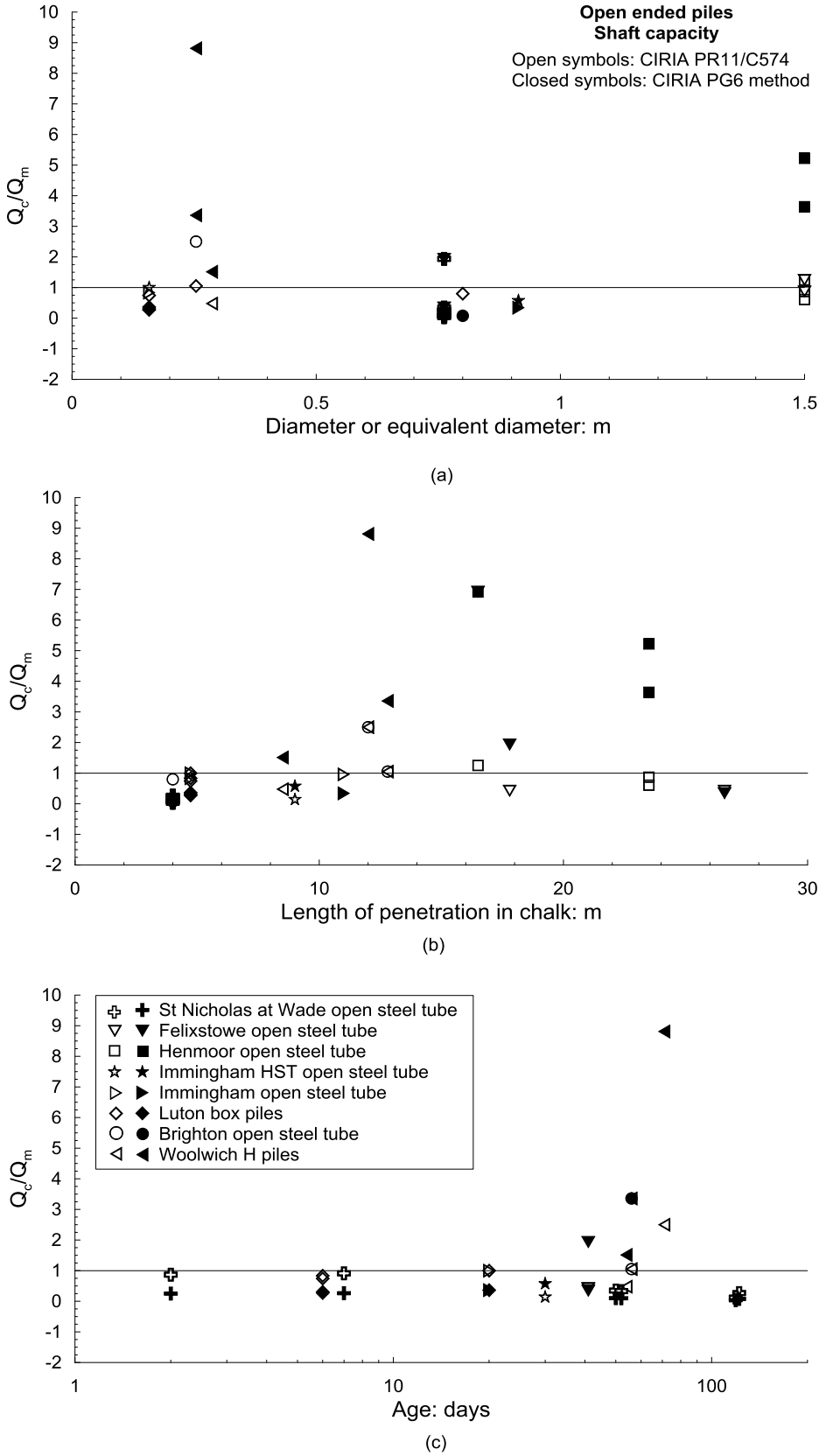


Figure 3-31: Ratio of calculated to measured shaft resistance during static tests of open-ended piles using CIRIA PG6 (Hobbs and Healy, 1979) and CIRIA C574 (Lord *et al.*, 2002) methods versus (a) diameter or equivalent diameter (b) length of penetration into chalk (c) pile age

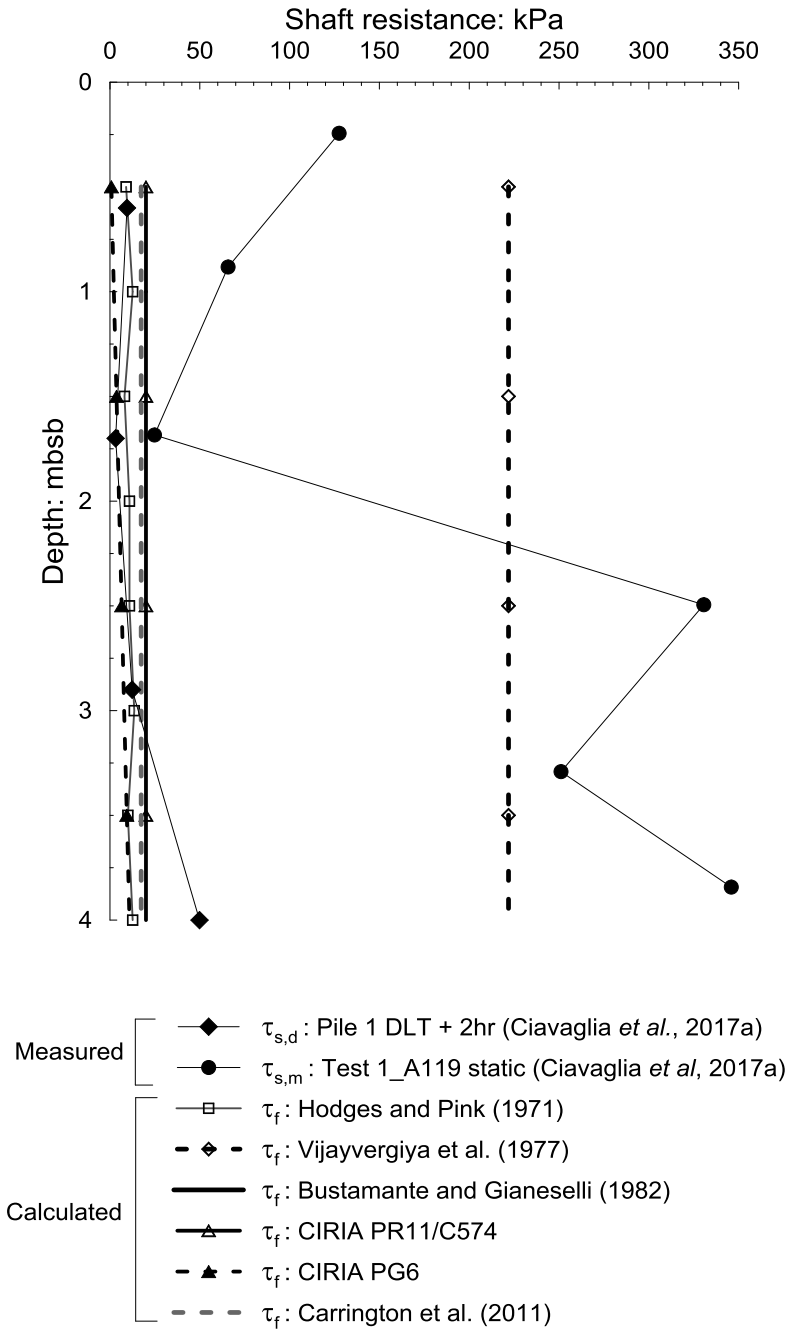


Figure 3-32: Comparison of current methods to predict shaft capacity in chalk with measured data

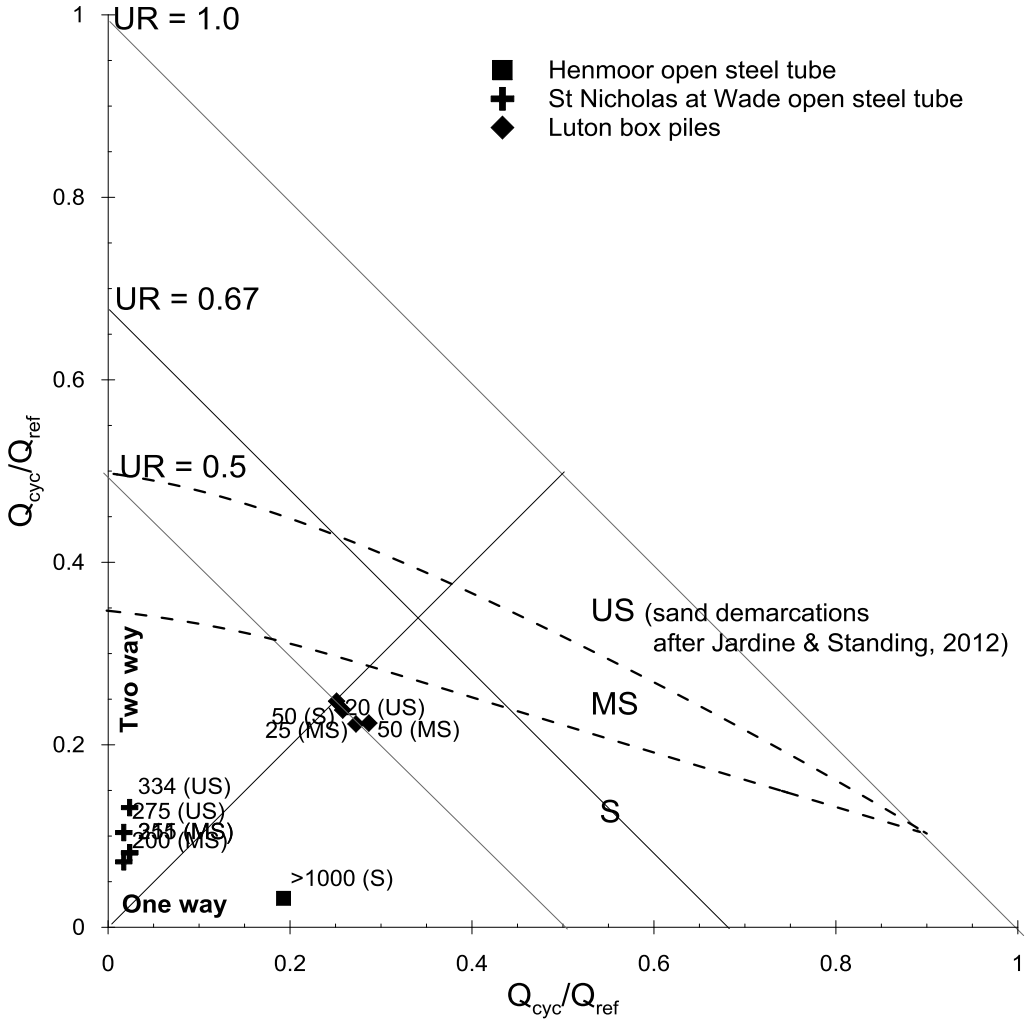


Figure 3-33: Cyclic loading tests in the database shown on a cyclic loading interaction diagram along with MS/S/US boundaries for sand after Jardine and Standing (2012)

3.7 Summary and concluding remarks

This chapter has reviewed the factors affecting the behaviour of driven piles and some common design methods applied currently to predict axial capacity in sands and clays that address the effective stress conditions during installation, equalisation and load testing. Equivalent procedures do not exist yet for chalk because the underlying fundamental processes are not understood and remain to be investigated thoroughly, particularly in relation to installation resistance, ageing behaviour and axial cyclic loading effects.

The current position regarding displacement piles in chalk and the review of available test data presented indicates that:

1. Driven piles installed in low-medium density chalk, with liquidity indices close to one, form a remoulded annulus of chalk around their shafts, which limits the radial effective stresses and shear resistances that can be mobilised. The properties of the remoulded annulus may vary with time;
2. The trends in base and shaft resistance appear to be related to the variation in CPT cone resistance with depth which requires further investigation and confirmation;
3. The available shaft shear stress mobilised by displacement pile shafts depends on factors including chalk density or grade, relative tip depth and time after installation;
4. Capacity increase appears to be also related to chalk density or grade and the relative tip depth. Set-up is significant for piles in low-medium density chalk although the underlying mechanisms are not fully understood;
5. Quantification of capacity-time trends is governed by the reference time chosen to assess early age capacity, which should be as close to the end of driving as practicable. Set-up is impacted significantly by the piles' previous loading history, with tests on previously failed piles showing ambiguous set-up trends. Defining "virgin" trends is key to tracking capacity increases with time accurately;
6. The limited database of pile load tests suggests a strong susceptibility of the capacity and stiffness of piles in chalk to axial cyclic loading, far more than seen in sands or clays, which is highly concerning. The effect of the piles' previous loading history cannot be discounted without further tests on virgin piles;
7. The predictive reliability of the current industry design method was shown to be low, with a mean Q_c/Q_m ratio for the database tested of 0.75 with a CoV of 0.7, highlighting the requirement for a new method to predict axial capacity.

8. The absence of well-founded design methods for displacement piles in chalk has led to the adoption of unreliable and potentially highly conservative design recommendations. The current design methods have been shown to predict with reasonable accuracy the early age capacity of long piles in low-medium density chalk, but to be highly conservative when compared to the results of static tests on aged piles.

The identified gaps in knowledge and design guidance shortcomings necessitate widely different choices when selecting design parameters for pre-formed driven piles in chalk that can impact significantly in projects involving potentially hundreds of large piles; Carrington *et al.* (2011). There is a clear need for reliable static and cyclic pile tests at chalk sites conducted at various ages, supported by high quality site characterisation, to provide benchmarks against which any potential predictive procedures may be developed, assessed and calibrated.

CHAPTER 4

Dynamic methods to determine axial pile capacity

4.1 Introduction

While static load tests are the best means of determining the axial capacity of a pile, indicative information on pile capacity and information on safe and efficient driveability and structural integrity can be obtained from dynamic pile tests. Proving axial capacity by dynamic pile testing requires significantly less time than static load testing and can be carried out on a large number of piles at a relatively low cost. The method is widely used in the offshore industry to predict and also prove capacity; the German BSH (2011) standard for design of offshore piles requires that dynamic pile tests are carried out on 10% of piles installed, to verify the capacity of principally axially loaded foundations.

Dynamic formulae, based on Newtonian impact principles, represent the oldest dynamic method used to determine pile capacity, a comprehensive review of which was given by White (2014). Closed-form solutions for the application of stress wave theory to piles developed around the world in the 1930s (Isaacs, 1931, Fox, 1932, Glanville *et al.*, 1938) but their use was initially limited by the complexity of the equations. A considerable advancement was made by the development of a computer program to simulate one-dimensional analysis by Smith (1962), which was then further advanced over the next three decades. Modern wave equation programs developed in North America are still based largely on Smith's original algorithm, often with some modifications (Goble and Rausche, 1976). A different approach, based on the method of characteristics, was adopted by the Dutch research group TNO (Middendorp, 1987), which in recent years has also been used in research oriented software (Randolph, 2008).

While a number of resistance models which simulate the soil response have been developed over the last thirty years (e.g. Simons and Randolph, 1985, Holeyman, 1985, Lee *et al.*, 1988, Salgado *et al.*, 2015) commercially available wave equation programs still use the original ideas of Smith to model the soil resistance.

This chapter gives an overview of modern dynamic methods used to determine axial resistance in piles, which were subsequently used to carry out the analyses of driven steel tube piles described in Chapters 5 and 6. A brief theoretical background of one-dimensional stress wave theory is given first. The numerical methods used for the solution of the one-dimensional wave equation are then outlined. The soil resistance models used widely in commercial software are then described, as are the more advanced soil resistance models utilised by the Author, followed by the applications of wave equation analysis in practice. The different software packages available are then contrasted and their relative merits assessed. Subsequently, a methodology for the analysis of the dynamic data is outlined which was adopted to carry out the analyses described in subsequent chapters. Finally, the accuracy of dynamic pile testing in routine analysis is discussed. Within this chapter, Sections 4.8.2, 4.9.2 and 4.10.1 were previously published whole or in part by Buckley *et al.* (2017b).

4.2 Wave equation theory & background

When a pile is struck by a hammer, an elastic wave is generated at the point of impact creating a compressive force pulse which, for a uniform pile, propagates down the pile at a constant speed. A pile installed in the ground to some depth and subjected to such a hammer impact can be idealised as a one-dimensional wave propagation problem in the elastic half space. The wave equation for a vibrating string developed by D'Alembert (1747) was combined by Isaacs (1931) with the research of Saint-Venant (1856) into the problem of an elastic bar fixed at one end and struck axially. The pile is treated as a free elastic rod and movement in the axial direction is considered only. The equation of motion for a pile of cross sectional area, A is given by:

$$\frac{\partial F}{\partial z} = \rho A \frac{\partial^2 w}{\partial t^2} \qquad 4\text{-}1$$

Where F is the axial force on the pile, ρ is the mass density of the pile material, t is time and w is the axial displacement in the z (vertical) direction. The axial stress, σ in the pile is related to the axial strain, ε, by Hooke's Law:

$$\sigma = E\varepsilon \quad 4\text{-}2$$

The strain is related to the displacement by:

$$\varepsilon = \frac{\partial w}{\partial z} \quad 4\text{-}3$$

Therefore using Eq. 4-2 and 4-3, the axial force on the pile can be expressed as:

$$F = EA\varepsilon = EA\frac{\partial w}{\partial z} \quad 4\text{-}4$$

Substitution of Eq. 4-4 into Eq. 4-1 gives the one-dimensional wave equation for propagation of stress waves in a pile:

$$\frac{\partial^2 w}{\partial t^2} = c^2\frac{\partial^2 w}{\partial z^2} \quad 4\text{-}5$$

where c is the compressional wave speed in an unconfined rod, $c = \sqrt{E/\rho}$. As waves travel down the pile, they are affected by the static and dynamic resistance of the soil, as well as by system damping effects. A wave which reaches the toe will be reflected as either a tensile or compressive force pulse, depending on the boundary conditions.

In reality, an embedded pile is not a free rod and the total (shaft and base) ground resistance, T_t must be considered, modifying Eq. 4-5 to:

$$\frac{\partial^2 w}{\partial t^2} = c^2\frac{\partial^2 w}{\partial z^2} \pm T_t(t) \quad 4\text{-}6$$

Where the total energy of the incident and reflected force pulses is greater than T_t, the pile will be advanced into the ground resulting in a permanent "set" or displacement.

4.3 Numerical methods for the solution of the one dimensional wave equation

The work of Isaacs (1931) was followed by a comprehensive study commissioned by the British Building Research Station which led to a paper by Fox (1932) on stress phenomena in piles during driving. Glanville *et al.* (1938) published a solution to the wave equation which allowed the first estimates of the stresses involved in pile driving. Both researchers advanced the theory that pile driving was a phenomenon which could be simulated using one-dimensional wave propagation theory, however their work involved a number of simplifying assumptions that were necessitated by the lack of computing power available at the time. The first comprehensive solution to the problem

was developed by Smith (1962) who utilised a finite difference approach with numerical integration of Eq. 4-6. In Smith's approach, the hammer and pile are discretised into a series of masses, connected by linear springs. The dynamic equilibrium equations are solved in the time domain using small time increments. The soil reaction to the movement of the pile, T_t in Eq. 4-6 is represented by springs, dashpots and plastic sliders distributed along the shaft and at the toe.

An alternative solution of the one-dimensional wave equation can be achieved using the method of characteristics. The solution was obtained by Saint-Venant (1867) who applied the principles of conservation of mass and momentum to water flow in an open channel. The method reduces a partial differential equation (here the wave equation) to quasi-linear ordinary differential equations along curves known as characteristics. The general solution is the sum of f(z - ct) a wave of fixed shape moving at speed, c and g(z + ct) a wave of fixed shape moving in the opposite direction at the same speed. The shapes remain fixed, but the sum of both shapes is a general shape which changes in time. The solution consists of the two functions f and g, which represent the downward travelling and upward travelling waves respectively (Haberman, 2013):

$$w(z,t) = f(z - ct) + g(z + ct) \tag{4-7}$$

Taking both compressive strain and the downwards z direction as positive, gives the strain, ε and stress, σ and as:

$$\varepsilon = -\frac{\partial w}{\partial z} = -(f' + g') \tag{4-8}$$

$$\sigma = E\varepsilon = -E(f' + g) \tag{4-9}$$

The downward (d) and upward (up) travelling components of velocity and force are calculated as:

$$v = v_d + v_{up} = -\frac{\partial w}{\partial t} = -cf' + cg' \tag{4-10}$$

$$F = F_d + F_{up} = EA\varepsilon = -EA(f' + g') \tag{4-11}$$

From Eq. 4-10:

$$v_d = -cf' \quad v_{up} = cg'$$

From dynamic equilibrium at the pile head, the applied impact force is proportional to the pile particle velocity by a factor Z, known as the pile impedance:

$$F(t) = Zv(t) \tag{4-12}$$

$$Z = \frac{EA}{c} \tag{4-13}$$

From Eq. 4-10 and Eq. 4-11:

$$F = F_d + F_{up} = -EA(f' + g') = -cZ(f' + g') = Zv_d - Zv_{up}$$

$$F_d = Zv_d \quad F_{up} = -Zv_{up} \quad v = v_d + v_{up} \quad \Rightarrow \quad Zv = F_d - F_{up}$$

$$F + Zv = 2F_d$$

$$F - Zv = 2F_{up}$$

$$\Rightarrow F_d = \frac{F + Zv}{2} \tag{4-14}$$

$$\Rightarrow F_{up} = \frac{F - Zv}{2} \tag{4-15}$$

The solution, for a frictionless free rod, was first applied successfully to the problem of pile driving by De Josselin de Jong (1956), although he incorporated base resistance only. The method was adapted to include shaft resistance by Voitus van Hamme *et al.* (1974) based on the assumption that the friction along the pile shaft can be represented by a number of concentrated friction forces which can easily be dealt with numerically. The parts of the pile between these points are assumed to have zero friction. At each boundary there must be equilibrium of forces and continuity of velocity. The waves travelling up and down the pile are affected by the total (dynamic plus static) shaft resistance, T_s at each of the boundaries as shown on Figure 4-1, giving, for equilibrium of forces:

$$F_d^i + F_{up}^r = F_d^t + T_s \tag{4-16}$$

For continuity of velocities:

$$v = (v_d + v_{up}) = \frac{F_d^i}{Z} - \frac{F_{up}^r}{Z} = \frac{F_d^t}{Z}$$

$$\Longrightarrow F_{up}^r = 0.5T_s \tag{4-17}$$

where F_d^i and F_d^t are the downward incident and transmitted waves respectively and F_{up}^r is the upward reflected wave. It follows from Eq. 4-17 that between time t_0, the start of the force application, and $t_{0+2L/c}$, when the wave has travelled to the bottom of the pile

and back to the measurement level, the upward wave from each boundary is equal to $0.5T_s$ at that boundary. This allows T_s to be calculated from the first travel of a wave along the pile.

The pile is considered to be comprised of a number of elements of length, Δl and impedance Z. The solution is obtained numerically by constantly moving through each node, at each time step, $t+\Delta t$, calculating the internal pile force, the velocity and the soil resistance and updating the displacements (Randolph, 2008). The pile displacement, w_p is calculated from:

$$w_{p\,(i,t+\Delta t)} = w_{p(i,t)} + v_{p(i,t)}\Delta t \qquad 4\text{-}18$$

Similar to the finite difference method, the method of characteristics models the total soil response, T_t using different combinations of springs, dashpots and plastic sliders located at the base, and at the frictional boundaries along the shaft. With both, the form of the soil pile reaction model, described in the following sections, is independent of the numerical method adopted. A direct comparison between the solution of the wave equation using the above approach and that of Smith (1962) is discussed in Section 4.8.2, where it is shown that they give broadly similar results when using the same parameters and soil resistance models.

4.4 Dynamic pile testing in practice

Piles which are monitored dynamically during driving are fitted with accelerometers and strain gauges near the pile head and above ground level (Figure 4-2), which measure the strain and acceleration response with time for each hammer blow. The first measurements of these kind were taken in the UK by Glanville *et al.* (1938) with significant advances made in the 1960s (Housel, 1965). There are typically two sets of diametrically opposite strain gauges and two sets of diametrically opposite accelerometers. The outputs are averaged between the sensors with suitable checks on the data for consistency. The data are interpreted in real time via a monitoring system e.g. a Pile Driving Analyser (PDA) which allows the stresses induced in the pile to be assessed during driving along with the pile integrity. An approximate estimate of the pile capacity can also be obtained from the measurements using closed form solutions and empirical correlations to static pile test results e.g. the CASE method (Goble and Rausche, 1970), the Impedance Method (Beringen *et al.*, 1980) or the TNO method (Foeken *et al.*, 1996).

The resulting accelerations measured at the pile head are integrated to give velocity, v_p and displacement, w_p of the pile with time during a hammer blow. The measured strain, ε from the strain gauges is used to obtain the force, F in the pile section. Above ground level, where the pile is unaffected by soil resistance, the reflected traces of F and Zv should be equal for a uniform pile. The reflected traces of F and Zv from below ground level are affected by the total (static and dynamic) soil resistance as per Eq. 4-6 and a suitable resistance model (discussed later) is required to simulate these effects. The measurement of F and Zv continues until the pile has come to rest and the final permanent displacement has been reached. The sampling rate is generally greater than 5000 samples per second.

Post-processing analysis of the F and Zv signals obtained from the strain gauges and accelerometers during a hammer impact to determine axial pile capacity is known as signal matching. A numerical method is used to simulate the wave propagation along the pile during a hammer blow. The measured Zv signal is generally used as the input boundary condition, eliminating the need to model the pile hammer separately. The aim of the analysis is to match artificially generated signals of either F or Zv with those measured at the pile head. For a free beam, the artificial signal differs from the measured by an amount equal to the total soil resistance. The signal matching process consists of iteratively changing soil resistance along the pile, by varying input parameters to the adopted soil resistance model, until a good quality match is obtained. The method therefore allows the Soil Resistance to Driving (SRD) to be determined with each blow, and with advancement of the pile tip. The parameters obtained in this way should not be considered as a unique set, but rather as the best fit to each particular data set, by one particular user. The process of matching individual signals is discussed further in Section 4.9.4.

Signal matching can be used to assess the change in pile capacity with driving up to the End of Driving (EoD) and also over time in Beginning of Restrike (BoR) tests. A restrike test involves returning to the pile some period of time after installation and subjecting it to one or more hammer blows at a sufficient energy to mobilise the ultimate resistance. The ratio of the BoR resistance to the EoD resistance can be used to assess the pile "set-up" or increase in capacity with time.

One-dimensional stress wave theory can also be used to forward predict SRD and displacement for a given hammer blow. This, so called "driveability" problem, is the inverse of a signal matching analysis. The aim of this analysis is to assess what size and

type of hammer is required to drive a pile to the required depth, without generating excessive driving stresses. In order to carry out a driveability study, the SRD at the pile base and along the shaft must be modelled in a similar manner as during the signal matching process. It is also necessary to know the pile dimensions and to model the response of the hammer. Hydraulic hammers were used to drive the piles described in Chapter 5 and 6 with external power sources used to induce downward velocity in a metal ram. The hammer itself can be modelled using analytical solutions, by numerical modelling of the entire hammer system or by using a signature force time response supplied by the hammer manufacturer (Randolph, 2008).

The output of a driveability analysis is a plot of SRD versus hammer blows per penetration, required to overcome that SRD. Plots of hammer blows per penetration against depth can also be developed for each pile. After pile driving, the latter can be compared to the actual blow counts per penetration with depth to assess the effectiveness of the SRD prediction methods. Driveability predictions therefore rely on correctly simulating the hammer response and on the reliable estimation of SRD, since there is no measured data available with which to compare the result. Methods to estimate SRD are discussed further in Section 4.9.3.

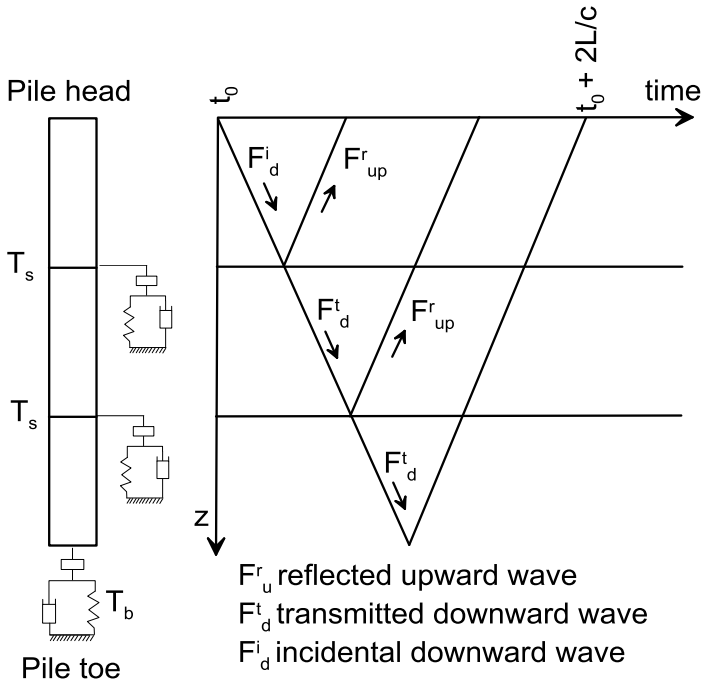
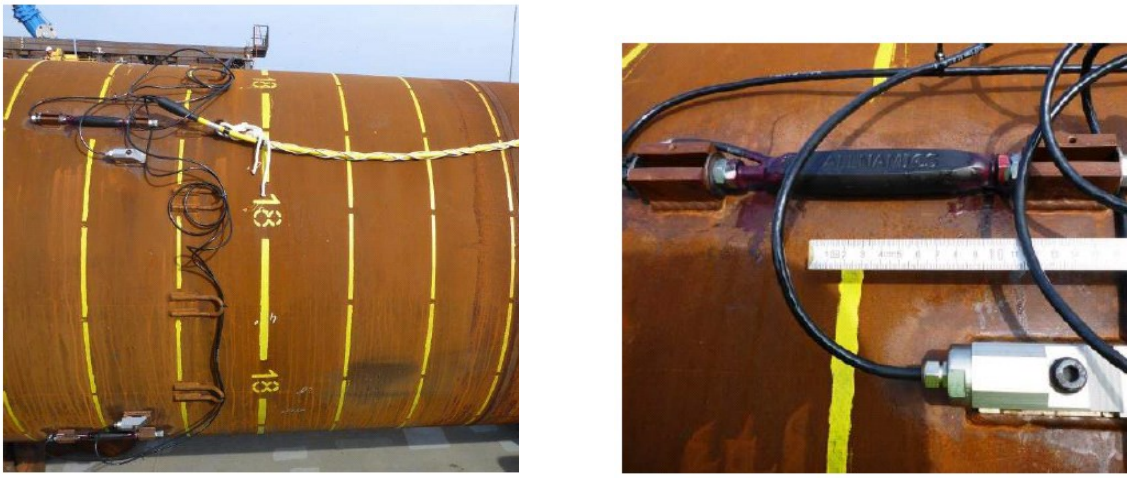


Figure 4-1: Schematic illustration of method of characteristics and waves affected by soil resistance; adapted from Middendorp and Verbeek (2006)



(a) (b)

Figure 4-2: Strain gauges and accelerometers near the pile head (a) installation/cable handling (b) sealed and fixed sensors (Bilfinger, 2015a)

4.5 The use of soil resistance models

The engineering benefit of the methods described above relies on the accurate representation of the dynamic response of the soil during pile driving. Pile installation causes cyclic loading and significant rate effects to be imposed in the surrounding soil. The accuracy of the result depends on the quantification of these effects. Along with plastic deformation of the soil immediately adjacent to the shaft, the dynamic response of the soil continuum during driving, shown schematically on Figure 4-3, includes:

- Radiation damping – due to energy dissipating in the far-field remote from the pile; and
- Hysteretic damping – energy dissipating due to the soil's loading and unloading behaviour.

Along the shaft, shear stress is mobilised as the pile moves downward. Once this reaches the limit shaft resistance, a thin shear band forms along the shaft. Plastic deformation in this band is caused by high strain rates which results in a higher than static resistance in the shear zone, due to viscous enhancement of strength. Viscous effects result in higher strengths under fast rates of loading related to the relative velocity between the pile and the soil. Viscous effects are of particular significance in fine grained soils, where water layers surround the particles and prevent mineral to mineral contact, resulting in a potentially strong viscous resistance; Litkouthi and Poskitt (1980).

Outside of the plastic shear zone, the soil undergoes predominantly cyclic vertical shear loading, with the vertical shear wave mode dominating. Energy is dissipated by non-linear hysteretic damping, with the damping ratio of the soil increasing with increasing cyclic shear strain. In the far-field, energy is also dissipated by radiation damping. Radiation damping occurs as the energy is spread over a larger volume of material, as it moves away the hammer source.

At the base, there is no relative slip between the pile and the soil and the propagation of stress waves causes the pile to penetrate the soil plastically. Plastic penetration occurs when the base resistance of the pile is exceeded, analogous to the bearing capacity mechanism of shallow footings. Within the zone of deformation beneath the pile, shown on Figure 4-3, energy is dissipated by radiation and hysteretic damping.

4.6 Shaft and base models after Smith (1962)

4.6.1 Original model formulation

The soil models used currently in most software applications to model the shaft and base response are based on the rheological model developed by Smith (1962) as shown on Figure 4-4. The soil mass is represented by a linear spring and a plastic slider in parallel with a dashpot. The spring represents the relative movement of the pile and soil prior to the limit of the slider. The dashpot models the viscous enhancement of soil resistance. The total (static + dynamic) resistance at a shaft node given by:

$$T_s = T_s^S + T_s^D = K_s w_p + C_s v_p \qquad 4\text{-}19$$

where the superscripts S and D indicate the static and dynamic resistances, K_s is the spring constant and C_s is the dashpot constant. The parameter J_s, with units of s/m, was introduced by Smith (1962), to simplify the problem in terms of computational effort giving:

$$T_s = T_s^S(1 + J_s v_p) \qquad 4\text{-}20$$

Eq. 4-20 effectively considers damping as a product of the static soil resistance, a damping factor and the instantaneous pile velocity. The unit resistance along the pile shaft can be further developed from Eq. 4-19:

$$\tau = \min\left(k_s w_p, \tau_{stat}\right)(1 + c_s v_p) \qquad 4\text{-}21$$

where τ_{stat} represents the limit of the plastic slider and the advent of plastic behaviour. The dashpot coefficient c_s can be expressed in terms of J_s and τ_{stat}:

$$c_s = \frac{C_s}{A_s} = J_s \tau_{stat} \qquad 4\text{-}22$$

where A_s is the surface area of the shaft. The spring stiffness for the shaft, k_s is expressed in terms of the displacement (Shaft quake, $q_{k,s}$) to mobilise τ_{stat} shown on Figure 4-4 (b):

$$k_s = \frac{K_s}{A_s} = \frac{\tau_{stat}}{q_{k,s}} \qquad 4\text{-}23$$

The implementation of the traditional soil resistance models in routine software programs often also includes an asymmetric elasto-plastic model, as also shown on Figure 4-4 (b), which models a lower tensile shaft resistance on unloading ($U_n\tau_{stat}$) and a different unloading stiffness such that:

$$k_{s,ul} = \frac{K_{s,ul}}{A_s} = \frac{U_n \tau_{stat}}{q_{ku,s}} \quad 4\text{-}24$$

Where U_n is an unloading factor (<1) and $q_{ku,s}$ is the unloading quake which differs from the loading quake. The inclusion of a lower tensile shaft resistance on unloading raises the later portion of the artificial upward wave, since it allows for less "negative" shaft resistance.

The base resistance in the Smith model is represented in a similar manner to Eq. 4-19 to 4-24, where $q_{b,stat}$ is the limit base resistance, denoted in all terms by the subscript "b":

$$T_b^S = A_b \left(\min\left(k_b w_p, q_{b,stat}\right)(1 + c_b v_p)\right) \quad 4\text{-}25$$

$$k_b = \frac{K_b}{A_b} = \frac{q_{b,stat}}{q_{k,b}} \quad 4\text{-}26$$

$$c_b = \frac{C_b}{A_b} = J_b q_{b,stat} \quad 4\text{-}27$$

The limiting shaft and base resistances depend on the soil conditions. Quake and damping are empirical constants obtained from back analysis of driving records and pile load tests. Values of quake and damping from the literature lie within a relatively small range; Smith (1962) suggested $q_{k,s}$ and $q_{k,b}$ equal to 2.5mm, J_s equal to 0.16 s/m and J_b equal to 0.492 s/m, from the limited data available for correlation at that time. A decade after the work of Smith, Coyle *et al.* (1973) estimated dynamic parameters from full scale pile load tests and suggested the parameters varied with soil type; two to four times higher shaft damping factors were proposed for silt and clay, thought to be due to the higher viscosity associated with cohesive soils. Negligibly low damping factors were suggested at the toe in clay. Hannigan *et al.* (2006) argue that damping factors are not constant for any soil type and vary with time after driving. This was supported by work by Castelli and Hussein (1998) and by Liang's (2000) statistical re-analysis of 611 driven piles previously reported by Paikowsky *et al.* (1994) which showed quake values which varied minimally between EoD and BoR and damping factors which appeared to be more influenced by time after driving than by soil type. Alves *et al.* (2009) back analysed dynamic parameters and showed that they varied with time for piles in soft clay, thought to be related to the dissipation of driving generated pore pressures. Ng and Sritharan (2013) attempted to correlate dynamic soil parameters with cone penetration and standard penetration tests with limited success.

The lack of satisfactory correlation between measurable soil quantities and the dynamic parameters is unsurprising since the Smith dashpot attempts to capture together all of the damping effects shown in Figure 4-3 and does not consider hysteretic damping, radiation damping or viscous effects separately. Simons (1985) emphasised that radiation damping is particularly important when elastic displacement is occurring, prevailing where piles are driven almost to refusal. In general, and as described by Loukidis *et al.* (2008) the mechanics of pile driving are not described well by the Smith model. The configuration of the model means that the dashpot is active before and after reaching τ_{stat}, giving the same amount of damping before and after sliding, for both the base and the shaft.

4.6.2 Modifications to the original model

The TNO soil model of Middendorp (1987) is a variant on the Smith soil resistance model. The spring, dashpot and slider have the same configuration, but the static and dynamic resistances are uncoupled, e.g. at the shaft:

$$T_s = T_s^S + T_s^D \quad 4\text{-}28$$

$$T_s^S = w_p \, A_s k_s \quad 4\text{-}29$$

$$T_s^D = v_p \, A_s c_s \quad 4\text{-}30$$

The parameter c_s has units of MNs/m^3 and as a result, the TNO model can be used to input the dynamic resistance separate from the static resistance. While this is an improvement on Eq. 4-20, this form of the soil resistance model shares the limitations of the Smith model discussed above.

Several authors have proposed modifications to the Smith damping constants based on laboratory testing that shows that the dependence of soil strength on velocity is non-linear. A power law for how shear strength varies with velocity under dynamic conditions was first suggested by Coyle and Gibson (1970) from their results of triaxial tests with soil samples loaded dynamically by a falling mass. A power law relationship is therefore often used in place of Eq. 4-20:

$$T_s = T_s^s(1 + J_s' v^{\beta_s}) \quad 4\text{-}31$$

Where J'_s and β_s are modified Smith parameters which account for the dependence of soil strength on velocity and have been determined in a number of experimental studies. Dayal and Allen (1975) carried out cone penetration tests in sand and clay in the laboratory at different penetration rates. Heerema (1979) investigated rate effects on

interface friction between sand and steel. Litkouthi and Poskitt (1980) and Brown (2004) carried out rapid model pile load tests in clay. The resulting values of J'_s and β_s (along with J'_b and β_b where the subscript b indicates the base node) from the studies in clay are shown in Table 4-1.

Dayal and Allen (1975) observed no rate effects in cone resistance or sleeve friction in sands at velocities as high as 0.8 m/s. Heerema (1979) also found no gain in strength with velocity for sands. Only Coyle and Gibson (1970) observed rate effects; recommendations for sands from that study, for both base and shaft, are β_s/β_b values between 0.18 and 0.26 and J'_s/J'_b between 0.34 and 0.56.

The value of the exponent at the shaft and base (β_s or β_b) is generally taken in practice as 0.2, independent of the soil type. Loukidis *et al.* (2008) give correlations for J' in sands and clays based on Lee *et al.* (1988) who collated the data from various experimental studies. For clays, $\beta_s = \beta_b = 0.2$ and the damping factors at the shaft and base are given by:

$$J'_s = 1.65 - 0.75\left(\frac{s_u}{p_a}\right) \quad 4\text{-}32$$

$$J'_b = 1.2 - 0.63\left(\frac{s_u}{p_a}\right) \quad 4\text{-}33$$

Where s_u is the undrained shear strength and p_a is the atmospheric pressure. For sands, $\beta_s = \beta_b = 0.2$, the damping factor at the shaft is considered negligible and the damping factor at the base is given by:

$$J'_b = 1.5 - 0.083(\varphi' - 30°) \quad 4\text{-}34$$

where φ' is the angle of shearing resistance. Loukidis *et al.* (2008) adopt J'_b equal to 0.3 for sands regardless of φ'

Table 4-1: Viscosity parameters for clay based on research studies

Test pile	J'_s (s/m)	J'_b (s/m)	β_s	β_b
Coyle and Gibson (1970)	0.95 - 1.55		0.11 - 0.25	
Dayal and Allen (1975)	0.93	0.49	0.34	0.23
Heerema (1978)	-	-	-	-
Litkouthi and Poskitt (1980)	0.78 - 2.1	0.44 - 1.0	0.16 - 0.57	0.17 - 0.37
Brown (2004)	1.26	-	0.34	-

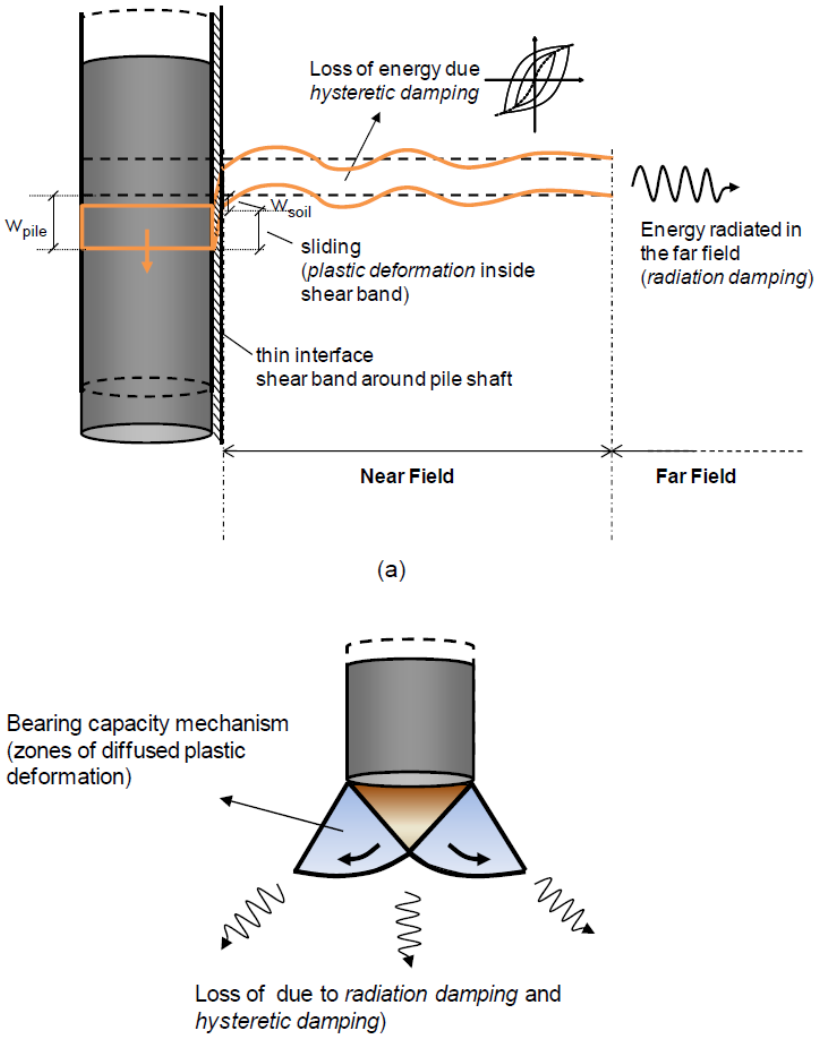


Figure 4-3: Dynamic mechanisms at a) the shaft and b) the base (Loukidis *et al.*, 2008)

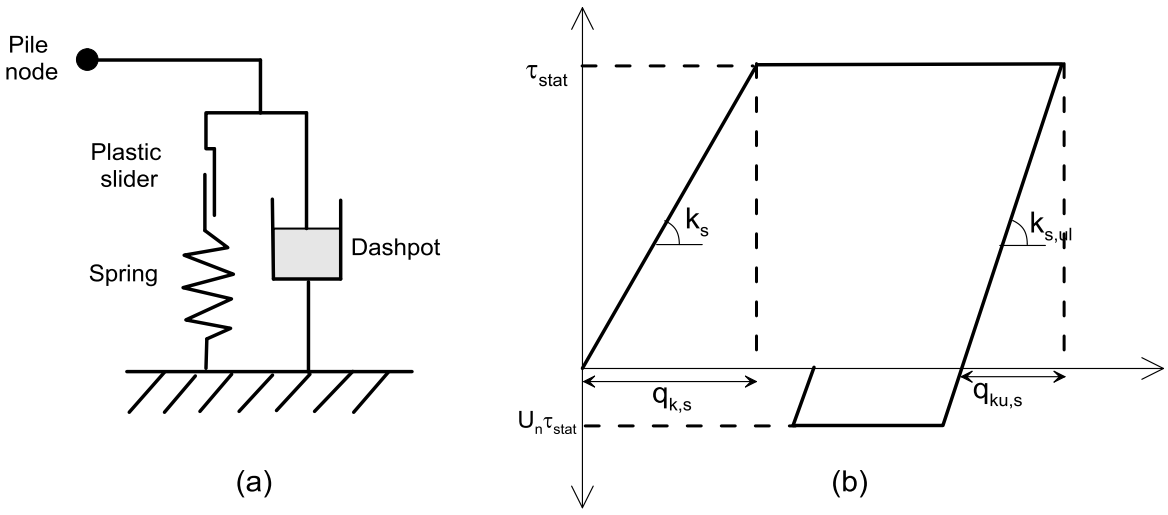


Figure 4-4: Traditional soil resistance models (a) model configuration adapted from Smith (1962) (b) elasto-plastic behaviour at a shaft node

4.7 Soil resistance models after Simons and Randolph (1985) and Deeks and Randolph (1995)

Several other rheological models have been proposed to better simulate the mechanics of pile driving (e.g. Holeyman, 1985, Simons and Randolph, 1985, Randolph and Simons, 1986, Deeks and Randolph, 1995, Salgado *et al.*, 2015). Two of these models have been considered by the Author and used in the research; the Simons and Randolph (1985) model for behaviour along the pile shaft (also described in Randolph and Simons (1986)) and the Deeks and Randolph (1995) model used to simulate behaviour at the pile base.

The Randolph and Simons (1986) shaft model is based on the closed-form analytical solution of Novak *et al.* (1978) for soil acting on the shaft of a vertically vibrating, rigid, infinitely long pile. The model, shown schematically on Figure 4-5, consists of a spring and radiation dashpot connected in parallel. The latter system is connected in series to a plastic slider and a viscous dashpot which are connected in parallel. The spring and radiation dashpot represent the far field response, while the slider and viscous dashpot model the shear band around the pile shaft, subjected to viscous rate effects.

The solution considers the pile as a series of independent horizontal layers, similar to static load transfer analyses. The complex reaction of an elastic soil disk acting on an element at the pile-soil interface, resulting from harmonic motion $w(t)=\omega\exp(i\omega t)$, was given by Novak *et al.* (1978):

$$\tau = \frac{G}{2\pi R}(S_{\omega 1} + iS_{\omega 2})w \qquad 4\text{-}35$$

The spring and dashpot constants $S_{\omega 1}$ and $S_{\omega 2}$ are functions of the dimensionless frequency factor, a_0:

$$a_0 = \frac{\omega R}{V_s} \qquad 4\text{-}36$$

Where V_s is the shear wave velocity of the soil.

During dynamic loading, the shear stress applied and the resulting displacement are no longer in phase due to the effects of material and radiation damping. The dynamic stiffness coefficients $S_{\omega 1}$ and $S_{\omega 2}$ describe this in-phase and out-of-phase stiffness, respectively. $S_{\omega 1}$ and $S_{\omega 2}$ can be expressed in terms of Bessel functions, and are shown in Figure 4-6 as a function of a_0.

At high dimensionless frequencies, $S_{\omega 1}$ is practically constant, while $S_{\omega 2}$ is proportional to the frequency. Simons and Randolph (1985) found that, for the frequencies associated with pile driving, i.e. a_0 between 1 and 10, $S_{\omega 1}$ and $S_{\omega 2}$ can be approximated by π and $2\pi a_0$, respectively. They proposed that the response of the soil in the far field, prior to slip, is described by a spring in parallel with a dashpot such that, in a similar form to Eq. 4-19, along the shaft:

$$\tau = k_s w + c_s \frac{\delta w}{\delta t} \leq \tau_{stat} \qquad 4\text{-}37$$

$$k_s = \frac{G}{D} \qquad 4\text{-}38$$

$$C_s = \frac{G}{V_s} = \sqrt{G\rho_s} \qquad 4\text{-}39$$

Eq. 4-39 is based on elastic wave propagation and therefore the correct shear modulus is the maximum value, G_{max} since soils are elastic only in the small strain range.

Where τ, calculated by Eq. 4-37, remains below τ_{stat}, the limit of the plastic slider, the spring and radiation dashpot dominate the response and the pile and soil move together. Once τ exceeds this value, i.e. during pile-soil slip, the spring and dashpot system is disconnected and the pile and soil displacements are calculated separately. During slip, the viscous dashpot augments the shear strength of the soil to account for rate effects in the thin shear band. The strength in the interface, τ_{inter} is a function of the relative velocity between the pile and soil, Δv:

$$\tau_{inter} = \tau_{stat}\left(1 + \alpha_s \left(\frac{\Delta v}{v_0}\right)^{\beta_s}\right) \qquad 4\text{-}40$$

Where v_0 is a normalizing velocity (= 1 m/s), and α_s and β_s are viscosity parameters. The above equation is similar to Eq. 4-31 with α_s approximately equal to J'_s and β_s as described previously. During slip, the behaviour is controlled by the slider and the viscous enhancement. The soil displacements are calculated constantly, by solving Eq. 4-37 with a fixed value of τ_{stat}. The condition for re-joining of the pile and the soil is when the value of τ calculated using *soil* displacement and *pile* velocity, $\tau_{s,p}$ falls below τ_{stat} (Randolph and Simons, 1986), i.e. where:

$$k_s w_s + c_s v_p \leq \tau_{stat} \qquad 4\text{-}41$$

Open-ended steel pipe piles can mobilise shaft resistance along their internal shaft area as well as the external area. Randolph (1987) describes a model for the soil plug

inside open-ended piles, which is essentially the same as that shown for the shaft in Figure 4-5, with the near-field soil node representing the internal shaft resistance, and the far field node representing the soil at the centre of the plug. The spring stiffness for the soil plug element is taken as double that outside of the pile. The internal shaft resistance is therefore considered explicitly, which is not possible with the traditional resistance models described in Section 4.6.

Deeks and Randolph (1995) assessed the performance of the widely used base resistance model derived from the Lysmer and Richart (1966) closed-form solution for the motion of a circular rigid footing on the surface of an elastic half space and subjected to vertical transient load. Deeks and Randolph (1995) carried out finite element modelling to assess the performance of several rheological model configurations. They found the best coincidence with finite element results occurred for the configuration shown in Figure 4-5, which is essentially similar to the Randolph and Simons (1986) shaft model. The primary difference is the addition of two lumped masses, one connected to the pile node (m_0) and one mass (m_1) connected through a second radiation dashpot (c_1). The spring and dashpot are the same as in the Lysmer and Richart (1966) model where the response of a circular footing of radius R is given by:

$$Q = K_b w + C_b w \leq q_{b,stat} \quad 4\text{-}42$$

$$K_b = \frac{4GR}{(1-\nu)} \quad 4\text{-}43$$

$$C_b = \frac{4R^2}{(1-\nu)}\sqrt{G\rho_s}\beta_0 \quad 4\text{-}44$$

The second radiation dashpot is described by

$$C_1 = \frac{4R^2}{(1-\nu)}\sqrt{G\rho_s}\beta_1 \quad 4\text{-}45$$

And the subsidiary masses by:

$$m_0 = \frac{4R^3\rho_s}{(1-\nu)}\alpha_0 \quad 4\text{-}46$$

$$m_1 = \frac{4R^3\rho_s}{(1-\nu)}\alpha_1 \quad 4\text{-}47$$

Where β_0, β_1, α_0, and α_1 are model parameters that depend on Poisson's ratio, ν. Deeks and Randolph (1995) found that for undrained conditions where ($\nu = 0.5$) the mass m_1 is equal to zero and therefore the second radiation dashpot has no effect. The parameter

β_0 adopted in Eq. 4-44 is equal to 0.8 and the parameter α_0 adopted in Eq. 4-46 is equal to 0.16 (Randolph, 2008). Randolph (1990) argues even that in clays, where viscous effects are important, radiation damping will dominate the response at the tip. Therefore, in contrast to the shaft reaction model, there is no viscous enhancement of base resistance included in the version of the model used by the Author. A summary of the adopted equations, for both the base and shaft models used by the Author, is given inTable 4-2.

Table 4-2: Summary of equations and parameters using Simons and Randolph (1985) and Deeks and Randolph (1995) models in IMPACT

	No.	Parameter
Shaft resistance	$\tau = k_s w + c_s v \leq \tau_{stat}$	
Spring	$k_s = \frac{G}{\pi D}$	G, D
Radiation dashpot	$C_s = \frac{G}{V_s} = \sqrt{G\rho_s}$	G, ρ_s
Viscous effects	$\tau_{inter} = \tau_{stat}\left(1 + \alpha_s\left(\frac{\Delta v}{v_0}\right)^{\beta_s}\right)$	α_s, β_s
Total base resistance	$Q = k_b w + c_b v \leq q_{b,stat}$	
Spring	$K_b = \frac{4GR}{(1-\nu)}$	G, D
Radiation dashpot	$C_b = \frac{4R^2}{(1-\nu)} 0.8\sqrt{G\rho_s}$	G, D, ρ_s
Subsidiary mass	$m_0 = 0.16\frac{4R^3\rho_s}{(1-\nu)}$	G, D, ρ_s

4.7.1 Sensitivity of model parameters

The sensitivity of the primary model parameters used in the adopted shaft and base models are explored below. Two hammer blows from the Wikinger dataset (WK70-1 Blow 815 and WK70-1 BoR1) are used for comparison and to illustrate the performance of the model and the variation of the result with three primary parameters; the shear modulus, G and the viscosity parameters, α_s and β_s. The general sensitivity of the result to changes in shaft and base capacity is discussed in Section 4.9.4 in the context of matching individual signals. The ground conditions generally consist of glacial deposits of stiff clay and medium dense sand underlain by Grade A1/B2 low-medium density structured chalk. Both the Wikinger dynamic test dataset and the ground conditions encountered at the site are described fully in Chapter 5.

Shear modulus

An "operational", less-than-elastic shear modulus is often substituted for G_{max} in order to account for soil non-linearity and stiffness degradation with increasing shear

strain. The appropriate G value to be used in the analysis can be difficult to ascertain since the shear strain amplitude varies with distance from the source and with time (Loukidis *et al.*, 2008). The effect of varying the shear modulus from G_{max} to an operational value, G_1 has been investigated for two distinct cases: i) for a hammer blow where the overall pile capacity is low (easy driving) and ii) for a hammer blow where the pile capacity is high (hard driving).

A hammer blow with *dominant viscous* effects (WK70-1 Blow 815) at one element along the pile shaft (22.2m depth and in chalk) is considered first. Where the capacity is high, the spring and radiation dashpot dominate the response over the majority of the hammer blow. Conversely, where the capacity is low, viscous effects dominate along the shaft and as a consequence the spring and radiation dashpot are activated only towards the latter portion of the record. The latter point is demonstrated on Figure 4-7 which shows the calculated spring and radiation dashpot for values of the shear modulus equivalent to 10, 50 and 100% of G_{max}, shown for the whole blow where the spring and dashpot are both inactive and active. The values of G_1 are equivalent to G_1/τ_{stat} ratios of $\approx$ 260, 1300 and 2650.

When the pile and soil are connected the shear stress is calculated as per Eq. 4-37, as shown in Figure 4-7 (c). When the pile and soil are disconnected, the pile and soil displacements are calculated separately, and the response is dominated by Eq. 4-40 and thus τ_{inter}. The condition for re-joining of the pile and soil is when the response at a pile node, $\tau_{s,p}$, calculated using soil displacement and pile velocity (Eq. 4-41) falls below the input parameter τ_{stat}. This is illustrated for the same hammer blow and element as above in Figure 4-8; $\tau_{s,p}$, can be seen to lie well above τ_{stat}, falling below τ_{stat} only in the very latter portion of the blow when the pile is almost at rest. At that point, the spring and dashpot are reactivated. The behaviour is similar for all three cases considered of 10, 50 and 100% of G_{max}.

The implications of this behaviour are that, when the response is similar along the *whole pile* length, the upward travelling wave, F_{up}, used primarily in signal matching, is relatively unaffected by a change in G_{max} until the latter portion of the record, where the spring and radiation dashpot are re-engaged when $\tau_{s,p}$ falls below τ_{stat}. Capacity changes along the pile or at the base have no effect on this portion of the record. Therefore for easy driving, where viscosity effects are dominant, a change in G_{max} does not affect the

upward wave (and therefore the resistance required) to obtain a good match between measured and computed F and Zv, where $\tau_{s,p}$ is greater than τ_{stat} along the pile shaft.

The overall evolution of soil and pile displacements at the same pile element are shown on Figure 4-9. The soil displacements can be seen to be strongly affected by the variation in $G_{max.}$ The pile displacements, which can also be used to match the response at the pile head in signal matching, are affected in the latter portion of the record only. Therefore, changing G_{max} by factors of 2 or 10 only influences the pile set or permanent displacement towards the end of a blow, as the pile comes to rest. An operational (reduced) shear modulus can be seen to simulate the rebound of the pile. Conversely, using $G=G_{max}$ leads to a stiffer response and no rebound of the pile on unloading.

Next, a hammer blow where the overall capacity is high (WK70-1 BoR1) and the response is dominated by the spring and radiation dashpot is shown in Figure 4-10 for the same element. Again the calculated radiation dashpot and spring are shown in this Figure where they are both inactive and active. Values of the shear modulus equivalent to 10, 50 and 100% of G_{max} are considered as in the easy driving case. The high capacity can be seen to lead to a stiffer response of the spring and dashpot system initially. The same hammer blow is shown on Figure 4-11 where $\tau_{s,p}$ (the condition for re-joining in Eq.4-41) falls below τ_{stat} for the main part of the signal. The spring and radiation dashpot are therefore engaged for almost all of the record and the response is primarily a function of the shear modulus and the soil density. The pile and soil are only disconnected, and the viscous dashpot engaged, between approximately 17.8 and 19.3ms (Figure 4-11). Consequently, the upward wave is affected over the main part of the signal by changes in G_{max}. In cases where G was reduced to $0.1G_{max}$ along the pile length it was necessary to increase the input SRD resistance by approximately 10% to obtain a good match. This contrasts with the easy driving case discussed above where viscous effects dominated and the choice of G had little or no effect on the upward wave.

The evolution of soil and pile displacements at the pile element level with time for the hard driving case are shown on Figure 4-12. Considerably less pile displacement is observed for this higher energy blow. Both the pile and soil displacements are affected by the change in G_{max} over the majority of the blow. The adoption of a lower value of G_{max} leads to greater overall displacement, accompanied by a larger rebound of the pile due to the softer response during the latter portion of the blow.

Viscosity parameters

The viscosity parameters, α_s and β_s, used in Eq. 4-40 to calculate the interface shaft resistance τ_{inter} are considered next. The parameters affect the response of the pile, and thus the displacement, in cases where the spring and dashpot system are disconnected during the blow. As discussed above, this occurs for the main part of the signal where the overall static resistance is low, such as is shown on Figure 4-9. Most researchers take α_s (or J'_s) as approximately 0.2, with a range of β_s values adopted that depend on the soil type. Values of β_s of 0.2, 0.3, 0.4 and 0.5 have been considered here maintaining an α_s value of 1. Values of α_s of 0.3, 0.5, 1 and 1.5 have also been adopted, taking β_s as 0.2. The range of parameters considered is shown on Figure 4-13, where their effect on τ_{inter}/τ_{stat} is also demonstrated for a range of relative velocities, Δv (between pile and soil). The static friction in the interface is clearly augmented by the use of Eq. 4-40 to simulate viscous effects e.g. adopting an α_s value of 1 and a β_s value of 0.2 increases the static resistance by a factor more than two-fold for a typical range of the relative velocity, Δv.

The easy driving blow (WK70-1 815) considered in the previous section was used to demonstrate the effect of the viscosity parameters on the response during a hammer blow. In this case the operational shear modulus used in the calculation of the spring and radiation dashpot was 10% G_{max} and G/τ_{stat} was approximately 260. The effect of both viscosity parameters on the evolution of τ_{inter}/τ_{stat} is with pile displacement is shown on Figure 4-14. As α_s and β_s decrease, the proportion τ_{inter}/τ_{stat} decreases, which leads to a lower dynamic resistance at the interface and a greater accumulation of pile displacement. It is clear from Figure 4-14 that the parameter α_s has a strong influence on the response; values of α_s in the region of 0.3, which are often adopted for sands (Loukidis *et al.*, 2008) lead to twice the accumulation of displacement than is calculated when an α value of 1.0 is adopted.

The influence of the viscosity parameters on the upward travelling wave, F_{up} and the pile head displacement is explored on Figure 4-15. Over the majority of the blow, where the velocity is increasing, there is little effect of a change in β_s on F_{up} or on the pile head displacement. Once the velocity decreases towards a minimum at the pile toe, (at time $t_{m+2L/c}$) the effect of a change in β_s is seen more clearly, with a general trend of a reduction in F_{up} with increasing β_s; Figure 4-15 (a). This is accompanied by a decrease in pile head displacement with increasing β; Figure 4-15 (b). The reason for this behaviour is evident by comparison with Figure 4-14 (a). The parameter β_s can therefore be expected to affect F_{up}, in this case, in the vicinity of the base, and the head pile displacement in the

latter portion of the record. An increase in β_s therefore yields a similar result to increasing the pile base resistance, causing a peak in F_{up}. As a result, a change in the parameter β_s here affects the capacity obtained near to or on the base.

Figure 4-15 (c) shows the effect of a change in α_s on F_{up} for the same hammer blow. A change in α_s can be seen the affect the whole of the record, with an increase in α causing an increase in F_{up}. Figure 4-15 (d) shows a similar effect on the mobilisation of pile head displacement which increases with decreasing α_s. The implications of Figure 4-15 (c) and (d), for this case, are that a change in the pile shaft and base capacity are required in order to achieve a good match, where α_s is varied. Therefore for easy driving cases, the parameter α_s can have a stronger influence on the capacity than the shear modulus or parameter β_s.

4.7.2 Limitations of existing models

The shaft and base models described above represent a significant improvement on the traditional rheological model of Smith (1962). However, the models described do not consider soil non-linearity or hysteresis and are based on steady-state harmonic solutions, whilst the pile response during driving is highly transient in nature. In addition, the Deeks and Randolph (1995) base model does not consider embedment effects on stiffness and radiation damping, since it is based on a closed-form solution for a footing on the surface of an elastic half space. Loukidis *et al.* (2008) anticipate that stiffness and damping will be greater in the field than calculated by base models based on the Lysmer and Richart (1966) analogue. The parameters in these models do however include physical soil properties such as shear modulus and soil density which can be measured in site investigations. Both the Randolph and Simons (1986) and Deeks and Randolph (1995) models separate the response before and after pile slip and effectively eliminate radiation damping once plastic penetration begins, a significant improvement on the Smith model.

Several other soil resistance models have been developed in the last thirty years which account for other aspects of behaviour shown in Figure 4-3 including soil non-linearity, hysteretic damping, highly transient motion and embedment effects (Holeyman, 1985, Nguyen *et al.*, 1988, El Naggar and Novak, 1994, Michaelides *et al.*, 1998, Holeyman *et al.*, 1996, Salgado *et al.*, 2015). The analyses presented in Chapter 5 and 6 use the models discussed within this section. These more advanced models therefore fall outside the scope of the thesis and are not considered further.

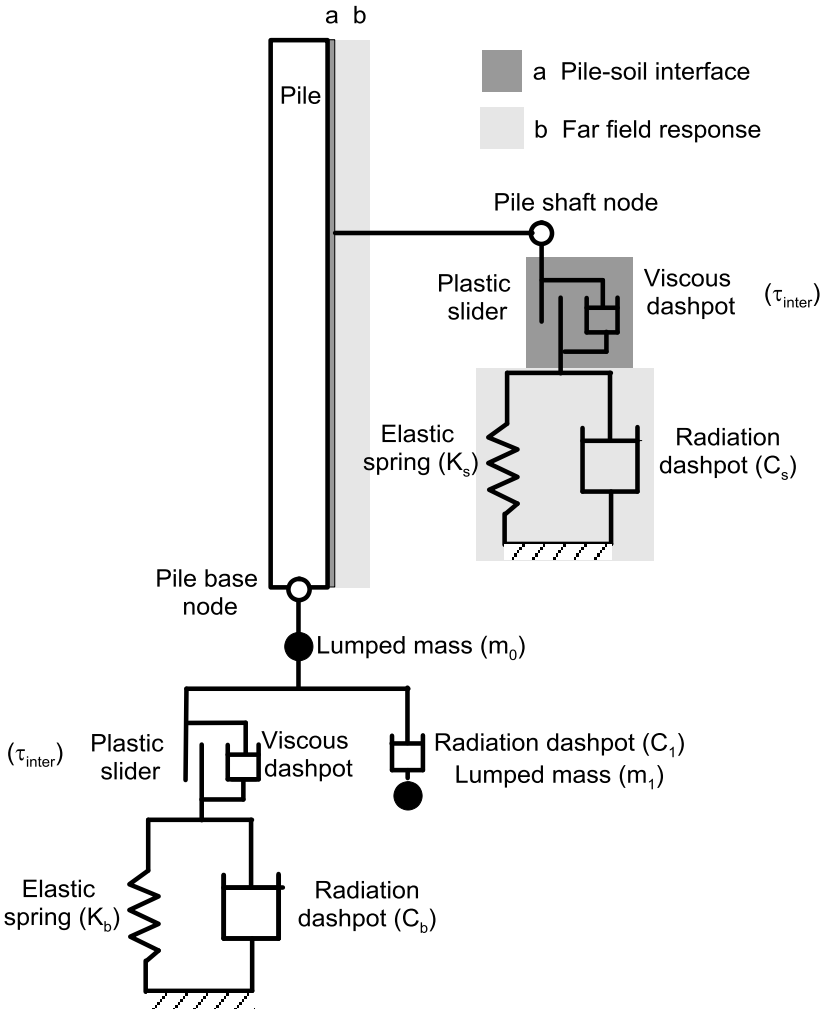


Figure 4-5: Rational soil resistance models adopted at the shaft and at the base; adapted from Randolph and Simons (1986) and Deeks and Randolph (1991)

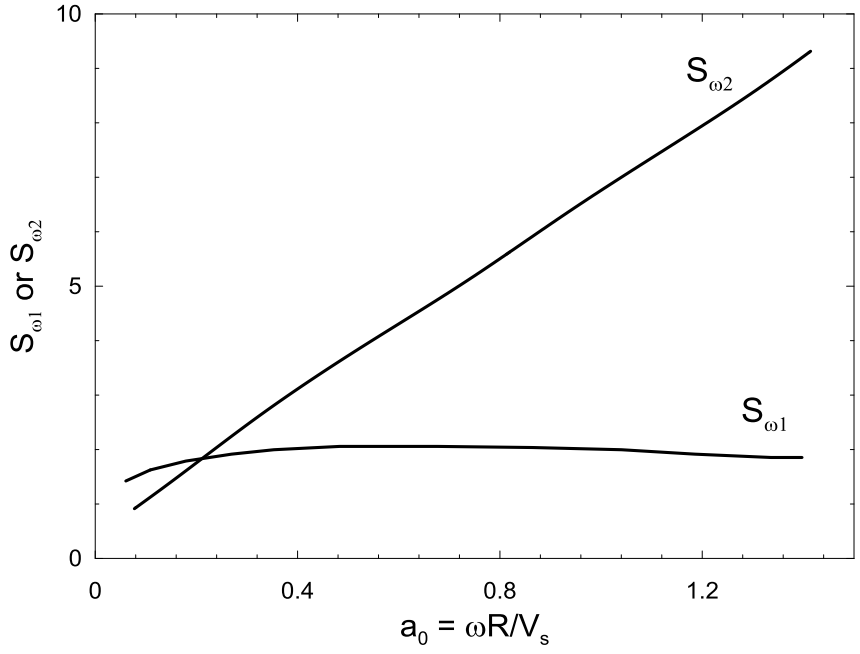


Figure 4-6: Variation of normalised stiffness coefficients $S_{\omega 1}$ and $S_{\omega 2}$ with frequency

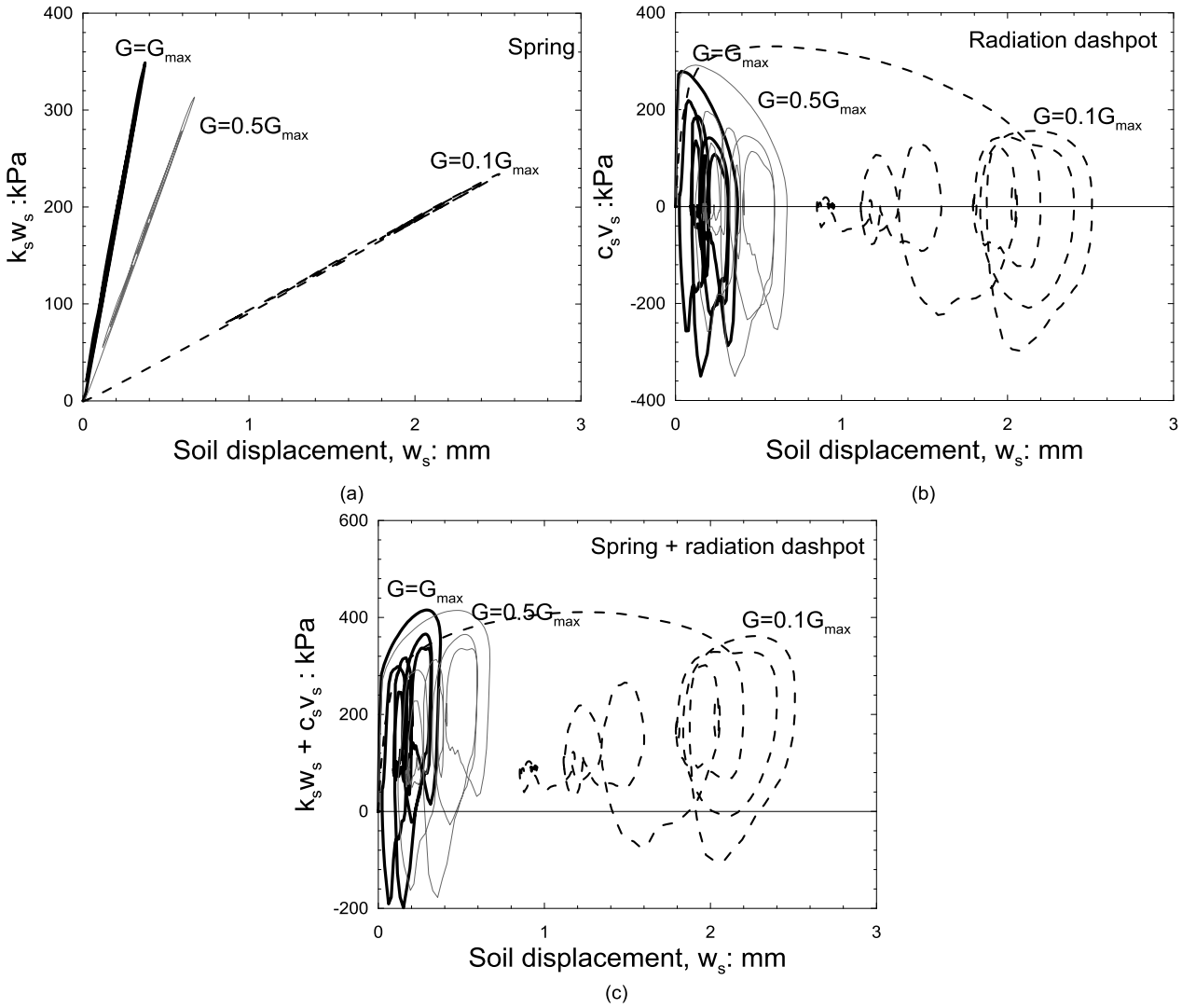


Figure 4-7: Effect of soil modulus on spring and radiation dashpot at a pile element for an easy driving case (a) spring b) radiation dashpot (c) total response Note: spring and dashpot shown in active and inactive cases

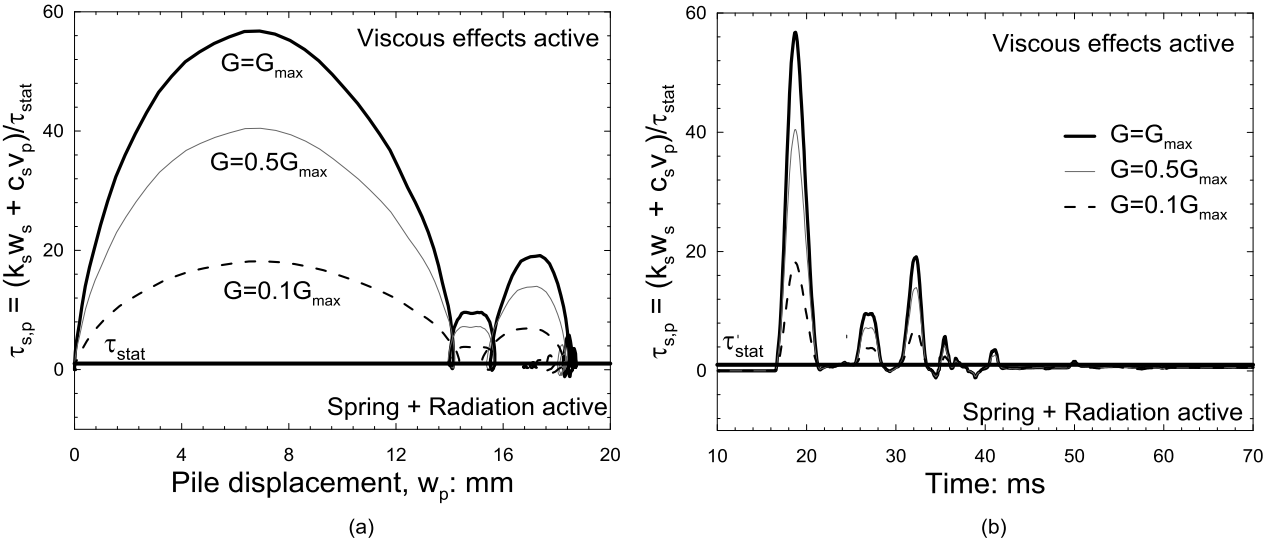


Figure 4-8: Illustration of condition for re-joining of pile and soil at a pile node for an easy driving case (a) $\tau_{s,p}$ versus pile displacement (b) $\tau_{s,p}$ versus time

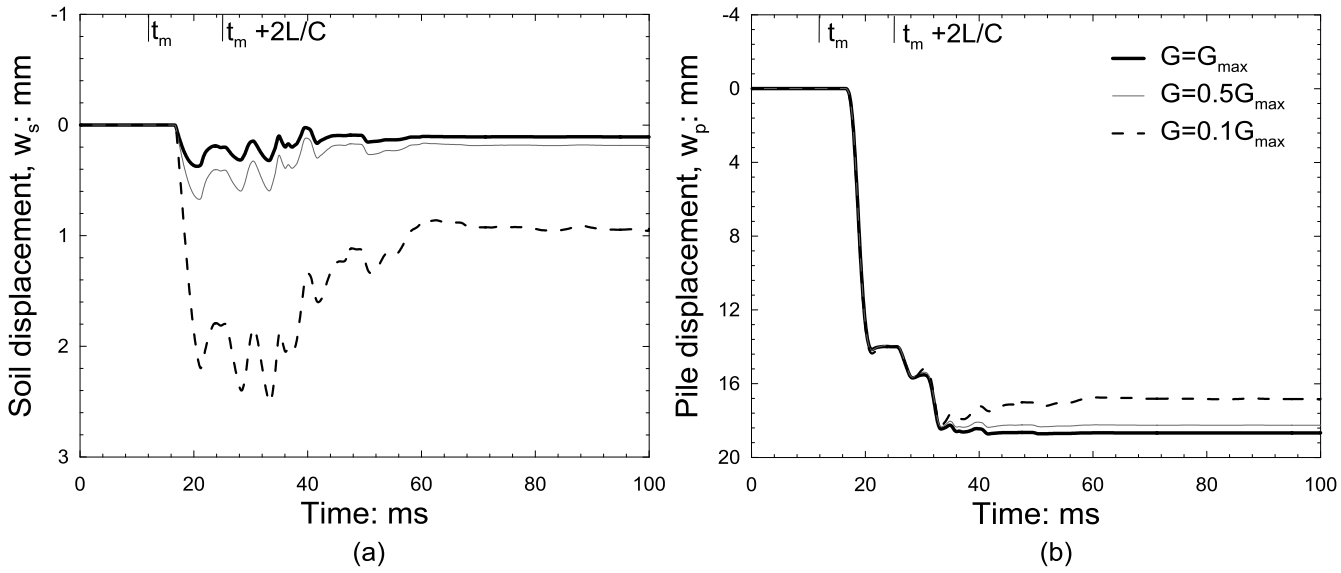


Figure 4-9: Displacements at a pile element during a hammer blow for an easy driving case (a) soil displacements (b) pile displacements

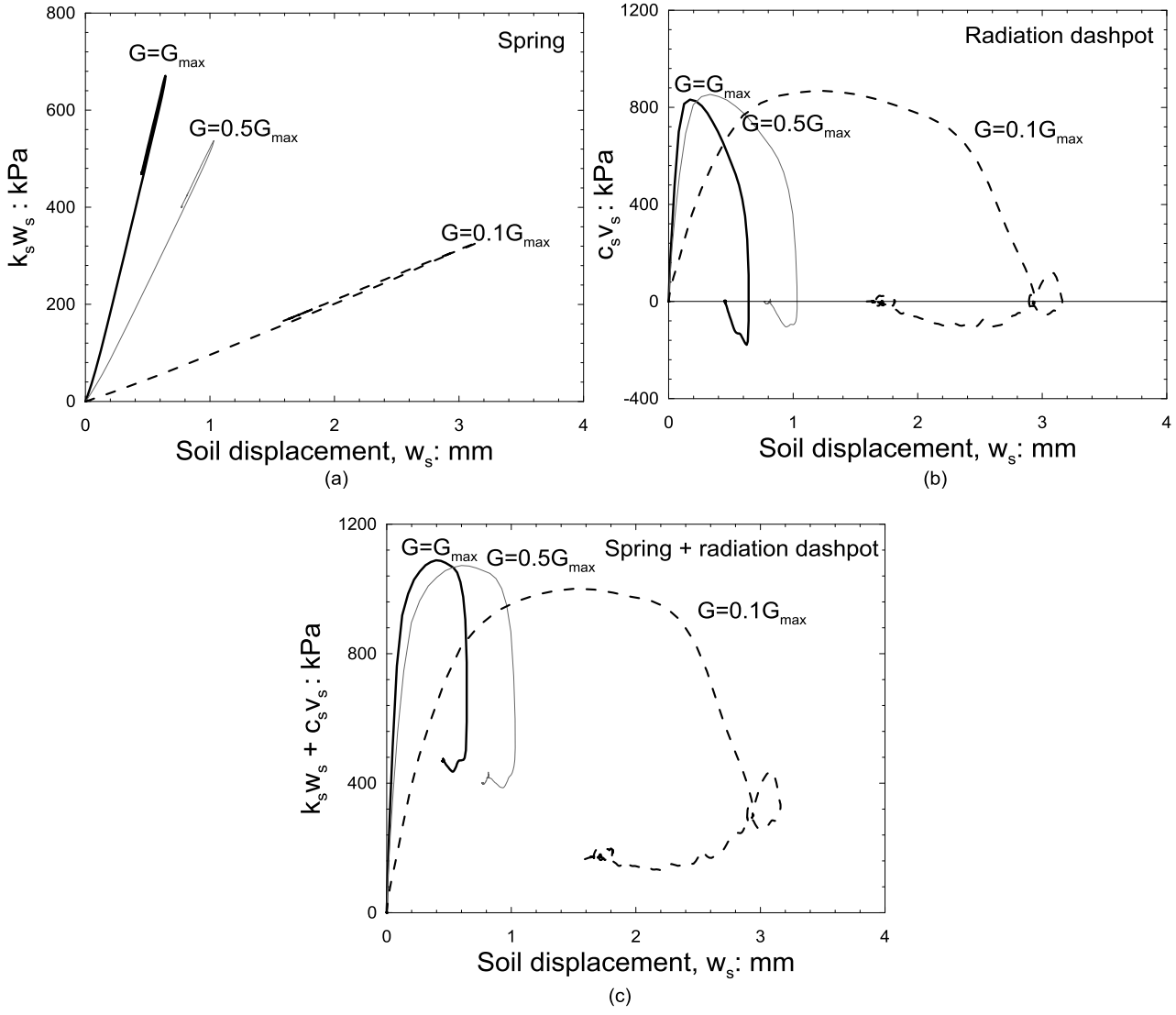


Figure 4-10: Effect of soil modulus on spring and radiation dashpot at a pile element for a hard driving case (a) spring b) radiation dashpot (c) total response

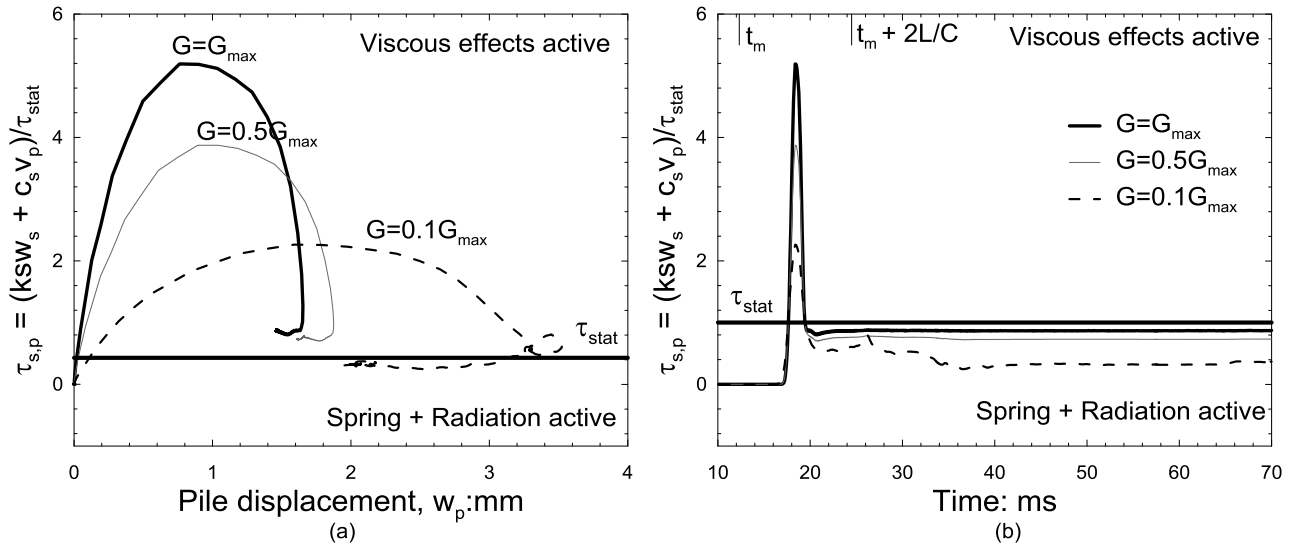


Figure 4-11: Illustration of condition for re-joining of pile and soil at a pile node for a hard driving case (a) $\tau_{s,p}$ pile displacement (b) time

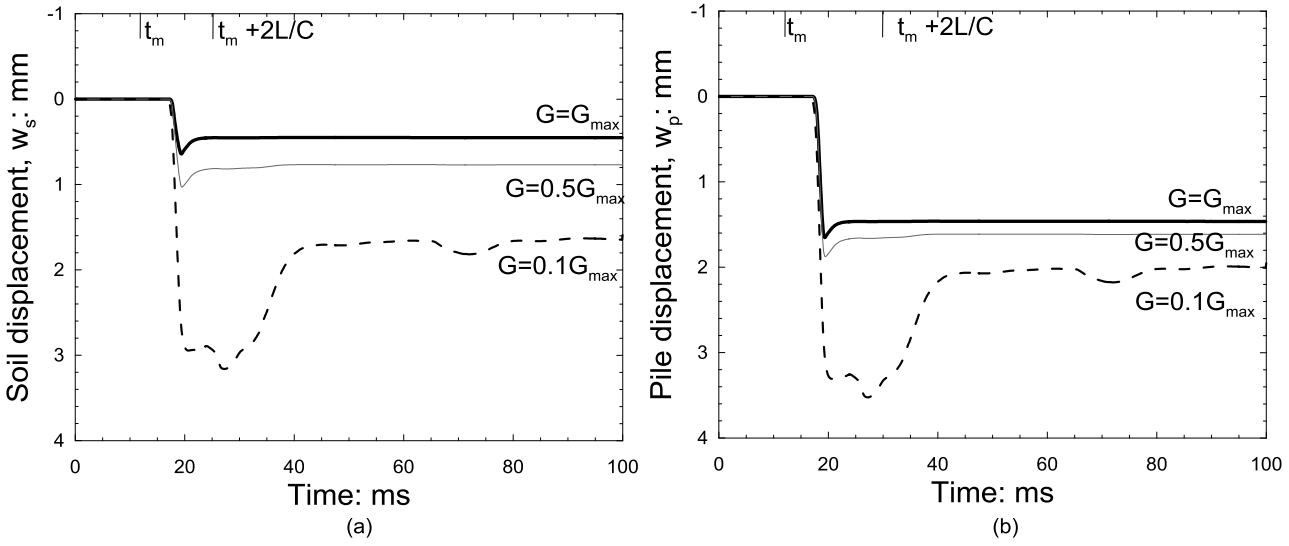


Figure 4-12: Displacements at a pile element during a hammer blow for a hard driving case (a) soil displacements (b) soil displacements

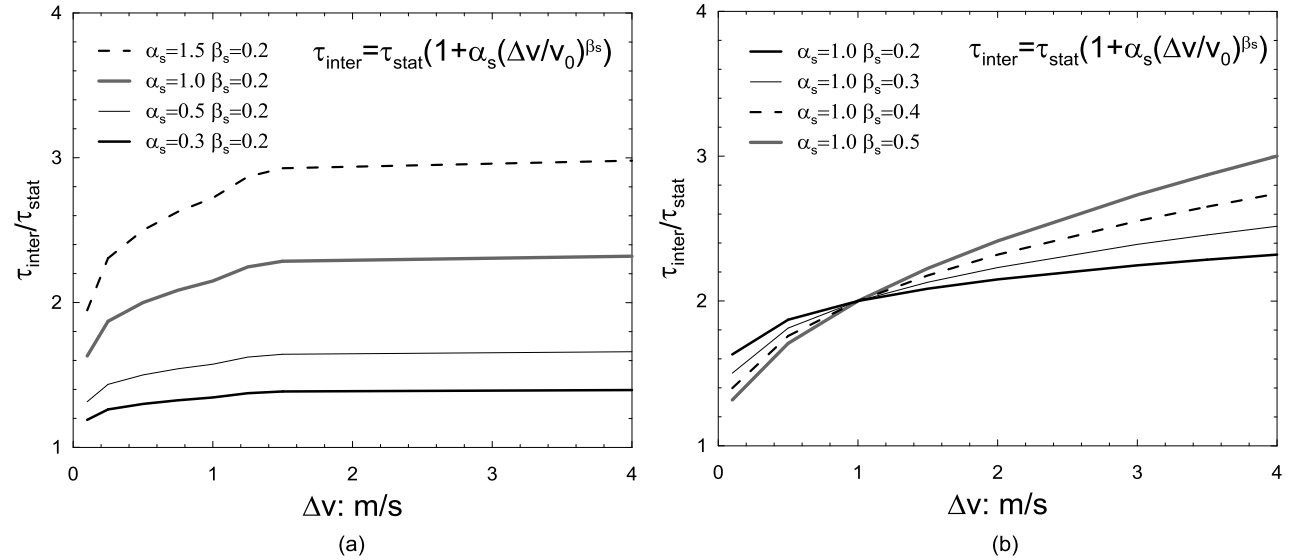


Figure 4-13: Viscosity parameters considered and the effect τ_{inter}/τ_{stat} (a) vary β (b) vary α

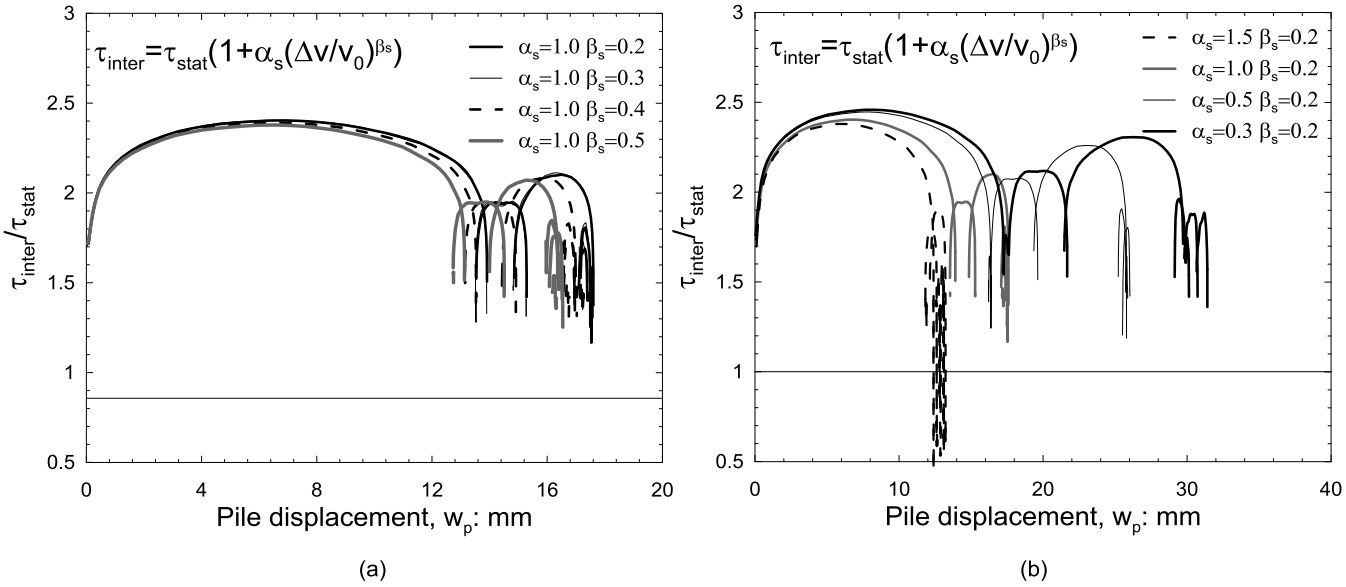


Figure 4-14: Evolution of τ_{inter}/τ_{stat} with pile displacement (a) vary β (b) vary α

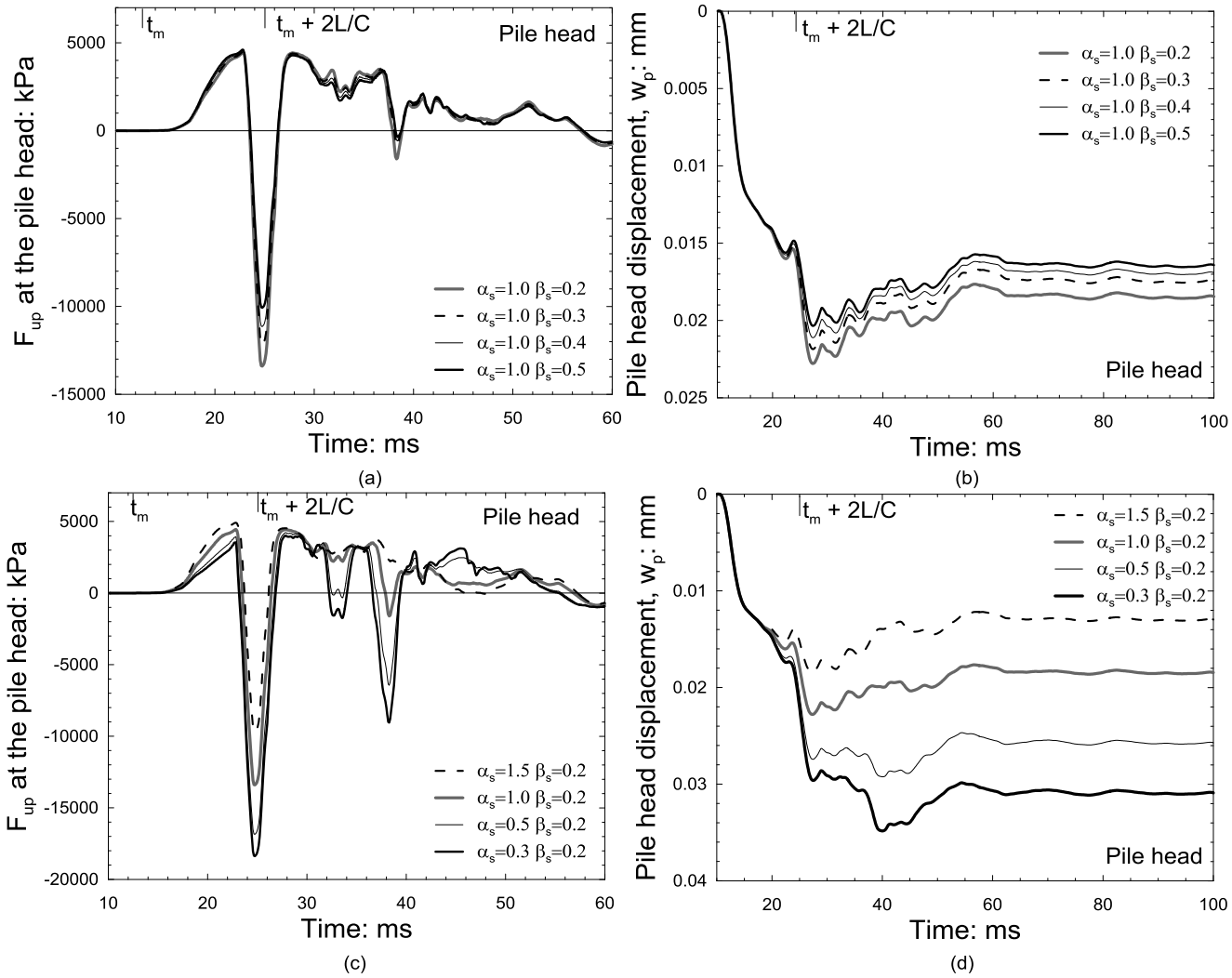


Figure 4-15: Effect of (a) varying β on upward travelling wave (b) varying β on pile head displacement (c) varying α on upward travelling wave (d) varying α on pile head displacement

4.8 Wave equation implementation in software

4.8.1 Commercial & research codes

The most widely used software program in industry is the Case Pile Wave Analysis Programme (CAPWAP) for signal matching or GRLWEAP for driveability studies (Rausche *et al.*, 1985). Both programs are developed by Pile Dynamics Inc. in North America and use Smith's lumped mass finite difference approach and the traditional soil resistance models described in Section 4.6. Allwave-DLT is a similar software program, developed by Allnamics in the Netherlands which utilises the alternative method of characteristics approach (Section 4.6) as discussed by Middendorp and Verbeek (2006) and the traditional Smith (1962) and TNO (Middendorp, 1987) soil resistance models. Allwave-DLT is similar to both the original computer program PILEWAVE developed by Hollandsche Beton Groep (HBG) and released in 1974, and to TNOWAVE which was released in the Netherlands in 1978. As both codes developed over the past 40 years, various features have been introduced to improve the performance of the interaction models. These include using asymmetric elasto-plasticity (Eq. 4-24), "uncoupled" resistance (Eq. 4-28), rate effects on strength (Eq. 4-31), as well as modelling a pile plug by addition of lumped masses and the inclusion of a "toe gap" beneath the pile to account for pile rebound during hard driving. The soil resistance models of Simons and Randolph (1985) and Deeks and Randolph (1991) have been implemented in signal matching codes used primarily for research purposes e.g. K-WAVE (Matsumoto and Takei, 1991) and IMPACT (Randolph, 2008), the latter being used by the Author for the majority of analyses presented in this thesis. A summary of the soil resistance models and additional features available in each of the codes used in the research is given in Table 4-3.

Table 4-3: Capabilities of the signal matching codes used in the research

	CAPWAP	**Allwave-DLT**	**IMPACT**
Numerical method	Finite difference	Characteristics	Characteristics
Soil resistance models	Smith	Smith TNO	Smith Simons & Randolph Deeks & Randolph
"Uncoupled" resistance	Yes	Yes	Yes
Asymmetric models	Yes	Yes	No
Rate effect on strength	No	Yes	Yes
Model internal shaft	No	No	Yes
Additional masses	Yes	Yes	Yes
Toe gap	Yes	Yes	No

4.8.2 Comparison between numerical methods

No examples were found in the literature of direct comparisons between codes which use the two numerical methods described in Section 4.3; Smith's lumped mass finite difference approach and solutions obtained using the methods of characteristics. Kawabata *et al.* (1994) report the results of dynamic and static tests on three steel tube piles carried out 6 days and 30 days after EoD. The results were analysed using CAPWAP, which uses Smith's original lumped mass finite difference approach and DLTWAVE (similar to Allwave-DLT) which uses the method of characteristics. While both sets of analyses gave reasonable predictions of the overall capacity and load displacement behaviour, the overall results differ since they were carried out by different operators, introducing their separate individual bias into the result. Tchepak (1992) describes a case study where CAPWAP was used to analyse the EoD result, while DLTWAVE was used to analyse the capacity at restrike, 12 months later. The two capacities obtained differed significantly due to set-up effects, so a direct comparison could not be established.

A direct comparison of the two numerical methods was made by the Author to assess whether the implementation of the traditional rheological soil models in codes which utilise different numerical methods leads to the same result. A BoR blow was selected to compare the numerical methods from the Wikinger dataset. Signal matches were carried out by the same operator using both CAPWAP and Allwave-DLT and the same model parameters. CAPWAP uses the Smith approach to calculate damping forces via Eq. 4-22. An uncoupled analysis was performed in Allwave-DLT using the TNO soil model, where the damping factors can be input separately from the static capacity (Eq. 4-28 to 4-30). The first estimates of shaft and base resistances were taken from the available site investigation results. The mobilised shaft resistance and stiffness calculated from the CAPWAP analysis were then input into Allwave-DLT. The dashpot coefficients for the TNO model were calculated from J_s, assumed in the CAPWAP analysis from Eq. 4-22. The key parameters used in both codes are summarised in Table 4-4.

The calculated upward travelling force waves obtained from both programs are compared with the measured signal on Figure 4-16. The two codes' predictions can be seen to closely match the measured signal and to be almost identical. Small differences are observed in the latter portion of the record which can be attributed to differences in

the interpolation of the parameters between shaft nodes; both codes indicate overall static shaft resistance of 32 MN with 1MN mobilised at the base.

Table 4-4: Summary of parameters used in comparison of numerical methods

Parameter	Value
Shaft damping, J_s	0.65
Base damping, J_b	1.38
Shaft quake, $q_{k,s}$ (mm)	3.5
Base quake, $q_{k,b}$ (mm)	2.3
U_n (%)	25
Unloading shaft quake (%$q_{k,s}$)	100
Unloading base quake (%$q_{k,b}$)	30

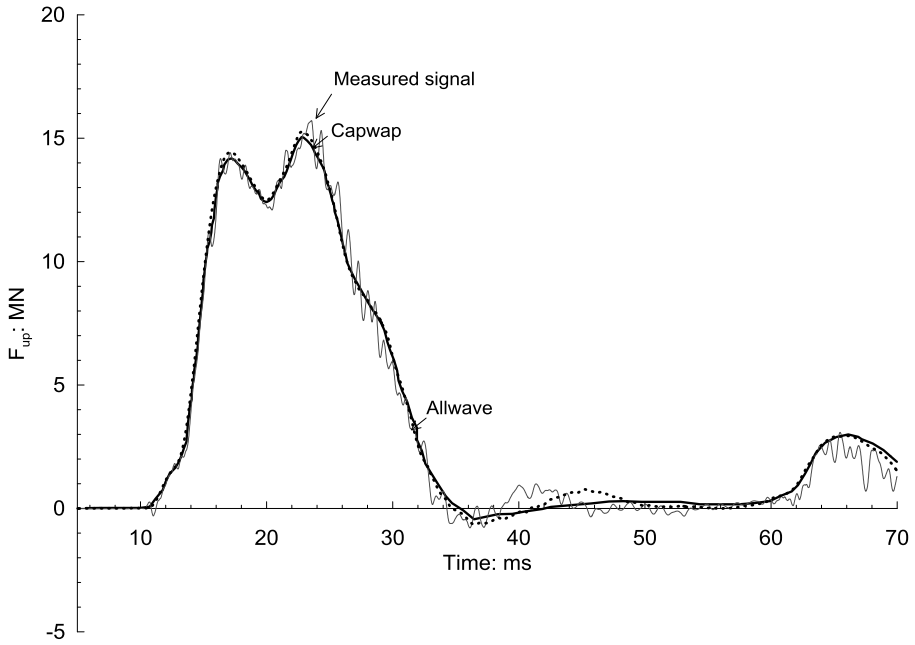


Figure 4-16: Comparison of upward travelling waves with different numerical methods

4.9 Signal matching methodology

The previous sections have outlined the theory of one-dimensional wave propagation in piles, the numerical methods used to obtain the solution and the rheological models used to model the soil response. This section describes the methodology adopted by the Author to carry out signal matching of the measured dynamic test data, obtained at both the Wikinger offshore wind farm and the Kent test site. The results of these analyses are described in full in Chapter 5 and Chapter 6.

4.9.1 Data quality assessment

The quality of the signal matching results are strongly influenced by the quality of the measured F and Zv signals from the strain gauges and accelerometers. An offshore pile installation can involve thousands of hammer blows. There are typically many hammer blows available over given penetration ranges and the most suitable and highest quality blow should be chosen to give the most useful result. Inferior data can be a result of pile bending, transducers which are not fixed securely to the pile, electronic noise, overload of the sensors, or from sensors which have not been calibrated correctly. The Author has carried out very minor data adjustment of recorded signals to avoid introducing unnecessary errors into the signal matching process.

Over time periods which involve reflections from depths above ground level and below the measurement level, i.e. for the free pile stick up, F and Zv should be equal and the upward travelling wave should equal zero (Figure 4-17). An exception to this point is where a change of cross-section (and therefore pile impedance) or pile damage exists above ground level. Where the difference is small, the F record can be replaced by Zv above ground level. As a general rule, records with erroneous or unreasonable measurements (such as indications of poor proportionality between F and Zv) should be discarded. In this respect, it can be useful to compare consecutive blows to assess data quality. Where two sets of sensors are available on the pile at the same instrumentation level, the outputs should be compared for consistency. For a blow applied axially, the output from the strain gauges should be identical and any difference implies eccentricity of the applied force pulse. Equally the instrument outputs should be compared to assess whether any bending occurred and a blow with minimal bending effects should be chosen.

Where there is significant noise in the data (due to electronic interference, or from an impedance change above ground level), a moving average filter can be applied to the signals to achieve a smoother trace which is easier to match. It is important that a scaling factor is then applied to the data where this moving average results in, for example, a different maximum F or Zv. Both the F and Zv signals should approach zero at the end of the hammer blow. The displacement time graph obtained from double integration of acceleration should approach a constant value equal to the pile permanent displacement or “set”. An F record which approaches zero at the end of the blow indicates that the transducers are fixed well to the pile (Pile-Dynamics, 2006).

The pile capacity during a hammer blow can be under-predicted if insufficient energy and force have been applied by the hammer to fully mobilise the base and shaft

resistance. A rule-of-thumb used in practice is to require a record with a minimum set per blow of ≈3mm (Rausche *et al.*, 2008). For blows at restrike, the first blow in which the capacity has been mobilised fully should be adopted, to avoid causing degradation of the capacity with further blows and under-predicting the capacity at BoR. Equally at the EoD, the last possible blow of reasonable quality should be selected to ensure a representative reference point is available for assessing capacity and set-up effects.

4.9.2 Parameter selection

An indicative list of unknowns applying to wave equation analyses in well-known commercial codes (e.g. CAPWAP and Allwave-DLT) is given in Table 4-5. There are $3N_s + 3$ primary unknowns, where N_s is the number of pile shaft nodes. The remaining parameters are only used to improve match quality and do not affect the mobilised resistance. This increases the number of unknowns to $3N_s + N_p + 8$, where N_p is the number of elements in the internal soil plug. The choice of dynamic parameters has a significant effect on driveability predictions, particularly in conditions where typical parameters are not available. Several studies indicate changes in the dynamic parameters with time, adding further uncertainty to the parameters shown in Table 4-5 (Svinkin, 1996, Castelli and Hussein, 1998, Hannigan *et al.*, 2006).

Table 4-5: Summary of unknowns in typical commercial codes

Parameter	No.	Type
Shaft resistance	N_s	Primary unknown
Base resistance	1	Primary unknown
Shaft quake	N_s	Primary unknown
Base quake	1	Primary unknown
Shaft damping	N_s	Primary unknown
Base damping	1	Primary unknown
Shaft unloading quake	1	Improve match
Base unloading quake	1	Improve match
Yield factor	1	Improve match
Base gap	1	Improve match
Base plug	1	Improve match
Shaft plug	N_p	Improve match

The unknowns in the case of the adopted models described in Section 4.7 are shown in Table 4-6. There are $3N_s + 3$ primary unknowns, of which $2N_s + 2$ can be determined from the soil density and shear modulus. The addition of the non-linear dependence of strength on velocity increases the unknowns to $5N_s + 3$. Although there remains uncertainty in the selection of these viscosity parameters, typical values of α_s and

β_s have been given previously (Section 4.6). Applying these reduces the number of unknowns to $3N_s + 3$, i.e. the same as the number of primary unknowns in typical commercial codes.

Table 4-6: Summary of equations, parameters and source using IMPACT

Parameter	No.	Source
Shaft resistance	N_s	In situ tests[1]
Base resistance	1	In situ tests[1]
Shaft spring stiffness	N_s	G[1]
Base spring stiffness	1	G[1]
Shaft radiation dashpot	N_s	G,ρ_s
Base radiation dashpot	1	G,ρ_s
Viscosity parameters	$2N_s$	Empirical

1. Indicative only

The displacement generated by a hammer blow during dynamic pile testing is generally significantly less than the limit of 10% of the pile diameter commonly used to define static failure. Therefore full base capacity is rarely mobilised during a dynamic pile test. As a result, pile driving prediction methods often include a factor to account for this partial mobilisation which increases the number of unknowns by 1 for both sets of models. The signal matching results presented in Chapter 5 and Chapter 6 used the soil models described in Section 4.7 and employed IMPACT, and the parameters listed in Table 4-6. The parameters adopted for the specific sites, gauged from the ground investigation results are discussed within the relevant chapters.

4.9.3 Assessment of soil resistance to driving (SRD)

There are several methods available in the literature to estimate the soil resistance to driving or resistance during installation. While similar to the axial capacity of a single pile, SRD is affected by rate effects during a high strain dynamic pile installation and also by the existence of excess pore water pressures in fine grained soils which build up during driving. The long-term static pile capacity mobilised during a slow static load test is not equivalent to the SRD, due to the effects of equalisation, ageing and consolidation.

There are methods available to evaluate SRD from site investigation data such as CPTs. These are used primarily in forward driveability prediction studies, which were discussed in Section 4.4. However these methods can also be used as a first estimate of the SRD for input into the signal matching procedure and this section gives a brief review of two of these methods; the method suggested by Alm and Hamre (2002) for sands and clays and Dührkop *et al.* (2017) for chalk. Both methods include expressions to account

for length effects i.e. "h/R or h/R*" or "friction fatigue" (discussed in Chapter 2), and were calibrated using large diameter piles and utilising modern underwater hydraulic hammers. Both methods were calibrated using the traditional Smith soil resistance models (Section 4.6).

Large (>1.5m) diameter offshore piles are unlikely to plug during installation due to the inertia force of the soil plug. Rausche and Hussein (2000) showed that for an assumed plug length of 3m and at a 50g acceleration, the inertia of the plug would be 190kN and 4800kN for a 0.3m and 1.5m diameter pile installed in sand, respectively. It is therefore often assumed that large diameter offshore piles are installed in a "fully coring" manner. For open-ended piles, the total SRD is the sum of the pile shaft and base resistance such that:

$$SRD = \pi\left(D\int_0^{L_p}\tau_{fi,ext}\,dz + D_i\int_0^{H_p}\tau_{fi,int}\,dz\right) + q_{ba}A_{ann} \qquad 4\text{-}48$$

Where $\tau_{fi,ext}$ and $\tau_{fi,int}$ are the external and internal shaft resistances, q_{ba} is the annular base resistance and A_{ann} is the annular steel area. Shaft friction is known to be a major contribution to the overall SRD, however the extent to which large diameter offshore piles mobilise $\tau_{f,int}$ remains a point of debate. While Dutt *et al.* (1995) argue that internal shaft resistance does not contribute to the resistance during driving, little evidence is cited to support this assumption. To date it has not been possible to take reliable effective shaft stress measurements, such as those described in Chapter 7, on open-ended driven piles. Jardine *et al.* (2005a) considered, from the results of instrumented pile and pile plug resistance tests, that internal shaft resistance is small and concentrated near the bottom of the pile, effectively contributing to the overall base resistance. The Author's comparison of dynamic restrike tests and static tension tests conducted at the same time, described in Chapter 5, also suggest that external shaft resistance provides the main resistance during a hammer blow.

Alm and Hamre (2002)

The most widely cited methods to predict SRD for clay and sand in the literature are those suggested by Alm and Hamre (2002) The methods were developed from back analysis of 164 different piles at 16 offshore sites in the North Sea, for pile diameters between 1.8 and 2.7m and an average diameter to wall thickness ratio, D/t_w of 40. The piles were driven with modern hydraulic underwater hammers such as the Menck MHU and IHC Hydrohammer. The maximum pile penetration was 90m. The general equation is given as:

$$\tau_{fi} = \tau_{res+}(\tau_i - \tau_{res})e^{-kh} \quad 4\text{-}49$$

where τ_{fi} is the total (internal and external) shaft resistance during driving, τ_i and τ_{res} are the initial and residual shaft resistances and h is the distance from the pile tip to the individual soil layer. The shape factor, k describes the degradation of shaft resistance with pile penetration and increases with increasing corrected CPT cone resistance, q_t:

$$k = \frac{\sqrt{\frac{q_t}{\sigma'_{vo}}}}{80}$$

For clays:

$$\tau_{res} = \text{CPT } f_s \quad 4\text{-}50$$

$$\tau_i = \frac{q_t}{250}\left(1 - \frac{1}{400}\frac{q_t}{\sigma'_{vo}}\right) \quad 4\text{-}51$$

$$q_{ba} = 0.6q_c \quad 4\text{-}52$$

With sands, τ_i reflects the ICP sand method calculation for radial effective stresses (Jardine *et al.* (2005a) as described in Section 3.3.4) with an adjustment to account for excluding the h/R* term.

$$\tau_i = \frac{q_t}{76}\left(\frac{\sigma'_{vo}}{\sigma'_{vo}}\right)^{0.13} \tan\delta' \quad 4\text{-}53$$

$$\tau_{res} = 0.2\tau_i \quad 4\text{-}54$$

$$q_{ba} = 0.15\left(\frac{q_t}{\sigma'_{vo}}\right)^{0.2} \quad 4\text{-}55$$

Eq. 4-55 results in q_{ba} values which increase with density and range from 0.35 to 0.55 times q_t. Since the sand method is based on the ICP formulation, which assumes that shaft resistance acts on the external pile surface area only, the method recommends applying 50% of τ_{fi} calculated by Eq. 4-49 to the internal and external shaft areas. For standard drivability calculations, using traditional models which do not model the internal shaft resistance separately, the assumed ratio of internal to external shaft resistance has no practical effect since at individual nodes, both internal and external shaft resistance are lumped together.

Eq. 4-52 and 4-55 effectively account for the reduced base resistance mobilised during a hammer blow due to lower pile tip displacements induced than during a slow

static loading test to failure. Displacements during a hammer blow are generally a maximum of 2% of the diameter, considerably lower than the displacement used to define failure in a static test, of 10%D.

Dührkop *et al.* (2017)

Dührkop *et al.* (2017) presented a method to predict driveability in chalk based on back analysis of a database of offshore driving records. Different values of unit shaft resistance and end bearing were applied that depended on the intact dry density of the chalk as summarised in Table 4-7.

Friction fatigue was partly accounted for by assigning different values of τ_{fi} and q_{ba} at the bottom and top of the layer respectively, although this introduces inconsistency into the model when the pile tip penetrates a chalk layer without reaching the base of the layer. The ICP-05 and UWA-05/UWA-13 methods, along the Alm and Hamre (2002) described include the *relative* tip depth, h in their formulations which avoids this issue. Duhrkop *et al.* recommend increasing SRD by a factor of three over a distance of 0.5m to account for the rapid and significant set-up which was observed during operational pauses in driving of up 1.5 hours.

Table 4-7: Driving resistance recommendations after Dührkop *et al*. (2017)

	Chalk density			
	Low	**Medium**	**High**	**Very high**
Unit skin friction, τ_{fi} (kPa)[1]	9	Top: 10 Bottom: 25	Top: 40 Bottom: 80	80
Unit end bearing, q_{ba} (MPa)	18	Top: 20 Bottom: 50	Top: 80 Bottom: 160	160

1. Applied to the internal and external shaft areas

4.9.4 Signal matching of individual signals

Signal matching is generally carried out by comparing the time series of the measured upward travelling wave, F_{up} calculated using Eq. 4-15, with the artificial wave created using the input velocity or force signal from the hammer. The upward travelling wave is shown schematically in Figure 4-17. As a second check, the measured displacement over the blow, obtained from double integration of the acceleration, is also compared to the computed displacement. The measured permanent set or residual displacement developed after all oscillations have dissipated is an important variable to assess in signal matching, since it depends on the energy losses in the soil and thus the work done by the shaft and base resistances (Loukidis *et al.*, 2008).

In the first interval up to time, t_0, there are no reflections measured in the upward travelling wave, since the wave is travelling through a free length and no soil resistance acts on the pile (Figure 4-17). In the time between t_0 and $t_{0+2L/c}$ the upward wave is affected by the downward movement of the pile due to the mobilisation of shaft resistance and this portion of the wave is used primarily for carrying out the signal match. Layers of higher or lower shaft capacity can be observed where the slope of F_{up} changes and these can be related to relative depths below ground level. The parameters are therefore changed iteratively along the shaft to obtain a good match in this region.

The portion of the record close to $t_{0+2L/c}$, where reflections come from close to the base, is affected by both the shaft resistance close to the base and by reflections from the pile tip itself. A tension wave (free pile end) reflected from the base manifests as a reduction in F_{up}, while a compression wave (fixed pile end) reflection causes a peak in F_{up}. The base resistance is again changed iteratively in this region to obtain a good match, but it can be difficult in cases of low overall shaft and base capacity to completely separate reflections from the base and shaft.

Reflections in the interval after $t_{0+2L/c}$ are more difficult to interpret due to the combined influence on the reflections of shaft and base resistance from different depths. As discussed in Section 4.9.2, the unloading behaviour of the pile can influence the match in this region, as can the overall damping at the base and shaft. It can therefore be difficult to achieve a perfect match in the latter portion of the record. The means of qualitative assessment of individual signal matches is discussed in the next section.

4.9.5 Qualitative assessment of match quality

Signal match quality assessment is used to objectively assess the relative quality of a particular match. Match quality assessment is specific to each blow. Each blow has its own optimum match and reliability level. Matches on piles with high shaft resistance generally give a higher quality than those with high base resistance due to clearer reflections in the time up to 2L/c.

The general formula for calculating match quality, M_q given by Middendorp (2015) and used to assess the signal matches carried out by the Author is given by:

$$M_q(\%) = \sum_{i=istart}^{i=iend} \frac{|F_m(i) - F_c(i)|}{(i_{end} - i_{start})F_{max}} \text{ x } 100 \qquad 4\text{-}56$$

Where i_{start} = start index of the interval and i_{end} = end index of the interval, F_m is measured upward wave value, F_c is the calculated upward wave value and F_{max} is the

maximum value of measured force. M_q is assessed on the upward wave separately over 6 specified intervals, as shown in Table 4-8. The overall match quality is:

$$M_{q,overall} = \frac{M_{q1} + M_{q2} + 2M_{q3} + 2M_{q4} + 2M_{q5} + 2M_{q6}}{9} \quad 4\text{-}57$$

The match quality at each interval and the overall match quality is classified into six categories, with the best "excellent" match considered as < 1% and any match > 4% requiring "improvement". Weighting is applied to the later portions of the record and the whole record is included in the assessment. To obtain a good estimate of the final displacement, Randolph (1993) considers it necessary to match up to at least a time of 4L/c. This is necessary to properly estimate both the viscous component of the shaft resistance and the final displacement.

Table 4-8: Match quality intervals; after Middendorp (2015)

MQ	**Start (time)**	**End (time)**	**Represents**
MQ_1	t_0	t_0+2L/C	Start - toe
MQ_2	t_0+2L/C	Start + (2 x $n_{samples}$: F_{max} to t_0+2L/C)	Toe 1
MQ_3	t_0+2L/C	Start + (4 x $n_{samples}$: F_{max} to t_0+2L/C)	Toe 2
MQ_4	t_0+2L/C + (2 x $n_{samples:}$ F_{max} to t_0+2L/C)	t_0+2L/C + $n_{samples\_2L/C}$	After toe
MQ_5	t_0+2L/C + $n_{samples\_2L/C}$	Start + 2$n_{samples_2L/C}$	4L/c - 6L/c
MQ_6	t_0+2L/C + 2$n_{samples_2L/C}$	Last value	6L/c - end

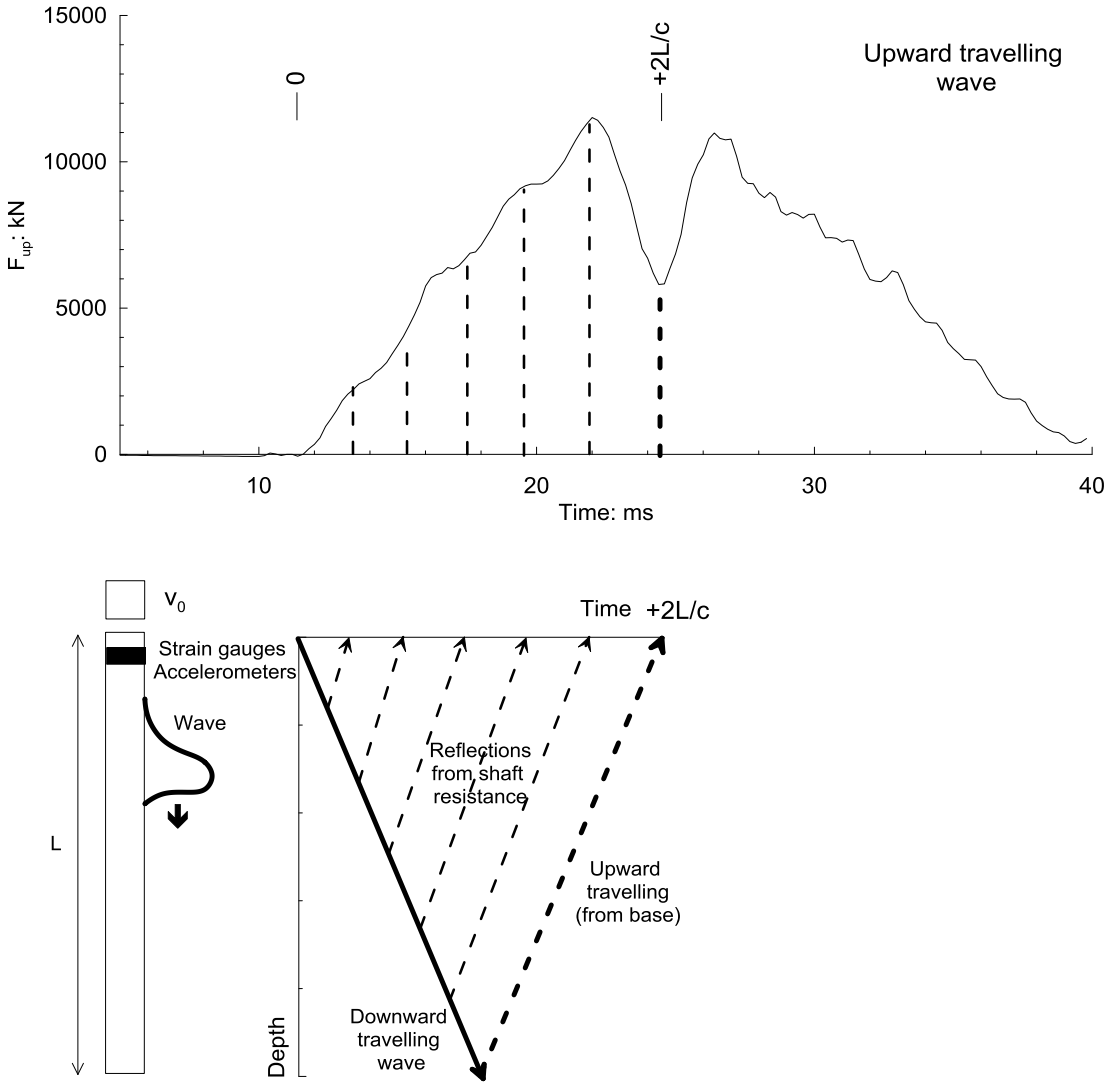


Figure 4-17: Upward travelling wave and schematic of stress waves in a pile; adapted from Randolph (2008) - data from Wikinger dataset

4.10 Accuracy of dynamic pile testing

The previous sections outlined a methodology for carrying out signal matching. It is important to ensure that good quality input data are used, utilising soil models whose parameters have links to physical meaningful soil parameters and ensuring that the soil resistance is related consistently to the ground profile and if possible to *in-situ* test results. A means of objectively comparing match quality was also outlined. Nonetheless, there remains uncertainty in the use of dynamic pile tests to assess axial capacity, as has been discussed by several authors (e.g. Danziger *et al.*, 1996, Chambers and Lehane, 2011). Svinkin (2004) emphasised that site-specific correlation between dynamic pile tests and high quality static load tests is important and depends on the time between tests and the time after installation (set-up trends), the piles' loading history and sequence of tests, the pile type, whether ultimate resistance is mobilised and the overall quality of the input data. The following sections address some uncertainties in dynamic pile testing and methods of reducing that uncertainty where applicable.

4.10.1 Dependency of the solution on the operator

It is well established that the signal matching or driveability analysis solution is non-unique and that multiple approximations with similar fits to the measured signals can be found. The non-uniqueness leads to potential bias in the results obtained by different operators. Fellenius (1988) describes a study where 19 participants each performed CAPWAP analyses of four blows, of varying complexity. This resulted in total capacity variations from the mean of between 5 and 14%. The variations in base and shaft resistances are not discussed in detail, although base resistance variations are reported as the primary reason for the deviations. To investigate the effect of different operators on the analysis of the Wikinger data set, the hard driving blow (WK70-1 BoR1) from the Wikinger pile discussed in Section 4.8.2 was analysed by three independent operators using the CAPWAP software program. CAPWAP was utilised since it was available to all three operators. Only the site investigation data, measured signal and pile dimensions were shared with the operators. Operator 1 was the Author while Operator 2 and 3 were experienced practitioners from Fugro France. The choice of soil resistance model and associated parameters was made by the individual analysts but was limited to the models available within CAPWAP (Table 4-3). As well as varying the standard Smith parameters, Operator 3 used the optional extension of shaft radiation damping in CAPWAP, to consider the far-field damping response in conditions of hard driving.

The resulting mobilised shaft resistance obtained from all three signal matches is shown in Figure 4-18 (a). The interpretations made by the three operators were qualitatively similar, e.g. a lower resistance band was interpreted between 18 and 22m depth, which was unexpected from the given site profile. The CAPWAP match qualities, MQ (Rausche *et al.*, 2000) obtained by the three operators varied between 1.7 and 1.9, indicative of a good quality match. The total shaft capacity (Q_s) estimates fell within ±4% of the mean. Significant differences in the split between base (Q_b) and shaft resistance (Q_s) were obtained, highlighting the particularly variable base solutions. The differences in base capacity predictions led to total capacities (Q_t) falling within approximately ±10% of the mean value. It is worth noting that very similar shaft and overall capacities were obtained by operators 1 and 2, who used the same soil resistance model.

As noted earlier, signal matching is inherently more difficult in situations where the overall resistance is low (easy driving conditions) due to lower shaft resistances and less clear reflections in the time up to 2L/c. To assess operator dependency for such conditions, analyses were carried out by two operators, for an EoD blow on one of the Wikinger piles where the total resistance was low. The mobilised shaft resistance profiles indicated on Figure 4-18 (b) show a different qualitative interpretation between the two operators. The operators could only obtain MQ values between 4 and 5, indicative of a lower quality match. Despite the variation in interpreted distribution of shaft friction, the variation in total shaft capacity was within ±4% of the mean value. The overall capacity was within ±2% of the mean value.

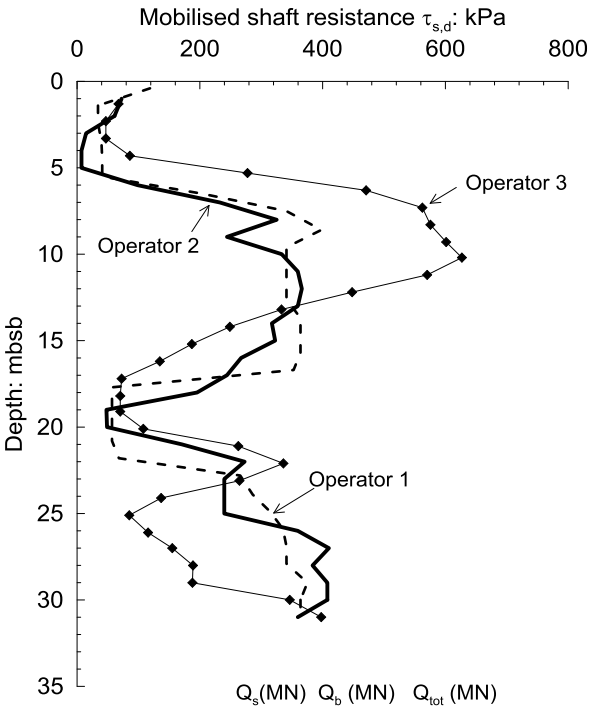
4.10.2 Comparison with static load tests

The compressive pile capacity obtained from a dynamic pile test is often compared with the results of a static load test (SLT), on the same, or similar piles to assess the reliability of the dynamic pile test result. It is now well accepted that the capacity of driven piles increases with time in sands and most clays (Skov and Denver, 1988, Jardine *et al.*, 2006, Karlsrud *et al.*, 2014). The ratios between dynamic pile tests (DPT) and SLT have no real meaning unless the two types of test are conducted at the same time, to account for changes in pile capacity with time. Good agreement is reported between capacities from DPT and SLT by e.g. Goble *et al.* (1975), Rausche *et al.* (1985) and Riker and Fellenius (1992), although these studies took no account of the time elapsed between pile installation and load testing. Paikowsky *et al.* (1994) report DPT and SLT on 204 piles installed in various materials which gave ratios varying from 0.4 (under prediction) to 1.7 (over prediction).

Lim and Lehane (2015b) outline the primary concerns of researchers when using capacity determined from a DPT as a reference point to determine pile capacity and assess set-up trends. The use of EoD as a reference to assess pile set-up can be misleading where large excess pore water pressures are generated during driving in soils that cannot achieve full dissipation at EoD, leading to high set-up factors before any other processes apply. The choice of a corresponding reference time, t_{ref} for EoD capacity can also differ between researchers ranging from immediately after the final hammer blow, (t_{ref} equal 0) to t_{ref} equal 1 day (Svinkin *et al.*, 1994, Bullock *et al.*, 2005a). For piles installed in materials such as chalk, which can display very rapid increases in capacity (Chapter 5) t_{ref} should be taken as close to zero as possible.

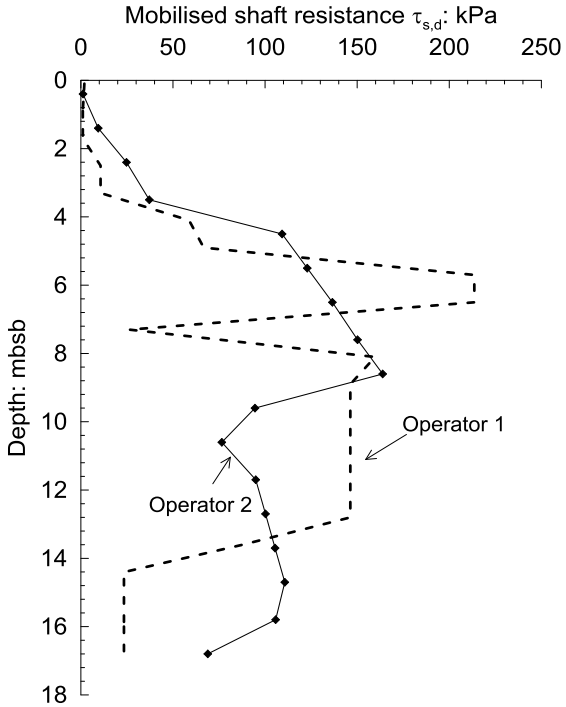
The under-mobilisation of ultimate resistance due to insufficient energy and force applied to the pile head can also lead to over-estimation or under-estimation of pile set-up, as discussed in Section 4.9.1. The accurate separation of end bearing from shaft resistance to facilitate comparison of change in shaft resistance with time can also be a concern.

The coincidence of dynamic and static capacities can be strongly affected by the piles' loading history; testing of previously failed piles can lead to different results to when fresh or "virgin" capacities are considered only. Lahrs and Kallias (2013) showed up to four-fold over-prediction of capacity by DPT when compared to SLT for piles installed in chalk in Henmoor, Germany (Chapter 3). However, the piles had been subjected to multiple restrike tests at varying ages prior to the static load test. The Wikinger tests results presented in Figure 5-48 show that during restrike tests, the capacity-time trends are disrupted when the pile is subjected to several blows at 100% of the energy. The importance of accounting for time effects and previous loading history and of using, wherever possible, "virgin" piles for static and dynamic testing is critical when comparing the results of static and dynamic pile tests. These considerations were addressed explicitly in the Wikinger offshore pile testing campaigns discussed in the next chapter.



	Q_s(MN)	Q_b (MN)	Q_{tot} (MN)
Operator 1	32.0	0.6	32.6
Operator 2	33.0	1.0	34.0
Operator 3	34.5	4.3	38.8

(a)



	Q_s (MN)	Q_b (MN)	Q_{tot} (MN)
Operator 1	6.7	0.3	7.0
Operator 2	6.2	0.5	6.7

(b)

Figure 4-18: Example of operator dependency for (a) a BoR (hard driving) blow (b) an EoD (easy driving) blow

4.11 Concluding remarks

This chapter has presented a review of dynamic methods used to assess axial pile capacity at a particular period in time. The use of dynamic testing has become more common over the last 20 years and is now adopted routinely by the offshore industry to verify capacity.

One-dimensional stress wave theory has been successfully applied to the problem of pile driving, with modern methods relying on mostly one of two numerical methods. However, the soil resistance models adopted by the industry have not advanced significantly since the 1960s, with more advanced models generally used only in research. The latter models have physically defined parameters which can largely be determined experimentally, so removing some of the uncertainty associated with the largely empirical constants used traditionally.

The results of signal matching exercises are a function of the resistance models adopted and can vary between operators. The quality of the result and the reliability of the analysis depends on the methodology adopted. The accuracy of the result can be quantified by comparison with static load tests on fresh piles, conducted at the same age as the dynamic load tests but with each involving a different "virgin" pile.

The relative ease of dynamic pile testing and the associated reduced testing times mean that many piles can be tested by dynamic means in the time taken to carry out a static load test. The tests also provide a means of verifying capacity in situations where static load tests are impracticable, either logistically or economically. However static load tests remain the preferred and most accurate way of determining pile capacity

CHAPTER 5

Static and dynamic pile tests at the Wikinger offshore windfarm

5.1 Introduction

While static load tests are the most accurate means of determining axial pile capacity, test execution in the offshore environment can be complicated by logistical concerns, varying met-ocean conditions and high water depths. Dynamic pile tests are routinely adopted as a substitute, due to the perceived prohibitively high static test costs. Onshore test sites with analogous ground conditions are often utilised as a cost effective alternative to carry out static testing, where testing conditions can be more easily controlled (e.g. Al-Shafei *et al.*, 1994, Lahrs and Kallias, 2013). As a result there are relatively few examples in the literature of full scale offshore static tests, with most tests on pile diameters less than 1.3m and in water depths less than 20m: e.g. Thomas *et al.* (2010), Matlock *et al.* (1998), Brzezinski and Baba (2012). Angemeer *et al.* (1973) report the largest scale and water depth axial static tension and compression tests to date, of which the Author is aware, on 508mm diameter open-ended steel tubes in water depths up to 122m installed in Calcareous sand in the Bass Strait, Australia.

This chapter describes the results of innovative offshore pile test experiments, conducted by Bilfinger Marine & Offshore Systems in connection with the Wikinger offshore windfarm, currently under construction by Iberdrola. The windfarm includes seventy wind turbine generators and one offshore substation, in water depths of between 34.8 and 41.7m. Each WTG is supported by a jacket structure and founded on four 2.7m diameter tubular steel piles, with the substation supported by six similar 3.67m diameter piles. The piles will carry their environmental loads by predominantly axial push-pull

loading plus associated lateral loads. The results have not been published to date and the analysis of the raw results of the pile test programme forms an integral part of this thesis.

This chapter begins with a description of the study objectives and methods adopted. A brief overview of the geology and stratigraphy at the windfarm is then given as well as a description of the test sites included in the study. An overview of the engineering behaviour of the deposits encountered is then provided. The pile test campaigns are then described followed by discussion and interpretation of the results obtained. The site investigation information and laboratory testing included are primarily taken from the two campaigns carried out by GEO and Gardline Geosciences Ltd. between 2012 and 2013 and the supplementary work carried out by Fugro (2013). The laboratory work carried out at Imperial College is mentioned where relevant.

5.2 Study objectives and methodology

5.2.1 Motivation for experimental investigation

Wikinger is located in the Baltic Sea, 34km north-east of the island of Rügen, in German waters, where the final design must be submitted to and approved by the local federal body; the Bundesamt für Seeschifffahrt und Hydrographie, or BSH. The BSH Standard (BSH, 2011) requires the pile design to conform to the EC7 framework (DIN, 2009) and the German national annexe (DIN, 2012). The latter requires that the capacities of predominantly axially loaded piles are proven by field measurements made after installation, due to concerns over the limited database of large pile tests to prove capacity in the materials encountered. Dynamic pile tests are required by the BSH on at least 10% of wind turbine locations and EC7 requires dynamic tests in fine grained soils under tensile loads and at least one static test in order to calibrate the dynamic capacity. The difficulties in achieving these requirements in offshore projects are well known and were discussed by Jardine *et al*. (2015).

It is well accepted that the axial capacity of piles in sands and clays increases with time after driving due to consolidation, equalisation and ageing (e.g. Skov and Denver, 1988, Jardine *et al.*, 2006, Karlsrud *et al.*, 2014, Rimoy *et al.*, 2015). Figure 5-1 shows the capacity-time trends from static tension tests as interpreted by Rimoy *et al.* (2015) for previously untested steel piles at four sand sites; Blessington, Ireland, Larvik, Norway and Dunkirk, France. Following the approach of Jardine *et al.* (2006), the first-time measured static tension capacities, Q_m, are normalised by the ICP-05 (see Chapter 3 and

Jardine *et al.*, 2005a) estimated pile capacities. Figure 5-1 indicates that the intact ageing characteristic (IAC), or capacity growth trend is tri-linear. The static tension capacity, one day after installation, obtained from dynamic tests at Larvik and Dunkirk and from a static test at Blessington, falls below the calculated ICP-05 equalised capacity. The equalised capacity is reached at approximately 10 days after installation, after which the capacity increases further with time, reaching over double the ICP-05 capacity post 100 days and tending to stabilise with time after approximately 200 days.

Dynamic pile tests are generally carried out within the first day after installation, while axial capacity design methods are intended to reflect capacity between 10 days after installation in sand, as illustrated on Figure 5-1, and after full pore pressure equalisation in clays (Jardine *et al.*, 2005a). The implicit assumption of the German requirements is that working capacity can be predicted more accurately by short-term dynamic tests than by forward prediction using calibrated axial capacity models based on high quality site investigation and static pile test databases.

The Eurocode EC7 requirement for static tests to calibrate the offshore dynamic tests can be met by access to verified reliable tests conducted on piles of similar geometry, installed using similar procedures in comparable ground conditions. The piles at Wikinger are founded on a range of profiles comprising different proportions of Weichsellian glacial till and low-medium density Maastrichtian chalk. The current state-of-the-art practice for assessing axial capacity in stiff clay tills is to employ the standard API/ISO "α-method" approach, the ICP-05 (Jardine *et al.*, 2005a) effective stress methodology (supported by the necessary site investigation and laboratory test data) or to use a CPT-based method that includes the ICP-05 dependency on relative pile tip penetration, see for example Lehane *et al.* (2017). These procedures are expected to give tolerably reliable predictions in stiff glacial clays, although this has yet to be verified by any offshore static pile testing.

Current axial capacity design procedures in low-medium density chalk are known to be highly uncertain as the database of tests is limited and consists of mixed quality experiments (Chapter 3). Iberdrola first considered the onshore tests presented by Lahrs and Kallias (2013) at a test site in Germany. However as argued in Section 3.5.1, the experimental design and execution of these tests led to ambiguous results which could not be applied reliably without leading to excessively long pile lengths.

The strict regulatory requirements and uncertainty over installed capacity and cyclic loading effects in chalk led Iberdrola to carry out two way axial cycling on previously failed piles (Section 3.5.1) at the Kent test site and finally to execute the offshore dynamic tests and axial static and cyclic pile load tests at Wikinger (Barbosa *et al.*, 2015, Barbosa *et al.*, 2017) described here. The testing campaign formed the basis of a Joint Industry Research Project led by Ibderdrola and supported by Innovate UK, with a research team from IC who analysed the results with technical input from the Geotechnical Consulting Group, as was described in Section 1.2.

5.2.2 Testing campaigns at Wikinger

Two field testing campaigns were carried out at Wikinger; one at the pre-construction stage, prior to finalisation of the pile design and one during production piling for the windfarm. The two phase pre-construction (PC) testing campaign consisted of:

- **Phase 1:** Installation of nine (dynamic monitoring of six) 1.37m diameter piles at three WTG locations that typified the variable ground conditions expected across the site: WK38, WK43 and WK70;
- **Phase 2:** One tensile static load test and one dynamic test on separate piles, at each test site, following equalisation periods of between 11 and 15 weeks.

A further set of dynamic experiments became available from Wikinger subsequently, from the production piling (PP) stage, during which a total of 286 large diameter offshore piles were installed. The production piling test campaign was required to satisfy the BSH requirement of dynamic tests on 10% of WTG locations.

5.2.3 Experimental aims

The experiments at Wikinger were planned to investigate:

1. Dynamic pile resistances during driving and during any pauses in driving using instrumentation fitted near the pile head;
2. The end of driving short-term capacities developed in the glacial till and chalk;
3. The long-term capacity available in the glacial till and chalk; and
4. Trends in capacity change with time for virgin piles, under static and dynamic loading, up to 3.5 months after installation.

The pre-construction test piles were scaled down from the production pile size in order to reduce the testing costs, with slenderness ratios (L_p/D) which varied from 12 to

22 and a diameter to wall thickness ratio (D/t_w) of 34. The production piling tests were carried out on working piles, whose L_p/D ranged from 7 to 16 and D/t_w from 49 to 74.

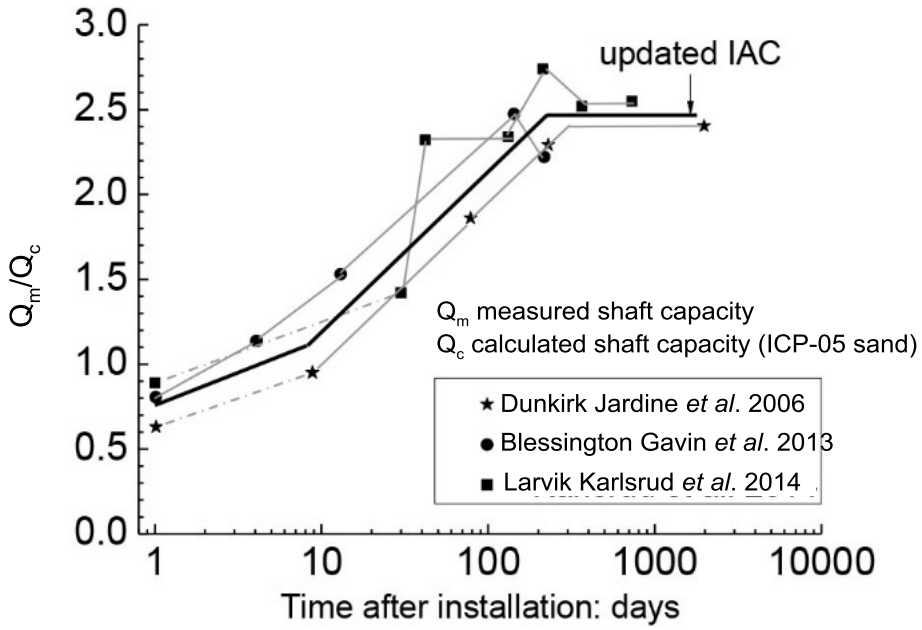


Figure 5-1: Static tension capacity-time trends from first time tests on steel pipe piles driven in sand at 3 sand sites, normalised by ICP-05 tension capacities (adapted from Rimoy *et al.*, 2015)

5.3 Geology and stratigraphy at the windfarm

Wikinger lies at the south-eastern margin of the Arkona basin, formed as part of the Baltic Basin during the Pleistocene era. Upper Cretaceous chalk and chalky limestone underlie the Quaternary sediments found in the area (Obst *et al.*, 2017) with geophysical studies indicating that the Quaternary-Cretaceous boundary reaches its greatest depth (90mbsl) close to the island of Rügen (Lemke, 1998). The thickness of the cretaceous section exceeds 400m along the south coast of the Baltic Sea (Šliaupa and Hoth, 2011).

Ground conditions across the Wikinger site generally consist of upper Pleistocene glacial till deposits and low-medium density structureless and structured chalk from the Upper or Late Cretaceous of Maastrichtian age. Narrow sub-glacial channels or tunnel valleys are incised into the chalk in some locations. The channels appear to strike primarily NE-SW at Wikinger based on geophysical surveys, which is typical within the Arkona basin (Obst *et al.*, 2017). Across the windfarm they are up to 63m deep, 100 to 1200m wide and are more pronounced at the southern extent. The deposits which bury the channels are heterogeneous and termed “fluvioglacial” (CIJV, 2013). In the NE corner of the windfarm a limestone of different properties was encountered, thought to be similar

to the cherty limestone identified by Obst *et al.* (2017) at the adjacent Arkona OWF, and to belong to a NW-SE trending area of Upper cretaceous or Danian sediments.

Following the last ice age, the area underwent isostatic uplift caused by glacial rebound, which was followed by deposition of post-glacial Holocene (recent) soft marine sediments on top of the glacial till. These deposits have a mean thickness of 1.4m and are not encountered at all locations. According to the German Earthquake Zonation map (DIN 4149:2005) the project area has only very minor seismic activity.

5.4 Description of test sites

Figure 5-2 shows an overview of all WTGs, the offshore substation (OSS) and the test sites included in this study. The minimum distance between the WTGs is ≈700m. Details of the eight test sites considered are given in Table 5-1, including total length of pile penetration (L_p) as well as pile penetration through Holocene deposits ($L_{p,hc}$), glacial till deposits ($L_{p,gt}$), fluvioglacial deposits ($L_{p,fgt}$), chalk ($L_{p,chlk}$) and the penetration of the CPT at the relevant location ($L_{p,cpt}$)

Figure 5-2 also includes contours of the depth from the seabed to the top of the glacial till. While some of the test sites indicate cover of Holocene mud up to 5m e.g. WK08 and WK11, the till can be seen to lie generally less than 2mbsb, outcropping at surface primarily in the southern half of the site. The glacial incised channels are 9.2 to 9.5m thick at two of the test sites (WK08 and WK42). Figure 5-3 shows a similar plot of chalk depths below the seabed. The minimum depth to the glacial till-chalk boundary lies at ≈6.5m and in localised areas is up to 30m; at the test sites the minimum depth is 6.6m at WK70.

The test sites were chosen by the designers (COWI/IMS) to characterise both the representative and most adverse ground conditions across the site, as required by DIN (2009). Locations where the depth from the seabed to the top of chalk layer was greater than 10m were considered representative (WK08, WK11, WK13, WK38 and WK42). Locations where the depth to the top of chalk is less than 10m are considered the most adverse (WK43, WK70 and OSS). The test sites were chosen based on the presence of an "advanced borehole" where significant laboratory testing had been carried out. As shown in Table 5-1, only some of the test sites included a full cone penetration test profile to the pile penetration depth, which presents some challenges in interpretation, further discussed in Section 5.6. At the test sites, WK13 and WK38 can be considered as glacial till

dominated, WK08 and WK42 are dominated by a combination of glacial and fluvioglacial deposits and OSS, WK43 and WK70 are dominated by low-medium density chalk. WK11 has almost equal proportions of till and chalk within the depth of influence of the test piles.

Table 5-1: Details of the test sites and pile penetrations at Wikinger included in the study

Test site	Testing stage	L_p (m)	$L_{p,hol}$ (m)	$L_{p,gt}$ (m)	$L_{p,fgt}$ (m)	$L_{p,chlk}$ (m)	$L_{p,cpt}$ (m)
OSS	Production	46.3	2.0	8.3	-	36.0	35.7
WK08	Production	27.9	4.1	9.5	9.5	4.8	49.3
WK11	Production	31.1	4.5	12.0	-	14.6	33.3
WK13	Production	25.8	3.0	15.9	-	6.9	24.2
WK38	Pre-construction	16.6	1.9	11.7	-	3.0	11.2
WK42	Production	19.9	0.1	9.9	9.2	0.7	50.4
WK43	Pre-construction	30.7	-	10.3	-	20.4	11.0
WK70	Pre-construction	31.0	-	6.6	-	24.2	7.4

The following sections report on the ground conditions and key soil parameters, placing special attention on the data required to test the application of the ICP-05 clay method (Jardine *et al.*, 2005a) to the glacial till layers and to help develop more reliable design procedures in the chalk strata.

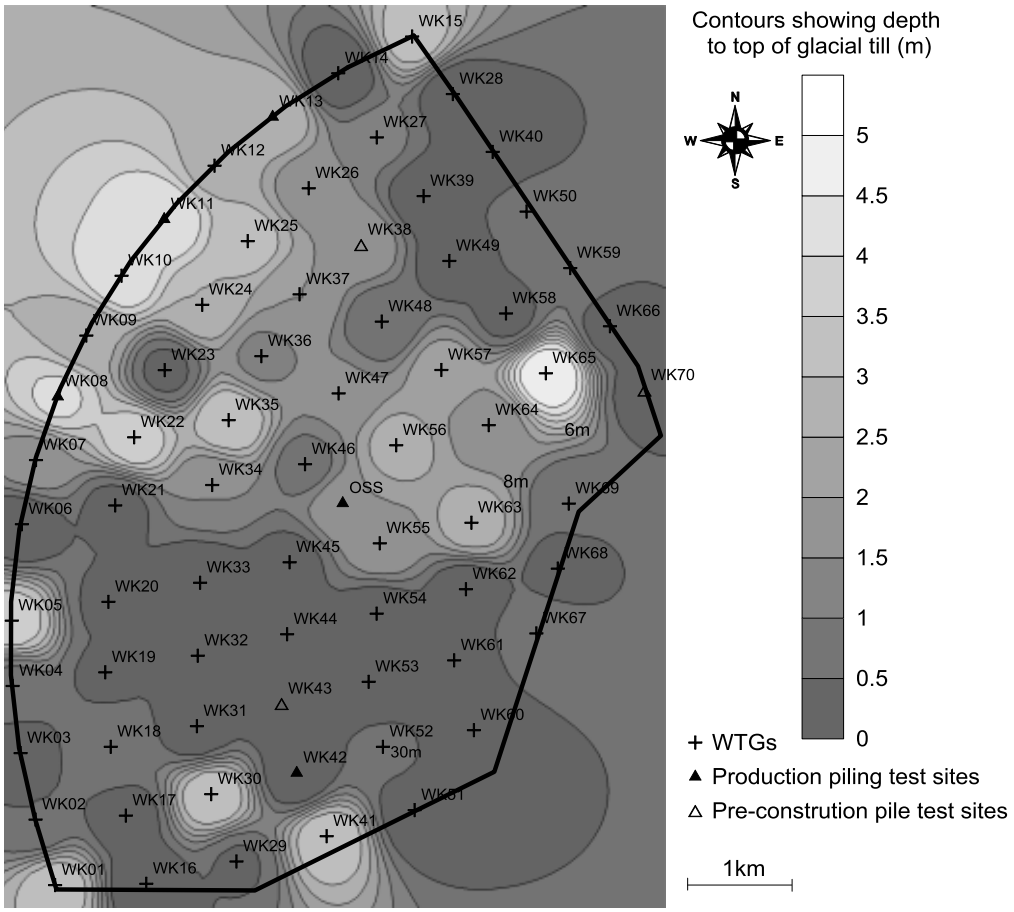


Figure 5-2: Depth from seabed to top of glacial till at the Wikinger OWF (data from CIJV, 2013)

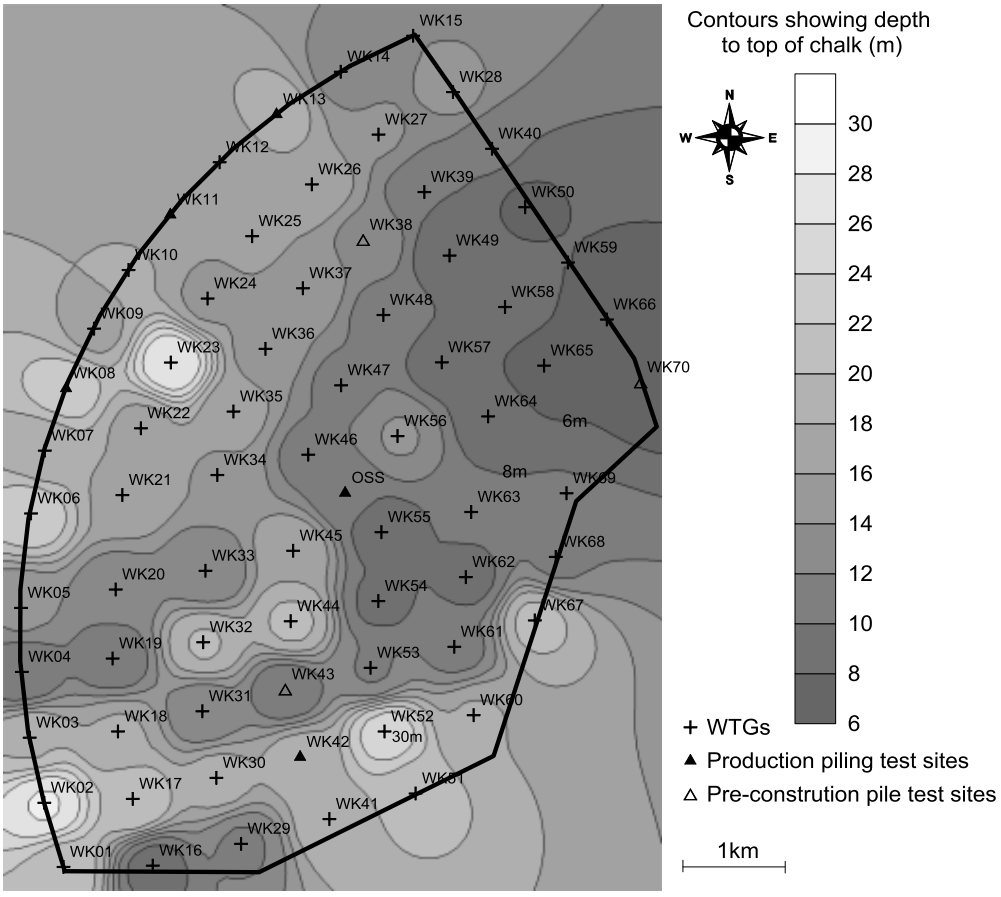


Figure 5-3: Depth from seabed to top of chalk at the Wikinger OWF (data from CIJV, 2013)

5.5 Glacial till deposits encountered at the test sites

5.5.1 Description & occurrence

Several authors have shown that the complex interaction between different glacial and tectonic process which lead to the formation of glacial deposits determines the nature of the sediments (e.g. Boulton and Deynoux, 1981). Obst *et al.* (2017) detail a litho-stratigraphical classification of glacial till units based on seismic profiles and boreholes at the adjacent Arkona OWF. The primary unit was identified as reworked till or flow till consisting primarily of silt, but also with high clay, sand and gravel content. Deposits encountered in the boreholes at Wikinger are described as medium to high strength, firm to very stiff, grey to dark greyish brown, sandy gravelly clay. Kessler *et al.* (2012) note that some tills include lenses of sand and gravel between units or embedded within the till itself, which can vary significantly in geometry and composition. Discrete layers of medium dense sand, up to 1.5m thick were encountered within the clay till at the test sites. The fluvioglacial deposits encountered classified as stiff, sandy, silty, gravelly clay with cobbles.

5.5.2 In-situ testing

A typical PCPT profile from WK42, which penetrated both the glacial and fluvio-glacial deposits, is plotted on Figure 5-4. Corrected cone resistance, q_t in the glacial till lies between 5 and 15MPa with discrete peaks up to 50MPa associated with medium dense sand layers. Sleeve friction, f_s lies between 100 and 300kPa. Penetration pore pressures measured at the u_2 position show a general trend of negative values between -100 and -250kPa, with discrete peaks seen in the positive measurements up to 1MPa. In the fluvioglacial till, q_t and f_s are consistently higher than in the glacial till at approximately 10MPa and 400-600kPa respectively. Penetration u_2 values are positive and reach up to 1MPa.

Secant shear stiffness interpreted from unloading reloading loops during High Pressure Dilatometer (HPD) tests in the glacial till at WK11 are shown in Figure 5-5, conducted and interpreted by Cambridge-Insitu (2013). The secant shear moduli have been determined using the method given by Whittle (1999) for non-linear behaviour, since soil behaviour is linear elastic only at very small strains. A power law is fitted to the reloading part of the cycle and the change in G_1 with shear strain over a range of strain levels is determined from a power function.

The method is thought to provide reliable estimates of secant shear modulus (G_{hh}) at values of shear strain between 0.01 and 1%. Also shown on Figure 5-5 is the maximum shear modulus, G_{max}, for very small strains in the G_{vh} direction, estimated using the correlation with q_t in clays given by Mayne and Rix (1993). Although the latter was not developed for glacial tills, and G_{hh} and G_{vh} need not have the same values in anisotropic soils, the resulting values are plausible extensions of the power law curves interpreted by Cambridge-Insitu (2013).

5.5.3 Index testing

Measured soil index properties are summarised in Table 5-2 for the test sites. The Atterberg limit tests indicate a low plasticity, inorganic clay or sandy clay with a limited range of plasticity. Figure 5-6 shows the range of particle size distributions from grading and hydrometer analyses. The glacial till comprises primarily silt and sand particles and classifies between a silty/clayey sand and a sandy silt/clay, with a clay fraction generally less than 15% and a gravel fraction less than 20%. The grading curves for the fluvioglacial till range from similar values to the glacial till through to soils of silt and clay that classify as a slightly sandy, silty, clay with fine gravel. The medium dense sandy layer within the glacial till, where sampled, showed sand fractions of up to 97%.

Table 5-2: Index properties from the 8 test sites in glacial till and fluvioglacial till

	Glacial till			Fluvioglacial till		
Parameter	**n**	**Mean**	**StDev**	**n**	**Mean**	**StDev**
Water content, w_c (%)	173	12.8	3.8	6	13.4	2.1
Passing 425um sieve (%)	36	83.8	6.3	2	82.0	1.4
Liquid limit, w_l (%)	58	21.5	4.5	5	20.8	3.6
Plastic limit, w_{pl} (%)	58	12.7	1.7	5	12.6	1.3
Plasticity index, I_p (%)	58	8.8	3.4	5	8.1	2.0
Bulk density, γ_{bulk} (Mg/m^3)	30	2.2	0.2	3	2.2	0.1
Dry density, γ_d (Mg/m^3)	30	1.9	0.2	-	-	-
Specific gravity, G_s	46	2.69	0.01	4	2.69	0.01

5.5.4 Undrained shear strength and critical state parameters

Undrained shear strength profiles are critical to applying the API/ISO "α-methods" in clays, described in Chapter 3, however measurements of s_u depend markedly on the technique by which they are determined. Unconsolidated undrained triaxial (UU) tests and anistropically consolidated undrained (CAU) triaxial tests employed at Wikinger can be used to estimate s_u, along with approximations made from cone resistance.

Estimates of s_u from cone resistance are made using an empirical cone factor, N_{kt} by the following equation:

$$s_u = \frac{q_t - \sigma_{vo}}{N_{kt}} \quad 5\text{-}1$$

Profiles of s_u from cone resistance in the glacial till are shown on Figure 5-7 at three of the test sites (WK08, WK38 and OSS) along with the results of UU and CAU tests. The effective stress paths and stress-strain plots from the latter are shown on Figure 5-8. The s_u profile ranges between 200 and 1000kPa with good agreement between laboratory CAU tests and Eq. 5-1 values when a site specific N_{kt} factor of 22.5 is adopted (see also Appendix A-4). Note that the CAU strengths are taken as those applying after 20% axial strain. The results are typical of tests on samples across the site which failed in a ductile manner, mobilising high s_u as result of significant dilation at failure, characteristic of over-consolidated non-brittle soils. The undrained tests on glacial till appear to reach critical state with M_{tc} = 1.44 (φ'_{cv}=35.5°) with their end points falling on a unique line in specific volume - mean effective stress space, with slope λ = 0.07 (C_c = 0.161) and Γ at p′=1kPa of 1.68. The latter value of C_c is consistent with values reported by Gens (1982) on samples of Cromer till, by Jardine (1985) for Magnus till and by Ushev (2018) for Cowden till. The oedometer tests, shown on Figure 5-9, were not taken to sufficient pressures to define a NCL line in v-lnp′ space.

5.5.5 Stress state and yield stress ratio

The ICP-05 clay design procedure relies critically on establishing the profiles of yield stress ratio in any clay layers. Deposits formed in the sub-glacial system were consolidated under the overlying ice. Subsequent wasting of ice and post depositional changes such as groundwater lowering and freeze-thaw activity acted to decrease the effective stresses (Trenter, 1999). YSR profiles were assessed using oedometer tests in the glacial and fluvioglacial till on intact samples, which showed acceptably clear yield points when specific volume was plotted versus mean effective stress on logarithmic axes (Figure 5-9). YSR is defined as:

$$YSR = \frac{\sigma'_{vy}}{\sigma'_{v0}} \quad 5\text{-}2$$

where σ'_{vo} is the effective overburden pressure and σ'_{vy} is the effective vertical yield stress which can sometimes be obtained from oedometer tests, but may be difficult to resolve in tests on stiff glacial tills (Lehane, 1992). An estimate of YSR can also be obtained from CAU triaxial tests sheared at the *in-situ* vertical effective stress. Estimates can also be

made from the ratio s_u/σ'_{vo} which is often related to YSR using relationships such as that given by Jardine *et al.* (2005a):

$$\frac{s_u}{\sigma'_{v0}} = \left(\frac{s_u}{\sigma'_{v0}}\right)_{nc} YSR^{0.85} \quad 5\text{-}3$$

where $(s_u/\sigma'_{vo})_{nc}$ is the value from CAU compression tests on K_0 consolidated samples, which lies between 0.25 and 0.35 for a range of materials. The above relationship is only valid for low plasticity clays that fail in a ductile manner such as those that were shown on Figure 5-8.

The results from oedometer and CAU tests on glacial till and fluvioglacial till were used to develop the trend with depth shown on Figure 5-10. Both deposits appear overconsolidated in the upper portion and YSR generally decreases with depth. No results are available at the top of the profile, with the trend suggesting a highly over-consolidated upper section and a limit of YSR = 60 was imposed above 3.8m. The trend shown can be used to determine a nominal profile of the coefficient of earth pressure at rest, K_0 by the relationship given by Mayne and Kulhawy (1982):

$$K_0 = (1 - \sin\varphi')YSR^{\sin\varphi'} \quad 5\text{-}4$$

Using a φ' of 35.5°, Eq. 5-4 results in a maximum value of K_0 of 4.5 which reduces to a value of 1.1 at 20m depth. However, the complex geological processes present at glacial sites may well lead to quite different, and likely lower, K_0 profiles; see for example Jardine (1985).

5.5.6 Interface shear behaviour

Site-specific drained interface shear angles are also critical to any ICP-05 analyses undertaken in clay layers. The large strain interface shear behaviour was investigated by the Author through ring shear interface tests in the Bishop ring shear apparatus at Imperial College (Bishop *et al.*, 1971). The apparatus is shown in Figure 5-11. Torsional shear is applied to specimens by constantly rotating the interface in the same direction while the sample remains fixed, to reach displacements representative of ultimate conditions. A loading yoke and torque arm is connected to the upper confining ring in the apparatus and the rotational load is measured by two connected load cells. Vertical load is applied to the sample via a dead weight system. The friction between the confining rings or "ring load" is measured using a separate proving ring below a rigid crosshead beam. Vertical displacement is measured using two Linear Variable Differential Transformers (LVDT).

Rotational displacement is measured using a scale on an annular plate fixed below the loading yoke.

The Author's tests are summarised on Figure 5-12. Three tests were carried out on specimens subsampled from cores held at Gardline Geosciences Ltd. The glacial till was first sieved to remove particles greater than 425μm, since coarse particles can affect the results due to scale effects in the apparatus. The remaining material was then remoulded and placed in two layers, as close to natural moisture content as practicable.

The annular interfaces used in the test were formed of mild steel, shot-blasted to a similar roughness to that of a typical steel tubular pile ($R_a \approx 10\mu m$). The method of measuring surface roughness of the steel interfaces is discussed further in Chapter 6. The test procedure followed is that given by Jardine *et al.* (2005a) and consisted of the following stages:

(a) After sample placing and set up, a total normal stress was applied to the sample, representative of the radial effective stress in the ground, σ'_{ri}, acting after pile installation at the relevant depth and subsequent consolidation. In this case σ'_{ri} varied between 100 and 140kPa;
(b) A total of 25 fast shearing pulses were applied to the sample to simulate driven pile installation, at a constant rate of 500mm/min for 200mm which resulted in a total of 5m displacement. Each pulse was followed by a pause period of 10 minutes;
(c) Following the fast shearing stage, a gap of 0.1mm was opened between the interface and confining rings by inducing a tensile ring load to minimise friction during slow shearing;
(d) A second consolidation stage was then applied to the sample with a vertical stress approximately equivalent to the induced tensile load plus the equalised effective radial stress acting on the pile after all pore pressures have dissipated, σ'_{rc};
(e) The sample was then subjected to drained shearing at a constant rate of 7±0.001μm/min. Shearing was continued until ultimate conditions were reached (>20mm displacement) and the interface friction angle δ'_{ult} could be determined reliably.

The results shown in Figure 5-12 are broadly consistent with each other, reaching δ'_{ult} angles of between 26.5 and 28°, well below the φ'_{cv} value quoted earlier. In all three cases, δ'_{peak} was reached at a displacement less than 2mm and δ'_{ult} was reached at

displacement of less than 10mm. The values of δ'_{ult} represent reductions of less than 0.5° on the δ'_{peak} values. The shearing did not appear to be strongly affected by the stress level range (200 to 300kPa). While Lehane and Jardine (1994b) report lower ultimate angles (22-24°) for a glacial clay at Cowden, where the fines content was significantly higher (30% clay and 50% silt), Jardine (1985) reported higher values for Magnus till and Iverson *et al.* (1998) demonstrated the tendency for ultimate friction angles in glacial till to reduce with increasing clay content. When examined upon completion of the test, all three samples had adhered to the interface. There was no evidence of polishing or formation of a shear surface at the interface.

5.5.7 Sensitivity

Certain clay soils have a higher strength in their undisturbed (intact) state than they do in the reconstituted state, where the latter is free of any natural structure. The ICP-05 procedure takes account of sensitivity when assessing axial capacity in clays and input parameters have to be assessed on a case-by-case basis when applying the methodology. "Sensitive" soils show ratios greater than unity between their intact s_u values and those from remoulded samples tested at the same void ratio or water content. Sensitivity can also be defined in terms of one dimensional compression, where $S_t = \sigma'_{vy}/ \sigma'_{vy}*$, σ'_{vy} is the pre-consolidation pressure of the natural material and $\sigma'_{vy}*$ is the vertical effective yield stress of the reconstituted material at the same specific volume as σ'_{vy} (Chow, 1997, Cotecchia and Chandler, 1997).

Sedimentary clays deposited in a marine environment and leached after deposition tend to have high sensitivity, which in extreme cases can exceed 500 (Lambe and Whitman, 2008). Most glacial tills have low sensitivity due to the remoulding which takes place contemporaneously with deposition (Clarke, 2017). Low sensitivity for Cowden till was indicated by oedometer tests reported by Lehane (1992) and Ushev (2018) and from the results of drained triaxial tests on undisturbed and remoulded/reconstituted samples reported by Gens and Hight (1979) and Marsland and Powell (1985). A similar conclusion was reached by Long and Menkiti (2007) for the Dublin boulder clay. No triaxial or oedometer tests are available on remoulded samples to assess the soil sensitivity, and it is assumed to be relatively un-cemented and insensitive with $S_t = 1$.

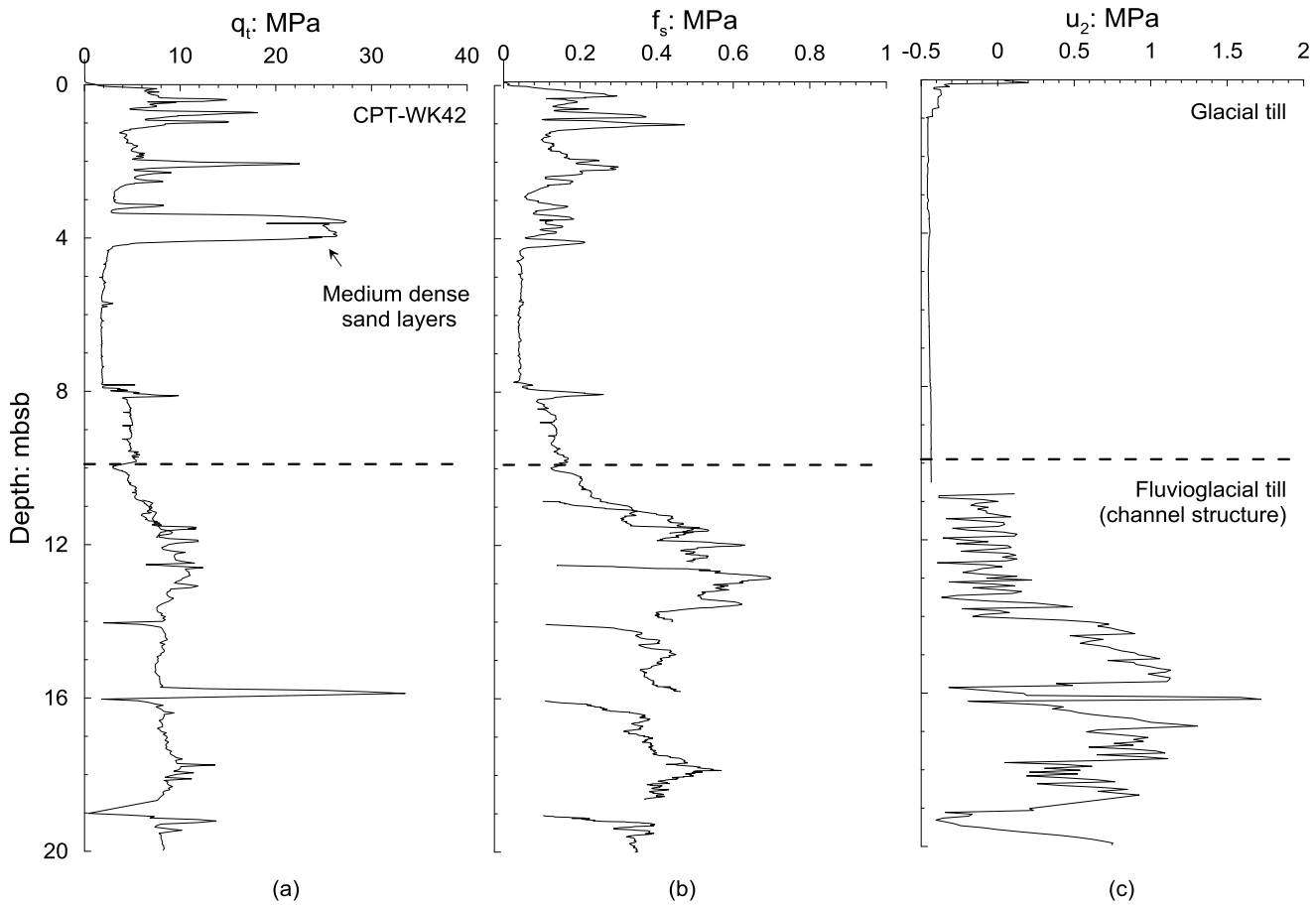


Figure 5-4: Envelopes of PCPT results in fluvioglacial and glacial till

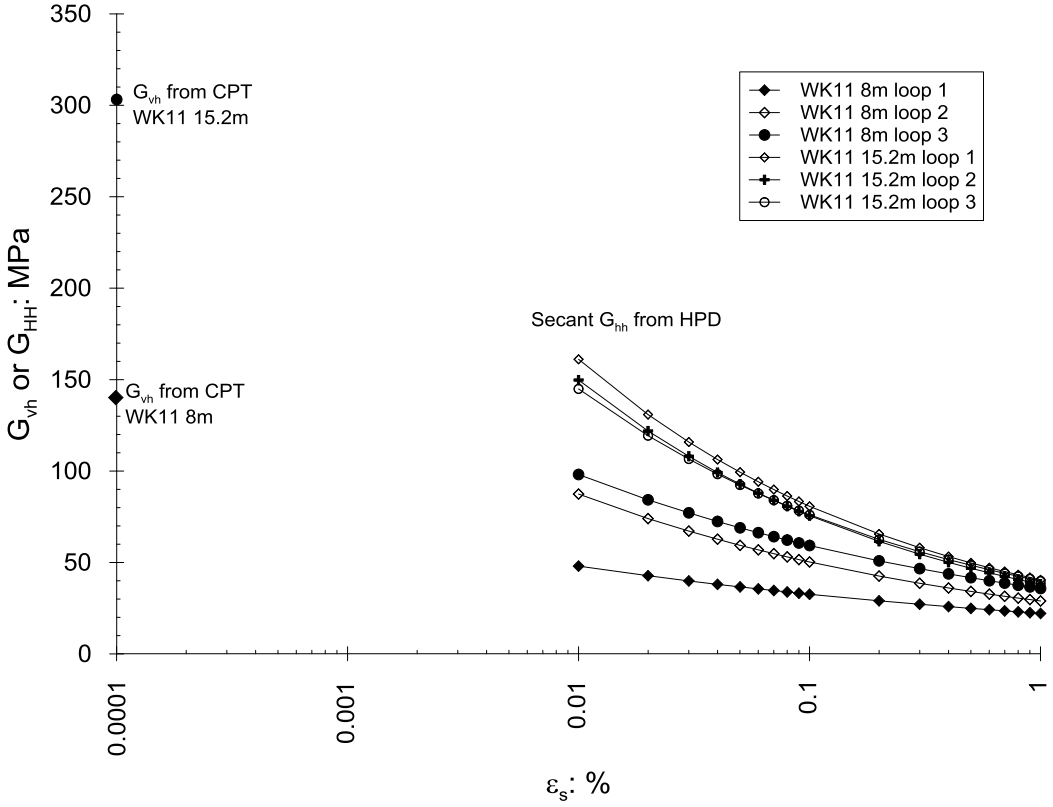


Figure 5-5: Secant shear stiffness from pressuremeter tests as interpreted by Cambridge-Insitu (2013) in glacial till, also showing G_{vh} from PCPT correlation at the same depths

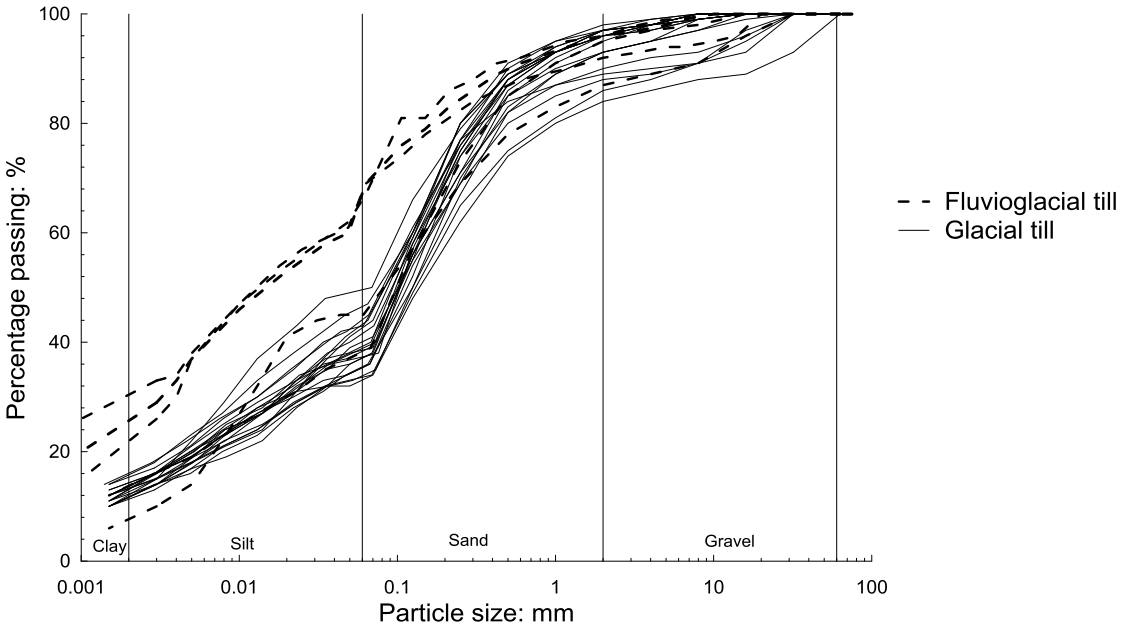


Figure 5-6: Grading curves in till from hydrometer tests carried out at the 8 test sites

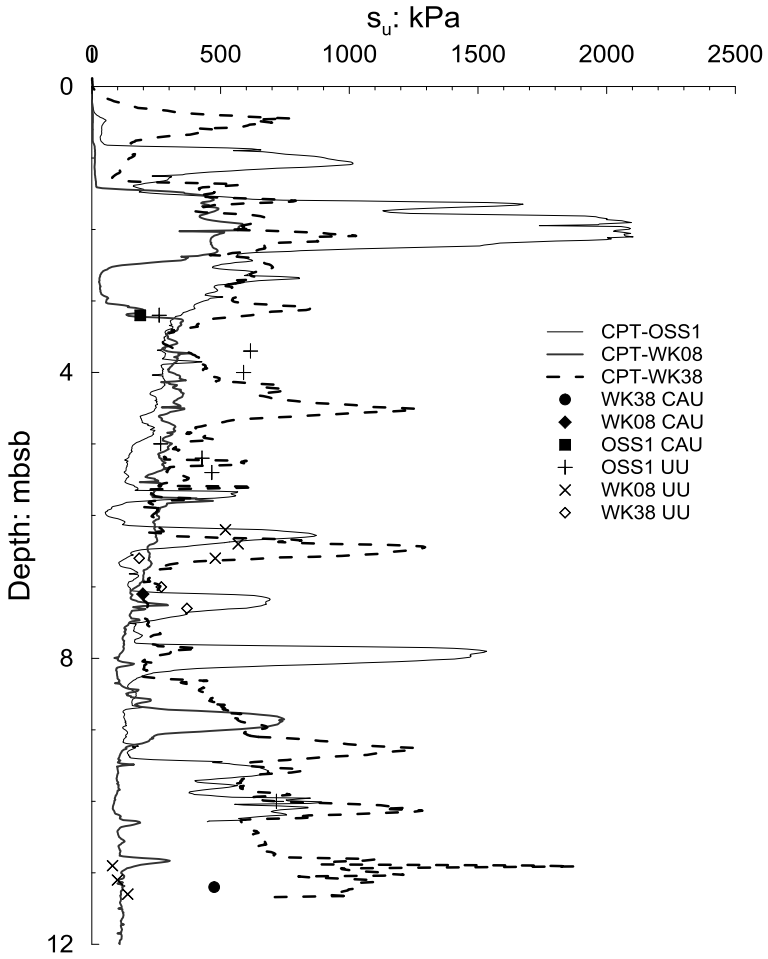


Figure 5-7: Undrained shear strength profiles in glacial till at three test sites based on PCPT correlation (Nkt = 22.5), CAU tests and UU tests

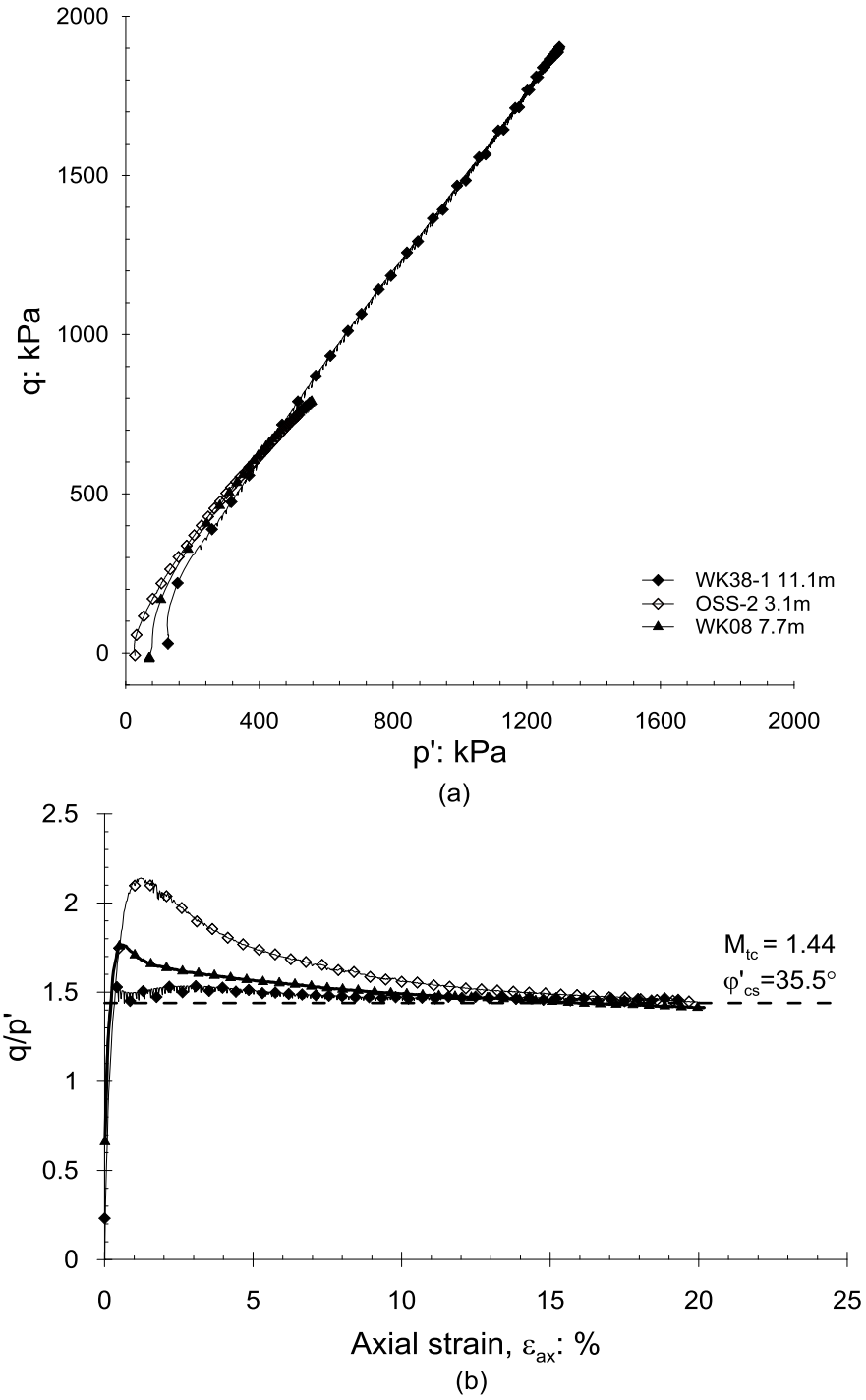


Figure 5-8: CAU triaxial tests on samples of glacial till from the test sites (a) effective stress paths (b) q/p' versus axial strain

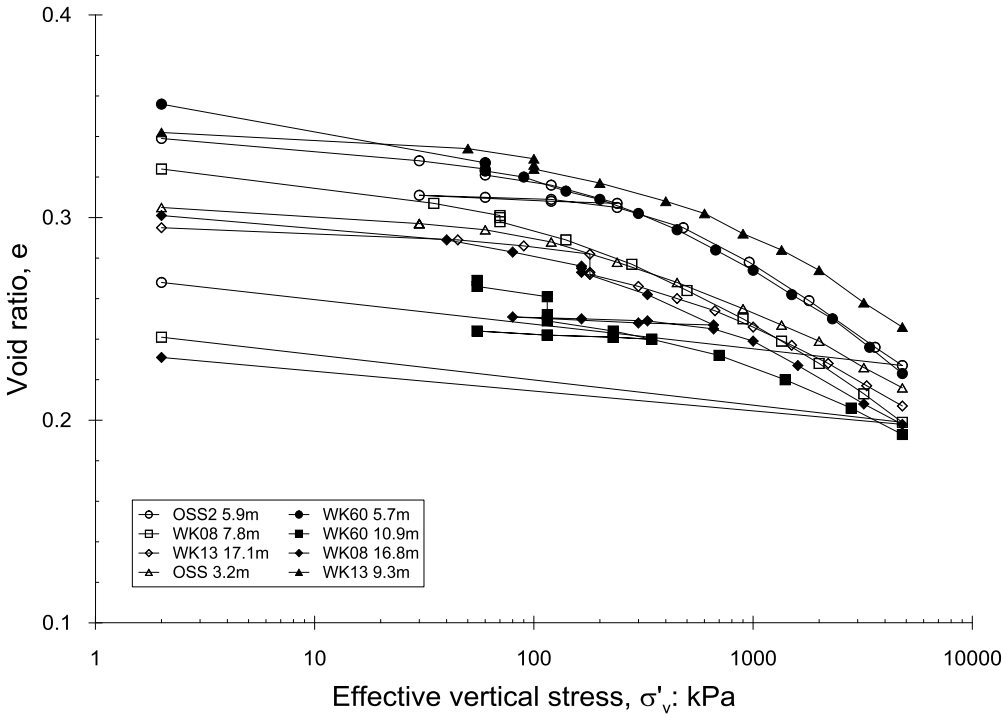


Figure 5-9: Oedometer tests on intact samples of glacial till

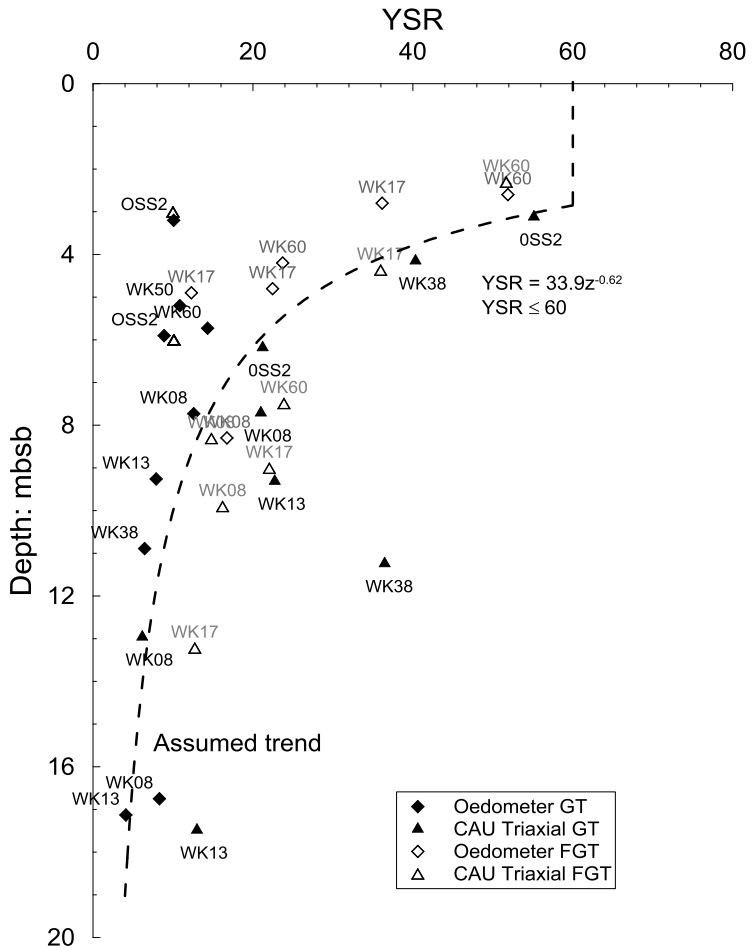
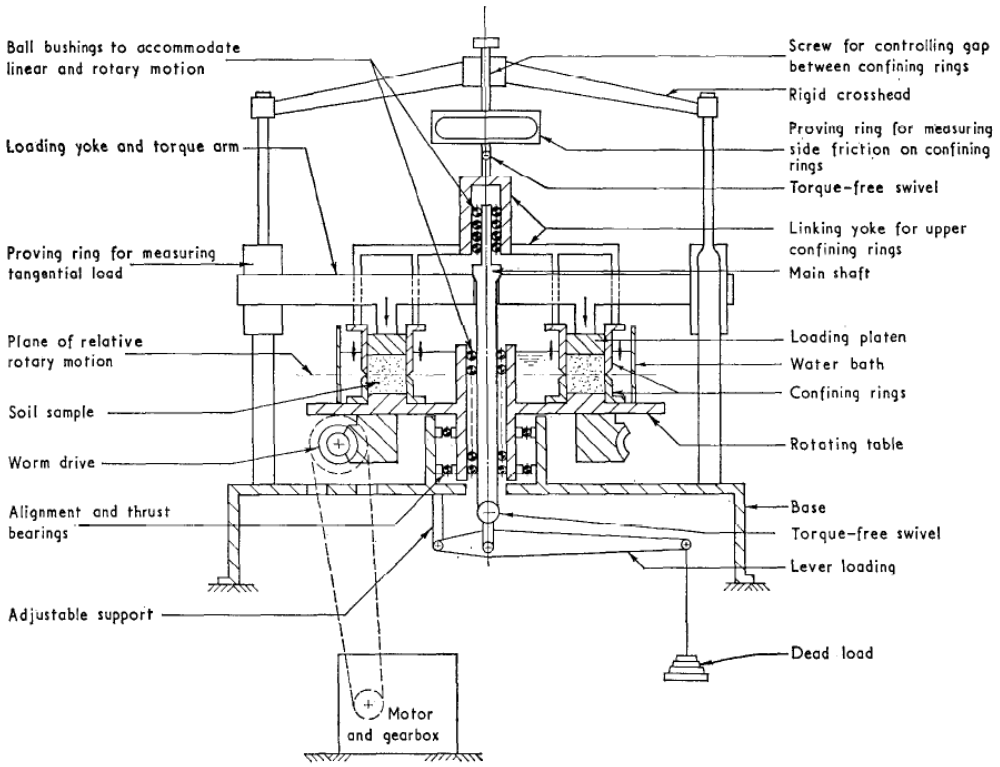
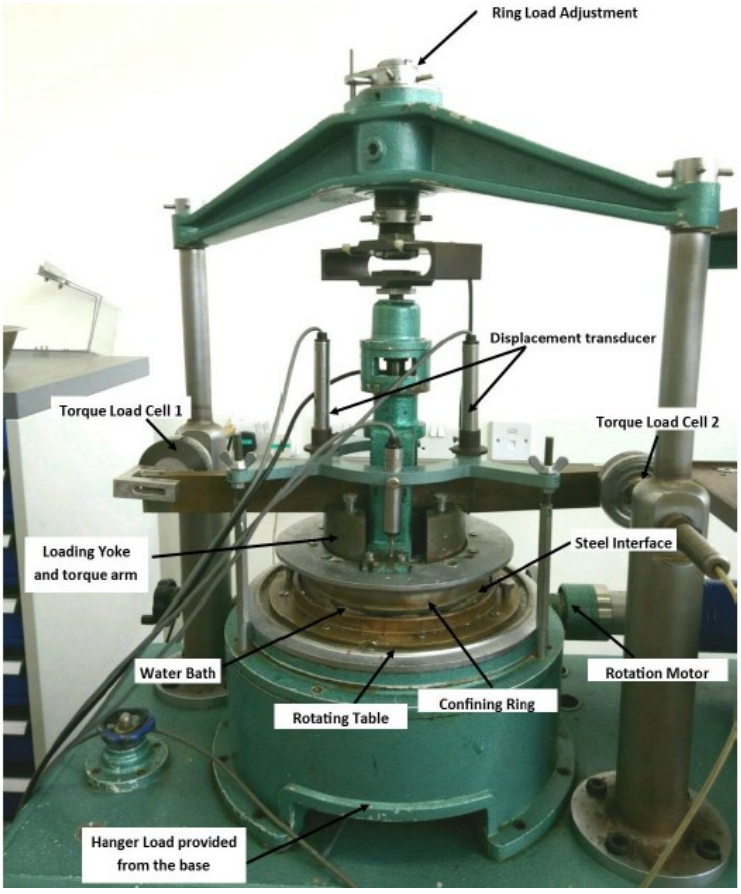


Figure 5-10: Yield stress ratio with depth in glacial till interpreted from oedometer and triaxial test results



(a)



(b)

Figure 5-11: Bishop ring shear apparatus (a) simplified principles of operation (Bishop *et al.*, 1971) (b) photo of apparatus (Chan, 2017)

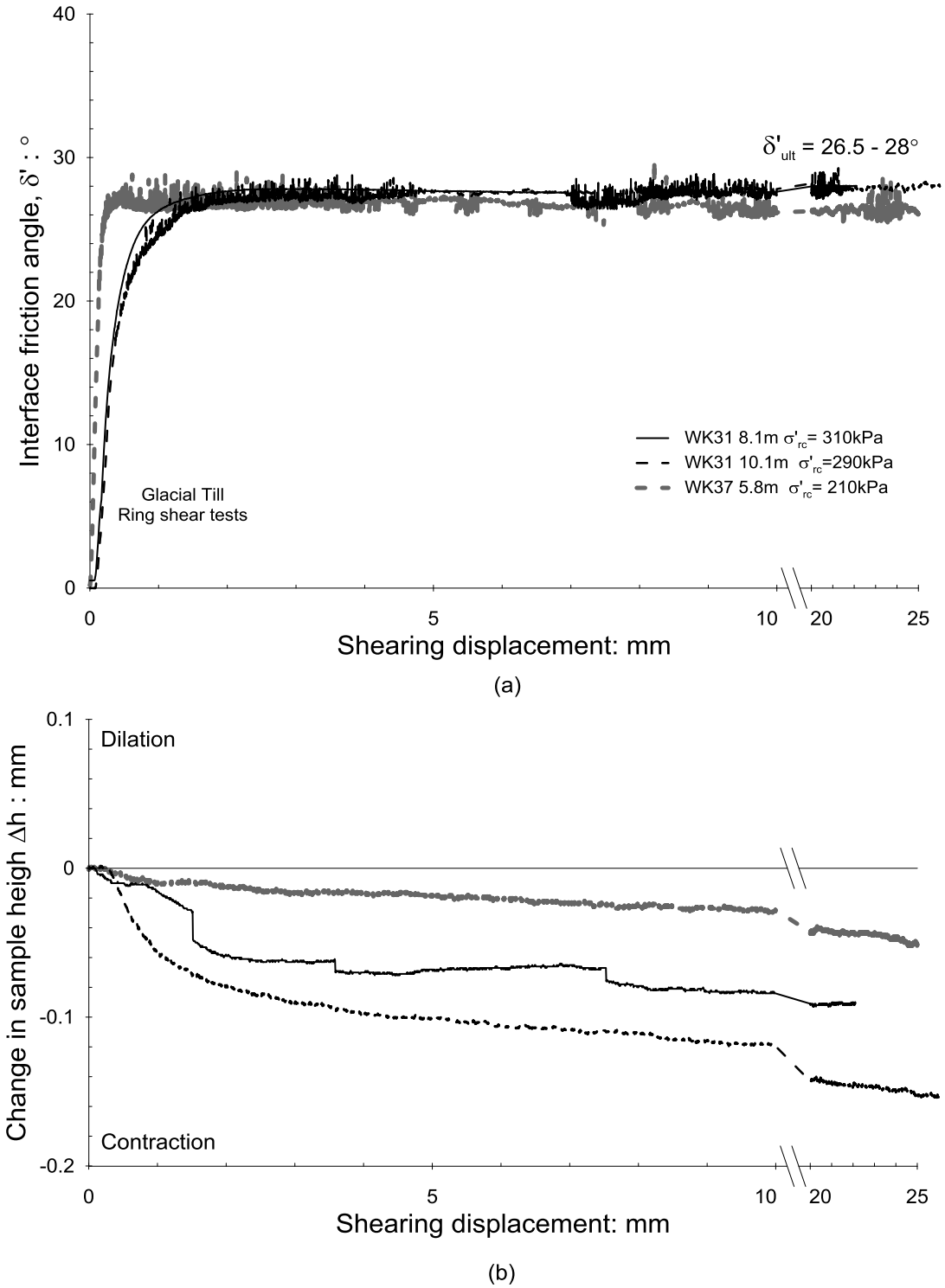


Figure 5-12: Ring shear tests on samples of glacial till conducted at Imperial College (a) interface friction angle versus displacement (b) change in sample thickness versus displacement

5.6 Maastrichtian chalk encountered at the test sites

5.6.1 Description & occurrence

Chapter 2 gave an introduction to the engineering behaviour of chalk with a focus on low-medium density material. The chalk encountered at Wikinger is of Maastrichtian age, with high proportions of calcium carbonate ($CaCO_3$), moderate weathering and narrow to closed discontinuities. Flint bands and nodules are occasionally encountered. Two distinct CIRIA grades (Lord *et al.*, 2002) can be identified:

a) Structureless, low density chalk, Grade D_m/D_c, located at 60% of WTGs and at six out of the eight test sites. At the test sites, the thickness varies from 0.2 to 5.2m with a mean of 4.4m;
b) Structured low-medium density chalk, Grade A1/A2, extremely weak, closely spaced, closed or clean fractures. This type of chalk is encountered by the piles across the site at 87% of WTG cases and at all of the test sites.

5.6.2 In situ testing

The relative merits and disadvantages of using CPT tests to classify chalk were discussed in Chapter 3, noting difficulties which can be summarised as:

- Achieving penetration through high density Grade A chalk or through significant flint layers;
- The lack of a consistent CPT-based classification system for chalk, due to its highly variable nature, the nature of fractures and their infill material;
- The need to average the data over an appropriate penetration interval to remove discrete sharp peaks in q_t and f_s thought to be caused by a build-up of penetration resistance followed by grain crushing and/or closing of discontinuities (Power, 1982, Smith, 2001).

At Wikinger, PCPTs were carried out from both the sea-bed and by a down-hole wireline method. The latter procedure consists of alternate cone penetration (≈3m) and drill-out segments to reach depths not achievable with seabed PCPTs. The PCPT traces recorded by the discontinuous downhole method generally lead to a greater number of resistance peaks. The recommendations of Smith (2001) were adopted when analysing the Wikinger data, and corrected cone resistance, q_t, f_s and u_2 were averaged over 300mm intervals. The effect of this averaging procedure is explored on Figure 5-13 and Figure

5-14 for tests conducted (i) from the sea bed and (ii) by a down-hole wireline method, respectively. The average trace can be seen to reduce greatly the discrete peaks in q_t.

Figure 5-13 and Figure 5-14 indicate that average q_t in structureless chalk lies between 5 and 10MPa, while averaged f_s is close to 100kPa and u_2 is approximately 3MPa. In structured grade A chalk, averaged q_t values fall between 10 and 20MPa with discrete peaks up to 60MPa. The sleeve friction, f_s generally lies between 200 and 400kPa while values of u_2 are remarkably high and increase with depth, reaching 10MPa close to 30mbsb.

Shear wave (V_s) and compression (V_p) wave velocities were investigated in the chalk using digital P-S suspension logging probes suspended in 17 boreholes. Shear wave velocity generally ranges from 0.8 to 1.1km/s increasing only slightly with depth; discrete peaks are thought to be due to the influence of higher strength layers or flints. Compression wave velocity is close to 2km/s and also remains constant with depth. These results are consistent with the ranges given by Obst *et al.* (2017) at the adjacent Arkona windfarm. A weak trend for G_{max}, to increase with depth, z was interpreted from the V_s measurements by CIJV (2014b) as:

$$G_{max} = 17.3z + 895 \text{ (MPa)} \quad 5\text{-}5$$

Full PCPT profiles are available for only four out of the eight static and dynamic test sites at Wikinger as indicated by $L_{p,cpt}$ in Table 5-1. In most cases, the seabed PCPT reached refusal at the top of (or close) to the top of chalk, and for these cases downhole PCPTs were not used to advance the profile. A correlation between average q_t and shear wave velocity from P-S logging has been developed for the Wikinger site to address this data gap. Figure 5-15 plots corrected cone resistance q_t against V_s from P-S logging at eight sites in structureless and structured chalk, at depths ranging from 9.5 to 63mbsb. The correlation generally relies on downhole tests, which are not available at all depths. Peaks in V_s associated with flints and not seen in the cone resistance profiles have been excluded as have results in the Danian limestone formation. The trend of increasing V_s with q_t shown in Figure 5-15 indicates the following relationship:

$$q_t = 21.04V_s^{1.09} \quad 5\text{-}6$$

where V_s is in km/s and q_t is in MPa. Eq. 5-6 can be seen to lead to a reasonable estimate of q_t in the chalk (Figure 5-15 (b)) with the average ratio of calculated to measured q_t equal to 1.01 with a standard deviation of 0.16. The mean trend from the V_s measurements is converted to q_t and plotted on the q_t envelope from across the site on Figure 5-16.

Estimates of q_t can be made for the deeper sections at WK43 and WK70 where the tests terminate at 11m and 7.4m, respectively and the piles reach ≈31mbsb. A data gap of 10m also exists in WK43 between 11 and 21.5m where no V_s measurements are available. Similarly V_s measurements are not available at WK70 between 7.4 and 11.5m. Interpolation using the average mean trend from similar sites has been used to synthesise a continuous profile of q_t between these depths. The relationship shown in Figure 5-15 is highly site specific and is likely to vary widely between sites with different chalk grades and intact dry densities.

5.6.3 Index testing

Chalk properties measured at the eight test sites are summarised in Table 5-3. While intact dry density is generally less than 1.5Mg/m^3, indicative of a low density chalk, Figure 5-17 indicates a medium density layer in WK38 and WK43 above ≈20mbsb and medium to high density chalk in WK70 above ≈25mbsb. Comparison of the natural moisture content (NMC) and saturated moisture contents (w_{sat}) indicates the chalk was within 3% of full saturation when tested (Figure 5-18) with its natural moisture content lying close to the phase relationship between w_{sat} and IDD. The results from WK70 on samples of structured M-H density chalk deviate from the trend with NMC lower than expected at a given density and samples which do not appear close to saturation. The layer may be part of the (Danian) limestone of different properties encountered in the NE corner of the windfarm. This layer is further discussed in Section 5.9 in the context of the pile installation results.

Both the structureless and structured chalk comprise almost entirely $CaCO_3$, with contents of 88 and 93% respectively. No grading curves are available on the material, but the particle size can be expected to be predominantly silt-sized (Clayton, 1978). Unconfined compression strength tests are shown on Figure 5-19, on saturated samples from the test sites, plotted against IDD of the same sample. As discussed in Chapter 2, the nature of the test and the sample requirements limit its application to structured chalk. IDD is generally directly related to UCS q_u, following the trend for saturated samples given by Matthews and Clayton (1993). Based on this trend, for typical IDD values of 1.4-1.55Mg/m^3 (low density) q_u ranges from 1.1 to 3.0MPa, and for medium density (IDD = 1.55-1.7Mg/m^3) between 3 and 5MPa. The q_u values at the test sites, and across the Wikinger site, fall well below this trend and lie between 0.2 and 0.8MPa. Taking UCS = $2s_u$, where s_u is the undrained strength, indicates that the UCS test strength forms a lower bound to the (450 to 600 kPa) undrained strength range found in undrained triaxial tests.

Table 5-3: Index properties from the 8 test sites in structureless and structured chalk

	Structureless			Structured		
Parameter	**n**	**Mean**	**StDev**	**n**	**Mean**	**StDev**
Water content, w_c (%)	20	30.5	8.7	149	28.4	4.7
Saturated water content, w_{sat} (%)	-	-	-	128	28.9	4.2
Degree of saturation, S_r (%)	1	100	-	126	97	0.1
Bulk density, γ_{bulk} (Mg/m^3)	2	2.28	0.42	143	1.95	0.1
Intact dry density, IDD (Mg/m^3)	-	-	-	143	1.52	0.1
Specific gravity, G_s	3	2.71	0.01	23	2.70	0.02
UCS, q_u (MPa)	-	-	-	55	0.39	0.24
Calcium carbonate (%)	3	88.3	5.7	30	93.2	9.4

5.6.4 Intact chalk strength & stiffness

The behaviour observed in CAU triaxial tests is shown on Figure 5-20 for intact samples of structureless, structured low and medium density chalk. The behaviour is consistent with that reported in the literature, exhibiting a high stiffness pre-yield with significant dilation, followed by failure in a brittle manner (e.g. Jardine *et al.*, 1985, Addis and Jones, 1990, Leddra *et al.*, 1993). The values of s_u applying at the end of the test at ≈20% strain, ranged from 450 to 600kPa. Two separate peak failure envelopes are identified for low and medium density samples. Low density samples show peak φ′ values of 36° with c′ of 150kPa. Cohesion appears to increase with IDD, consistent with a more cemented fabric; peak φ′ in medium density samples was similar at 36.4° however cohesion was closer to 200kPa.

The small strain stiffness, G_{vh} interpreted from the P-S logging V_s measurements in intact chalk and using a mass density equal to 1.95Mg/m^3 is shown Figure 5-21, available at five of the test sites, along with the envelope of measurements from across the site.

The formation and stress history of chalk suggests that it is not significantly affected by changes in overburden stress. Cementation at grain contacts likely occurred contemporaneously with deposition allowing chalk to support high overburden pressures without any consolidation (Clayton *et al.*, 2002). The results of six oedometer tests, at depths of between 19 and 45mbsb, shown on Figure 5-22, indicate YSR between 6 and 9 which did not vary significantly with depth.

5.6.5 Putty chalk strength, stiffness & time effects

An annulus of putty, or remoulded chalk, is known to form around the shafts of driven piles during installation (Hobbs and Atkinson, 1993, Muir Wood *et al.*, 2015). A laboratory investigation of "putty" or remoulded chalk behaviour was carried out on samples from Wikinger at Imperial College by Doughty (2016) as reported by Doughty *et al.* (2018) and summarised briefly here. The aim of the study was to investigate the effects of time on putty strength and stiffness in connection with the strong influence of time on capacity reported from the field (Chapter 3). The putty was formed by compaction of undisturbed samples at their natural moisture content using a 2.5kg Proctor compactor. The putty was placed in a compaction mould and 10 x 27 blows were applied or until further compaction was not possible, ensuring throughout that the chalk remained close to its natural moisture content. The chalk generally reached a smooth consistency, with an assessed undrained strength of around 4kPa, within the first 100 blows (Figure 5-23).

Fall cone tests, used to determine s_u of the putty formed by compaction, provided evidence that modest thixotropic increases in s_u occur with time at room temperature under conditions of constant water content. Putty samples were filled into open-ended Perspex cylinders and left to age for periods ranging from 1 minute to 28 days. The samples were preserved by wrapping in layers of cling film, foil and wax prior to the tests. Small variations in water content, of <0.8%, occurred over the test programme. A clear trend of increase in s_u was observed with time, with s_u doubling every ≈3 log cycles, from 3.7kPa initially to 12.3kPa after 28 days. The rate of increase appeared to accelerate within the first day.

Samples of putty were consolidated in a triaxial cell and sheared either immediately or allowed to age under constant mean effective stress for up to 14 days. The consolidation and shearing stages of specimens consolidated to mean effective stress, p' values between 100 and 200kPa and subjected to undrained ageing for 0, 7 and 14 days post-consolidation are shown in specific volume-mean effective stress space in Figure 5-24. The effective stress paths and secant stiffness for all four tests are shown on Figure 5-25 and Figure 5-26 while the stress-strain behaviour is shown on and Figure 5-27.

All samples were denser-than-critical state at the end of consolidation (and creep) under constant p' (Figure 5-24) with a state parameter, $\psi < 0$ (Been and Jefferies, 1985). The single test on un-aged putty (TX4) showed similar behaviour during shear to a medium dense granular material. This "zero" day test was in fact sheared ≈18.5 hours after placement, following saturation and consolidation. The behaviour was strongly

contractive initially, with an excess pore water pressure of ≈90kPa generated at very small strains, followed by transition to strongly dilative behaviour at the phase transformation point. Sample TX4 was placed at a looser state than the tests presented in similar work by Razoaki (2000), discussed in Chapter 2, to mimic conditions in the field, and was not permitted to form structure either by ageing or in a consolidometer, leading to different initial behaviour than seen in that study. A common critical state angle of shearing resistance was found by both authors, corresponding to $c'=0$ and $M_{tc}=1.24$ ($\varphi' \approx 31°$).

The samples aged in triaxial cells under constant load showed similar behaviour to the similar tests conducted earlier by Razoaki (2000); see Figure 2-24. Samples consolidated to the same stress level (100kPa) and subjected to undrained shearing at ages of 7 and 14 days (TX2 and TX3) showed a higher initial stiffness when compared to the un-aged test, assumed to be due to the effects of drained ageing (creep), and/or re-cementation at grain contacts. The increases in stiffness were on the order of 200 to 300%. The beneficial effects on stiffness reduce significantly at shear strains of approximately 0.1% with the aged tests converging onto a single line (Figure 5-26). The stiffness and stress-strain behaviour observed is similar to the behaviour of intact chalk at high stresses which exhibit an initial yield point where bonds are broken down followed by strain hardening to failure; see Chapter 2 and Addis and Jones (1990). This behaviour contrasts sharply with the unaged test which showed a ductile response. Figure 5-24 illustrates that after some initial contraction all four tests dilated towards a common CSL with parameters $\lambda = 0.07$ and $\Gamma = 2.188$. At the end of the test, the shear strength also showed an increase with time; for samples consolidated at the same stress level, s_u increased by a factor of 3.3 over 7 days and 8.2 over 14 days; Figure 5-27.

The results can be interpreted within the multiple kinematic surface framework of Jardine (1992) discussed in Section 2.9.1. The small strain stiffness behaviour shown in Figure 5-26 illustrates that the initial stiffness, which determines the size of the recoverable linear elastic Y_1 kinematic sub-yield surface, is increasing with time, likely due to the effects of cementation (Jardine, 1992). No unload-reload paths were carried out therefore the hysteretic response cannot be assessed. Figure 5-25 includes possible locations of the outer Y_3 bounding surface which also appears to increase in size and change shape with ageing. The response of the 7 and 14 day tests are similar, indicating that the most marked change in material properties occurs within the first week. Confining pressure was also shown to have an effect on the elastic region; samples consolidated at

the same age (7 days) to 200kPa showed a further expansion of the yield surface over the 100kPa tests.

The primary conclusions of the study conducted on putty samples from the site by Doughty (2016) are:

(a) Intact samples of low-medium density chalk lie close to their liquid limit at their natural water content. When compacted at their natural moisture contents they degrade readily to a consistent putty material, which may barely support its own weight, with an assessed s_u of approximately 4kPa;
(b) Thixotropic effects were found to lead to modest increases in strength under conditions of constant water content due to re-cementation and/or structural changes within the material;
(c) At the end of consolidation or consolidation and creep under constant p′, the stress states in all four triaxial tests were on the dense side of critical ($\Psi<0$). Subsequent shearing led to an initial contraction followed by phase transformation and dilation to critical state;
(d) The greatest increases in strength are caused by drained consolidation after puttification. Following testing, the samples were described as firm to stiff compared to the soft putty installed initially in the triaxial tests. The assessed post-test strength increased with increasing confining pressure and the associated reductions in void ratio;
(e) Undrained triaxial tests on samples consolidated to the same p′ showed that initial undrained strength and initial stiffness increase with age. The region of stress space within which the behaviour was linear elastic also appeared to increase with age, controlling the point at which large volume changes occurred during shearing. At shear strains of >0.1% the beneficial effects of age on stiffness were significantly reduced.

The results have important implications for the interpretation of pile capacity changes with time and are discussed further in Section 5.9. Further details of the tests are provided by Doughty (2016) and Doughty *et al.* (2018).

5.6.6 Interface shear behaviour

Interface ring shear tests were carried out by Fugro (2013) on samples of remoulded chalk taken at Wikinger, as summarised on Figure 5-28. The test procedure

adopted, based on BSI (1990a), differs slightly from the method described in Section 5.5.6 and consisted of the following stages:

(a) Consolidation to a normal stress representative of the radial effective stress at the relevant depth;
(b) Fast shearing at a rate of 674°/min followed by a short period to allow for equalisation and then a slow shearing stage at a rate of 0.024°/min.

The confining pressure was then increased and (a) and (b) were repeated at a higher stress level. The mild steel interfaces had an average centre line roughness, R_a of 10μm. All nine tests were conducted on structured low density grade A1/A2 chalk at stress levels between 112 and 554kPa. The results, shown in Figure 5-28(a), indicate δ'_{ult} angles of between 32 and 34°. The δ'_{ult} values appear slightly affected by confining stresses. For samples consolidated to between 112 and 297kPa, δ'_{ult} ranged from 32 to 34° with a mean of 33.2°. This range increased to between 33 and 34° with a mean of 33.6° for samples consolidated to between 446 and 594kPa. Figure 5-28 (b) shows the change in specimen height as a function of vertical displacement during slow shearing. The general trend is for dilation initially prior to δ'_{peak}, with a magnitude generally less than 0.015mm or $1.5R_a$, followed by contraction with continued shearing.

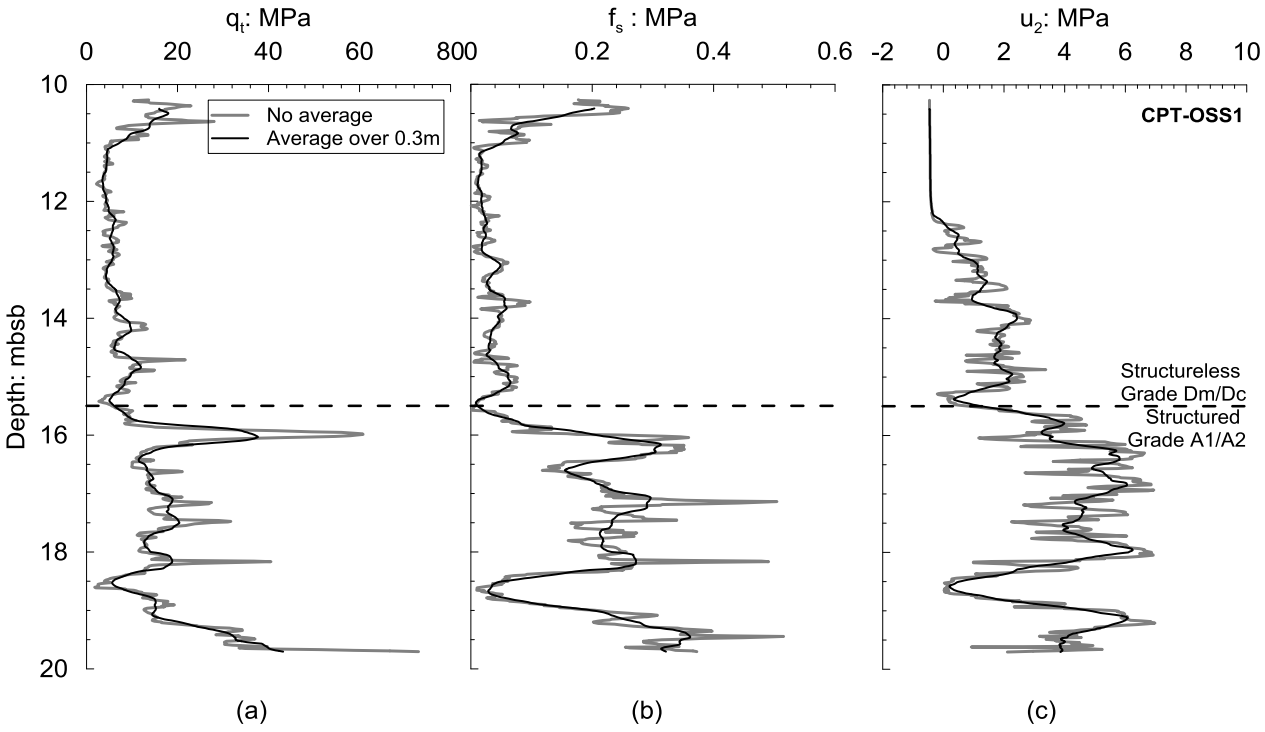


Figure 5-13: Effect of averaging PCPT parameters over 300mm for tests conducted from the seabed (a) cone resistance (b) sleeve friction (c) penetration pore pressures

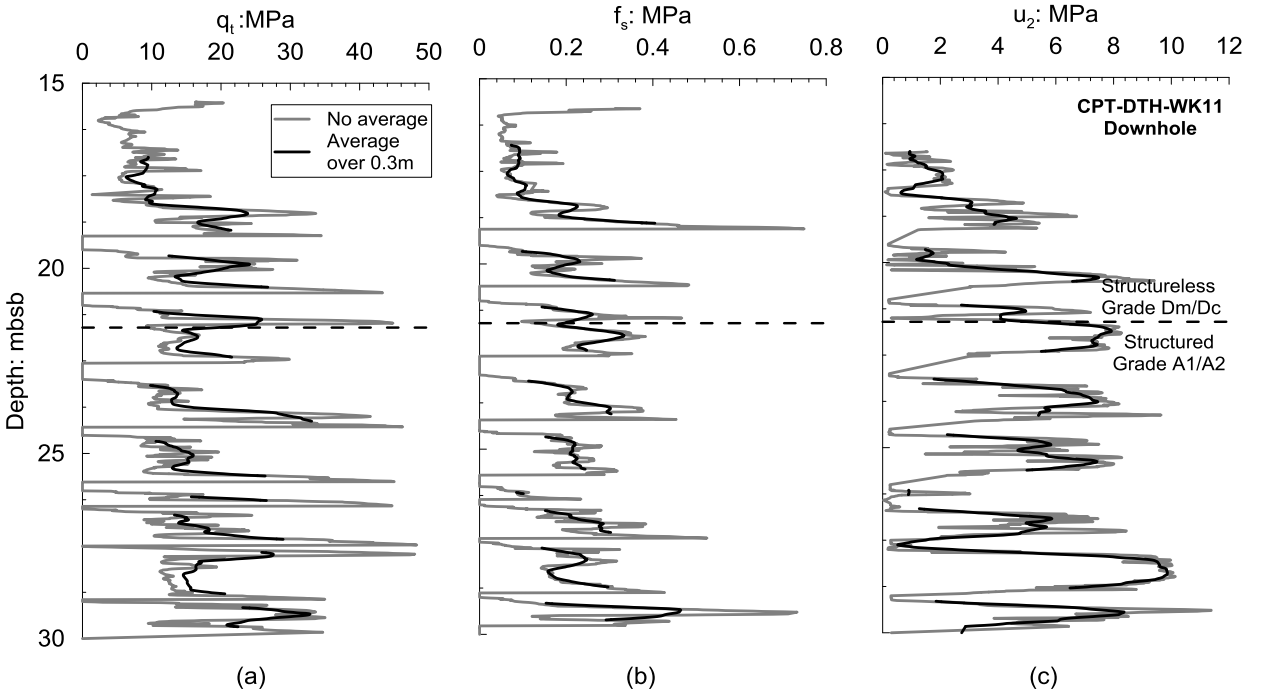
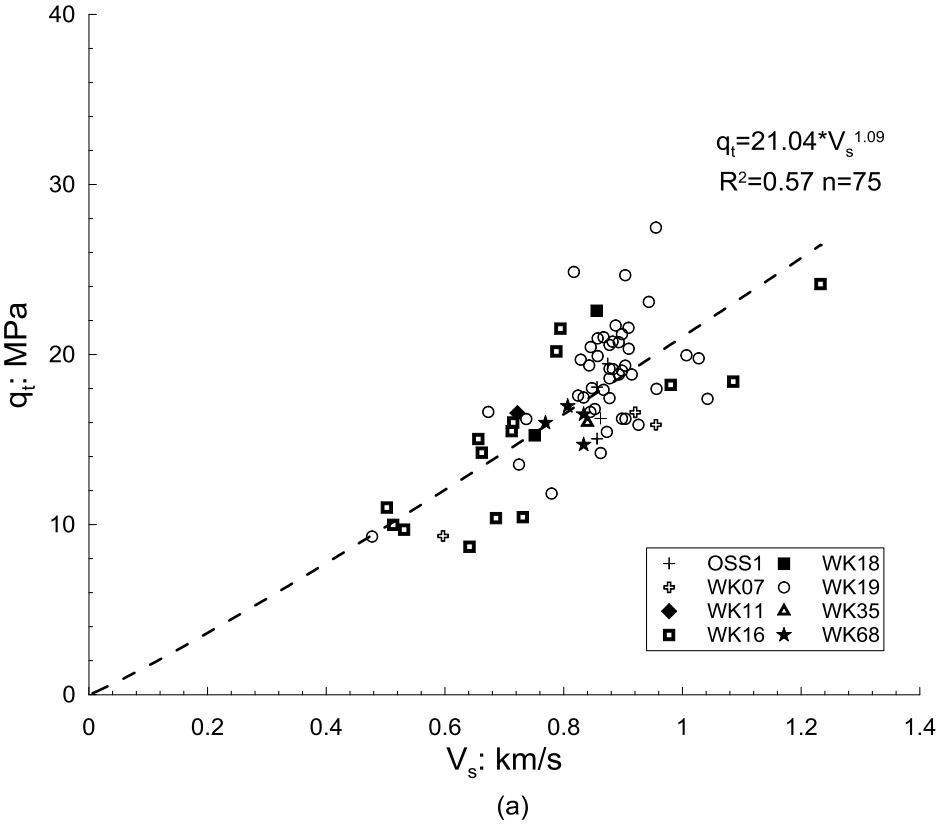


Figure 5-14: Effect of averaging PCPT parameters over 300mm for tests conducted by down-hole wireline (a) cone resistance (b) sleeve friction (c) penetration pore pressures



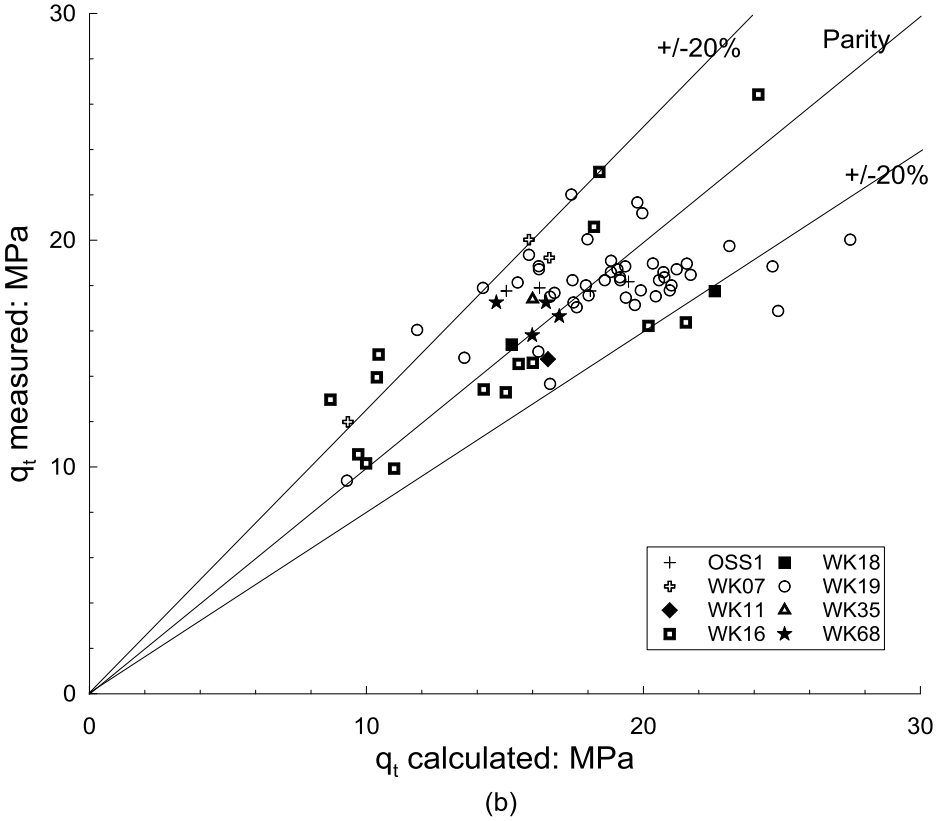


Figure 5-15: Correlation between cone resistance and cone resistance in chalk developed from the results at eight sites

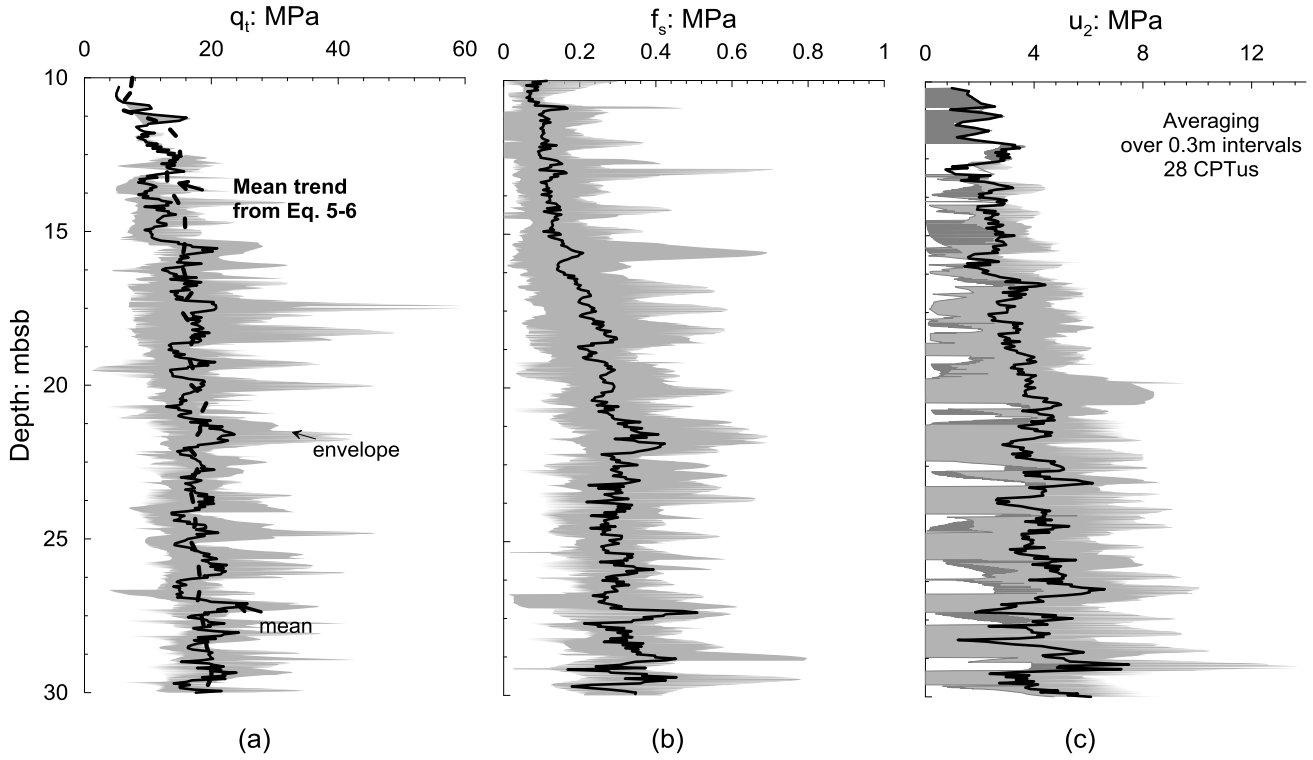


Figure 5-16: Envelopes of PCPT results in Grade A1/A2 chalk (a) cone resistance (b) sleeve friction (c) penetration pore pressures

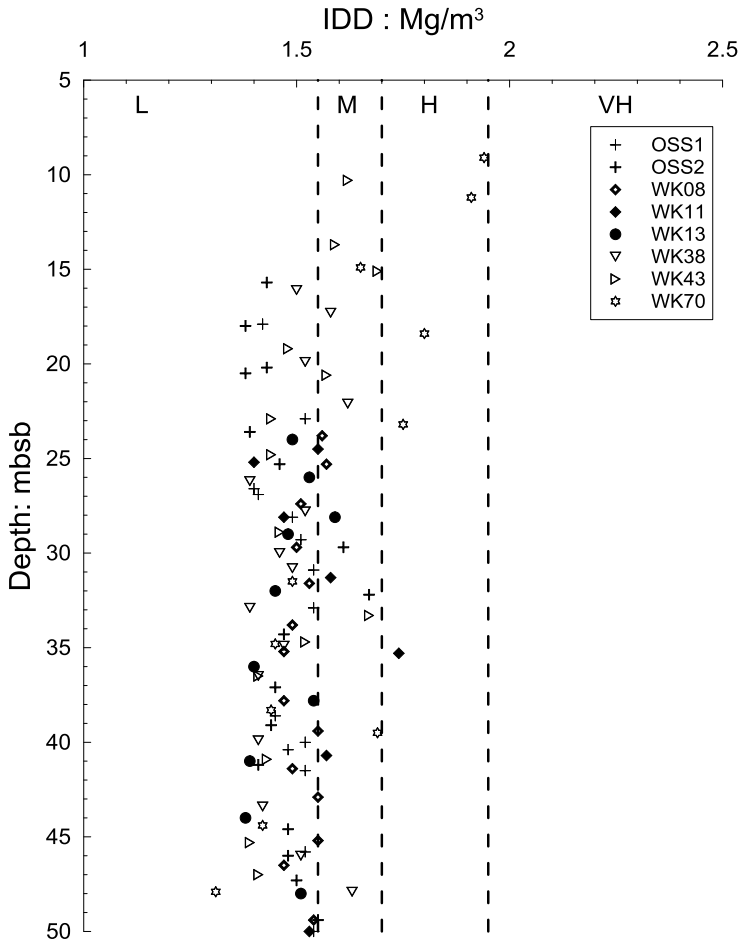


Figure 5-17: Intact dry density at the test sites with depth

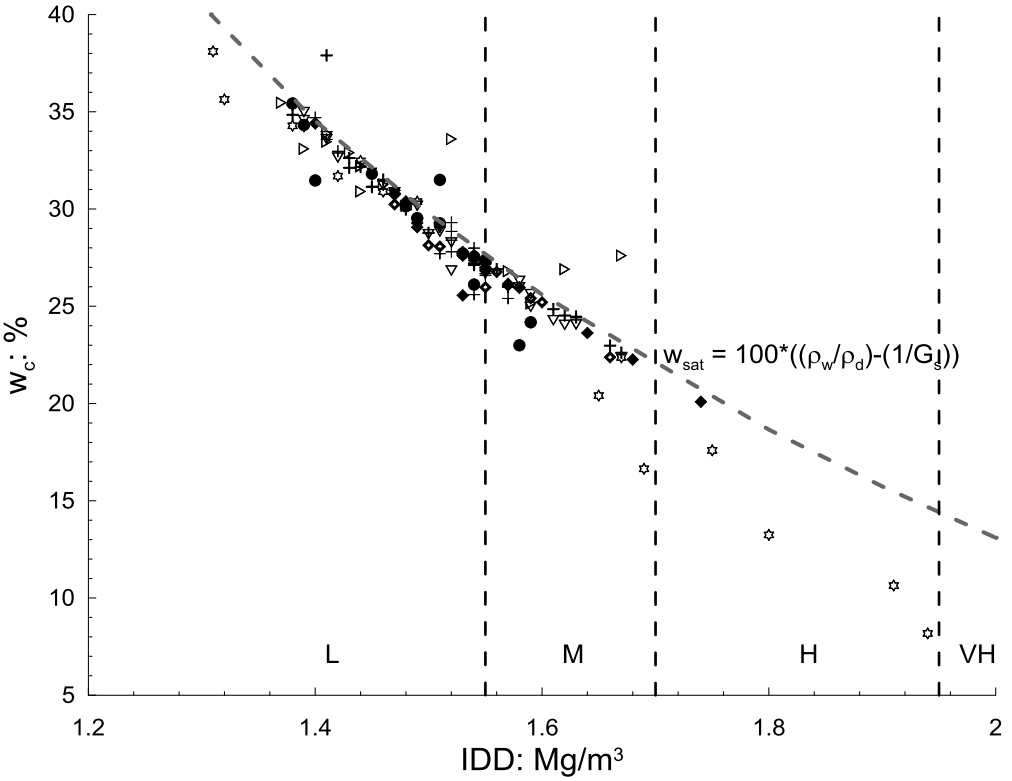


Figure 5-18: Intact dry density relationship with natural moisture content

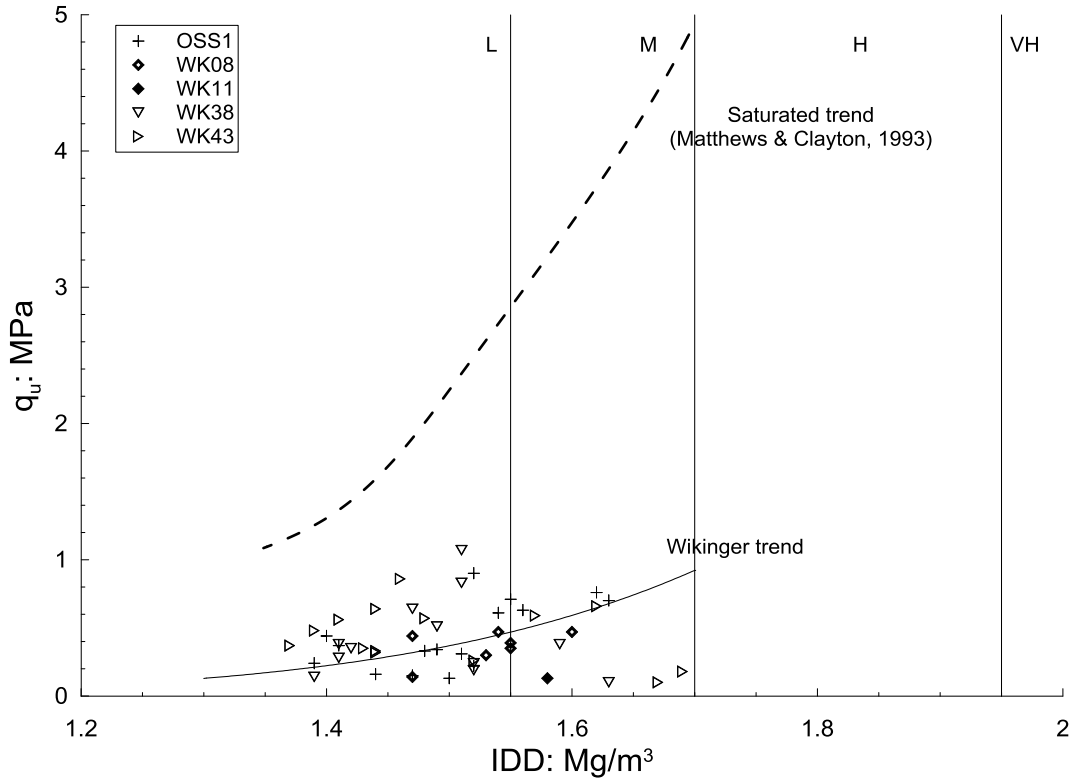


Figure 5-19: Relationship between unconfined compressive strength and IDD in chalk

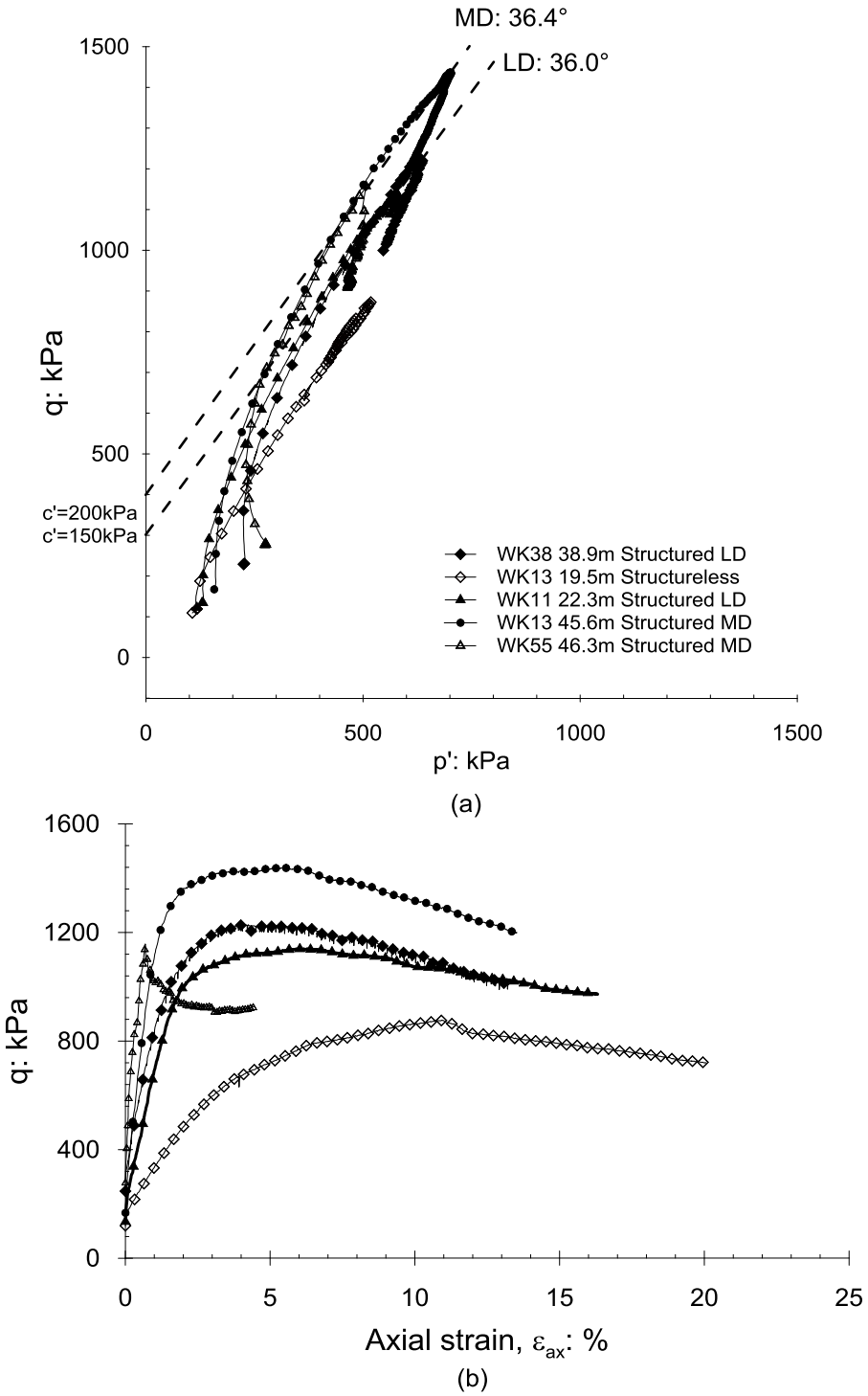


Figure 5-20: Triaxial tests on samples of intact structured and structureless Wikinger chalk (a) effective stress paths (b) deviator stress versus axial strain

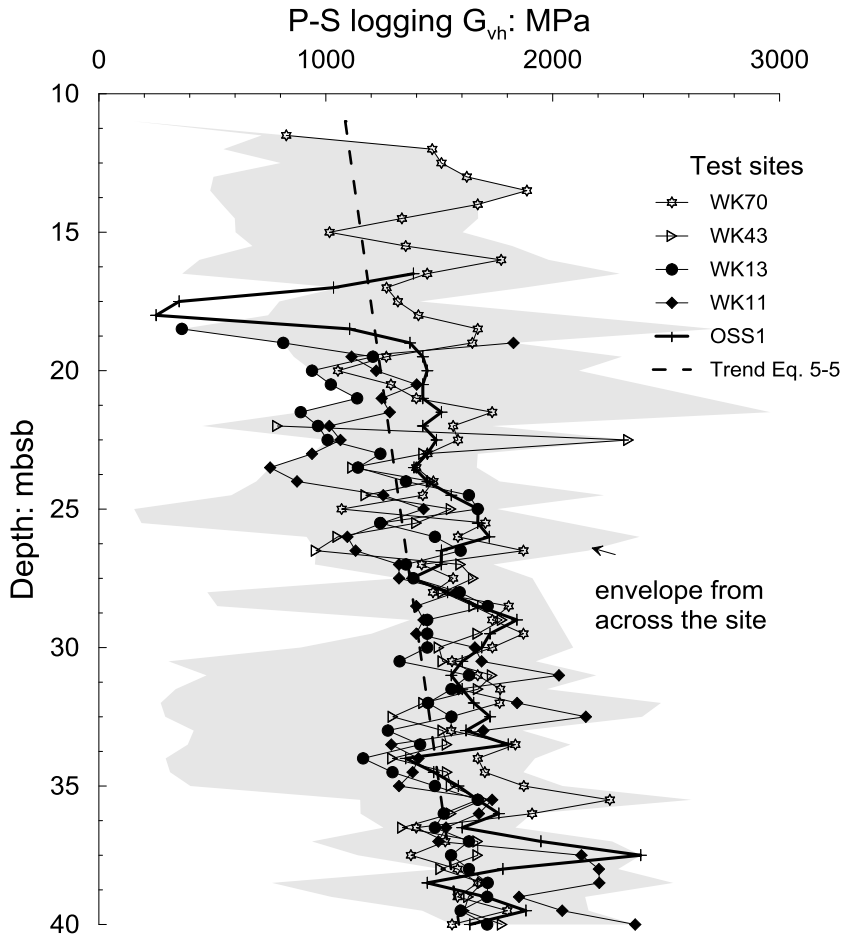


Figure 5-21: Shear modulus, G_{vh} in chalk from suspension P-S logging at the test sites

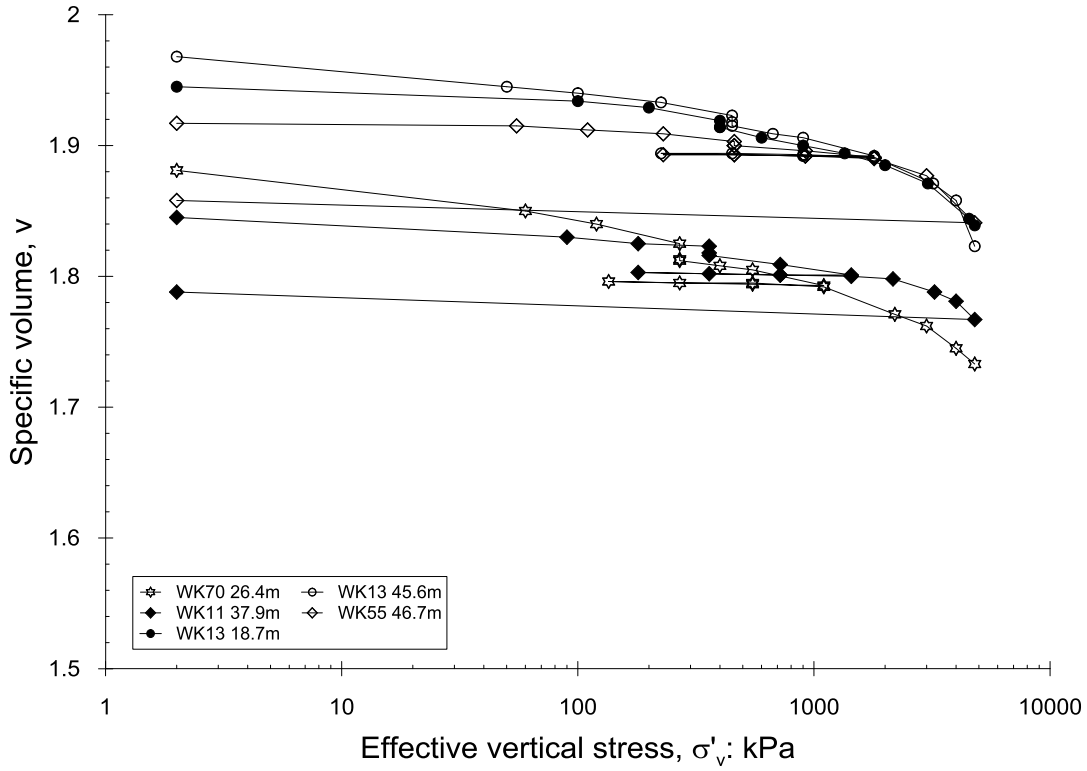


Figure 5-22: Oedometer tests on samples of intact chalk



Figure 5-23: Putty chalk preparation in the laboratory using a 2.5kg Proctor compactor

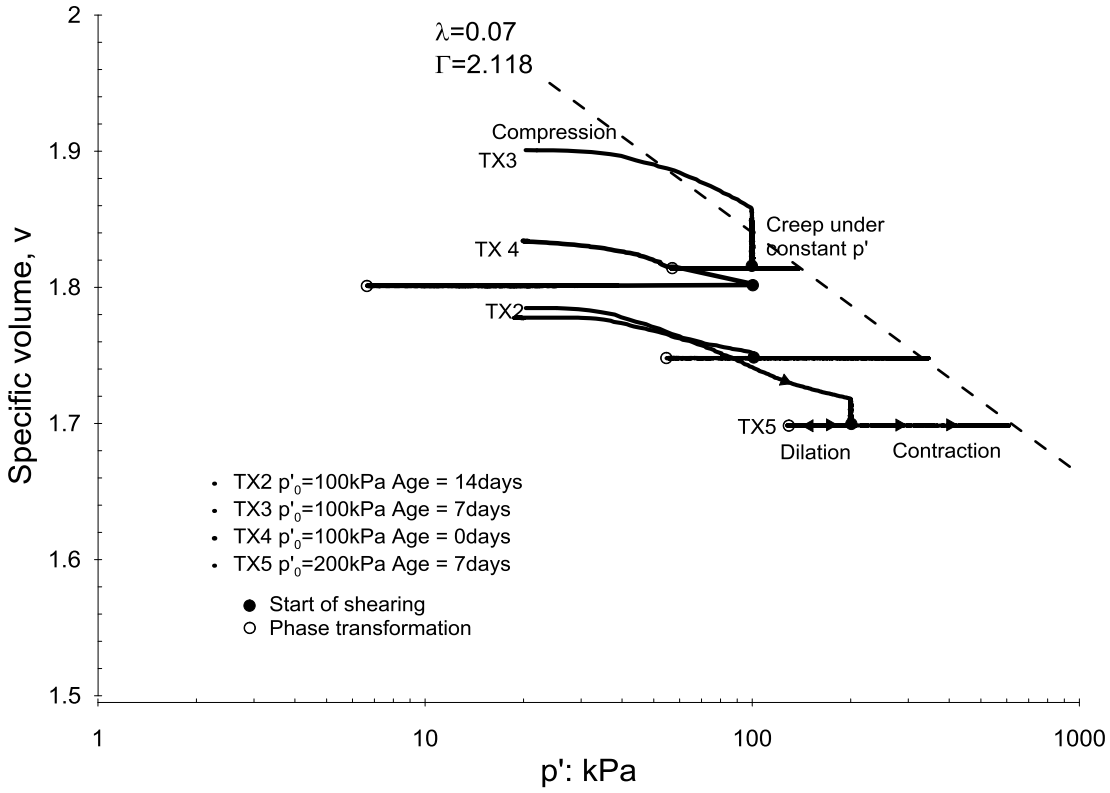


Figure 5-24: Consolidation and undrained shearing on chalk putty samples from Wikinger (Doughty, 2016, Doughty *et al.*, 2018)

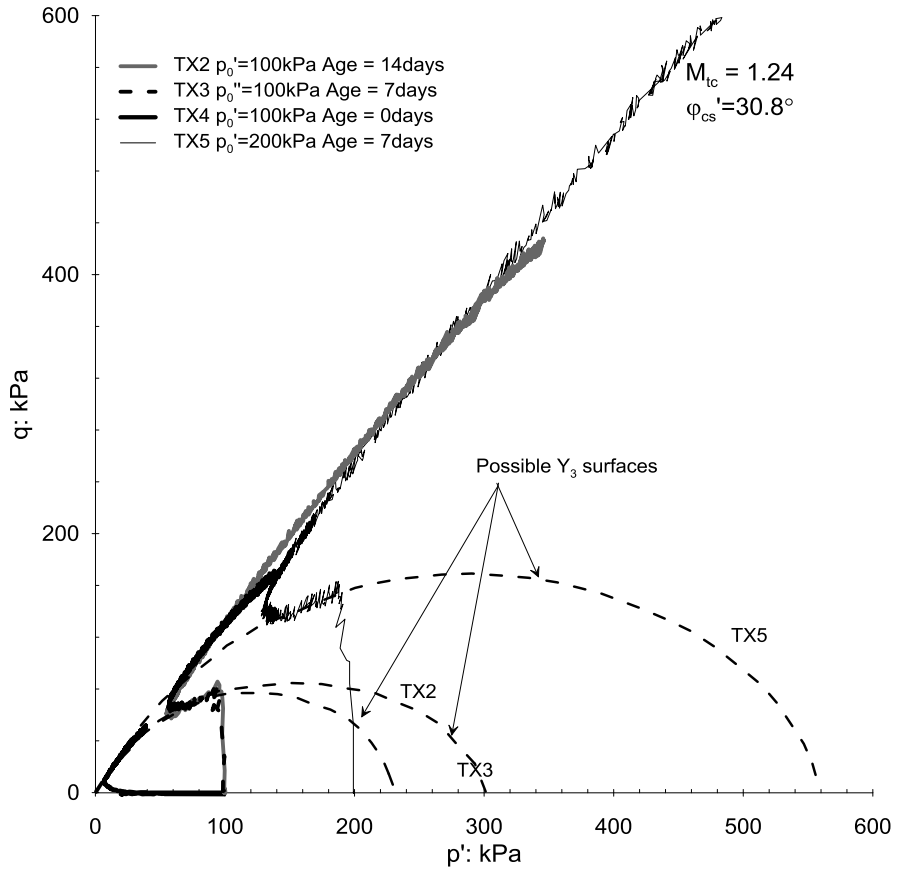


Figure 5-25: Undrained triaxial tests on chalk putty samples - stress paths and interpreted bounding surfaces (Doughty, 2016, Doughty *et al.*, 2018)

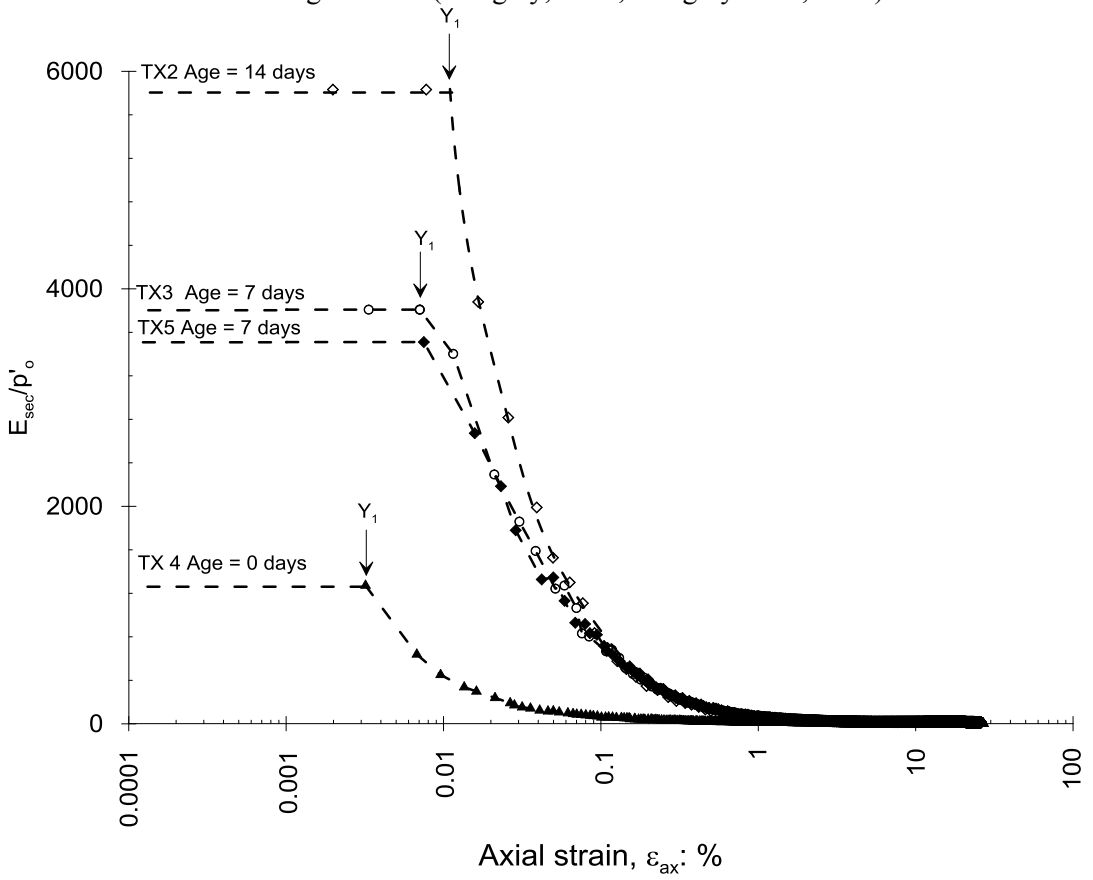
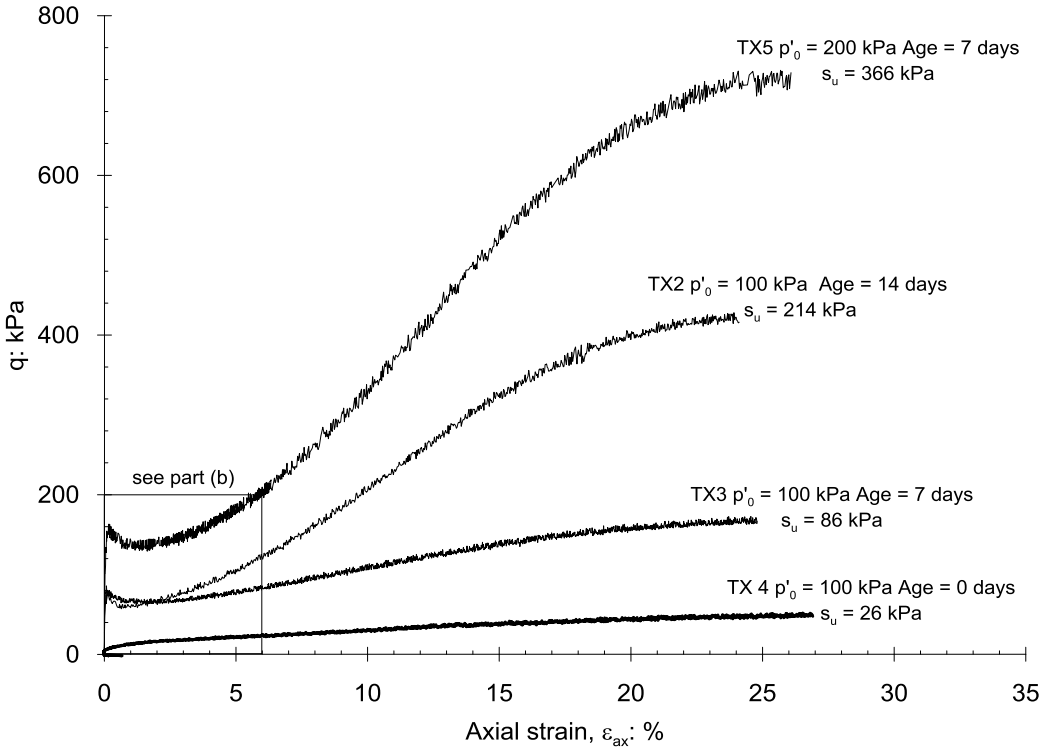
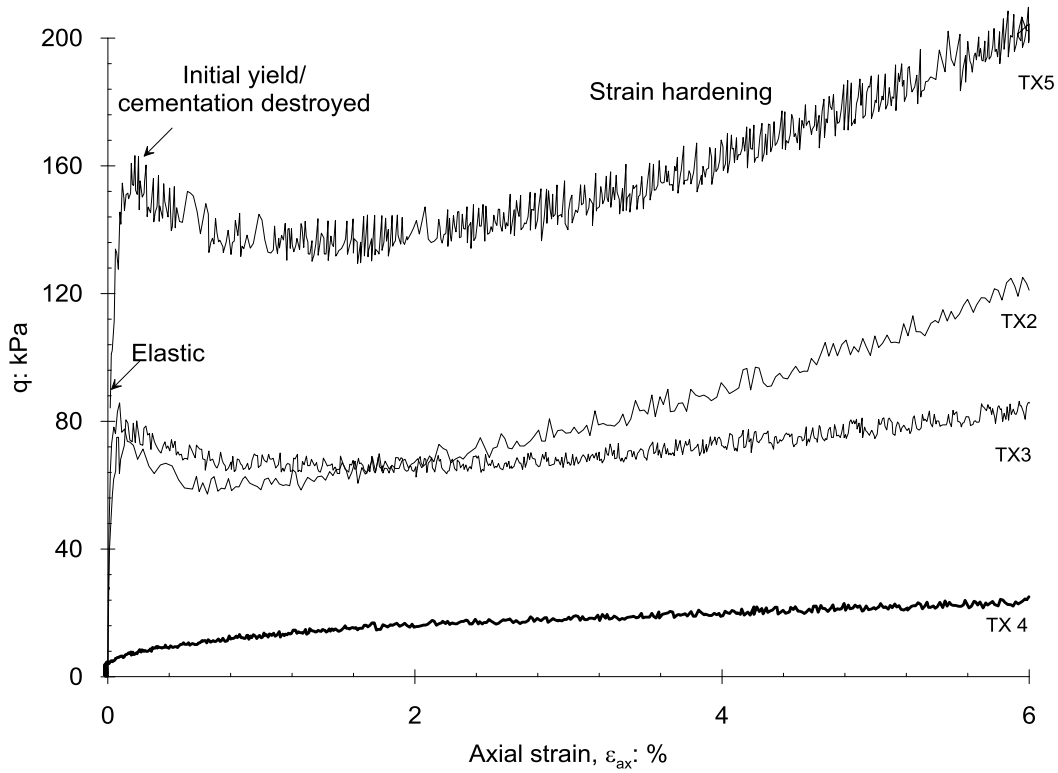


Figure 5-26: Secant stiffness normalised by initial mean effective stress for aged and unaged triaxial tests on chalk putty (Doughty, 2016, Doughty *et al.*, 2018)



(a)



(b)

Figure 5-27 Undrained triaxial tests on chalk putty samples – stress – strain behaviour during shearing (Doughty, 2016, Doughty et al., 2018)

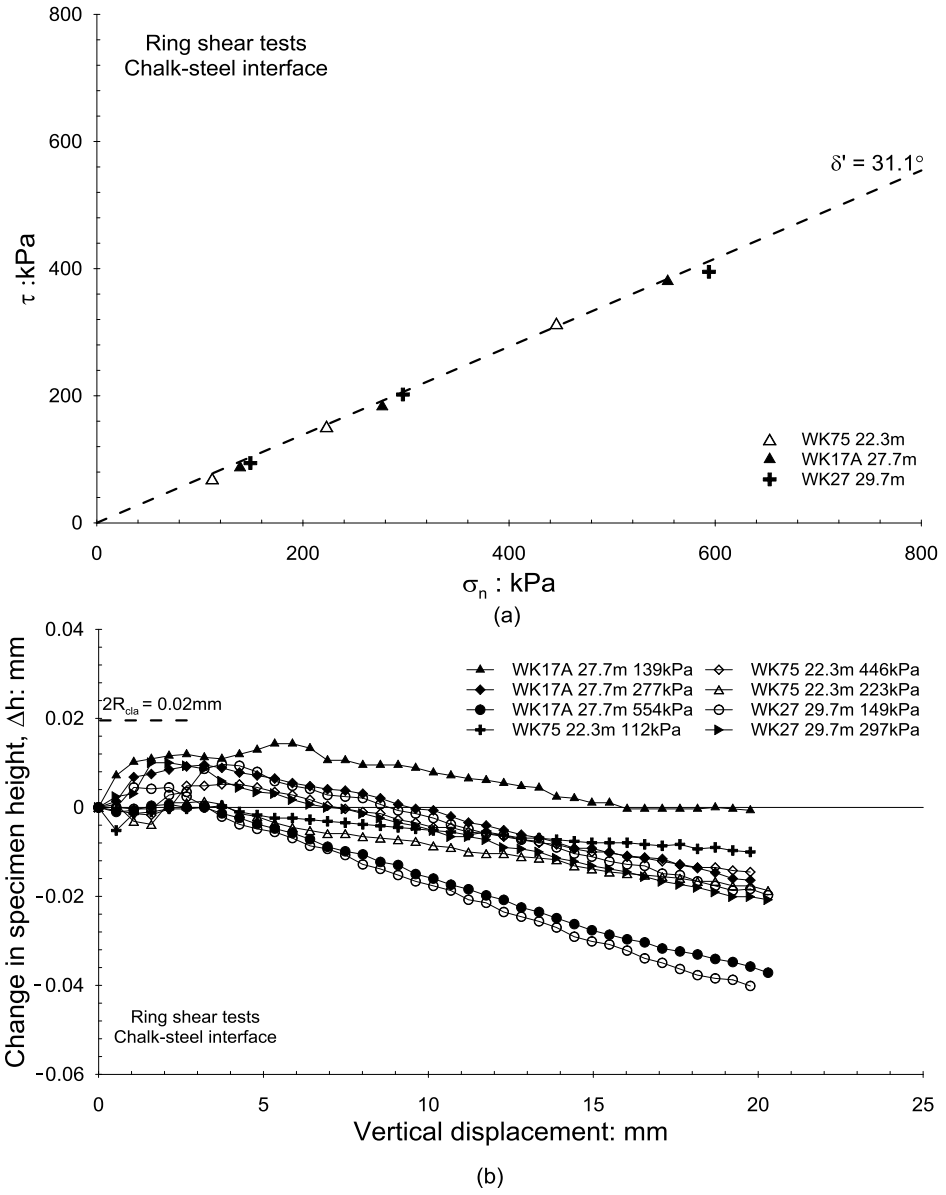


Figure 5-28: Ring shear tests on chalk samples using mild steel interfaces (Fugro, 2013)

5.7 Pre-construction pile test campaign

An overview of the pile details and test execution during the main pile test campaign are given here to frame the analysis of the results, drawing on detailed information on the offshore pile tests available in the Pile Load Test Concept Report Rev 2.1 (CIJV, 2014a), the interim and final pile test reports (Bilfinger, 2015a, b) as well as Barbosa *et al.* (2015) and Barbosa *et al.* (2017).

5.7.1 Pile configurations & installation

At each of the pre-construction test sites, three 1.37m diameter steel tubular piles (Steel Grade S355) with a wall thickness, t_w of 40mm, were driven as summarised in Table 5-4. A recapitulation of the ground conditions at each site is provided in Table 5-1. The piles were installed in a straight line with a centre to centre spacing of 8.33m. At each site, Pile 1 was subjected to a dynamic test only, Pile 2 was subjected to a static tension test only and Pile 3 was an un-failed reaction pile. The piles were installed using a Menck MHU 800S hydraulic underwater hammer with a maximum energy of 820kJ above water and a ram weight of 45.4tons, with a total submerged weight of 111 tons. Four strain gauges and four accelerometers were attached to test Piles 1 and 2 at each site, which remained 700mm above the sea bed at the end of installation. A schematic illustration of the sensor positions is shown in Figure 5-29(a).

To ensure the required installation tolerances could be achieved, which was key for the success of the static tests, the piles were installed through a custom built "triplex template", shown on Figure 5-29 (b). The template was first lowered on to the seabed and the pile was guided by a hydraulically foldable upper guide support system and by a lower guide which could be adjusted to allow the instrumentation to pass through. Once on the seabed, the system could be levelled using adjustable footplates. The template height was adapted to the pile length; varying from 10m at WK38 to 15m at WK43/WK70.

The self-weight (SW) penetration of the piles (Table 5-4) was generally less than 0.4m at WK43 and WK70 where the piles were placed directly on to the stiff glacial till. At WK38, where the piles were placed onto soft Holocene deposits the SW penetration was higher, reaching up to 2.6m. Figure 5-30 shows blow count profiles for the six instrumented piles, which typically involved 15 to 25mm penetration per blow in the glacial till and 25 to 50 mm of penetration per blow in the chalk. The depths where driving was paused for operational reasons are indicated on this Figure with the pauses further detailed on Table 5-5.

Table 5-4: Summary of test pile installation

Test pile	D (m)	L (m)	L_p (m)	SW pen (m)	Total Blows	Driving time (mins)		Date	Plug level[4] (mbsb)
						Total	Net		
WK38-1	1.37	21.8	16.6	2.6[1]	544	105	34	02/10/2014	-
WK38-2	1.37	21.8	16.6	0.9[1]	593	132	46	01/10/2014	-0.79
WK43-1	1.37	35.7	30.7	0.4[1]	1069	85	63	10/10/2014	-2.65
WK43-2	1.37	35.7	30.7	0.3[1]	1183	74	66	09/10/2014	-2.57
WK70-1	1.37	36.0	31.0	0.3[1]	1192	62	54	13/10/2014	-2.67
WK70-2	1.37	36.0	31.0	0.03[1]	961	80	46	12/10/2014	-2.38
OSS-C2	3.7	50.6	46.3	0.7[2]	4571	157	146	18/05/2016	-
OSS-C4	3.7	50.6	46.2	1.0[2]	4679	144	134	14/05/2016	-
WK08-A	2.7	31.4	27.9	-[3]	1729	58	49	17/07/2016	-
WK11-A	2.7	35.0	31.1	-[3]	1655	64	51	01/08/2016	-
WK13-A	2.7	30.0	25.8	-[3]	1889	59	47	20/08/2016	-
WK42-B	2.7	23.0	19.9	0.8[2]	1889	84	73	16/04/2016	-

1. Self-weight penetration of pile only.
2. Self-weight penetration of pile, hammer and follower
3. Measurement not always possible due to poor visibility
4. Plug level is negative where plug is above the seabed

Table 5-5: Significant pauses (>5 min) during test pile installation

Test code[1]	L_p (m)	Blow Number	Duration (mm:ss)	Tip Stratum	$L_{p,\ chlk}$ (m)
WK38-1_DPT_EOP1	6.06	59	42:05	Glacial till	-
WK38-1_DPT_EOP2	13.3	375	28:52	Glacial till	-
WK38-2_DPT_EOP1	5.1	87	43:09	Glacial till	-
WK38-2_DPT_EOP2	10.3	237	10:56	Glacial till	-
WK38-2_DPT_EOP3	13.3	423	31:55	Glacial till	-
WK43-1_DPT_EOP1	11.9	454	16:06	Chalk	1.6
WK43-1_DPT_EOP2	25.4	927	05:51	Chalk	15.1
WK43-2_DPT_EOP	13.9	507	08:54	Chalk	3.6
WK70-1_DPT_EOP	11.7	412	08:25	Chalk	5.1
WK70-2_DPT_EOP1	11.9	389	08:59	Chalk	5.3
WK70-2_DPT_EOP2	24.2	757	25:22	Chalk	17.6
OSS-C2_DPT_EOP	35.7	3510	09:59	Chalk	25.3
OSS-C4_DPT_EOP	36.0	3484	09:43	Chalk	25.6
WK-08A_DPT_EOP	16.7	761	07:16	Glacial till	-
WK-13A_DPT_EOP	15.9	824	07:39	Glacial till	-
WK-42B_DPT_EOP	8.55	536	11:24	Glacial till	-

1. Test code for driving pause: Pile number_Dynamic Pile Test_ End of Pause_Pause number

At the end of installation, the piles had a stick up above the seabed of ≈5m. The internal soil column remained 0.8m above the seabed in the glacial till dominated WK38. At the chalk dominated locations, WK43 and WK70, the soil plug reached ≈2.5m above the sea bed. This indicates that the piles were fully coring during installation (IFR=1), as

expected based on the diameter and the inertia of the plug. At the end of pile installation, the sensor cables from the strain gauges and accelerometers were stored on the seabed using specially designed spools and the piling template was removed.

5.7.2 Static and dynamic testing system

An 18.46m long loading beam was placed with its centre over Pile 2 (Figure 5-31(a)). The loading beam was connected to the test pile (2) via a 1.17m diameter locking tool which fitted into pre-formed grooves in the top of the pile. Pressure plates were connected to the two reaction piles. Four hydraulic actuators were placed on top of the beam, capable of applying a total tensile load of 15MN with a stability of ±150kN. The load was applied to Pile 2 by reacting against the other two piles with load measured by four load cells connected to the actuators. The load cells were accurate to ±50kN with a resolution of ±20kN.

Pile head displacement was measured using the Norwegian Geotechnical Institute (NGI) subsea cylindrical extensometer system with its own independent reference frame. The self-installing system was placed onto a custom made sleeve on the top of the test pile (Figure 5-31(b)) to prevent the sleeve landing on the pile. Three extensometers spaced circumferentially around the pile were fixed between the sleeve and the ring by three latches. The extensometers were made of magneto-strictive linear position transducers, which measure absolute distance between a position magnet and the end of a sensing rod. The NGI system has a travel of 400mm with a very high accuracy and stable resolution, with the displacement measurements kept within the required accuracy of ±0.25mm. The system was rigidly connected to the independent displacement monitoring reference frame, supported by four 8m x 8m mudmats spaced at a distance of ≈13m (9.5D) from the centre of Pile 1.

Dynamic restrike tests were carried out on the dynamically instrumented piles installed at all three sites (WK38-1, WK43-1 and WK70-1) after the static test by first retrieving the cables from the seafloor and checking the functionality, followed by the application of three hammer blows at full energy to Pile 1 using the same hammer as during driving. An underwater camera connected to the displacement reference frame monitored the displacement of the pile per blow, using a pointer system and pre-made pile markings. The primary technical risks associated with undertaking the novel offshore tests were mitigated against by including redundancy in the measurement and loading system.

5.7.3 Static load test procedure

The static loading tests were considered complete when (a) clear pile failure developed giving a total pile head displacement exceeding 10% of the diameter (137.2mm), (b) a creeping failure was observed where the semi-logarithmic creep rate, k_c exceeded 4mm/log cycle after 30 minutes, or (c) the load reached the maximum test load (15MN). The k_c criterion was scaled up from the EA-Pfähle (2014) recommendation to reflect the test pile dimensions, with k_c defined as:

$$k_c = \frac{s_b - s_a}{\log\left(\frac{t_b}{t_a}\right)} \qquad 5\text{-}7$$

where s_a and s_b are the pile head displacements at time t_a and time t_b respectively. The load test procedure and maximum allowable creep values are shown on Figure 5-32.

The pile was loaded in three steps to the designer's characteristic tensile capacity, $R_{t,c}$ (Appendix A-3) followed by unloading to $0.4R_{t,c}$. Loading then continued in incremental steps that varied between 2.5% and 20% of the expected maximum load depending on k_c in the previous step, following EA-Pfähle (2014). Each load step was applied in three minutes giving loading rates of 0.13-1.0MN/min. The general procedure was to apply a loading increment, monitor creep for a minimum of 30 minutes and apply the following criteria:

- If k_c < 2mm/log cycle after 30 minutes the next loading step can be applied as normal. If k_c is between 2mm/log cycle and 4mm/log cycle after 30 minutes half of the next load step is applied;
- If k_c > 4mm/log cycle after 30 minutes, the creep period is extended to 60 minutes and k_c is reassessed. If, after 60 minutes, k_c remains >4mm/log cycle for another 60 minutes, loading is terminated and the pile is unloaded.

The pile was unloaded in four loading steps, the first two reaching $R_{t,c}$ with holding periods of 10 minutes each.

5.7.4 Testing programme

The testing programme and test codes are summarised in Table 5-6. End of driving dynamic tests were conducted on each of the six instrumented piles. After waiting periods of between eleven and fifteen weeks, a static load test was conducted on each test pile followed by a restrike test on an adjacent pile. The equalisation periods were chosen to

allow an estimate of the piles' long-term set-up behaviour to be determined. A limited packet of one-way axial cycling was applied following the static test on WK38-2.

Table 5-6: Summary of pile test codes and test histories during test campaigns

Test pile	Test code[1]	Pile age		Test type
		Days	mins	
WK38-1	WK38-1_DPT_EOD	0	0	Dynamic test end of driving
	WK38-1_DPT_BOR	108	278	Dynamic test beginning of restrike
WK38-2	WK38-1_DPT_EOD	0	0	Dynamic test end of driving
	WK38-2_SLT_108	108	-	Static test on aged pile
	WK38-2_CYC_108	108	-	Post static failure cyclic test
WK43-1	WK43-1_DPT_EOD	0	0	Dynamic test end of driving
	WK43-1_DPT_BOR	78	335	Dynamic test beginning of restrike
WK43-2	WK43-2_DPT_EOD	0	0	Dynamic test end of driving
	WK43-2_SLT_78	78	-	Static test on aged pile
WK70-1	WK70-1_DPT_EOD	0	0	Dynamic test end of driving
	WK70-1_DPT_BOR	77	989	Dynamic test beginning of restrike
WK70-2	WK70-2_DPT_EOD	0	0	Dynamic test end of driving
	WK70-2_SLT_77	77	-	Static test on aged pile
OSS-C2	OSS-C2_DPT_EOD	0	0	Dynamic test end of driving
	OSS-C2_DPT_BOR	0	240	Dynamic test beginning of restrike
OSS-C4	OSS-C4_DPT_EOD	0	0	Dynamic test end of driving
	OSS-C4_DPT_BOR	0	130	Dynamic test beginning of restrike
WK08-A	WK08-A_DPT_EOD	0	0	Dynamic test end of driving
	WK08-A_DPT_BOR1	0	14	Dynamic test beginning of restrike
	WK08-A_DPT_BOR2	0	376	Dynamic test beginning of restrike
	WK08-A_DPT_BOR3	59	230	Dynamic test beginning of restrike
WK11-A	WK11-A_DPT_EOD	0	0	Dynamic test end of driving
	WK11-A_DPT_BOR1	0	15	Dynamic test beginning of restrike
	WK11-A_DPT_BOR2	0	375	Dynamic test beginning of restrike
WK13-A1	WK13-A_DPT_EOD	0	0	Dynamic test end of driving
	WK13-A_DPT_BOR	0	360	Dynamic test beginning of restrike

1. The test code nomenclature gives the pile name (e.g. WK38-1), the type of test (DPT = dynamic pile test, SLT = static pile test CYC = cyclic pile test) and the time of the test (EOD or Beginning of Restrike (BOR) for dynamic tests and number of days for the static tests).

5.8 Production piling dynamic test campaign

At each of the WTG sites, four 2.7m diameter production piles, each with t_w of 40.5-54.0mm, were installed in a grid with the naming convention shown in Figure 5-33. The OSS was supported by six 3.67m diameter piles, with t_w of 50-60mm, installed in a rectangular configuration. One pile was monitored dynamically at each test site during driving in a similar manner to the pre-construction test piles. At the OSS, two of the six

piles were monitored. Six relevant DPTs at five sites have been analysed by the Author, as were summarised previously on Table 5-4.

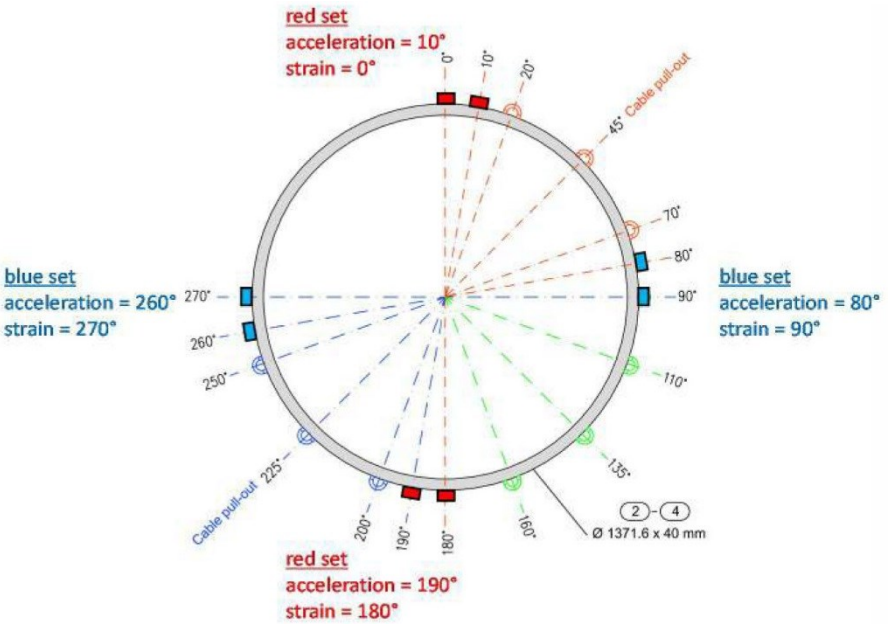
5.8.1 Production pile installation

The production piles were installed using a Menck MHU 1200S under-water hydraulic hammer rated to a maximum energy of 1200kJ above water and a ram weight of 72.8 tons. Four strain gauges and four accelerometers were attached to each test pile which remained 200 to 1000mm above the seabed at the end of installation. The self-weight penetrations of the piles with hammer and follower attached were always less than 1m, where recorded (Table 5-4). Blow count profiles for installation of the six test piles are shown on Figure 5-34 along with the operational pauses during driving where were detailed in Table 5-5. The piles typically penetrated by between 10 and 20mm per blow in both the glacial till and chalk.

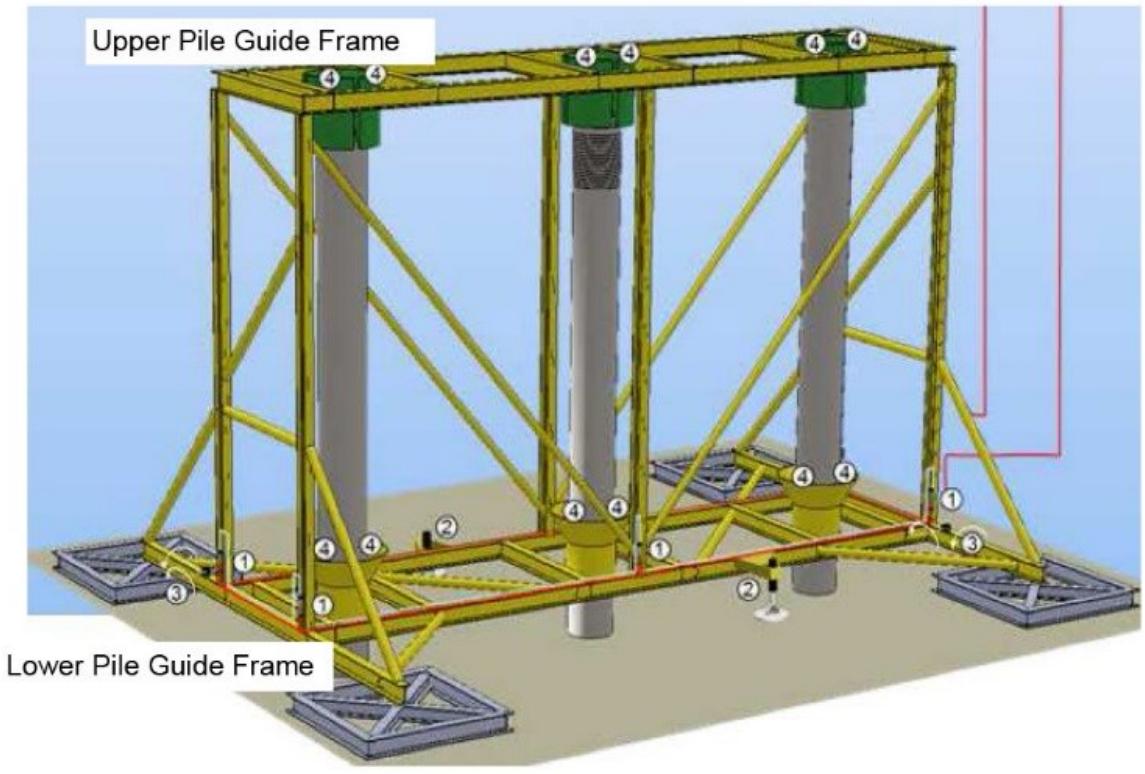
The height of the internal soil column was not measured during production piling. However, a dredge tool was required to remove the soil from all piles above the last shear key, located 4m from the pile top. This indicates that, similar to the pre-construction test piles, the production piles were fully coring during installation. The sensor cables from the strain gauges and accelerometers were again stored on the seabed ready for the subsequent restrike test.

5.8.2 Testing programme

Similar to the pre-construction campaign, EoD tests were conducted on each of the piles (Table 5-6, previously). Restrike tests were then conducted at times after installation of between 14 minutes and 67 days. The aim of the restrike tests was to confirm the pile capacity which in some cases (as at WK08) led to the application of multiple restrike tests to the same pile.



(a)



(b)

Figure 5-29: Pile installation at Wikinger (a) schematic of sensor positions around the test piles (b) Triplex template used to guide installation of test piles (Bilfinger, 2015a)

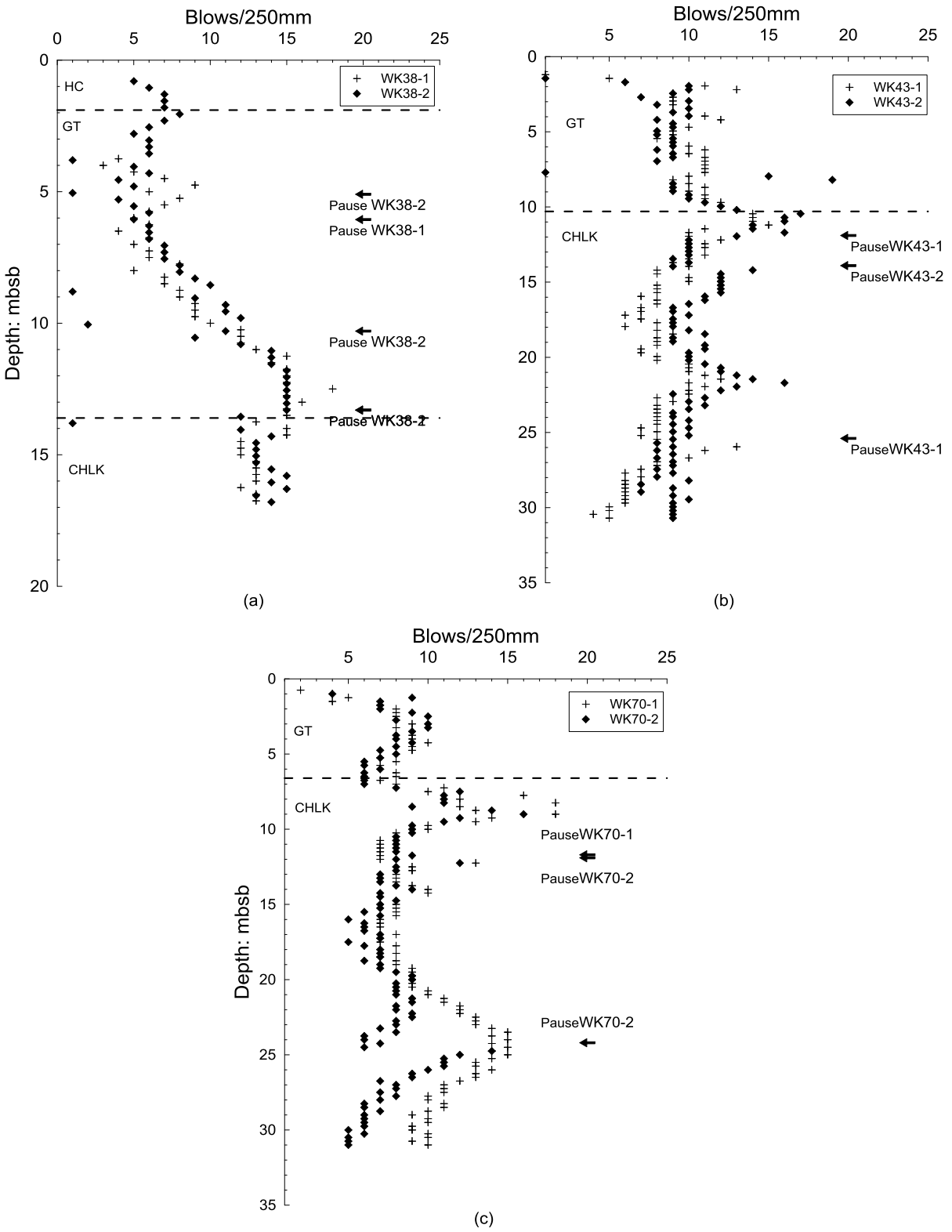
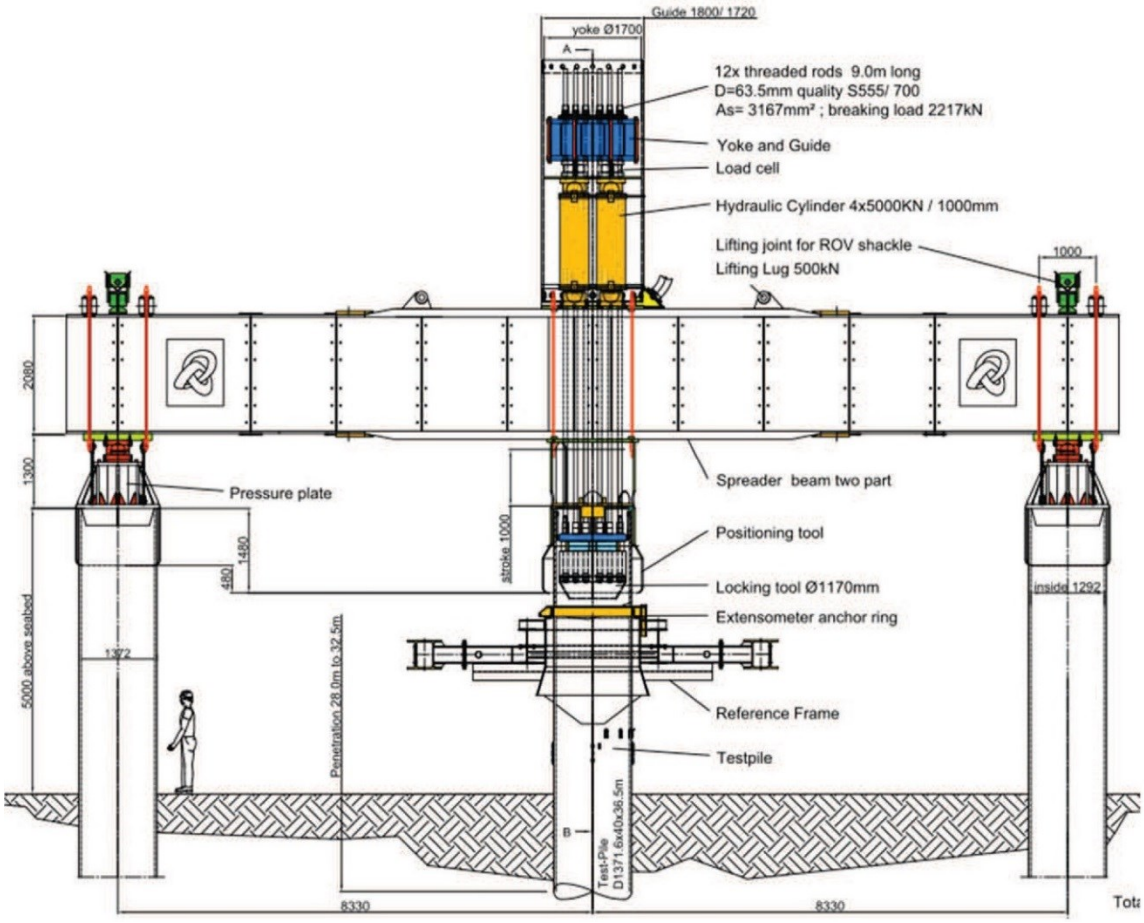
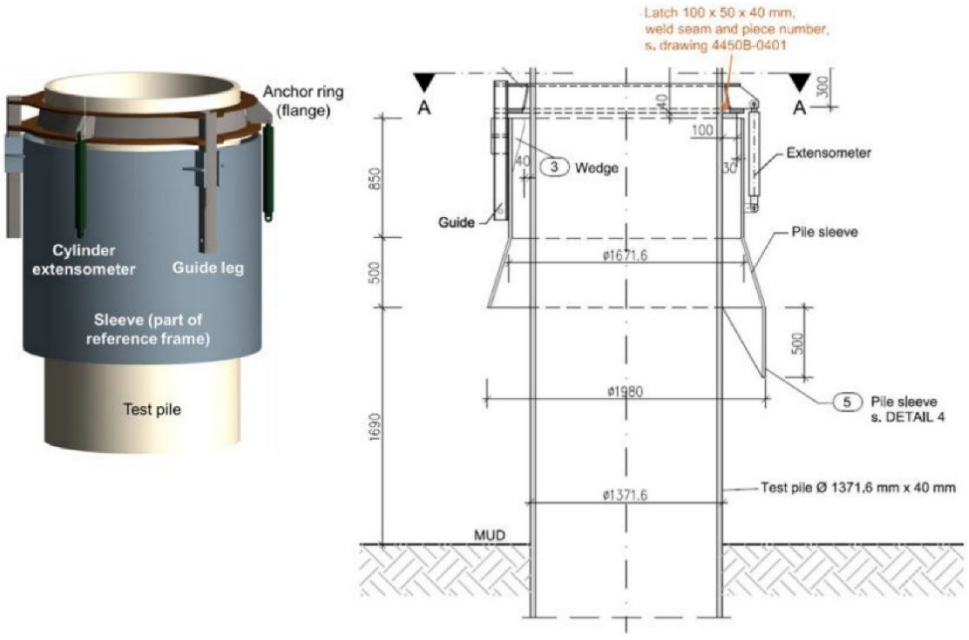


Figure 5-30: Recorded blow counts during installation of PC test piles including pauses during installation detailed in Table 5-5 (a) WK38 (b) WK43 (c) WK70



(a)



(b)

Figure 5-31: Offshore tensile load test system at Wikinger (a) test pile configuration and spreader beam (b) displacement monitoring system (Bilfinger, 2014)

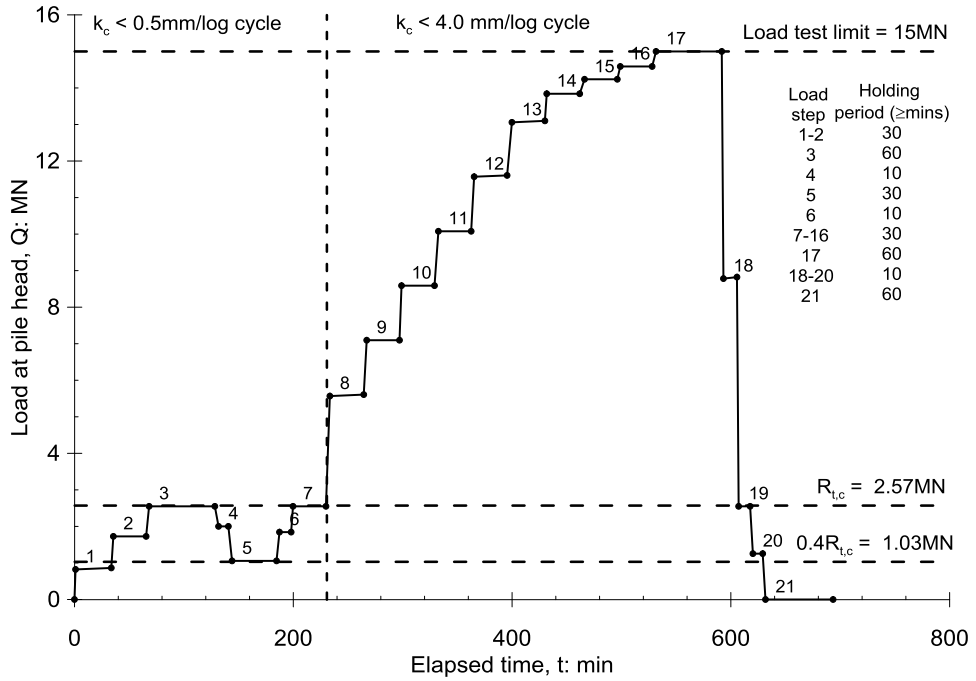


Figure 5-32: Static test loading procedure for offshore tests at Wikinger for loading up to 15MN (adapted from Bilfinger, 2014)

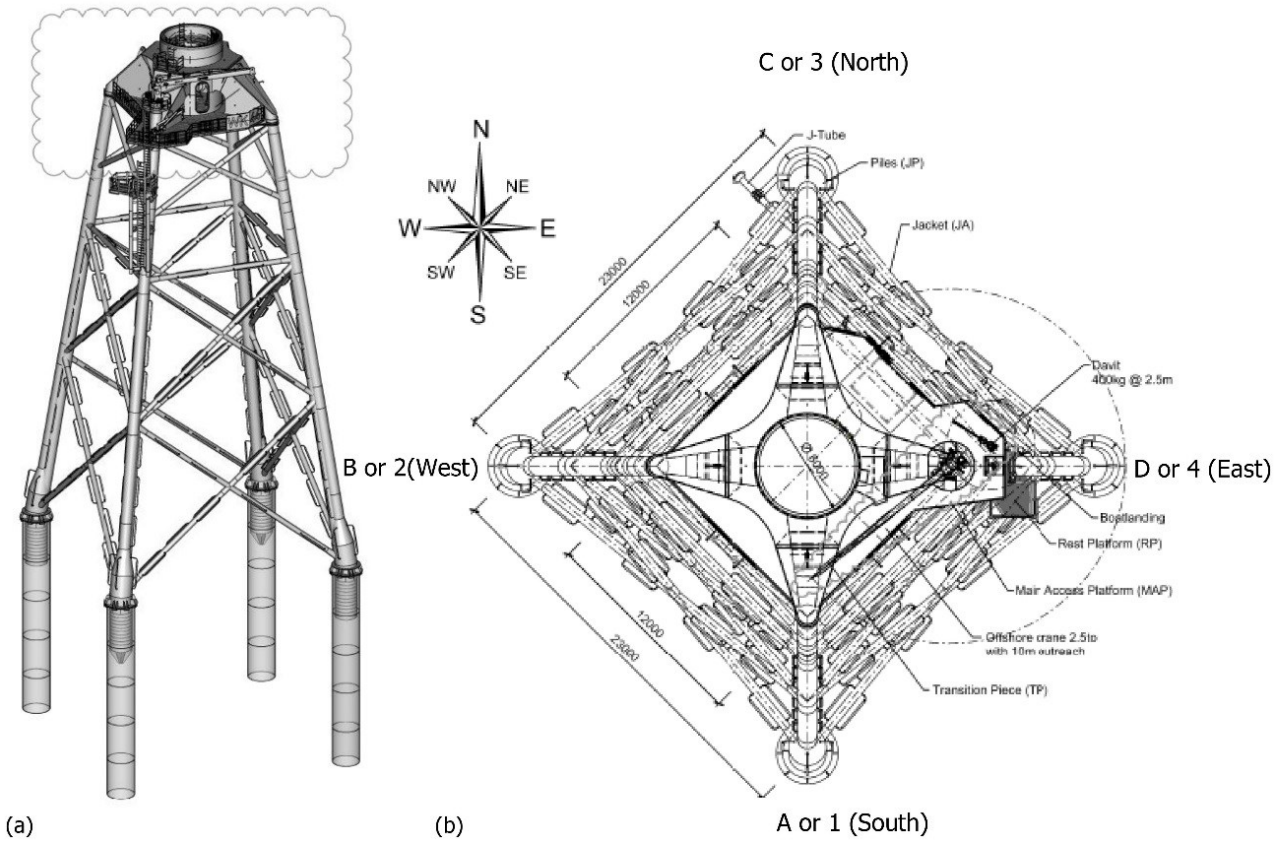


Figure 5-33: Jacket foundations at Wikinger (a) Isometric 3D view of the jacket foundation (b) jacket plan view from top to bottom showing pile locations (CIJV, 2016)

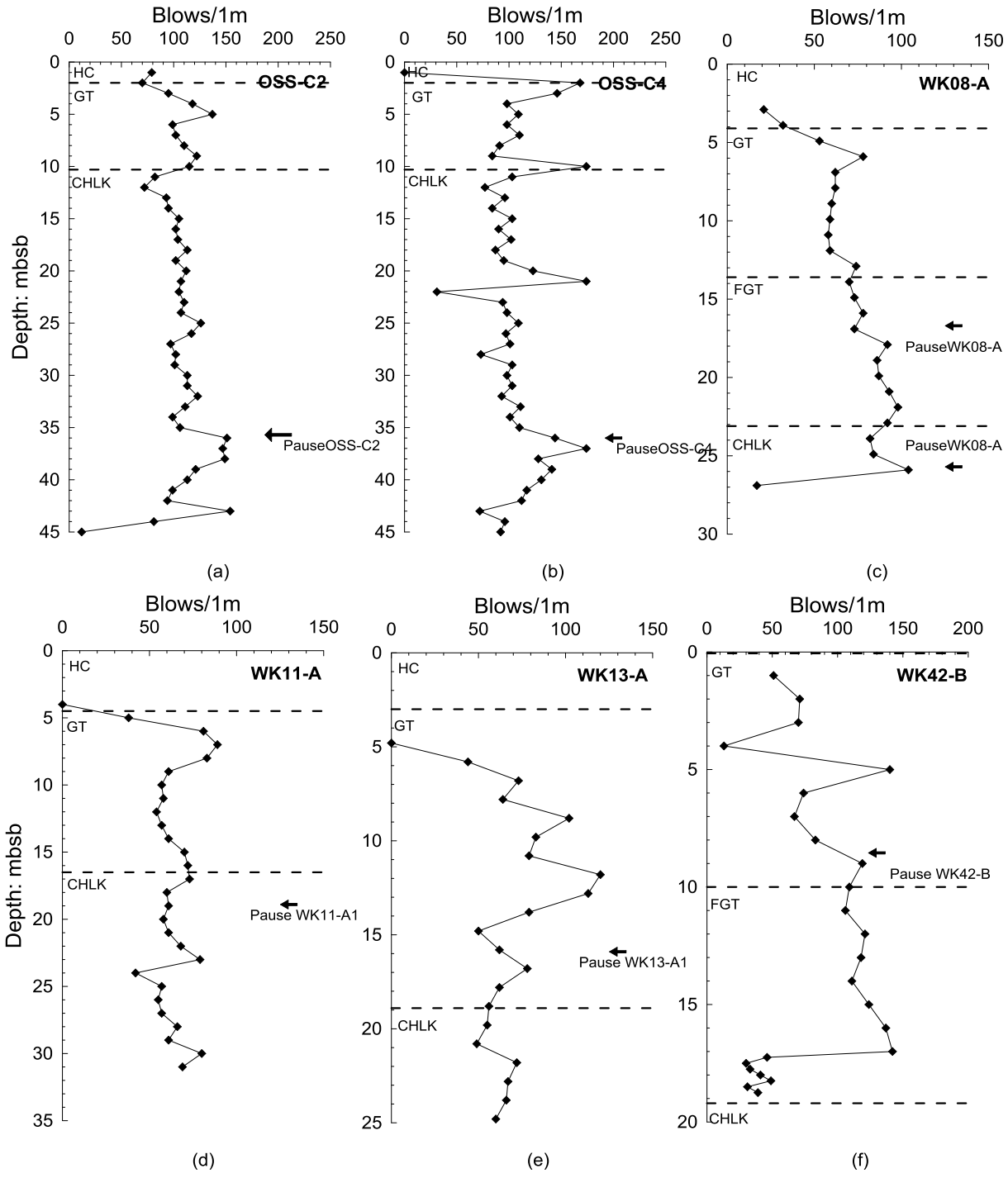


Figure 5-34: Blow counts recorded during installation of production piling DPTs at Wikinger

5.9 Results & interpretation

The results of the static and dynamic pile tests from both the pre-construction and production piling campaigns are considered within this section, broadly separated into; (a) base capacity from dynamic tests (b) installation pile resistance, (c) changes in installation resistance with driving (d) load displacement behaviour during static tension tests (e) prediction of capacity in the glacial till and (f) time effects on capacity.

5.9.1 Adopted dynamic parameters for signal matching

Methods of back analysis of dynamic pile tests were discussed in Chapter 4. The change in pile capacity with pile penetration can be determined from the results of signal matching, allowing assessment in given layers of any relative penetration or "h/R*" effects, where h is distance of any horizon layer above the pile tip and R* is the effective pile radius for an open-ended tubular pile. Blows near the end of driving can be used to assess the short-term capacity of each pile, and as a reference point to assess pile ageing by comparison with a blow after installation e.g. at beginning of restrike (BoR). The Author's analysis of the Wikinger dataset employed the IMPACT software (Randolph, 2008) adopting the Randolph and Simons (1986) soil model for the shaft and the Deeks and Randolph (1995) model at the toe. In both models, the input parameters are linked to measurable soil properties as discussed in Chapter 4.

First estimates of the shaft and base resistance were gauged from the site investigation. The soil density and shear moduli, G, were determined from the results presented in Section 5.5 and 5.6. As discussed in Chapter 4, the values of G were secant values, G_1 degraded from the small strain, G_{max} values to account indirectly for soil non-linearity following Alves *et al.* (2009) and Salgado *et al.* (2015). In the glacial till, the best matches were obtained using G_1 close to $200\sigma'_{vo}$ following the recommendations of Lee *et al.* (1988) for sandy soils which resulted in G_1/G_{max} ratios of <0.3. In the chalk, the trend with depth obtained from the P-S logging V_s measurements was used to estimate G_{max} with depth (Eq. 5-5), which was then reduced to $G_1=0.2G_{max}$ for input into the program. The same values of shear modulus were adopted at the end of driving and beginning of restrike, effectively assuming that the degraded secant stiffnesses are unaffected by time over these strain ranges (see Figure 5-26).

The viscosity parameters, α_s and β_s (Eq. 4-40) along the shaft were adopted based on the correlations given by Loukidis *et al.* (2008) based on Lee *et al.* (1988) who collated the data from various experimental studies. For clays, $\beta_s = \beta_b = 0.2$ and the value of α_s at the shaft is given by:

$$\alpha_s = 1.65 - 0.75\left(\frac{s_u}{p_a}\right) \quad 5\text{-}8$$

Where p_a is atmospheric pressure. For both the till and the chalk, β_s was taken as 0.2 consistent with the recommendation of Randolph (2008). The adopted value of α_s in the chalk was 1.1, taking s_u from remoulded samples to reflect the soft behaviour expected in the annulus of chalk putty close to the shaft. However, substitution of the intact strength for glacial till into Eq. 5-8 gives a negative value of α_s, as the correlations were not developed for high strength insensitive clays such as those encountered at Wikinger. In the glacial till, a value of α_s of 1.15 has been adopted, which gave the best quality signal matches. This value is consistent with the ranges given in Table 4-1 for clay, and with Randolph (2008) who advocates α_s up to 1 and higher for clay soils.

IMPACT includes explicit modelling of internal shaft resistance (Randolph, 2008). For the cases investigated, similar quality signal matches could be obtained by varying the ratio of internal to external shaft resistance from zero to 0.2. The quality of the signal match reduced significantly if the ratio of internal to external shaft resistance increased above 0.2. The piles were fully coring during installation and therefore it was assumed that shaft resistance occurred on the external area only to simplify the analyses. Residual base stresses were ignored. The signal match quality (Eq. 4-57) for the total of 70 blows analysed from Wikinger during this study ranged from 1.18% (good) to 3.84% (good/fair) with a mean of 2.85% (good/fair) and a standard deviation of 0.69%. A summary of governing equations and parameters adopted during the signal matching analyses at Wikinger is given in Table 5-7.

Table 5-7: Summary of equations and adopted parameters using models in IMPACT

	No.	Glacial till	Chalk
Shaft resistance	$\tau = k_s w + c_s v \le \tau_{stat}$		
Spring	$k_s = \frac{G}{\pi D}$		
Radiation dashpot	$C_s = \frac{G}{V_s} = \sqrt{G\rho_s}$	$G = G_1$ $G_1 = 200\ \sigma'_{vo}$ (MPa) $\rho_s = 2.2$ G/cm^3 $\alpha_s = 1.15$ $\beta_s = 0.2$ $\nu = 0.5$	$G_{max} = (895+17.3z)$[1] $G = G_1 = 0.2\ G_{max}$ (MPa) $\rho_s = 2.2$ G/cm^3 $\alpha_s = 1.1$ $\beta_s = 0.2$ $\nu = 0.5$
Viscous effects	$\tau_{inter} = \tau_{stat}\left(1 + \alpha_s\left(\frac{\Delta v}{v_0}\right)^{\beta_s}\right)$		
Base resistance	$Q = K_b w + C_b v \le q_{b,stat}$		
Spring	$K_b = \frac{4GR}{(1-\nu)}$		
Radiation dashpot	$C_b = \frac{4R^2}{(1-\nu)} 0.8\sqrt{G\rho_s}$		
Subsidiary mass	$m_0 = 0.16\frac{4R^3\rho_s}{(1-\nu)}$		

1. Trend from P-S measurements across the site

5.9.2 Base resistance from dynamic tests

Field research with the Imperial College Pile showed that static end bearing was related to cone resistance in sands and clays (Jardine *et al.*, 2005a). In that method, annular base resistance at static failure, $q_{ba,\ 0.1D}$ is, for fully coring piles in sands, taken equal to the cone resistance $q_{c,1.5D}$, averaged 1.5D above and below the penetration depth to account for partial embedment effects. The method acknowledges that this may overestimate the true annular resistance and make allowance for a small contribution from the internal shaft friction. For fully coring piles in clay, $q_{ba,0.1D}$ is taken similarly as $q_{c,1.5D}$ with values 60% higher possible if loading occurred sufficiently slowly to allow drainage to occur. The UWA-05 (Lehane *et al.*, 2007) method for sands assumes that full plugging occurs during static loading and gives $q_{b,0.1D}$ equal to approximately $0.2q_{c,1.5D}$ for a typical tubular offshore pile with D/t_w=40, with $q_{b,0.1D}$ applied over the gross area including the plug. Both methods are intended to represent the static base capacity after full equalisation, and the interaction between the pile and soil during driving is not considered.

The base resistance mobilised during a dynamic pile test can be more difficult to ascertain than the shaft resistance, due to the difficulties separating the response from the lower shaft elements and the base itself. In addition, the displacement mobilised during a dynamic pile test is generally less than the criterion of 10%D which defines static capacity. Back analyses of open-ended pile driving records indicate ratios of q_{ba}/q_t of 0.6 for clays, 0.35 for loose sands and 0.55 for dense sands (Alm and Hamre, 2002, Schneider and Harmon, 2010). There is currently no information in the literature which describes the partial mobilisation of q_{ba} in chalk during driving.

Base resistance is available from the 70 driving blows analysed at Wikinger as part of this study. The Wikinger piles were fully coring during installation therefore the base resistance mobilised during a hammer blow is assumed to act on the steel annulus, with q_{ba} less than $q_{ba,0.1D}$. The resulting $q_{ba}/q_{t,1.5D}$ ratios in the glacial till varied with pile displacement and ranged from 0.16 to 0.75 with a mean of 0.48 and a standard deviation of 0.16. As discussed in Section 5.9.1, shaft resistance was assumed to act on the external area only. In the chalk, ratios of $q_{ba}/q_{t,1.5D}$ also varied with displacement per blow, generally ranging from 0.25 to 0.80 with a mean of 0.51 and a standard deviation of 0.14.

5.9.3 Pile resistance at the end of installation

Figure 5-35 shows examples of the compressive local dynamic shaft resistance, $\tau_{s,d}$ with depth interpreted from the dynamic measurements made during the pre-construction pile test campaign. An example signal match is shown on Figure 5-36 in terms of the measured and back calculated force (F) and velocity times impedance (Zv) signals, the upward wave and the measured and calculated displacement.

At the end of driving, the shaft resistance mobilised in the soft Holocene deposits appears to be negligible. Values in the glacial till lie primarily between 30 and 200kPa and show a tendency to reduce with h/R*, e.g. Figure 5-35 (a). The results at WK38 indicate variations in mobilised shaft resistance in the glacial till even between piles at the same location which may be attributable to the presence of sand lenses within the deposit. A similar trend of dependence on h/R* is observed in chalk with $\tau_{s,d}$ up to 300kPa observed close to the pile tip, reducing to values as low as 10kPa higher up along the shaft. The presence of the high to very high density chalk (or Danian Limestone) layer shown on Figure 5-18 (a), was reflected in the end of driving data at this location with $\tau_{s,d}$ reaching 80kPa between approximately 10 and 15mbsb at both locations and falling outside the general trends discussed above for the lower density chalk (Figure 5-35(c)).

In the majority of cases, any increases in capacity developed at discrete depths over pauses in pile driving disappeared after driving recommenced and progressed and were hardly evident at the end of driving, suggesting any capacity increase is destroyed by the effects of continued driving, as discussed further in Section 5.9.6.

The end of driving shaft, base and total capacities found by signal matching analyses on all twelve test piles examined from the pre-construction and production test campaigns are summarised in Table 5-8 along with τ_{avg}, the dynamic test shaft capacity averaged along the *shaft length*. Along the shaft, τ_{avg} can be seen to reduce with increasing penetration, with the lowest value of 24kPa being associated with the maximum penetration of the pile into chalk of 36m (OSS-C2_DPT_EOD). The relationship between the degree of penetration into chalk, or the effect of h/R*, and mobilised shaft resistance, as the pile penetrates, was explored further using the dynamic monitoring data, as discussed in the following section.

Table 5-8: Pile capacities at the end of driving for all twelve EoD tests

Test code	Q_s (MN)	Q_b (MN)	Q_{tot} (MN)	τ_{avg}[1] (kPa)	L_p (m)	$L_{p,chlk}$ (m)
WK38-1_DPT_EOD	4.76	2.85	7.61	67	16.6	3.0
WK38-2_DPT_EOD	5.34	3.35	8.69	75	16.6	3.0
WK43-1_DPT_EOD	3.46	1.34	4.80	26	30.7	20.4
WK43-2_DPT_EOD	4.78	3.35	8.13	36	30.7	20.4
WK70-1_DPT_EOD	5.31	2.01	7.31	40	31.0	24.2
WK70-2_DPT_EOD	4.61	1.17	5.78	35	31.0	24.2
OSS-C2_DPT_EOD	12.84	8.14	20.98	24	46.3	36.0
OSS-C4_DPT_EOD	15.36	4.07	19.43	29	43.3	36.0
WK08-A_DPT_EOD	14.23	3.05	17.28	60	27.9	4.8
WK11-A_DPT_EOD	7.65	5.41	13.07	30	31.1	14.6
WK13-A_DPT_EOD	14.80	0.68	15.48	67	25.8	6.9
WK42-B _DPT_EOD	14..09	3.05	17.14	86	19.9	0.7

1. Along the whole pile length in glacial till and chalk

5.9.4 Effect of penetration depth on shaft resistance during driving

The change in shaft capacity with increasing pile penetration in chalk was investigated by examining blows recorded during different stages of the driving process for the test piles. The tendency for local $\tau_{s,d}$ to reduce with increasing h/R* was used to evaluate a general trend for chalk. A total of 14 blows, summarised on Figure 5-37, were analysed to examine the effects of "continuous" pile driving prior to any interruptions. Pauses in pile driving are known to significantly affect capacity and to disrupt the "h/R*" trends (discussed later). The pile diameter ranged from 1.37 to 3.67m, the penetration into chalk varied from 14.9 to 25.6m and h/R* varied between 1.0 and 52.5. The data shown on Figure 5-37 were obtained in the following manner:

- For each signal match carried out, the resulting values of $\tau_{s,d}$ were converted to initial radial effective stresses at failure, σ'_{ri} taking $\sigma'_{ri} = \tau_{s,d}/\tan\delta'_{ult}$, with δ'_{ult} equal to 32° (Section 5.6.6);
- The resulting σ'_{ri} values were normalised by the corrected cone resistance, q_t at the relevant depth and plotted against h/R*. Normalisation of σ'_{ri} in this manner assumes that there is a link between σ'_{ri} and cone resistance for chalk, as has been found in sands (Chow, 1997), which is discussed further in Chapter 7.

Also shown on Figure 5-37 are the trends interpreted from the static ICP sand design method (Jardine *et al.*, 2005a) and the industry's best current method for predicting soil resistance to driving in sands (Alm and Hamre, 2002). The trends shown are for a

40m long 3.67m diameter pile and a constant q_t profile of 15MPa. Figure 5-37 shows the interpreted power law trend between σ'_{ri}/q_t and h/R* and indicates a tendency for the magnitude of degradation to increase slightly with pile diameter which is not fully captured by the inclusion of the equivalent radius R*. The latter suggests a further parameter is required to capture these effects, which is discussed further in Chapter 8.

5.9.5 Long-term load displacement behaviour

(a) Glacial till dominated WK38

The static load test at WK38-2 on the relatively short (16.6m penetration) pile installed primarily in glacial till gave the load displacement results shown in Figure 5-38. The net pile head loads (less the weight of the soil plug and steel), Q_{net}, have been converted to τ_{avg} along the pile length ($\tau_{avg}=Q_{net}/\pi DL_p$), to allow results from piles of different length to be compared. It is assumed that no negative end bearing occurs since the piles were founded in fractured chalk which is relatively free draining. The following points are noted with respect to Figure 5-38:

1. Static tension failure was reached at a net pile head load of 8.8MN (τ_{avg}=122kPa) and a displacement of ≈20.7mm. The pile did not develop a brittle failure but exceeded the creep load failure criterion when the final load step was applied. The pile underwent an additional 8.5mm of displacement at a rate of 0.07mm/min under constant load until unloading commenced;
2. The creep rates, k_c developed under constant load remained less than 0.1mm/log cycle until loading increased beyond $R_{t,c}$ after which the creep rates followed a power law trend with increasing load (Figure 5-39 (a)). The failure load corresponded to a creep load of ≈3.5mm/log cycle;
3. The failure shaft resistance was 65% higher than that measured in WK38-2_DPT_EOD indicating an *overall* (glacial till and chalk) set-up factor of 1.65, assuming that tensile and compressive shaft resistances are equal. A higher factor would apply if tension resistance was lower than compression resistance;
4. The restrike test carried out on the adjacent pile at the same age, WK38-1_DPT_BOR gave a compressive τ_{avg} of 136kPa which was 11% higher than the static tensile failure resistance;
5. The designers' expected characteristic design resistance of 80kPa (detailed in Appendix A-3), falls close to that measured at EoD. The designers' upper bound

prediction for failure resistance of 207kPa was 70% higher than the static failure value.

Following the static test, the pile was unloaded to near zero load and two packets of one way axial cyclic loading were applied at two loading levels (Figure 5-40). The first consisted of 10 cycles at a utilisation ratio (UR) or inverse factor of safety (FoS) of 0.62 times the static failure load. The loads were then increased to give a UR of 0.84 for 10 further cycles. The permanent accumulated cyclic displacements, shown on Figure 5-41(a) normalised by pile diameter, remained low (<0.05%) for the first 10 cycles. When the loads were increased, displacements accumulated rapidly at ≈1mm/cycle, reaching 15mm or 1.1% D at the end of the test.

The cyclic loading and unloading stiffnesses, shown on Figure 5-41(b) normalised by the stiffness in the first cycle, exhibit a similar trend. Very little change in stiffness was observed over the first 10 cycles, but the final 10 cycles led to stiffness reductions between 25 and 35% by the end of the test. The cyclic loading results are not surprising considering the loading levels applied maximum loads to within 13% of the peak capacity (FoS ≈ 1.13). It was intended to carry out the single cyclic loading test at a chalk dominated location which was thought to be more susceptible to cyclic loading, however this proved impossible for operational reasons. Nonetheless, the result represents the only offshore axial static and cyclic load test in glacial till, reported to date, of which the Author is aware.

(b) Chalk dominated WK43 and WK70

The static load tests on WK43-1 and WK70-2 with ≈31m long piles installed predominantly in chalk gave the load displacement results plotted in Figure 5-42 and Figure 5-43. Ultimate failure conditions were not achieved in either test, as the safe structural limit of the test rig was reached, at 15MN (τ_{avg}≈106kPa), before the failure of either pile occurred. It is worth noting that the maximum test rig limit was designed based on the upper bound designers' estimate for WK38 (Appendix A-3) and the higher capacities that developed at the chalk dominated sites were unexpected by the designers.

A number of methods exist to extrapolate incomplete pile load tests. The five that have been used to predict the piles' ultimate capacity are summarised in Appendix A-3. Three of the methods assume a hyperbolic or parabolic load displacement curve and extrapolate the result accordingly (Chin, 1970, 1971, Brinch Hansen, 1963, Decourt,

1999). The fourth and fifth methods are based on extrapolation of the semi-logarithmic creep rate, k_c versus applied load curve to criteria of 3mm/log cycle and 4mm/log cycle, respectively. All five methods were checked through application to the test which reached full failure (WK38-1_SLT_108). The hyperbolic/parabolic extrapolation methods over-predicted the result by between 15 and 60%. Extrapolation of the k_c-τ_{avg} curve to k_c between 3mm/log cycle and 4mm/log cycle led to values which were within 5% of the actual failure load, and this method appears the most appropriate.

Figure 5-42 and Figure 5-43 show the range of values resulting from the application of all five extrapolation methods. For both WK43-2_SLT_78 and WK70-2_SLT_77 the failure load adopted for analysis of the results is that found from extrapolation of the k_c-τ_{avg} curves to k_s of 3 mm/log cycle, as shown in Figure 5-39 (b) and (c).

The following points are noted in relation to the WK43-1_SLT_78 test as shown on Figure 5-42:

1. The limit of the test rig, which was sufficient to mobilise τ_{avg} of 106kPa at a displacement of 10.1mm, was 2.9 times higher than the characteristic design load (Appendix A-3) and 15% higher than the designers' upper bound capacity estimate for that pile. In fact, the designers' characteristic resistance of 37kPa was close to that measured at the end of driving (WK43-2_DPT_EOD);
2. Extrapolation of the k_c-τ_{avg} curve to a k_c of 3mm/log cycle indicated failure with τ_{avg} of 158kPa, representing a 440% increase in overall (glacial till and chalk) shaft resistance over that measured in WK43-2_DPT_EOD, under compressive loading;
3. The restrike test carried out on the adjacent pile at the same age, WK43-1_DPT_BOR gave a compressive τ_{avg} of 138kPa, 13% lower than the extrapolated tensile failure load;

At the second chalk dominated test site the following points are noted in relation to WK70-2_SLT_77 and Figure 5-43:

1. The limit load of the test rig was reached at a displacement of 6.1mm. The deviation of the maximum load from the designers' expected value was similar to that seen in WK43-1_SLT_78;

2. Extrapolation of the k_c-τ_{avg} curve to 3mm/log cycle indicated tensile failure at an average τ_{avg} of 168kPa. This *overall* failure resistance (in the glacial till and chalk) was 490% higher than that measured under compression in WK70-2_DPT_EOD;
3. The restrike test carried out on the adjacent pile at the same age, WK43-1_DPT_BOR gave τ_{avg} of 207kPa, 23% higher than the extrapolated static tensile failure load.

The stiffness evolution with loading for all three static tests has been considered using the loading stiffness, k_{stat} (=ΔQ/disp) defined from a reference point, which was taken after the unload reload loop shown on Figure 5-32. The stiffness is normalised by the initial maximum reference secant stiffness, $k_{s,ref}$, defined by considering the first load step, $Q_{s,ref}$ defined at the same reference point. The stiffness ratio $k_{stat}/k_{s,ref}$ is plotted against the ratio $Q/Q_{s,ref}$ on Figure 5-44 for the load steps following the unload-reload loop. The global secant stiffness is shown to be highly non-linear. The un-failed response of WK43 and WK70 are naturally stiffer than that of the failed shorter pile, WK38-2, whose secant stiffness had reduced by over 90% by the point when failure was reached. However, the unfailed piles show a continued reduction in stiffness with loading, and had reduced by more than 80% when loading had to be halted at the safe limit of the test rig.

The static test results, summarised in Table 5-9, demonstrate that aged pile capacity is far greater 11 to 15 weeks after installation than at the end of driving. The magnitude of this capacity increase was observed to be significantly greater at the two chalk dominated sites. The interpreted shaft and base resistances, from the signal matching analysis in the chalk and glacial till at end of driving and after equalisation periods are discussed next, to investigate these trends further.

Table 5-9: Static tension failure loads for offshore pile tests at Wikinger

	WK38-2	**WK43-2**	**WK70-2**
Time after driving (days)	108	78	77
Tensile failure load, Q_t (MN)	9.33	-	-
Pile and chalk self-weight (MN)	0.53	0.87	0.87
Net tensile failure load, Q_{net} (MN)	8.80	20.90*	22.44*
Average tensile shaft resistance, τ_{avg} (kPa)	122	158*	168*
Compressive EOD shaft load, Q_s (MN)	5.34	4.78	4.61
Global set up factor, Λ	1.65	4.37	4.86

* Based on extrapolation of creep rates to k_c = 3mm/log cycle

5.9.6 Time effects on shaft resistance from dynamic tests

The increases in pile capacity with time observed during the static tests can be further explored by analysis of the dynamic monitoring data, employing two specific datasets for this purpose:

1. Comparing the capacity analysed from the beginning of restrike (BoR) blow recorded after 11 to 15 week equalisation periods with the corresponding EoD blow on the same pile;
2. Comparing, over the driving pause periods, the capacities from end of pause (EoP) blows with the corresponding beginning of pause (BoP) blows on the same pile.

The effect of a pause period on the force (F) and velocity times impedance (Zv) signal *measured* during a dynamic test is demonstrated on Figure 5-45 at EoD and BoR on the same pile, 77 days after installation. A clear increase in the measured F trace is observed in the +77 day blow, along with a decrease in measured Zv. Recalling from Chapter 4 that an increase in the measured upward wave, F_{up} indicates an increase in shaft capacity and that $F_{up} = (F-Zv)/2$, indicates a significant increase in capacity over this time period. A similar trend for F_{up} to increase with time is observed over operational pauses in driving as demonstrated on Figure 5-46, where the upward wave, F_{up} from the blow immediately after and immediately prior to a driving pause are compared.

Figure 5-47 shows typical profiles of local $\tau_{s,d}$ along the pile length obtained from back analysis of the dynamic tests at EoD and BoR at two locations. It is useful at this point to consider the effects of continued driving on capacity which has increased with time during an equalisation period or over a driving pause. Repeated high energy blows and increasing pile penetration are expected to negate any beneficial time effects on capacity. To illustrate the effect of multiple restrike blows on mobilised capacity, a signal match was performed on the first 100% energy restrike blow along with subsequent blows during the same restrike test at WK11-A, WK13-A1, WK43-1 and WK70-1. The length of the pauses was given previously in Table 5-5. Figure 5-48 plots the set-up factor obtained at each blow against number of restrike blows for (a) chalk and (b) glacial till. For WK43-1 and WK70-1 where the piles penetrated between 20.4 and 24.2m into chalk, a reduction in capacity of between 10 and 15% is observed between the first and second full energy blows. For WK11-A, which had a penetration into chalk of 14.6m at the time of restrike, the set-up reduced by 11% between blows 1 and 5 and by a further 7% between blows 5 and 10. WK13-A, which penetrated 6.9m into chalk, reduced by 16% over the

first and second blows. In the glacial till, with the exception of WK43-1, the results indicate small variations in the set-up trends with number of blows.

A similar analysis can be carried out over the operational pauses in driving. Following Figure 5-46, Figure 5-49 shows, at the same location WK70-1, the shaft resistance back analysed from the blow (i) immediately prior to the pause (412) (ii) immediately following the 8 minute pause (413) and (iii) 2, 7, 17, 27 and 37 blows after the end of the pause, equivalent to further penetrations of 0.04, 0.15, 0.4, 0.7 and 1.0m. Shaft capacity can be seen to increase markedly in chalk over the 8 minute pause in driving, indicated by the shaded portion in the figure, by factors of 1.2 in the glacial till and 2.0 in the chalk. The capacity reduces with further driving, at a more significant rate per blow than seen when multiple blows are applied to equalised capacity during a restrike test (Figure 5-48), with the majority of the beneficial time effects being destroyed once the pile had penetrated by a further 1m or approximately 30 blows.

The results further illustrate the strong degradation which can occur in chalk capacity under hammer blows, and that multiple restrike tests can lead to disruption of set-up trends in a similar manner to repeated static tests on the same pile.

5.9.7 Quantification of set-up trends

In total, 26 cases are available to examine dynamically tested set-up trends over both long-term equalisation periods and operational pauses. Although noting that changes in Q_b with time are more difficult to ascertain, due to the relationship between displacement per blow and capacity mobilisation, the results indicate that only modest changes in base capacity, Q_b occur over time (<20%) which did not appear to be related to the founding material.

The set-up factors for shaft capacity are interpreted from the trends shown on Figure 5-50 for glacial till and Figure 5-51 for chalk. The τ_{avg} values were close to 38kPa at EoD in the glacial till. Figure 5-50 (a) indicates that set-up in the glacial till developed gradually, and was generally less than 2 with a maximum factor of approximately 3.2 seen in WK43-1_DPT_BOR at 78 days. Empirical relationships have been suggested to represent such trends in clays and sands (Skov and Denver, 1988, Mesri *et al.*, 1990, Bogard and Matlock, 1990, Tan *et al.*, 2004). The set-up in the glacial till may be incomplete as the trend of capacity increase does not appear to stabilise with time. As a result, the semi-logarithmic time function suggested by Skov and Denver (1988) appears

appropriate for the glacial till. The trend, also shown on Figure 5-50 (a), calculates the set-up factor, Λ as;

$$\Lambda = \frac{\tau_{avg}(t)}{\tau_{avg}(t = t_{ref})} = 1 + M\log\left(\frac{t}{t_{ref}}\right) \quad 5\text{-}9$$

Where $\tau_{avg}(t)$ is the resistance measured at time, t after installation and $\tau_{avg}(t= t_{ref})$ is the initial reference resistance measured at time, t_{ref}. The parameter M depends on soil type and represents the capacity change with time. The trend shown in Figure 5-50 corresponds to $t_{ref} \approx 0.01$days and M = 0.4, which gives a 40% increase in capacity per log cycle of time. Over the installation pauses in the glacial till, which varied from 2 to 43 minutes, very little change in capacity was observed, with the set-up factor remaining close to 1.

Applying the analytical approach of Teh and Houlsby (1991) allows an estimation of the time for 50% dissipation of excess pore water pressure dissipation, or 50% of capacity gain to occur. In the absence of dissipation tests, a coefficient of horizontal consolidation c_h of $\approx 2x10^{-7}$ m^2/s is estimated based on the range given by Robertson *et al.* (1992) for glacial till. Scaling up the pore pressure dissipation times for a standard 43.8mm diameter PCPT by the ratio (R^*/R_{cpt}), and using a rigidity index, I_r of 500, indicates times for 50% pore water pressure dissipation of 7 and 23 days for the 1.37m and 3.7m diameter piles respectively. This is in broad agreement with the trend shown in Figure 5-50, which indicates that set-up was still ongoing at these times, and was not fully complete when the final test was conducted.

The τ_{avg} developed in the chalk at EoD depended strongly on the degree of penetration of the pile tip into the layer, reducing from 123 to 17kPa after penetrations into chalk of 4.8 and 36m respectively. Installation pause data indicate that set-up in the chalk, shown on Figure 5-51, occurred instantaneously with shaft resistance doubling in as little as 8 minutes and reaching four-fold after 90 minutes, consistent with observations made by Dührkop *et al.* (2017) as discussed in Section 4.9.3. Set-up factors reached between 5.3 and 5.8 after 78 days (Figure 5-51) and again appeared affected by the amount of penetration into the material. For penetrations into chalk of less than 5m (generally less than 20% of total penetration), the maximum set-up factor was between ≈2 and 3 over the same 78 day time period. The trends in capacity increase are therefore related to the trends in h/R* (Figure 5-37), as is discussed further in Chapter 8.

The hyperbolic relationship between capacity gain and time, suggested by Tan *et al.* (2004) appears appropriate for the chalk and has been fitted to the data where $L_{p,chlk}$

was greater than 5m (h/R* > 21 for the 1.37m diameter piles and 12 for the 3.7m diameter piles) as shown in Figure 5-51. The set-up factor, Λ is defined as:

$$\Lambda = \frac{\tau_{avg}(t)}{\tau_{avg}(t = t_{ref})} = \Lambda_{ult}\left(m + (1-m)\left[\frac{t/T_{50}}{1 + (t/T_{50})}\right]\right) \quad 5\text{-}10$$

where $\tau_{avg}(t)$ is the resistance measured at time, t after installation, $\tau_{avg}(t= t_{ref})$ is the initial reference resistance measured at time, $t_{ref.}$, Λ_{ult} is the ultimate set up factor, T_{50} is the time required to reach 50% and m is an empirical parameter (around 0.2) used to improve the fit at the early (t < 1day) age. The trend shown in Figure 5-51 (b) corresponds to T_{50} of 29 minutes, Λ_{ult} of 5.6 and m equal to 0.18.

Excess pore water pressure dissipation is expected to be extremely rapid in the chalk due to the high porosity and nature of the fractures. Applying a similar analysis to that described above to predict t_{50} around the large diameter piles indicates time for 50% dissipation of pore water pressure of between 11 and 40 minutes for a rigidity index I_r (=G/s_u) of 3000, which is also in broad agreement with the trend shown in Figure 5-51 (b).

5.9.8 Predictions of shaft capacity at the till dominated site

Section 3.3.2 provided an overview of current axial capacity design methods for displacement piles in clay, developed following reviews of predictions with the API method which showed significant biases and skews in predictions with respect to pile length (or L_p/D) and yield stress ratio (YSR) or apparent OCR; e.g. Chow (1997), Jardine *et al.* (2005a). As discussed in Chapter 3, Lehane *et al.* (2017), as part of a JIP, assessed the performance of the ICP-05 clay method using a newly assembled database of pile tests. The latter method did not appear to perform as well, overall, as previously reported. It was recognised that this was related, at least partly, to the very small number of sites for which the necessary site investigation information existed and the exclusion of all of the ICP tests because of their small diameter and jacked installations. Several other critical cases were also excluded, while retaining in the greatly reduced database a large proportion of tests from low OCR silty clay sites, including Lierstranda in Norway, where very low axial capacities had been measured showing remarkably low net cone resistance values. Potential problems had been raised by Chow (1997) and Jardine *et al.* (2005a) with several of the tests. Ridgway and Jardine (2007) set out how such sites such as Lierstranda might be recognised and recommended that the ICP should not be applied in such conditions.

Lehane *et al.* (2017) report that a CPT based method, suggested by Lehane *et al.* (2012b) following a similar database study and termed "UWA-13", provided generally good predictions for shaft resistance in the larger database of tests for which reliable CPT data existed. The method relates shaft resistance to net cone resistance, q_t in the clay retaining the ICP-05 h/R* term (Eq. 3-15) and reducing the lower limit on h/R* to 1. Two expressions were proposed, as were shown in Eq. 3-19 and 3-20, with and without inclusion of the pile shaft clay interface friction angle and effective overburden pressure.

The performance of the ICP-05 clay method in predicting shaft capacity for the clay glacial tills at Wikinger is assessed here along with the UWA-13 method and the API method, using the results of the static test conducted at the glacial till dominated site. This test (WK38-2_SLT_108) conducted 108 days after driving, showed a net tensile failure load of 8.8MN. The dynamic restrike test conducted at the same time on an adjacent pile had a shaft capacity in close correspondence (11% higher see Section 5.9.5) to the static tension test to failure. The signal matching results indicated that 69% of the capacity is attributable to the glacial till. Therefore it can be assumed that 6.07MN was mobilised in the glacial till during the static test. In order to predict the capacity applying in the glacial till layer during the statc tension test, five different methods were considered:

1. The ICP-05 clay methodology (Jardine *et al.*, 2005a) described in Section 3.3.2 with parameters (YSR, S_t and δ') as set out in Section 5.2 applied to the full glacial till thickness;
2. As above but with the ICP-05 sand methodology (Section 3.3.4) applied in the dense sand layers that comprised approximately 20% of the section and were indicated by high cone resistance;
3. The UWA-13 expression suggested by Lehane *et al.* (2012b) which includes the interface friction angle and overburden pressure in the formulation (i.e. Eq. 3-19) applied to the full glacial till thickness;
4. As above but with the UWA-13 expression which does not include the interface friction angle or the overburden pressure (i.e. Eq. 3-20);
5. The API alpha approach, described in Section 3.3.2 using the undrained strength calculated using a site specific N_{kt} factor of 22.5 (See Appendix A-4) and assuming only external shaft resistance acts during a static tension test. .

Table 5-10 summarises the ratios of calculated to measured shaft capacity (Q_c/Q_m) where Q_m is the measured capacity in the glacial till during the static test. Overall, both the API method and the UWA-13 method (both formulations) tended to over-predict the

capacity, assessed 108 days after driving, showing Q_c/Q_m ratios of approximately 1.55 and 3.2, respectively. The use of the ICP-05 clay method plus the ICP-05 sand in the assessed sand layers under-predicted the capacity by approximately 12%. The ICP-05 clay method, applied to the glacial till layer, provided the closest match to the capacity measured 108 days after driving, under predicting the result by just 4% in this case.

However the set-up trend in the glacial till, shown on Figure 5-50 suggests that the increases in capacity with time had not stabilised fully when the testing was carried out. Noting that the methods are intended to predict capacity after full equalisation has occurred, the Q_c/Q_m ratios calculated using all five methods should further reduce over time. This may lead to an improvement in the UWA-13 prediction with time and to the ICP-05 methods becoming more conservative. However, this test suggests that it is inadvisable to adopt the UWA-13 method for high YSR insensitive glacial tills such as those encountered at Wikinger.

Table 5-10: Summary of pile capacity predictions in glacial till for the static tension test on WK38-2 conducted 108 days after driving

Test code	**Q_c (MN)**	**Q_m (MN)**	**Q_c/Q_m (MN)**
ICP-05 clay	5.85	6.07	0.96
ICP-05 clay + ICP-05 sand	5.37	6.07	0.88
UWA-13 (Eq. A6-1)	20.02	6.07	3.30
UWA-13 (Eq. A6-2)	19.51	6.07	3.21
API alpha method	9.43	6.07	1.55

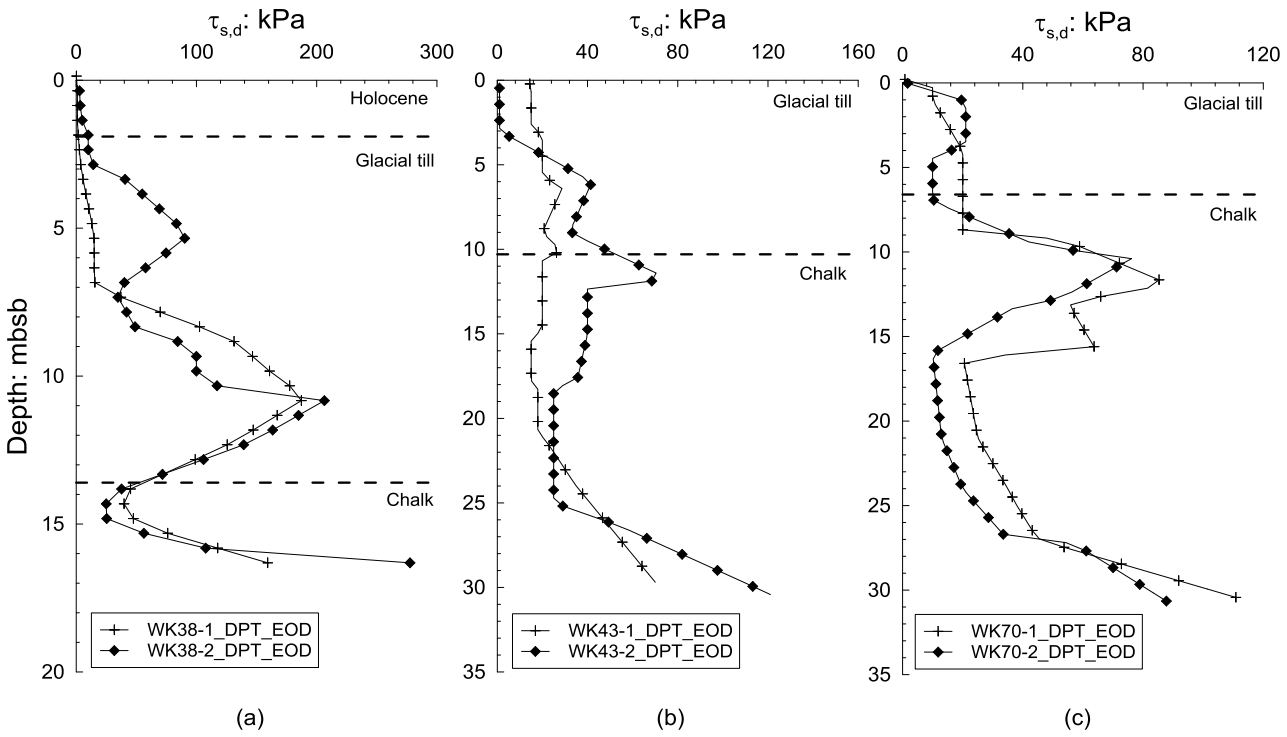


Figure 5-35: End of driving shaft resistance of pre-construction piles from back analysis of dynamic measurements

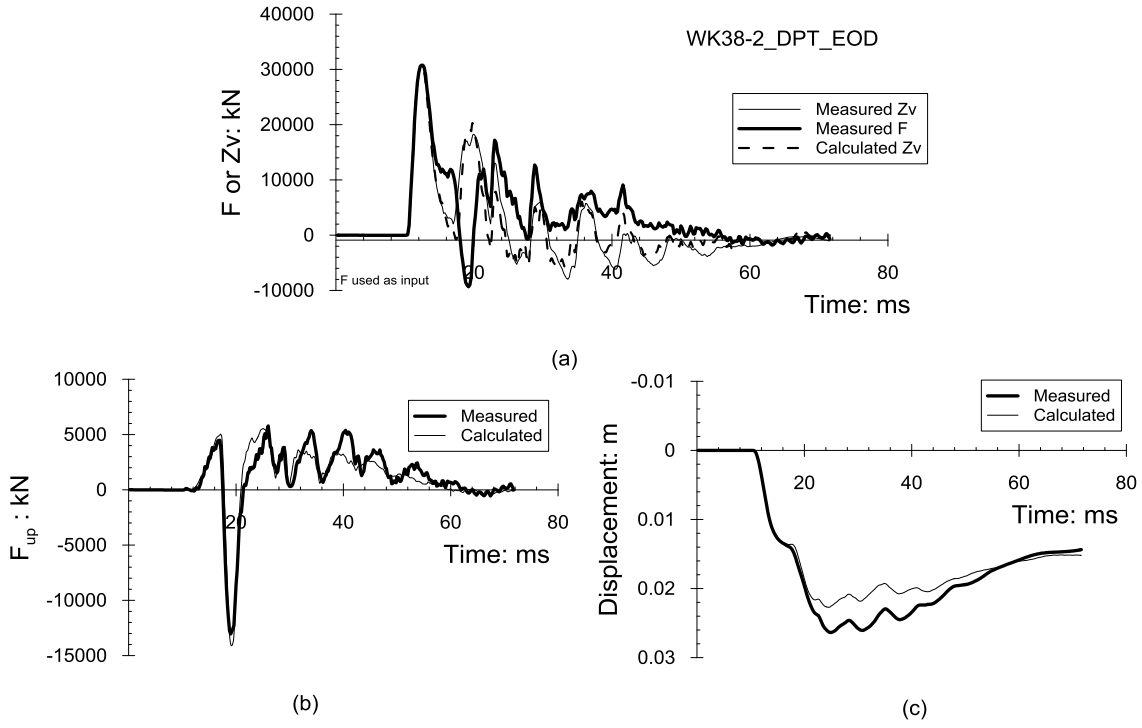


Figure 5-36: Example signal match from blow WK38-2_DPT_EOD: measured and calculated (a) force and velocity times impedance (b) upward travelling force (c) displacement

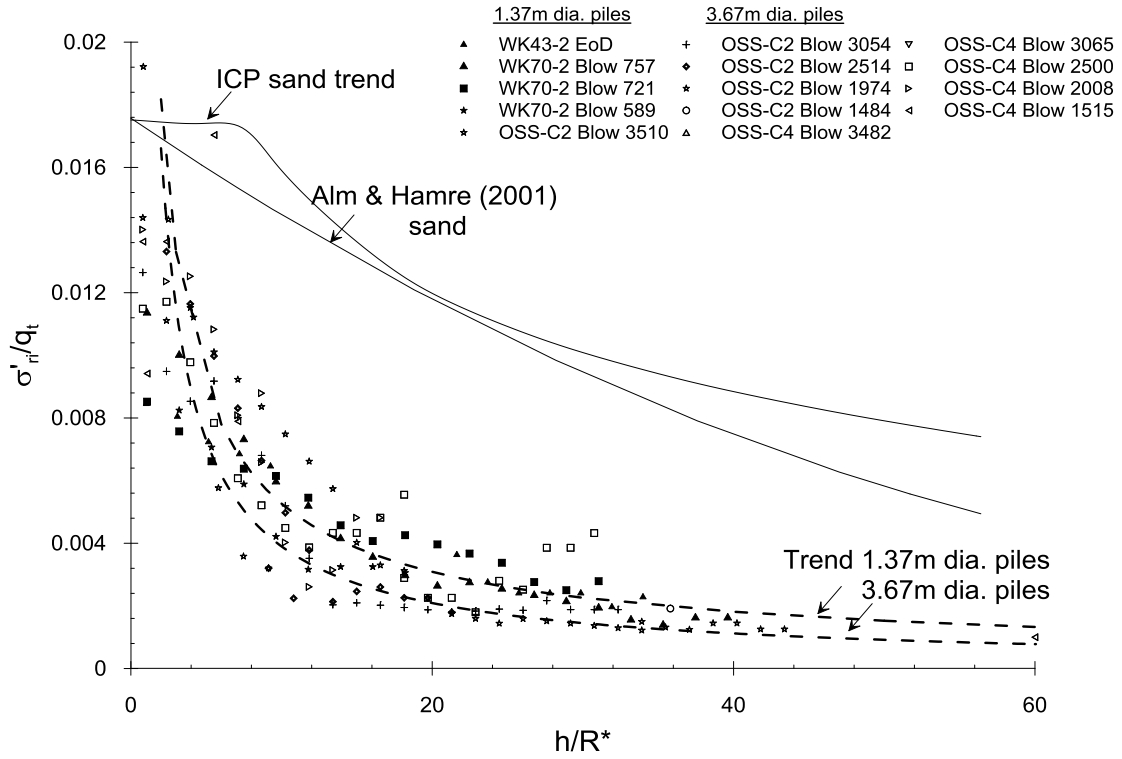


Figure 5-37: Trend of normalised radial effective stress reduction with normalised distance from the pile tip for 15 driving blows in chalk

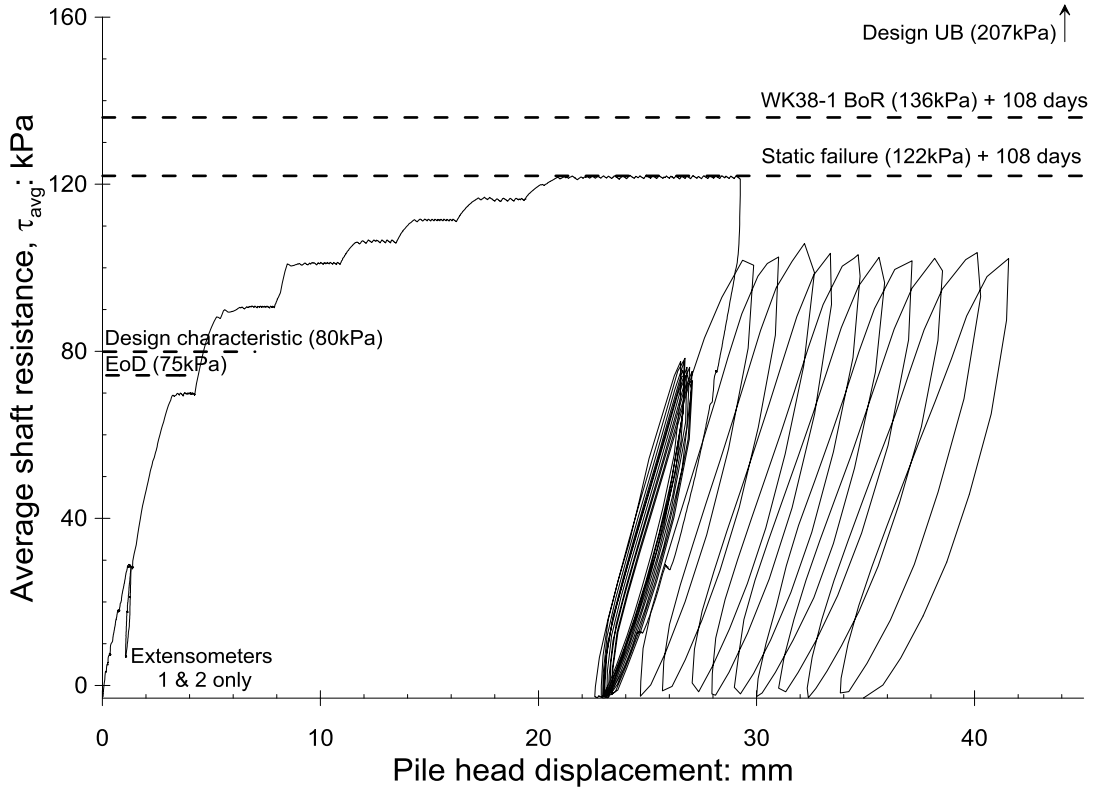


Figure 5-38: Load – displacement behaviour during static axial tension test WK38-2_SLT_108

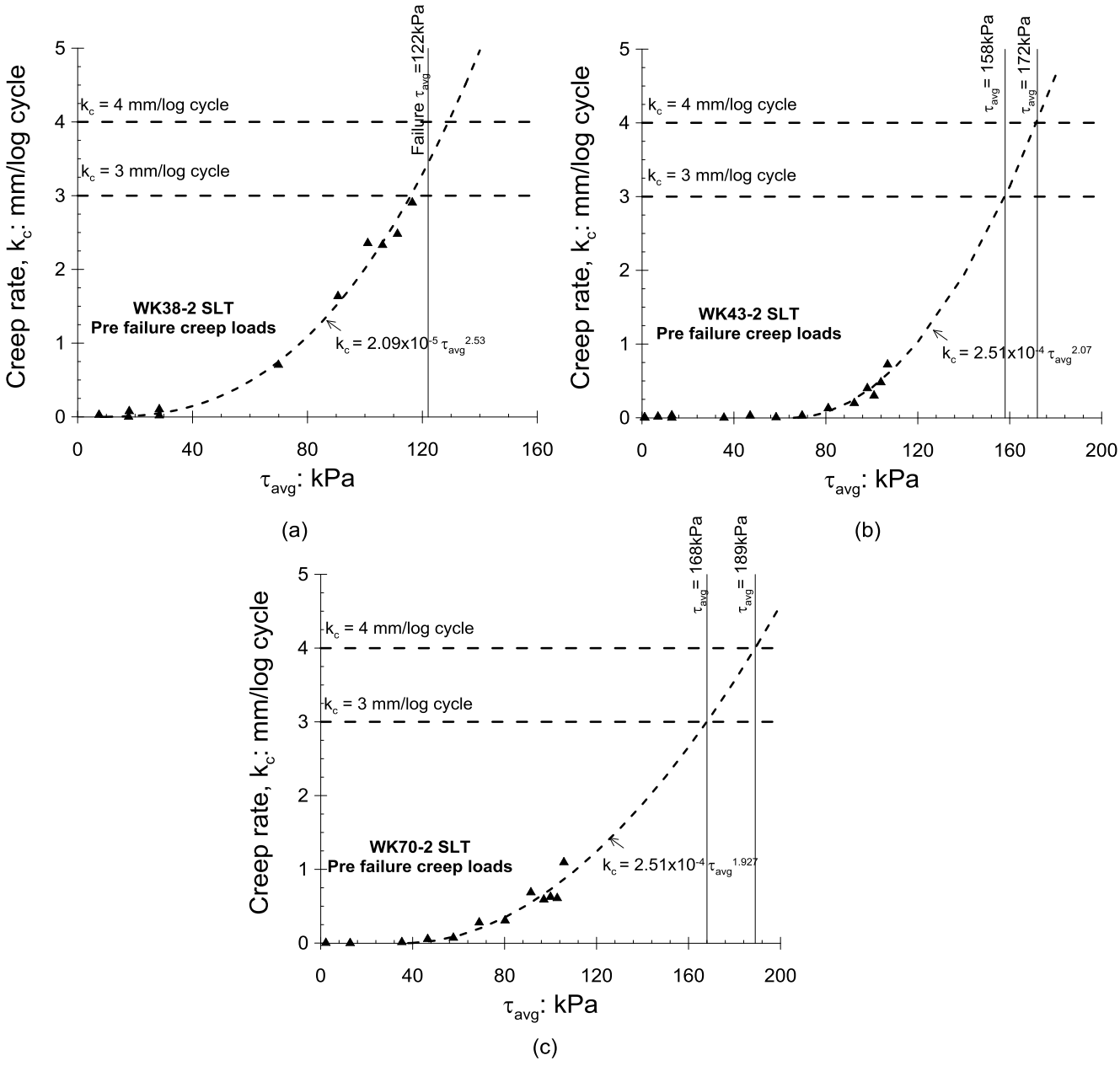


Figure 5-39: Extrapolation of creep rates to failure (a) Wk38-2 (b) WK43-2 (c) WK70-2

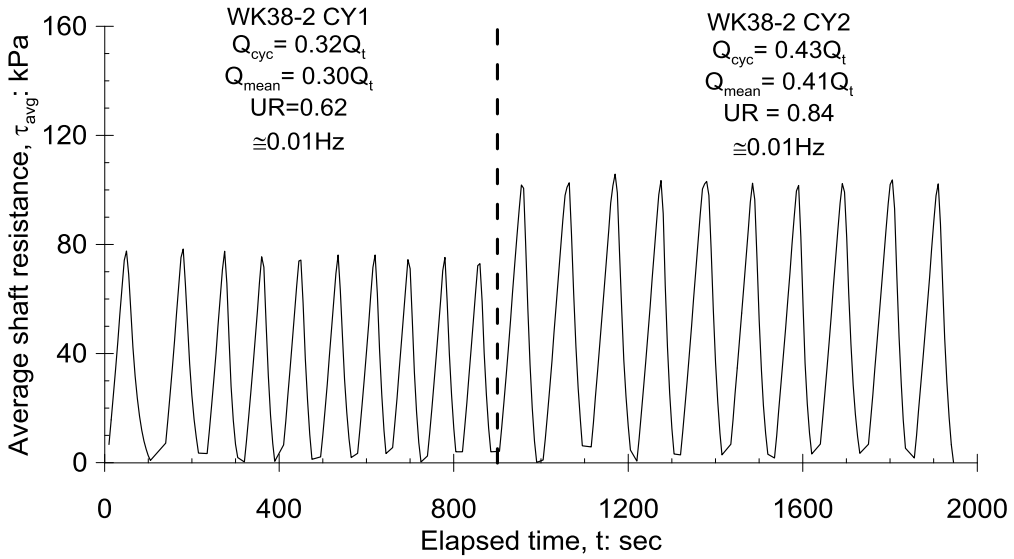


Figure 5-40: Average shaft resistance against time mobilised during WK38-2_CYC_108

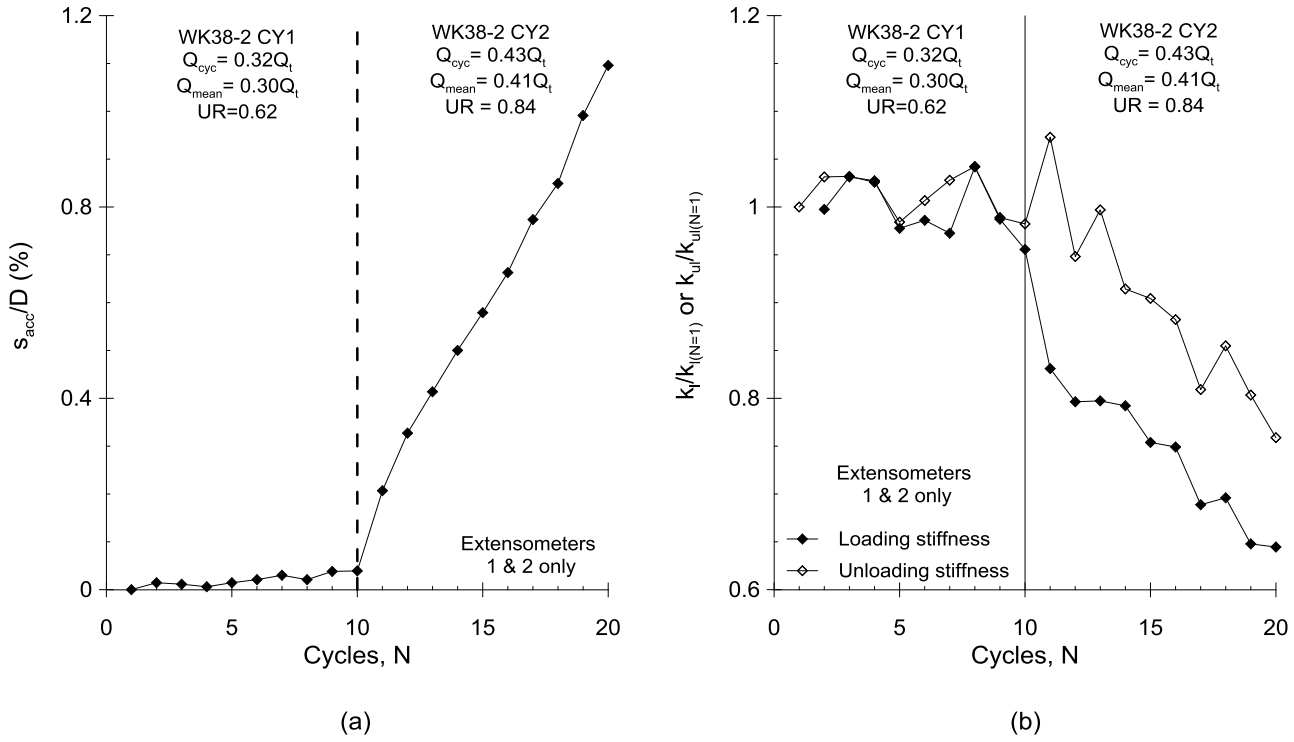


Figure 5-41: WK38-2_CYC_108 (a) permanent cyclic displacements normalised by pile diameter (b) cyclic loading and unloading stiffness

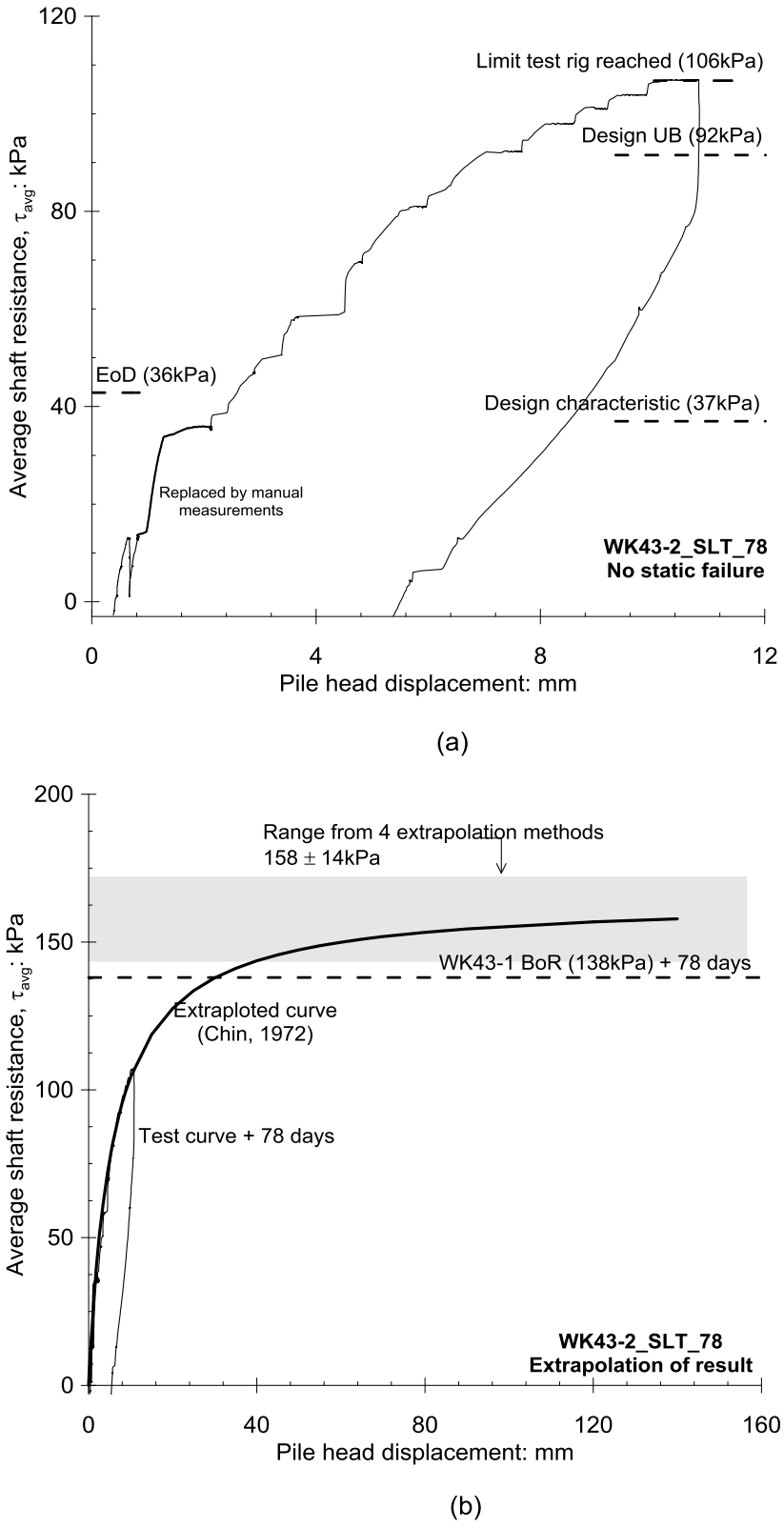
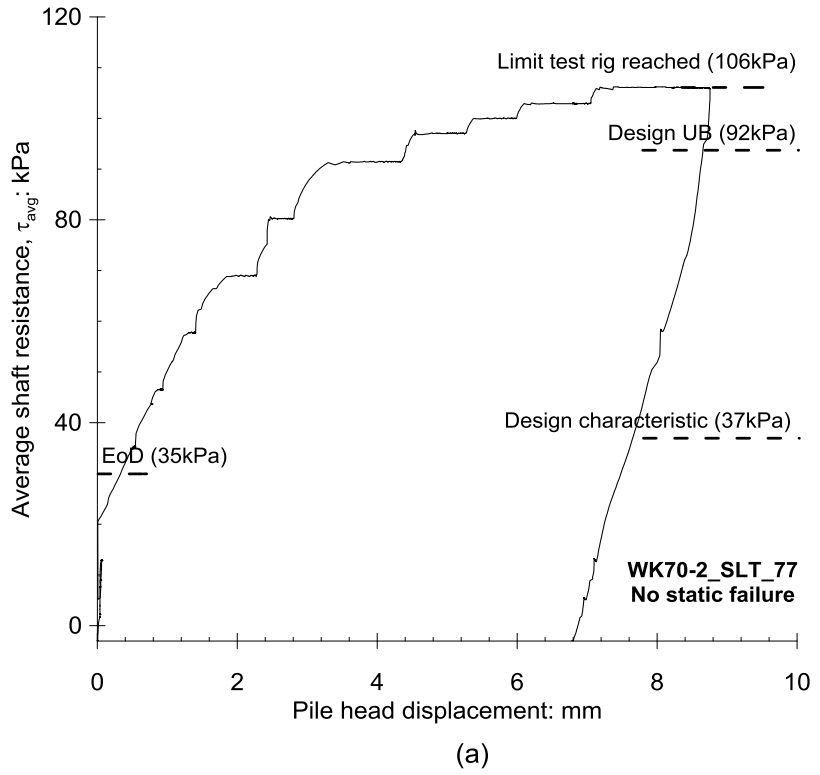
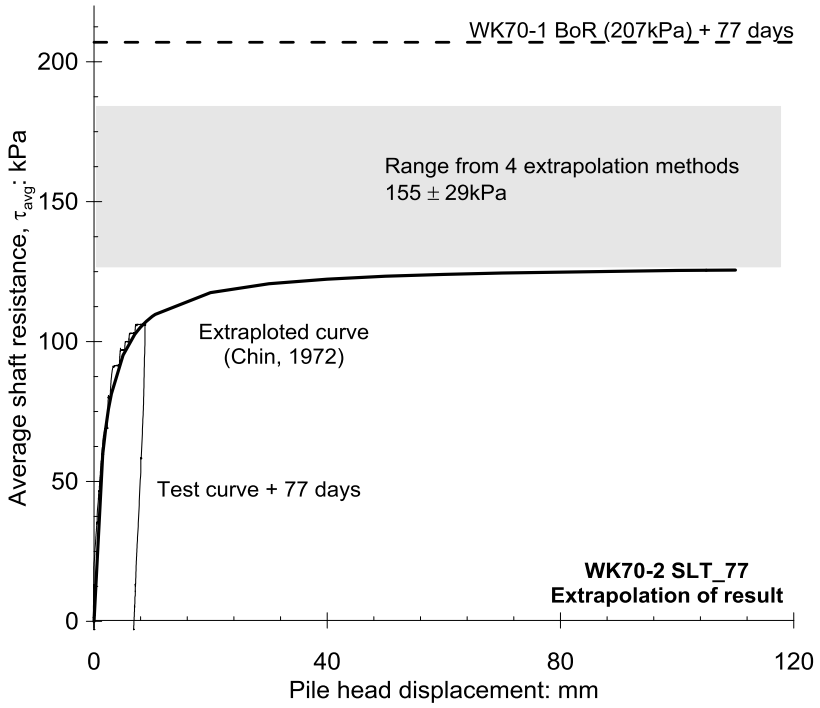


Figure 5-42: Load – displacement behaviour during static axial tension test on WK43-2



(a)



(b)

Figure 5-43: Load – displacement behaviour during static axial tension test on WK70-2

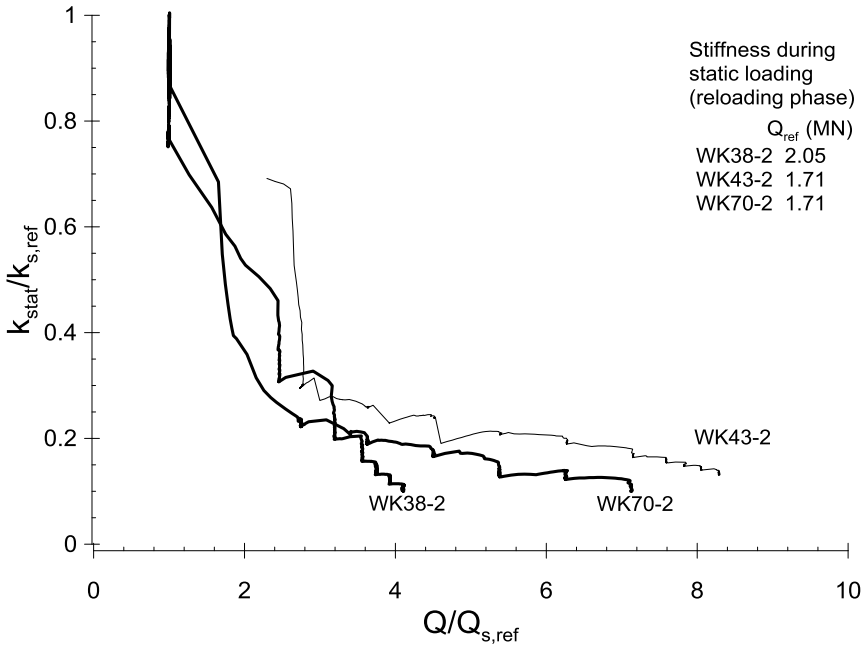


Figure 5-44: Stiffness evolution during SLT tests on WK38-2, WK43-2 and WK70-2

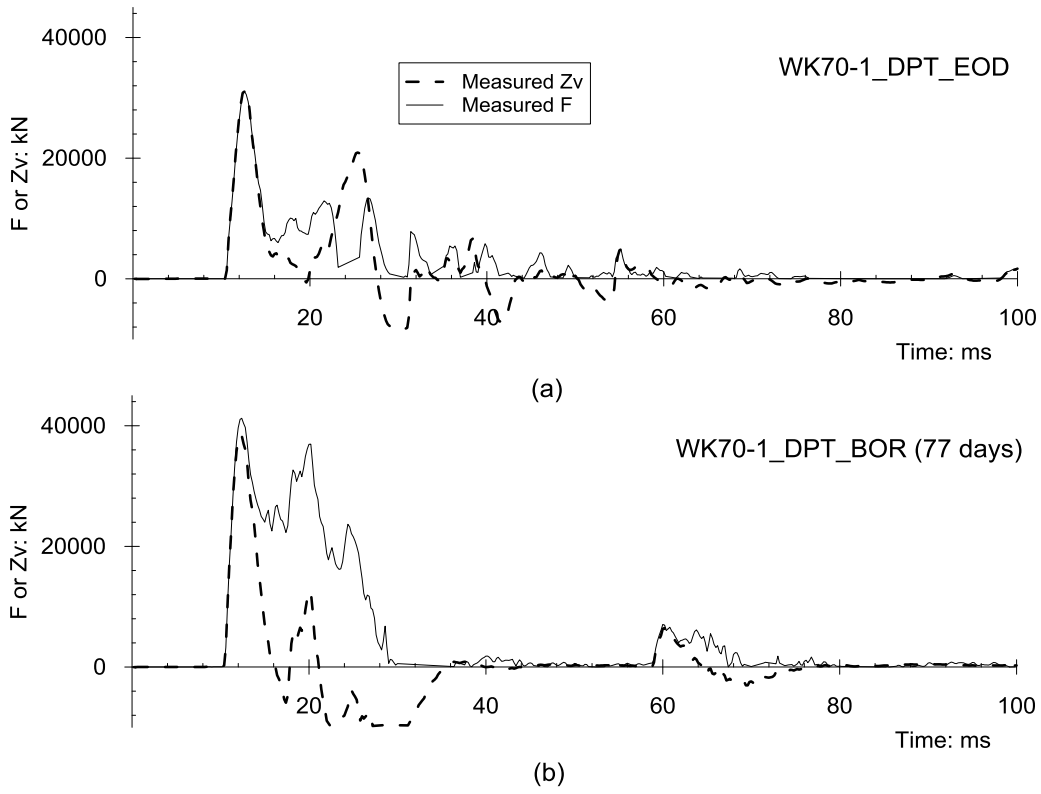


Figure 5-45: Demonstration of change in F and Zv traces with time at WK70-1 (a) at End of Driving (b) at Beginning of Restrike 77 days after driving

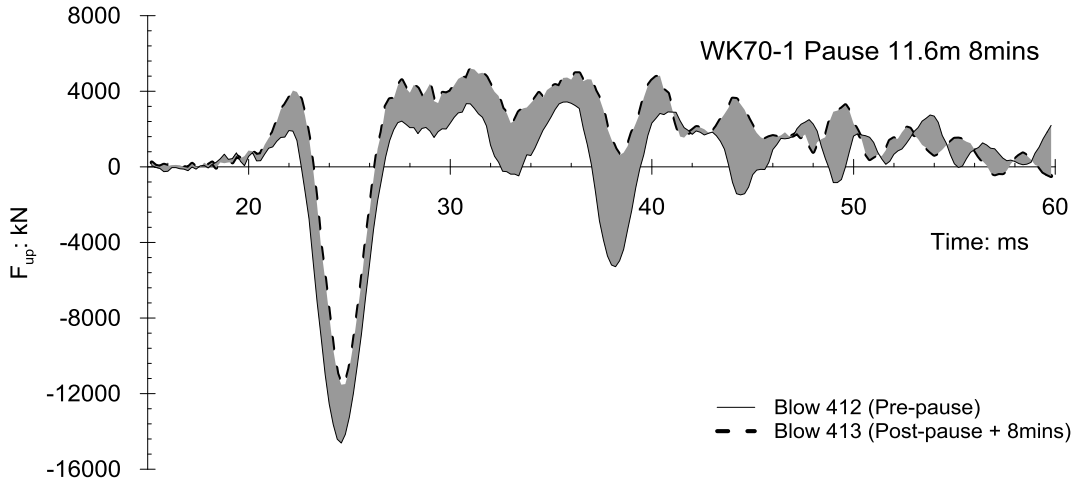


Figure 5-46: Demonstration of change in F_{up} traces with time over a pause in installation

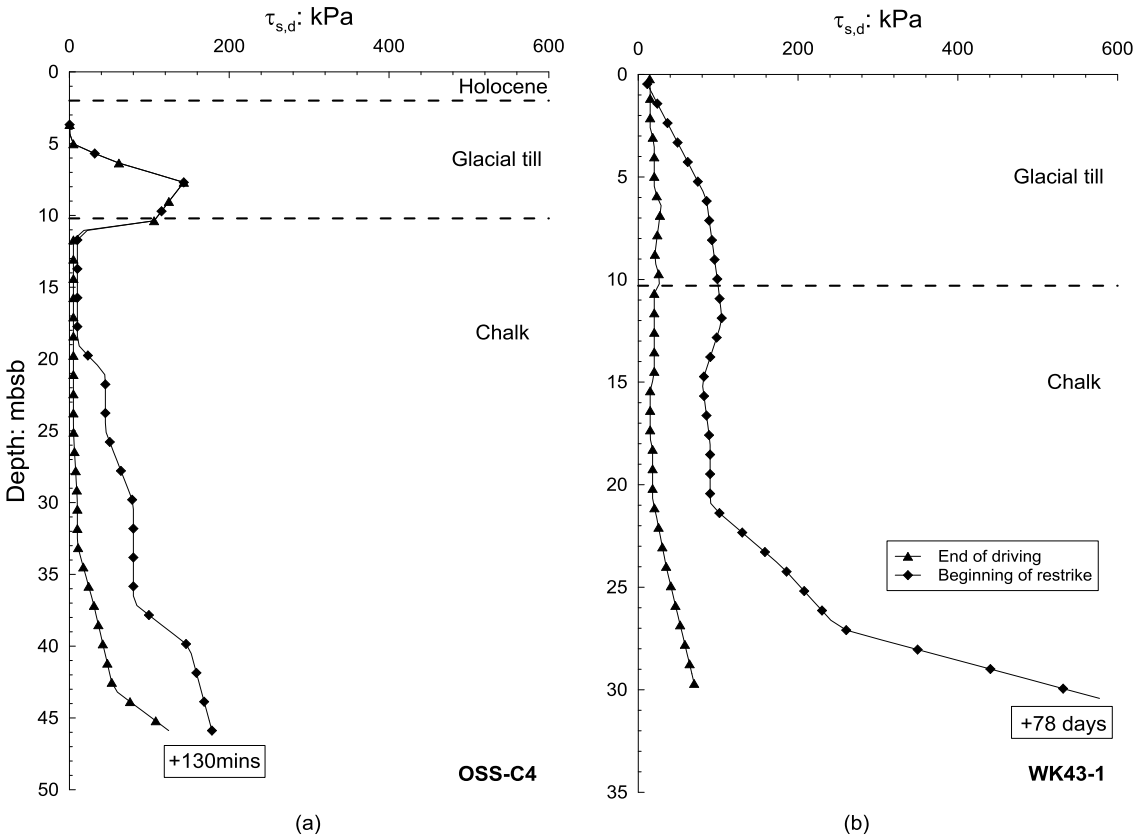


Figure 5-47: Shaft resistance profiles at EOD and BOR from pre-construction test campaign

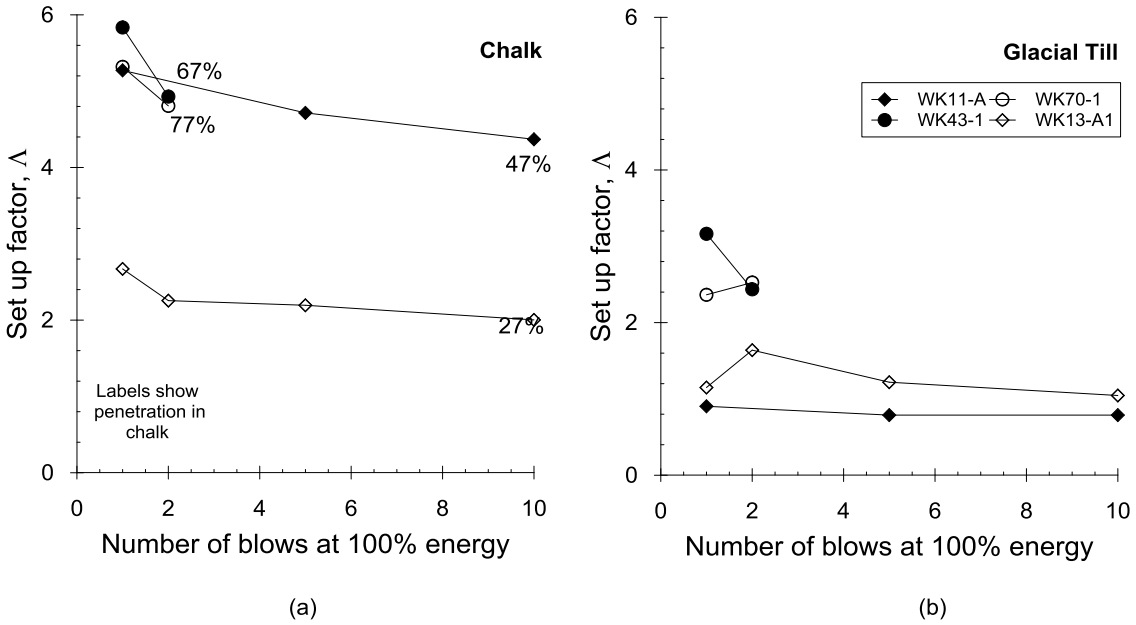


Figure 5-48: Effect of multiple restrike blows on pile set-up factor (a) in chalk (b) in glacial

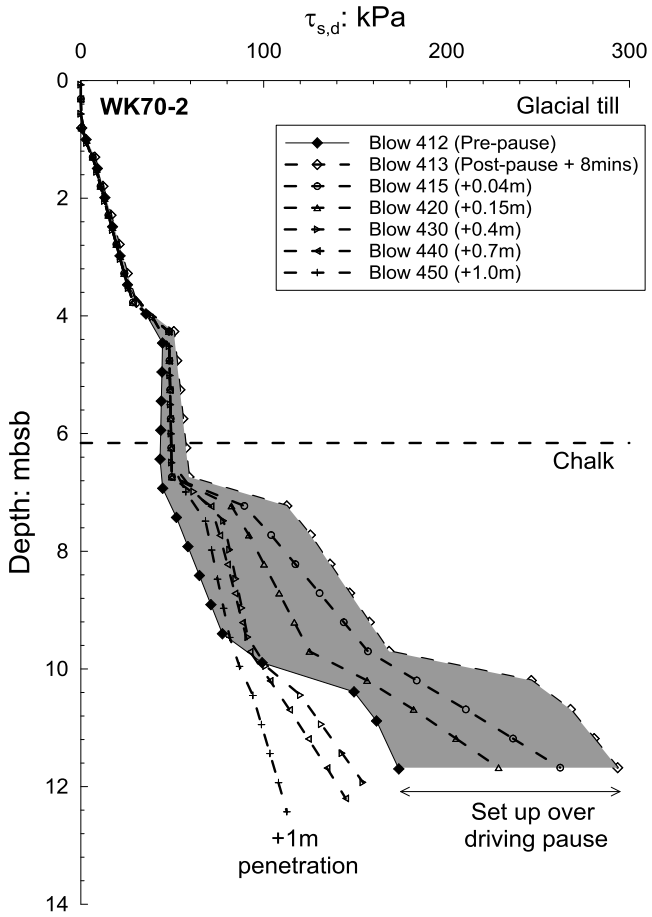


Figure 5-49: Change in shaft resistance immediately following a driving pause and with subsequent driving – location WK70-2

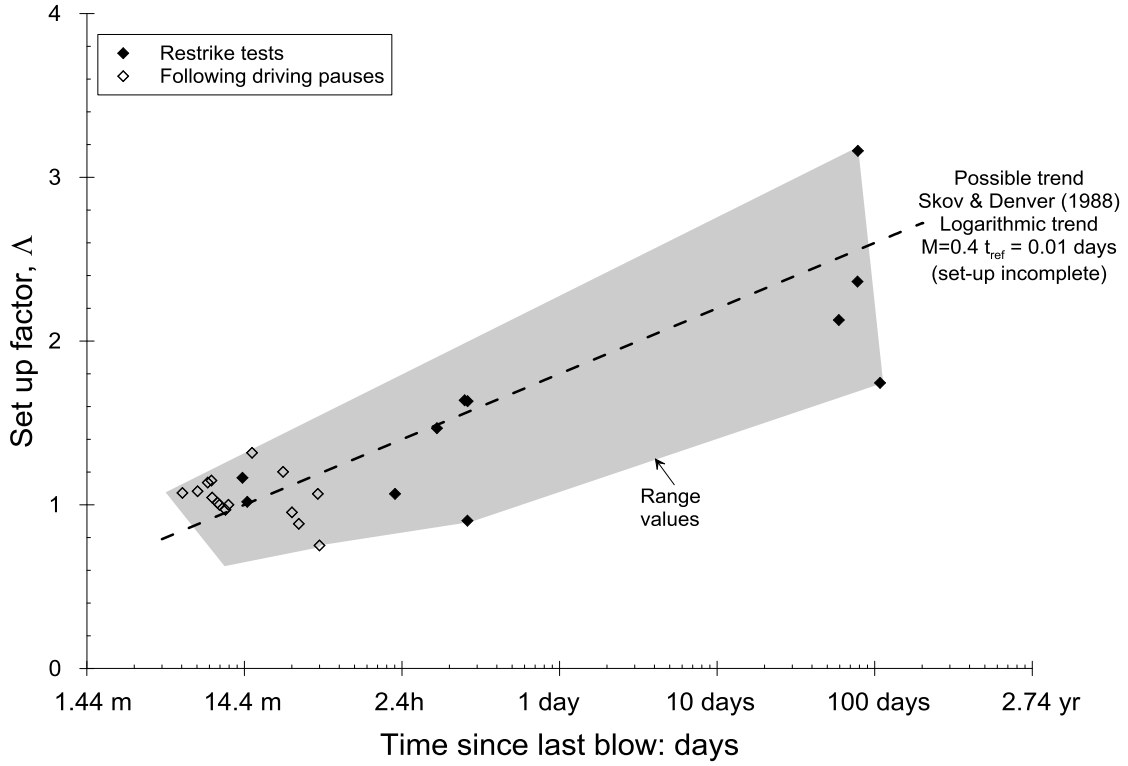
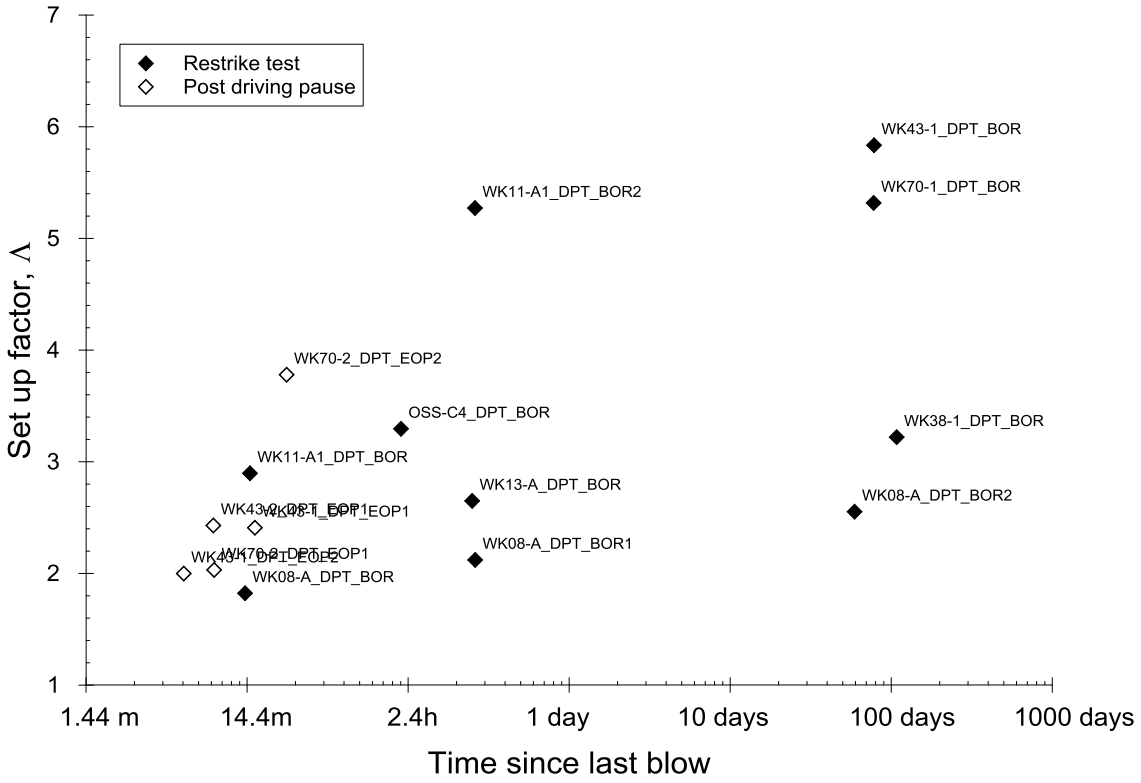
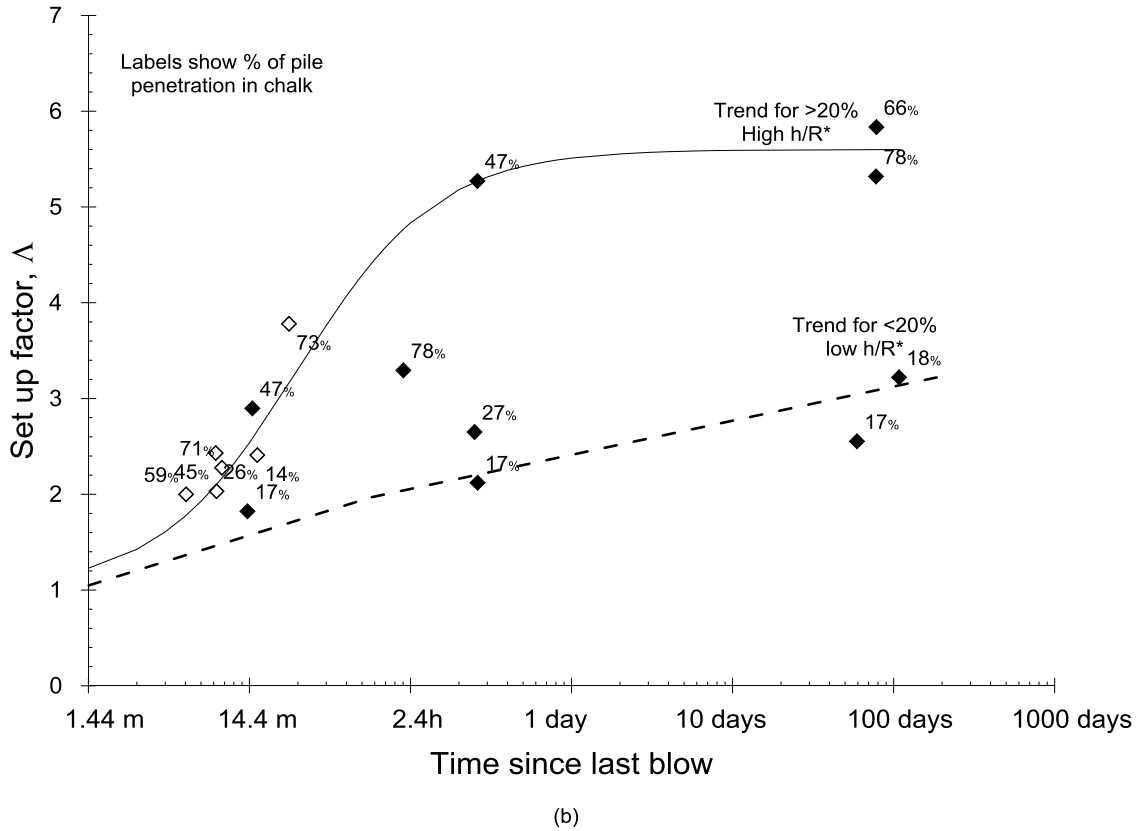


Figure 5-50: Set-up trends in glacial till from dynamic restrike tests and from blows following driving pauses with logarithmic capacity increase trend



(a)



(b)

Figure 5-51: (a) Set-up trends in chalk from dynamic restrike tests and from blows following driving pauses (b) with interpreted trend

5.10 Summary and concluding remarks

This chapter has described the experimental aims and objectives of a novel static and dynamic testing programme on piles of between 1.37 and 3.7m diameter, installed offshore at the Wikinger offshore windfarm. The ground conditions and engineering behaviour of the encountered materials were outlined, with laboratory experiments conducted by the Author and by others to support the interpretation of the results. The behaviour observed in the multiple novel axial static and cyclic tests and dynamic tests conducted in glacial till and chalk was then described. The following primary conclusions emerge from the results:

1. Tests in the laboratory showed that compaction of intact samples of chalk at their natural moisture content causes rapid degradation to a putty with a very low undrained strength. Subsequent consolidation resulted in significant increases in strength and initial stiffness over time. Thixotropic effects were found to be less significant;
2. Low average shaft resistances were observed in chalk during driving which showed a clear trend to reduce with increasing relative penetration (h/R*) into chalk. Analysis of the dynamic data showed the local shaft resistance falling rapidly with h/R*. The relative amounts of degradation observed during pile driving in chalk are far larger than expected for sands or clays by the current industry best methods;
3. The shaft resistances at the end of driving observed in the glacial till also showed a tendency to reduce with increasing penetration or h/R*, although the trends were less marked than those seen in chalk;
4. The static load tests at the predominantly chalk locations did not reach failure due to the set-up capacities being far greater than the characteristic design predictions;
5. The static test conducted at the glacial till dominated site, which reached full failure, showed good agreement with the results of the dynamic restrike test conducted at the same time;
6. Capacity change over time was tracked separately in the glacial till and chalk by comparing the aged and unaged static and dynamic tests. Capacity increase in the glacial till was gradual, reaching factors of between two and three by the end of the programme. The capacity increases in chalk were far more significant,

reaching over 500%, and followed a hyperbolic trend that was 50% complete less than an hour after installation;

7. The trends in capacity increase with time also appear related to the trends in capacity change with h/R* with more significant increases seen for larger penetrations into chalk or higher relative tip depth, h;
8. The application of multiple restrike blows to piles that had experienced long-term set-up was shown to reduce their capacities, starting from the first blow. Beneficial time effects observed during operational pauses were also shown to be degraded by further hammer blows or pile penetration.

The novel tests results represent a valuable dataset, which prompted the Author to carry out further experiments on driven and jacked test piles at an analogous onshore test site. These tests are described in the following Chapters 6 and Chapter 7.

CHAPTER 6

Static and cyclic driven pile tests at St. Nicholas-at-Wade

6.1 Introduction

This chapter describes a programme of static, dynamic and cyclic pile tests conducted at an onshore test site in Kent, South East England on driven open-ended tubular steel piles. The tests were planned to address the significant design guidance shortcomings for axial capacity of piles in chalk identified in Chapter 3 and to supplement the Wikinger offshore test results described in Chapter 5. The tests were carried out in tandem with the highly instrumented jacked "Imperial College Pile" tests, conducted at the same site, the results of which are discussed in Chapter 7.

The chapter begins by describing the experimental aims of the study, followed by a description of the test site and the ground conditions encountered. The pile details, testing programme and experimental procedures follow before the main observations, interpretation and the primary conclusions of the testing programme are outlined. Sections 6.4 to 6.10 were published previously, either whole or in part, by Buckley *et al.* (2017a) and Buckley *et al.* (2018a).

6.2 Experimental aims

While the onshore pile tests described in this chapter involved relatively small piles, they were conducted in a purely chalk profile and multiple piles could be installed at the same location. The testing times and procedures could be more easily controlled than in the offshore

environment, which facilitated a systematic investigation of how ageing and cyclic loading affected driven steel piles over an eight month period. The testing programme incorporated the lessons learned from the review of available pile test data, described in Chapter 3, as well as the Wikinger offshore testing. The experimental testing programme carried out at the test site between October 2015 and July 2016 aimed to investigate:

- Dynamic resistances during and at the end of pile driving, using PDA instrumentation fitted near the pile head;
- How pile installation and subsequent static and cyclic testing affect the chalk surrounding the pile shaft;
- Tension (shaft) capacity-ageing trends for virgin piles over 8 months after installation through static tests;
- The impact of re-testing piles which had been previously subjected to static tension failure; and
- How multiple 'virgin' piles respond to large numbers of one-way (non-dynamic) axial load cycles after 8 months of ageing after driving.

The static and cyclic tests were conducted in tension to allow the shaft friction capacities to be determined without the need for base instrumentation, which was not feasible for the tests in this study.

6.3 Test site at St Nicholas-at-Wade

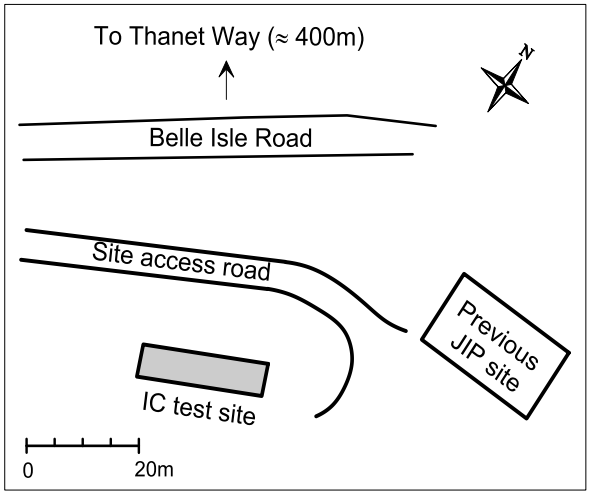
The test site is located in a previous chalk quarry, close to the village of St. Nicholas-at-Wade on the Isle of Thanet (UK Grid: TR 25419 66879) and approximately 15km west of the town of Margate, Kent (Figure 6-1 (a)). The quarry was previously used to provide material for the nearby Thanet Way road embankment. As a result, all overburden and weathered chalk has been removed to expose structured chalk from the ground surface. The quarry was selected as a trial investigation site in 2007 by Thanet Offshore Wind Ltd. because the ground conditions are similar to those encountered at the Thanet Offshore Windfarm, located approximately 30km from the site in the Southern North Sea. The suitability of various *in-situ* geotechnical investigation techniques in chalk was examined during this phase (SETech, 2007). Joint Industry pile testing programmes of static and cyclic lateral pile tests, led by Wind Support Ltd., were subsequently conducted between 2011 and 2013, along with axial testing of the same piles (Dührkop *et al.*, 2015, Ciavaglia *et al.*, 2017a, b). The results of those tests

were discussed in Section 3.5.1. An associated site investigation campaign included five boreholes to a maximum depth of 20.5m and CPTs/PCPTs to a maximum depth of 17m, along with chalk specific laboratory testing (Fugro, 2012a, 2012b).

The land was rented by Imperial College in October 2015 and utilised as a research pile testing site; Figure 6-1(b) shows an overall site plan including the location of the IC site and the previous JIP test site. Figure 6-2 (a) shows the layout of the previous JIP site including the test piles, the associated boreholes and PCPTs. Finally, Figure 6-2 (b) shows a plan of the IC test site, which is located on flat ground approximately 60m away from the previous study area. New PCPTs, dissipation tests and seismic cone penetration tests (SCPT) were undertaken in this area, supervised by the Author. Interface ring shear tests on samples taken from the site were also conducted at Imperial College.



(a)



(b)

Figure 6-1: (a) St Nicholas-at-Wade test site location (UK Grid: TR 25419 66879) (b) overall site plan showing IC test site and previous JIP

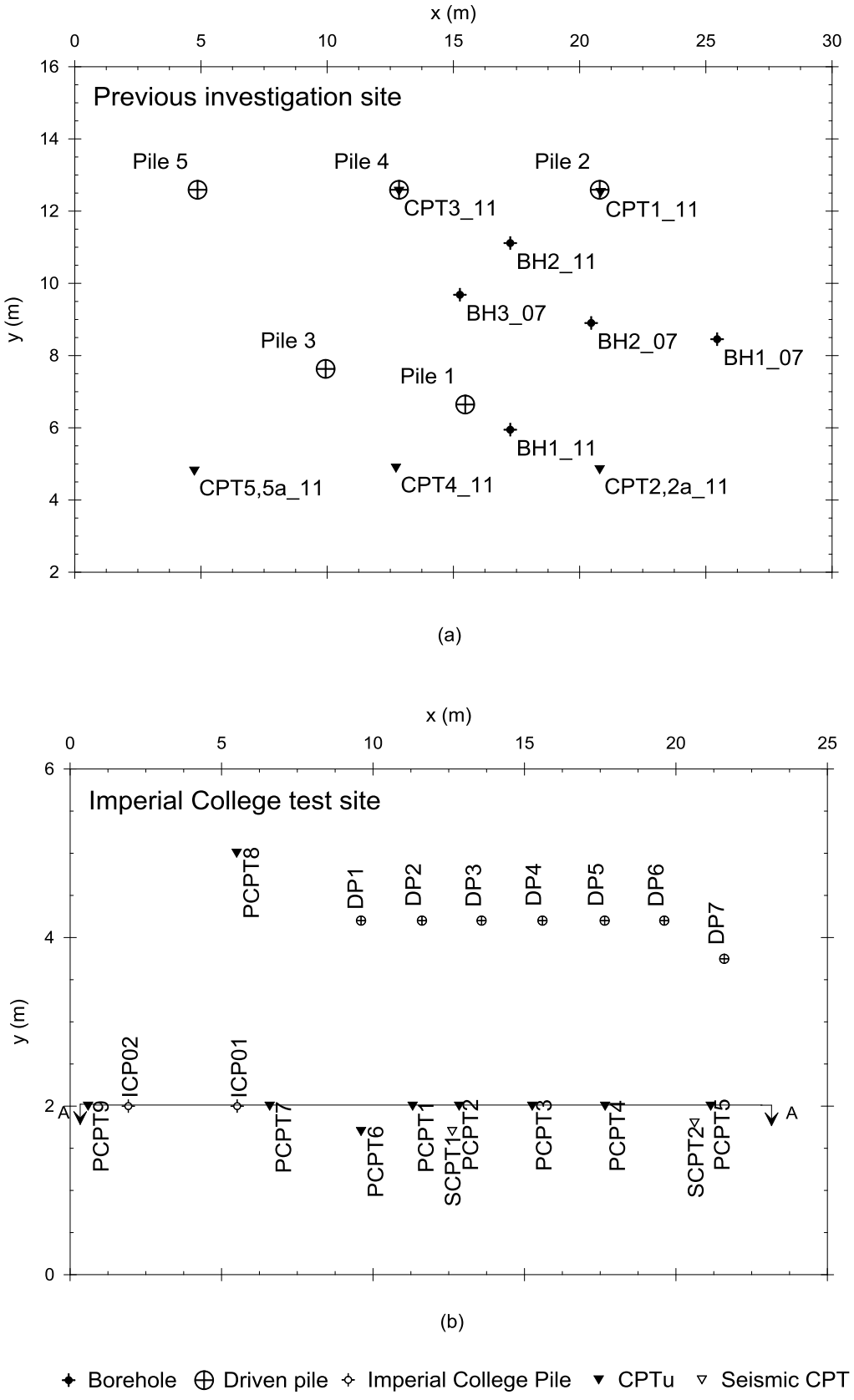


Figure 6-2: (a) Piles and site investigation at the previous JIP site (Ciavaglia *et al.*, 2017a, b) (b) piles and site investigation at the IC test site

6.4 Ground conditions

6.4.1 Geology & stratigraphy

The site falls within the North Downs of East Kent, an area primarily underlain by the Upper Cretaceous Chalk Group, with chalk generally encountered from surface on the Isle of Thanet (Aldiss *et al.*, 2004). Both the Margate and Seaford Chalk formations found on Thanet form part of the White Chalk Subgroup, which comprises 98.6% calcium carbonate (Hancock, 1975) and is generally equivalent to a combination of the Middle and Upper Chalk within the traditional classification system. The Margate Chalk is a facies of the Newhaven Chalk Formation, which generally comprises white chalk without marl seams and few flints overlain unconformably by the Thanet Sand formation. The Seaford chalk underlies the Margate Chalk and comprises mainly soft blocky white chalk with seams of small to very large flint nodules. On the Isle of Thanet, the boundary between the Seaford and Margate formations is defined by the Barrois' sponge bed which is a 200 to 300mm thick yellowish iron stained nodular sponge bed. Approximately 6m below the Barrois' sponge bed lies a conspicuous almost continuous tabular flint seam termed "Whitakers Three Inch" flint band (Aldiss *et al.*, 2004, Mortimore, 2014b).

Figure 6-3 shows the correlation developed by Prof. Mortimore between the stratigraphy encountered at the test site, the closest onshore section located at North Foreland and offshore borehole No. 7 at the Thanet OWF (ChalkRock, 2007). Rotary core samples from the site, taken during the 2007 site investigation (SETech, 2007), were assessed by Prof. Rory Mortimore, in order to correlate the stratigraphy to that encountered offshore, with two primary successions described:

1. **From 0 to 7.6m:** Pure white chalk with occasional small flints and few macrofossils which forms part of the lower Margate Chalk formation and contains the Barrois' sponge bed at ≈6.3m;
2. **From 7.6m to the end of the borehole:** chalk containing regular flint bands which forms part of the Seaford chalk formation and contains the Whitakers Three Inch Flint Band at between 14 and 15m depth.

The chalk classifies as CIRIA Grade B2/B3 within the Margate chalk formation (Bowden *et al.*, 2002), with discontinuities open to less than 3mm and a fracture spacing of between 60 and 200mm. The grade varies between B3 and A2 within the Seaford chalk

encountered at greater depths, with A2 representing chalk with closed discontinuities spaced between 200 and 600mm. Only Margate Chalk is encountered by the test piles. Groundwater was encountered at 11.6m below the quarry base during borehole drilling conducted in early February 2007.

6.4.2 In-situ testing

Figure 6-4 plots a typical PCPT profile from a test conducted at the Imperial College test site, including the penetration pore pressures measured at both the tip (u_1) and shoulder (u_2) positions. Within the depth of influence of the test piles, corrected cone resistance, q_t generally lies between 10 and 20MPa and sleeve friction, f_s lies between 100 and 500kPa. Thin discrete and discontinuous flints were encountered which gave sharp local peaks in q_t up to 60MPa that were not thought to influence the pile tests unduly. Figure 6-5 plots the variation in q_t along Section A-A as shown on Figure 6-2, indicating that q_t varied moderately spatially across the site. Figure 6-6 compares the envelopes of q_t, f_s, and u_2, measured at both the IC and previous test sites. Both q_t and f_s are slightly higher at the IC test site with a similar range of pore pressures observed between the two sites.

At the IC test site, the shaft load during a PCPT installation was assessed by measuring the total axial force required to advance the cone and the rods, Q_{tot} and comparing it to the load measured by the cone tip, Q_{tip} as shown on Figure 6-7 (a). This allowed the overall shaft stress along the advancing cone and steel rods, τ_{cpt} to be determined:

$$\tau_{cpt} = \frac{Q_{tot} - Q_{tip}}{A_s} \qquad 6\text{-}1$$

where A_s is the area of the shaft. Figure 6-7 (b) compares this shaft stress with the sleeve friction, f_s measured approximately ≈120mm from the cone tip, illustrating the strong effects of increasing penetration on reducing the available shaft stress. The sleeve friction measurements were generally between 100 and 800kPa, while the average shaft stresses along the whole length were less than 100kPa and reduced with depth to less than 20kPa at 11.5mbgl. The influence of length effects on reducing the ratio of τ_{cpt} normalised by q_t is explored further on Figure 6-7 (c), which illustrates that τ_{cpt}/q_t follows an approximate power law relationship with L_p/D, where L_p is the penetration of the CPT.

The penetration pore pressures are remarkably high across the site, reaching 10MPa within the depth of interest at the u_1 position and 6MPa at the u_2 position. Dissipation tests conducted at 3.5 and 3.6m depth using 43.8mm diameter piezocones showed 50% dissipation

of excess pore water pressure after 4 to 13 seconds at the u_2 position. The latter indicate horizontal consolidation coefficients, $c_{h,piezo}$ of ≈ 1 x 10^{-3} m^2/s, assuming a suitably high rigidity index in the surrounding intact chalk (≈ 3000) and applying the approach of Teh and Houlsby (1991). The dissipation test results are also consistent with results from the site obtained by Diambra *et al.* (2014).

The degree of pore pressure dissipation during a cone penetration test can be assessed using a normalised velocity, V (Finnie and Randolph, 1994) defined as:

$$V = \frac{vD}{c_h} \qquad 6\text{-}2$$

where the standard tip velocity, v is 20mm/s. The critical values of V, where the behaviour transitions from drained to undrained, depend on which method is used to define c_h, as the normally consolidated values seen in oedometer tests ($c_{h,nc}$) fall well below those measured in a dissipation test ($c_{h,piezo}$) which in turn fall below those applicable in lightly overconsolidated states, $c_{h,oc}$. Centrifuge tests indicate a transition to fully undrained conditions at V values of between 10 and 100 when $c_{h,nc}$ is substituted (Finnie and Randolph, 1994, Randolph, 2004, Cassidy, 2012, Suzuki, 2014). If $c_{h,piezo}$ is considered approximately equal to five times $c_{h,nc}$ (Fahey and Lee Goh, 1995) for the chalk tests, the transition range reduces to 2 and 20. The CPT penetration corresponds to a normalised velocity, V≈0.8, indicating that partially drained conditions apply. Assuming the CPT end bearing failure mechanisms extend approximately two diameters below their tips leads to similar conclusions, as the dissipation tests indicate 40 ± 15% pore pressure dissipation in the 3.6 seconds required for the pile tip to pass through its earlier failure zone to reach fresh chalk.

The effect of penetration rate on q_t was assessed during PCPT08 at the IC test site. The standard rate of penetration of 20mm/s was reduced manually in steps to a minimum stable value of approximately 5mm/s, or V≈0.022, between 5.02 and 5.9mbgl. The value of q_t, was compared to q_t over the same interval at the adjacent standard rate PCPT06, termed $q_{t,ref}$ (Figure 6-8 (a)). Figure 6-8 (b) plots q_t/q_{ref} against the normalised velocity for the variable rate test. At the standard dimensionless velocity, V of the CPT of 0.8 the ratio of q_t/q_{ref} is by definition equal to 1. As the penetration rate was reduced the value of q_t/q_{ref} increased reaching a maximum of 1.7, associated with increasing degrees of consolidation around the advancing cone tip. The results appear consistent with the centrifuge test results and with the cone end bearing failure mechanism described above, with the transition from partially drained to fully drained behaviour occurring at a V value close to 0.05.

At the previous JIP site, $V_{s,hv}$ (i.e. propagating horizontally and polarised vertically) and $V_{s,hh}$ (propagating horizontally and polarised horizontally) were measured from cross-hole seismic tests along with $V_{s,vh}$ (propagating vertically and polarised horizontally) from P-S suspension logging conducted below 8m depth (SETech, 2007, Fugro, 2012b). At the IC test site, $V_{s,vh}$ was found from SCPTs carried out to a maximum 5m depth. Figure 6-9 (a) compares measurements of shear wave velocity, V_s with depth from the four different methods, while Figure 6-9 (b) shows these as shear modulus, G variations with depth where $G = \rho_s V_s^2$ and ρ_s is the soil density. The cross-hole seismic results indicate some stiffness anisotropy for the intact chalk mass with $V_{s,hv}$ approximately 10 to 20% higher than $V_{s,hh}$. Where overlaps are available, the SCPT $V_{s,vh}$ measurements were similar to the crosshole $V_{s,hv}$ measurements, while the downhole P-S logging indicated generally 10% lower values than both sets of crosshole measurements.

Several studies have shown that ultrasonic shear velocity in chalk increases with increasing density and reducing porosity. Figure 6-10 shows the shear wave velocity, $V_{s,vh}$ measurements from P-S suspension logging measured at the test site plotted against IDD at the same depth. Figure 6-10 also shows the results for structured chalk from the Wikinger OWF (Grade A1/A2), the Thanet OWF (Grade B2/B5), Sheringham Shoal OWF (Grade B3/B5) and Site A which is a North Sea OWF site (Grade A3/B5). Also shown on this plot are laboratory measurements of ultrasonic velocities taken on intact chalk samples, at a 7.5MPa confining stress, from the Dan, South Arne and Danish North Sea oil fields (Røgen *et al.*, 2005). Those authors chose only samples without fractures or visible inhomogeneities. In all cases, the *in-situ* results fall below the trend interpreted from laboratory samples, which may be attributable to differences in stress level or to the presence of fractures in the chalk mass.

As discussed in Chapter 2, Clayton *et al.* (1994) showed that the small strain stiffness measured using surface Rayleigh wave tests at three sites, which ranged from low to high intact dry density, was less than the small strain stiffness measured with local hall effect strain gauge instrumentation during uniaxial compression tests in the laboratory on 38mm diameter samples. For low-medium density chalk, V_s measured *in-situ* ranged from 390 to 810m/s and increased with depth and V_s measured in the laboratory ranged from 695 to 1255m/s. Apparent increases in V_s with IDD were far more marked for the tests conducted on laboratory samples. The difference was attributed to low stiffness discontinuities having poor contact within the chalk under *in-situ* stresses and a dominant impact on the stiffness characteristics of the chalk mass. Within the field measurements shown on Figure 6-10, there is a broad trend of increasing

$V_{s,vh}$ with increasing chalk grade and therefore decreasing discontinuity spacing. In addition to material anisotropy, the *in-situ* stiffness of the intact chalk mass is likely to be anisotropic and related to the nature and orientation of the discontinuities.

6.4.3 Index testing

Classification tests from across the site are summarised in Table 6-1, within the depth of influence of the test piles. Figure 6-11 plots bulk and intact dry density profiles along with the water content and saturated content variations with depth. Intact dry density, IDD ranges from 1.39 to 1.54 Mg/m^3 with a medium density layer encountered between 2.98 and 3.3 where IDD increases to 1.64 Mg/m^3. While the groundwater table is located far below the quarry base, the degree of saturation remains high above the water table (90-100%). Chalk specimens crushed from the test site quarry samples indicate predominantly silt sized grains; see Figure 6-12 after Bialowas *et al.* (2016) and Chan (2017). Both authors formed the samples by grinding intact samples into a powder and adding water where necessary. In those tests, D_{50} ranged from 2.7μm to approximately 6μm. Bundy (2013) showed that D_{50} for samples of Culver and Newhaven chalk can range from 1 to 10 μm, with the predominant minimum particle size between 2 and 4 μm, depending on the sample preparation method and grinding time in a Tema mill machine. Unconfined compression strength tests from the site carried out by SETech (2007) indicate q_u values between 2 and 3MPa broadly consistent with the expected (low density) q_u range of 1.1 to 3.0MPa for IDD values of 1.4 to 1.55Mg/m^3 presented by Matthews and Clayton (1993).

Table 6-1: Classification and index tests from 0 to 7m depth (SETech, 2007, Fugro, 2012a)

Test site	Testing stage
Intact dry density, IDD (Mg/m3)	1.38 – 1.64 (1.49)
Natural moisture content, wc (%)	28 – 33 (29.9)
Degree of saturation, S_r (%)	90 - 100
Liquid limit, w_l (%)	30 – 31 (30.6)
Plasticity index, I_p (%)	5 – 8 (6.4)
Unconfined compressive strength, q_u (MPa)	2.1
Specific gravity, G_s (Mg/m3)	2.71

6.4.4 One-dimensional compression

One dimensional compression and swelling curves are shown on Figure 6-13 for both intact and remoulded samples from the same depths from oedometer tests carried out by Fugro (2012a). The compression curves on intact samples showed sharp yield points which occurred

between 1.6 and 3MPa for four samples which had IDD between 1.41 and 1.49 Mg/m^3. Yielding was observed as a dramatic reduction in volume, of approximately 20 to 30%, associated with progressive de-structuring of the intact chalk and reductions in void ratio (Clayton *et al.*, 2002). The results from remoulded samples, also shown on Figure 6-13, are consistent with those presented by Clayton and Matthews (1987) for oedometer tests on chalk slurries (Figure 2-21). Similar to granular materials, at low effective stress levels, void ratio is a function of the initial void ratio of the material and a set of non-coincident intrinsic compression lines results. A unique void ratio-effective stress curve was not approached even at stress levels of 1MPa, with the compression curves indicating only small volume changes. The results indicate that structure or bonding was not fully destroyed by remoulding of intact samples, and significant de-structuring of the material or bond breakage does not occur until stress levels in excess of 1MPa are reached (Figure 6-13).

6.4.5 Triaxial stress paths

Intact chalk is markedly brittle, failing at less than 0.1% local axial strain in triaxial tests (Jardine *et al.*, 1984). Lord *et al.* (2002) indicate intact c' values from 100kPa to > 2 MPa, with $36° < \varphi' < 42°$. Remoulded chalk generally mobilises φ' between 29 and 34° with $0 < c' <$ 10kPa (Clayton, 1978, Razoaki, 2000, Bundy, 2013). Peak failure stresses from triaxial tests on intact and remoulded samples from the site, conducted by Fugro (2012a), are shown on Figure 6-14. Consolidated drained triaxial tests on *intact* samples show a markedly brittle response with best fit peak $c' = 390$kPa and $\varphi' = 41°$ developing at small strains (<0.2%) , while undrained triaxial compression tests on remoulded samples showed ductile behaviour with tentative peak φ' angles of between ≈36 and 38° (for low and medium densities respectively), when zero c' is assumed. Figure 6-15 shows the effective stress paths and stress-strain behaviour of consolidated undrained triaxial compression tests on remoulded samples, as consolidated both isotropically and under K_0 conditions. Figure 6-16 presents the stress-strain behaviour observed during drained triaxial compression tests on intact samples. The axial strains shown in Figure 6-15 and Figure 6-16 are interpreted from the Fugro results, and show average local strain measurements (made with Hall effect gauges) plotted as solid lines up to the points where the sensors become less reliable than the external strain measurements. The latter were adopted to construct the later stage stress-strain curves and are plotted as dashed lines. A key point to note is the marked brittleness shown by the drained test on intact samples after they reached peak deviator stress at relatively small strains (<0.2%). Figure 6-17 shows the variation in equivalent secant shear modulus (G=E/3) with shear strain (ε_1- ε_3) from both

triaxial tests and multi-stage resonant column tests on remoulded samples. The shear moduli of remoulded chalk, which forms around the shaft of driven piles, is significantly lower than both (i) those from the *in-situ* SCPT or cross-hole tests shown on Figure 6-9 (b) and (ii) the ranges expected from laboratory tests on similar intact samples reported by Matthews *et al.* (2000) and Clayton and Heymann (2001).

6.4.6 Interface shear behaviour

Earlier studies have found that the interface shearing resistance of sands increases with the interface surface roughness, until an upper bound "critical" value is reached, which is close to the internal friction angle of the material. The latter is associated with interlocking of sand grains at the interface as the particle size approaches the surface roughness, forcing the shearing mechanism into the sand mass (Kishida and Uesugi, 1987, Jardine *et al.*, 1993, Ho *et al.*, 2010). Jardine *et al.* (1993) showed that the residual friction angle, δ'_{ult} decreases with increasing stress level associated with suppressed interface dilation.

The large strain interface shear behaviour of samples of chalk from the test site was investigated using the Bishop ring shear apparatus at IC. Tests were conducted by the Author and also by Derek Chan for his MSc thesis. The tests were planned to investigate (i) the residual interface shear strength of remoulded chalk (ii) the effect of interfaces of different materials and varying interface roughnesses on interface shear strength and (iii) the effect of ageing under constant load on the interface shear behaviour.

The apparatus and general test procedure were described in Section 5.5.6 with the apparatus shown previously on Figure 5-11 and Figure 5-12. Further details on the tests are provided in Table 6-2 and by Chan (2017). Both mild steel (MSt) and stainless steel (SS) interfaces were considered in the study. Three MSt and one SS interface were shot-blasted at IC to "standard" R_a values of 9.88μm and 8.3μm respectively. Four MSt and three SS interfaces were manufactured to an "enhanced roughness" by an external contractor. The enhanced R_a varied between 12.93 and 15.11μm for the MSt interfaces, similar to that of an offshore pile, and between 11.48 and 13.36 μm for the SS interfaces. Three "smooth" polished SS interfaces were also used for comparison, where R_a was equal to 1.22 μm. The latter were intended to investigate the interface shearing behaviour between the chalk and a PCPT friction sleeve which has a similar roughness, discussed further in Chapter 7.

The roughness measurements were made by the Author using a Taylor Hobson "Talysurf" surface profiling machine. A total of four measurements, individually 100mm long,

were made for each of the annular interfaces. A Gaussian weighted average filter was passed through the data to obtain the value of R_a. An example of a surface measurement result on an interface, made prior to shearing, is shown on Figure 6-18.

A total of thirteen tests were carried out on samples from the site; Table 6-2 summarises the pre and post-test values of interface R_a, the peak interface friction angle, δ'_{peak} and δ'_{ult} at a shearing displacement of both 10 and 40mm. The maximum displacement mobilised during the static tests on the driven piles was close to 16mm, while the maximum mobilised during static testing of the jacked piles was approximately 9.5mm. Twelve of the tests were sheared after 12 hours. One test, MSt-RGH-200kPa-aged, was consolidated to 200kPa and allowed to age under load in the apparatus for 25 days, while measuring the change in sample height.

Table 6-2: Summary of ring shear tests on samples from the site (after Chan, 2017)

Test code[1]	R_a (μm)		δ'_{peak} (°)	δ'_{res} (°)	
	Pre-test	Post test		10mm	40mm
MSt-STD-200kPa	9.88	10.01	33.4	31.8	32.8
MSt-STD-400kPa	9.88	10.01	35.8	35.0	33.8
MSt-RGH-100kPa	12.93	9.88	31.5	31.5	31.8
MSt-RGH-200kPa	15.11	10.72	33.2	32.5	31.6
MSt-RGH-400kPa	15.11	11.82	35.6	35.0	35.0
SS-SMT-100kPa	1.22	1.22	29.8	28.9	26.2
SS-SMT-200kPa	1.22	1.22	30.5	30.1	30.5
SS-SMT-400kPa	1.22	1.22	31.5	31.5	31.5
SS-STD-100kPa	8.3	8.03	31.0	30.7	29.7
SS-RGH-100kPa	13.36	11.92	31.4	30.1	30.2
SS-RGH-200kPa	11.48	-	33.8	33.3	32.2
SS-RGH-400kPa	11.48	-	35.5	34.8	33.9
MSt-RGH-200kPa_aged[2]	13.91	9.87	36.0	35.7	34.5

1. Test code nomenclature gives interface type (MSt = mild steel, SS = stainless steel) then roughness type (STD = standard roughness, RGH = enhanced roughness, SMT = smooth) and consolidation stress level (e.g. 100kPa).
2. Aged test held under constant load post consolidation for 25 days prior to shearing

The twelve early age tests show both δ'_{peak} and δ'_{ult} varying with R_a and with stress level with an overall range for δ'_{peak} of 32.8±2.1° and of 31.6±2.3° for δ'_{ult} measured at 40mm displacement. Considering the effects of interface roughness, Figure 6-19 (a) plots δ'_{ult} (at 40mm displacement) normalised by the soil-soil friction angle of remoulded chalk of ≈33° (Section 6.4.5) against the relative roughness, $R_n = R_a/D_{50}$. The tendency for sliding to occur within the soil mass has been shown previously to increase with R_n; Uesugi and Kishida (1986). As illustrated on Figure 6-19 (a), for the values of R_n considered, the peak stress ratio attained appears to be independent of the interface properties suggesting failure occurs in the chalk

mass. Taking a D_{50} value of 3 to 6μm indicates R_n values of 2.1 to 5.0 for the mild steel tests, and 1.9 to 4.5 for the stainless steel tests, both well above the R_{crit} limit of approximately 0.1 defined for sands. The values of δ'_{ult}/φ' are generally between 0.9 and 1.05 for the mild steel and stainless steel tests also indicating that failure occurred within the chalk mass.

Granular particles in contact with an interface will dilate as the particles must move away from the interface in order for sliding to occur. Rough surfaces interlock with soil particles forcing particle rearrangement to occur regardless of stress level or density; DeJong and Westgate (2009) showed that dilation occurs at the interface even for loose samples, with particle-interface interlocking overcoming the tendency for contraction based on the low initial density. Contraction was shown to occur elsewhere in the sample based on global measurements of vertical movements. Figure 6-19 (b) plots the maximum observed dilation Δr versus R_n for the chalk tests. Tests using mild steel interfaces showed that Δr ranged from 14 to 24μm equivalent to 0.9 to 1.9 times R_a. The stainless steel interface tests indicated Δr between 6 to 25.5μm, equivalent to between 0.4 and 2.2 times R_a. A trend of increasing Δr with R_n was not observed, with similar values of Δr observed in all tests, also consistent with shearing occurring within the chalk mass, where dilation is largely independent of the interface properties. Both δ'_{peak} and δ'_{ult} also appeared to increase with stress level e.g. considering the MSt-STD tests and the MSt-RGH tests conducted on interfaces of similar roughnesses at stress levels between 100 and 400kPa. As shown in Figure 6-19 (c), the magnitude of increase in δ' was highest between 100 and 200kPa and appeared to level off between 200 and 400kPa.

Figure 6-20 (a) plots the interface friction angle against displacement for one of the early age tests, conducted at 200kPa, along with the ageing test for comparison. Figure 6-20 (b) plots the change in sample height, Δh for the same tests, indicating that the samples all dilated initially before contracting to ultimate conditions. The aged chalk sample mobilised higher δ'_{peak} and δ'_{ult} angles of 36 and 34.5° respectively. Comparison with the early age test indicates an increase in δ'_{peak} and δ'_{ult} of 2.6° and 2.9° respectively, equivalent to an increase in local shear stress, τ_f of approximately 10%. The vertical displacement remained constant over the ageing period. At the end of the test, rust was observed on the interface which had diffused into the sample, possibly disrupting the pre-formed shear mechanism and forcing a new mechanism to occur under chalk-chalk conditions. Visual observation indicated a change in properties and a significant increase in strength. After testing, it was no longer possible to remould the sample by finger pressure.

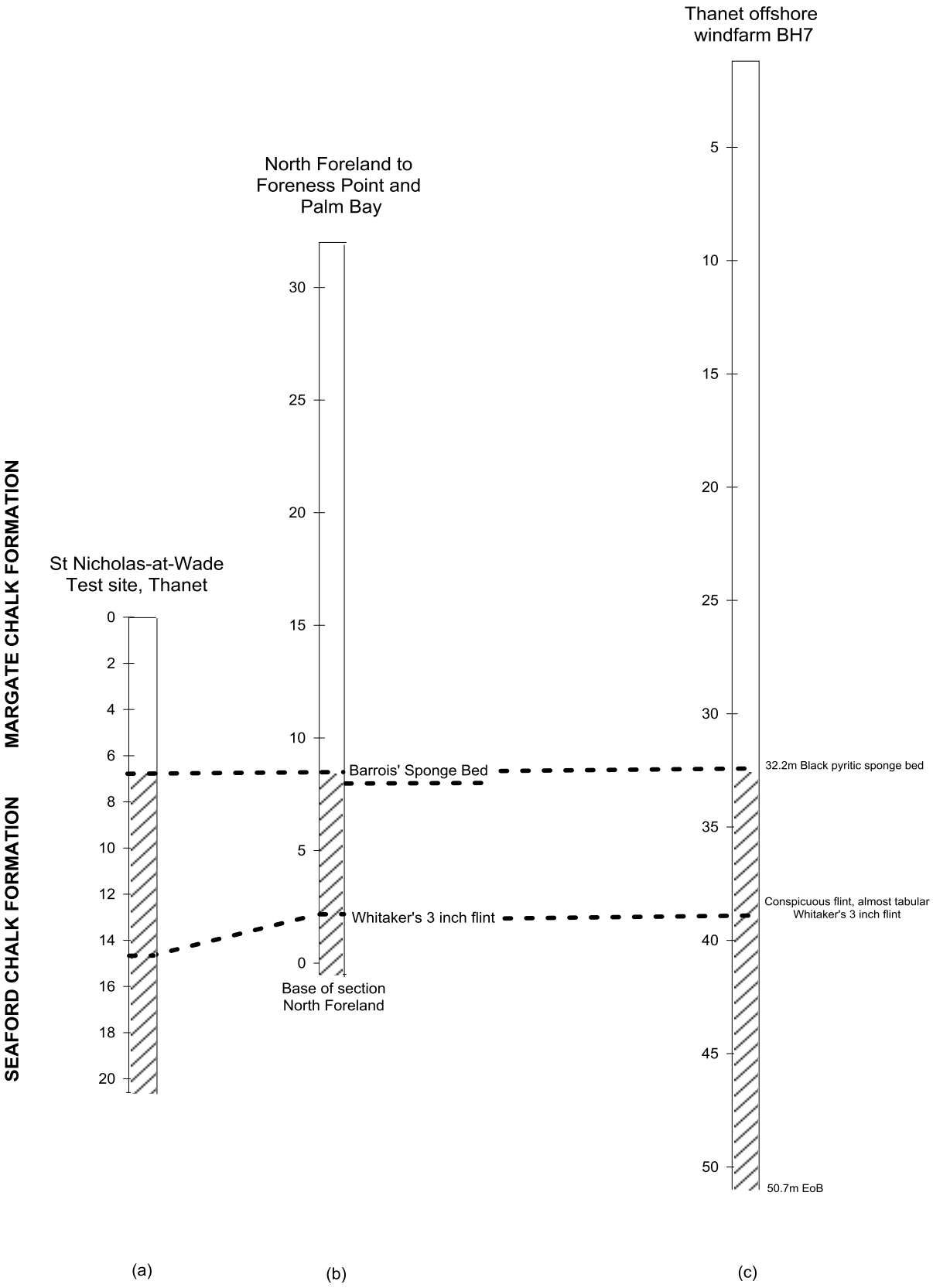


Figure 6-3: Correlation of stratigraphy encountered at the test site with the closest onshore section located at North Foreland and offshore borehole No. 7 at the Thanet Offshore Windfarm as carried out by Prof. Rory Mortimore (adapted and simplified from ChalkRock, 2007)

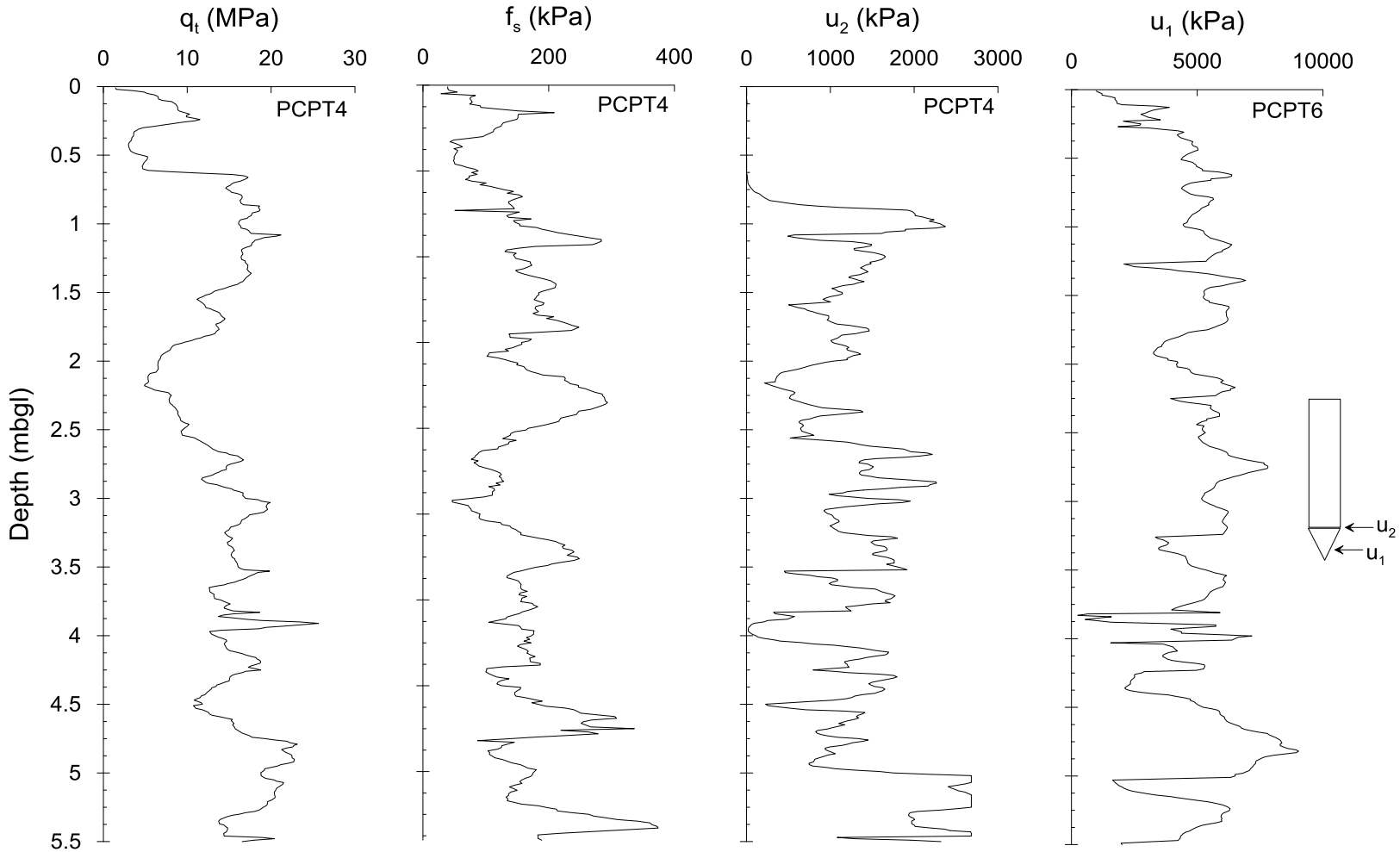


Figure 6-4: Typical profiles of cone resistance, q_t, sleeve friction, f_s, pore pressure at the sleeve position, u_2 and pore pressure at the u_1 position measured at the Imperial College test site

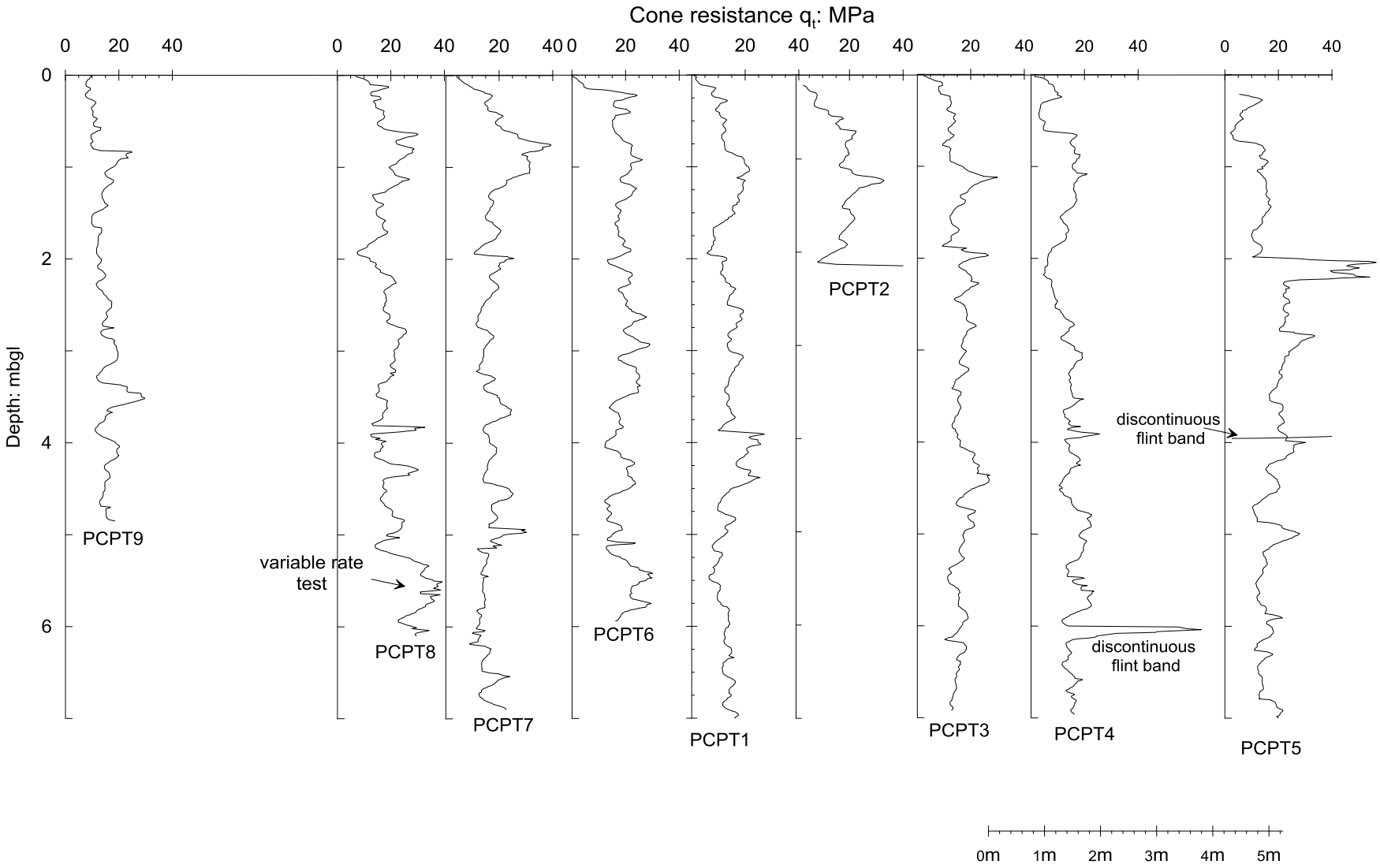


Figure 6-5: Section A-A cone resistance with depth across the Imperial College test site

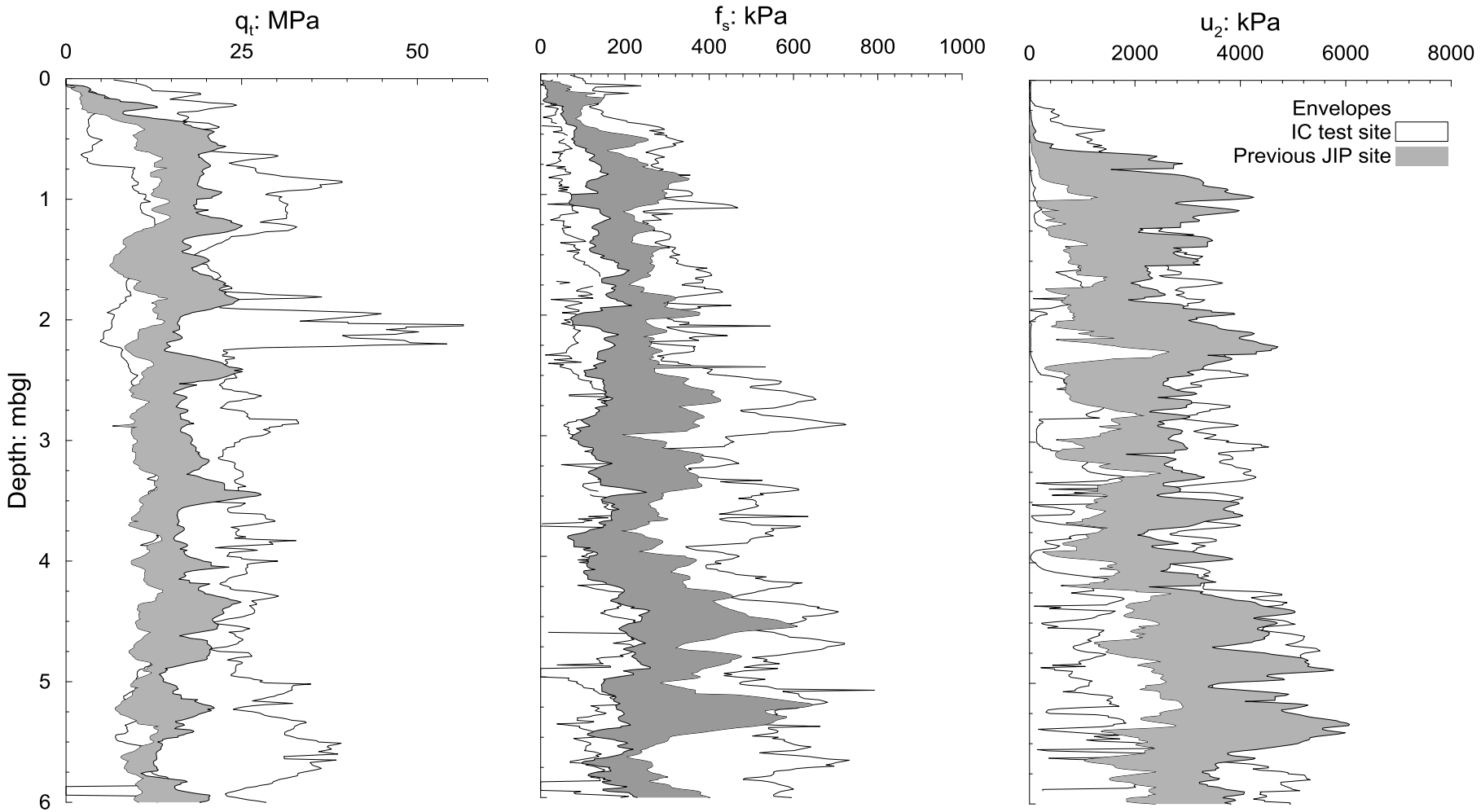


Figure 6-6: Envelopes of CPT test parameter profiles at the Imperial College test site compared to those at the previous JIP site

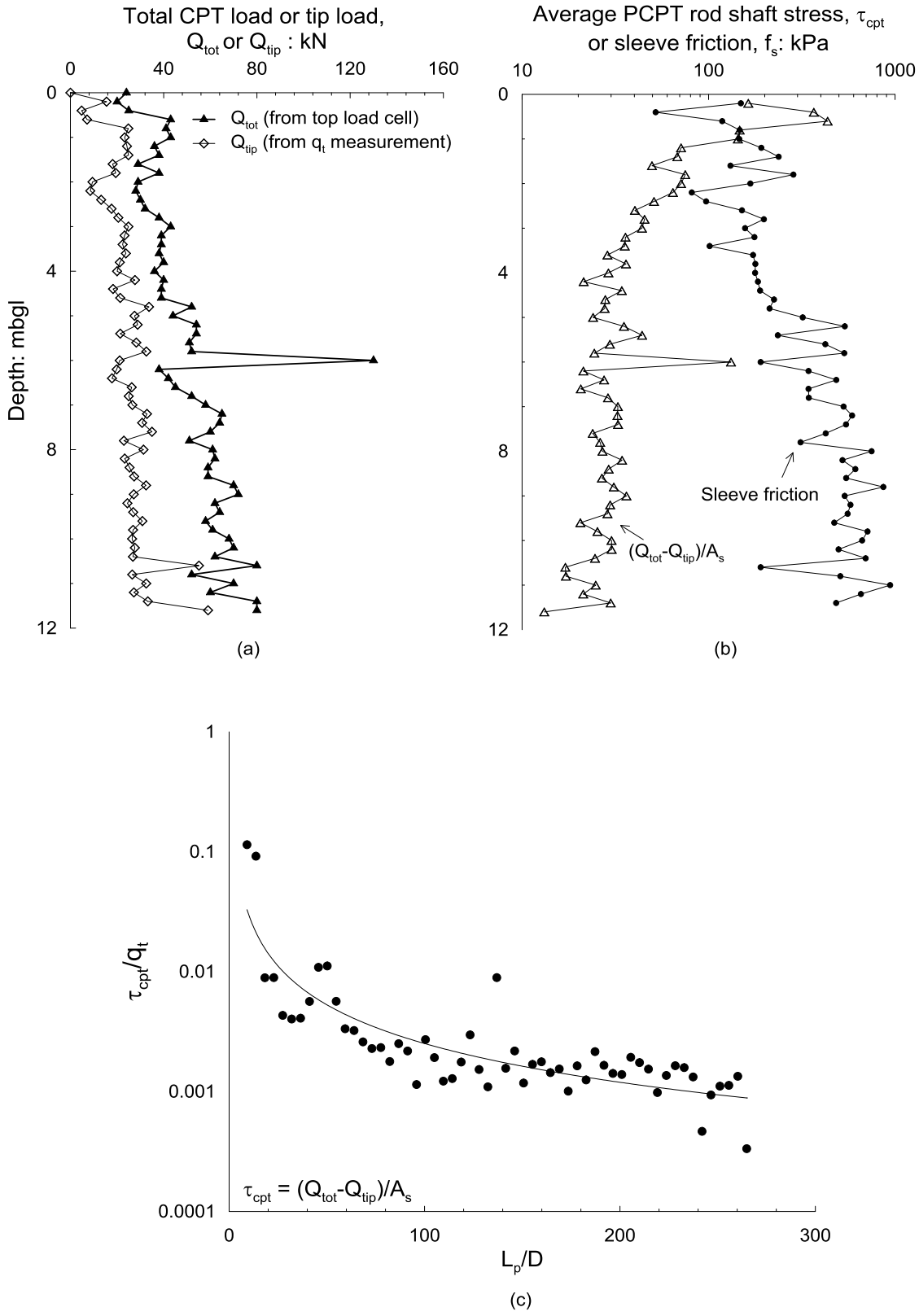


Figure 6-7: Measurement of PCPT load during installation (a) total load measured in the CPT truck compared with load on the tip (b) average shaft stress during penetration on CPT rods, τ_{cpt} compared with sleeve friction measurements, f_s (c) τ_{cpt}/q_t versus length of penetration normalised by diameter

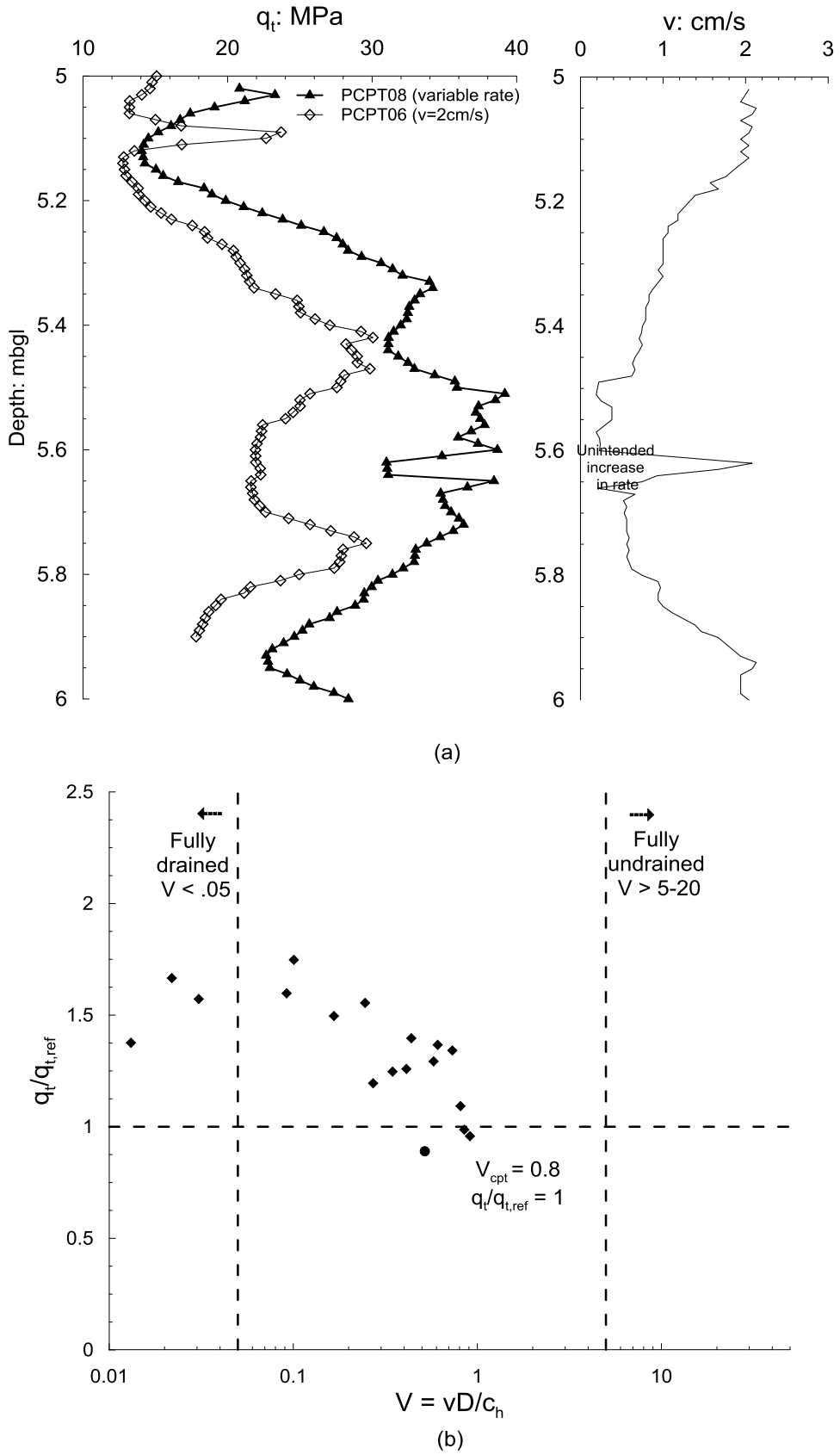


Figure 6-8: Effect of variable penetration rate on cone resistance at PCPT08. Adjacent PCPT06 also shown where penetration was at a rate of 2cm/s (b) cone resistance during variable penetration versus normalised velocity

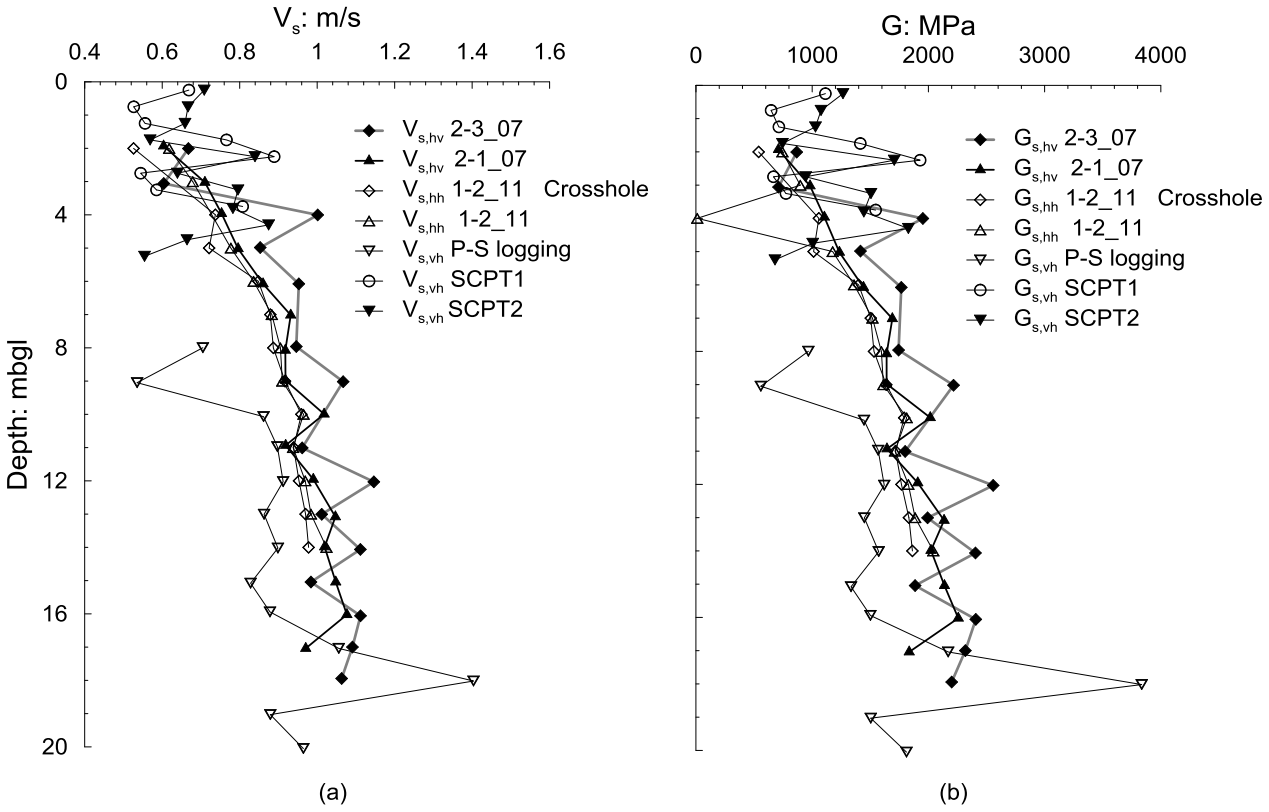


Figure 6-9: Shear wave velocity and shear modulus crosshole, P-S suspension logging and SCPT

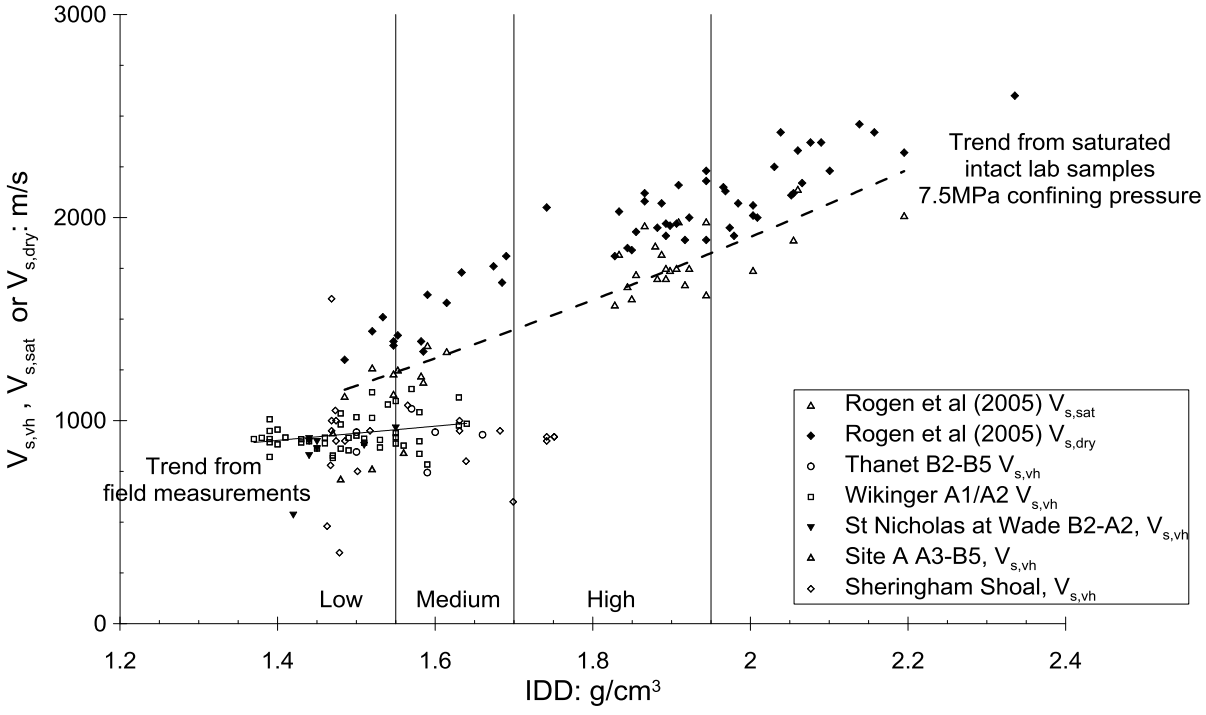


Figure 6-10: Shear wave velocity versus IDD at the site compared with other sites

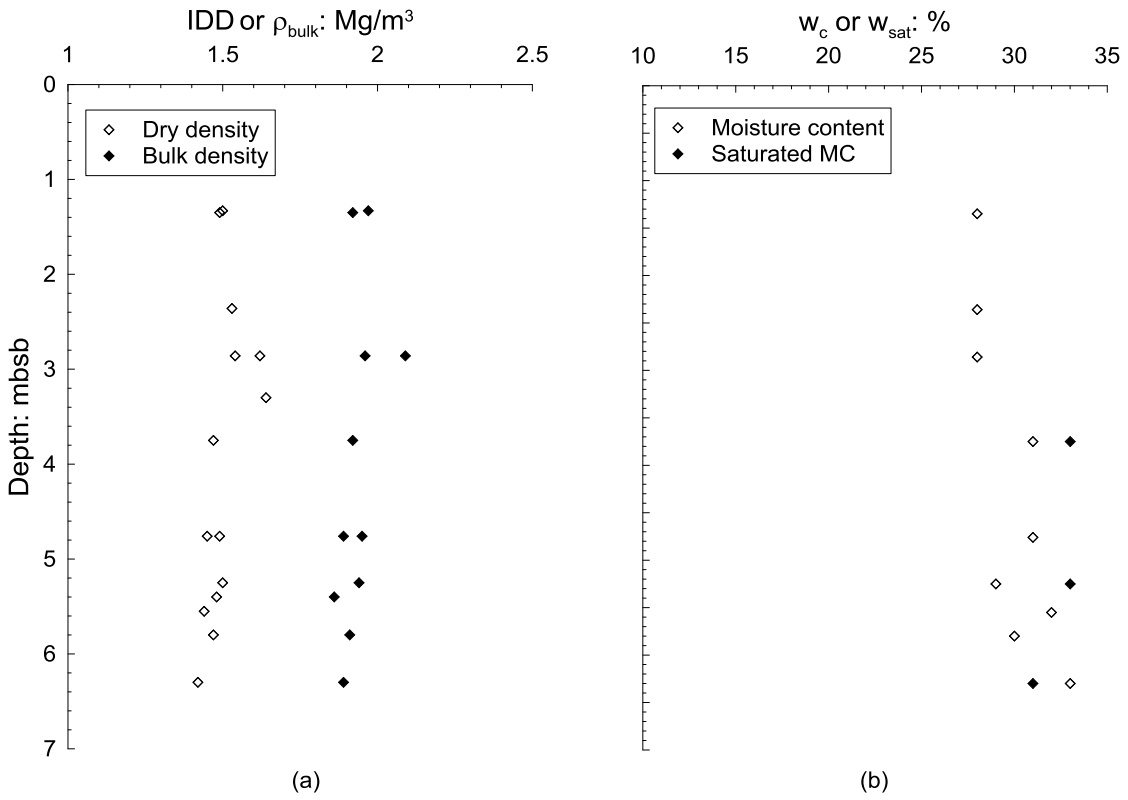


Figure 6-11: (a) Bulk density and dry density profiles (b) moisture content and saturated moisture content at the previous JIP site (data from Fugro, 2012a, SETech, 2007)

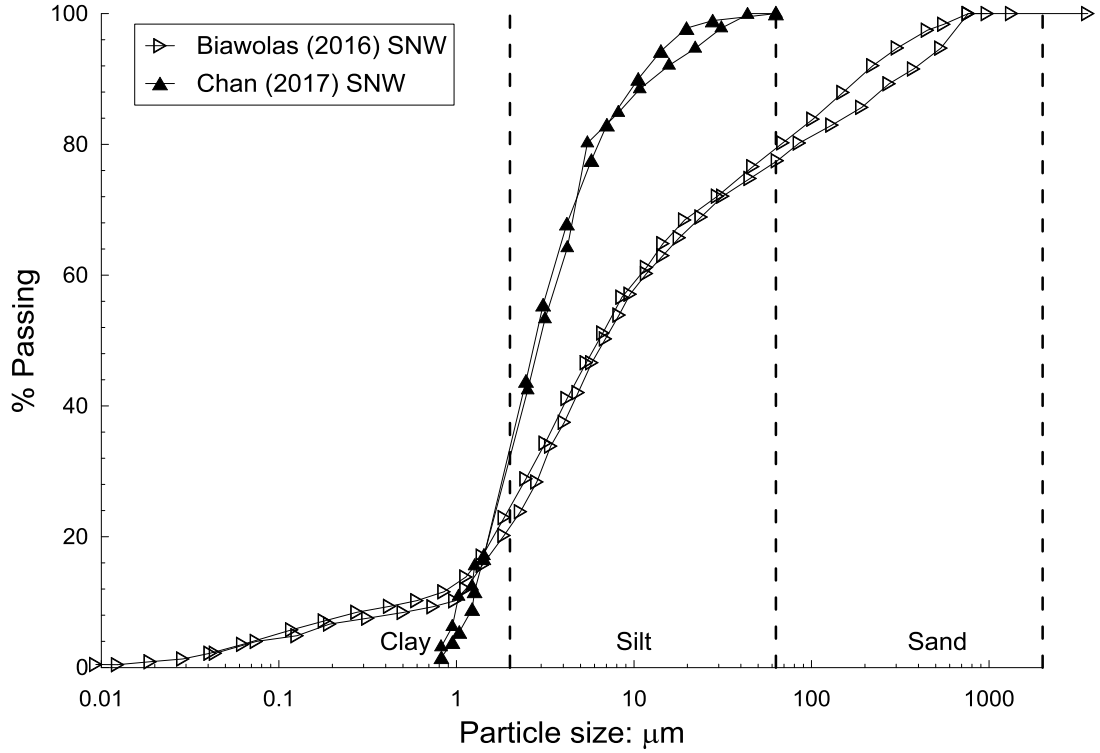


Figure 6-12: Grading curve from samples of crushed chalk at the test site (Bialowas *et al.*, 2016)

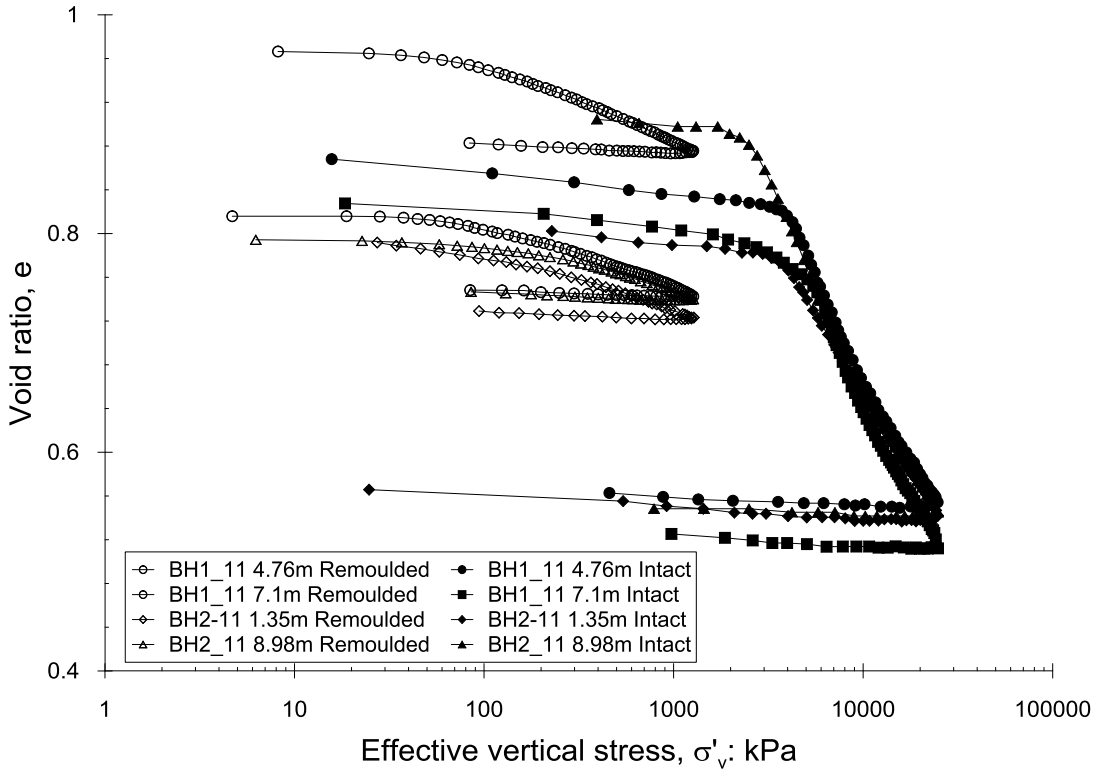


Figure 6-13: One dimensional compression and swelling curves from oedometer tests on intact and remoulded samples (data from Fugro, 2012a)

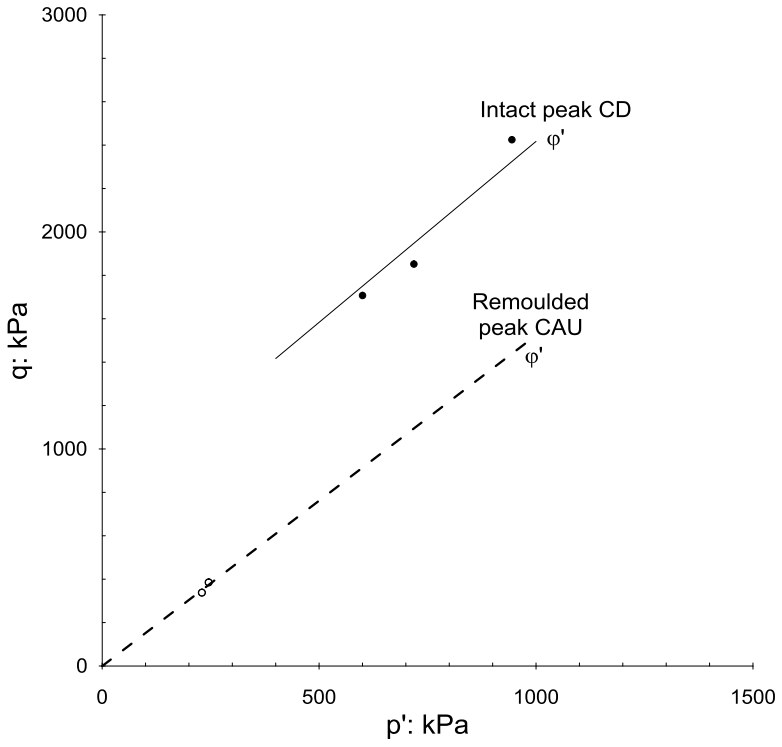


Figure 6-14: Peak failure envelopes interpreted from Consolidated Drained (CD) and Consolidated Undrained (CU) triaxial tests on intact and remoulded samples (data from Fugro, 2012a)

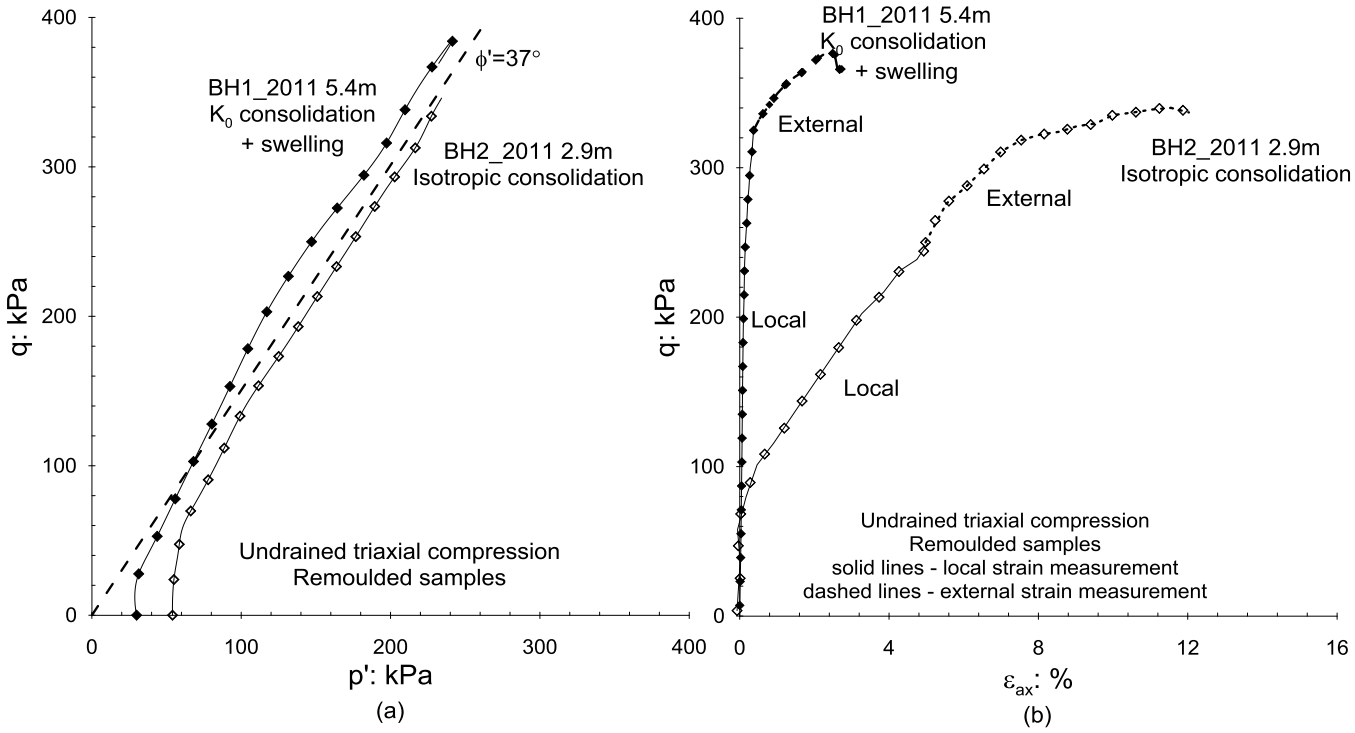


Figure 6-15: (a) Undrained triaxial tests on remoulded samples (a) stress paths in q-p′ space (b) q-ε_{ax} (data from Fugro, 2012a)

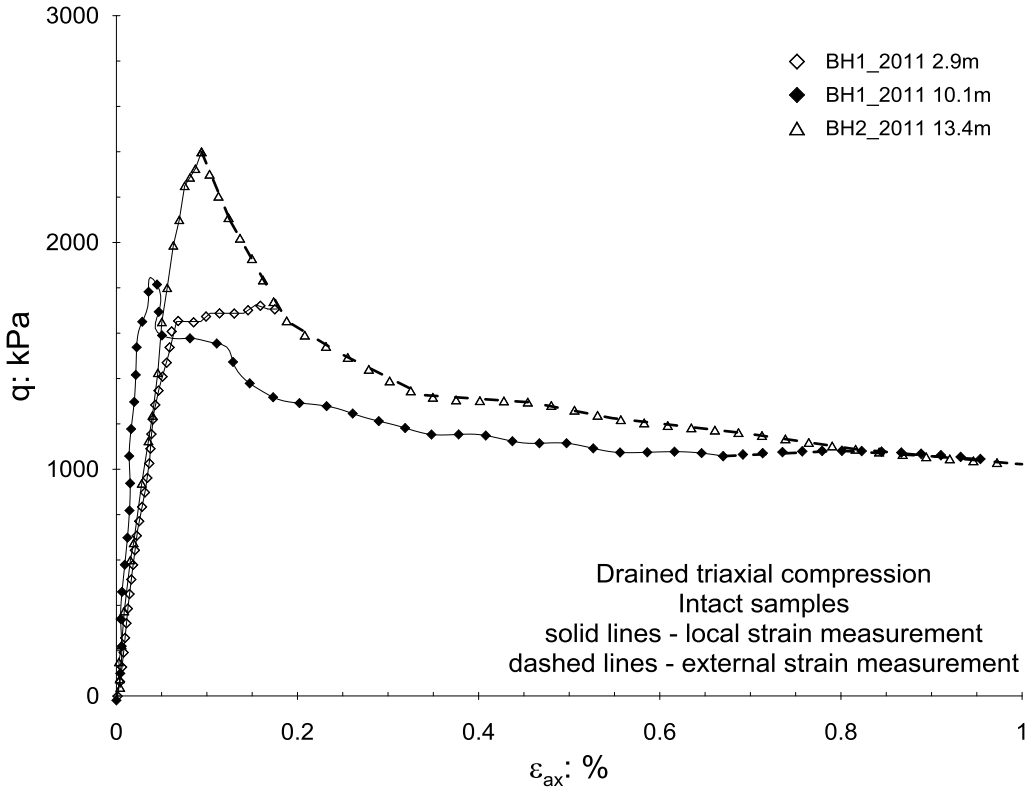


Figure 6-16: Drained triaxial tests on intact samples (data from Fugro, 2012a)

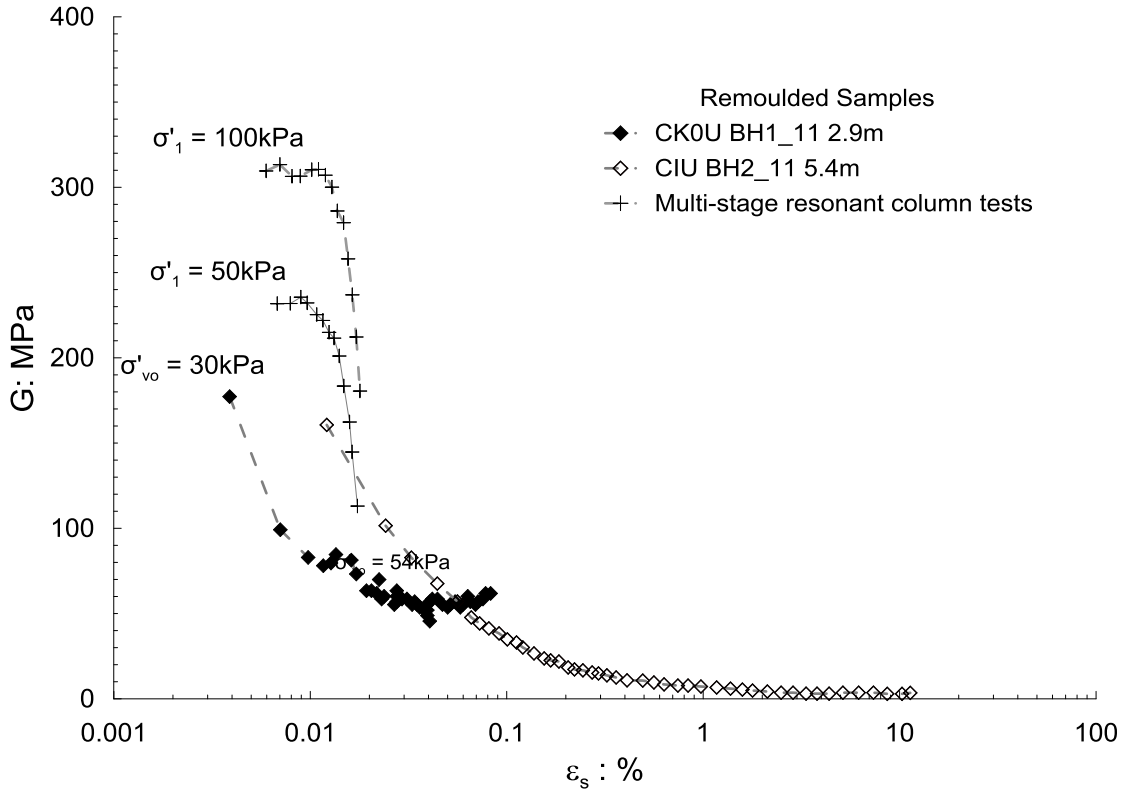


Figure 6-17: Shear modulus from triaxial stress path tests and multi stage resonant column tests on remoulded samples (data from Fugro, 2012a)

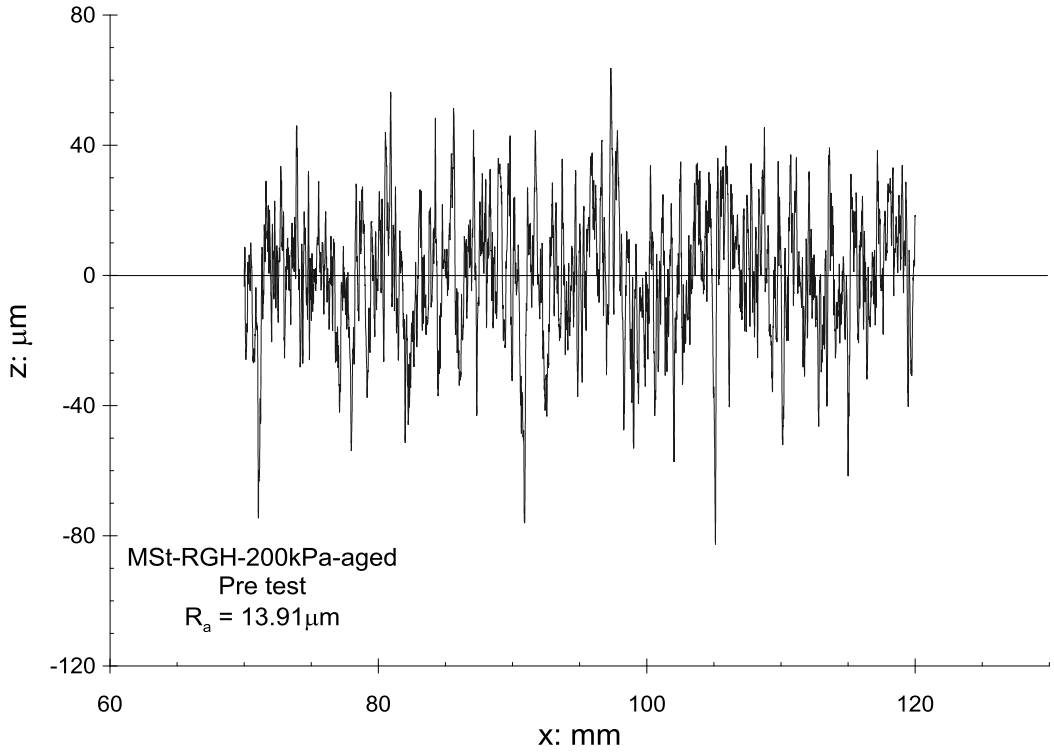


Figure 6-18: Example of pre-test roughness measurement of ring shear interface using Talysurf (MSt-RGH-200kPa)

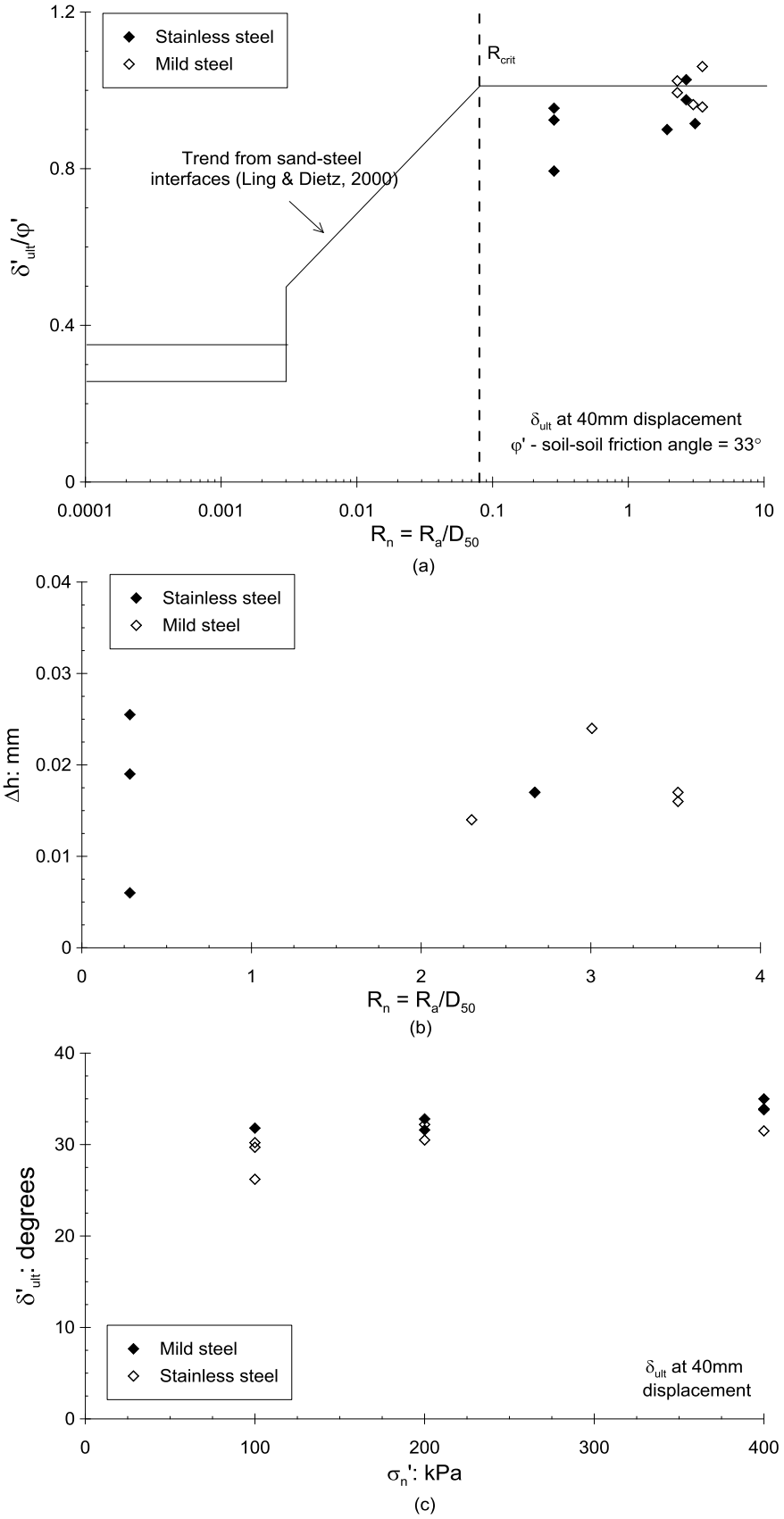


Figure 6-19: (a) effect of relative roughness on δ normalised by the soil-soil friction angle ϕ (b) change in sample height versus relative roughness (c) ultimate interface friction angle versus stress level (data from Chan, 2017)

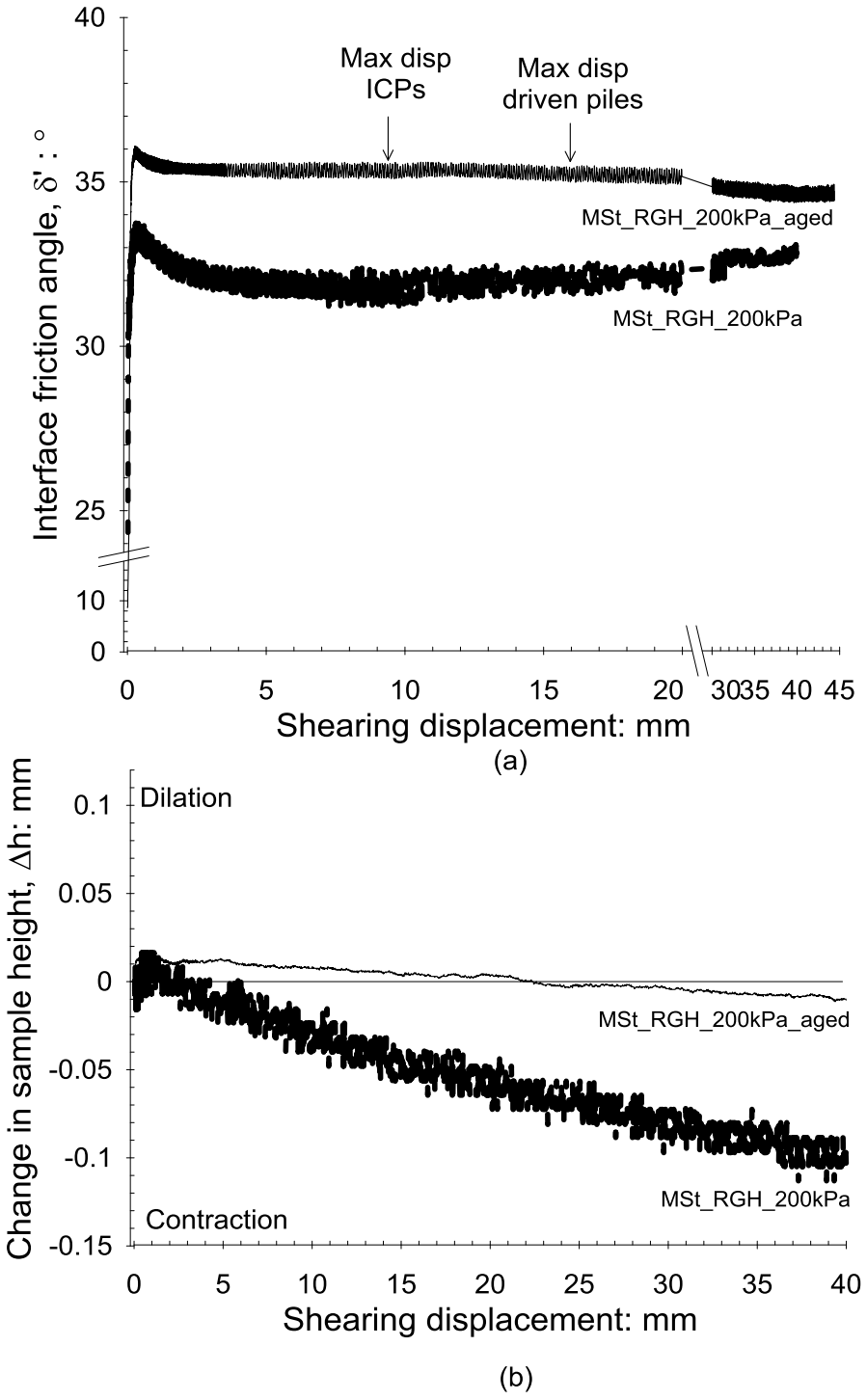


Figure 6-20: Comparison between aged and unaged large strain interface ring shear tests at IC in the Bishop apparatus on samples from the St Nicholas-at-Wade test site (a) interface friction angle versus displacement (b) change in sample height (data from Chan, 2017)

6.5 Pile and driving details

6.5.1 Pile details

A total of seven 139mm diameter open-ended steel tubular piles (API 5CT Grade L80/N80) with an average wall thickness, t_w of 8.5mm and R_a of approximately 10μm were driven at the St. Nicholas-at-Wade test site on 19th October 2015. The piles were driven to penetrations of approximately 5.5m by Green Piling Ltd. using a 4 tonne Juntann hydraulic impact hammer (SHK100-4) with a maximum energy of 49kNm. A stick up of between 0.5m (DP2, DP3, DP5, DP6) and 1.0m (DP1, DP4, DP7) was left above ground level to facilitate the subsequent static and dynamic testing. The blow counts per 250mm penetration were recorded during the drive and are plotted on Figure 6-21. When released from the pile gripper, the piles initially fell under their own weight, by distances of between ≈0.75 and 1.0m. Blow counts over the entire drive were generally less than 10 per 250mm penetration, increasing slightly with depth.

In most cases, coring behaviour was observed, with the internal soil columns of DP1, DP4 and DP5 rising between 0.26 and 0.83m above ground at the end of driving and falling 0.18 to 0.43m below ground with the other four piles. The volume of chalk displaced by the steel was equivalent to 0.019m^3 or a height inside the steel tube of 1.6m, if all the chalk was displaced upwards during driving.

6.5.2 Pile resistance at the end of driving

Three of the piles had a stick up of up to 1m to facilitate dynamic testing, which was conducted on DP1, DP4 and DP7. Strain gauges and accelerometers were placed 0.5m from the top of each pile and the driving data were recorded using the Pile Driving Analyser (PDA) software. The intrinsic limitations and uncertainties of inferring static capacity from dynamic driving monitoring were highlighted by Lim and Lehane (2014), including the effects of carrying out tests following delays after driving, which can include time-dependent capacity increases. The latter was avoided by installing the dynamic instrumentation prior to pile installation and monitoring uninterrupted continuous driving. Back analysis of the measured force and velocity signals was conducted using IMPACT (Randolph, 2008) which includes explicit modelling of both internal and external shaft resistance. The soil density and intial shear modulus were determined from the laboratory test results and *in-situ* measurements

(Figure 6-9), respectively. As with the analysis of the Wikinger data (Chapter 5), and consistent with the approach adopted by Salgado *et al.* (2015) the shear modulus used in the analyses was an operational secant modulus, G_1 projected down from the elastic small strain (G_{max}) data as approximately 20% G_{max}. The viscosity parameters, α_s and β_s were both adopted as 1.0 in this case in order to obtain a good match. The best quality signal matches were obtained by applying 85-90% of the shaft resistance on the outer area, consistent with trends reported from instrumented piles driven in sand by Chow (1997). This differs slightly from the approach adopted at Wikinger, where shaft resistance was assumed to occur only on the external area to simplify the analysis of the approximately 70 blows considered.

Figure 6-22 shows the partial measured and calculated velocity and force time histories from a typical result. From the three results, the average end bearing at the end of driving, including the contribution from the internal shaft resistance was 15.8MPa. The average external compressive shaft load at EoD was 39.3kN. The final profiles of total (internal and external) shaft resistance against depth for all three piles are shown in Figure 6-23. Average external EoD shaft shear stresses were between 15 and 17kPa, similar to the 11 to 23kPa range of unit τ_{avg} reported between 2 and 12 hours after driving for 762mm diameter 4m long open-ended steel tubes driven at the same site (Ciavaglia *et al.*, 2017a).

The average shaft stresses on the 139mm diameter piles fall 15 to 25% lower than the CIRIA 20kPa static capacity recommendation in low-medium density chalk (Lord *et al.*, 2002). Markedly higher local resistances were interpreted from the dynamic tests over the lower 1 to 1.5m of the shaft, which tended towards the CPT sleeve friction values value of 200kPa and decayed with additional distance, h above the tip. These trends are similar to the trends seen in average shaft resistance and sleeve friction measurements from the CPT reported in Section 6.4.2 and shown on Figure 6-7.

6.5.3 Drainage characteristics during driving

The seven open-ended piles each took between 4 and 16 minutes to drive leading to average penetration rates of between 5.7 and 22.9mm/s. Substitution of these field velocities and $c_{h,piezo}$ into Eq. 6-2 indicates partially drained behaviour for the piles with normalised velocities of between 0.25 and 3.07. The latter considers the piles as open-ended with the equivalent effective radii, R* determining the dissipation rates. The local excess pore pressures remaining in the chalk at any level after the tip passes during driving will dissipate with continued pile penetration and increasing h. The h values at which any remaining tip generated

pore pressures can be expected to dissipate by 50% are between 210 and 690mm, obtained by scaling up from the piezocone dissipation times, t_{50} by the ratio of $(R^*/R_{cpt})^2$ and applying the driving velocity ranges of the piles. At greater h values, where longer times will have elapsed after the local excess pore pressures were generated at the tip, higher degrees of pore pressure dissipation can be expected. The annulus of chalk putty, formed around the shaft, is also likely to experience degrees of consolidation and reductions in void ratio that depend similarly on h/R*. The surrounding stiff chalk mass will provide kinematic restraint which will reduce the effective stresses acting on the pile shaft due to the putty's own volume straining, which will be accommodated primarily by radial shrinkage. Lower degrees of consolidation around the pile shaft are likely to apply to larger piles during driving and/or those that penetrate more rapidly such as in the free falling pile runs that can occur when installing large monopiles in chalk (Norrie, 2015, Carotenuto *et al.*, 2018).

6.5.4 The effects of pile installation on the surrounding chalk mass

Following the end of the pile load testing programme, 274 days after driving, two piles (DP1 and DP7) were partially exhumed, in order to examine the conditions surrounding their shafts after ageing and testing. Pile DP1 had been subjected to two cyclic tests, the second reaching failure, and a post failure static tension test 21 days prior to excavation. Pile DP7 had been subjected to a cyclic test which did not reach failure followed by a post cyclic static tension 27 days prior to excavation.

The trial pits, carried out along one face of the driven pile, were approximately 1.5m wide and were excavated to a maximum depth of 1.1m. The conditions were logged with the help of Dr. James Lawrence from Imperial College. Figure 6-24 shows a schematic description of the chalk fabric developed around the piles. Figure 6-25 shows variations in the water content with depth, z and radial distance from the pile centre, r normalised by the pile radius, R. Further details on the pile exhumation inspections are given in Appendix A-5. The conditions observed around the pile can be summarised as:

- **Zone A:** 0-14mm from pile wall, remoulded chalk (assumed to have puttified during driving) with no distinct fabric features. A 1-2mm thick mottled brown oxidised surface adjacent to the surface of the pile giving evidence of redox reactions taking place involving the pile steel. Water contents (w_c) range from 19.5 to 24.9% (average = 22.8%), falling below the undisturbed far-field average of 29.9%;

- **Zone B:** 14-50mm from pile wall – intact chalk with gritty fragments, crumbles between fingers into dice-sized blocks. Evidence of recent fracturing with no iron staining; (w_c) ranges from 25 to 28% (average = 26.5%). This zone is discontinuous and was not encountered at all depths;
- **Zone C:** Intact chalk which breaks into bigger blocks. Fractures are iron-stained (old) and open to <3mm; (w_c) ranges from range 26.4 and 31.3%, with the average of 28.4% slightly lower than the far-field mean.

The remoulded zone's thickness, t_{zone} varied from 0.59 to 1.64 times the pile wall thickness. Muir Wood *et al.* (2015) exhumed a previously tested 762mm diameter pile at the same site and report a remoulded annulus of 0.78 to 1.57 times t_w. The same authors found remoulded zones formed around steel driven plates whose width amounted to approximately 40% of the varying plate thickness.

Evidence of the conditions under which the remoulded zone formed was presented in the present study by natural fractures and marl seams which terminated and curved sharply downwards at the zone's outer edge. There was no sign of any shear surface close to the pile, or within the chalk mass, having formed during static loading, that could be separated confidently from the remoulded zone that formed during driving. As argued earlier, the remoulded zone probably underwent at least partial contemporaneous consolidation during driving that contributed to the driving 'h/R*' effects identified in Figure 6-23 through, likely temporary, relaxation of the shaft radial effective stresses. Jardine *et al.* (2006, 2013a) argue that similar radial effective stress reductions take place around piles driven in sand and that subsequent creep processes allow the arching mechanisms generated around the shafts to relax and lead to radial effective stress gains that contribute to shaft capacity growth with time.

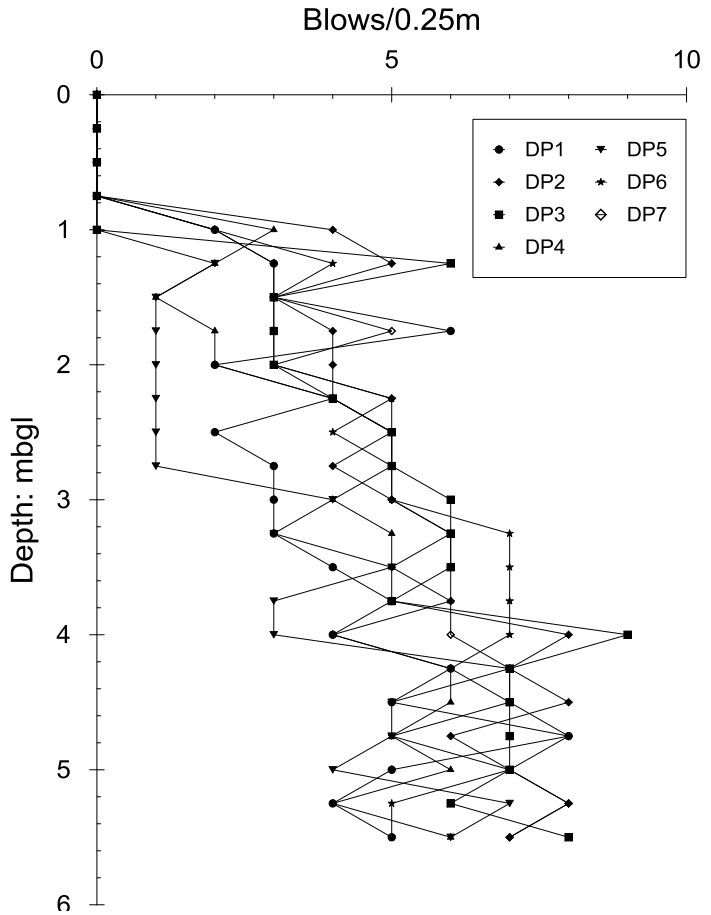


Figure 6-21: Blow counts/250mm penetration during installation of 139mm diameter test piles

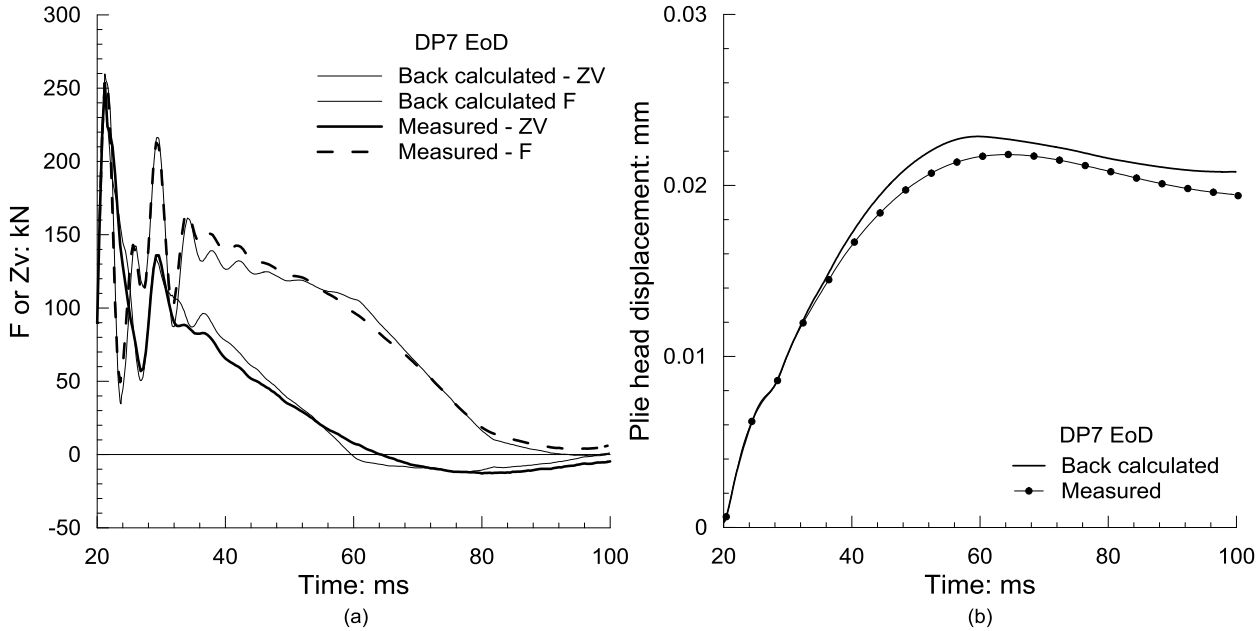


Figure 6-22: Example of a signal match found with IMPACT for pile DP7 (a) force and velocity times impedance (b) pile head displacement

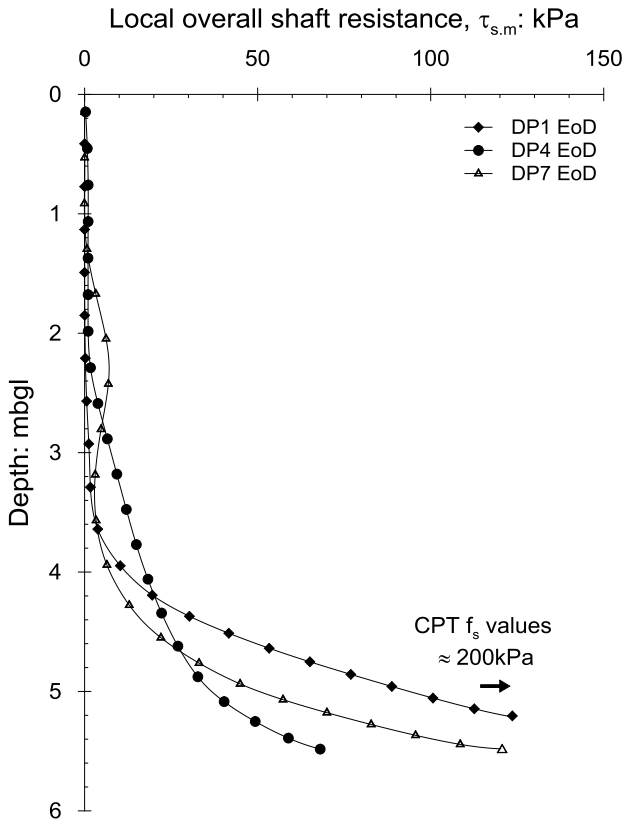


Figure 6-23: Profiles of overall resistance at EoD from analysis of dynamic pile test

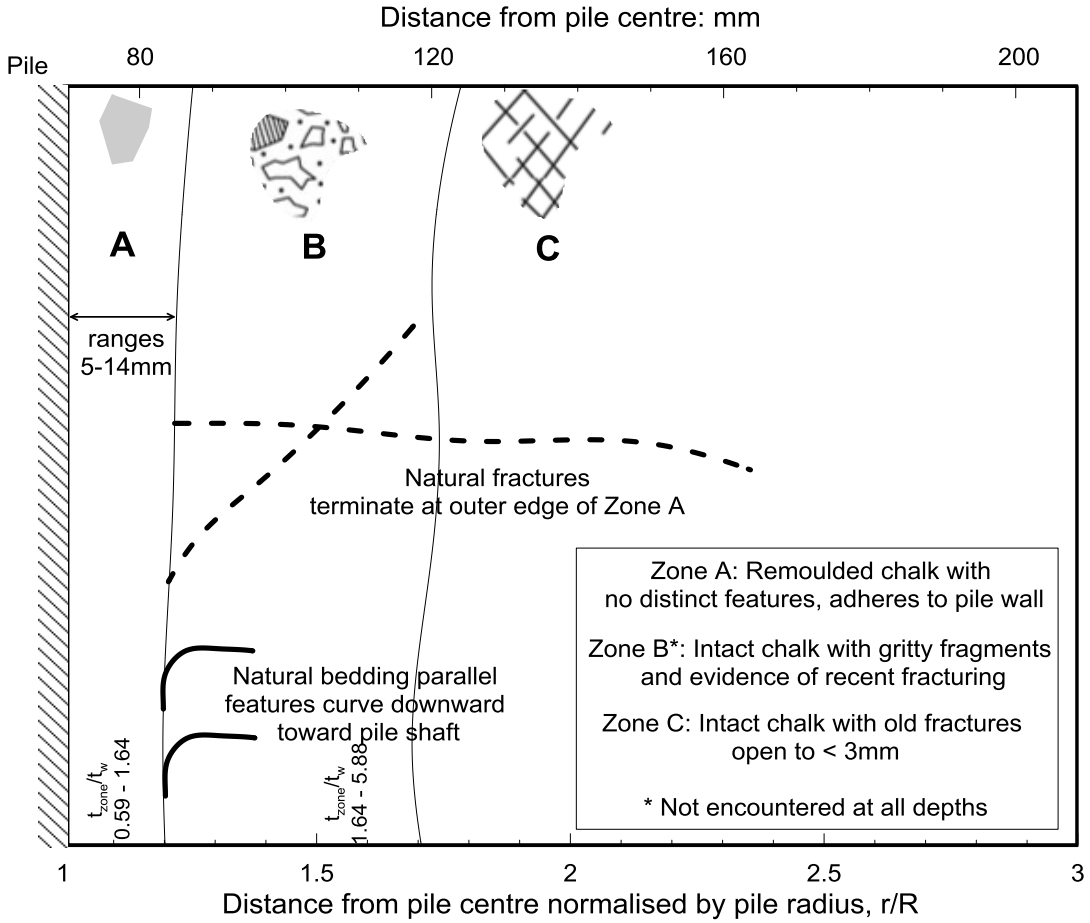


Figure 6-24: Schematic of conditions in chalk surrounding 139mm diameter test piles

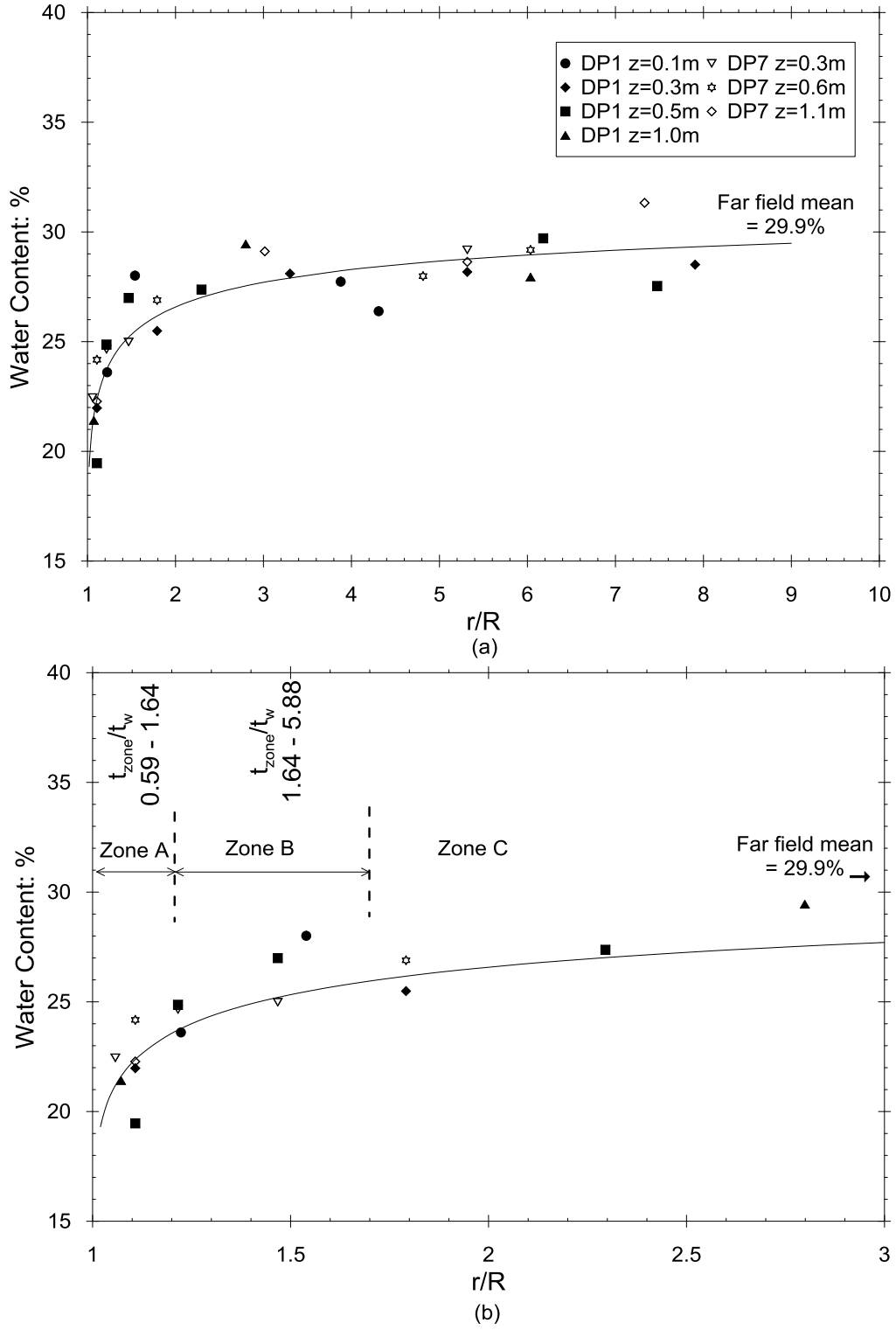


Figure 6-25: Radial water content profiles with radial distance from the pile centre normalised by pile outside radius R (a) near and far field (b) near field

6.6 Testing programme

The analysis of the dynamic pile tests described in Section 6.5.2 provided estimates of the piles' average compressive shaft resistance at the end of pile driving. The post-driving ageing trends were investigated using 'slow' static maintained load tension tests conducted at four ages on three virgin piles and one previously tested pile. The pile test codes and test histories are shown on Table 6-3. The test code nomenclature refers to the pile number (e.g. DP1), then the test type (CY=cyclic, T=first time static tension, TPC = post cyclic static tension) and the number of experiments previously completed up to and including that test. The effects of axial cyclic loading on aged piles were investigated through the separate programme summarised in Table 6-4, testing four virgin piles 247 to 255 days after driving.

Table 6-3: Summary of pile test codes and test histories for ageing trends

Test pile	Test code	Age (days)	Comment
DP2	DP2-T1	10	Static test on previously untested pile
	DP2-T2	227	Static test on a previously failed pile
DP3	DP3-T1	106	Static test on previously untested pile
DP6	DP6-T1	246	Static test on previously untested pile

Table 6-4: Summary of pile test codes and test histories for cyclic loading effects

Pile	Test code	Age (days)	Mode	Comment
DP1	DP1-CY1	253	Cyclic	Low level cyclic test on previously untested pile
	DP1-CY2	253	Cyclic	Second cyclic test immediately after DP1-CY1
	DP1-TPC	253	Static	'Quick' static test post cyclic failure
DP4	DP4-CY1	249	Cyclic	Low level cyclic test on previously untested pile
	DP4- TPC	249	Static	'Quick' static test post DP4-CY1
	DP4-CY2	255	Cyclic	Second cyclic test on DP4 (Retest)
DP5	DP5-CY1	254	Cyclic	Low level cyclic test on previously untested pile
	DP5-CY2	254	Cyclic	Second cyclic test immediately after DP5-CY1
	DP5-TPC	254	Static	'Quick' static test post cyclic failure
DP7	DP7-CY1	247	Cyclic	Cyclic test on previously untested pile
	DP7- TPC	247	Static	'Quick' static test post cyclic failure

The first cyclic experiment, DP7, imposed 1000 medium level cycles with a period of 30 seconds before a 'quick' static maintained load test to failure in tension, which took 25 minutes to complete. Piles DP1, DP4 and DP5 were all subjected to ≥1000 relatively low-level

cycles, which led to little or no stiffness loss and modest displacements. Two of the three piles (DP1 and DP5) were then subjected, without delay, to cycling at higher normalised load levels, employing comparable periods. Similar 'quick' tension load tests to failure followed in both cases. Pile DP4 was initially subjected to 1000 relatively low-level cycles, followed by a 'quick' static test to failure. A second higher level cyclic test was performed 6 days later.

6.7 Experimental procedures

The static and cyclic tests were all conducted with the load and control equipment shown in Figure 6-26 to Figure 6-28 which was designed and built at Imperial College. The A frame and loading beams were made of UK Parallel Flange Channel (PFC) and Square Hollow Section (SHS) steel sections. A 36mm diameter high tensile Macalloy steel bar was connected to the pile head via a specially made connection piece. The bar passed through a recess in the loading beam, a hollow 'NCB' design load cell, an actuator, a flat plate and a nut. Load was applied by expanding the hollow jack using either a hand pump or a portable electrical Enerpac XC1202 hydraulic pump and reacting against the loading frame. The system was capable of applying up to 480kN of tension load to the driven piles safely. A pressure gauge attached to the hydraulic system gave a check measurement of the applied load.

The load was transferred to the ground via railway-sleeper mat style foundations placed on level ground. Pile head displacements were monitored by three Linear Variable Differential Transformers spaced evenly circumferentially around the pile and attached to an independent reference frame supported on stands set 1m from the pile centre (Figure 6-27). The 'slow' static test loads were applied in increments of 10% of the expected failure capacity, each imposed over 1 minute, followed by monitored pause periods that extended as failure approached. Pile failure was defined as either:

1. Pile head displacement reaching 10% of the diameter, D; or
2. The semi-logarithmic pile creep-displacement rate, k_c measured under constant load exceeding 0.2mm/log cycle of time after ten or more minutes.

The creep rate criterion was scaled from the German EA-Pfähle (2014) criterion of k_c > 2mm per log cycle of time to reflect the test pile dimensions and keep compatibility with the Wikinger field load tests. The load steps and creep pause durations depended on the creep monitoring data. Ten to twelve load steps were required to reach failure and tests took two to

three hours to complete. The additional 'quick' load tests were performed following selected cyclic tests that led to failure in less than thirty minutes.

The cyclic loading system, designed by Mr. Duncan Parker, was based around a standard Arduino Uno microcontroller computer programmed with a proportional closed loop control algorithm, which used the load cell to provide a feedback signal. Additional circuitry enabled the switching of the modified Enerpac hydraulic pump for loading the actuator, and of a solenoid valve for unloading, as shown schematically on Figure 6-29. The pump and valve were binary on/off type devices and switching in short pulses of varying duration allowed for proportional control. Control parameters such as set point, dead band, and cycle period could be arbitrarily set using commands from an attached laptop, which also served to log test data (Figure 6-30). The typical sample rate was approximately 3Hz. The system was designed to be fully operable using either a standard single phase mains supply, or using a large capacity lead acid battery.

The cyclic loading system could impose two to four cycles per minute (0.03 to 0.06 Hz) for thousands of cycles and control the peak loads to ±2%. Sine wave loading was not achievable with the systems available. The adopted square wave, plus twin exponential section, cyclic load characteristic is shown in Figure 6-30, where the average (Q_{mean}) and cyclic (Q_{cyc}) loading components are also defined. The cyclic loading parameters associated with each test, discussed later, refer to the *current* net static tension shaft capacity, $Q_{net} = Q_{ref}$ of each pile, proven by the independent static test results. Cyclic failure manifests as rapidly accumulating permanent displacement and decreasing global stiffness and failure was defined as either:

1. The permanent pile head displacement reaching 10%D; or
2. A sudden increase in the rate of displacement accumulation, indicative of decreasing stability and approaching cyclic failure.

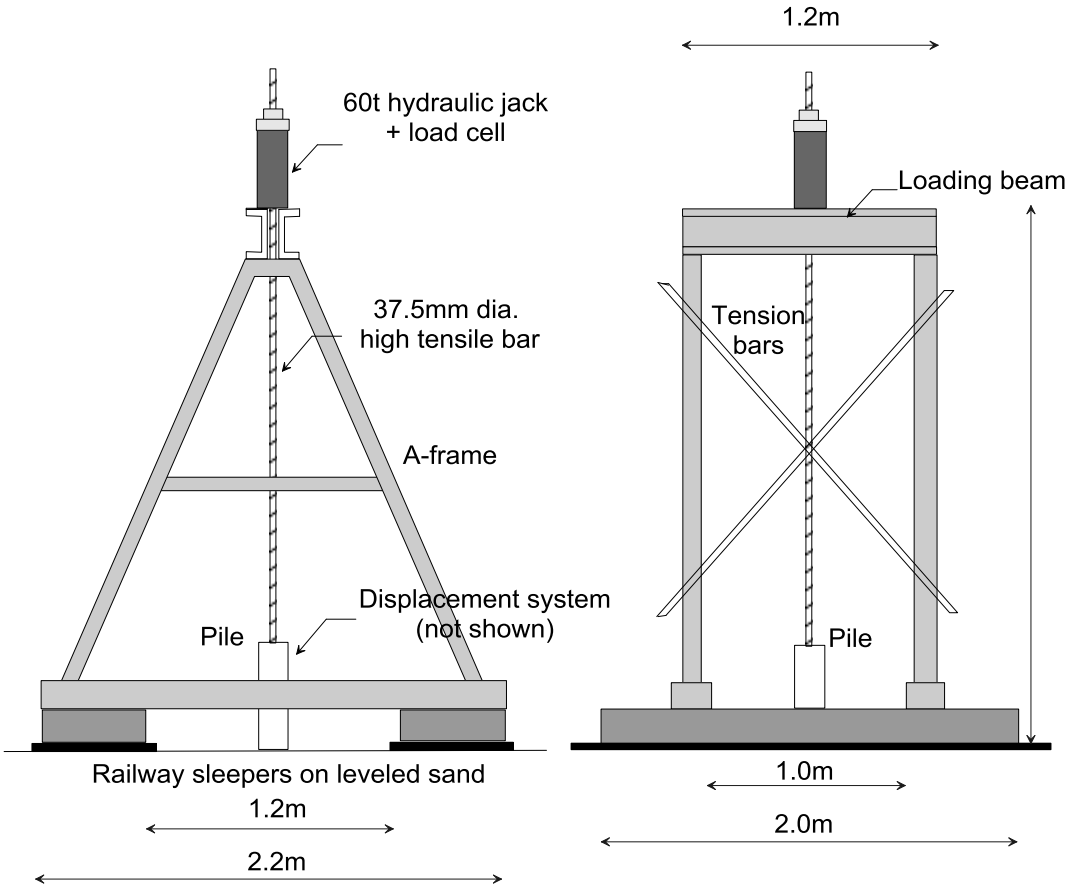


Figure 6-26: Schematic of load test system used in the axial static and cyclic investigation

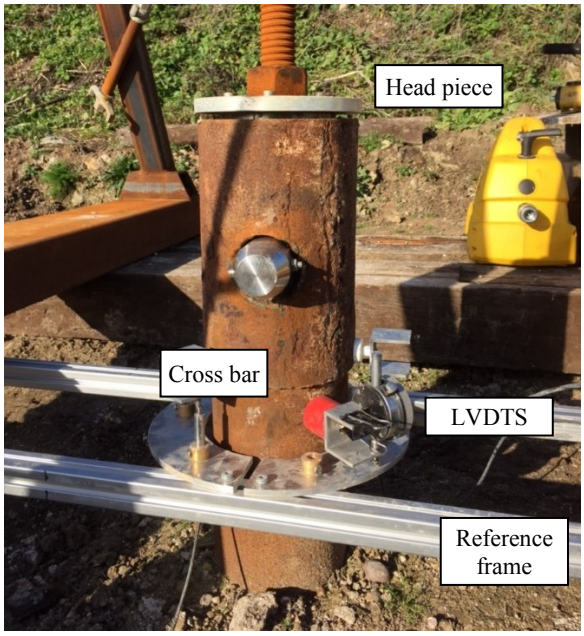
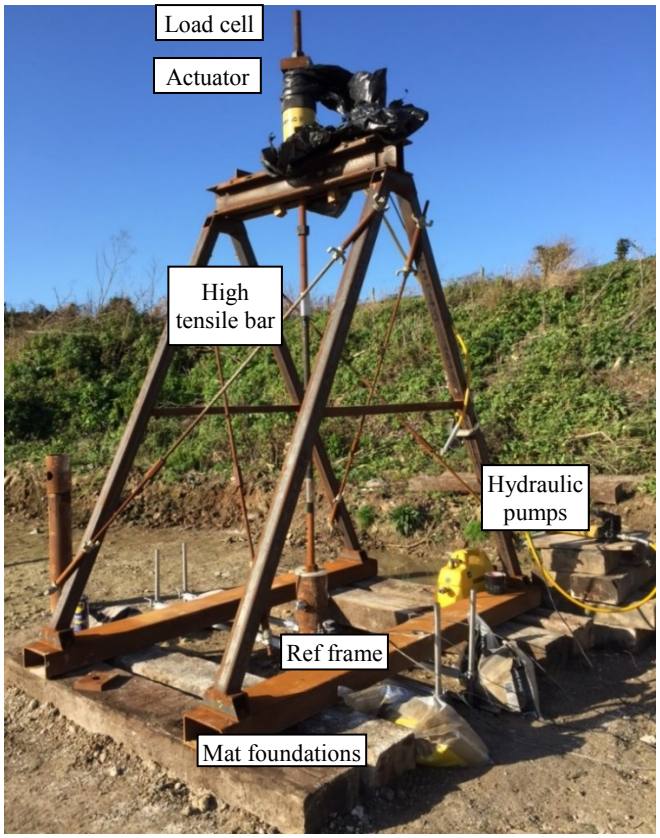
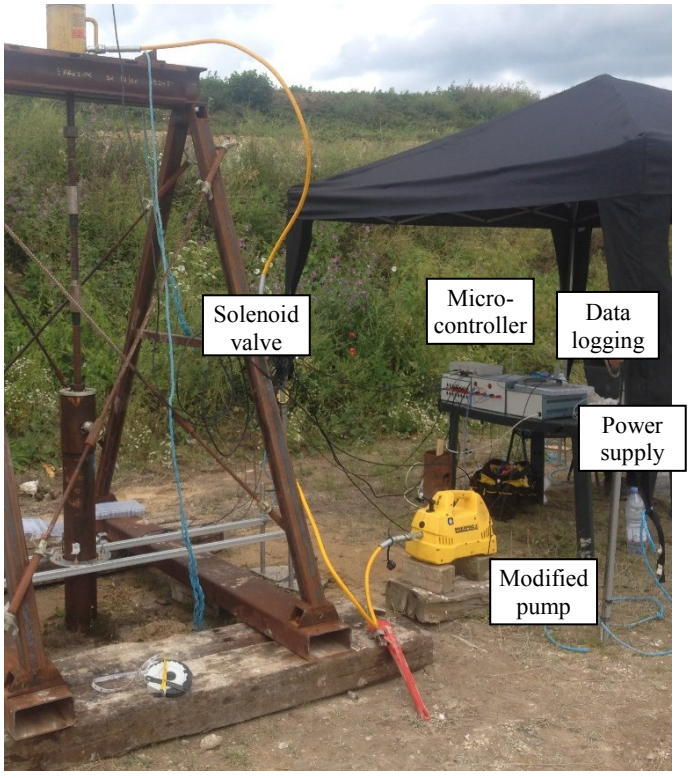


Figure 6-27: Pile head piece and displacement monitoring system



(a



(b)

Figure 6-28: (a) overview of load testing system (b) including cyclic loading system

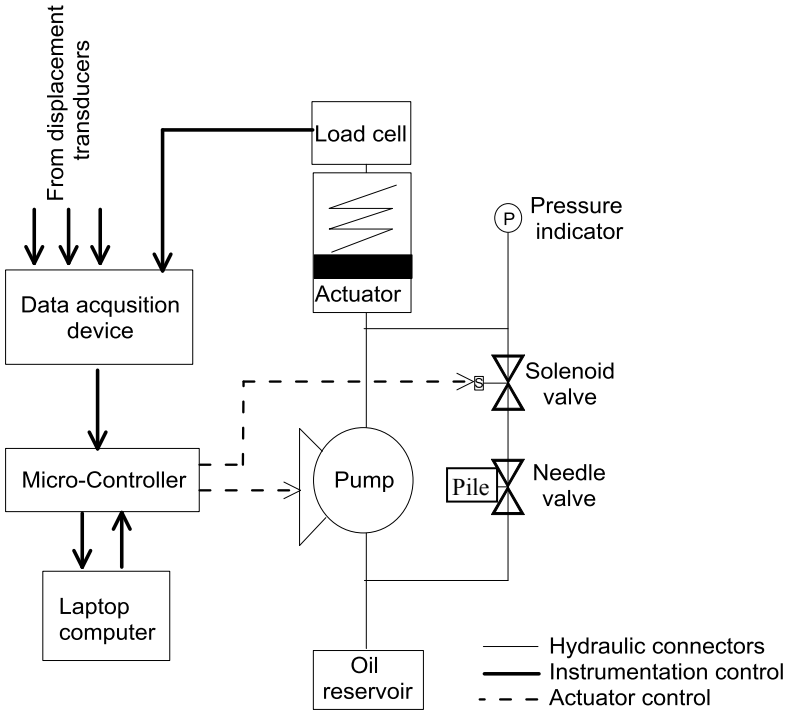


Figure 6-29: Schematic of cyclic load test system

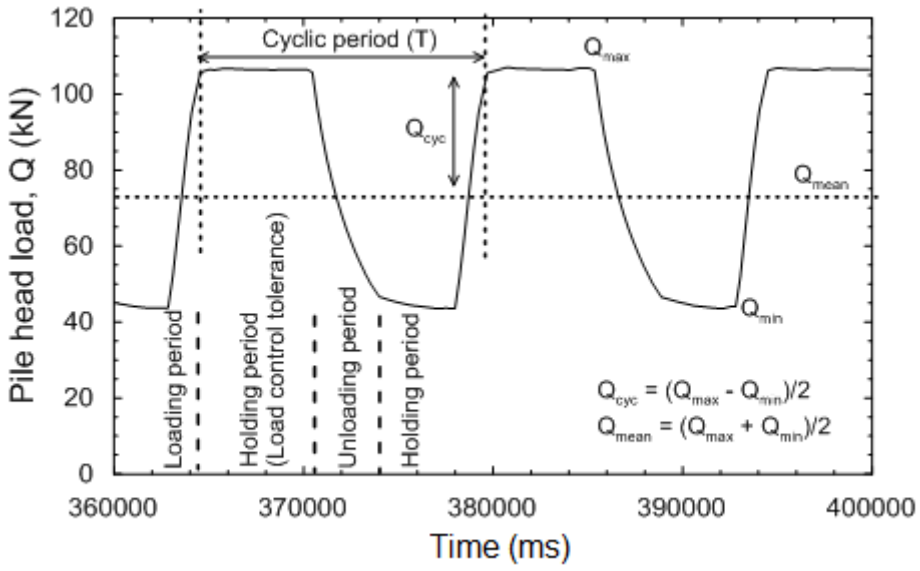


Figure 6-30: Schematic illustration of cyclic loading conventions and cyclic loading control parameters

6.8 Ageing Observations

Tension tests were conducted to failure 10, 106 and 246 days after driving on three virgin piles; DP2, DP3 and DP6, which gave the peak capacities, corrected for pile and chalk plug self-weight, summarised in Table 6-5. Reverse end bearing is assumed negligible, as the fractured chalk drains very rapidly and final static holding periods were typically greater than 30 minutes, far exceeding the dissipation time anticipated for any reverse end bearing mechanism to occur.

The piles' overall net axial load displacement responses are converted to average shaft stress, τ_{avg} versus displacement curves and shown on Figure 6-31 where $\tau_{avg} = Q_{net}/A_s$ and A_s is the area of the shaft. Also shown on Figure 6-31 are the average compressive EoD shaft stresses mobilised by DP1, DP4 and DP7 at the end of driving as described in Section 6.5.2. Global secant stiffness can be quantified as load change ΔQ from the initial 'nip-load', applied to ensure loading system stability, divided by total displacement from the same origin. The three tests' stiffness trends are plotted over the course of each stage in Figure 6-32, along with the retest on pile DP2. The stiffness-load trends show highly non-linear trends from their first increment onwards, as is common in soils (Jardine *et al.*, 2005b). All three virgin curves share broadly similar initial stiffness of 100 to 200kN/mm at a 20kN load level, with the 106 and 246 day aged piles also showing similar stiffnesses over a range of loading levels. The re-tested pile shows significantly stiffer behaviour initially, which subsequently degraded at lower load levels than the virgin pile.

Table 6-5: Post ageing and end of driving capacities of virgin piles in the static capacity study

Test code	Age (days)	Shaft Capacity[1] (kN)	Shaft Resistance[2] (kPa)	Capacity Change[3] (%)
DP2-T1	10	94	39	+239
DP3-T1	106	186	77	+473
DP6-T1	246	206	86	+524

1. Includes correction for pile and soil self-weight
2. External - only external shaft resistance is assumed to be mobilised during a static tension test
3. Calculated based on average external compressive shaft capacity from three DPT results (= 39.3kN)

Figure 6-33 (a) plots the set-up factor, Λ, calculated as $\tau_{avg}(t)$ from the peak static tension loads at time, t after installation divided by τ_{avg} ($t = t_{ref}$) interpreted from the dynamic tests at the end of driving, against time. The closed symbols indicate the Intact Ageing Characteristic (IAC) of the virgin piles (Jardine *et al.* (2006)), while the open symbol shows

the retest on pile DP2, completed 227 days after installation and 217 days after its initial ten day static tension test to failure. If compression and tension shaft capacities are equal, then Figure 6-33 indicates a set-up factor, Λ of 5.2 after 246 days for the fresh piles, with mean τ_{avg} growing from ≈16 to 86 kPa. Most of the beneficial ageing occurs over the first 100 days; the rates of change slow with time and may tend to a final equilibrium.

Similar to the Wikinger results, the hyperbolic relationship suggested by Tan *et al.* (2004) appears appropriate to describe the capacity increase in chalk. The set-up factor, Λ is defined as:

$$\Lambda = \frac{\tau_{avg}(t)}{\tau_{avg}(t = t_{ref})} = \Lambda_{ult}\left(m + (1 - m)\left[\frac{t/T_{50}}{1 + (t/T_{50})}\right]\right) \quad 6\text{-}3$$

Where $\tau_{avg}(t)$ is the resistance measured at time, t after installation, τ_{avg} (t= t_{ref}) is the measured soon after installation, Λ_{ult} is the ultimate set up factor, T_{50} is the time required to reach 50% of the ultimate value and m is an empirical parameter (around 0.2) used to improve the fit at the early (t < 1day) age. The curve plotted on Figure 6-33 corresponds to Λ_{ult} of 5.72, m = 0.2 and T_{50} = 27 days. The single re-test confirmed that beneficial ageing was disrupted by previous static failure; the pre-failed DP2 showed 32% less gain in capacity over its ten to 227 day age range than the equivalent virgin pile DP6.

A similar trend was observed in the tests on 762mm diameter piles at the St. Nicholas-at-Wade reported by Ciavaglia *et al.* (2017a), shown on Figure 6-33 (b). The average shaft resistance for the static tests on the same pile at 6, 50 and 119 days after installation was compared to the result of the dynamic test on Pile 1, obtained 2 hours after installation. A similar trend is observed between the two sets of tests with the larger 762mm diameter re-tested piles reaching a higher overall set-up of 8.1 after 119 days when compared to a dynamic test two hours after installation and a set-up factor of 7.4 when compared to static tension test, 2 days after installation. The higher overall set-up factor observed may be attributable to scale effects or to the piles' testing history. The pile was retested once under dynamic loading and three times under static loading over a 119 day period.

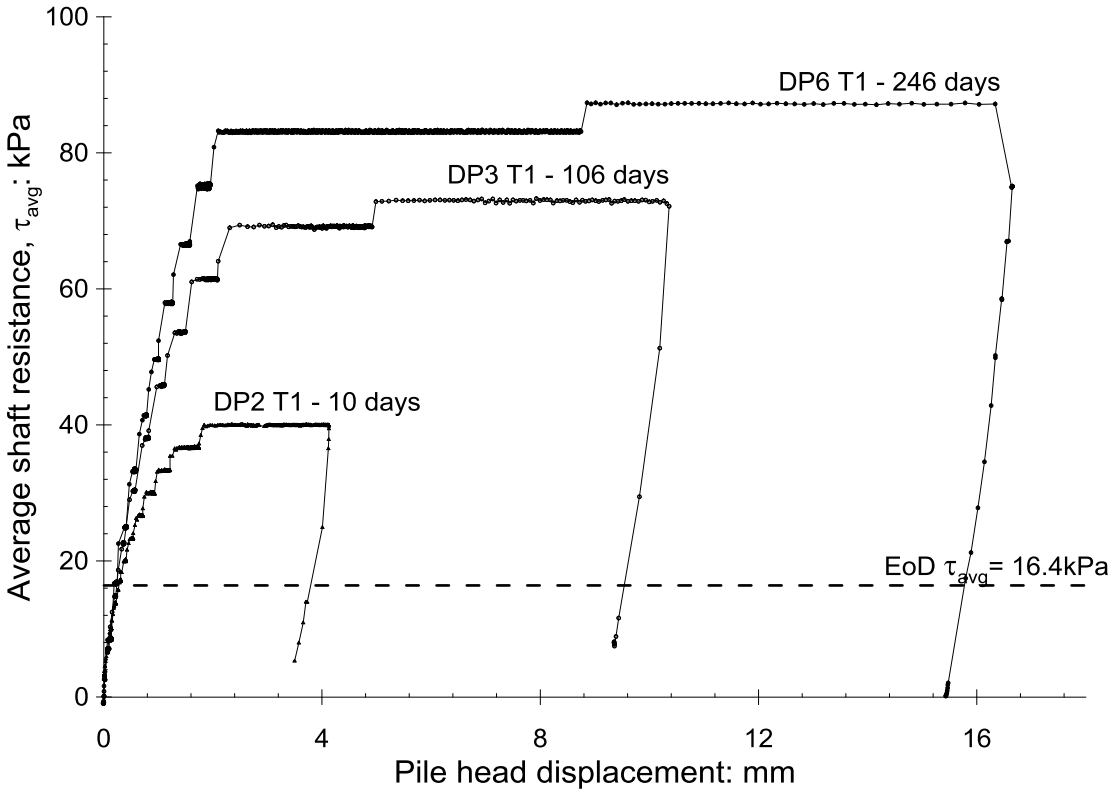


Figure 6-31: Average shaft resistance versus pile head displacement for first time tension tests to failure on DP2, DP3 and DP6

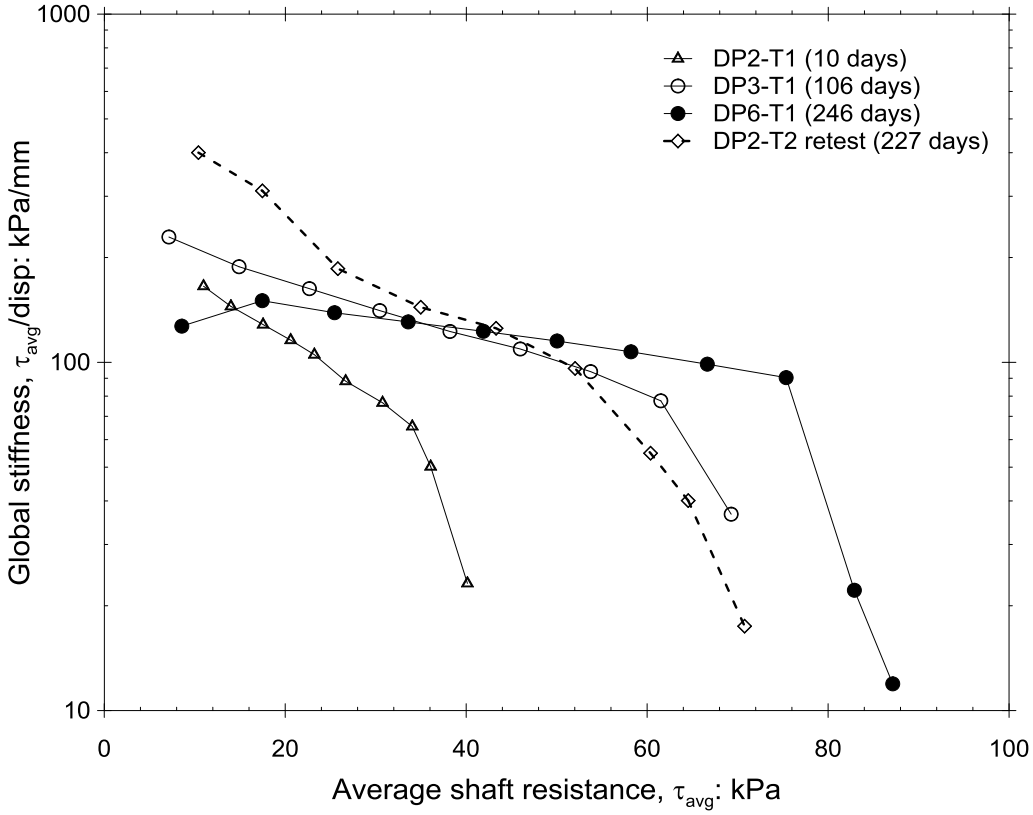


Figure 6-32: Global stiffness versus average shaft resistance for first time tension tests to failure on DP2, DP3 and DP6 and retest on DP2

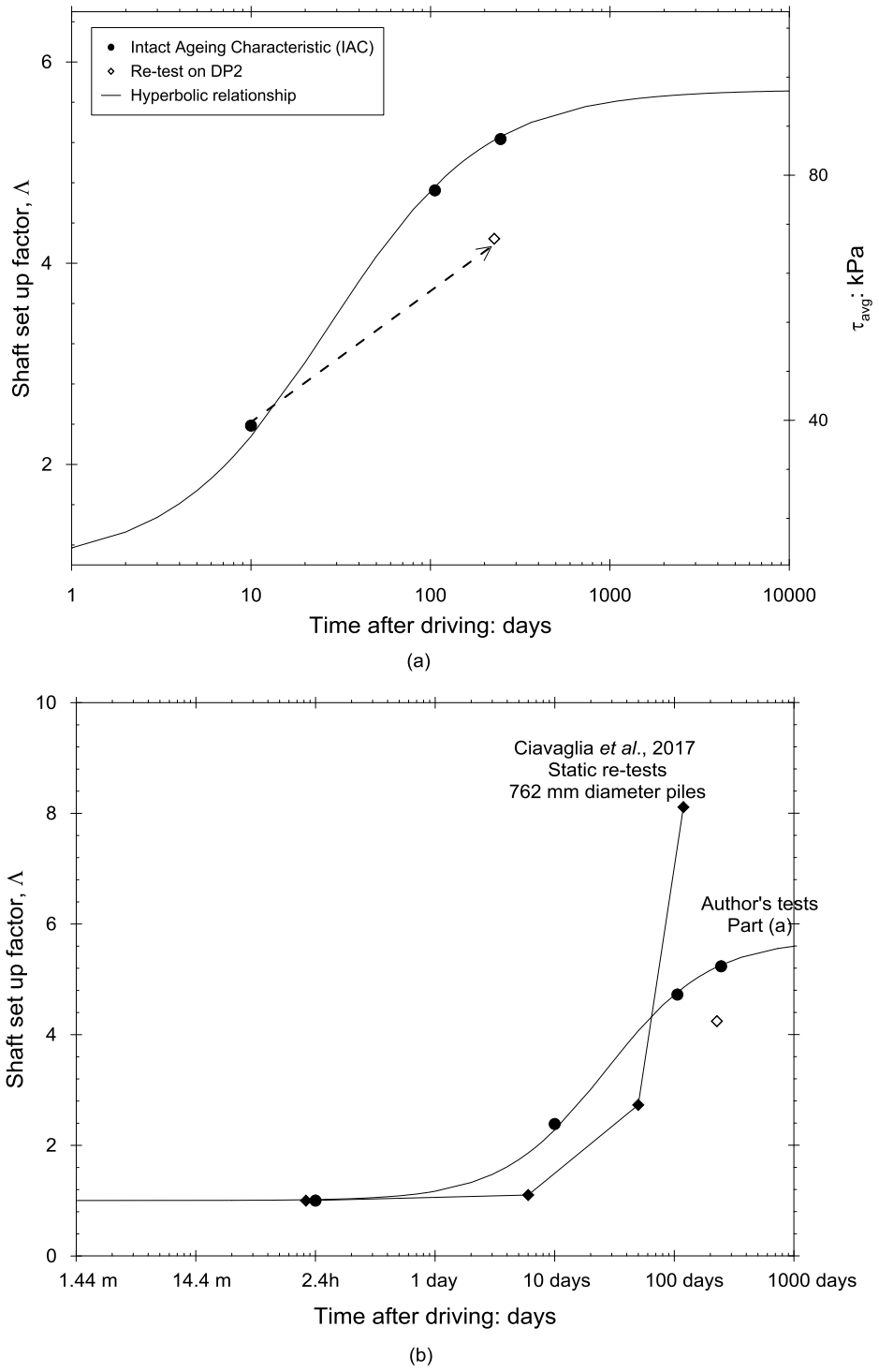


Figure 6-33: (a) Shaft capacity growth with time for first time tension tests on pile DP2, DP3, and DP6 and re-test on DP2 (b) trend from (a) compared with trend from re-tests on 762mm diameter piles reported by Ciavaglia *et al.* (2017a)

6.9 Cyclic test results & interpretation

The test results are summarised in Table 6-6. The definitions of the accumulated cyclic displacement parameters applied to the cyclic tests were given by Rimoy *et al.* (2013) and are shown on Figure 6-34. A typical test result in terms of average shaft resistance mobilised versus displacement is shown on Figure 6-35.

The growth of permanent cyclic displacement, s_{acc} normalised by D, with the number of cycles, N, is plotted for the six cyclic experiments in Figure 6-36 and Figure 6-37. The four non-failing tests (Figure 6-36 a to d) follow approximately constant logarithmic gradients once N > 20. The implied power law trends have the form:

$$\frac{s_{acc}}{D} = CN^{\chi} \qquad 6\text{-}4$$

where C and χ are non-dimensional fitting parameters. The re-test presented in Figure 6-36 (e) shows a broadly comparable but more staggered trend. The two unstable tests, presented in Figure 6-37, failed at low N values and, as discussed later, demonstrated marked losses of shaft capacity.

Table 6-6: Summary of cyclic loading test outcomes

	One way axial cyclic loading									Post cyclic tension loading	
Test code	**Q_{min} (kN)**	**Q_{max} (kN)**	**Q_{ref} (kN)[1]**	**Q_{cyc}/Q_{ref}**	**Q_{mean}/Q_{ref}**	**UR[2]**	**Period T (s)**	**No. of cycles[3]**	**Class**	**Q_{pc} (kN)**	**Capacity change (%)[4]**
DP1-CY1[5]	40	103	207.6	0.15	0.34	0.50	15	>1059	MS/S	-	-
DP1-CY2	40	164	207.6	0.30	0.49	0.79	30	5	US	117.6	-43
DP4-CY1	82	145	207.4	0.15	0.55	0.70	15	>1004	MS/S	216.8	+5
DP4-CY2[6]	49	146	207.8	0.23	0.47	0.70	20-30	>1003	S	-	-
DP5-CY1	4	99	207.7	0.23	0.25	0.48	15	>1000	MS/S	-	-
DP5-CY2	5	146	207.7	0.34	0.36	0.70	30	32	US	158.4	-24
DP7-CY1	24	120	207.3	0.23	0.35	0.58	30	>1000	MS/S	177.9	-14

1. Reference capacity Q_{ref} at the time of the test calculated from Eq. 6-3.
2. UR = Utilisation Ratio = Q_{max}/Q_{ref}
3. prefix ">" : no cyclic failure when number of cycles reached
4. When compared to Q_{ref}
5. Marginally higher cyclic loads were applied initially than intended for three cycles; these have not been included in the cycle number or permanent displacement trends
6. Re-test on a pile previously failed in static tension and subjected to cyclic loading
7. All loads given in Table are net loads (measured load less pile and chalk self-weight)

The six tests' normalised Q_{mean} and Q_{cyc} loading components are plotted on an axial cyclic interaction diagram (Karlsrud *et al.*, 1986, Poulos, 1988, Jardine and Standing, 2000,

2012) on Figure 6-38. In this figure, the numbers of cycles imposed are also noted, falling below 1000 for the two tests that failed cyclically. The tension capacities employed to normalise the loads for each test age were obtained from Eq. 6-3 as given in Table 6-6. The top-left to right-bottom diagonal in this diagram represents the static failure conditions, where the Utilisation Ratio of tension shaft capacity, UR = Q_{max}/Q_t is equal to 1. The line representing the minimum UR = 2/3 recommended by API working stress design (WSD) guidance for extreme offshore environmental loading cases is also shown, along with an UR = 0.5 line. Tentative contours of N = 10, 100 and 1000 are plotted to indicate the conditions under which cyclic failure could be expected under given normalised cyclic load combinations.

6.9.1 Axial cyclic stiffness

The experiments also revealed how global cyclic secant stiffness evolved during each cyclic test. Stiffness was assessed by the loading or unloading terms, k_l and k_u defined by Rimoy *et al.* (2013) as shown on Figure 6-34. Figure 6-39 (a) shows the loading stiffness trends, normalised by the first cycle value, for the four unfailed tests. Two of these showed k_l and k_u increasing consistently under cycling and reaching gains of up 30% at N = 1000. The two other "unfailed" tests showed stiffness reducing up to 200 cycles, before increasing to reach almost 1.05 times the initial value at N = 1000. Figure 6-39 (b) presents the two failed tests' trends: DP1-CY2 showed stiffness degrading from the first cycle falling by over 60% prior to final failure. Degradation was less marked in DP5-CY2 initially, but reached a similar level before final cyclic failure. As expected, stiffness degradation was generally slightly steeper on re-loading than on un-loading so leading to displacement accumulation during cycling, as shown on Figure 6-40. Re-test DP4-CY2, completed 6 days after test DP4-CY1 and a subsequent tension test to failure, showed gentler degradation trends and more stable normalised behaviour (Figure 6-39 (a)) than the initial cyclic test at lower load levels. It appears that stiffness recovers and normalised resistance grows with time following cyclic or static failure.

6.9.2 Impact on tension capacity

The post-cyclic tension tests are also summarised in Table 6-6. Those following the "unfailed" experiments DP4-CY1 and DP7-CY1 indicated relatively modest changes in capacity (5% increase and 14% reduction respectively) when compared to the static trends predicted by Eq. 6-3. However, cyclic failure led to more marked losses of 24% and 43% following DP5-CY2 and DP1-CY2, respectively.

6.9.3 Cyclic stability criteria

Cyclic axial loading tests on piles driven in clays and sands show trends that have been classified as Stable, Metastable or Unstable (Karlsrud *et al.*, 1986, Poulos, 1988, Jardine and Standing, 2000, Tsuha *et al.*, 2012, Jardine *et al.*, 2012). The working definitions applied by Jardine & Standing (2012) and Rimoy *et al.* (2013) in their interpretation of open tube piles driven in dense sand at Dunkirk were discussed previously in Section 3.2.5.

Table 6-6, previously, also lists the outcomes of the cyclic loading tests. Applying the above categories, two of the tests (DP1-CY2, DP5-CY2) are clearly unstable. The remaining four (DP1-CY1, DP4-CY1, DP5-CY1 DP7-CY1) classify as stable in terms of reaching 1000 cycles without failure, or significant loss in operational tension capacity, but meta-stable with regards to accumulated displacements. The transition between unstable and metastable or stable behaviour appears to be abrupt. Fully stable behaviour was not observed, except in test DP4-CY2, which had been pre-failed, within the limited region of the interactive diagram that could be explored. Bearing in mind the tests involved purely one-way loading at UR $\geq$ 0.48, the stable region of behaviour appears to be more limited than was found, for example, for Dunkirk sand by Jardine and Standing (2012). Jardine *et al.* (2012) emphasise that higher cyclic Q_{cyc}/Q_{net} amplitudes are likely to have a greater impact in two-way loading tests conducted with maximum loads set to achieve the same UR values; UR is not an adequate parameter on its own to predict the impact of cyclic loading.

6.9.4 Permanent accumulated displacements

Under the limited loading range investigated, the virgin piles' permanent displacement accumulation trends correlate with UR. The unstable tests showed different accumulated displacement trends; test DP1-CY2 subjected to cyclic and average loads equivalent to a 'static' UR of 0.79, accumulated displacements of 2.3 to 3.4mm from its start and failed in 5 cycles. Displacement accumulation was more gradual in unstable test DP5-CY2 (under a 'static' UR of 0.70) remaining below 0.1mm/cycle for the first 9 cycles, before more rapid accumulation led to failure in 32 cycles.

Three of the four Stable/Meta-stable tests (DP1-CY1, DP5-CY1 and DP7-CY1) exhibited consistent behaviour when subjected to cycling at loads equivalent to 0.48 < UR < 0.58. While their displacement accumulation rates may have stabilised eventually, they followed the power law function given as Eq. 6-4 over 20 < N < 1000, with coefficients C and χ of 0.0015 ±0.0004 and 0.32 ±0.03 respectively; see Figure 6-41. The remaining MS/S test

(DP4-CY1), whose loads implied an equivalent static UR of 0.70, followed a steeper power law trend (C= 0.0008, χ=0.49) that might have accelerated and led to eventual failure if cycling had continued. The global trends must reflect locally progressive top-down degradation (Jardine *et al.*, 2012) that can only be checked through the use of local instrumentation. The coefficient C, can therefore be expected to vary with chalk profile, pile shaft length and cross section. Figure 6-42 shows the permanent displacements plotted on cyclic stability interaction diagrams, considering cases with N = 3, 10, 20, 100, 300 and 600. Contours are indicated for s_{acc}/D ratios of 0.2%, 0.5% and 2.0% for these one way cyclic tests. Further tests are required to examine potential pile scale effects and the influence of high-level two-way loading. Finally, Figure 6-43 collates the contours of s_{acc}/D shown on Figure 6-42 and plots them as 3D surfaces to express how displacements change with Q_{mean}/Q_{ref}, Q_{cyc}/Q_{ref} and N.

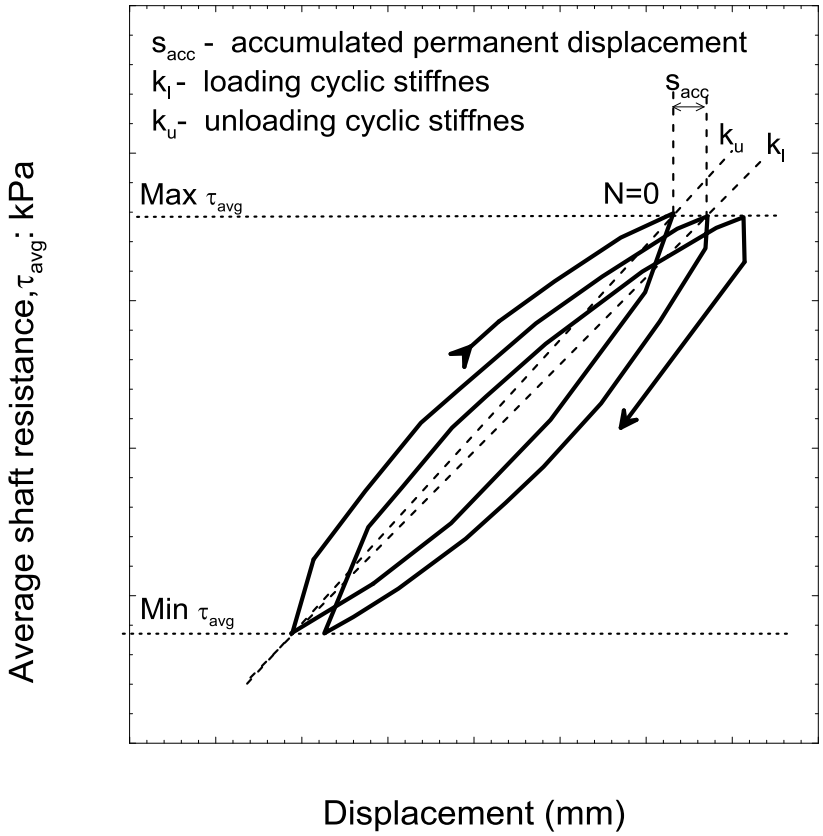


Figure 6-34: Definitions of cyclic displacement and stiffness; adapted from Rimoy *et al.* (2013)

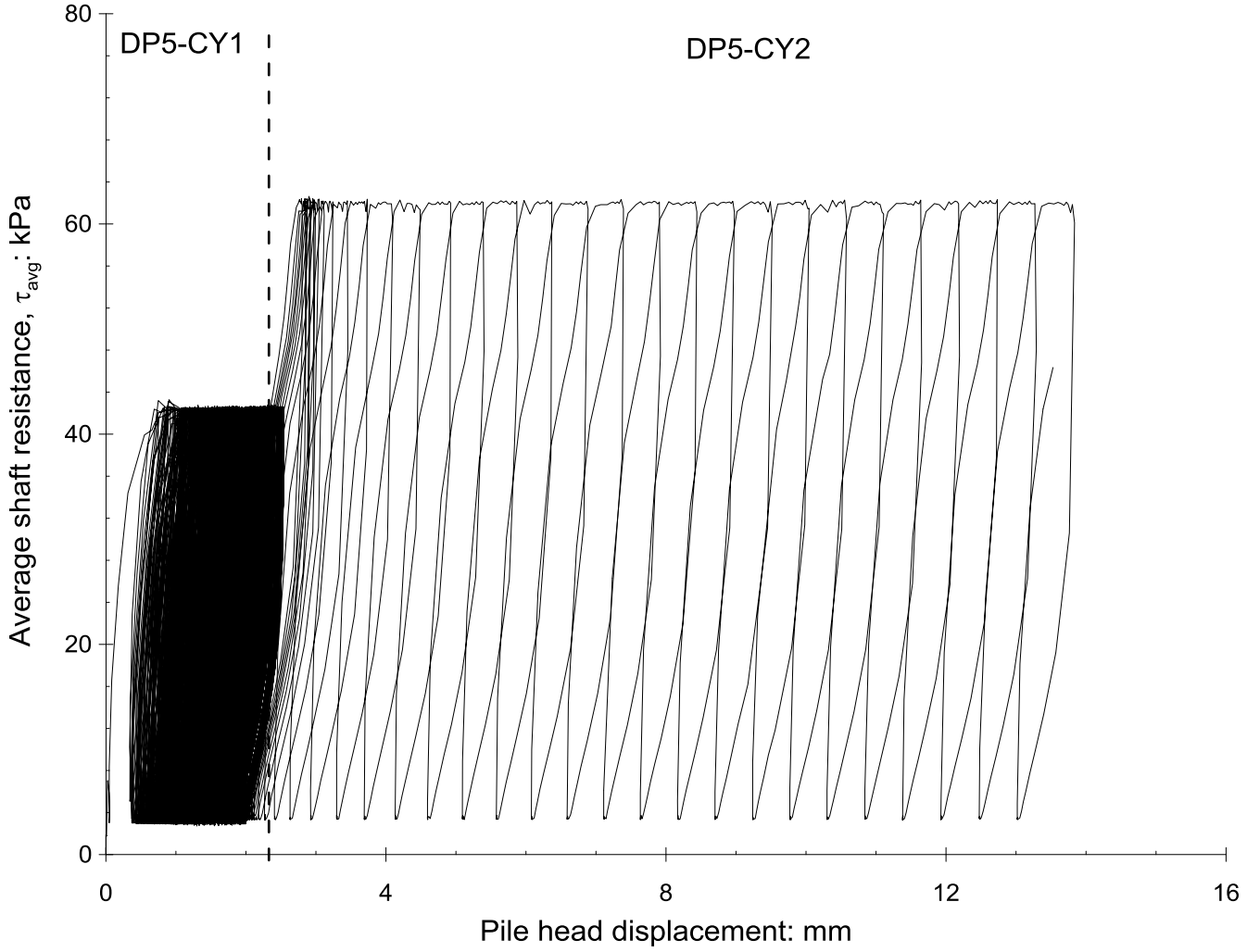


Figure 6-35: Average shaft resistance versus time during cyclic load tests DP5-CY1 and DP5-CY2

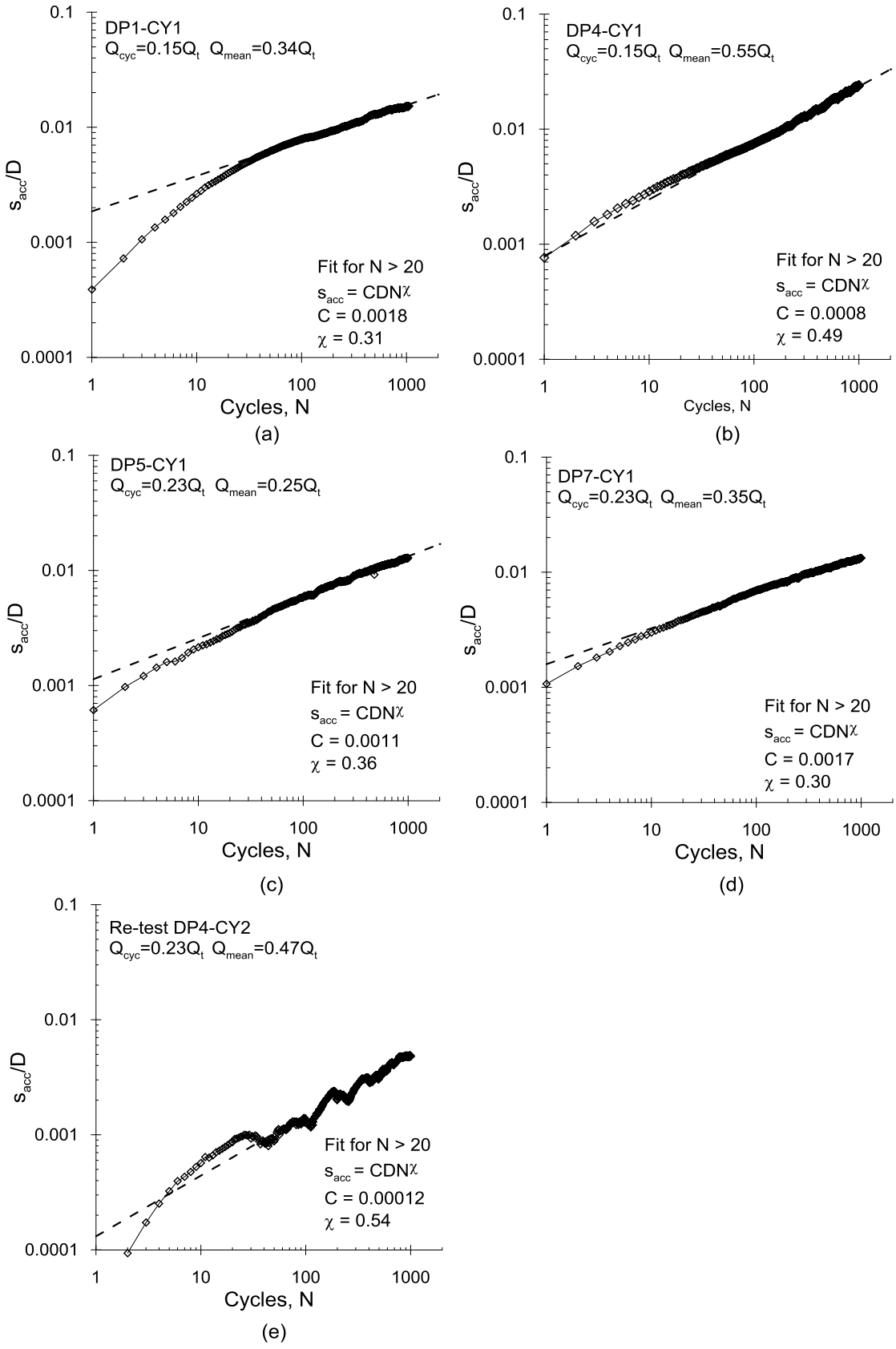


Figure 6-36: Permanent accumulated cyclic displacement normalised by pile diameter for unfailed tests (a) DP1-CY1 (b) DP4-CY1 (c) DP5-CY1 (d) DP7-CY1 and (e) re-test DP4-CY2

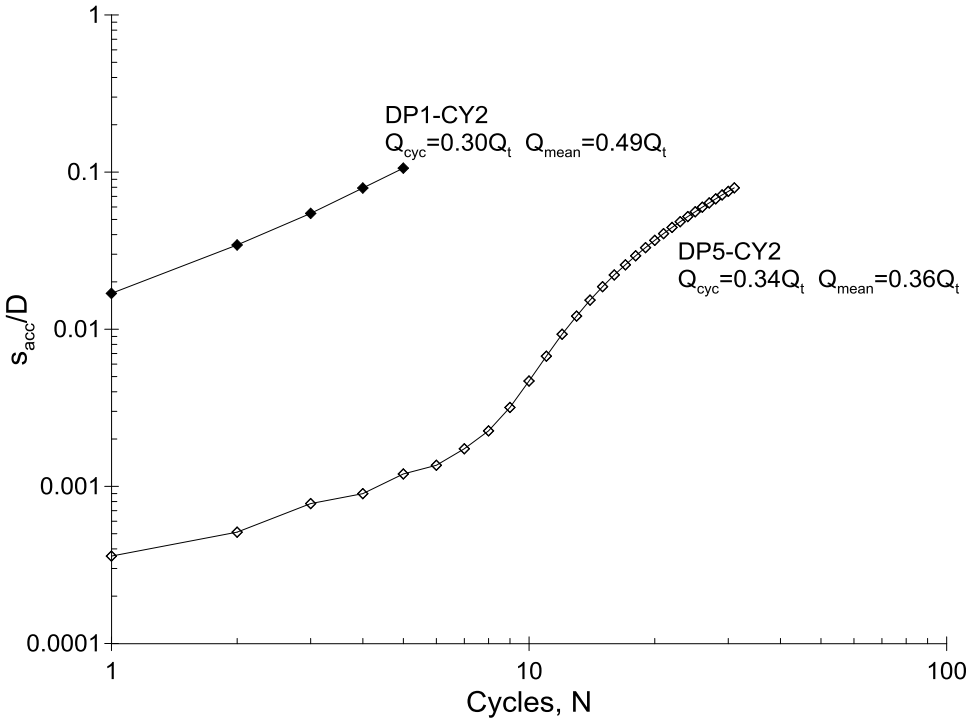


Figure 6-37: Permanent accumulated cyclic displacement normalised by pile diameter for failed tests DP1-CY2 and DP5-CY2

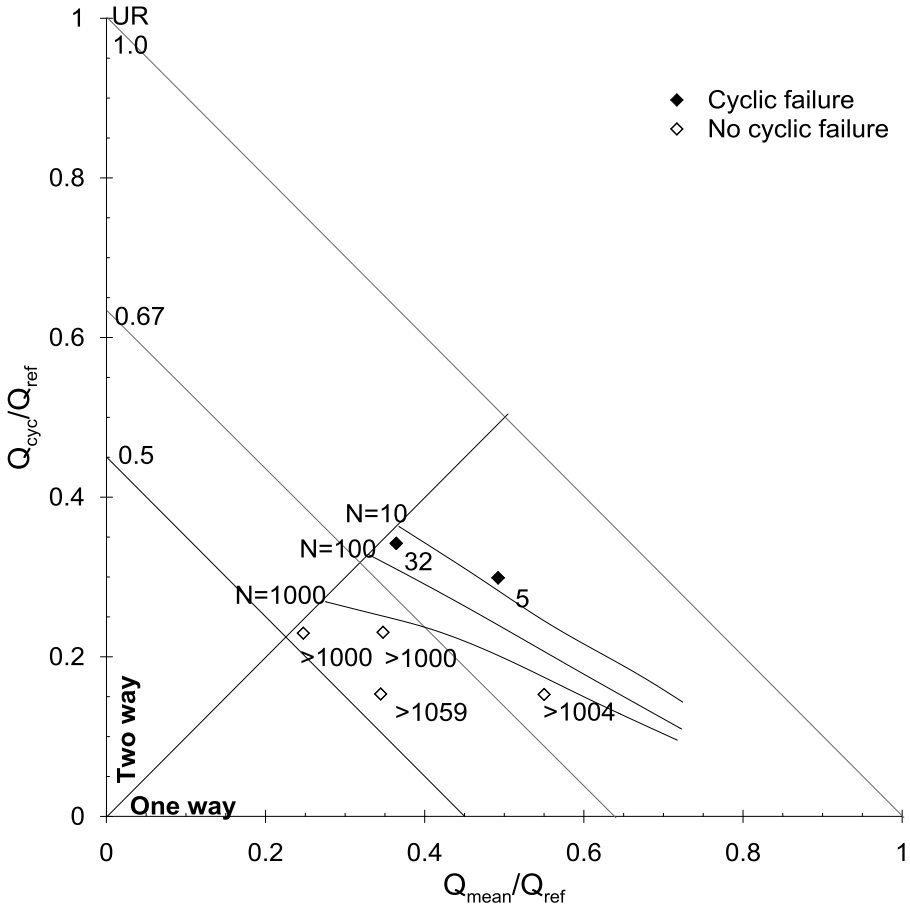


Figure 6-38: Cyclic loading interaction diagram with number of cycles either to failure or to the end of test if unfailed

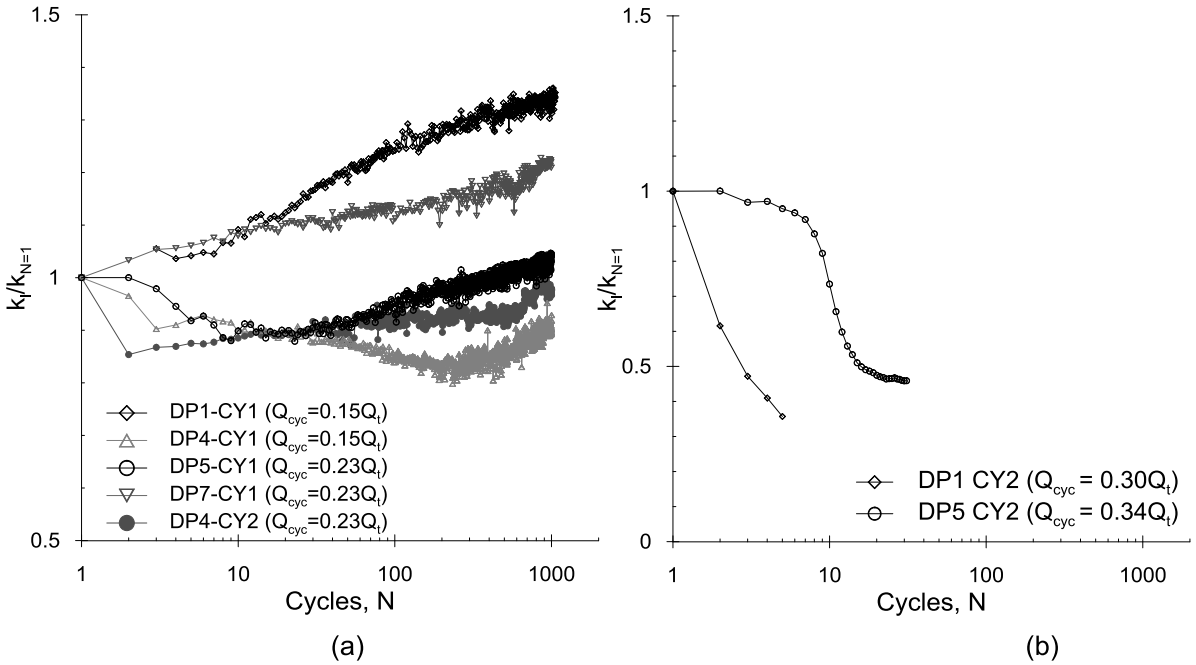


Figure 6-39: Global axial loading stiffness for (a) unfailed tests (b) failed tests

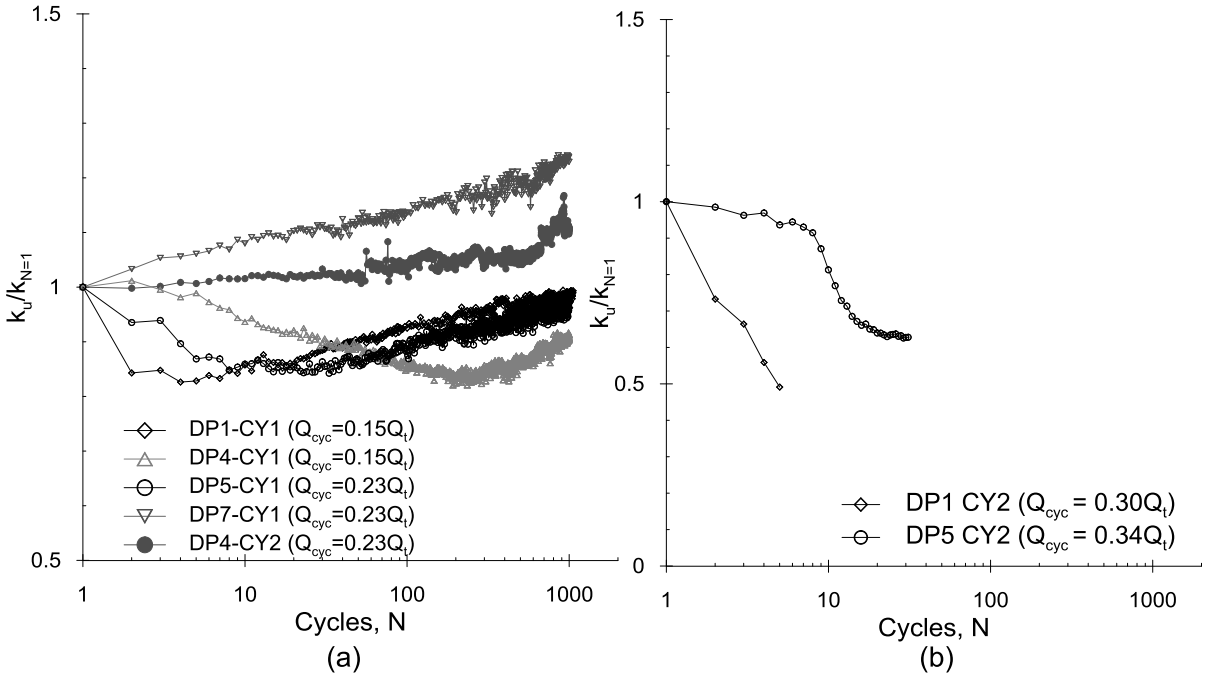


Figure 6-40: Global axial unloading stiffness for (a) unfailed tests (b) failed tests

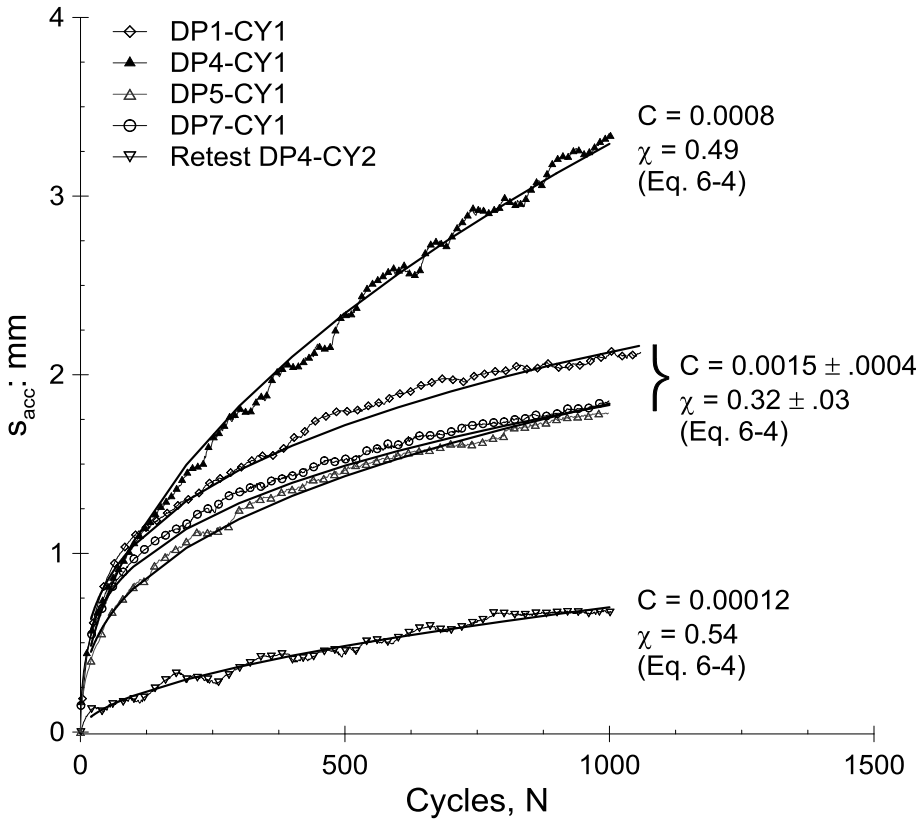


Figure 6-41: Permanent accumulated displacement with cycles for meta-stable/stable tests on natural scale with power law fits and parameters shown

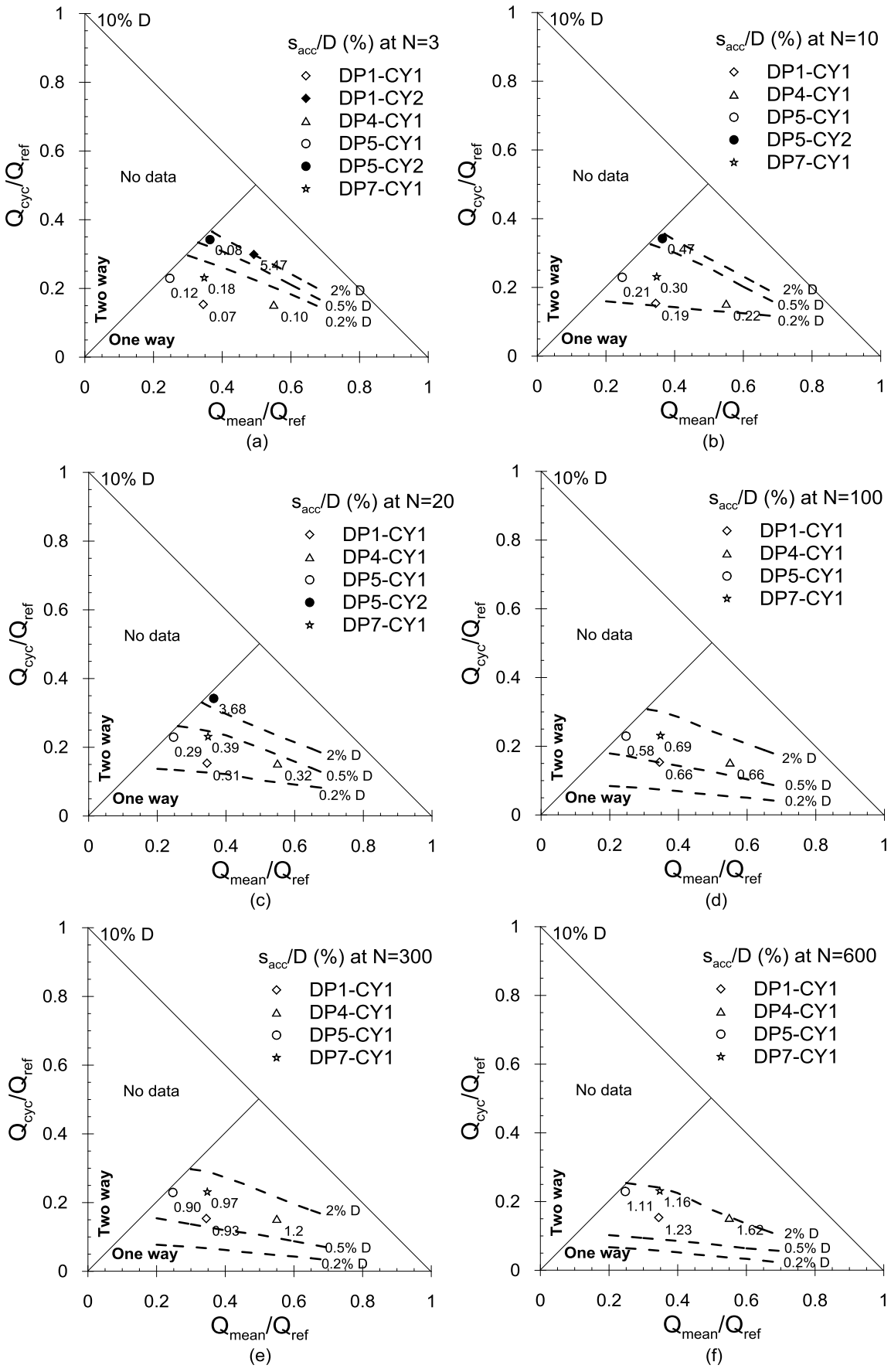


Figure 6-42: Cyclic interaction charts showing accumulated displacements (normalised by pile diameter) at (a) N=3, (b) N=10, (c) N=20 (d) N=100 (e) N=300 and (f) N=600

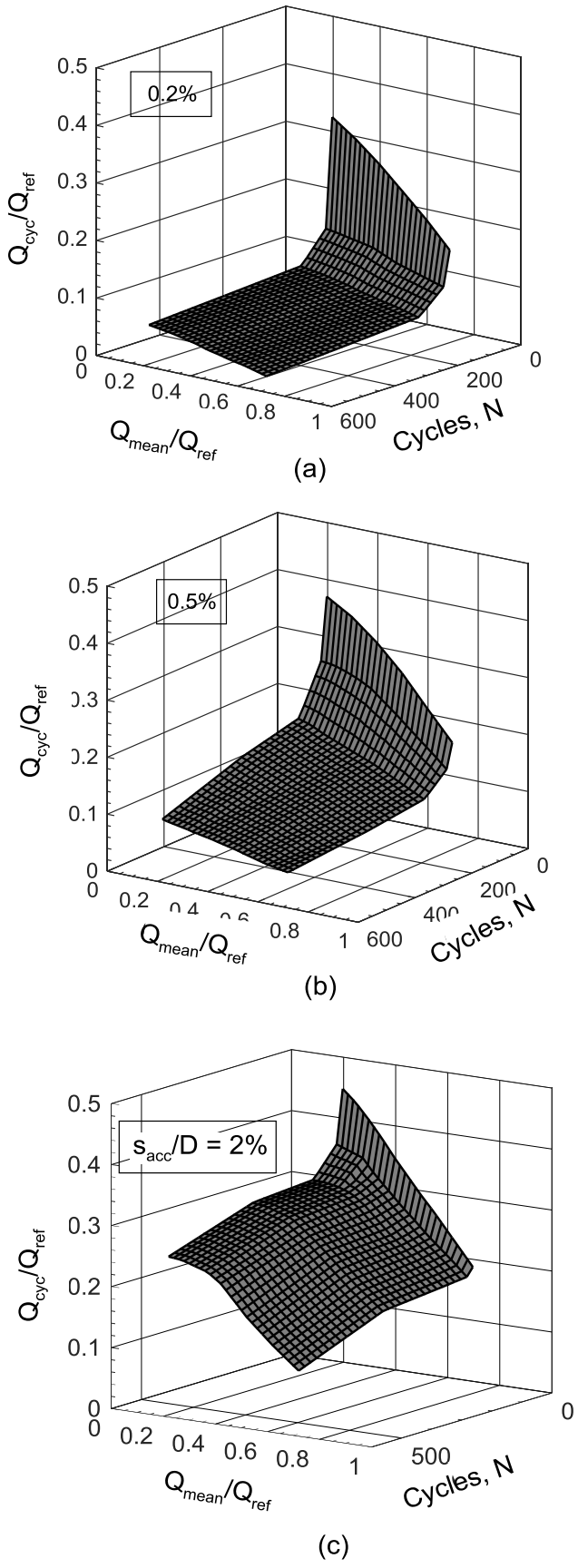


Figure 6-43: 3D plot showing variation of s_{acc}/D with N, Q_{cyc}/Q_{ref} and Q_{mean}/Q_{ref} for s_{acc}/D of a) 0.2% b) 0.5% and c) 2.0%

6.10 Summary & concluding remarks

This chapter described the site conditions and chalk properties at a site where a programme of static and cyclic loading tests was undertaken on open-ended steel tubular piles driven in low-medium density chalk. The ground conditions at St. Nicholas-at-Wade show similarities to those encountered at the Wikinger OWF described in Chapter 5. A more comprehensive review of the conditions at both sites is provided in Chapter 8. The following similarities and differences are noted here:

- At both sites, low-medium density structured chalk is encountered with IDD which is generally less than 1.55Mg/m^3;
- Similar to Wikinger, the chalk at St. Nicholas-at-Wade is at, or close to, full saturation;
- Within the depth of influence of the test piles, a similar proportion of flints is seen as in the Wikinger chalk;
- The chalk at Wikinger (Grade A1/A2) has closed fractures which are spaced between 200 and 600mm leading to tighter chalk blocks to those present at St. Nicholas-at-Wade;
- At both sites, average cone resistance, sleeve friction and penetration pore pressures lie within similar ranges;
- Unconfined compressive strength at St. Nicholas-at-Wade is significantly higher than that seen at Wikinger which, as discussed in Chapter 5, falls below published trends.

This chapter also reported the results of a programme of static and cyclic tests designed to supplement the results obtained at the Wikinger offshore test site. The summary of the test outcomes provided within this chapter showed:

1. Notably low shaft resistances during driving along the piles' main shaft lengths;
2. A significant effect of installation rate on cone penetration resistance in chalk, thus reflecting that both the CPT and pile installation were partially drained events;
3. A strong dependence of local shaft resistance on relative distance above the pile tip (h/R*) from the results of dynamic tests which mirrored the trends seen when the average load on the CPT was measured;
4. Marginally lower average shaft driving resistances than the CIRIA static design guidance values;

5. Driving remoulded the chalk, created a puttified zone and probably generated very high excess pore pressures near to the pile tip. Rapid excess pore water pressure dissipation during and after driving led to markedly lower water contents close to the shaft;
6. Static tension capacities increasing markedly after driving. Gains exceeding 500% were interpreted after eight months, leading to average shaft stresses that exceeded the low-medium density guidance value by a factor of 4.3;
7. A hyperbolic shaft capacity trend with time that was 83% complete 100 days after installation. A single re-test conducted 8 months after one pile's first static failure showed a positive ageing trend, although its capacity fell well below that of the undisturbed piles;
8. Evidence from field observations and laboratory tests of changes in residual shear strength with time, for chalk-steel interfaces aged under load. However, the latter are equivalent to increases in local shear stress of approximately 10%, which is too low to explain the observed long-term increases in shaft capacity of the driven piles;
9. Similarly, short-term reconsolidation of chalk putty that was too rapid to explain, on its own, the observed long-term increases in shaft capacity;
10. Other mechanisms are required, such as consolidation of chalk putty (contemporaneously with pile driving) followed by long-term creep and the breakdown of arching, allowing radial total stress re-growth which may provide explanations for the observed ageing trends, taken in combination with potential re-cementing and the redox chemical reactions that were noted to have occurred close to the pile shafts;
11. A range of responses to axial cyclic loading imposed with a range of loading combinations around 250 days after driving. One-way (non-dynamic) cycling that involved equivalent 'static' utilisation ratios >0.70 led to clearly unstable behaviour with rapid accumulation of displacement, stiffness loss, failure in far less than 100 cycles and marked degradation in operational shaft capacity. One-way tests conducted with $0.48<UR<0.70$ led to broadly stable capacities and cyclic stiffness remaining constant or growing as cycling continued. However, the piles' accumulated displacement trends did not stabilise within 1000 cycles, suggesting only meta-stability. Greater degradation can be expected at the same UR values under high-level two-way loading;
12. The permanent displacement accumulation trends followed under the stable/metastable tests developed proportionally with N, raised to an exponent of

≈1/3 that appeared to be insensitive to the loading parameters within the limited range (one-way $0.48 < UR < 0.70$) considered. Higher exponents applied in the unstable range. Further investigation is required to explore the potential effects of pile scale and chalk density, as well as the cyclic response under a wider range of cyclic loading conditions.

The experiments provide the first systematic study of which the Author is aware into the effects of undisturbed ageing and cyclic loading of previously unfailed piles driven in chalk. Overall, guidance based on driving monitoring and early age tests appear to be potentially highly conservative, while cyclic tests on aged piles showed responses that varied between stable and unstable, depending on the loading conditions. Parallel investigations were made into the governing effective stress processes with highly instrumented Imperial College Piles, as described in the next chapter.

CHAPTER 7

Instrumented pile tests at St. Nicholas-at-Wade

7.1 Introduction

Field studies by Bond (1989), Lehane (1992) and Chow (1997) with highly instrumented displacement Imperial College Piles (ICP), jacked into sands and clays, have led to increased understanding of behaviour and significant advances in practical axial design methods for driven piles. Experiments conducted in sands showed for the first time that local shaft radial effective stresses and pile base resistances followed the same trends as cone resistance. Tests in both sands and clays demonstrated that an effective stress Coulomb law controlled shaft failure and also identified the strong influence of relative tip depth, h on reducing the shaft radial and shear stresses with increasing penetration (Bond and Jardine, 1991, Lehane *et al.*, 1993, Chow, 1997). The results of the above extended testing programmes led to radically different design methods for clays and CPT-based axial capacity design methods for sands (Jardine *et al.*, 2005a, Lehane *et al.*, 2005b), which are now employed widely in practice (see Overy, 2007, Merritt *et al.*, 2012, Hampson *et al.*, 2017, or Rattley *et al.*, 2017). The sand methods are also incorporated into the current API RP2A and ISO 19902:2007 recommended practice for offshore pile design.

This chapter reports experiments designed to achieve similar insights into the behaviour of piles driven in chalk. As noted previously, the mechanical behaviour of displacement piles in chalk and the governing effective stress processes remain poorly understood. The entirely empirical design methods described in Chapter 3 have poor reliability and lead to considerable

uncertainty in design, especially when applied for large offshore wind farms (Carrington *et al.*, 2011).

The programme of ICP tests reported in this chapter was carried out at the St. Nicholas-at-Wade test site described in Chapter 6. The tests were planned to advance fundamental understanding of displacement pile behaviour in chalk and to supplement the tests on un-instrumented driven tubular steel piles described in Chapters 5 and 6, for which equivalent measurements were not feasible. The experimental aims are outlined first, followed by a description of the ICP pile, its instruments and their calibration. The experimental procedures are then described, followed by the main results, interpretation and the conclusions from this element of the field testing. The material presented in Sections 7.3 to 7.7 has also been reported previously, either whole or in part, by Buckley *et al.* (2017a) and Buckley *et al.* (2018b).

7.2 Experimental aims

The instrumented pile employed measures radial total stress σ_r, local shear stress τ_{rz}, and pore water pressure, u at fixed points on the pile shaft, allowing effective stress conditions to be determined along the shaft during pile installation, equalisation and long-term monitoring and load testing. The experimental testing programme carried out at the St. Nicholas-at-Wade test site was designed to investigate the fundamental effective stress behaviour of displacement piles in chalk including:

1. Installation local shaft effective stresses (σ_r and τ_{rz}) and base stresses (q_b) mobilised during installation and their relationship to pile installation rate, chalk properties and in particular *in-situ* CPT cone resistance and increasing penetration or relative tip depth (h/R);
2. The effect of extended monitoring periods following installation on the load displacement behaviour and local shaft effective stresses; and
3. The effective stress paths followed at points along the pile shaft during static and cyclic pile tests and their relationship to the behaviour seen in laboratory tests.

7.3 The Imperial College instrumented pile

7.3.1 Background

The instrumented displacement pile was developed by the Soil Mechanics section at Imperial College, starting in 1983. The original body of the pile was used by researchers at the University of Southampton to examine the effects of electro-osmosis on pile capacity (Johnston, 1972, Butterfield and Johnston, 1973). Jardine (1985) revamped the pile at Imperial College adding extra load cells and pore pressure sensors and obtained the first field measurements in a pilot study involving in London Clay at Canon's Park, North London. While these data were interesting and useful, the instrument systems did not perform optimally.

A PhD thesis by Bond (1989) was dedicated to first re-designing the instruments to deliver research quality data, and then applying the equipment in an extended series of tests at Canon's Park. In collaboration with Cambridge *in situ* Ltd., and after consideration of various options, Bond (1989) arrived at a fully effective device which was named the Imperial College Pile (Bond *et al.*, 1991). Lehane (1992) proceeded to conduct a further eleven pile tests at three sites in the UK and France; at Labenne in loose dune sand, at Cowden in stiff heavily over-consolidated glacial till and at Bothkennar in soft sensitive clay. Chow (1997) added an extra instrumentation level and completed a further eleven tests in normally consolidated clay-silt at Pentre and, after adding higher capacity axial load cells, in dense marine sand at Dunkirk. Pellew (2002) was the most recent researcher to use the 102mm diameter pile at IC, to study the behaviour of bored piles at Canon's Park, installing the pile within a low viscosity grout tremied into marginally oversized pre-bored holes. A 36mm diameter, 1m long "mini ICP" pile, with three instrument clusters, was also developed at Imperial College in conjunction with Cambridge *in situ* Ltd. (Jardine *et al.*, 2009) and installed in uniform sand in a calibration chamber at Grenoble-INP as part of several studies into the behaviour of displacement piles in sand (Yang *et al.*, 2010, Tsuha *et al.*, 2012, Jardine *et al.*, 2013b, Rimoy *et al.*, 2015).

Sections of the 102mm diameter pile were loaned to Professor Barry Lehane at the University of Western Australia (UWA) in 2010 and used to study behaviour in various Perth sands (Lim, 2014, Lim and Lehane, 2015a) and an Australian residual soil (Orea Velazquez, 2015). The equipment was returned to Imperial College in October 2015 for the Author's work described in this chapter, in which Professor Lehane and a colleague (Mr. Tom Pine) also participated.

7.3.2 Pile configuration

The closed-ended 102mm diameter Imperial College Piles' main shaft sections are tubular with a 9.5mm wall thickness. With the exception of their stainless steel Surface Stress Transducer (SST) sections, the piles are made from molybdenum steel and had typical centre line average roughness (R_a) of ≈5μm at the time of installation at St. Nicholas-at-Wade. High axial loads were expected in chalk and the dual instrument clusters adopted were identical to the higher capacity cells employed by Chow (1997) for tests in dense marine sand at Dunkirk. They are distinguished in Figure 7-1 by their *leading* and *following* positions, as defined by their ratios of, h, height above the pile tip, normalised by the pile radius, R. Each cluster includes:

- An axial load cell (ALC), which measures axial load in the pile (Figure 7-2);
- Two diametrically opposite pore pressure transducers (PPT) which measure pore water pressure (Figure 7-3); and
- An SST, which measures σ_r and τ_{rz} on the pile surface, as well as temperature (Figure 7-4).

7.3.3 Instruments & calibrations

The instruments' design, development and calibration procedures are described by Bond *et al.* (1991). The instruments were calibrated prior to the first pile test at UWA by Dr. Jit Kheng Lim and again by the Author prior to and following the final tests at St. Nicholas-at-Wade. The instruments were calibrated against known forces in the laboratory, or in the case of the surface stress transducers, in a specially designed calibration rig.

Axial load cells

The ALCs connect to the pore pressure units as shown in Figure 7-2 and are strain gauged at a thin wall section. The strain gauges are arranged in a Poisson bridge configuration with four pairs of gauges; one set in the axial direction and the other in the circumferential direction, giving one bridge voltage output per axial load cell. High axial loads were expected at the Kent site, and therefore the 175mm long high capacity load cells manufactured for Chow's (1997) tests at Dunkirk were used. The ALCs, which have a nominal capacity of 405kN at 0.2% axial strain, were calibrated in the structures laboratory at Imperial College using a 600kN SATEC Series universal testing machine, which had an accuracy of ±0.5% for the applied load. The cells were first subjected to 5 load-unload cycles to the maximum load to "exercise" the cells before being loaded to 300kN (in compression) giving the six point

calibration results shown on Figure 7-5 for ALC1 (*leading* cluster) and ALC2 (*following* cluster).

Pore pressure transducers

The pore pressure transducers were mounted in specially machined ports and comprise a sintered stainless steel porous disc fitted on an acetyl co-polymer mounting block, which is turned to lie flush with the curved pile surface (Figure 7-3). Pore pressure is measured by a Druck PDCR 81 miniature pressure transducer which is attached to the back of the block, with a small O-ring between the transducer and the sintered stainless steel porous disc. The pore pressure probes were prepared for the test in two stages:

1. The porous stones were bolted inside specially made brass chambers and saturated with silicone oil, using cycles of positive pressurisation to approximately 300kPa and depressurisation to vacuum, in order to remove trapped air, following the method described by Chow (1997);
2. Once the stone was saturated, one side of the brass chamber was opened and a bath of silicone oil was attached to retain saturation. The transducer and the O-ring were then clamped to the mounting block. The pore pressure transducers were calibrated inside the brass chamber following saturation by connecting the probes to a Budenberg dead weight tester. The probes were transported to site sealed inside the brass chamber.

Replacement PDCR81 transducers were required following damage that occurred during extraction of the pile following the first test of the programme. The obtained pore pressure calibration coefficients are listed in Table 7-1

Table 7-1: Calibration coefficients for the pore pressure transducers used in this study

Cluster	**Transducer**	**ICP01 (kPa/V)**	**ICP02 (kPa/V)**
Leading	PPTa	350	363
	PPTb	342	319
Following	PPTc	332	347
	PPTd	312	361

Surface stress transducers

The surface stress transducer measures stresses through a (97.5 x 77.5mm) window pane fixed to a “Cambridge” three axis load cell (Figure 7-4). The window pane moves when subjected to radial and shear stress and causes the strain gauged radial and shear webs to

deflect. The window pane and load cell are housed in a window frame with a special rubber seal between their edges. The window pane is in turn connected to the main cell housing, with the SST occupying 26% of the pile circumference. A "Dowty" bonded seal is placed inside the final top screw in the window pane, and a large O-ring is fitted at the top of the cell which together ensure water tightness of the cell. Each cell outputs two radial stress circuits at the top and bottom, plus one shear circuit and one temperature circuit measured through an integrated circuit device. The radial total stress measurements are accurate to typically ± 3kPa and the shear stress measurements to typically ± 1.5kPa (Bond *et al.*, 1991).

Calibrations were conducted at the University of Western Australia prior to the first test and at Cambridge *In-situ* Ltd. after repair work conducted during and shortly after the test programme. The calibration rig, purpose-built at Cambridge In-situ Ltd. at Little Eversden, Cambridgeshire, is shown on Figure 7-6. The system has similar principles to the Imperial College rig designed originally by Bond (1989) and consists of a dead weight biaxial jig which applies radial stress through a specially manufactured top platen attached with screws to the window pane. Shear stress is applied through a system of pulleys and a frame also connected to the window pane with a line of action set to act parallel to and through the surface of the cell. It is noted that positive shear stress is taken here as that induced when the soil resists compression loading of the pile.

As well as direct calibration of the radial and shear stress sensors, the calibrations also considered the cells' cross sensitivities related to the effects of:

1. Axial load on the radial and shear strain gauge output;
2. Shear stress on the radial strain gauge output;
3. Radial stress on the shear strain gauge output; and
4. The effect of temperature changes on all the gauges.

The effect of axial load on the radial and shear strain gauge output was assessed using data from the pile installation pushes, where the SST was still "in air" and above the ground. In this condition, axial load causes the shear and radial webs to deflect and induces a change in the zero point of the radial and shear sensors, which can be monitored and used to correct the results for the effects of axial load.

Figure 7-7 shows an example of an SST calibration result. The radial stage consists of varying σ_r by applying increments of load to the platen, with zero shear stress initially and then with constant values of positive τ_{rz} followed by constant values of negative τ_{rz}. The shear stage

consists of varying τ_{rz} in increments up to the maximum calibration load, while keeping σ_r either at zero or at a constant value.

The two calibration stages are used to assess both the direct sensitivity of the sensor to their measured stress, and the cross sensitivity between the radial and shear circuits (points 2 and 3 above). Some cross sensitivity is unavoidable as the radial webs carry some shear load and vice versa, although the cell design minimises these interactions. When the radial cells are configured to give average readings for each SST, the relationship between applied loads and output signals is as follows, after Bond (1989):

$$\sigma_r = c_{11}\left\{\frac{(V_0/V_i)_{c1} + (V_0/V_i)_{c2}}{2}\right\} + c_{12}(V_0/V_i)_s \quad 7\text{-}1$$

$$\tau_{rz} = c_{21}\left\{\frac{(V_0/V_i)_{c1} + (V_0/V_i)_{c2}}{2}\right\} + c_{22}(V_0/V_i)_s \quad 7\text{-}2$$

where σ_r and τ_{rz} are the radial total stress and shear stress respectively, c_{ij} are the calibration coefficients, V_0 and V_i are the output and input voltages (V_i =5V) and subscripts c and s refer to the radial and the shear circuits, respectively. The calibration factors c_{11} and c_{12} are obtained from the radial calibration stage, and the factors c_{21} and c_{22} from the shear calibration stage. Multiple regression analysis is used to fit the data based on the three variables i.e. applied stress, radial circuit voltage output and shear circuit voltage output. The calibration coefficients are summarised in Table 7-2. Over the two sets of calibrations, the cross sensitivity of σ_r to τ_{rz} (i.e. c_{12}/c_{22}) was less than 0.042 kPa/kPa and the cross sensitivity of τ_{rz} to σ_r (i.e. c_{21}/c_{11}) was less than 0.0049kPa/kPa. These are consistent with the values reported by Bond (1989) for his original calibrations, for which he gave c_{12}/c_{22} less than 0.04kPa/kPa and c_{21}/c_{11} less than 0.005kPa/kPa.

Laboratory investigations have shown that temperature increases cause expansion of the SST's radial webs, and under registration of stresses (Lehane, 1992); changes in temperature therefore affect the output from the radial and shear circuits. This has been addressed in earlier work by incorporating temperature sensors into the instrument clusters and conducting checks in environments subject to significant diurnal temperature cycles. The current sensitivity of the measurements to temperature was assessed at UWA and at IC where the instruments were logged continuously under zero load for up to a week under conditions

where the diurnal ambient peak to trough temperature changes were approximately 10ºC/day. The maximum difference between the initial conditions in air and the final temperatures after installation in the ground in the Author's tests was approximately 8ºC. Temperature calibrations were derived and applied to adjust the initial zero values relating to signals recorded when the pile was in the ground. This was useful particularly over the installation phase, where the instrument temperatures increased during jacking as a result of the high frictional tip loads, and cooled during the installation pauses.

Table 7-2 Direct and cross sensitivity factors for the radial and shear stress transducers

SST	Test	Sensitivity	Radial circuit – R1 (kPa/V)	Shear circuit[1] (kPa/V)
SST1	ICP01	Direct sensitivity (c_{11}/c_{12})	816.5	209.3
		Cross sensitivity (c_{12}/c_{21})	3.3	7.5
	ICP02	Direct sensitivity (c_{11}/c_{22})	791.2	211
		Cross sensitivity (c_{12}/c_{21})	3.9	8.8
SST2	ICP01	Direct sensitivity (c_{11}/c_{22})	897.6	131.4
		Cross sensitivity (c_{12}/c_{21})	0.65	-3.3
	ICP02[2]	Direct sensitivity (c_{11}/c_{22})	1128.1	136.0
		Cross sensitivity (c_{12}/c_{21})	-1.3	-3.5

1. Shear stress applied is calculated by dividing force applied by the area of the window pane. This area also accounts for half of the width of the hot bonded rubber seal which follows the edges of the window pane.
2. Re-strain gauged following ICP01 which accounts for different calibration factors

7.3.4 Instrument performance

Completely accurate measurements of σ_r and τ_{rz} are difficult to obtain and instrument malfunctions can occur during field testing. However, the ICP configuration includes redundancy that allows cross checking and error identification. The SSTs' local τ_{rz} measurements can also be cross checked with the average shear stresses, interpolated from the axial load measured by the cells located above and below the sensor and σ'_r can be checked for consistency by dividing the τ_{rz} measurements taken at failure by tanδ' values obtained in laboratory interface shear tests. The dual radial sensor circuits and pore pressure transducers available in each cluster provide back-up that proved useful in the Author's experiments.

Bond *et al.* (1991) recognised that the SSTs' asymmetric design makes them susceptible to bending under high axial load. This was not unduly significant at the initial clay and loose sand test sites, where end bearing and overall axial loads were relatively low. However, Chow (1997) found that the high installation and compression test loads developed in dense marine sand caused the SSTs to deflect asymmetrically and under-register both σ_r and τ_{rz}. High end

bearing loads were anticipated for, and experienced in, the chalk tests that would lead to stress under-registration when the pile was penetrating downwards, but have no effect when the pile head load was zero (i.e. during an installation pause), or negative and relatively low, as in tension tests. To avoid the SST measurement difficulty under high compression loads, the analysis of the installation data therefore concentrates primarily on the stationary radial effective stresses measured during a pause in penetration, immediately prior to a stress reversal (see Figure 7-17, later). The performance of the various instruments during the Author's tests is further discussed in Appendix A-6.

7.3.5 Data acquisition

The UWA in-house "DigiDaq" data acquisition system was used to capture data during the Author's tests at St. Nicholas-at-Wade, using equipment loaned by Prof. Lehane. The system can facilitate data streaming of eight channels at 100Hz per box of input, with 8 boxes of input allowed, and simultaneous data recording at high speed of up to eight channels at 1MHz per box. The system has an integrated signal conditioner that powers the cells, amplifies the outputs, digitises the data and interfaces with the data logging PC. The system consists of a laptop connected to a signal conditioning box via an Ethernet cable, with both the laptop and the box connected to a power supply. The system is not capable of long-term data capture without a PC connection and as a result the laptop and the box must be connected to a power supply at all times while the pile is logging.

The SST strain gauges have a typical output of 5mV when energised at 10V and were amplified 1000 times to give outputs of ±5V. A total of fourteen channels were provided by the two DigiDaq boxes employed during this study, allowing two radial, one shear and one temperature circuit, as well as one axial load and two pore pressure circuits to be recorded per cluster.

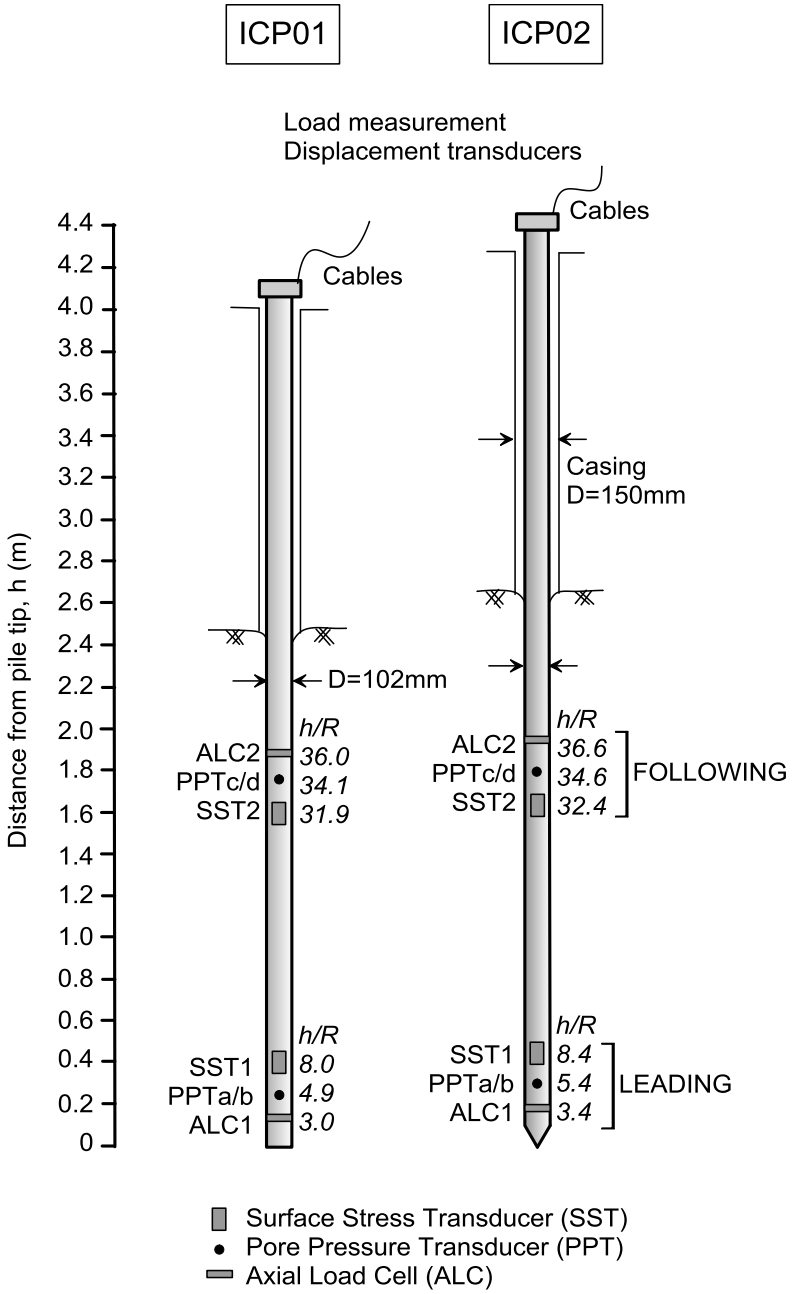


Figure 7-1 ICP configuration used during tests in chalk a) ICP01 b) ICP02

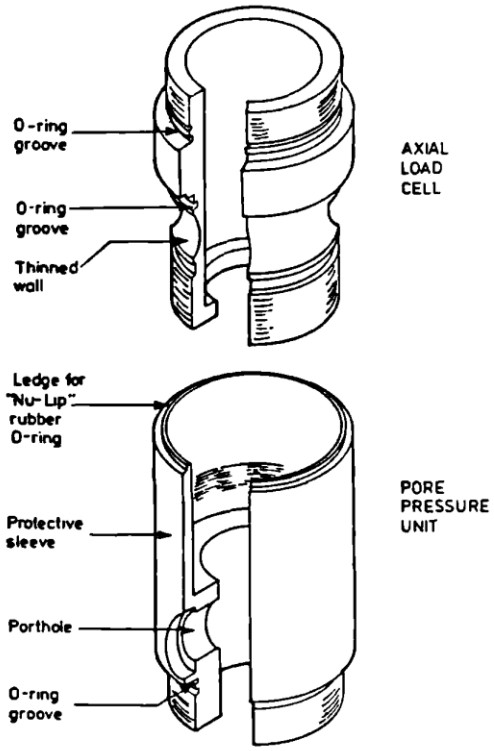


Figure 7-2 The combined axial load cell and pore pressure unit (Bond, 1989)

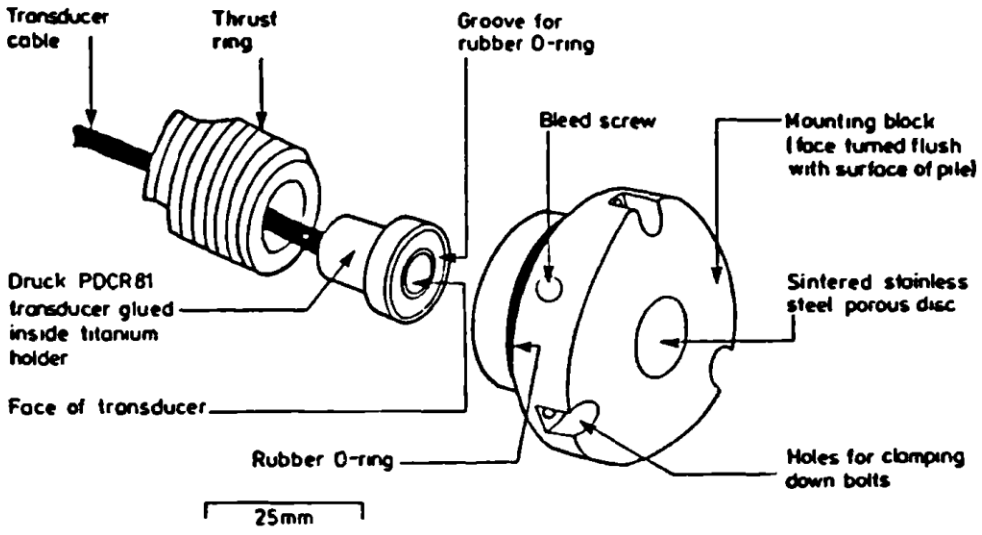


Figure 7-3 The pore pressure probe (Bond, 1989)

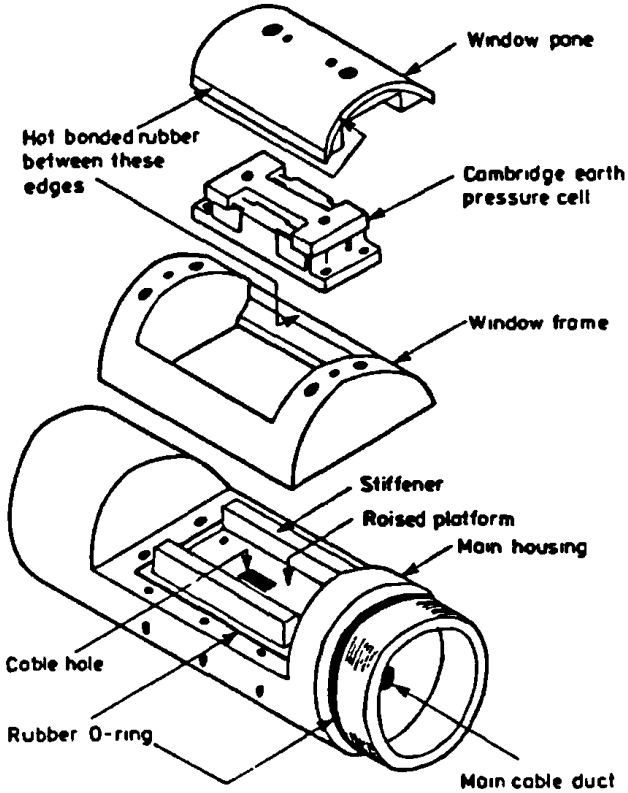


Figure 7-4 The surface stress transducer (Bond, 1989)

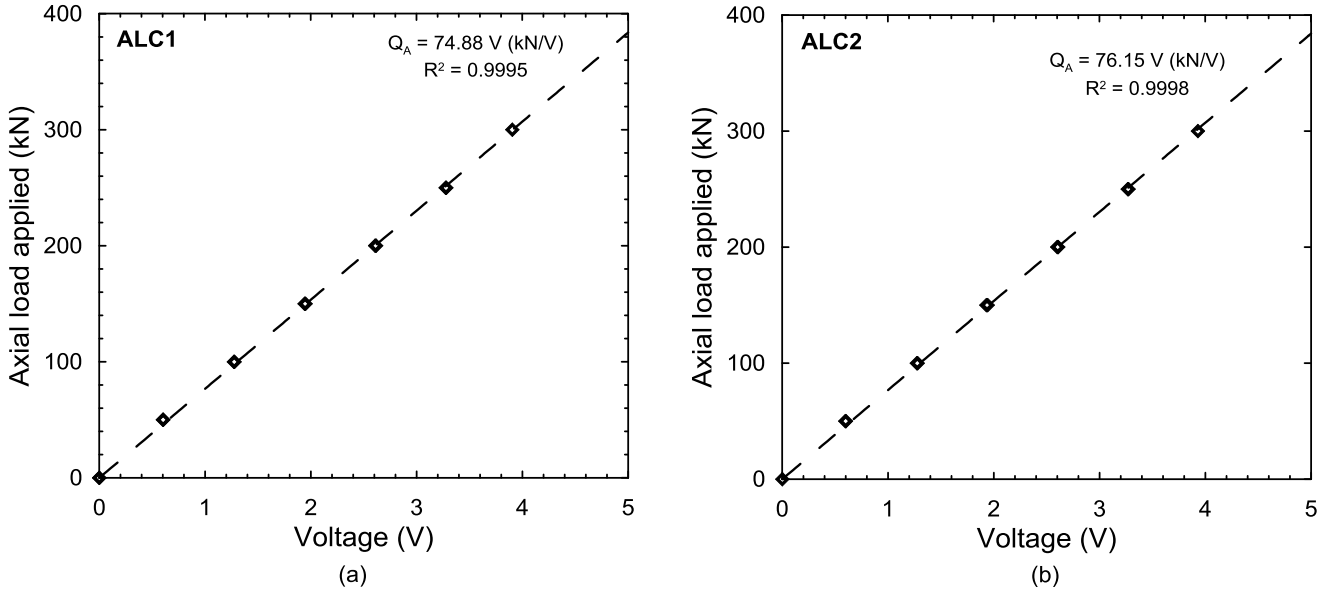


Figure 7-5 Calibration of axial load cells at a) ALC1 (leading cluster) and b) ALC2 (following cluster)

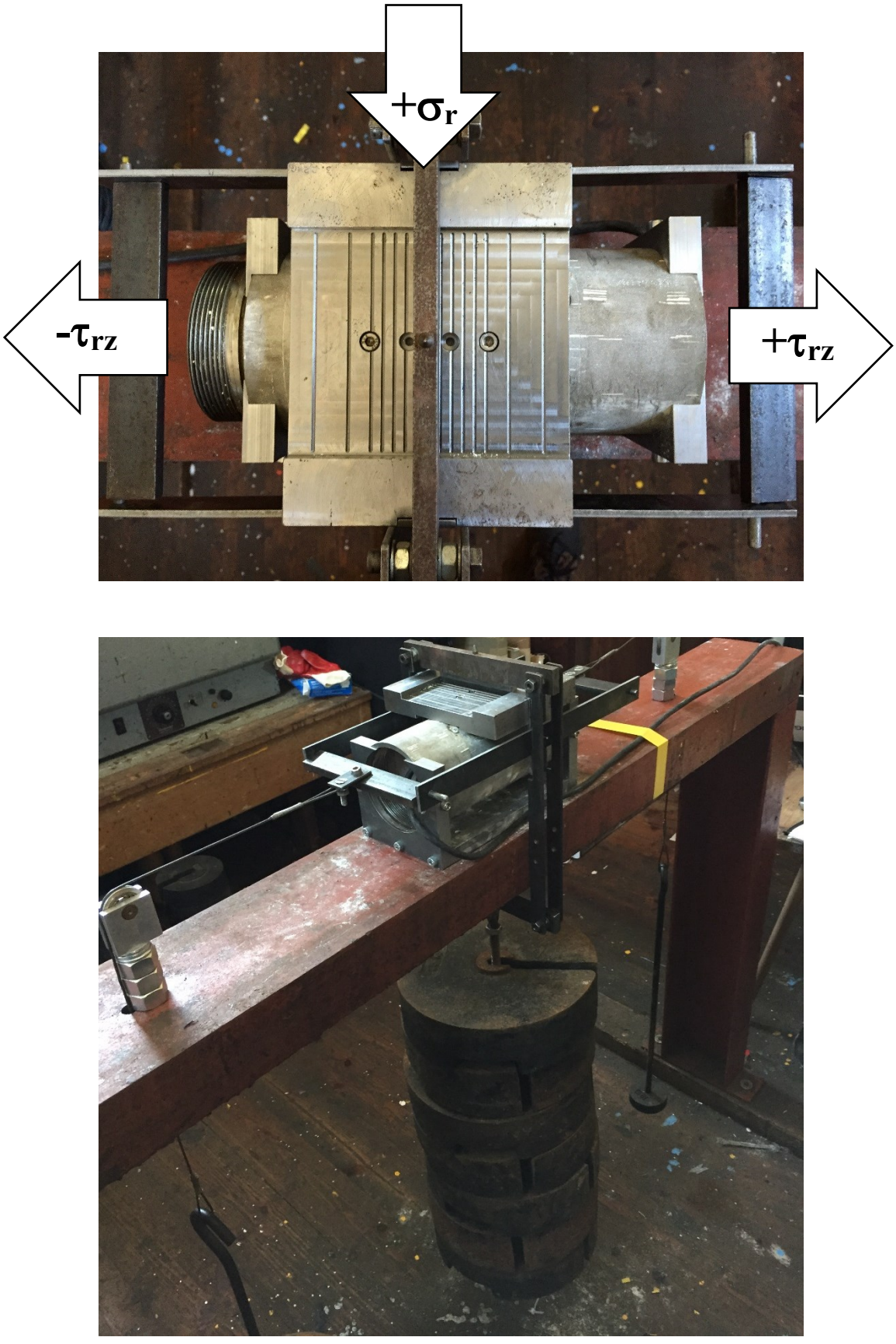


Figure 7-6 Calibration of radial and shear stress circuits in the surface stress transducers in a dead weight bi-axial calibration jig

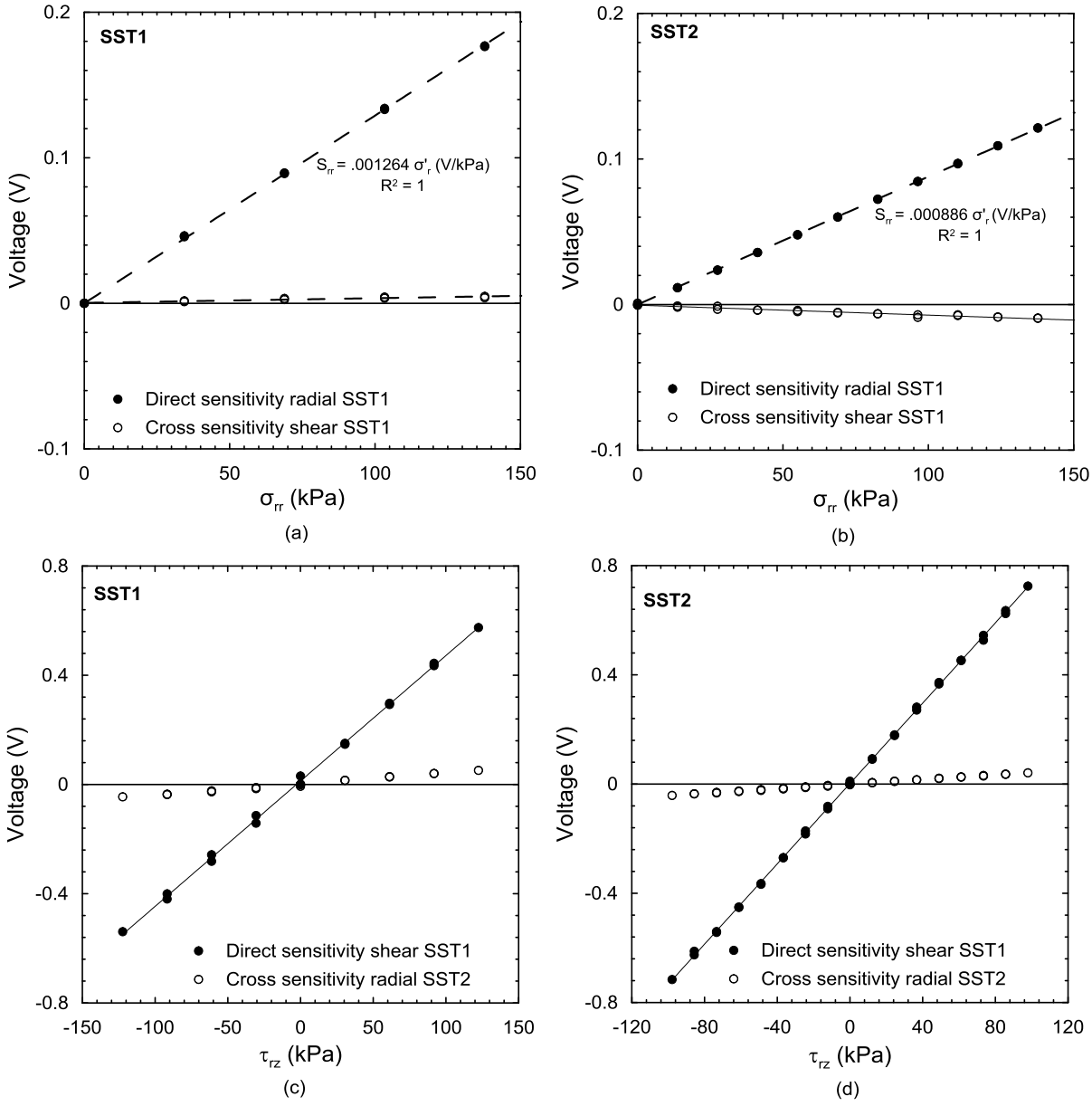


Figure 7-7 Calibration of surface stress transducers using purpose built bi-axial calibration jig for a) radial circuit SST1 b) radial circuit SST2 c) shear circuit SST1 and d) shear circuit SST2

7.4 Experimental procedures

7.4.1 Test preparation

To avoid overloading the ALCs under the high end bearing loads anticipated, the piles were installed from a free depth, 1.6m below current ground level, through 150mm diameter PVC casings placed in a backfilled trial pit. The pits were formed using an excavator with a small bucket. The ICP sections were assembled on site, and placed initially inside the cased hole before the first installation push was applied, with the tip at 1.6m depth.

The first test, ICP01, experienced slight water ingress into the pile over time that affected some strain gauges. The earlier ICP testing programmes employed a Hylomar "liquid" gasket sealant between all joints to avoid this problem; by-passing this time consuming process did not prove to be successful. To mitigate the effects of water ingress during the second test (ICP02), the pile was packed with silica gel sachets above each instrument cluster to trap any moisture which entered the pile and prevent it from reaching the instruments.

During installation and load testing the pile instruments, data loggers and laptop were run from a small petrol-driven generator, as during the driven pile tests described in Chapter 6. Over the long-term monitoring periods, the pile instruments, data logger and laptop were energised using a parallel wired bank of up to ten heavy duty 115Ah 12V lead-acid batteries. The DC supply from the batteries was converted to AC current to power the Digidaq system and the PC using a power inverter.

7.4.2 Pile Installation

The piles were installed by jacking against a 30 tonne CPT truck equipped with a 270kN hydraulic ram. Installation took place under displacement control, at jacking rates which varied (unavoidably) but averaged at 4.8mm/s and 3.4mm/s for ICP01 and ICP02 respectively (Figure 7-8), with 50mm strokes separated by 60 to 90 second zero-load pauses. The latter were chosen to ensure a similar degree of cycling to that experienced by open piles driven by the authors at the same site, which had penetrated by around 50mm per blow.

Installation force was measured by a load cell at the pile head or by the CPT truck's systems. All instruments were logged at 1 to 2 second intervals during installation. The process was not fully continuous. Apart from the intervals imposed between strokes, adding extra casing lengths led to total installation times of 80 to 124 minutes per pile, while only 4 to 15

minutes were required for the driven piles described in Chapter 6. The ICPs therefore inevitably experienced far slower penetration rates and far greater excess pore pressure dissipation during installation.

7.4.3 Equalisation and long-term monitoring

The instruments were monitored over the weeks following installation with readings every 5 minutes over ageing periods of 23 and 80 days that represent the longest duration ICP tests to date. The instruments were powered continuously over the relatively cold and wet 2015/16 winter, apart from four unintended short supply breaks. Instrument drifts (change in voltage output under zero load) were anticipated and the results were corrected by comparing instrument 'zero-values' established before and after each experiment, assuming constant drift rates between installation and extraction (Appendix A-6).

7.4.4 Load testing

The ICPs were subjected to tension load testing after their ageing monitoring periods using the load and control equipment described in Chapter 6 and shown on Figure 6-27. The ICP head piece, shown on Figure 7-9, which connects the pile to the load test system, consists of a flat plate and a coupler which screws into the uppermost pile casing. The head piece has a specially made recess which accommodates a 24mm diameter bar, which is secured with a nut below the flat plate. Five high tensile M10 bolts with a 30mm threaded length connect the flat plate to the threaded coupler, with an overall ultimate tensile capacity for the bolts of 390kN. The 37.5mm diameter Macalloy bar used for this test programme, with an ultimate tensile capacity of 570kN, was machined down to a 24mm diameter along a 100mm length to allow it to fit inside the pile head connection. This reduced the ultimate tensile capacity for the overall system to 230kN, which was adequate for the maximum anticipated failure tension loads.

Following each tension failure, the piles were unloaded to a small tensile load to retain system stability and approximately twenty (relatively high-level) one-way tension cycles were applied. The cycles were load controlled at 0.016Hz following a square wave pattern. During load testing, all pile instruments were logged every 1 to 2 seconds.

7.5 Testing programme

As summarised in Table 7-3, the testing programme began in October 2015 and was completed in February 2016 and consisted of the installation of two piles, followed by lengthy

monitoring periods which ended with static load tests to failure and post-failure cyclic loading tests. The *in-situ* test profiles from the site used to interpret the results are shown on Figure 7-10. The location of the *in-situ* tests and ICP piles was shown previously on Figure 6-2.

The piles were assembled on site using threaded casings, sealed with O-rings, to give total lengths of between 4.1 and 4.3m. This resulted in embedded lengths of between 2.5 and 2.7m (L_p/D = 24.5 to 26.5). The pile end conditions differed between tests; ICP01 was installed with a flat closed-end and ICP02 utilised a 60º conical tip to aid penetration if flint nodules were encountered, resulting in h/R values that differ slightly between tests (Figure 7-1). The leading ALCs were located above the pile tips and recorded the base loads plus minor contributions from the short (≈87 and 150mm) lengths of shaft below the base ALCs.

Table 7-3: Summary of 102mm diameter ICP test programme

Test	**ICP01**	**ICP02**
End condition	Flat base	Conical tip
Number of installation jacking cycles	51	56
Average dimensionless velocity, V_{pile}	0.46	0.33
Final Penetration (mbgl)	4.09	4.33
Length of embedment (m)	2.49	2.73
L_p/D	24.4	26.8
Installation date	27/10/2015	21/11/2015
First tension test date	19/11/2015	09/02/2016
Ageing period (days)	23	80

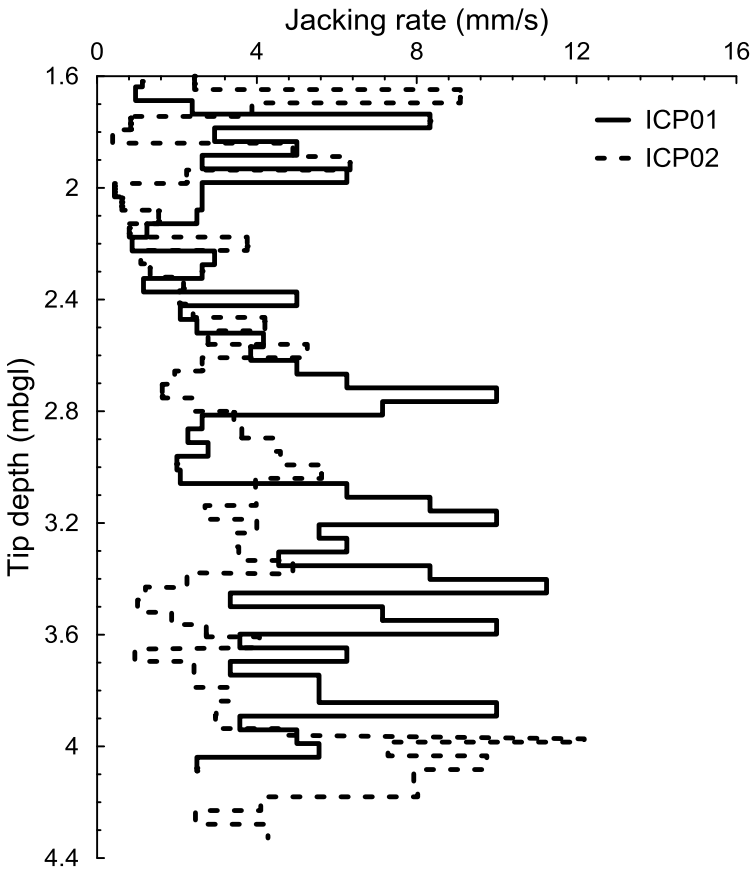


Figure 7-8 Pile jacking rate measured during installation of ICP01 and ICP02

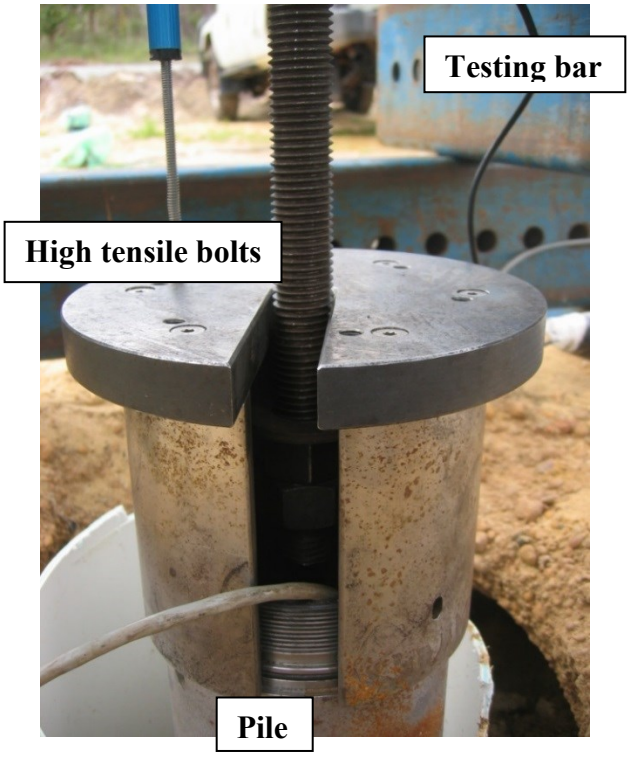


Figure 7-9 ICP head piece used for tension load test

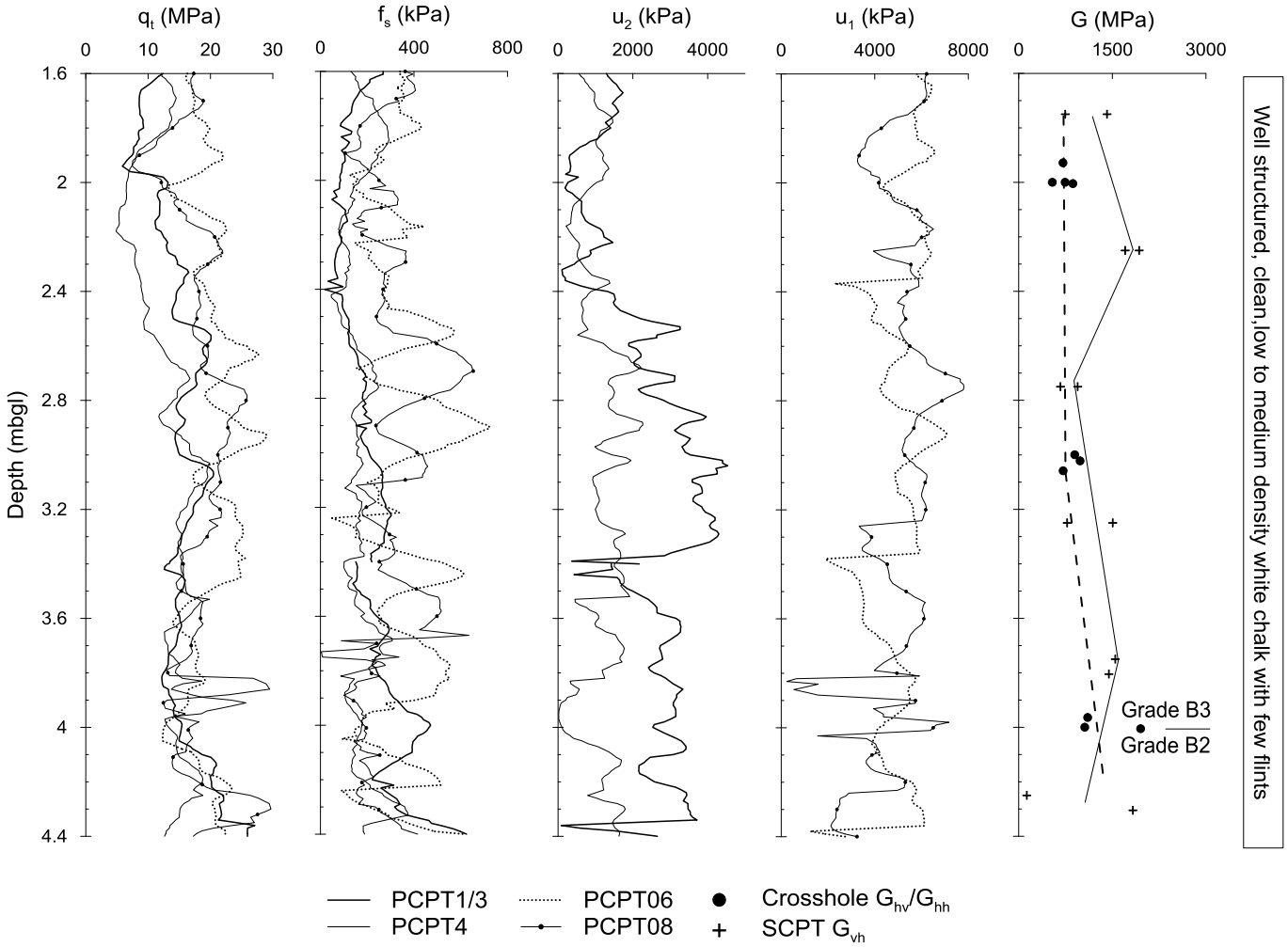


Figure 7-10 *In-situ* tests used in the analysis of jacked pile test results

7.6 Results & Interpretation

7.6.1 Installation resistance

The total axial force, Q_{tot} measured at the end of each penetration stroke are shown on Figure 7-11 along with the forces measured at the pile base, Q_b and the average shaft stresses, $\tau_{install}$ where:

$$\tau_{install} = \frac{Q_{tot} - Q_b}{\pi D L_p} \quad 7\text{-}3$$

and L_p is the pile penetration. Also shown on Figure 7-11 is the envelope of q_t measurements from across the test site. The lowermost load cell (ALC1) measurements include contributions from short lower sections of shaft, and therefore must be corrected to obtain an estimate of the true base load. The Q_b traces have been corrected by assuming that CPT sleeve friction values (measured at h/R ≈ 5.5) apply near the base such that:

$$Q_b = Q_{ALC1} - f_s \pi D h_{ALC1} \quad 7\text{-}4$$

Where:

Q_{ALC1} = load at the bottom-most load cell

h_{ALC1} = height of the bottom-most load cell above the tip

This assumption is considered reasonable since similar shear stresses (up to 280kPa) applied along these shaft lengths during static tension testing, as discussed later. Axial loads up to 270kN developed during installation pushes, comparable to those found in Chow's (1997) dense sand tests at Dunkirk. The base resistance, Q_b comprised ≈ 80% of the head load, Q_{tot} as in Chow's tests and in accordance with other piles jacked into weathered chalk (Hodges and Pink, 1971). Lower tip resistance contributions develop in clays, where Q_b typically comprises <20% of the total (Lehane, 1992, Lehane and Jardine, 1992b, Chow, 1997). As discussed in Chapter 6, PCPT tests identified laterally discontinuous, thin, high resistance flint bands. Figure 7-11 shows that $\tau_{install}$ was highest in a layer between 2 and 2.3m, but fell in both tests to approximately 50kPa as the tips penetrated to greater depths. While the overall average shaft resistance of 50kPa exceeds the CIRIA driven pile static capacity recommendation of Lord *et al.* (2002), the average

shear stresses recorded over the main shaft lengths, *between* ALC1 and the pile top, were on average 11kPa, falling well below the average calculated over the whole pile length (seen on Figure 7-11) and the CIRIA guideline value. Small residual ALC1 loads (typically <3kN) remained after unloading at the end of each jacking push, whose distributions with depth mirrored the profiles of $\tau_{install}$.

7.6.2 Penetration pore pressures

Pore pressure measurements were taken on the shaft, all of which were positioned high above the water table. The ambient pore water pressures in this region depend on infiltration rates and permeability gradients. Negative pressures can be expected under dry conditions, but small positive values appeared to operate at times over the 2015/16 winter as shown on Figure 7-12. Figure 7-13 shows the measurements along with those made during PCPT penetration, plotted in this instance against h/R where h is the distance from the pile or PCPT tip and R is the pile or PCPT radius. Low, typically <10kPa, penetration pore pressures were measured by the pile sensors located between 0.25 and 1.76m behind the pile tip, while, within the depth of interest, values exceeding 4MPa were measured at the PCPT u_2 position ≈38mm from the cone tip reaching as high as 7.8MPa at the tip (u_1). The location of the pore pressure measurements on the PCPT instrument are shown schematically on Figure 7-14.

The piles were installed under displacement control at variable jacking rates, which are equivalent to normalised velocities, V between 0.33 and 0.46, well below the minimum of 2 to 20 proposed in Chapter 6 for undrained conditions. Strong gradients of pore pressure with distance from the pile base are indicated in Figure 7-13, to which the piles' partially drained tip conditions contributed. Effectively drained conditions applied over most of the shaft above the tip, due to the reduced total stresses (as described later) and additional dissipation of pore pressures over the time taken for the upper shaft sections to reach any given chalk horizon. Partially drained pore pressure distributions were also assessed along the shafts of the tubular piles driven at the same site (Chapter 6), although their degrees of dissipation would have been lower, as the driven piles had larger diameters and far shorter total installation times.

7.6.3 Base resistance measurements

The closed-ended ICP end bearing load profiles shown on Figure 7-11 have similar forms to the CPT q_t profiles shown in Figure 7-10, with the exception of the higher

pile tip resistance band encountered between 1.9 and 2.3m. The pile base resistance can be evaluated from:

$$q_b = \frac{Q_b}{A_b} \qquad 7\text{-}5$$

Given their geometric similarities, it is reasonable to expect the above (closed-end) pile bearing pressures, corrected for the shaft contribution as described earlier, to correlate with the cone resistance. For deep penetration, $q_b = \alpha_t q_t$ is also predicted from strain path methods and cavity expansion solutions (Baligh, 1985, Randolph *et al.*, 1994) where α_t depends on penetration rate and pile-end geometry. Jacking under partially drained or drained conditions is known to increase tip resistance (Chung *et al.*, 2006) while positive rate effects apply under undrained conditions. The variable installation rates and geometries of the jacked piles results in α_t values between 1.0 and 1.6 which mirror the trends seen in variable rate cone penetration tests described in Chapter 6. Figure 7-15 shows the variation of α_t with non-dimensional velocity V (applying over an installation push for the pile) for the pile and PCPT, indicating the general trend for q_b/q_t to reduce with V and the limits for installation under drained or partially drained conditions. The relative scatter in this plot is considered attributable to variability in the correction of the base measurements with the sleeve friction values described as per Eq. 7-4. The parameter α_t can be seen to reduce with increasing V tending towards an α value of 1 when $V_{pile} = V_{cpt}$. Installation end bearing therefore appears to be controlled by cone tip q_t and the degree of local drainage.

7.6.4 Shaft effective stresses close to pile tips

It has been argued that closed-ended piles develop triaxial compression failure zones immediately beneath their tips during penetration (Jardine *et al.*, 2013a). The average vertical stress, σ_z (=σ_1) should then equal q_t (or q_b) beneath the tip, with:

$$\sigma_1 = q_t = \sigma'_z + u_1 \qquad 7\text{-}6$$

where u_1 is the average pore pressure over the cone tip. Applying the argument presented by Jardine *et al.* (2013a) for sands, the maximum moving radial effective stresses, σ'_{rm} applying immediately below the pile tip during rapid penetration can be calculated from the Mohr-Coulomb failure criterion for triaxial compression:

$$\sigma'_{rm} = \tan^2\left(45 - \frac{\varphi'}{2}\right)\sigma'_z - 2c'\tan\left(45 - \frac{\varphi'}{2}\right) \quad 7\text{-}7$$

where peak $\varphi' = 41°$ for intact chalk at the test site (Figure 6-15), and σ'_z beneath the tip $= q_t - u_1$. The mean u_1 pore pressures are approximately equal to $0.4q_t$ giving:

$$\sigma'_{rm} \approx 0.125q_t - 2c'\tan(24.5) \quad 7\text{-}8$$

beneath the pile tip during steady penetration. Taking c'=387kPa from Figure 6-14 gives $900 < \sigma'_{rm} < 2150$kPa on the pile axis at the tip (h=0). Moving to slightly higher locations, the CPT sleeve resistance values, f_s indicate "moving" effective stresses that are almost an order of magnitude lower, calculated from $\sigma'_{rm} = f_s/\tan\delta'_{cpt}$ by applying the measured interface shear angle, δ'_{cpt} of 30.5º, giving $100 < \sigma'_{rm} < 350$ at h/R = 5.5. The value of δ'_{cpt} of 30.5º was chosen based on the results of interface ring shear tests on samples from the site using stainless steel interfaces with similar roughness to the CPT cone sleeves and at normal effective stress of 200kPa, compatible with the mean σ'_{rm} values (Section 6.4.6). The near pile tip values of σ'_{rm} discussed above are compared below to the local radial effective and shear stresses measured at the SST locations measured higher above the tip on the pile shaft.

7.6.5 Local shaft effective stresses

Figure 7-16 shows the stationary radial effective, σ'_{rs} and stationary τ_{rz} stresses measured at the *leading* instrument during both ICP tests; the following instrument data are discussed later. The stationary stresses are chosen at the points shown on Figure 7-17 where the pile head load is zero, and are free of the bending effects described in Section 7.3.3 and Appendix A-6. Since the pile was installed under partially drained conditions and the stresses equalised rapidly after each stroke, σ'_{rs} can be considered equivalent to the equilibrium values applying shortly after installation to the same tip depth. The σ'_{rs} values were similarly low in both tests, varying from ≈20 to 60kPa, far below the values discussed in the previous section for the pile tip region. When the piles were stationary, the SSTs measured low negative τ_{rz} values, reflecting the shafts' tendency to resist locked-in toe forces when the head load was removed.

The *leading* SSTs profiles of σ'_{rs} correlate directly with the CPT q_t depth trends (see Figure 7-18), as has been noted previously for sands (Lehane, 1992, Chow, 1997) and incorporated into CPT pile design methods (Jardine *et al.*, 2005a, Lehane *et al.*,

2005b). The σ'_{rs}-q_t trends for ICP01, which had a flat bottomed end, exhibit a higher degree of scatter than those for ICP02, which utilised a conical tip. The average q_t/σ'_{rs} ratio is approximately 405 at the *leading* instrument.

The stationary radial stresses applying further along the shaft are shown on Figure 7-19, where σ'_{rs} is normalised by q_t and plotted against h/R for the last 500mm of penetration in each test. Also shown on this plot are trends observed in loose silica sand at Labenne (Lehane, 1992, Lehane *et al.*, 1993), dense Dunkirk sand (Chow, 1997) and uncemented calcareous sand (Lehane *et al.*, 2012a). The σ'_{rs}/q_t ratios can be seen to fall well below the measurements made at Labenne and Dunkirk and to fall closer to the calcareous sand trend. Only slight reductions in normalised σ'_{rs}/q_t were observed between the *leading* instrument (h/R = 8 – 8.4) and the *following* cluster (h/R = 31.9 – 32.4), suggesting that in chalk the extreme stress reduction that takes place between the pile tip and the shaft develops over a relatively short h/R range.

Further evidence is presented in Figure 7-20 by adding to the stationary SST measurements i) "moving" radial effective stresses inferred from the CPT f_s traces and ii) profiles of τ_{rz} found from back analysis of dynamic tests on piles driven at the site; Section 6.5.2. The three sources of evidence all point to low local shear resistances over the majority of the shaft and markedly higher resistances closer to the pile tip. Ciavaglia *et al.* (2017a) report a similar trend from their analysis of strain gauge measurements on open piles driven at the same site; shaft resistances four to six times higher applied on the lower half of their 762mm diameter piles which were driven to 4m embedment.

7.6.6 Long-term equalisation

Continuous monitoring tracked the variations between installation and final load testing in local shaft effective stresses. The trends in pore pressure, radial effective stress and shear stress over the first 10 minutes after the final jack push are shown on Figure 7-21, while the long-term σ'_{rs}, τ_{rz} and pore pressure trends are plotted against logarithm of time on Figure 7-22.

Only small excess pore pressures were seen that dissipated quickly and remained relatively stable at <4kPa. The ICP01 pile's radial effective shaft stresses fell by 11 to 26% over its 23 day ageing period, while ICP02's fell by 29 to 34% over 80 days thought to be due to strain creep over time. Radial total stress reductions dominated, although some discrete pore pressure peaks were observed that correlated with recorded rainfall

events, an example of which is shown on Figure 7-23 (data from Met-Office, 2016). Residual ALC1 loads of between 11.8 and 16.7kN were measured at the ends of installation for ICP01 and ICP02 respectively, which reduced to 3.7kN and 2.0kN at the end of the equalisation. The SST τ_{rz} values were primarily negative at the end of jacking and in most cases reduced towards zero over the monitoring periods.

7.6.7 Static Load testing

The two piles were subjected to stage-loaded tension testing after ageing, at which time the re-consolidation of any chalk putty to a lower water content would have been complete. The piles' average shaft stress-displacement curves are presented in Figure 7-24, where the average shaft stress, τ_{avg} is evaluated as:

$$\tau_{avg} = \frac{Q_{net}}{\pi D L_p} \qquad 7\text{-}9$$

And Q_{net} is the net tensile load (less the pile self-weight). The final static holding periods in both tests were ≥ 30 minutes. Pile ICP01 underwent minor axial realignment at low loads and showed a slightly softer initial response than ICP02. The piles' failures were defined by their displacement creep trends under constant load. In both cases the piles failed when the displacement creep rates exceeded 0.2mm/log cycle of time; the peak loads developed after pile head displacements of 1.43 and 2.58mm, respectively. The shaft stress, τ_{avg} mobilised during the tests on both ICP01 and ICP02 were ≈31.6 and 32.1kPa, respectively. These values are remarkably similar, despite the different ageing periods involved, which is further discussed in the following section.

The axial loads measured along the pile length at failure, shown on Figure 7-25, indicate tension failure loads of ≈ 9 ±1kN at the ALC1 position. Given that free-flowing drained conditions applied, and so no reverse end bearing could develop, the ALC1 loads imply local shear stresses of between 200 and 280kPa along the final section of the shaft positioned below the instruments, similar to the sleeve friction, f_s measurements described previously. These values far exceed the CIRIA 20kPa recommendation. However, the ALC measurements indicate significantly lower average shear stresses applied further along the pile shaft, leading to an average of 22kPa, which is similar to both the shaft stresses seen during installation and the current CIRIA recommendation for ultimate shaft resistance of 20kPa.

The ICP tests provided a unique opportunity to observe how the local effective stresses respond during load testing. Figure 7-26 shows the evolution of radial stress and shear stress with pile head displacement. The effective stress paths measured at the instrument clusters during one-way static loading are presented on Figure 7-27, where the τ_{rz} axis is negative under tension loading. The radial effective stresses increased during loading, as seen previously in sands and interpreted as constrained dilation at the interface (Lehane *et al.*, 1993, Chow, 1997). The shear and effective stresses mobilised at failure, τ_f and σ'_{rf} respectively show peak stress ratios δ'_f (= $\tan^{-1}$ (τ_f/σ'_{rf})) close to the δ'_{ult} angles seen in interface ring shear tests on samples from the site (Chapter 6). It appears that as with sands and clays ultimate shaft shear stress can be described by a Coulomb expression. The form for chalk is more similar to that proposed for sands (Lehane *et al.*, 1993) where:

$$\tau_f = (\sigma'_{rc} + \Delta\sigma'_{rd})\tan\delta'_{ult} \qquad 7\text{-}10$$

And σ'_{rc} = the equalised radial effective stress,

$\Delta\sigma'_{rd}$ = the change in radial effective stress during loading

δ'_{ult} = the ultimate interface friction angle.

Boulon and Foray (1986) showed that with sands, the magnitude of $\Delta\sigma'_{rd}$ is related to dilation at the sand-pile interface and can be estimated with a simple cavity expansion expression:

$$\Delta\sigma'_{rd} = \frac{2G\Delta r}{R} \qquad 7\text{-}11$$

The shear modulus, G in Eq. 7-11 should ideally be measured in the G_{hh} direction and may need to account for fabric, void ratio, strain level and non-linearity. The Δr term may be taken as $2R_a$ for sands in cases where the interface's relative roughness, R_n (R_n = R_a/D_{50} where D_{50} is the mean particle size) is less than the critical value, which for a perfectly rough response is approximately 0.1 (Kishida and Uesugi, 1987, Lings and Dietz, 2005).

Figure 6-12 indicates that the chalk's D_{50} is between approximately 3.0 and 6.0 μm, giving $R_n \approx 0.8$ to 1.7, and so far exceeding the perfectly rough limiting value. The SST sensors indicated $\Delta\sigma'_{rd}$ from ≈11 to 14kPa, in three cases and 96kPa in the remaining case. Locally instrumented triaxial tests on intact and reconsolidated chalk by Jardine *et al.* (1984) and Doughty (2016) showed that the behaviour is likely to be principally elastic

in most of the soil mass over the implied strain range. The undisturbed *in situ* seismic G_{hh} values shown in Figure 7-10 range from ≈400 to 1200MPa. However, locally lower G values may apply close to the shaft due to installation effects and re-consolidation. Multi-stage resonant column tests on samples taken from the site carried out by Fugro (2012a) indicated G_{vh} of 250 to 300MPa at the appropriate mean effective stress level for remoulded chalk (Figure 6-17). Substituting the G ranges of 250 to 1200kPa into Eq. 7-11 allows Δr to be estimated for these tests as falling mostly between 0.23 and 2.04μm, with one isolated high value of 9.8μm. The latter Δr values fall well below the piles' surface average peak-to-trough roughness value. The degree of radial expansion experienced appears to be several times smaller than with sands, probably due to the smaller grain size of the chalk and the higher ratio between the pile roughness and the D_{50} values of the chalk grains.

7.6.8 Change in static capacity with time

The trends with time in static shaft capacity can be determined most easily by comparing i) the shaft shear stresses mobilised at tension failure $\tau_{avg}(t)$ (Eq. 7-9) with ii) the average (positive compressive) shear stress, $\tau_{install}$ measured during the final jacking stroke (Figure 7-11). The installation stresses are higher and, neglecting any influences of displacement rate and variation in capacity with loading direction, shaft capacity reduced over time by 20% for ICP01 and 18% for ICP02. These losses are compatible with, although less marked than, the local radial effective stress trends presented in Figure 7-22.

The jacked, closed-ended, piles' ageing behaviours contrast strongly with those seen in the parallel tests on the open-ended driven piles at the same site discussed in Section 6.8. The latter's hyperbolic ageing trend curve indicated gains of 327 and 448% over 23 and 80 days respectively, building to 530% after 250 days (see Figure 7-28), similar to the trend reported by Ciavaglia *et al.* (2017a) for 762mm diameter open-ended tubular steel piles installed at the same site. For the driven piles, the set-up factor is obtained by comparing the average tensile shaft capacity along the pile length, $\tau_{avg}(t)$ from the static tension test with the end of driving compressive shaft capacity from the dynamic test $\tau_{avg}(t= t_{ref})$ interpreted from the dynamic tests at the end of driving, assuming that tensile and compressive shaft capacity are similar, even if not exactly equal. While dynamic pile tests are subjected to more uncertainty than static tension load tests, the trend shown on Figure 7-28 indicates that the static tensile shaft resistance more than doubled between the 10 and 106 day test ages, consistent with the indicated overall

capacity trend increase. The set-down shown by the jacked piles also contrasts sharply with the Wikinger full-scale offshore tests outlined in Chapter 5.

One possible ageing mechanism involving consolidation of the chalk putty annulus formed around the open pile and long-term radial stress growth post driving was outlined in Chapter 6, to explain the driven piles' strong set-up, while noting that redox reactions between the pile shaft and re-cementing of the puttified chalk could also be influential. The lack of set-up shown by the (mainly oxidisable molybdenum steel) jacked piles indicates that physico-chemical effects and re-cementing cannot be dominant. The two types of piles were installed into chalk of the same grade and density and allowed to equalise over similar time periods prior to failing under the same testing procedure, so the different ageing trends must originate in either i) the ICP's closed ends and/or ii) the piles' modes and rates of installation. The driven piles penetrated one to two orders of magnitude more rapidly than the ICPs. Also, no evidence was seen on extraction of the ICPs of any previously puttified zone, as was found adhering to the driven piles.

7.6.9 Stress changes during installation, equalisation and load testing

Soil elements whose initial states (characterised here by void ratio and mean effective stress, p′) are not at critical state, must change volume or mean effective stress during shear before they can attain critical states (Roscoe *et al.*, 1958). As discussed in Chapter 2, applying high mean effective stresses tends to suppress dilatancy in denser-than-critical cases and the definition of state must take stress into account (Been and Jefferies, 2006). The state parameter, ψ was introduced for sands by Been and Jefferies (1985) as a measure of the vertical distance to the critical state line (CSL) in void ratio mean effective stress space (e-lnp′) manifested by a soil element under its *in-situ* initial condition:

$$\psi = e - e_{cs} \qquad 7\text{-}12$$

$$e_{cs} = \Gamma - \lambda \ln p'_{cs} \qquad 7\text{-}13$$

where e_{cs} and p_{cs} are the void ratio and mean effective stress on the critical state line and Γ and λ are intrinsic soil parameters which define the critical state line. The state parameter is used in place of void ratio since it is the magnitude of dilation that determines strength. The sign of ψ determines whether the sand is in a denser-than-critical (ψ <0) or in a looser-than-critical (ψ >0) state. These two distinct possibilities lead to different facets of soil behaviour. During constant volume shearing, denser-than-critical samples may show a tendency for contraction initially and appear to reach a steady-state prior to

the onset of apparent dilation at high strains, termed the phase transformation point (Ishihara *et al.*, 1975). The more negative the state parameter the further from the CSL and the greater the magnitude of apparent dilation required to reach critical state. Conversely, under constant volume shearing, samples looser than critical ($\psi > 0$) tend to contract to critical state with no softening or dilation.

The stress changes occurring for chalk elements that were located initially on the pile axis during ICP pile installation, equalisation and load testing can be interpreted semi-quantitatively in terms of the state parameter framework. Stress states are considered here at depths below ground level, z, corresponding to the final depth of the SSTs at the end of installation. Four stress states are considered each, for both the following (Figure 7-29 (a)) and leading (Figure 7-29 (b)) instruments during pile installation. These correspond to the stresses, applying at depth z, (= 2.44 to 3.87mbgl), where:

A. The pile tip is above the instrument's final level, z;
B. The pile tip has just arrived at the instrument's final level, z;
C. The pile tip is below z and the instrument is at its final level at the end of installation;
D. The pile tip is below z and the instrument is at its final level at the end of the equalisation period.

A schematic diagram of the radial stresses applying on a soil element (i) adjacent to the shaft and (ii) below the tip on the pile axis of an incompressible pile is shown on Figure 7-30. The cylindrical coordinate system corresponds to r (in the radial direction), z (in the vertical direction) and θ (in the circumferential direction). Beneath the pile tip, there is rotational symmetry about the central pile axis, therefore there is no displacement in the θ direction and the displacements in the r and z directions are independent of θ. As argued by Jardine *et al.* (2013a), the average vertical stress, σ_z ($=\sigma_1$) equals q_t (or q_b) beneath the pile tip. The radial effective stresses at the tip were calculated previously using Eq. 7-8, giving $900 < \sigma'_{rm} < 2150$kPa on the pile axis at h=0. The subscript m on the effective stresses denotes the moving stresses. Because of axi-symmetry at the tip:

$$\sigma'_{rm} = \sigma'_{\theta m} \qquad 7\text{-}14$$

The mean effective stresses can then be calculated in terms of the principal effective stresses as:

$$p' = \left(\frac{\sigma'_{zm} + 2\sigma'_{rm}}{3}\right) \quad 7\text{-}15$$

The stress components applying on an element of soil adjacent to the pile shaft are also shown on Figure 7-30. In this case the radial effective stress, σ'_{rm} is likely to be the major principal effective stress, ($=\sigma'_1$). It is difficult to determine how the other effective stress components σ'_{zm} and $\sigma'_{\theta m}$ compare to σ'_{rm}. Measurements made in sand by Jardine *et al.* (2013b) show that $\sigma'_{\theta m}$ values may be comparable to, although lower than, σ'_{rm} close to the pile shaft. Similar trends were noticed in FEM analyses of the experiments by Zhang *et al.* (2014). It has been argued previously that the strain path followed by an element of soil, in a normally consolidated state, adjacent to a pile and loaded axially is comparable to that undergone by a sample in a simple shear test (Randolph and Wroth, 1981). Ignoring any cohesion the mean effective stresses at failure, can be estimated from:

$$p' = \left[\frac{\sigma'_{zm} + \sigma'_{\theta m} + \sigma'_{rm}}{3}\right] \quad 7\text{-}16$$

$$= \left[\frac{(1+b)\sigma'_{rm} + (2-b)\sigma'_{zm}}{3}\right] \quad 7\text{-}17$$

Where the parameter b, given by Bishop (1966) is calculated as:

$$b = \left(\frac{\sigma'_{\theta m} - \sigma'_{zm}}{\sigma'_{rm} - \sigma'_{zm}}\right) \quad 7\text{-}18$$

The value of b varies from 0 for triaxial compression tests up to 1 for triaxial extension tests. For plane strain tests, the value of b must be determined experimentally since $\varepsilon_\theta = 0$ and $\sigma'_{\theta m}$ is not known. Consistent with Randolph and Wroth (1981) a value of b equal to 0.5 is adopted which gives:

$$\sigma'_{\theta m} = \left(\frac{\sigma'_{rm} + \sigma'_{zm}}{2}\right) \quad 7\text{-}19$$

$$p' = \left(\frac{\sigma'_{zm} + \sigma'_{rm}}{2}\right) \quad 7\text{-}20$$

The failure state in simple shear can be calculated using one of three approaches, illustrated in Figure 7-31. The first, most conventional approach (a), assumes that planes parallel to the direction of shear are planes of maximum stress obliquity. In this case:

$$\sigma'_{rm} = \frac{\tau_{rz}}{\tan\varphi'} \quad 7\text{-}21$$

$$\sigma'_{zm} = \sigma'_{rm}(1 + 2\tan^2\varphi') \quad 7\text{-}22$$

The second approach (b) of co-axial plasticity (Davis, 1968) assumes that the poles of the stress and strain axes are coincidental. This leads to a critical state (zero dilation) condition with:

$$\sigma'_{rm} = \sigma'_{zm} \quad 7\text{-}23$$

The third approach (c), proposed by De Josselin de Jong (1972), indicates failure in simple shear occurs by sliding in conjunction with rotation on planes that are normal to the direction of shear, which are planes of maximum stress obliquity. In this case:

$$\sigma'_{rm} = \tau_{rz}\frac{1 + \sin^2\varphi'}{\sin\varphi'\cos\varphi'} \quad 7\text{-}24$$

$$\sigma'_{zm} = \frac{\tau_{rz}}{\tan\varphi'} \quad 7\text{-}25$$

For puttified and reconsolidated chalk, the φ'_{cs} angle of 31° is appropriate. Substitution into approaches (a), (b) and (c) gives mean effective stress, p' equivalent to $1.18\sigma'_{rm}$, σ'_{rm} and $1.36\sigma'_{rm}$ respectively. For simplicity, the foregoing analysis assumes that $p' \approx \sigma'_{rm}$ at the pile shaft, although the true value may be slightly higher.

A tentative illustration of the resulting effective stress states applying at depths (z) at which the instruments reach their final levels at the stages, A, B, C and D (Figure 7-29) are shown in specific volume, v – mean effective stress (v-logp') space on Figure 7-32. The critical state line adopted is that determined by Doughty (2016) from triaxial tests on remoulded samples of Wikinger chalk, which may differ from the CSLs applying at the St. Nicholas-at-Wade site. Points to note include:

- Prior to the pile reaching depth z, elements are at the *in-situ* stress state where $\sigma'_r = \sigma'_{r0}$ and the mean effective stress, p' is approximately equal to 40kPa (based on an assumed K_0 of 0.4). Assuming full saturation, the specific volume is calculated from:
  $$v = 1 + e = 1 + w_c G_s \quad 7\text{-}26$$
  where w_c is the natural water content measured at the site, at depth z, of between 28 and 31% and G_s is the specific gravity (≈2.7);
- As argued above, the maximum moving radial effective stresses, σ'_{rm} applying immediately below the pile tip during rapid penetration are between 900 and 2150kPa on the pile axis at the tip (h=0). For $\sigma'_{zm} = 0.6\ q_t$ (Section 7.6.4), and q_t of between 10 and 20MPa, this leads to values of p' of between ≈2600 and 5400kPa. Thus when the pile tip is at the instrument depth z, the element below the tip follows the stress path

(A-B) shown on Figure 7-32, assuming initially undrained conditions. The mean effective stresses reduce dramatically as the chalk loses its natural structure and eventually tends to its puttified state generating high pore water pressures;

- The pore pressure measurements taken along the pile shaft (Section 7.6.2) and the variation in base resistance with penetration rate (Figure 7-15) indicated that ICP installation was partially drained with consolidation occurring along the pile shaft during jacking, which was largely complete before the end of installation. The specific volume at the end of installation can be calculated using:

$$v = 1 + e = 1 + w_f G_s \qquad 7\text{-}27$$

where w_f is assumed to match the reduced water content trend with $w_f = 0.8 w_c$ value measured on samples taken adjacent to the driven pile shaft during pile exhumation inspections 274 days after driving (Section 6.5.4). It is important to recall however, that the final radial effective stresses acting on the ICPs were significantly lower than those seen on the shaft of the driven piles after full equalisation;

- At point C, the tip is below the instrument level and the instrument is at its final position. The end of installation values, σ'_{ri} measured at the SST locations immediately following the final jacking push were between 35 and 69kPa at the leading instrument and between 23 and 56 kPa at the following instrument. Taking σ'_{ri} equivalent to p', as argued above, results in the Path B-C;
- The radial effective stresses applying on the jacked ICP pile shaft tended to reduce during the equalisation period (Section 7.6.6) reaching equalised radial effective stresses. σ'_{rc} (=p') of between 11 and 37kPa at the leading instrument and between 11 and 12 kPa at the following instrument at 23 and 80 days after installation (Path C-D);
- At the end of equalisation, static tension testing to failure led to increases in radial effective stresses at failure, σ'_{rf} due to the effects of constrained interface dilation, reaching final values close to the end of installation values. However, if this process matched ideal elastic cavity expansion (Eq. 7-11), then the mean effective stresses would have remained unchanged in the surrounding chalk mass, with $\Delta\sigma'_z=0$ and $\Delta\sigma'_r = -\Delta\sigma'_\theta$. At the interface however, the "simple shear" boundary conditions will lead to $p' \approx \sigma'_{rm}$ as argued above.

The natural cemented structure of the chalk allows states to exist to the right of the critical state line (i.e. at point B). At both the end of installation and the end of equalisation the stress state (in void ratio mean effective stress space) is on the denser-

than-critical side, with a negative state parameter (ψ <0). The stress states applying during the ICP tests are compared further with those interpreted from the driven pile tests in Chapter 8.

7.6.10 Cyclic load testing

Limited packages of one-way axial cyclic loading were applied after the two ICP piles' first time static tests. In both cases, the first packet of cycles were imposed with $Q_{cyc}/Q_{ref} \approx 0.3$ and Q_{mean}/Q_{ref} of ≈ 0.4 where Q_{ref} was the earlier net static tension failure load. The levels were increased to Q_{cyc}/Q_{ref} of ≈ 0.4 and Q_{mean}/Q_{ref} of 0.45 for ICP01 and 0.5 for ICP02 for a second set packet of cycles. The first packet consisted of ten cycles in ICP01 and eleven cycles in ICP02. The second packet consisted of ten cycles in both cases, Figure 7-33 shows the evolution of accumulated permanent displacement, s_{acc} under cycling, indicating either metastable or unstable responses, in terms of the cyclic definitions adopted by Rimoy *et al.* (2013), when the maximum shaft loads ($Q_{cyc} + Q_{mean}$) amounted to 0.7 to 0.9 times Q_{ref}. Following the end of cycling, ICP02 was unloaded and subjected to a static tension test to failure that, as shown on Figure 7-24, indicated a 13% capacity loss. A further 5% loss of capacity would have been required to reach failure in this $Q_{max}/Q_{ref} \approx 0.82$ test, which might have been achieved within tens of cycles if the experiments had continued. Overall, the piles did not appear to be unduly sensitive to high level one-way cycling, similar to the cyclic tests on driven piles described in Chapter 6, although the effects of high level two-way axial cycling are likely to be more severe.

The SST instruments also revealed the local shaft stress response to cyclic loading as shown on Figure 7-34. As demonstrated in Figure 7-35, cycling invoked a similar shear and radial effective stress response to that under static loading. The effective stress path gradients led to σ'_r rising as τ_{rz} was applied in each cycle and also drifting as cycling continued. Comparison of the σ'_r measurements made on unloading after i) static testing and ii) cyclic testing indicated overall σ'_r reductions of up to 29% for ICP02, while ICP02 indicated a 5% reduction at the *leading* instrument and an increase of 27% at the *following* instrument, as indicated by points B and C on Figure 7-35. Very little change in pore pressure was observed during cycling at the rate applied (1 cycle per minute), as shown on Figure 7-36, and the radial effective stress trends reflect the total stresses falling in the kinematically constrained conditions applying close to the pile shaft. The substantially drained response observed is compatible with the consolidation analysis discussed previously.

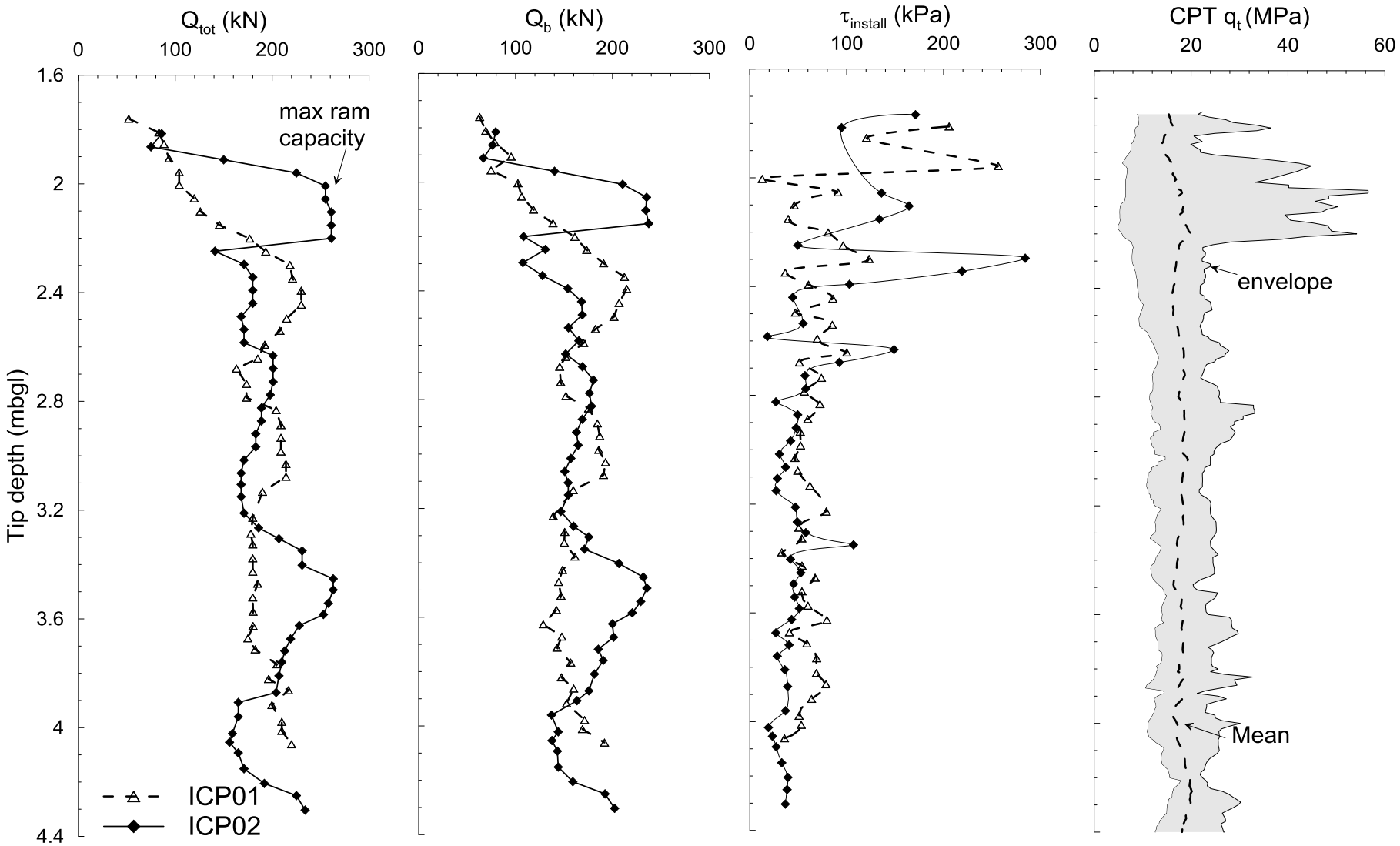


Figure 7-11 Force at the pile head during installation (Q_{tot}) force at the pile base (Q_b), average shear stress over the pile length ($\tau_{install}$) and envelope of q_t measurements

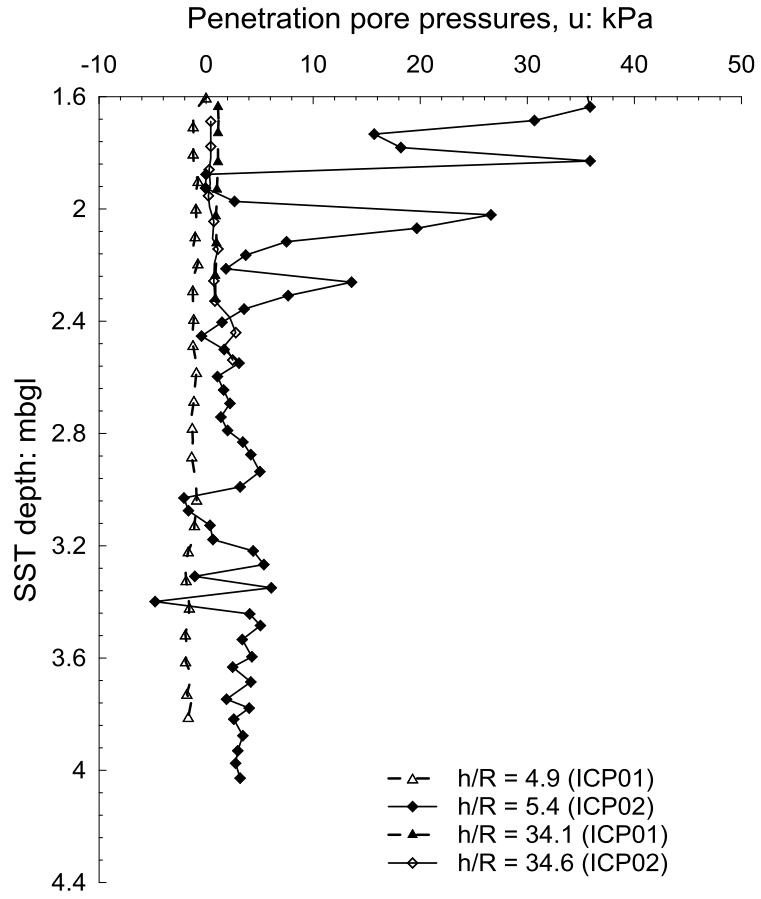


Figure 7-12 Pore pressures measured during penetration at both the leading and following instruments

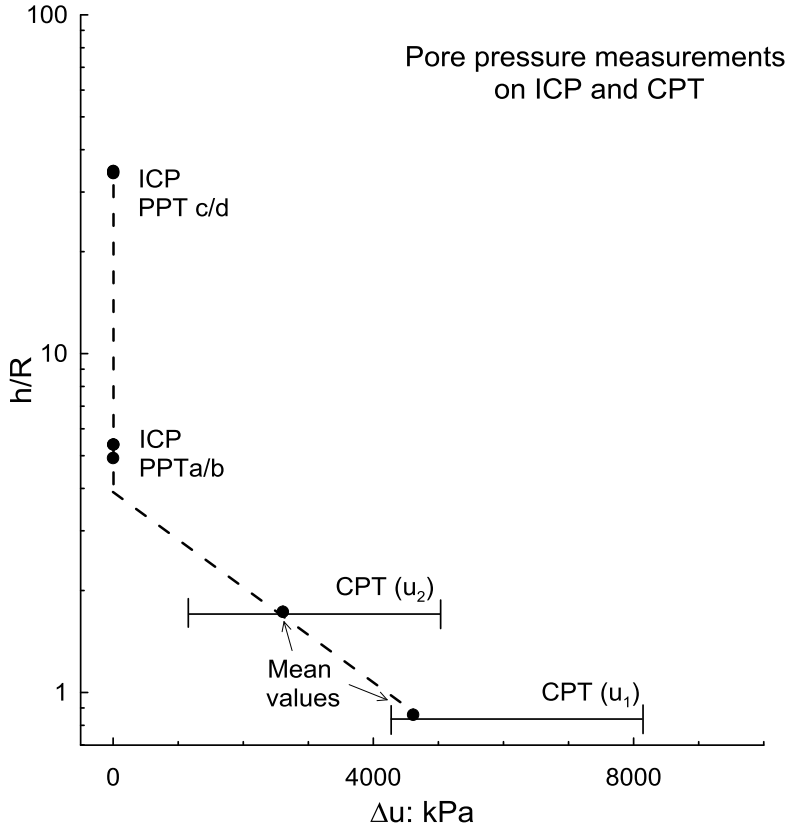


Figure 7-13 Variation in excess pore water pressure with normalised distance from the tip during PCPT and jacked pile penetration. Note: initial pre-installation pore pressures are small or negative

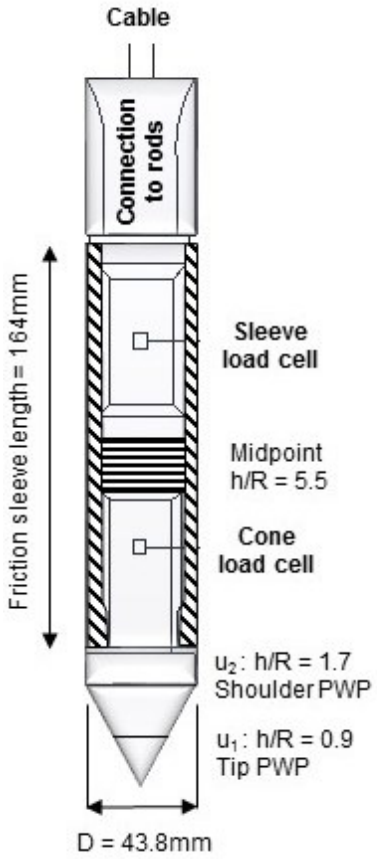


Figure 7-14 CPT measurement positions for IC CPTs after Lankelma (2016) and ASTM (2012)

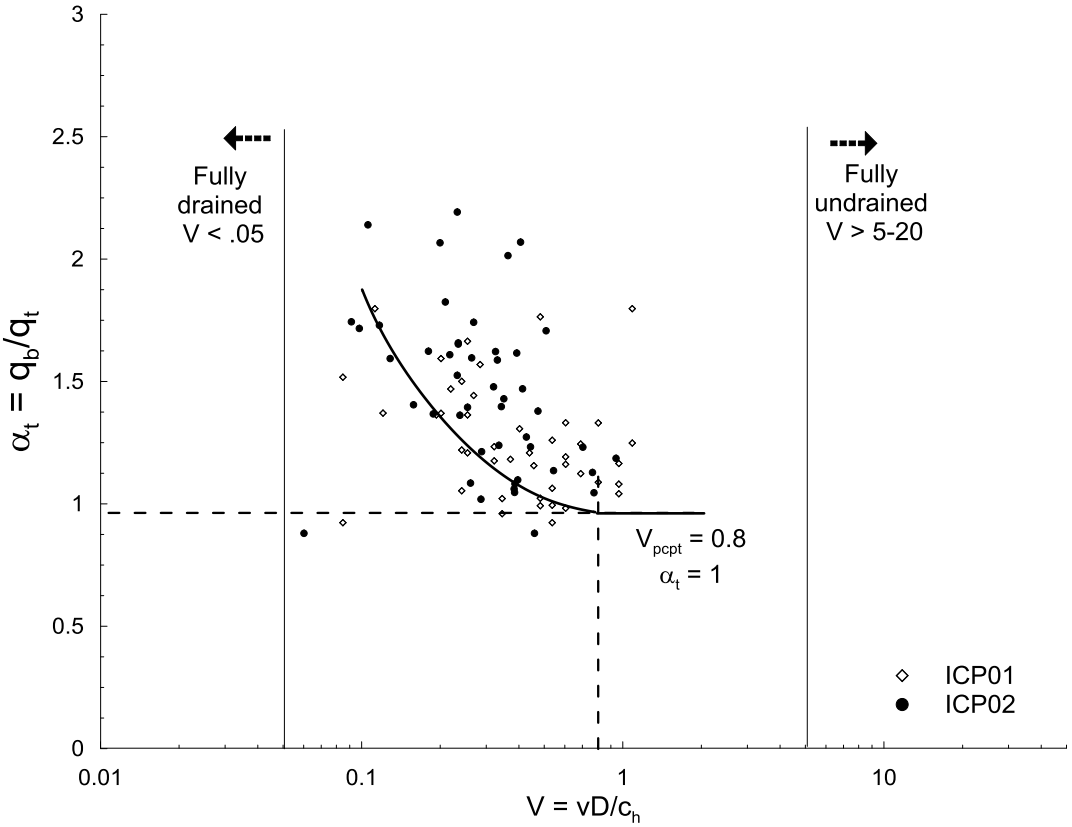


Figure 7-15 Variation in ratio q_b/q_t with normalised velocity for the jacked pile

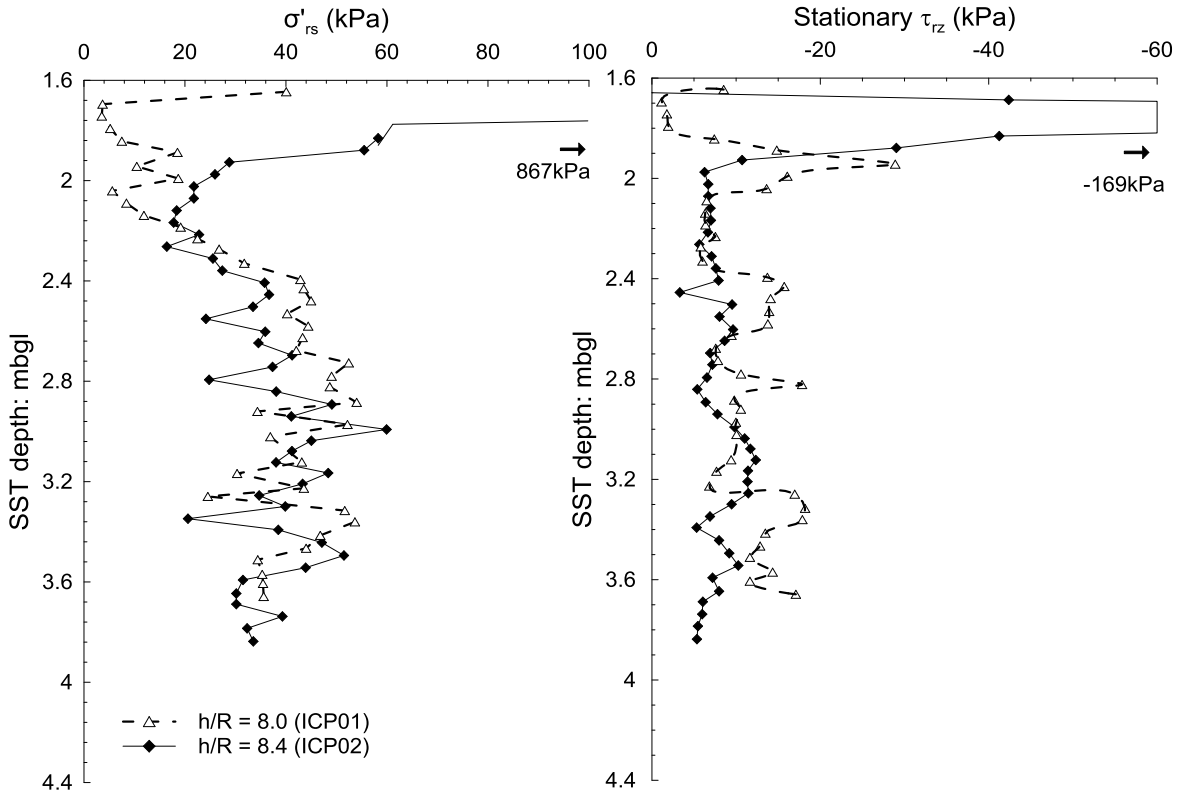


Figure 7-16 Profiles of SST measurements at the leading instrument during pauses in jacking a) stationary local radial effective stresses b) stationary local shear stresses

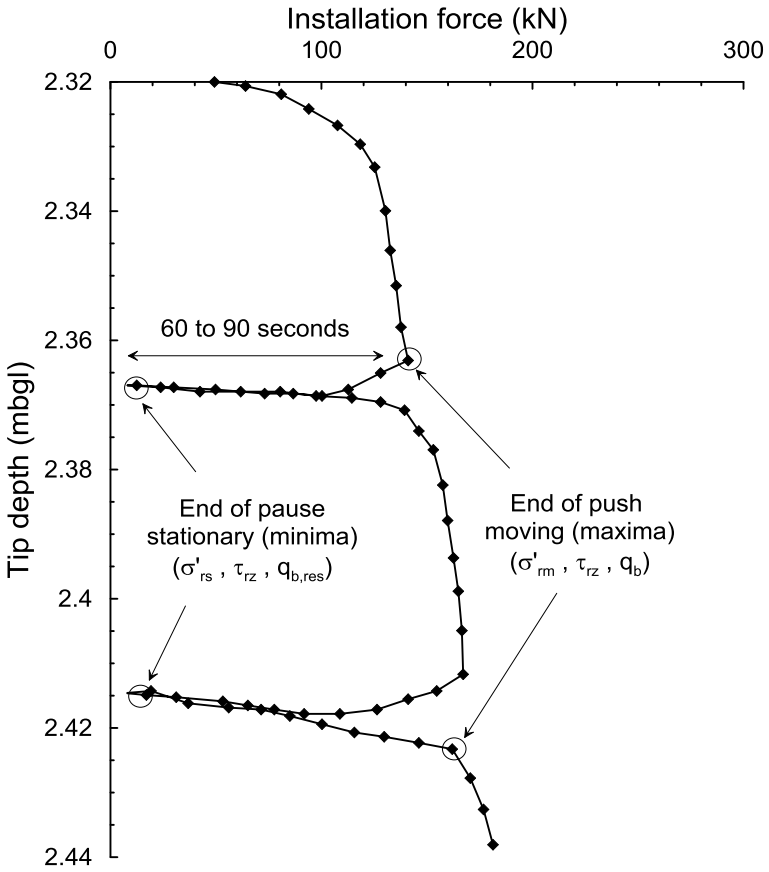


Figure 7-17 Illustration of stationary (minima) and moving (maxima) radial, shear and base stresses at the end of an installation push and at the end of a jacking pause

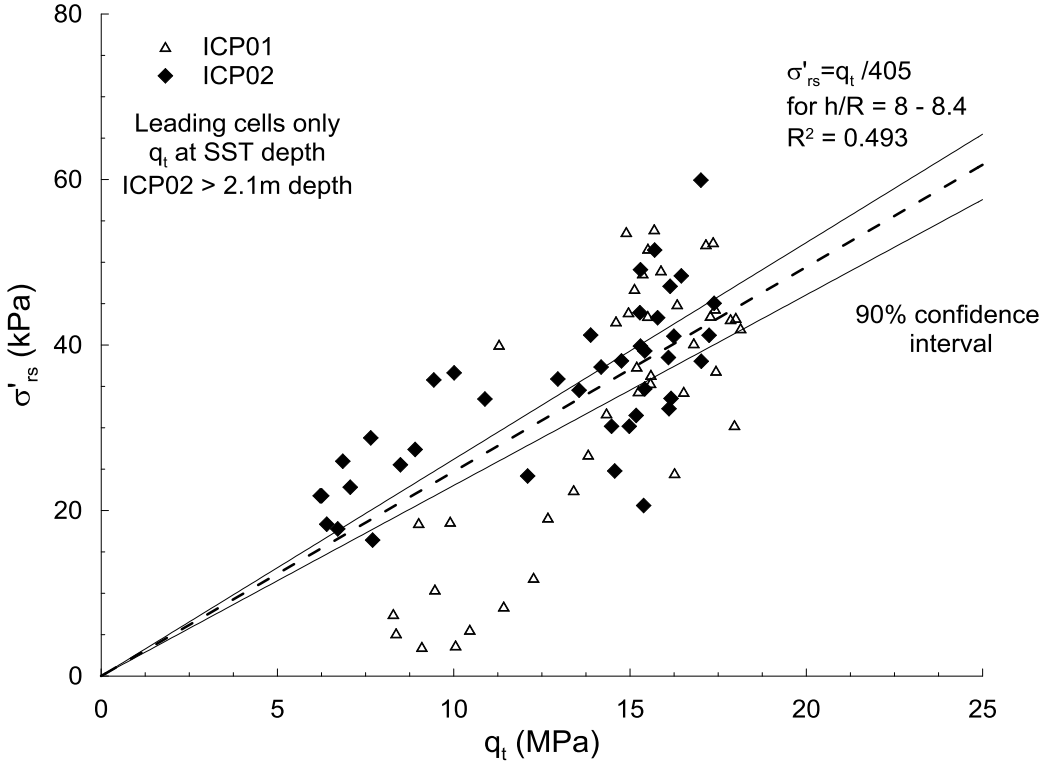


Figure 7-18 Relationship between cone resistance and radial effective stress at the leading instrument

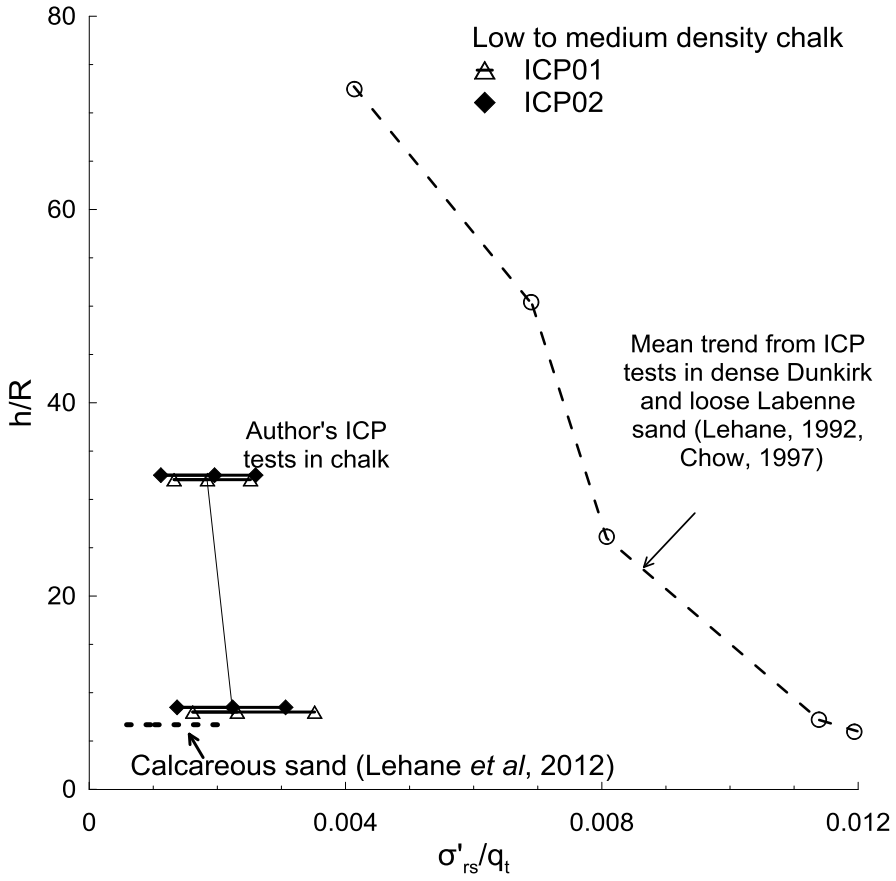


Figure 7-19 Normalised stationary radial effective stresses along the pile shaft during installation compared to historical measurements

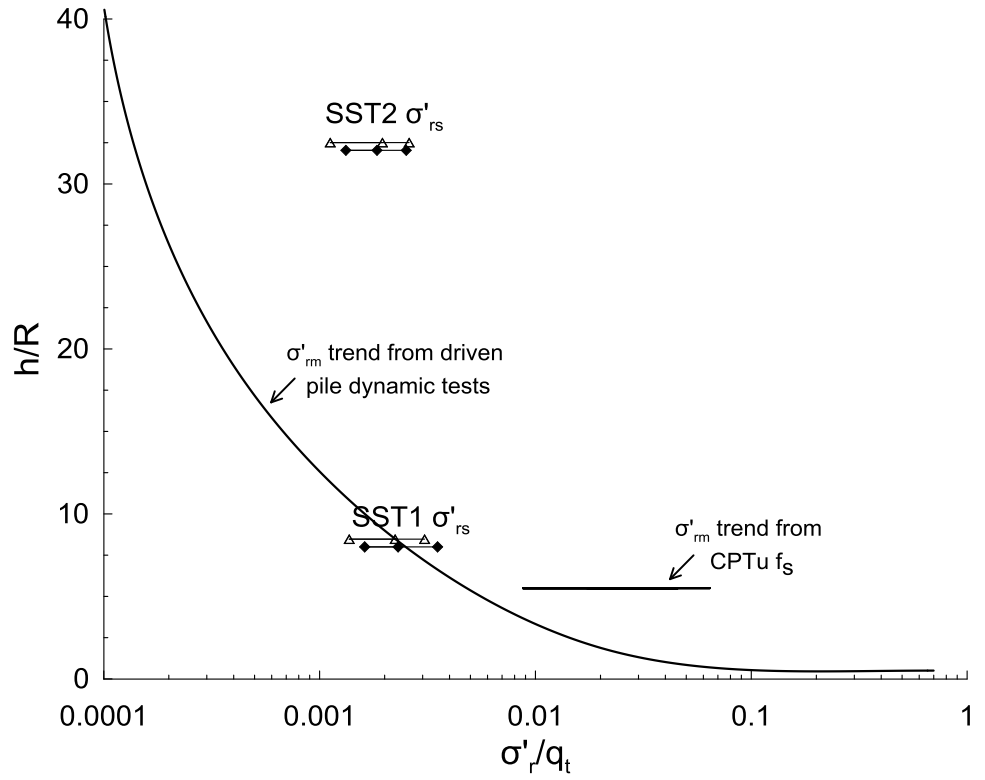


Figure 7-20 Normalised stationary and moving radial effective stresses from SST measurements, CPT f_s readings and back analysis of dynamic test data on driven piles

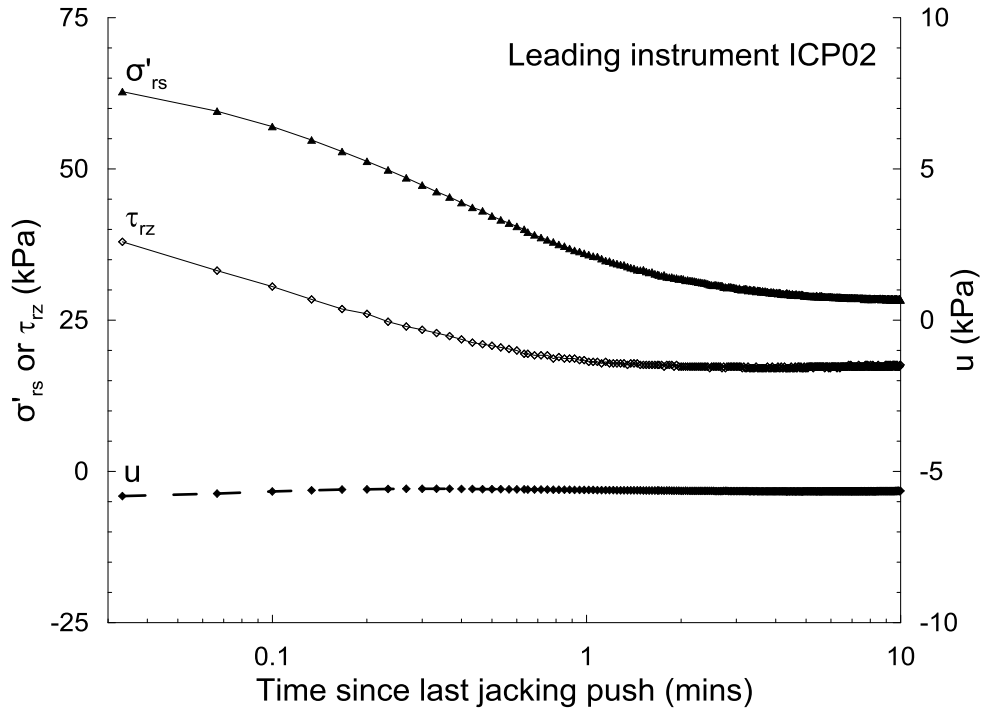


Figure 7-21 Typical short-term changes in local radial effective stress, local shear stress and pore water pressures

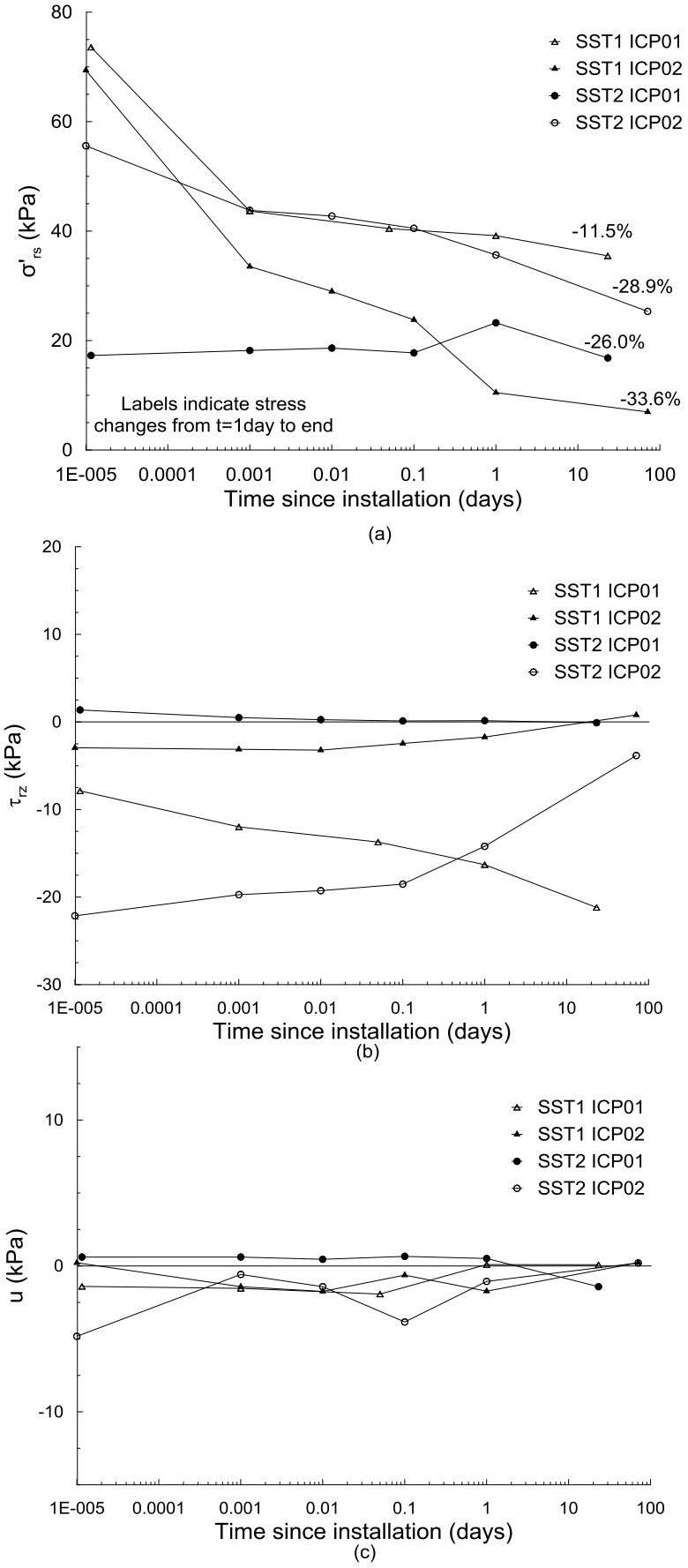


Figure 7-22 Variations with time over entire equalisation period of (a) local effective shaft radial stresses (b) local effective shaft shear stresses (c) pore water pressures

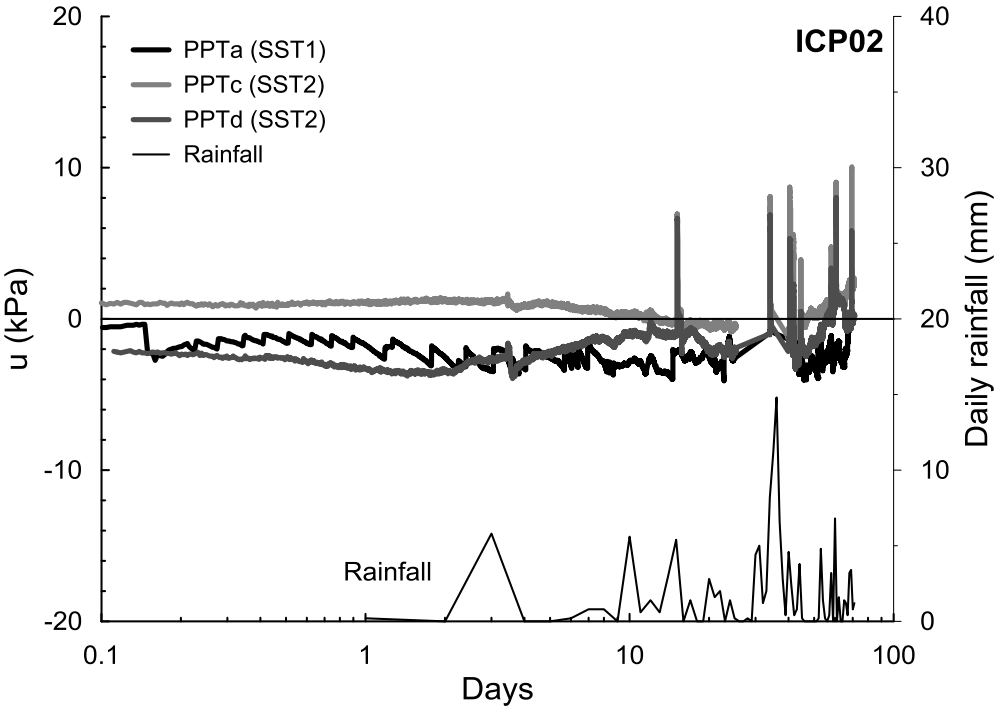


Figure 7-23 Long-term pore pressures with time compared with daily rainfall measurements taken at Manston airport (Met-Office, 2016)

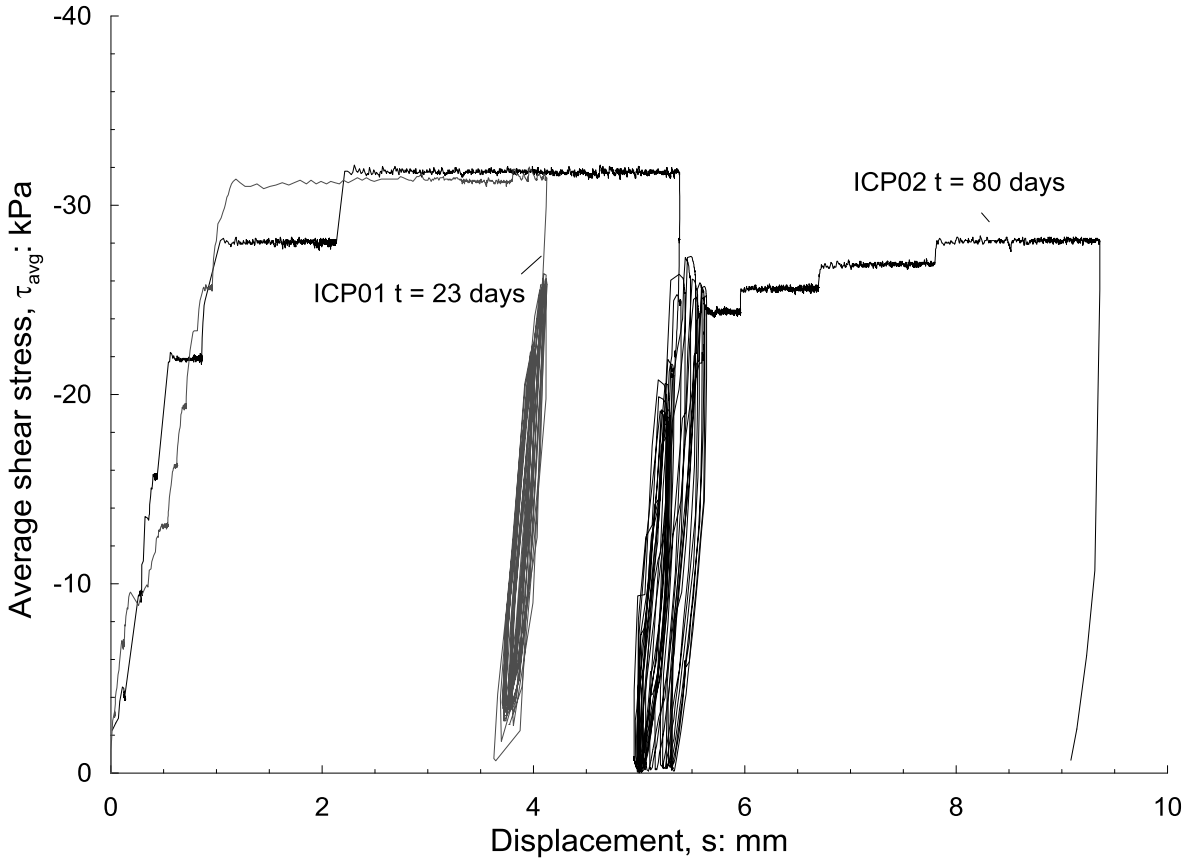


Figure 7-24 Average shaft resistance mobilised versus displacement during static tension and one way cyclic loading on ICP01 and ICP02

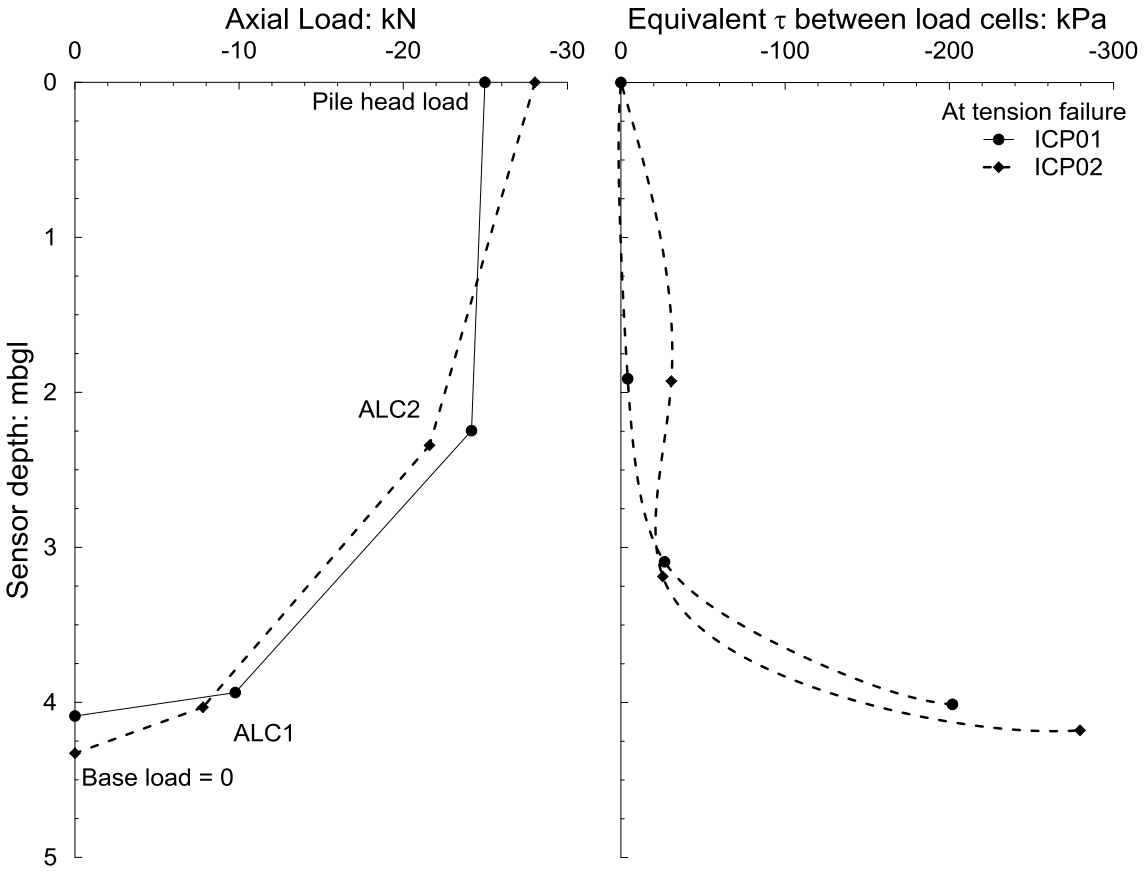


Figure 7-25 Variation in axial load and shear stress interpolated between the load cells along the pile length at the point of tension failure

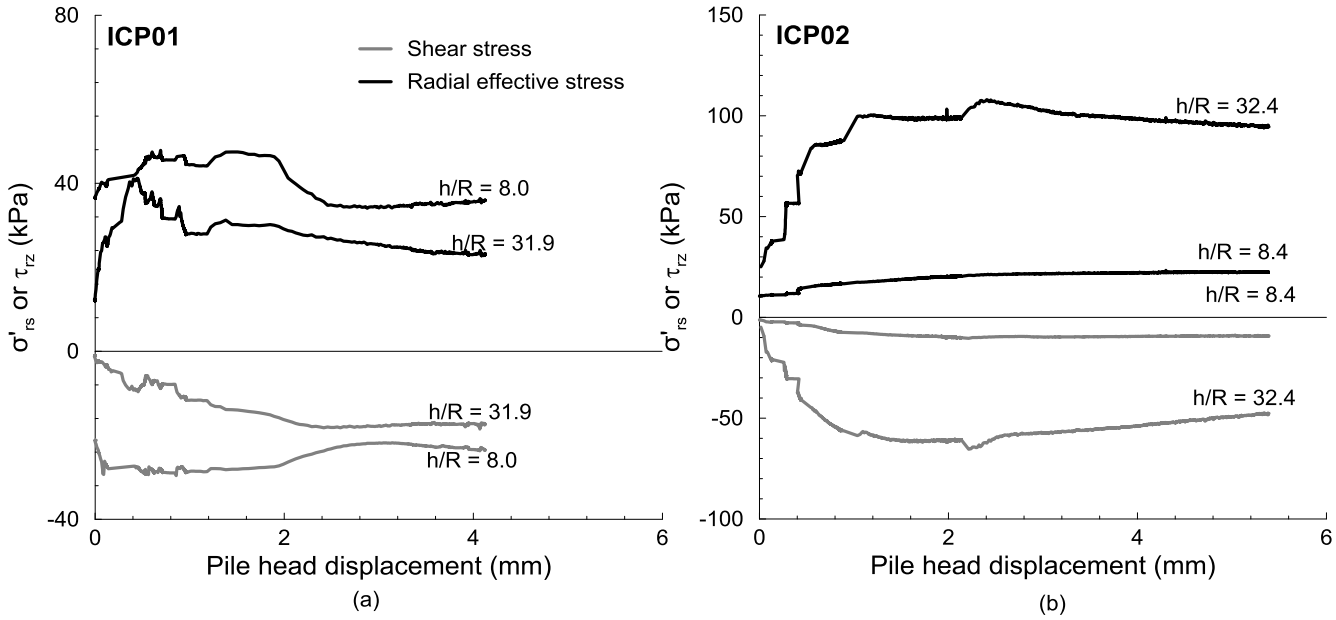


Figure 7-26 Evolution of radial stress and shear stress with pile head displacement during a static load test

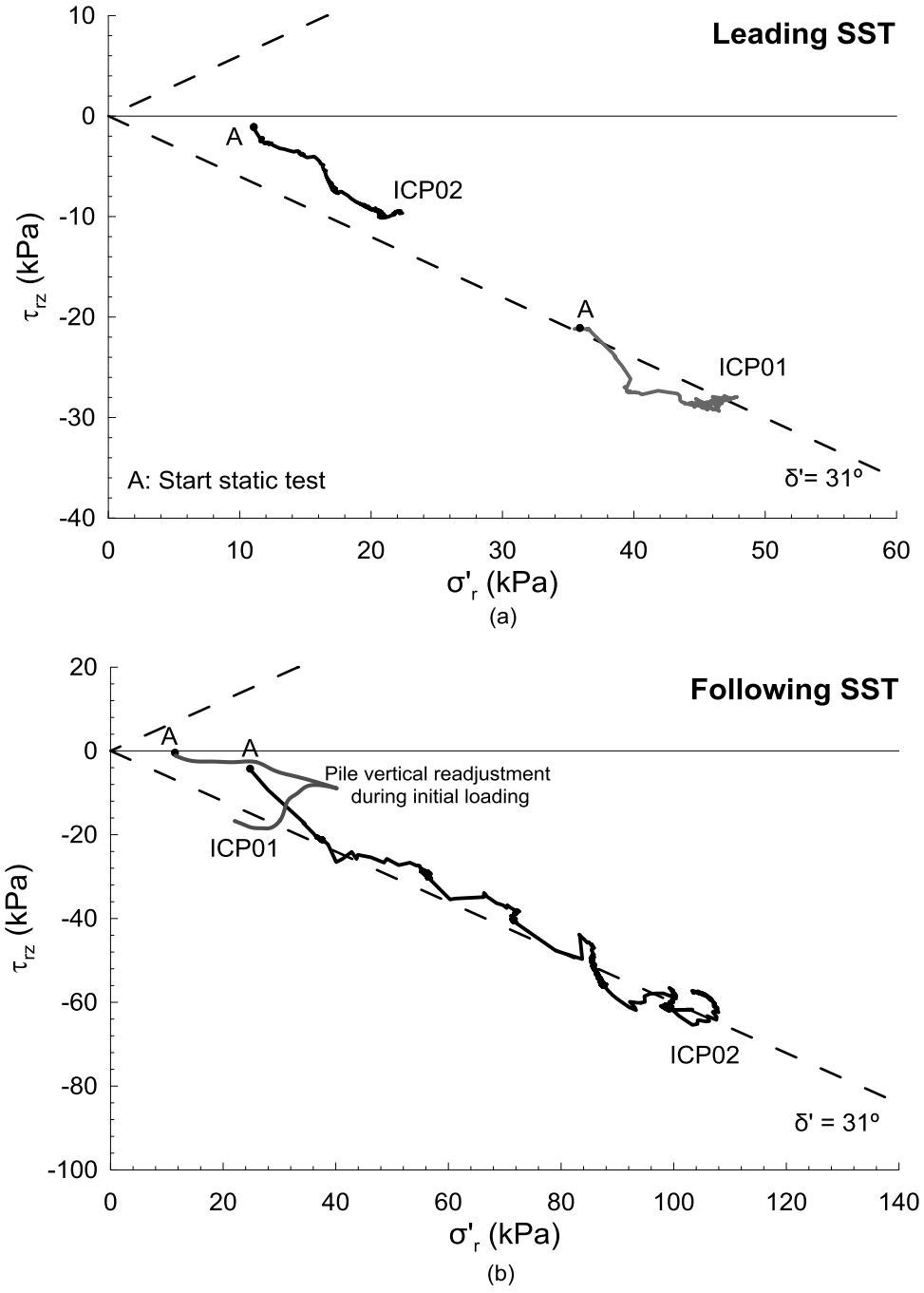


Figure 7-27 Effective stress paths during static tension loading at a) the leading SST1 and b) the following SST2

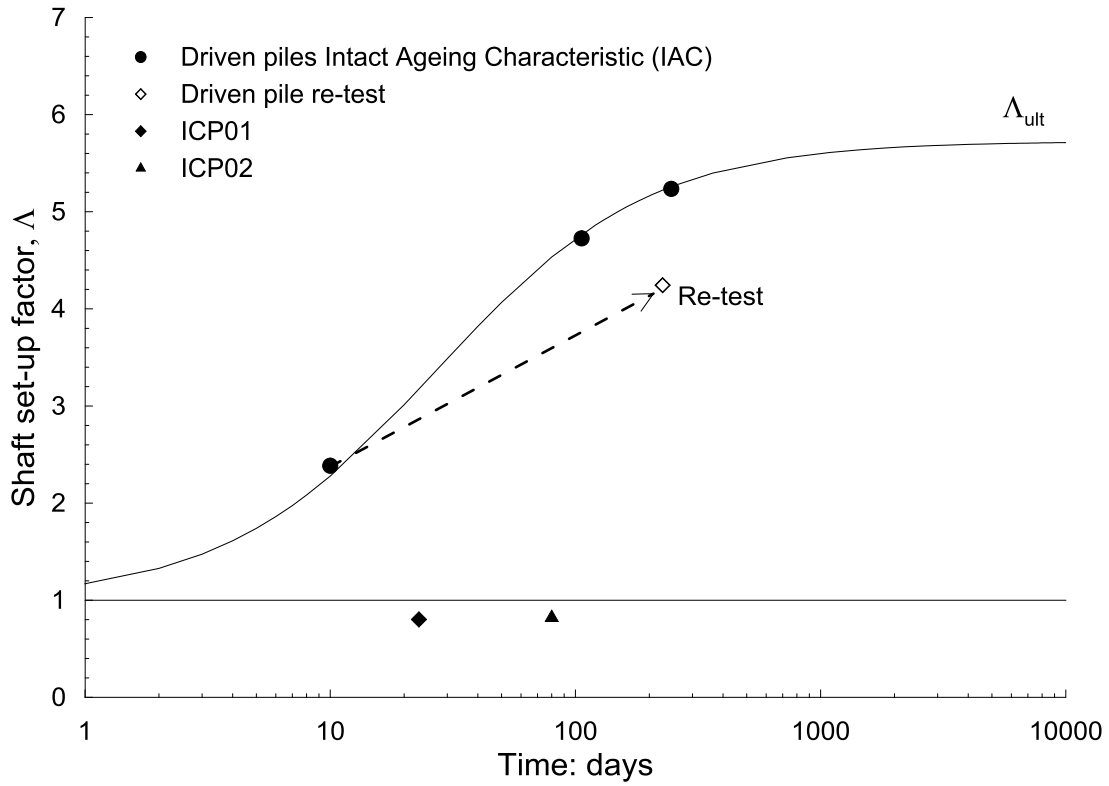


Figure 7-28 Comparison of set-up factors observed during static testing of jacked piles following equalisation periods with driven piles

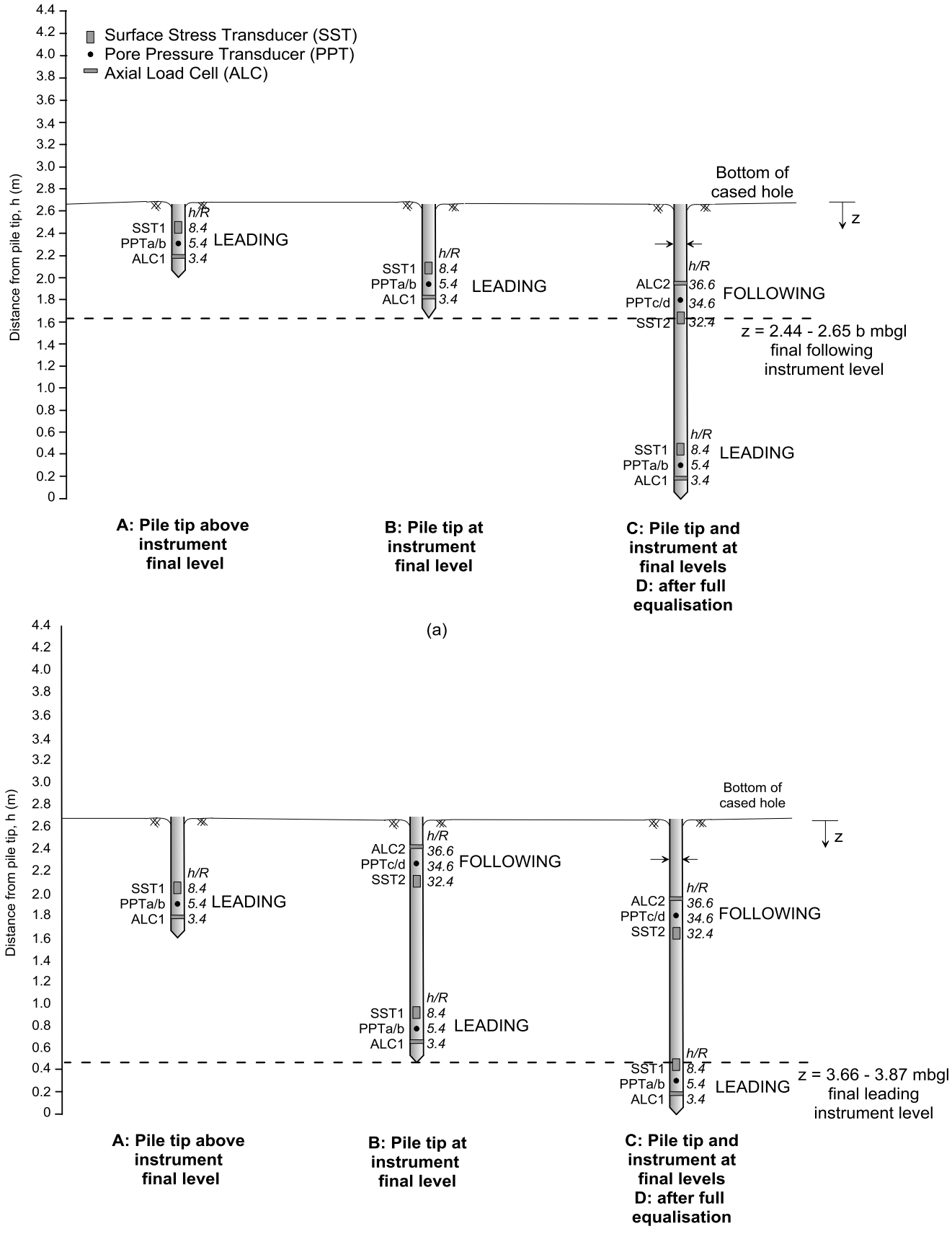


Figure 7-29 Two depths at which the effective stress states are considered during ICP penetration with (a) the final level of the following instrument (b) the final level of the leading instrument

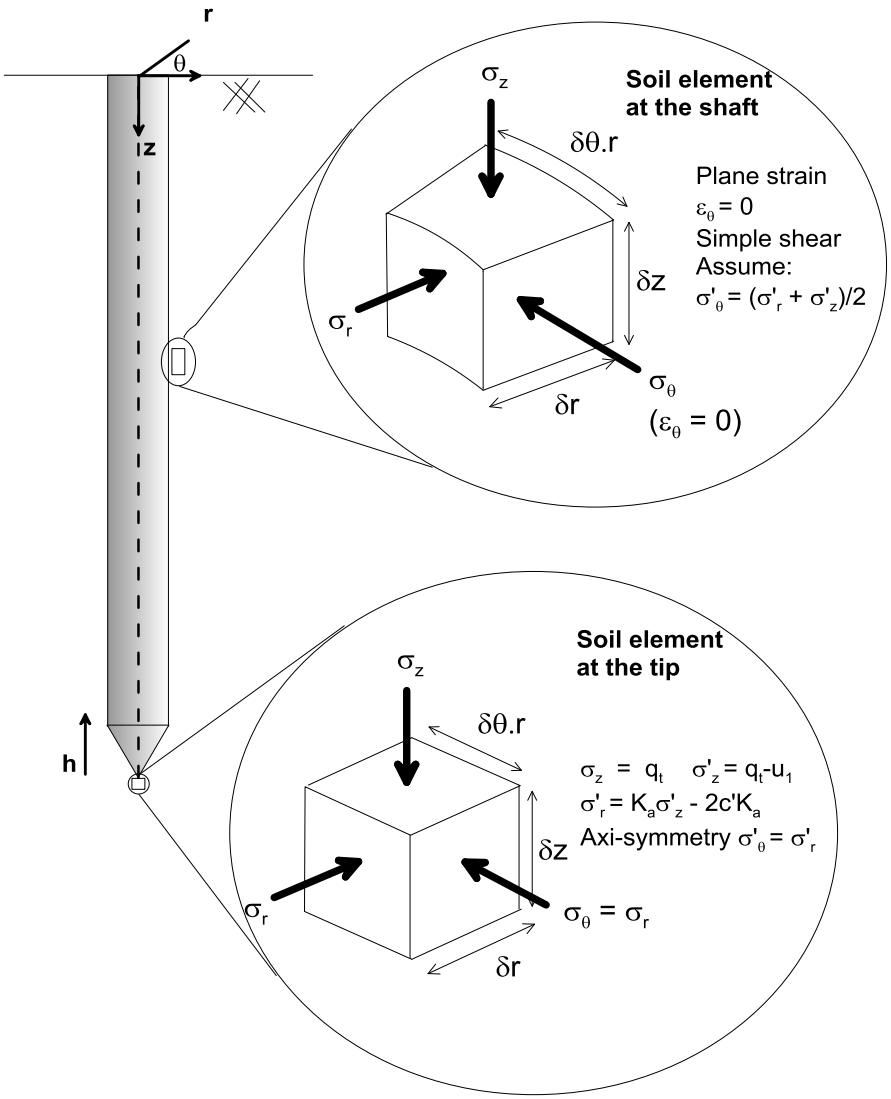


Figure 7-30 Schematic diagram of soil element at the ICP shaft and below the pile tip

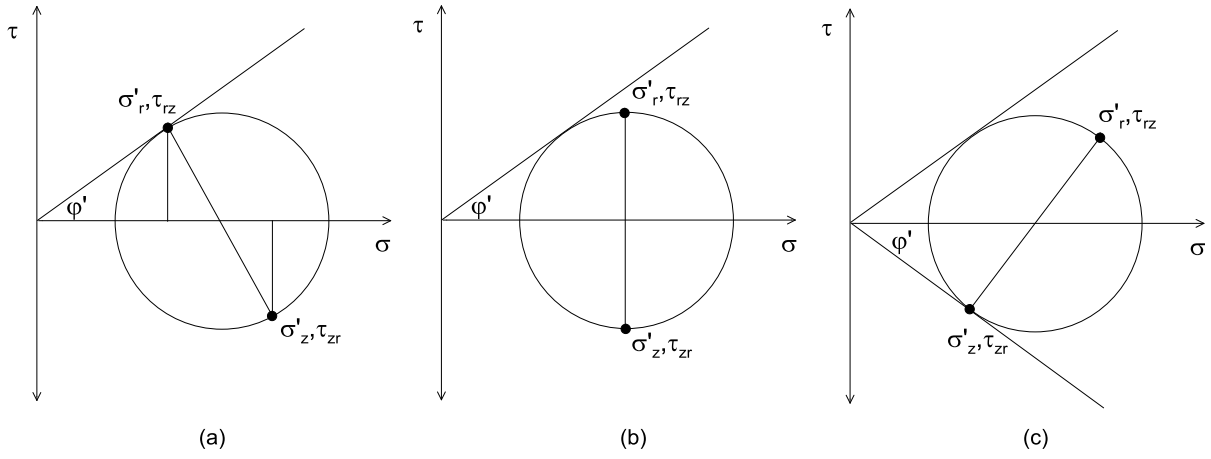


Figure 7-31 Mohr's circles for different assumed failure modes in simple shear (a) planes parallel to direction of shear are planes of maximum stress obliquity (b) co-axial plasticity at critical state (c) planes normal to direction of shear are planes of maximum stress obliquity

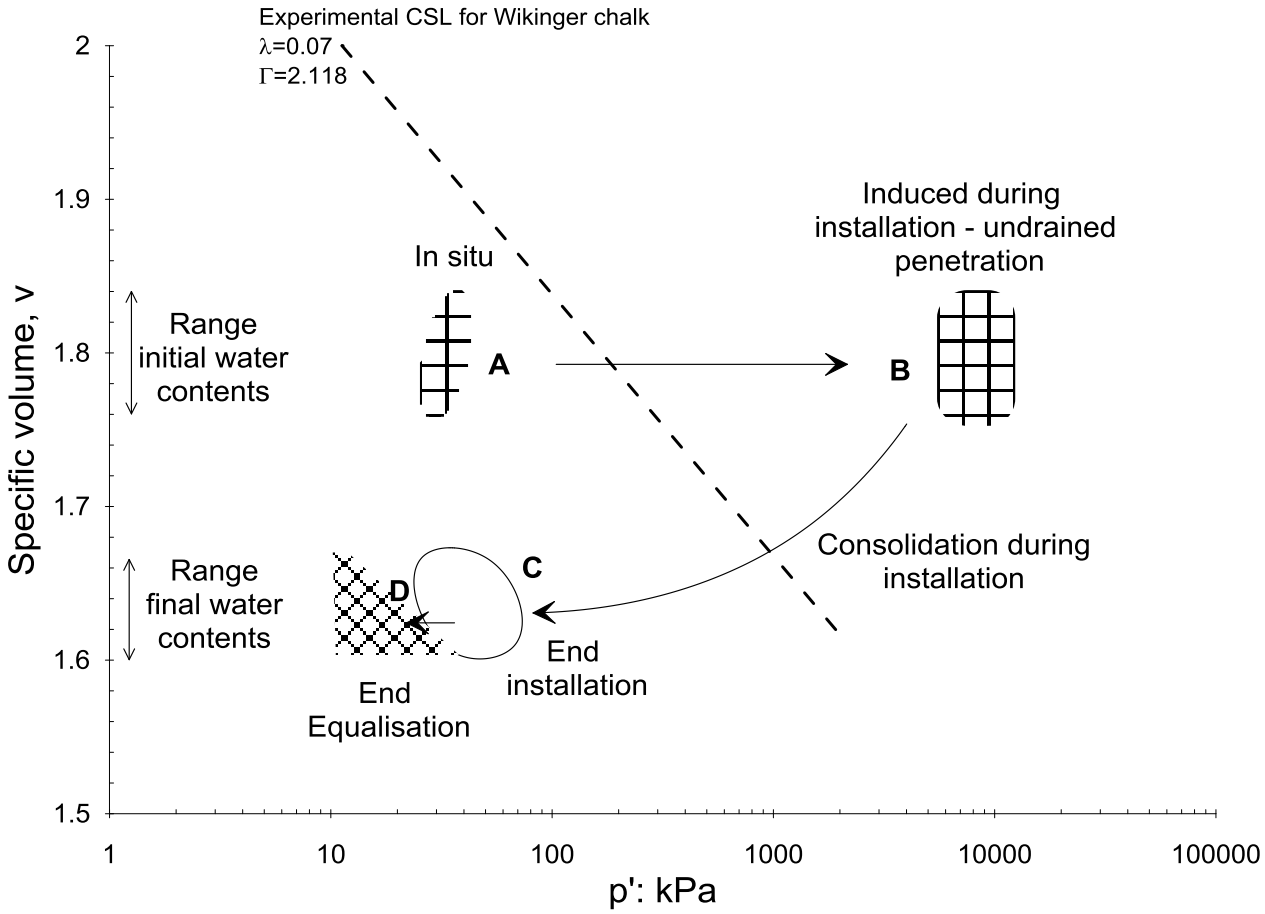


Figure 7-32 Illustration of stress state changes during ICP pile installation and equalisation

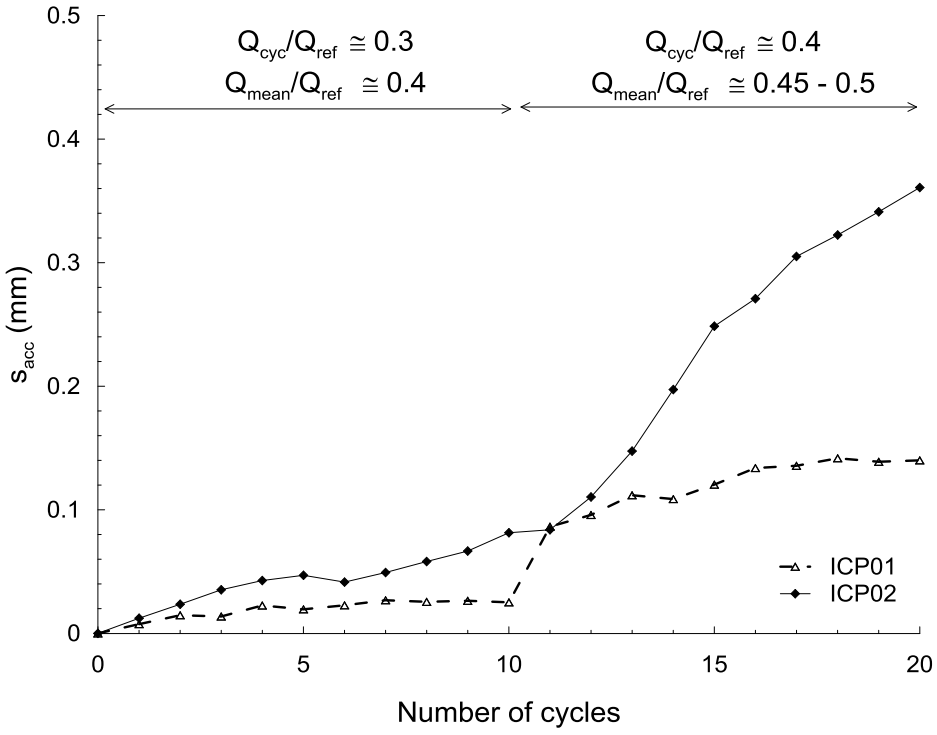


Figure 7-33 Evolution of permanent pile head displacement with number of cycles

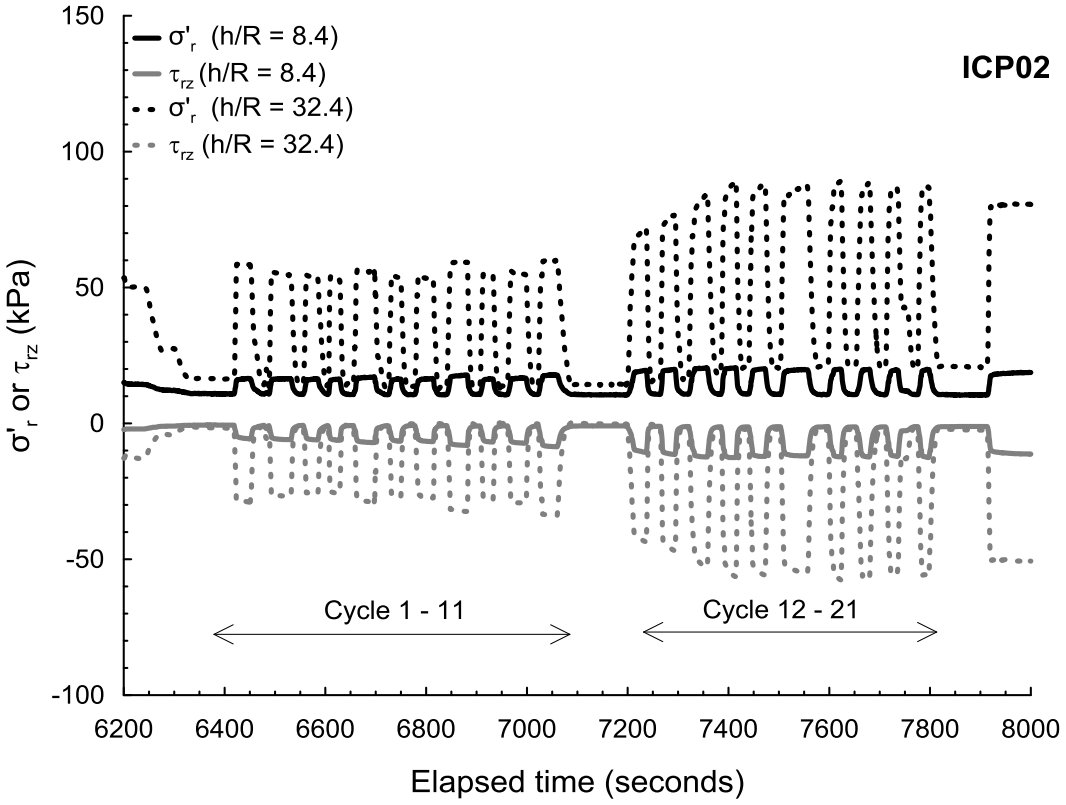


Figure 7-34 Example radial and shear stresses changes during cycling at the leading and following instruments during the test on ICP02

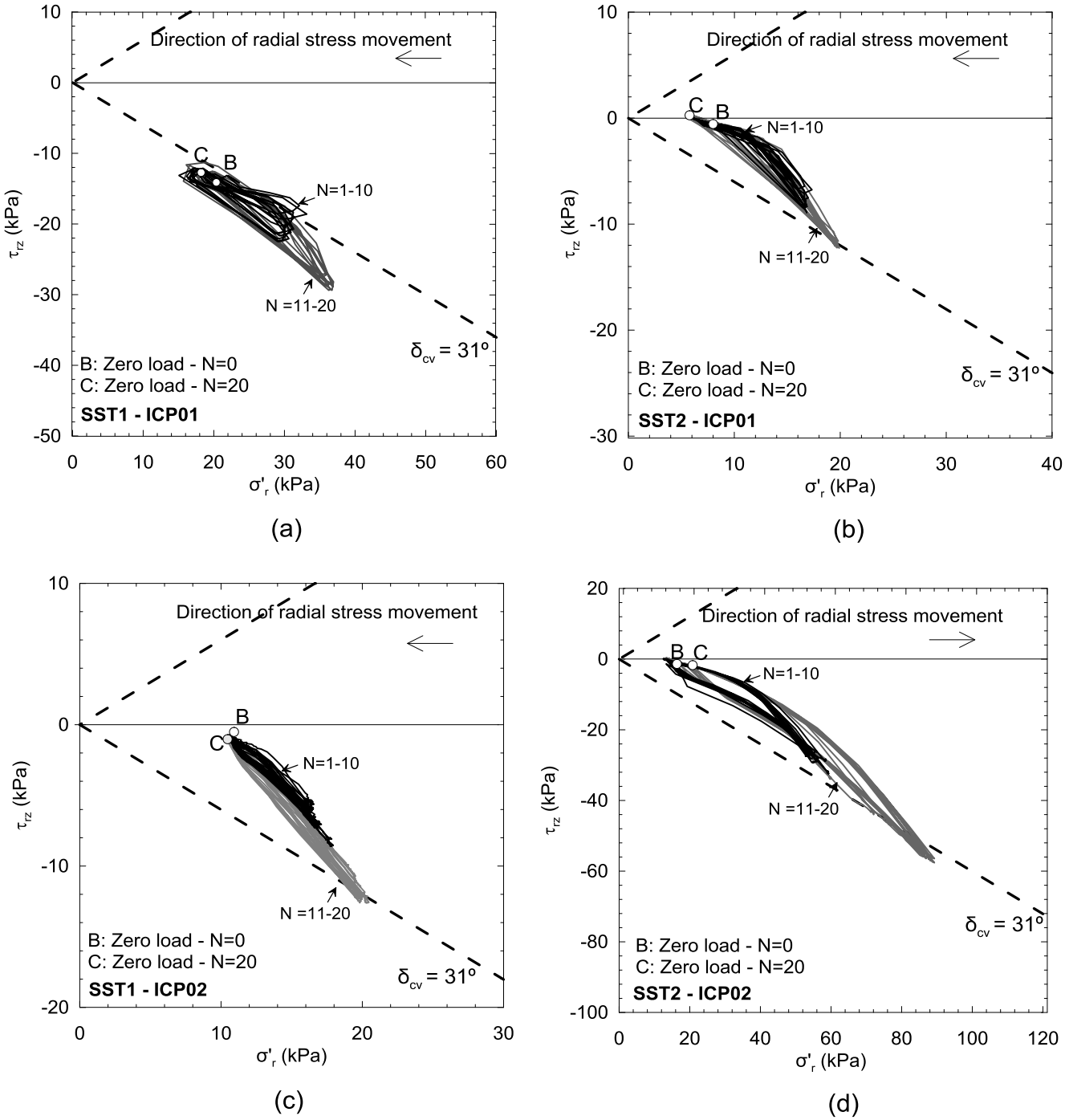


Figure 7-35 Effective stress paths during one way cyclic loading at a) leading SST1 during ICP01 b) following SST2 during ICP01 c) leading SST1 during ICP02 d) following SST2 during ICP02

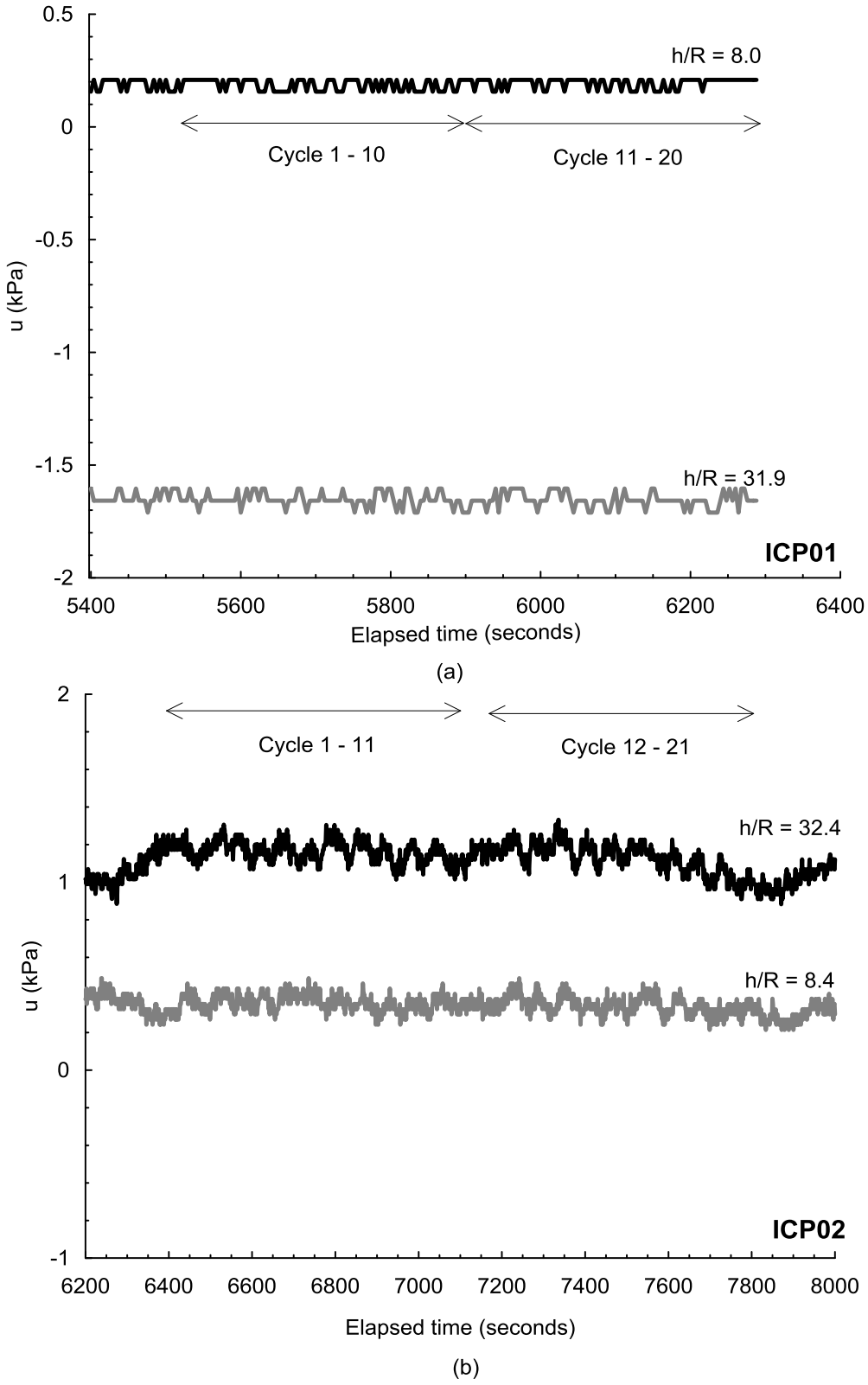


Figure 7-36 Changes in pore pressure with cycling at both instrument levels during (a) ICP01 and (b) ICP02

7.7 Summary & Concluding remarks

The programme of jacked ICP field model pile tests conducted at St. Nicholas-at-Wade presented in this chapter provided new insights into aspects of displacement pile behaviour in low-medium density chalk. The observations made include:

1. Base resistance varied directly with local cone resistance and depended on drainage conditions;
2. Shaft resistances are low during installation, with the jacked piles' average values exceeding those back analysed from open-ended piles driven at the same site due to the slower installation rate of the jacked piles;
3. Large excess pore water pressures are interpreted as having developed under the pile tip during penetration that dissipated rapidly as the tip advanced;
4. Low stationary radial effective stresses developed during pile installation that correlated directly with cone resistance, with ratios to q_t comparable to those in calcareous sands;
5. Strong reductions in shaft radial effective stresses, σ'_{rm} develop immediately after the pile tip passes any given horizon, with more gentle additional degradation applying further along the shaft. Still more reductions in σ'_{rm} with relative tip depth (h/R) apply to driven piles;
6. The effective stress paths recorded during static and cyclic loading tests show that shaft failure is controlled by a Coulomb law, with an interface shear angle similar to that mobilised in laboratory interface ring shear tests;
7. The radial effective stresses rise under static loading until interface dilation reaches its limit. The degree of radial expansion experienced at the interface appears to be far smaller than with sands, due to the higher ratio between the pile roughness and the silt sized crushed chalk grain size;
8. Long-term monitoring of the jacked piles showed total shaft radial stresses reducing with time after installation, falling by 11 to 34% after 23 and 80 days respectively;
9. Tension load tests showed shaft capacity reducing by similar proportions over the weeks that follow installation, in marked contrast with the strong set-up shown by open driven piles at the same site;
10. Geometry and/or installation method influence the ageing and subsequent loading behaviours and require further investigation.

Conclusions 1 to 7 are fully compatible with observations made at the same site with open-ended driven piles, described in Chapter 6, which developed far higher capacities than are recommended by the current CIRIA guidelines. The ICP tests provide key insights that will help guide new, more fundamental and reliable, effective stress based design methods for piles driven in chalk.

CHAPTER 8 Towards a new design approach for displacement piles in low-medium density chalk

8.1 Introduction

Current axial capacity design methods for piles driven in chalk were reviewed in Chapter 3 in connection with the associated database of pile load tests. The predictive reliability of the current industry standard design method was shown to be poor, with a mean calculated to measured shaft capacity ratio, Q_c/Q_m of 0.75 and a standard deviation is 0.52 (CoV = 0.7). Figure 8-1 shows the average shaft resistance along the pile shaft, τ_{avg} at end of driving (short-term) and after equalisation (long-term), for open ended piles, from the Author's tests in low-medium density chalk, along with the existing CIRIA database results (Lord *et al.*, 2002) and the extended database of tests described in Chapter 3. The average shear stress values at end of (or during) driving in the Author's tests were between 16 and 120 kPa and tend to reduce systematically with increasing pile penetration into the chalk, or h/R*. A similar trend for τ_{avg} to reduce with increasing pile penetration may be observed in the long-term equalised resistances which generally varied between 80 and 300kPa. The highest equalised local shaft capacity measurements are up to 15 times greater than the design τ_{avg} value of 20kPa recommended by Lord *et al.* (2002) for low-medium density chalk, and up to 2.5 times higher than the recommendation for ultimate shaft resistance (of 120kPa) in high density material.

The development of better design methods for piles in chalk has been impeded by a lack of both instrumented pile test data and the understanding they can bring regarding the fundamental underlying effective stress mechanisms. The Innovate-UK JIP research related to the Wikinger field testing programme described in Chapter 5, along with the Author's driven

pile tests and ICP tests conducted in low-medium density chalk, described in Chapters 6 and 7, provided important insights into the underlying fundamental effective stress processes, the capacity changes that occur with time and the behaviour under axial cyclic loading conditions for both small and large diameter piles.

This chapter utilises the understanding drawn from the Author's tests, as well as supplementary data from other sources, to map out a route towards better rules for predicting the axial capacity of open-ended and closed-ended displacement piles in chalk. Capturing the radial effective stresses applying on pile shafts is central to the proposed axial capacity design methodology. A new approach to predict short-term and long-term radial effective stresses is proposed, which is based on the key phenomena identified in earlier chapters, namely:

- The use of CPT cone resistance to allow for local variations in ground properties;
- Recognising the marked effect of the relative distance from the pile tip below any given chalk horizon being considered; and
- Addressing the chalk's interface effective stress shear failure characteristics.

Dilation induced changes in radial effective stresses during loading are also considered. The resulting preliminary recommendations for shaft capacity predictions are tested against the available database of high quality static tests, which is also used to re-evaluate the industry standard methods of estimating the axial shaft capacity of displacement piles in chalk (Lord *et al.*, 1994, Lord *et al.*, 2002). Preliminary conclusions regarding the base capacity of open-ended and closed-ended piles from the database are discussed, as are other design considerations such as the effect of loading direction, the effects of axial cyclic loading and possible interactions with lateral loading components.

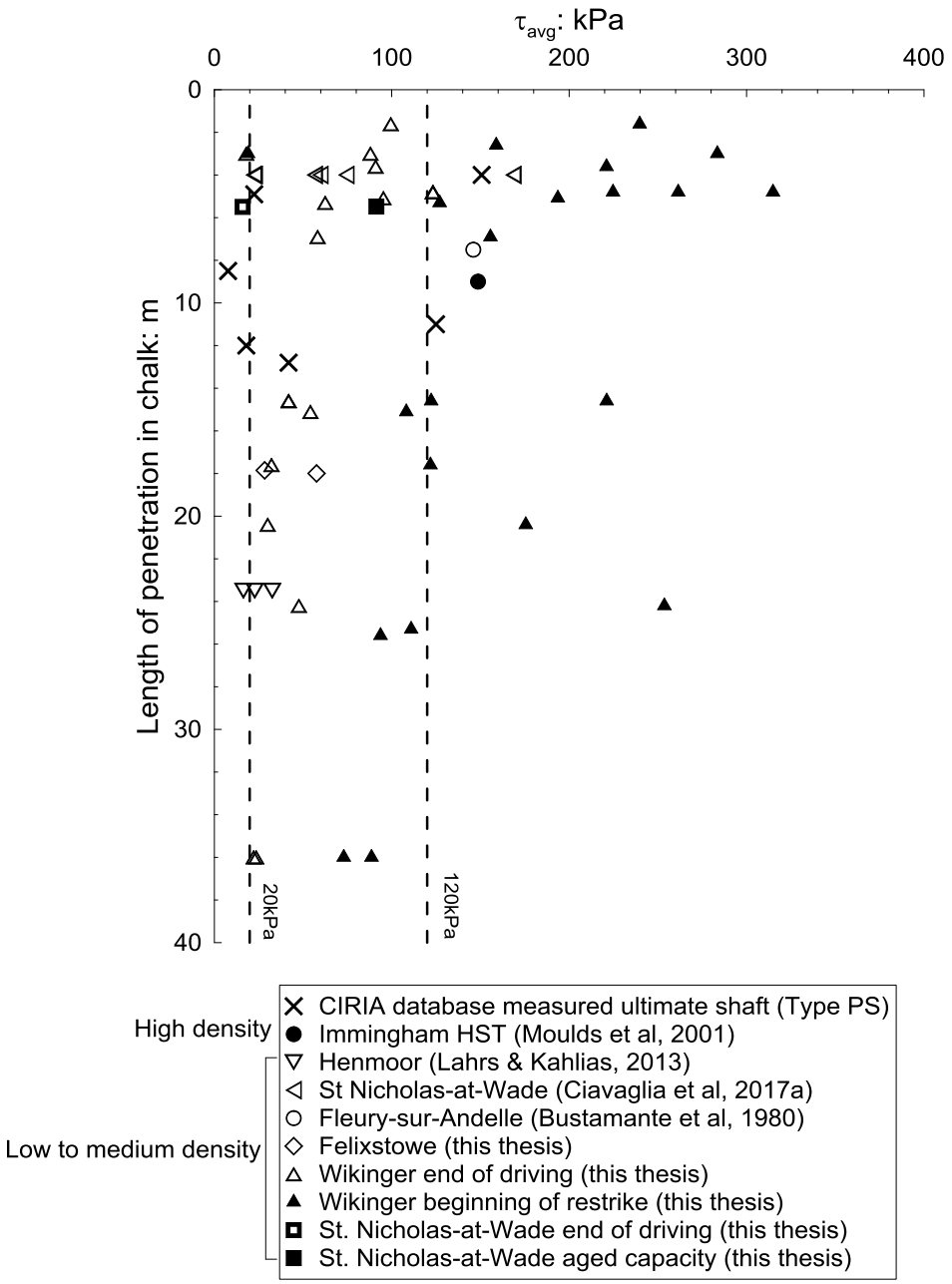


Figure 8-1: Comparison of average shaft stresses, τ_{avg}, for open-ended piles, from the CIRIA database, tests identified by the Author and the Author's tests

8.2 Current understanding of displacement piles in chalk

The behaviour observed in the static, cyclic and dynamic tests, described in Chapter 5, 6 and 7, conducted onshore and offshore in low-medium density chalk led to the following primary conclusions;

1. Low-medium density chalk can be encountered in the field at liquidity indices close to or exceeding unity;
2. Low average shaft resistances apply during and immediately after driving along the pile shaft length embedded in chalk, which tend to reduce markedly in any given layer with increasing penetration. Back analysis of dynamic tests allowed the significant trends in shaft resistance degradation with continued driving (or growing h/R*) to be tracked, which were shown to be considerably more severe than the reductions seen previously in sands and clays. Strain gauge measurements at static failure showed similar h/R* dependency;
3. The drainage characteristics of chalk appear to vary greatly, reflecting the macro-fabric of fissures specific to each site. The chalk was shown to be relatively free draining at St Nicholas-at-Wade, which led to partial drainage in CPT tests as well as jacked and driven pile installation. Behaviour during slow axial monotonic pile loading tests to failure was fully drained;
4. Driving of open-ended piles remoulds the chalk, creating a puttified zone, and probably generates very high excess pore water pressures near to the pile tip. Dissipation of pore water pressures during and after driving leads to a reduction in water content in the zone surrounding the pile shaft, which was observed directly at the onshore test site;
5. The highly instrumented ICP tests conducted at St. Nicholas-at-Wade demonstrated that the stationary radial effective stresses developed during installation correlated directly with the CPT cone resistance, mobilising far lower ratios to corrected cone resistance, q_t than are seen in fully drained silica sands, although the ratios observed were similar to those developed in high voids ratio crushable calcareous sands;
6. Tracking of the axial capacity changes over time showed that set-up is highly significant in chalk and shaft resistances can build to over 5 times the end of driving resistances over periods up to 8 months after installation. The time taken for pile set-up may be related to the nature of the fractures *in-situ* and rates appear to be fastest in cases where fractures are closed tightly;

7. Interface ring shear, triaxial and other tests conducted on aged samples showed that the set-up observed in the field is not due primarily to cementing or processes such as thixotropic hardening. Equally, the field tests at St. Nicholas-at-Wade showed that set-up is not related primarily to redox or other chemical reactions;
8. The effective stress paths measured during static and cyclic loading tests on the ICPs indicated that shaft failure is controlled by an effective stress Coulomb law, with interface shear angles at failure similar to the ultimate values seen in laboratory interface ring shear tests on appropriate samples;
9. Radial effective stresses are seen to increase during loading, which is interpreted as reflecting constrained interface dilation, similar to that seen in sands. However, a lower degree of radial expansion appears to apply in chalk compared to that observed in sands, which is interpreted as being due to the higher relative roughness of the interface (ratio between pile roughness and the mean particle size, D_{50}) due to the smaller silt-sized chalk particles;
10. The Author's test results indicate that the behaviour of displacement piles in chalk is similar in most respects to that seen in calcareous sands, mobilising relatively high base resistances during driving, with consolidation occurring during and immediately after driving. Radial effective shaft stresses and end bearing pressures follow the trends of CPT cone resistance, while "dilative" changes in radial effective stresses are observed during static loading to failure;
11. One-way axial cyclic loading of driven piles, imposed around 250 days after driving, led to responses that ranged from stable to unstable, depending on the loading combinations imposed. The aged and previously untested piles' ultimate axial capacities were relatively insensitive to one-way axial cycling for the considered loading levels and numbers of cycles. However, significant permanent displacements could develop under even relatively modest one-way cyclic loading levels. High level two-way cycling is also likely to prove more damaging than one-way cycling.

8.3 Data sources and comparison of the chalk encountered at the test sites

The following sections draw on the understanding described above and in previous chapters to develop preliminary correlations for the radial effective stresses and local shaft shear stress resistances applying on displacement piles in chalk.

A CPT-based design method has been adopted on the basis of observations made in the Author's tests and as a result, only sites where full cone resistance profiles or equivalent correlations are available could be selected. The results of pile tests from the three different test sites used to develop the tentative correlations for open and closed-ended piles, are considered first. The tests used to develop the correlations on open-ended piles are summarised in Table 8-1 and include;

- Static and dynamic tests on 762mm diameter piles installed onshore at the St. Nicholas-at-Wade test site described in Chapter 3 and by Ciavaglia *et al.* (2017a);
- Static and dynamic tests on 1.37m diameter piles and dynamic tests on 2.7 and 3.67m diameter piles installed offshore at the Wikinger offshore wind farm (Chapter 5);
- Static and dynamic tests on 139mm diameter piles installed onshore at the St. Nicholas-at-Wade test site (Chapter 6).

The correlations developed for the open-ended piles described above are also applied to a small number of high quality tests carried out by Bustamante *et al.* (1980) on closed-ended piles at Fleury-sur-Andelle, France (Table 8-2), which were described previously in Chapter 3. Further details regarding each of the tests considered to develop the correlations are available in Chapters 3, 5 and 6.

Table 8-1: Summary of open-ended tubular piles and relevant static and dynamic tests included in the study

Pile	Location	D (m)	L_p (m)	$L_{p,chlk}$ (m)	D/t_w	Test type	Age (days)
OSS	Wikinger	3.67	46.3	36.0	61	End of driving dynamic	-
WK11	Wikinger	2.7	31.1	14.6	67	End of driving dynamic	
						Restrike dynamic	0.26
WK43	Wikinger	1.37	30.7	20.4	34	End of driving dynamic	-
						Restrike dynamic	78
						Static load test	78
WK70	Wikinger	1.37	30.7	24.2	34	End of driving dynamic	-
						Restrike dynamic	77
						Static load test	77
DP6	St. Nicholas	0.139	5.5	5.5	16	End of driving dynamic	-
						Static load test	246
A_119	St. Nicholas	0.762	4.0	4.0	17	Static load test	119

Table 8-2: Summary of closed ended steel piles and H-piles at Fleury-sur-Andelle included in the study

Pile	Pile type	D or D_{eq}[1] (m)	L_p (m)	$L_{p,chlk}$ (m)	Test type	Age (days)
P1	Pre-cast concrete	0.204	10.35	≈7.4	Static load test	118
P2	Closed Steel tube	0.45	10.3	≈7.4	Static load test	693
P3	H pile	0.39	10.3	≈7.4	Static load test	394

1. Diameter or equivalent diameter.: $D_{eq} = \sqrt{4A_{gross}/\pi}$ where A_{gross} is the gross enclosed area of the pile

The type and grade of chalk encountered varies between the three test sites used to develop the correlations, and a comparison is provided here before considering the pile test results. Further details on each of the test sites are provided within the relevant chapters.

Ground conditions at the Wikinger test sites consist of upper Pleistocene glacial till deposits overlying low-medium density saturated structured chalk. The fractures are primarily closed and generally spaced between 200 and 600mm (Grade A1/A2). At the St. Nicholas-at-Wade (SNW) test site, low-medium density chalk is encountered from surface across the quarry floor. The chalk grade varies and generally improves with depth. Within the depth of influence of the test piles (4 to 5.5m) the fractures are spaced between 60 and 600mm and are generally open with discontinuity apertures of less than 3mm (Grade B2/B3). The groundwater level in the quarry is likely to vary seasonally and groundwater was encountered at 11.6m below the quarry base during borehole drilling conducted in early February 2007. Less detailed information is available from the Fleury-sur-Andelle (FSA) site; the ground conditions comprise clay and gravel with structureless chalk encountered between 2.9 and 9mbgl (assumed Grade Dm/Dc) underlain by low density structured chalk of unknown CIRIA grade. The piles at the site terminate at 10.3m.

Representative cone resistance profiles are provided for all three sites in Figure 8-2 to Figure 8-4. As discussed previously in Chapter 2, profiles of cone resistance in chalk frequently include a sequence of sharp peaks over small (<0.5m) intervals thought to be related to the presence of flints, as well as the manner in which penetration resistance "builds up and is then followed by grain crushing and closure of discontinuities" (Power, 1982). The profiles have been averaged over 0.3m penetration intervals to remove discrete peaks in resistance, as recommended by Smith (2001). At Wikinger, the cone resistance averaged in this way, q_t, falls between 15 and 20 MPa, while the discrete peaks reach up to 60 MPa. Average f_s generally lies between 200 and 400 kPa (far above that expected in remoulded chalk), while values of u_2 are remarkably high and increase with depth, reaching 10 MPa close to 30 mbsb (Figure 5-16). At

SNW, cone resistance is similar to that seen offshore at Wikinger lying between 10 and 20 MPa, while sleeve friction, f_s lies between 100 and 500 kPa. Thin discrete and discontinuous flints were also encountered which gave sharp local peaks in q_t up to 60 MPa. The penetration pore pressures reach 10 MPa within the depth of interest at the u_1 (tip) position and 6 MPa at the u_2 (shoulder) position. Cone resistance in the structureless chalk at Fleury was significantly lower than seen at either Wikinger or SNW, ranging between 2 and 6 MPa and only reaching 10 MPa in the structured material below approximately 9m depth.

Figure 8-5 (a) illustrates that the sites manifest similar water content and intact dry density trends with the test samples' results lying close to the full saturation line shown from Mortimore and Fielding (1990). Not shown on Figure 8-5 (a) are the high density chalk/Danian Limestone samples encountered between approximately 10 and 15 mbsb, which as discussed in Section 5.6.3, fall below this trend with intact dry density reaching values as high as 1.94 Mg/m^3. Intact dry density is largely less than 1.55 Mg/m^3 at Fleury and between 1.4 and 1.7 Mg/m^3 at Wikinger and SNW, indicating low-medium density chalk within the current classification scheme (Bowden *et al.*, 2002).

Figure 8-5 (b) plots the variation in unconfined compressive strength with intact dry density for the Wikinger and SNW sites. Intact dry density is often correlated directly with UCS q_u, following the trend for saturated samples given by Matthews and Clayton (1993) and by others (e.g. Bowden *et al.*, 2002). The q_u values at the Wikinger test sites, and across the Wikinger site, fall well below this published trend and lie between 0.2 and 0.8MPa. As discussed in Chapter 2, UCS results depend on the size of the sample, the method of the test and the platen friction and therefore should be considered as an index test as opposed to a true indicator of strength. Taking UCS = $2s_u$, where s_u is the undrained strength, indicates that at Wikinger the UCS test strength forms a lower bound to the (450 to 600 kPa) undrained strength range found in undrained triaxial tests. The UCS values encountered at SNW are generally between 2 and 3MPa and are broadly consistent with the expected (low density) q_u range of 1.1 to 3.0MPa for IDD values of 1.4 to 1.55Mg/m^3

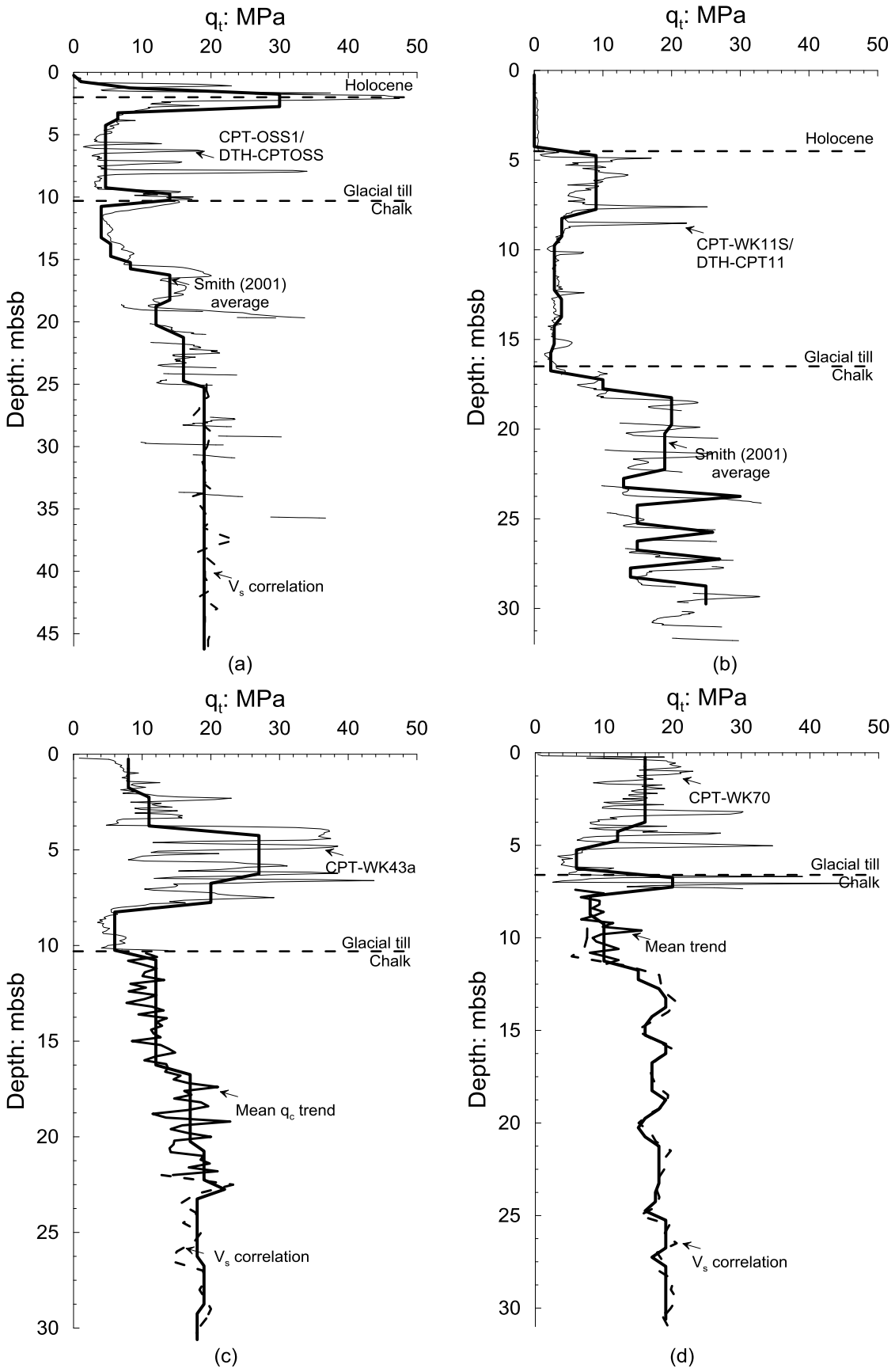


Figure 8-2: Cone resistance profiles from case studies at Wikinger (a) OSS (b) WK11 (c) WK43 (d) WK70

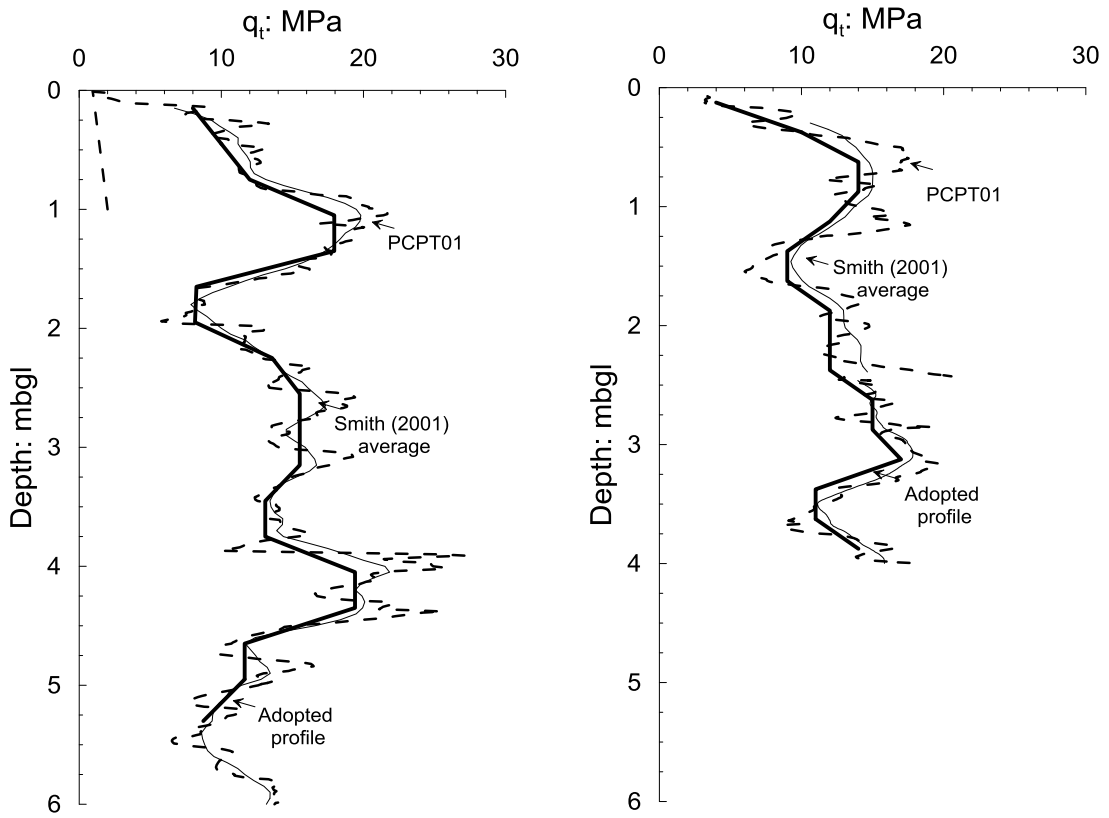


Figure 8-3: Cone resistance profiles from case studies at St. Nicholas-at-Wade (a) Imperial College site (b) Previous JIP site

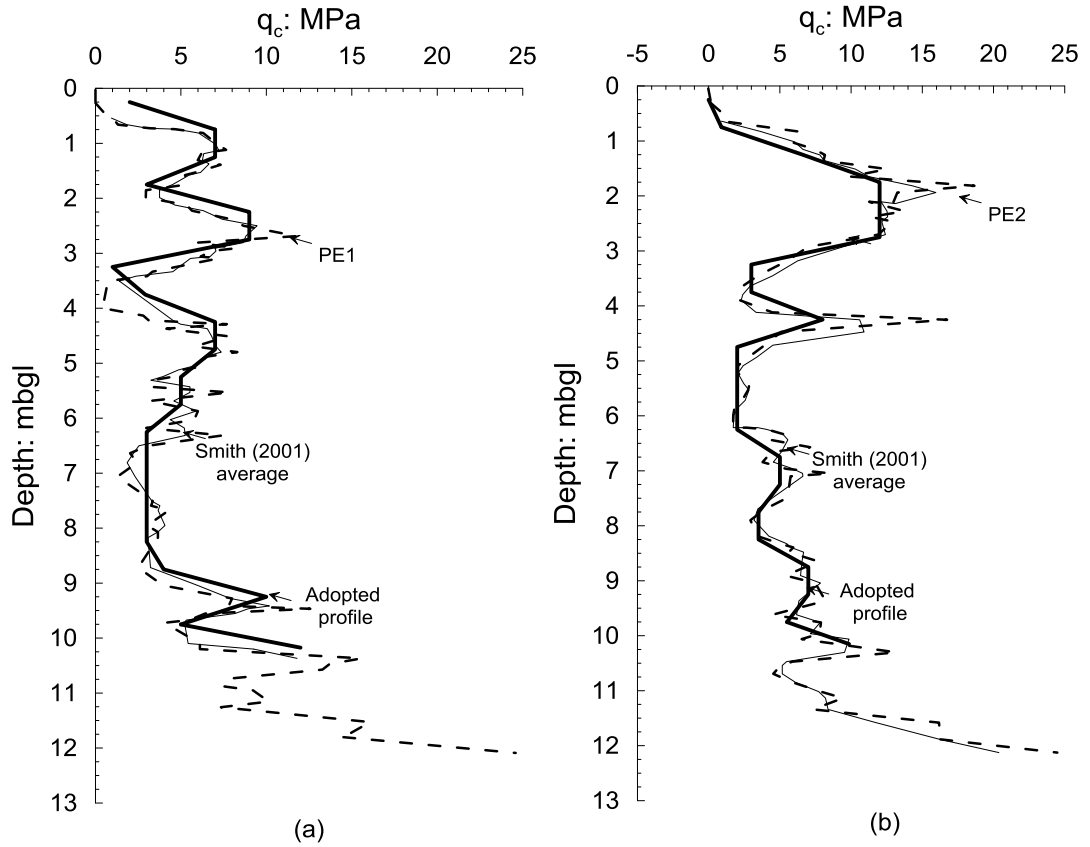
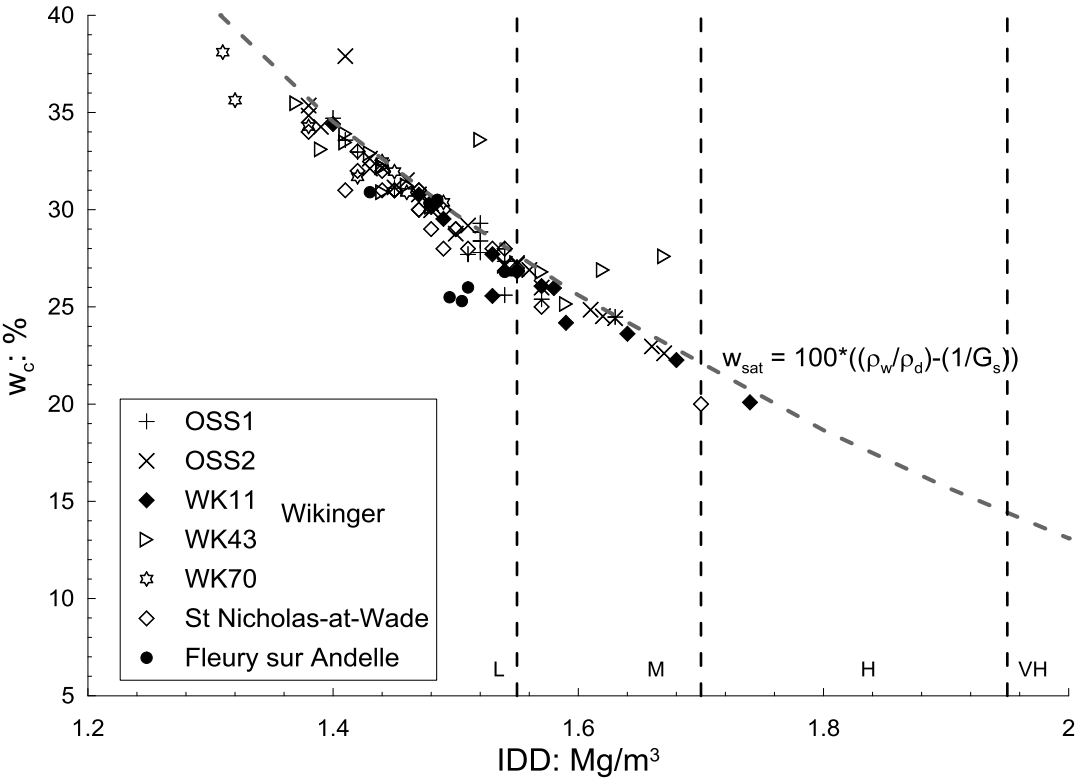
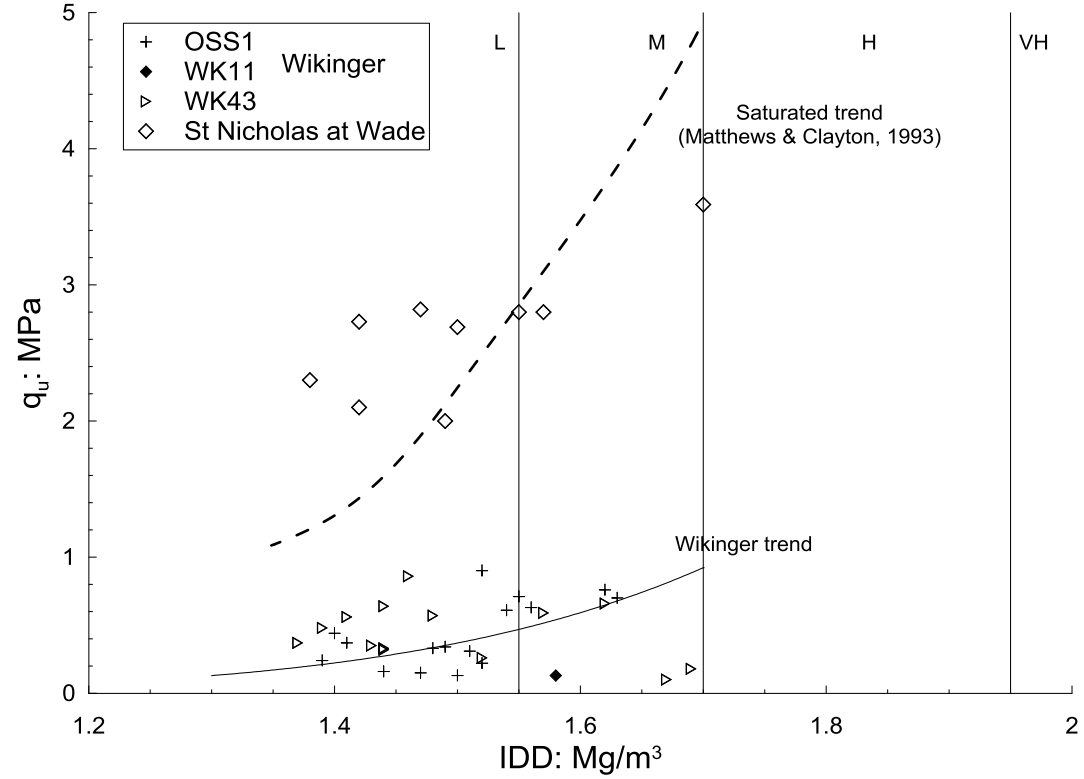


Figure 8-4: Cone resistance profiles from case study at Fleury-sur-Andelle (note uncorrected q_c as no information on pore pressures at the site)



(a)



(b)

Figure 8-5: Comparison between index properties at the three sites (a) water content versus intact dry density relationship (b) Unconfined compressive strength versus IDD

8.4 Base capacity of open and closed-ended piles

In order to determine the total compressive axial capacity of a driven pile foundation it is necessary to estimate the end resistance contribution. Previously, ICP field tests showed that static end bearing is closely related to cone resistance in sands and clays. The CIRIA PG6 and C574 design methods rely on a correlation with SPT measurements to predict base capacity, with $q_{b,0.1D} \approx 200N$ (kPa). A tentative correlation between $q_{b,0.1D}$ and q_c was also suggested by those authors which suggests $q_{b,0.1D} = 0.75$ to $1.0q_c$.

The majority of the Author's static tests discussed in previous chapters have been conducted in tension and give little information on base resistance mobilisation. However, the ICP tests, discussed in Chapter 7, demonstrated that:

- During jacked pile installation, high axial loads develop during the jacking pushes. The base resistance comprised approximately 80% of the total head load. While such findings would be remarkable in clays, similar ratios were seen in Chow's tests in dense sand at Dunkirk and are in accordance with other piles jacked into weathered chalk (Hodges and Pink, 1971);
- The proportion (q_b/q_t) of the end bearing normalised by the CPT values varied significantly with the non-dimensional velocity V ($V=vD/c_h$) during both CPT pushing and pile jacking;
- The ratio q_b/q_t tends to reduce with the non-dimensional velocity, and the results indicated the limits applying to installation under drained or partially drained conditions. When the non-dimensional velocities of the (closed-ended) pile and CPT were similar ($V_{cpt} = V_{pile,}$) the ratio q_b/q_t was approximately equal to 1. The latter confirms the finding of Hodges and Pink (1971) in weathered chalk (Figure 3-27).

The average base capacity mobilised beneath open-ended tubular steel piles can be expected to be far less than that beneath closed-ended piles of similar diameters, due to the softer response beneath the soil plug. As discussed in Chapter 4, the base resistance mobilised during a dynamic pile test can be more difficult to ascertain than the shaft contribution, due to the difficulties of separating the responses of the lower shaft elements from the base itself. The base contributions of large diameter open-ended tubular piles are likely to be concentrated under their annular tip areas, with additional contributions from the internal chalk plug that are transferred to the pile through internal shaft friction.

Base resistances interpreted from the dynamic tests at Wikinger indicated $q_{ba}/q_{t,1.5D}$ ratios (defined over the annular areas only with q_t averaged within 1.5D of the tip) in the chalk which varied with displacement and generally ranged from 0.25 to 0.80 showing a mean of 0.51 and a standard deviation of 0.14. The smaller diameter piles at St Nicholas-at-Wade, give $q_{ba}/q_{t,1.5D}$ ratios from dynamic tests of 0.7 to 0.8 during penetrations of around 50 mm to 70mm per blow, or 0.25 to 0.35 times the diameter. An estimate of $0.7q_{t,1.5D}$ therefore seems to be an appropriate preliminary proxy of the end bearing on the annulus during rapid penetration for the small diameter piles at St. Nicholas at Wade. For the large diameter offshore piles at Wikinger, a lower bound ratio of $0.5q_{t,1.5D}$ appears to be more appropriate. It is noted that in both cases the mobilisation of base resistance likely depends on the penetration per blow. It is also possible that the dynamic end bearing capacity of open-ended driven piles is dependent on pile diameter and wall thickness ratio in chalk, as it is known to be for piles driven in sand when tested under static conditions (Jardine *et al*., 2005a, Lehane *et al*., 2005)

While the above dynamic pile tests drove in an unplugged manner, their behaviour during static loading is less well understood and more difficult to quantify without a significant database of reliably instrumented compression load tests. Analysis of the static compression tests conducted on the 762mm diameter open-ended steel pile (Pile 4) installed at SNW was described by Iberdrola (2013) and reviewed in Chapter 3. The ratio of end resistance to cone resistance depends on whether the pile is assumed to be "plugged" or "unplugged" during static loading, which is unknown. Field load tests performed on instrumented open and closed ended piles driven into sand and reported by Salgado *et al.* (2002) suggest that, whether the piles are driven in an unplugged or plugged manner, the plug contributes to the static base capacity. They showed that the base resistance of the open-ended pile was 36% lower than the equivalent closed-ended pile and the plug resistance contribution was equivalent to 30% of the annular resistance. Consequently, the end bearing should potentially be applied separately to the annular and plug areas. Applying a ratio of $0.7q_{t,1.5D}$ to the annular area for the 762mm diameter pile test, indicates that end bearing on the soil plug is equivalent to approximately $0.28q_{t,1.5D}$. Assuming the pile is plugged, and applying the base load on the gross base area during static failure leads to $q_{b,0.1D}$ approximately equal to 5MPa (or $q_{b,0.1D}/q_{t,1.5D}$ equal to $0.34q_{t,1.5D}$). At Fleury-sur-Andelle, the static compression tests on closed-ended steel and concrete piles (Chapter 3) mobilised $q_{b,0.1D}/q_{t,1.5D}$ ratios over their total base areas of between 0.59 and 0.81 respectively.

The limited dataset available suggests that, for closed-ended piles, such as the ICP, $q_{b,0.1D}$ during static loading is approximately equal to $q_{t,1.5D}$, but may be significantly affected by pile scale, partial drainage during installation and therefore by the rate and mode of installation. Assuming unplugged behaviour, open-ended piles mobilise lower $q_{ba}/q_{t,1.5D}$ ratios under the annulus during a dynamic hammer blow of approximately 0.5 to 0.7 times the cone resistance.

A larger database of compression tests is required to develop more reliable empirical correlations between base resistance and cone resistance. Double-walled instrumented pile tests, such as those reported by Salgado *et al.* (2002), would also help to separate the base resistance components developed from the annular and plug (or inner shaft) areas.

8.5 Contributions to capacity due to interface dilation

The axial shaft capacity of displacement piles is strongly influenced by both friction and dilation at the soil-pile interface. Constrained contraction at the interface will result in a reduction in radial effective stresses during loading and a lower value of shaft stress at failure, τ_f and therefore axial capacity. Equally, constrained dilation at the interface will lead to increases in radial effective stress and higher values of τ_f that may offer potentially significant contributions to overall axial capacity, particularly for small diameter piles. The effects of interface dilation therefore must be considered in any design formulation.

8.5.1 Effect of relative interface roughness

The behaviour observed between a soil and a structural interface with a certain asperity height and spacing can be described by two general behaviour conditions (Dove and Jarrett, 2002):

1. Where the size of the soil grains are large compared to the asperity height and spacing as with a coarse sand grain in contact with a smooth interface. In this case small volume changes occur and very little dilation needs to occur relative to the grain size. Therefore the peak strength is controlled by particle contact conditions, material hardness and surface roughness at the grain contacts, as illustrated on Figure 8-6 (a);
2. Where the size of the soil grains are small compared to the interface asperity height and spacing as with a fine sand grain in contact with a rough interface. In this case large dilative

changes can be required relative to the grain size for slip to develop and the observed strength increases as the roughness increases and the grain size decreases.

A so called "saw tooth" dilative model is illustrated in Figure 8-6 (b), where shearing occurs due to the relative movement between two contacting saw blades. When subjected to a shear load, P, the surfaces must move both horizontally and vertically in order for movement to occur. The angle of relative movement between the two saw blades is analogous to the dilation angle of the soil. Figure 8-6 (c) shows a similar model to (b) but in this case considering a particulate soil material. Shear is resisted by the inter-granular friction, friction between the interface and the particles and by soil dilation.

DeJong and Westgate (2009) employed particle image velocimetry (PIV) to study direct shear interface tests and observed that granular particles in contact with an interface will dilate to some extent regardless of the particle type or the surface roughness, as the particles must move away from the interface in order for sliding to occur. They showed that dilation occurs *at the interface*, even with loose samples with a low or negative state parameter, with particle-interface interlocking overcoming any tendency for the granular assembly to contract under shear because of its initially loose state.

Interface roughness is known to have a significant effect on the frictional resistance between sand and steel and the magnitude of dilation. The friction between sand and different construction materials was found to be lower than the sand-sand friction by Potyondy (1961) and to reduce with the roughness of the interface. Uesugi and Kishida (1986) showed that the peak angle of interface friction, δ'_p mobilised in simple shear tests on sand is related to the ratio of interface roughness to mean sand grain size. The maximum relative roughness, $R_{n,max}$ is defined as:

$$R_{n,max} = \frac{R_{max}}{D_{50}} \qquad 8\text{-}1$$

where R_{max} is the maximum interface roughness measured over a length equal to D_{50}. The relative roughness, R_n can also be described in terms of the average centreline roughness, R_a:

$$R_n = \frac{R_a}{D_{50}} \qquad 8\text{-}2$$

Figure 8-7 illustrates the concept of relative roughness with a scheme of spheres in contact with a steel surface, for the smallest and largest values of D_{50}, in a test series presented

by Uesugi and Kishida (1986). The angle of sliding between large particles and rough steel (θ_j) is lower than the angle of sliding for a small particle against the same interface (θ_i). Correlation between friction and surface roughness therefore must consider the particle diameter. Uesugi and Kishida (1986) showed the tendency for sliding to occur within the soil mass increases with R_n and that for values of R_n larger than a critical roughness value, R_{crit} (approximately equal to 0.1) failure occurs in the soil mass and the peak stress ratio attained appears to be largely independent of the interface properties with the coefficient of friction ($\tan\delta'$) eventually reaching a constant volume value (Figure 8-8). Interface friction and dilation tend to reduce with increasing particle size (or decreasing R_n) until a relatively stable "smooth" value is reached at R_n of approximately 0.001 (Dietz, 2000). Equally, the interface shear and soil-soil shearing resistance angles converge to similar values when R_n exceeds 0.1. Ho *et al.* (2010) report large-displacement ring shear interface tests on silica sands that demonstrated that the δ'_{ult} values can vary with the test conditions and that large-scale particle crushing takes place during shearing over large relative displacement (as occurs during pile driving). The particle crushing was shown to dominate the interface shearing response and induce significant interface roughness changes.

8.5.2 Magnitude of dilation

It has been observed during static tests to failure on ICP piles jacked in sands that following an initial small reduction, the radial effective stresses tend to increase with loading, contributing an extra component of radial effective stress, $\Delta\sigma'_{rd,}$, interpreted as kinematically constrained dilation in the interface between the pile and soil (Lehane *et al.*, 1993). For each element along the pile shaft:

$$\tau_f = (\sigma'_{rc} + \Delta\sigma'_{rd})\tan\delta_{ult} = \sigma'_{rf}\tan\delta_{ult} \qquad 8\text{-}3$$

Boulon and Foray (1986) argued that with sands, the magnitude of $\Delta\sigma'_{rd}$ can be estimated by a simple elastic cavity expansion expression with $\Delta\sigma'_{rd}$ proportional to the shear modulus and inversely proportional to pile diameter:

$$\Delta\sigma'_{rd} = 2G\varepsilon_c \qquad 8\text{-}4$$

where ε_c is the cavity strain which is equal to the average movement of the soil grains, Δr due to dilation divided by the pile radius, giving:

$$\Delta\sigma'_{rd} = \frac{4G\Delta r}{D} \quad 8\text{-}5$$

The shear modulus, G should ideally be measured in the G_{hh} direction and may need to account for strain level and non-linearity. The friction coefficients and relative roughness values for industrial driven steel piles in sands tend to lie in the range between the maximum and minimum critical roughness values, where the magnitude of the Δr term can be approximated as twice the average interface roughness, $\Delta r \approx 2R_a$ (Chow, 1997, Jardine *et al.*, 2005a). Schneider (2008) argued that since the maximum dilation at the interface increases with the shear band thickness and therefore D_{50} (Foray *et al.*, 1998), Δr should be related to D_{50} and R_a and proposed the dimensionally consistent relationship:

$$\Delta r = 2.5 D_{50}^{0.4} R_a^{0.6} \quad 8\text{-}6$$

The Author's ICP tests in low-medium density chalk at the SNW site, described in Chapter 7, measured the local shaft effective stress paths which developed during static tension loading to failure. Example stress paths are shown on Figure 8-9, which demonstrate how the radial effective stresses measured at the instrument clusters tended to increase during loading due to constrained interface dilation, similar to the behaviour seen in sands and modelled using cylindrical cavity expansion theory (Eq. 8-5). The shear and effective stresses mobilised at failure, τ_f and σ'_{rf} showed peak stress ratios δ'_f (= $\tan^{-1}$ (τ_f/σ'_{rf})) close to the δ'_{ult} angles seen in interface ring shear tests on samples from the site.

In order to estimate the contribution of dilatational stress changes to the overall capacity of the tests considered, it is necessary to know the amount of dilation that occurs during loading. An indication of the magnitude of Δr in chalk for use in Eq. 8-5 may be determined from two sources:

1. Measurements taken by the SST sensors on the ICPs during static tension loading to failure which measure $\Delta\sigma'_{rd}$ directly, allowing an estimate of Δr to be made using Eq. 8-5, since both the diameter and operational shear stiffness are known;
2. Interface ring shear tests on samples of chalk, where the normal displacement during shear can be estimated and used as an indicator of Δr.

The correct D_{50} to use to calculate the relative roughness (Eq. 8-2) depends on the particle size distribution of the chalk putty formed around displacement piles during driving. The median grain size, D_{50} in chalk has been shown previously to depend on the method of preparation of the crushed chalk. Figure 8-10 shows variation between particle size

distributions from the SNW site carried out on samples by Bialowas *et al.* (2016) and Chan (2017). In both studies, the test samples were formed by grinding intact chalk into a powder and adding water where necessary. In those tests, D_{50} ranged from 2.7 to approximately 6 μm. Bundy (2013) reports that D_{50} for samples of Culver and Newhaven chalk can range from 1 to 10 μm, depending on the sample preparation method and grinding time in a Tema mill machine. His tests indicated the predominant minimum particle size was between 2 and 4μm consistent with the size of the individual coccolith laths (Clayton, 1983).

The ICPs are primarily made of molybdenum steel and had typical centre line average roughness, R_a of approximately 5μm at the time of installation. The D_{50} range shown on Figure 8-10 for the SNW samples of between ≈3 and 6 μm gives a range of R_n for the ICPs of 0.8 to 1.7, far exceeding the perfectly rough value, R_{crit} for sands described by Kishida and Uesugi (1987) and Lings and Dietz (2005) and shown as around 0.1 on Figure 8-8.

The SST sensors indicated that $\Delta\sigma'_{rd}$ ranged from 11 to 14kPa in three cases and 96kPa in the remaining case. The undisturbed *in-situ* intact seismic G_{hh} values at SNW within the depth of interest generally range from approximately 400 to 1200MPa. However, locally lower G values may apply close to the shaft due to installation effects and re-consolidation. Multi-stage resonant column tests on samples taken from the site carried out by Fugro (2012a) indicated G_{vh} of 250 to 300MPa at the appropriate mean effective stress level for remoulded chalk. Substituting absolute upper and lower bound G ranges of 250 to 1200kPa into Eq. 3-23 indicates Δr for these tests as falling between 0.23 and 2.04 μm, apart from one isolated high value of 9.8 μm. Approximating Δr as equal to 0.5μm from three of the tests gives Δr equal to $D_{50}/6$ to $D_{50}/12$ or $0.1R_a$.

The resulting Δr values fall well below the piles' surface average peak-to-trough roughness value and suggest that the degree of radial expansion experienced by the chalk is far smaller than the $2R_a$ to $2.7R_a$ (using Eq. 8-6) expected for sands. This reflects the higher ratio between the pile roughness and the silt sized crushed chalk grain size. The high relative roughness at the pile-chalk interface causes the surface to interlock with the soil and forces shearing out into the chalk mass where smaller absolute volume changes are required to allow shaft-to-chalk slip, developing in thin shear bands whose thickness is controlled by D_{50}.

Considering the alternative means of studying interface dilation, interface ring shear tests are available on samples of remoulded chalk from both Wikinger and SNW as summarised

in Chapter 5 and 6 and shown on Figure 5-28 and Figure 6-20. Tests performed on samples from both sites using mild steel interfaces, with R_a values of between 10 and 15 μm ($R_n \approx 1.7$ to 5.6) suggest Δr values of between 14 and 24 μm (or 2.3 to 8.0 times D_{50}). The latter values of Δr are equivalent to 0.9 to 1.9 times R_a, similar to the recommendation of $\Delta r \approx 2R_a$ for sands. However, these values are over 30 times larger than can be inferred from measurements made on the ICP shafts. The conflicting results are not fully understood and further investigation is warranted to determine the magnitude of Δr and its relationship to R_a and D_{50} in chalk. In the absence of further resolution of this discrepancy, a value of Δr equal to 0.5 μm is assumed in this chapter based on the ICP test results. This may be considered more conservative than adopting $\Delta r = 2R_a$ as in sands, since the contribution of dilation to overall capacity increases with increasing Δr. As shown later, assuming Δr equal to 0.5 μm leads to dilational components offering relatively small contributions to the overall long-term shaft capacities for most piles driven in chalk.

8.5.3 Prediction of interface dilation during pile loading

The dilation characteristics indicated by the ICP test measurements discussed in Section 8.5.2, have been used to develop a preliminary expression for $\Delta\sigma'_{rd}$, in which Eq. 8-5 is employed with Δr equal to 0.5 μm. Figure 8-11 shows the predicted and measured values of $\Delta\sigma'_{rd}$ from the ICP tests, calculated using Eq. 8-5. Figure 8-12 shows how the $\Delta\sigma'_{rd}$ profiles vary with pile size, illustrating the reduction in the dilation component with increasing pile diameter at the same site. For the 101mm diameter ICP piles, the dilation component calculated using Eq. 3-23 is between 4 and 16kPa, contributing 20.6% and 16.7% of the overall capacity in tension tests conducted at the end of equalisation for ICP01 and ICP02 respectively. The slightly larger 139mm diameter driven piles installed at the same site showed shaft capacity increases of up to 530% over 246 days. In their case $\Delta\sigma'_{rd}$ calculated using Eq. 3-23 falls between 3 and 17kPa, and dilation contributes 5.2% of the capacity of the pile measured by static testing after ageing. For the 762mm diameter piles at the same site, $\Delta\sigma'_{rd}$ lies between 0.5 and 2.1kPa and the contribution from dilation reduces to approximately 0.4% of the capacity measured by static testing after ageing. For the larger still offshore piles at Wikinger (1.37 to 3.7m diameter) dilation generally makes a less than 0.5% contribution to the piles' aged shaft capacities in tension. The shear stiffness adopted for the Wikinger tests is calculated using Eq. 5-5.

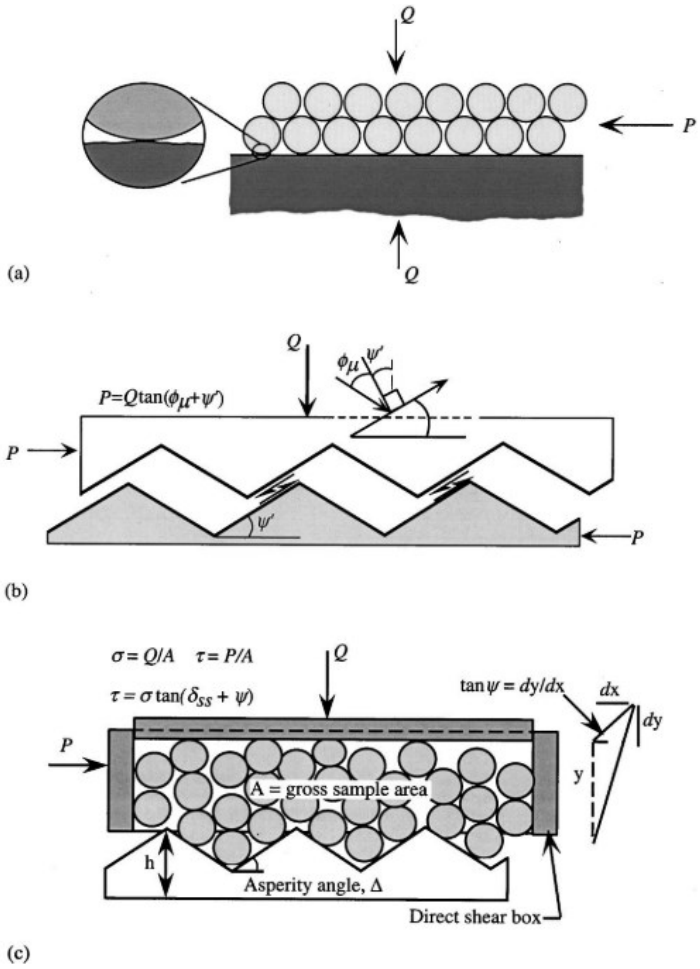


Figure 8-6: (a) schematic illustration of non-dilative interface (b) conceptual model of dilatancy and friction (c) idealised dilative interface system (Dove and Jarrett, 2002)

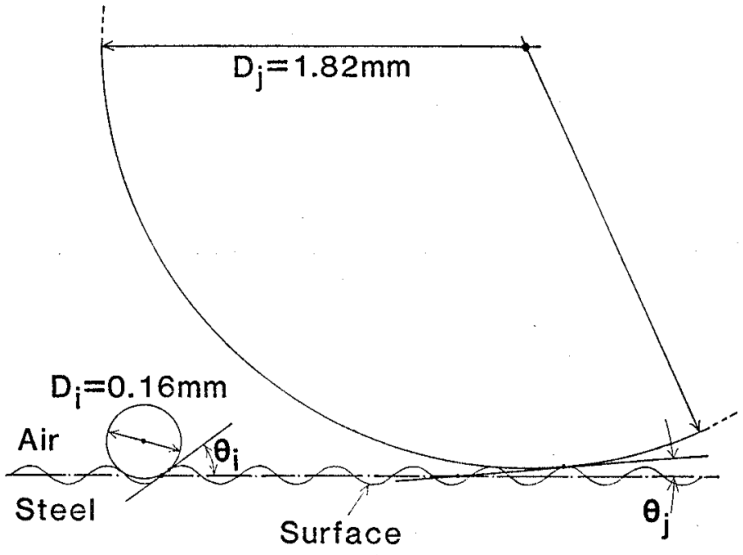


Figure 8-7: Interface sliding angle, θ, as a function of particle size/normalised roughness (Uesugi and Kishida, 1986)

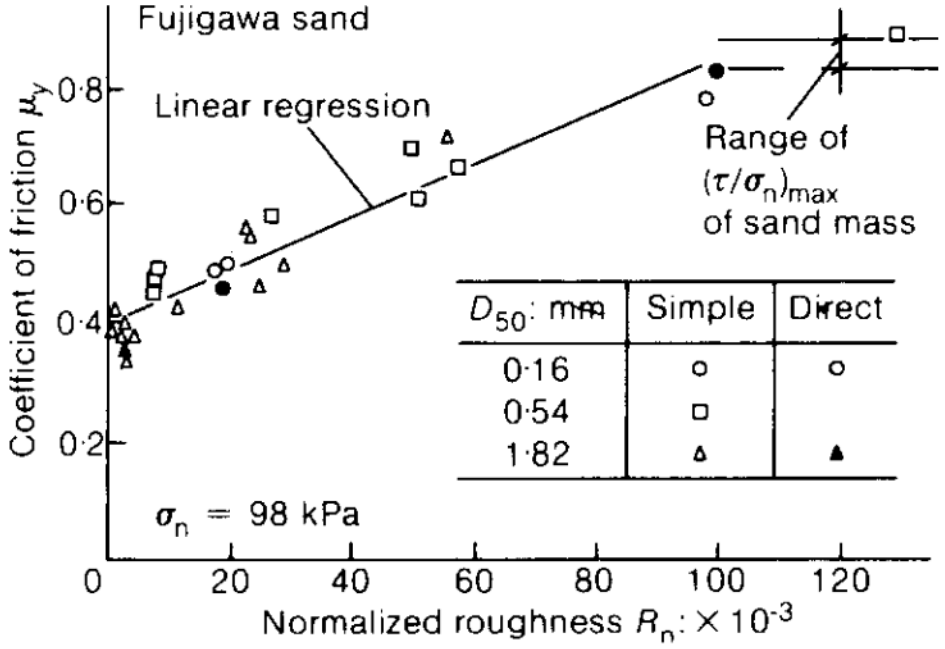


Figure 8-8: Concept of interface friction and normalised roughness (Kishida and Uesugi, 1987)

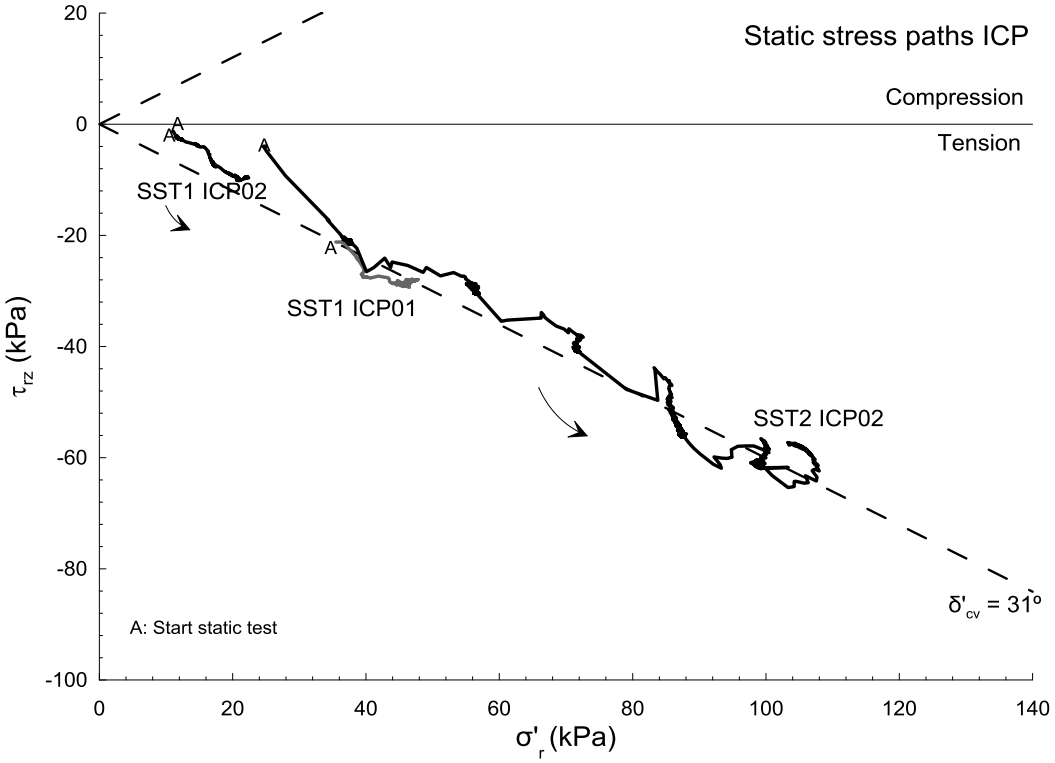


Figure 8-9: Typical stress paths measured by ICP instruments during static testing

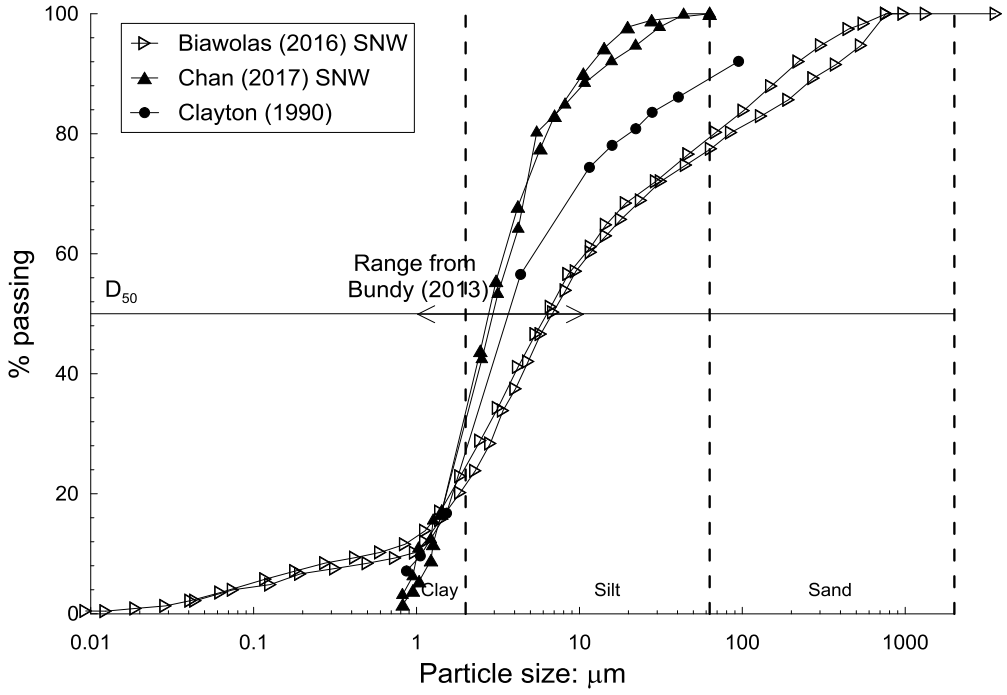


Figure 8-10: Variation in particle size distributions of crushed chalk

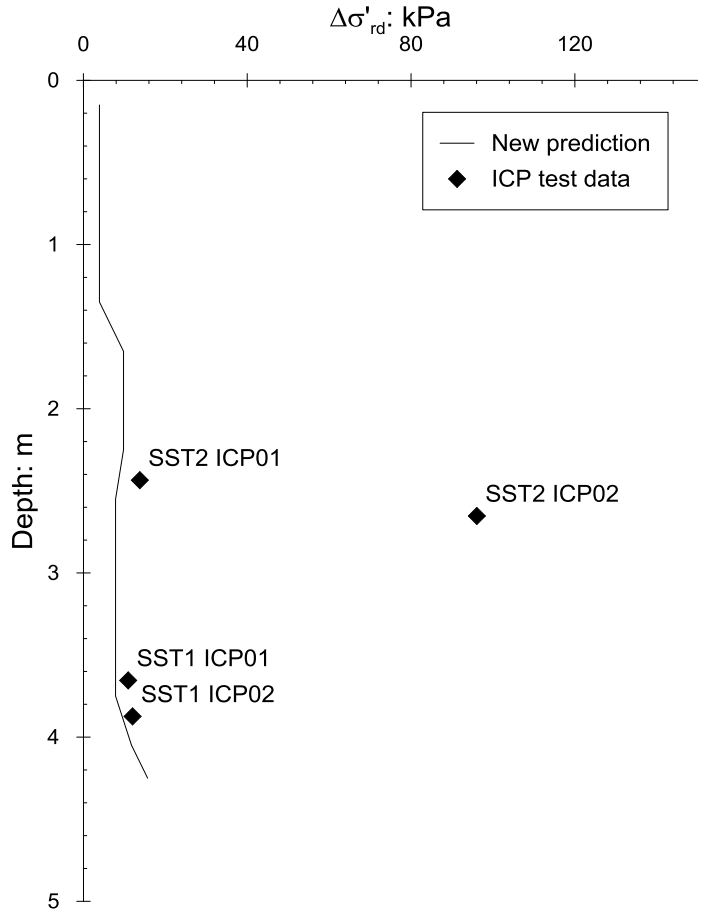


Figure 8-11: Predictions of $\Delta\sigma'_{rd}$ during loading of jacked ICP piles at St. Nicholas-at-Wade

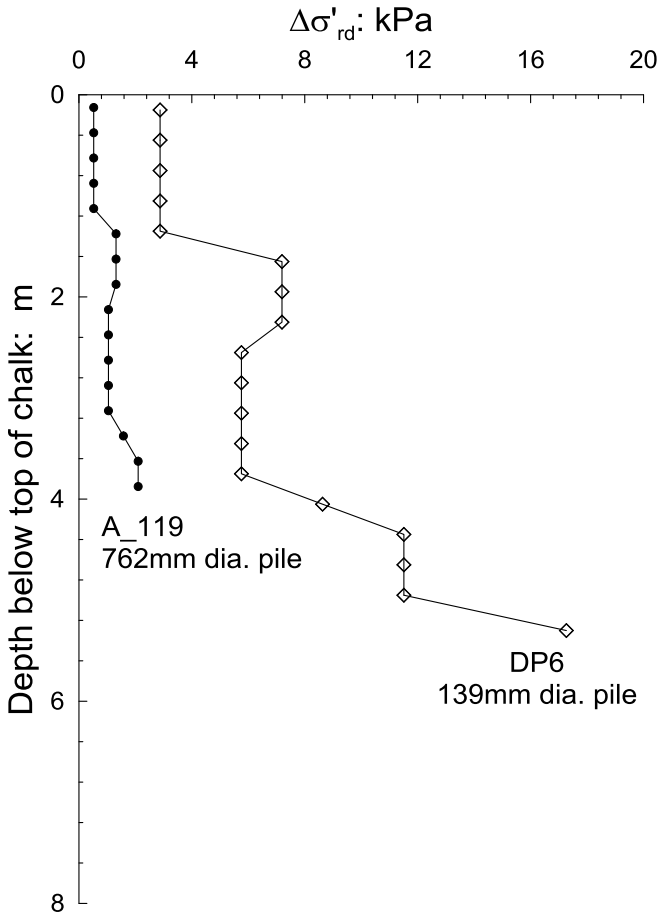


Figure 8-12: Predictions magnitudes of $\Delta\sigma'_{rd}$ for piles of different diameter in the case studies.

8.6 Stress changes during pile installation, equalisation and loading

Before moving to predict the radial effective stresses applying during pile installation, equalisation and loading to failure, it is important to understand the stress changes occurring over each of these stages. Figure 8-13 provides an example of the behaviour of remoulded chalk in constant volume triaxial tests performed on aged and unaged samples from the Wikinger site. All samples achieved denser-than-critical states at the end of consolidation (see Figure 5-24). Subsequent constant volume triaxial compression tests led to an initial contraction followed by strongly dilative tendencies at large strains that created substantial p′ increases under constant volume conditions.

The effective stress experienced by chalk elements that were located initially under the pile tip's annulus during driven pile installation, equalisation and load testing can be interpreted semi-quantitatively in terms of the state parameter framework, applied earlier to the ICP tests, described in Chapter 7 and shown on Figure 7-32. Effective stress states are considered for the 139mm diameter tubular piles at two depths below ground level, z_1 and z_2, of 2.75 m and 5.5m, representing points that were finally halfway along the shaft and near the tip of the driven, open-ended piles respectively. Four stress states are considered, as illustrated on Figure 8-14. These correspond to the stress systems, applying at depths z_1 and z_2, when:

A. The pile tip is above z_1 or z_2;
B. The pile tip has just arrived at either level;
C. The pile tip is below or at either z at the end of installation;
D. The pile tip is below or at either z at the end of the equalisation period.

For the depth, z_2 = 5.5mbgl, condition B is the same as condition C. Schematic diagrams of the stresses applying on a soil element either (i) immediately adjacent to the shaft and (ii) below the annulus of an incompressible pile are shown on Figure 8-15, which is similar to the representation shown previously in Figure 7-30 for the closed-ended pile. The cylindrical coordinate system corresponds to r (in the radial direction), z (in the vertical direction) and θ (in the circumferential direction).

It was argued in Section 8.4 that the average total vertical stresses beneath the open-ended steel pile's annulus, σ_z (σ_1) can be approximated as 0.7 times the cone resistance, q_t giving:

$$\sigma_1 = 0.7q_t = \sigma'_z + u_{ann} \quad 8\text{-}7$$

where u_{ann} is the average pore pressure over the annular area. While use could be made of the $u_1 \approx 0.4q_t$ relationship estimated from piezocone tests when considering the closed-ended pile case in the ICP analysis presented in Chapter 7, this approximate relationship cannot be applied to the annular case shown in Figure 8-15 because the total stress system is different and the σ_z value is 30% lower. It is more reasonable to assume that the plane-strain undrained shear strength applying to the annular case approximately matches the triaxial value calculated using the axially symmetric ICP case, where $\sigma'_z = q_t - u_1 \approx 0.6q_t$. In this case, u_{ann} is predicted to be much smaller than u_1. Since, $\sigma_z = 0.7q_t$ (Eq. 8-7) this gives u_{ann} approximately equal to $0.1q_t$.

Applying the argument presented by Jardine *et al.* (2013a) for sands, the maximum moving radial effective stresses, σ'_{rm} applying immediately below the annulus during rapid penetration can be calculated again from the Mohr-Coulomb failure criterion for triaxial compression:

$$\sigma'_{rm} = \tan^2\left(45 - \frac{\varphi'}{2}\right)\sigma'_z - 2c'\tan\left(45 - \frac{\varphi'}{2}\right) \quad 8\text{-}8$$

Assuming peak $\varphi' = 41°$ and $c' = 387$kPa from the earlier reported triaxial tests on intact chalk at the test site and noting the q_t range of 10 to 20MPa results in $900 < \sigma'_{rm} < 2150$kPa beneath the annulus at h=0. The subscript m on the effective stresses denotes the moving stresses. The boundary conditions immediately beneath the tip give rise to zero circumferential strain, so $\sigma'_{\theta m}$ is the stress in the plane-strain direction. If we assume, as in Eq. 7-19:

$$\sigma'_{\theta m} = \frac{\sigma'_{rm} + \sigma'_{zm}}{2} \quad 8\text{-}9$$

We can assess the mean effective stresses in terms of the principal effective stresses, giving p' between 3450 and 7080kPa.

The stress components applying on an element of soil adjacent to the pile shaft are also shown on Figure 8-15. As argued in Section 7.6.9, the mean effective stresses applying at the pile shaft can be approximated as:

$$p' \approx \sigma'_{rm} \quad 8\text{-}10$$

A tentative illustration of the resulting stress states applying at the final instrument levels, z at the stages, A, B, C and D (Figure 7-29) are shown in specific volume, v – mean

effective stress (v-logp′) space on Figure 8-16. The critical state line adopted is that determined by Doughty (2016) from triaxial tests on remoulded samples of Wikinger chalk, which may differ from the CSL applying at the St. Nicholas-at-Wade site. The following points are noted:

- Prior to the pile reaching depth z, elements are at the *in-situ* stress state where $\sigma'_r = \sigma'_{r0}$ and the mean effective stress, p′ is approximately equal to 40kPa (based on an assumed K_0 of 0.4). Assuming full saturation, the specific volume is calculated from:

  $$v = 1 + e = 1 + w_c G_s \qquad 8\text{-}11$$

  where w_c is the natural water content measured at the site, over the depth of interest, of between 28 and 31% (Figure 6-11) and G_s is the specific gravity (≈2.7);
- As argued above, the maximum mean effective stresses, p′ developed beneath the steel annulus falls between 3450 and 7080kPa. Thus when the pile tip is at the instrument depth z, the element below the tip follows the sharp increase in mean effective stress along Path (A-B) shown on Figure 8-16, assuming initially undrained conditions;
- The mean effective stresses reduce dramatically as the chalk loses its natural structure and eventually tends to its puttified state generating high pore water pressures;
- The consolidation characteristics at the site indicate that driven pile installation was partially drained, with consolidation occurring during driving and likely largely complete before the end of installation (see Section 6.5.3). The void ratio at the end of installation can be calculated using:

  $$v = 1 + e = 1 + w_f G_s \qquad 8\text{-}12$$

  where w_f is assumed to match the reduced water content value (= $0.8w_c$) measured from samples taken adjacent to the driven pile shaft during pile exhumation inspections 274 days after driving;
- At point C, the pile is at its final installation depth. Shaft radial effective stresses, σ'_{ri} applying at this stage can be estimated from the signal matching analysis, described in Section 6.5.2, by assuming a δ'_{ult} value of 32°. Taking $\sigma'_{ri} = p'$ gives p′ of between 6 and 145kPa at the shaft midpoint and just above the tip respectively, resulting in Path B-C;
- Noting that the radial effective stresses applying on the driven pile shafts in the tension tests increased by approximately 500% over the 246 day monitoring period and applying this set-up factor to the σ'_{ri} values, taking $\sigma'_{ri} = p'$, results in the ageing Path C-D applying during equalisation;

- As argued earlier, static tension testing to failure after full equalisation led to increases in radial effective stresses at failure, associated with the effects of constrained interface dilation which contributed approximately 5% to the overall axial capacity. However, if this process matches ideal elastic cavity expansion (Eq. 8-25) then the mean effective stresses will remain unchanged within the chalk mass, with $\Delta\sigma'_z=0$ and $\Delta\sigma'_r = \Delta\sigma'_\theta$. Any variations in the stress-regime in chalk-shaft interface may also be relatively small.

The natural cemented structure of the chalk allows states to exist to the right of the critical state line (i.e. point B) until the chalk is de-structured by large straining. However, by the end of the installation and equalisation stages the stress state in void ratio-mean effective stress space is on the denser-than-critical side, with a negative state parameter (ψ <0).

The interpretation shown on Figure 8-16 for the open-ended piles driven at St. Nicholas-at-Wade is not identical to that shown for the ICP tests Figure 7-32. The closed-ended ICPs were shown to develop higher stresses (σ'_1) beneath their tips during installation than were interpreted below the annuli of the driven piles. They also showed higher radial effective stresses, σ'_{ri} along the shaft at the end of installation than the driven piles, since the slower installation rates led to a greater degree of drainage and therefore consolidation around the pile shaft. The effective stresses measured on the ICPs tended to reduce slightly during equalisation. The radial effective stress measurements, σ'_{rc}, taken by the piles' surface stress transducers, reduced over time. The ICP radial effective stresses at failure under tension loading exceeded the end of equalisation values due to the effects of constrained dilation in the interface, reaching σ'_{rf} values which were close to those seen at the end of installation.

The final radial effective stresses on the ICPs were significantly lower than those interpreted on the shaft of the driven piles after full equalisation. The driven and jacked piles at the St. Nicholas-at-Wade site were installed into chalk of the same grade and density and allowed to equalise over similar time periods prior to static leading to tension failure using the same procedure. Both piles are made from similar materials with similar roughnesses, therefore the different ageing trends must be attributable to either i) the ICP's closed ends and/or ii) the piles' modes and rates of installation. The driven piles were installed one to two orders of magnitude more rapidly than the ICPs and no evidence was seen on their extraction of the remoulded and reconsolidated zone, which was found adhering to the driven piles.

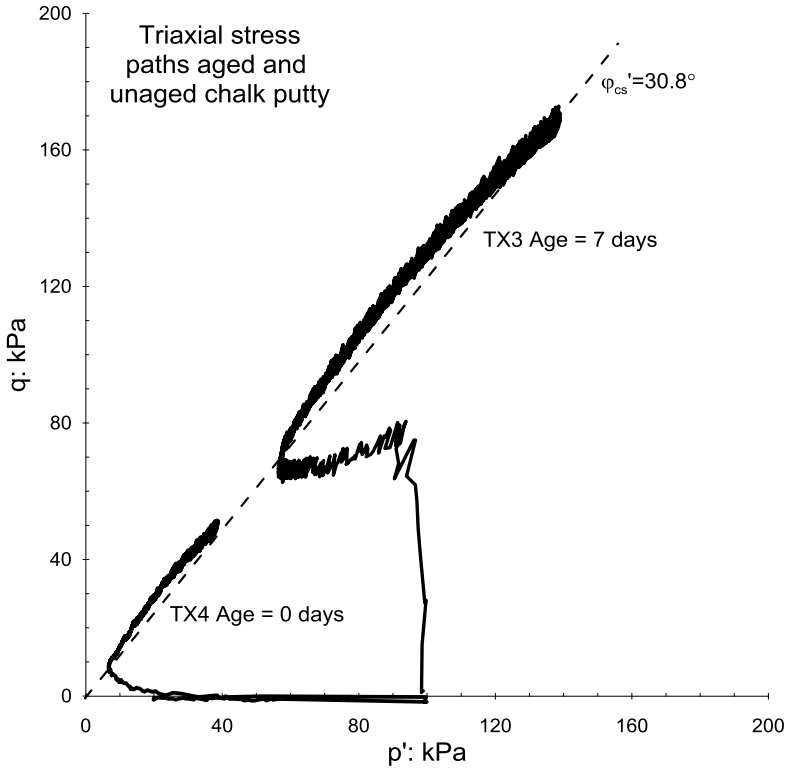


Figure 8-13: Typical effective stress paths from undrained triaxial tests to failure on remoulded chalk putty at 0 and 7 days (Doughty, 2016)

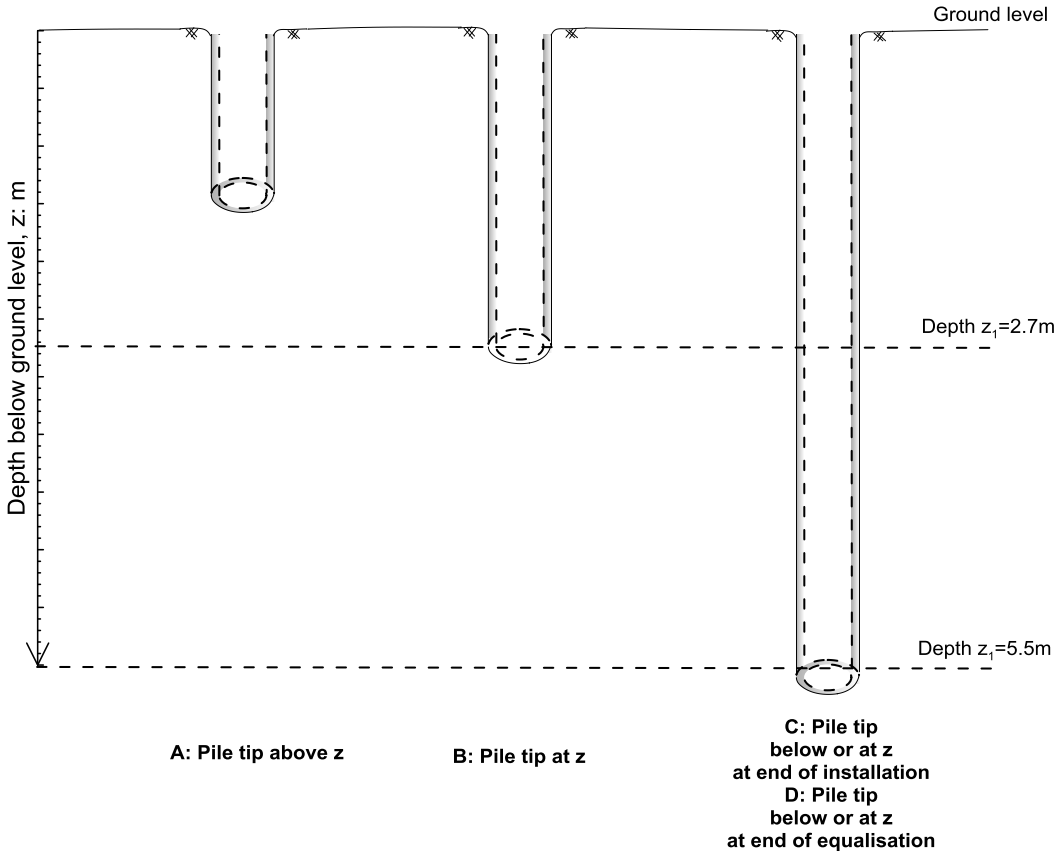


Figure 8-14 Illustration of stress states during driven pile penetration at a depth z

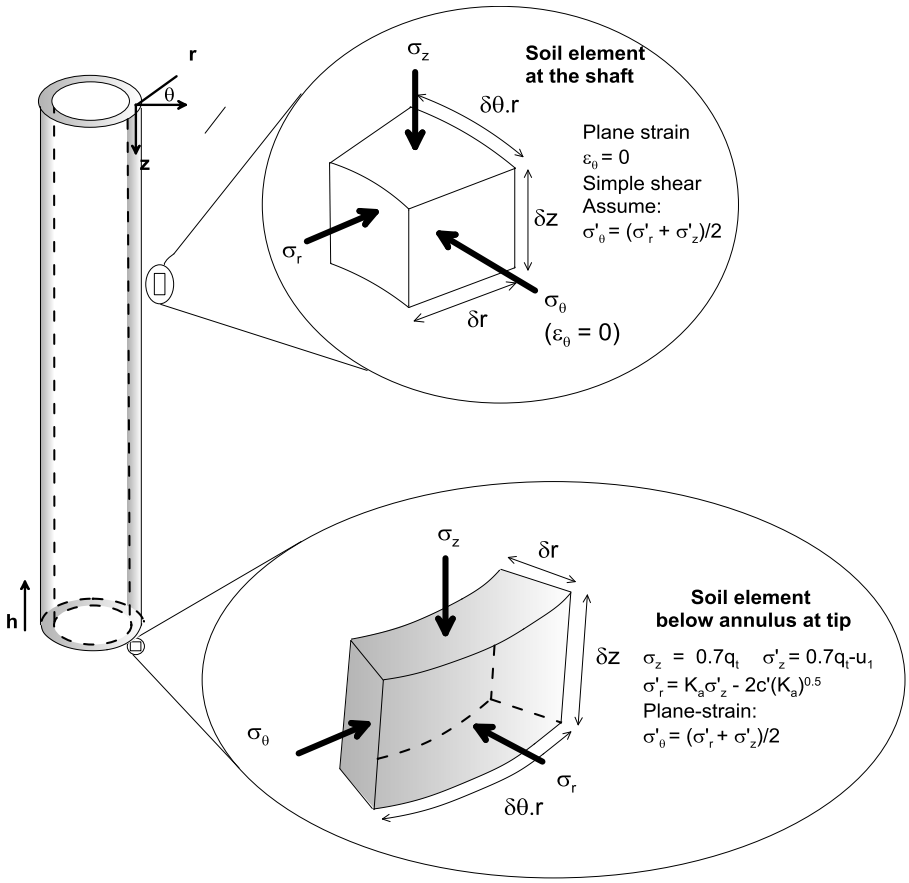


Figure 8-15 Schematic diagram of soil element at the shaft and below the steel annulus

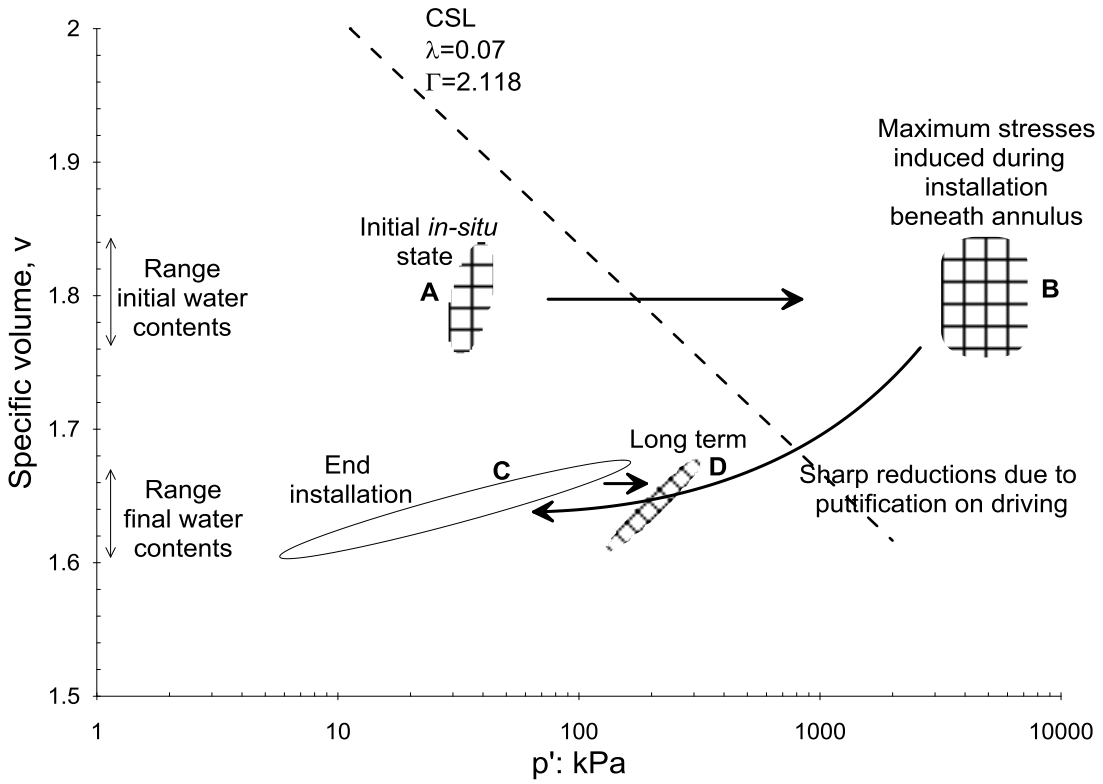


Figure 8-16: Illustration of stress states during installation, equalisation and ageing of driven piles

8.7 Adopted approach to estimate shaft resistance

Several approaches may be proposed to predict the shaft shear stresses applying at failure on displacement piles. The candidate proposals are discussed below and their relative merits contrasted:

a) Adoption of a single ultimate shaft resistance, τ_f along the whole pile length as is employed in the current CIRIA C574 design guidelines. Such a formulation would also have to take into account any beneficial time effects on capacity that are not considered by the current recommendations;

b) An alpha (α) type total stress or a beta (β) type effective stress approach which uses simple empirical correlations between shear stress at failure, τ_f and unconfined compressive or undrained shear strengths, or between shear stress at failure and overburden pressure, e.g.;

$$\tau_f = \alpha s_u \qquad 8\text{-}13$$

$$\tau_f = \beta \sigma'_{vo} \qquad 8\text{-}14$$

c) Modelling of local shaft failure using an effective stress Coulomb failure criterion which relates τ_f to the radial effective stress at the end of equalisation, σ'_{rc} and the ultimate angle of interface shearing resistance, δ'_{ult}, such that:

$$\tau_f = \sigma'_{rc} \tan \delta'_{ult} \qquad 8\text{-}15$$

The radial effective stresses could be related to the CPT cone resistance and the relative tip depth normalised by the pile radius, h/R as has been applied previously for sands (Lehane *et al.*, 1993, Chow, 1997, Jardine *et al.*, 2005a):

$$\sigma'_{rc} = \zeta q_t \left(\frac{\sigma'_{vo}}{p_a}\right)^{\kappa} \left(\frac{h}{R}\right)^{-\eta} \qquad 8\text{-}16$$

Neglecting the σ'_{v0} term in Eq. 8-16 leads to[1]:

$$\sigma'_{rc} = \zeta q_t \left(\frac{h}{R}\right)^{-\eta} \qquad 8\text{-}17$$

[1] The ICP-05 sand method's weak dependence on vertical effective stress, σ'_{v0}, is not included in this preliminary formulation due to the limited available dataset.

Parameter ζ is used to reflect the stress reduction from q_t to the radial effective stress immediately behind the pile tip. The h/R term and exponent η account for the observed rapid attenuation of radial effective stress above the pile base. For an open-ended tubular steel pile R is equal to the equivalent radius, $R^*=(R^2 - R_i^2)^{0.5}$):

$$\sigma'_{rc} = \zeta q_t \left(\frac{h}{R^*}\right)^{-\eta} \qquad 8\text{-}18$$

For $h/R \geq 8$.

Approach (a) and (b) were not considered further due to (i) the limitations of the α-type and β-type methods discussed in Chapter 3 and (ii) the Author's experiments on driven and jacked piles, described previously, which have shown that overall and local shaft capacities are sensitive to relative tip depth, h, variations in chalk properties with depth and the interface angle of shearing resistance, which cannot be captured using either of these approaches.

Approach (c) was considered the most appropriate since (i) the ICP pile tests described in Chapter 7 demonstrated that local radial effective stresses rise and fall with, and so follow the same trends as, cone resistance with depth, (ii) the analysis of the driven pile tests in Chapter 5 and 6 indicated strong dependence of the local shaft stress on relative tip depth (h/R or h/R*) and (iii) the ICP tests in chalk showed that local shaft failure follows an effective stress Coulomb law with stress ratios at failure similar to those seen in interface ring shear tests.

The parameters ζ and η in Eq. 8-18 which formulate the ICP sand method (Jardine *et al.*, 2005a) were obtained originally by Lehane *et al.* (1993) and Chow (1997) using similar instrumented pile tests to those described in Chapter 7 and then validated against an independent database of high quality instrumented static pile load tests. The appropriate parameters for use to predict short and long-term radial effective stresses in chalk require calibration before Eq. 8-15 to 8-18 can be used to predict the shaft stresses applying in chalk and the overall shaft capacity.

8.8 Increases in axial shaft capacity with time

The Author's static and dynamic pile tests described in Chapters 5, 6 and 7 confirmed the strong beneficial effects of time on shaft capacity which were also evident in the limited database of results described in Chapter 3. The magnitude of pile set-up observed in the chalk layers at Wikinger is similar to that reported in comparable layers at the onshore SNW test site in tests conducted on "virgin" piles. Tests at the latter site by Ciavaglia *et al.* (2017a) indicated

comparable, although more marked, increases in shaft capacity over similar time periods. The similarities in set-up trends between the tests conducted in saturated chalk at the (saline) offshore and (fresh-water) onshore sites suggests that the set-up trends are not dominated by water salinity.

Although the ultimate magnitudes of set-up are similar, Figure 8-17 shows that the capacity gain with time in chalk occurred at a far higher rate at Wikinger than was observed in the Author's static tests at the St. Nicholas-at-Wade site and in independent tests reported by Ciavaglia *et al.* (2017a). In those tests, time for 50% of the ultimate set-up to occur, T_{50}, appeared to increase with pile diameter, being around 27 days for the Author's 139mm diameter pile tests and 105 days for the 762mm diameter piles reported by Ciavaglia *et al.* (2017a). The Wikinger trends for larger pile diameters (1.37 to 3.7m) indicated much lower T_{50} values, which fell well below one hour. As argued below, this is most probably due to the Wikinger chalk's closed system of fractures. However, it is worth recalling that the Wikinger set-up trends are based primarily on dynamic pile tests which are subject to more uncertainty than static tests.

A hypothesis was presented in Chapter 6 to explain the set-up seen at the St. Nicholas-at-Wade test site, involving pore pressure dissipation which can lead to a reduction in void ratio and possibly relaxation of the surrounding radial effective stresses. The remoulded annulus formed around the pile reduces in volume as it consolidates after puttification leading to low shaft stresses developing, even after pore pressures dissipate, and creating an arching system outside the annulus. Strength gains due to consolidation are supported by the triaxial tests on chalk putty described in Section 5.6.5, which showed significant reductions in void ratio and increases in undrained shear strength post-consolidation. Over time, creep processes could allow the arching mechanisms generated by driving to relax and the radial effective stresses to increase and contribute to increases in capacity with time, through a mechanism similar to that suggested for sands by Jardine *et al.* (2006) and Jardine *et al.* (2013b). Relaxation of the arching mechanisms is likely to be more rapid for chalk masses with widely spaced tight fractures than those with an open and closely-spaced fracture system.

The more rapid rate of set-up seen at Wikinger following pore pressure dissipation may therefore be related to the differences in chalk grade and tightness of the chalk blocks *in situ*. At Wikinger, the fractures are closed or tight (and water filled) and spaced between 200-600mm (A1/A2), while at St. Nicholas-at-Wade the fractures are open to <3mm, air filled and

spaced between 60 and 200mm. The increases in capacity seen with time at both sites may also be attributable to, to a lesser extent:

(i) **Corrosion in the interface**: redox reactions at the interface could cause any shear surface formed during driving to migrate into the chalk mass, where shearing would have to develop under soil-soil conditions. It was argued in Section 8.5 that a high relative roughness exists between the interfaces of industrial steel piles and the silt-sized chalk grains that promotes chalk-chalk shearing even without any corrosion. Any further movement of the shear surface into the chalk mass could potentially produce an additional increase in shaft stress due to the increase in effective diameter (and effective surface area) as well as potentially greater radial dilation at failure;

(ii) **Internal re-cementing of chalk putty**: precipitation and re-cementation of calcite grains at grain contacts could act to increase the chalk's shear strength over time. However, the fall cone tests reported on samples of Wikinger putty chalk in Section 5.6.5 indicated that s_u increased only modestly due to thixotropy, far less than required to explain the large increases in shaft resistances seen in the field;

(iii) **Changes in interface shear properties with time due to cementing**; Chan (2017) investigated these effects using samples of chalk putty from the SNW site, as discussed in Section 6.4.6. The tests indicated increases in δ'_{peak} and δ'_{ult} of 2.6 and 2.9° respectively, when compared to a similar test on an unaged sample at the same stress level using the same interface material (see Figure 6-20). Considering, Eq. 8-15, an increase in δ'_{ult} of 2.9° (from 31.6 to 34.5°) could increase the shear stress at failure, τ_f by approximately 10%.

It is now appreciated that current CPT-based design methods for piles driven in sands have to define capacity within a particular time range after driving (e.g. Jardine *et al.*, 2005a, Lehane *et al.*, 2005b) and do not, at present, consider the short-term and long-term fully equalised radial effective stress cases separately. In the same way, static capacity design methods for clays are only considered applicable after all installation pore pressures have dissipated. Soil resistance to driving is generally addressed by different procedures to static long-term calculation methods. Consideration must therefore be given in any adopted approach to predict radial effective stresses in chalk to the markedly different magnitudes of stresses which are observed in the short-term, during pile driving, and in the long-term after full equalisation has occurred.

8.9 Short-term (driving) radial effective stress

8.9.1 Relationship between radial effective stress and cone resistance

The Author's instrumented ICP tests described in Chapter 7 and in earlier studies by Hodges and Pink (1971) and Bustamante and Gianeselli (1982) have shown that the profiles of local shaft stresses developed at failure in low-medium density chalk are related to the trends in local CPT cone resistance. Figure 8-18 shows, as an example, the stationary radial effective stresses measured at the *leading* instrument (SST1) during installation of the jacked highly instrumented pile ICP02 (Chapter 7). Also shown, plotted on a secondary axis, are the trends in cone resistance from the most relevant *in-situ* cone penetration test (PCPT4). During installation, elements close the pile shaft reach failure, following an effective stress Coulomb law. The stationary radial effective stresses were measured at the end of each installation push, immediately prior to a stress reversal, as shown schematically on Figure 7-17. The shapes of the cone resistance profiles developed in structured chalk are also likely to reflect local variations in the key factors that affect mass shear strength and density including; intact dry density, degree of cementation, fracture frequency, fracture infill and fissuring. The cone resistance traces appear to be affected by aspects of the above factors in ways that mirror how the stationary radial effective stresses vary with depth, for any fixed value of h/R or h/R*.

The σ'_{rs}/q_t ratios observed in the Author's experiments in chalk were shown in Chapter 7 to be significantly lower than those applying in silica sands by Lehane *et al.* (1993) and Chow (1997) and to fall closer to values reported in calcareous sands by Lehane *et al.* (2012a). The low ratios applying to both the chalk and calcareous sands are related to the high compressive stresses during driving beneath the pile base causing de-structuration in both cases that leads to severe reductions in radial effective stresses immediately behind the pile tip.

8.9.2 Interface shear behaviour

Laboratory interface ring shear tests were conducted at each of the test sites considered, employing the expected normal effective stress levels and using mild steel interfaces with similar roughness values to those of the driven piles (R_a generally between 10 and 15 μm). The values of δ'_{ult} obtained at Wikinger by Fugro (2013) ranged from 32 to 34° at normal stress levels between approximately 100 and 300kPa and a mean value of 33° is adopted in the treatment that follows. The interface ring shear tests run by the Author and by Chan (2017) for St. Nicholas-at-Wade, described in Chapter 6, demonstrated that δ'_{ult} ranged from 31.6° to 32.8°

at a normal stress level of 200kPa, and a value of 32° is adopted. At Fleury-sur-Andelle only the soil-soil angle of shearing resistance, φ' (=28°) is reported. In the absence of other information a value of $\delta'_{ult} = \varphi'$ is assumed in this case for the primarily structureless chalk encountered.

8.9.3 Reductions in stress with distance from the pile tip

The review of available pile test data described in Chapter 3 and the supplementary static and dynamic tests conducted by the Author on short and long driven piles showed that local shaft effective stresses reduce systematically with increasing pile length or pile penetration into chalk. Strain gauge measurements from static tests at failure and back analysis of dynamic pile tests showed that local shaft effective stress depends critically on the relative pile tip depth, h.

Back analysis of pile driving records from two offshore wind farm sites was carried out as part of two MSc projects at Imperial College in Summer 2017, aided by the Author (Ebensperger, 2017, Esper, 2017). The studies employed the Allwave-PDP software program (Allnamics, 2015) which predicts pile driveability using one dimensional wave equation theory and utilises the Smith soil resistance models described in Chapter 4. The aim of the analyses was to help develop a new formulation to predict soil resistance to driving in chalk. Driveability analyses were described in Section 4.4. The driveability analyses in this case followed the following approach:

1. Case histories were selected from each site where there were no interruptions during pile driving. The blow count profiles and q_t profiles were then determined for each case;
2. The hammers were simulated by applying characteristics that represented the particular hammers adopted in the piles' installation, employing signature traces available in library files built into Allwave-PDP, with modifications to account for the actual input energy;
3. The input shaft and base resistance were varied in the soil resistance models until a good match was obtained between measured and calculated blow counts;
4. In cases where sand or clay were encountered above the chalk, their resistance to driving was modelled using the Alm and Hamre (2002) method discussed in Section 4.9.3. The dynamic "Smith" model parameters used during the studies were those recommended by Alm and Hamre (2002) for sands and clays as given in Table 8-3;

5. Soil resistance to driving in the chalk was calculated continuously for each penetration assuming that Eq. 8-18 applies. This expression was implemented into a beta (development) version of the Allwave-PDP program by Middendorp (2016);
6. The parameters, ζ and η along with the lower limit on h/R* to calculate stress, σ'_{ri} (Eq. 8-18) were varied in the analysis, within reasonable bounds, until a good fit was obtained between the measured and calculated blow counts;
7. In the chalk, the Alm and Hamre (2002) sand parameters were adopted with the additional inclusion of a non-linear dependence of soil strength on pile velocity, see Section 4.7, applying Eq. 4-40 for β_s=0.2. The latter was adopted to be consistent with the Author's signal matching analyses for the Wikinger piles, described in Chapter 5.

Esper (2017) back analysed the blow counts from ten 4.1 to 4.7m diameter monopiles installed into low density Grade B3-B5 chalk at the Thanet offshore windfarm in the Southern North Sea. Ebensperger (2017) analysed the results from eight 2.7m diameter Wikinger production piles founded primarily in low-medium density Grade A1/A2 Maastrichtian chalk. For the monopiles, the parameter ζ, used in Eq. 8-18, was adopted as 0.031 (reflecting a shear stress reduction behind the tip of $\approx 5\% q_t$ for δ'_{ult} of 32°) and the resulting best fit for parameter η fell between 1.0 and 1.2 with a h/R* lower limit equal to 8. Ebensperger's (2017) analysis of the 2.7m diameter Wikinger piles, installed in low-medium density Grade A1/A2 chalk adopted the same value for ζ and led to lower best fit values of 0.8 to 1.0 for parameter η, along with the lower h/R* limit again equal to 8. The base capacity was input as a proportion of q_t in both sets of analyses with the ratio q_b/q_t varying from 0.4 to 1.0.

Table 8-3: Quake and damping parameters used in the drivability analysis (Alm and Hamre, 2002)

	Shaft		**Toe**	
Pile	**Quake, $q_{k,s}$ (mm)**	**Damping J_s (s/m)**	**Quake $q_{k,b}$ (mm)**	**Damping J_b (s/m)**
Sand	2.5	0.25	2.5	0.5
Clay	2.5	0.25	2.5	0.5
Chalk	2.5	0.25	2.5	0.5

8.9.4 Preliminary correlation for soil resistance to driving

The preliminary driveability studies by Esper (2017) and Ebensperger (2017) suggested that the rate of degradation in local (driving) shaft stresses with increasing relative tip depth, h, increases with either (or both) pile diameter and decreasing chalk density. The signal

matching analysis of the Wikinger dataset described in Chapter 5 allows a further examination of these effects, in this case for piles of varying diameter driven in chalk of the same grade and density, thereby isolating the effect of chalk grade (Figure 5-37). Signal matching offers a more representative means of determining changes in shaft capacity during installation than driveability back analyses since a single signal obtained during one blow is matched iteratively, as opposed to a driveability analysis where the operator attempts to match the measured and calculated blow count profiles. The signal matching carried out by the Author also employed the software code IMPACT (Randolph, 2008), the relative benefits of which were discussed in Chapter 4.

Figure 8-19 plots the radial effective stresses interpreted as applying at the end of installation against h/R*, obtained from signal matching by the Author using IMPACT. The data shown on Figure 8-19 were obtained in the following manner:

- For each signal match carried out, the resulting values of $\tau_{s,d}$ were converted to initial radial effective stresses at failure, σ'_{ri} taking $\sigma'_{ri} = \tau_{s,d} / \tan\delta'_{ult}$;
- The resulting σ'_{ri} values are normalised by the average corrected cone resistance, q_t at the relevant depth and plotted against h/R*.

The available results for shaft capacity at the end of driving are grouped by diameter on this plot which includes (a) the 2.7 and 3.67m diameter production piles installed at Wikinger (b) the 1.37m diameter Wikinger trial piles and (c) the 0.139m diameter piles installed by the Author at St. Nicholas-at-Wade. The power law relationship given in Eq. 8-18, is also shown on these figures with the parameters ζ and η varied by the Author to achieve matches to each dataset.

The best fit ζ and η parameters found at four pile scales from the Author's analyses shown on Figure 8-19 are summarised in Table 8-4 as set A1, along with the pile diameter and diameter-to-wall thickness ratio of the tests considered. The lower limit to h/R* was selected as 6, to better replicate the shaft resistances observed in static and dynamic tests close to the pile base, although it is possible that a still lower value may apply. Also shown are the ratios of calculated to measured shaft capacity (Q_c/Q_m) obtained by substituting each diameter-dependent set of parameters shown on Figure 8-19 into Eq. 8-18, and integrating Eq. 8-15 over the pile shaft. The mean (μ) and standard deviation (stdev) of the Q_c/Q_m values are also included. Good agreement is observed between the calculated and measured capacities for the

majority of the tests with the exception of test WK43-2, which exhibited an approximately 40% higher capacity than expected at the end of pile driving

The best fit parameters listed in Table 8-4 as set A1 are based primarily on pile diameters which range from 0.139m to 3.7m. During pile driving the chalk putty surrounding the pile controls the behaviour, which lies on the wetter-than critical side (Figure 8-16) therefore no interface dilation (described in Section 8.5) is likely to occur. The correlation for short-term radial effective stresses *during driving* will therefore take the form:

$$\tau_{fi} = \sigma'_{ri} \tan\delta'_{ult} \qquad 8\text{-}19$$

$$\sigma'_{ri} = \zeta q_t \left(\frac{h}{R^*}\right)^{-\eta} \text{ For } h/R \geq 6. \qquad 8\text{-}20$$

where τ_{fi} are the shear stresses during driving and qt is averaged over 300mm penetrations.

As evident in Table 8-4, and also seen on Figure 5-37, the rate of degradation appears to reduce with pile diameter, indicating that the geometrical system applying in the field is not fully captured by the simple characterisation involving the equivalent radius R*, whose formulation includes the pile wall thickness. This is evident by adopting a single set of parameters for all pile diameters, based on a best fit power law relationship through all of the data, which increases the mean Q_c/Q_m values and introduces a skew with diameter (Set A2 in Table 8-4).

To obtain a single expression for σ'_{ri}, that covers a range of diameters, it appears to be necessary to introduce a further geometrical factor into Eq. 8-20. Recalling from Section 6.5.4 that the thickness of the zone of puttified chalk depends primarily on pile wall thickness, t_w, it appears logical to investigate whether any systematic relationship exists with the best fitting ζ and η parameters and the non-dimensional wall thickness ratio, D/t_w. Figure 8-20 plots the variation in best fitting parameter η (from Table 8-4) against D/t_w. Also shown are both a power law and exponential function fitted to the data. A range of D/t_w of between 17 and 67 was investigated. Use of an exponential function to capture how η varies modifies Eq. 8-20 to:

$$\textbf{A3:} \quad \sigma'_{ri} = 0.031 q_t \left(\frac{h}{R^*}\right)^{-0.682 e^{0.0042 \frac{D}{t_w}}} \qquad 8\text{-}21$$

Adopting the power law relationship between η and D/t shown on Figure 8-20 leads to the relationship:

A4: $$\sigma'_{ri} = 0.031 q_t \left(\frac{h}{R^*}\right)^{-0.481\left(\frac{D}{t_w}\right)^{0.145}} \quad 8\text{-}22$$

The resulting η parameters obtained using Eq. 8-21 and 8-22 are summarised in Table 8-4 as options A3 and A4, respectively. Both parameter sets can be seen to lead to an equally promising match between the measured and calculated values. The simpler option A4, which is recommended for ease of calculations, offered a Q_c/Q_m mean of 0.97 and a standard deviation of 0.16. Figure 8-21 plots the calculated profiles of shaft resistance obtained using Eq. 8-22 (Option A4) along with the measured values from the signal matching results. Good agreement is observed between the measured and calculated profiles of shaft shear stress. Eq. 8-22 may be combined with Eq. 8-19 to predict soil resistance to driving for driveability assessments.

Table 8-4: Assessment of proposed correlation for end of driving shaft resistance for open-ended tubular steel piles

	h/R*	A1 – best fit parameters			A2 - single expression			A3 – exponential			A4 – power law		
Test	≥	ζ	η	Q_c/Q_m[1]	ζ	η	Q_c/Q_m[1]	ζ	η	Q_c/Q_m[1]	ζ	η	Q_c/Q_m[1]
OSS-C2_DPT_EOD	6	0.031	0.90	1.05	0.023	0.73	1.20	0.031	0.88	1.04	**0.031**	**0.87**	**1.13**
OSS-C4_DPT_EOD	6	0.031	0.90	1.07	0.023	0.73	1.22	0.031	0.88	1.06	**0.031**	**0.87**	**1.15**
WK11-A_DPT_EOD	6	0.031	0.90	0.93	0.023	0.73	1.02	0.031	0.90	0.95	**0.031**	**0.88**	**0.93**
WK43-1_DPT_EOD	6	0.031	0.77	1.01	0.023	0.73	0.83	0.031	0.79	0.96	**0.031**	**0.80**	**0.90**
WK43-2_DPT_EOD	6	0.031	0.77	0.71	0.023	0.73	0.58	0.031	0.79	0.67	**0.031**	**0.80**	**0.63**
WK70-1_DPT_EOD	6	0.031	0.77	1.03	0.023	0.73	1.13	0.031	0.79	0.99	**0.031**	**0.80**	**0.98**
WK70-2_DPT_EOD	6	0.031	0.77	1.06	0.023	0.73	1.17	0.031	0.79	1.01	**0.031**	**0.80**	**1.01**
DP6_DPT_EOD[2]	6	0.031	0.75	0.93	0.023	0.73	0.73	0.031	0.73	0.99	**0.031**	**0.72**	**1.02**
Mean				0.97			0.99			0.96			**0.97**
Std Dev				0.12			0.24			0.12			**0.16**

1. Shaft only and proportion in chalk only
2. Average of three dynamic tests at EoD

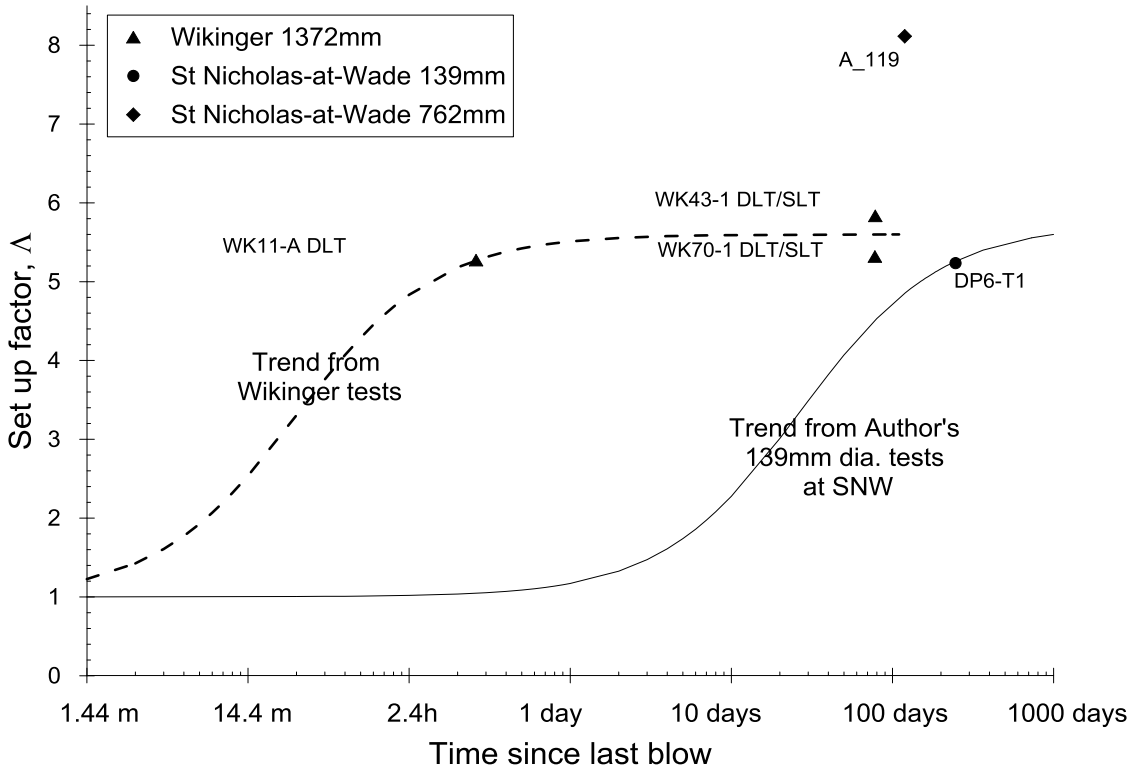


Figure 8-17: Set-up factors versus time since end of driving for three sets of tests

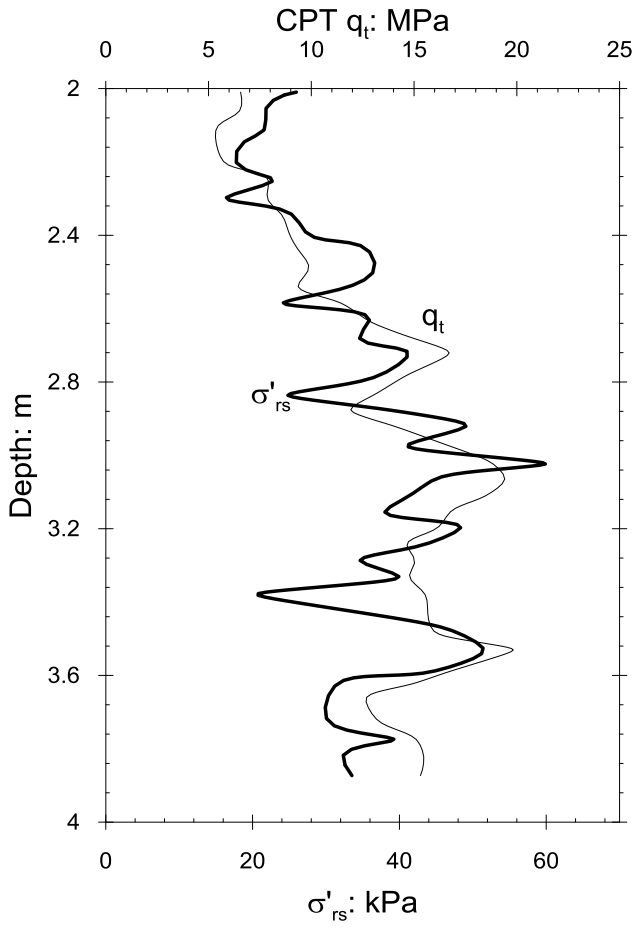


Figure 8-18: Illustration of variation in CPT cone resistance with radial effective stress (SST1 ICP02)

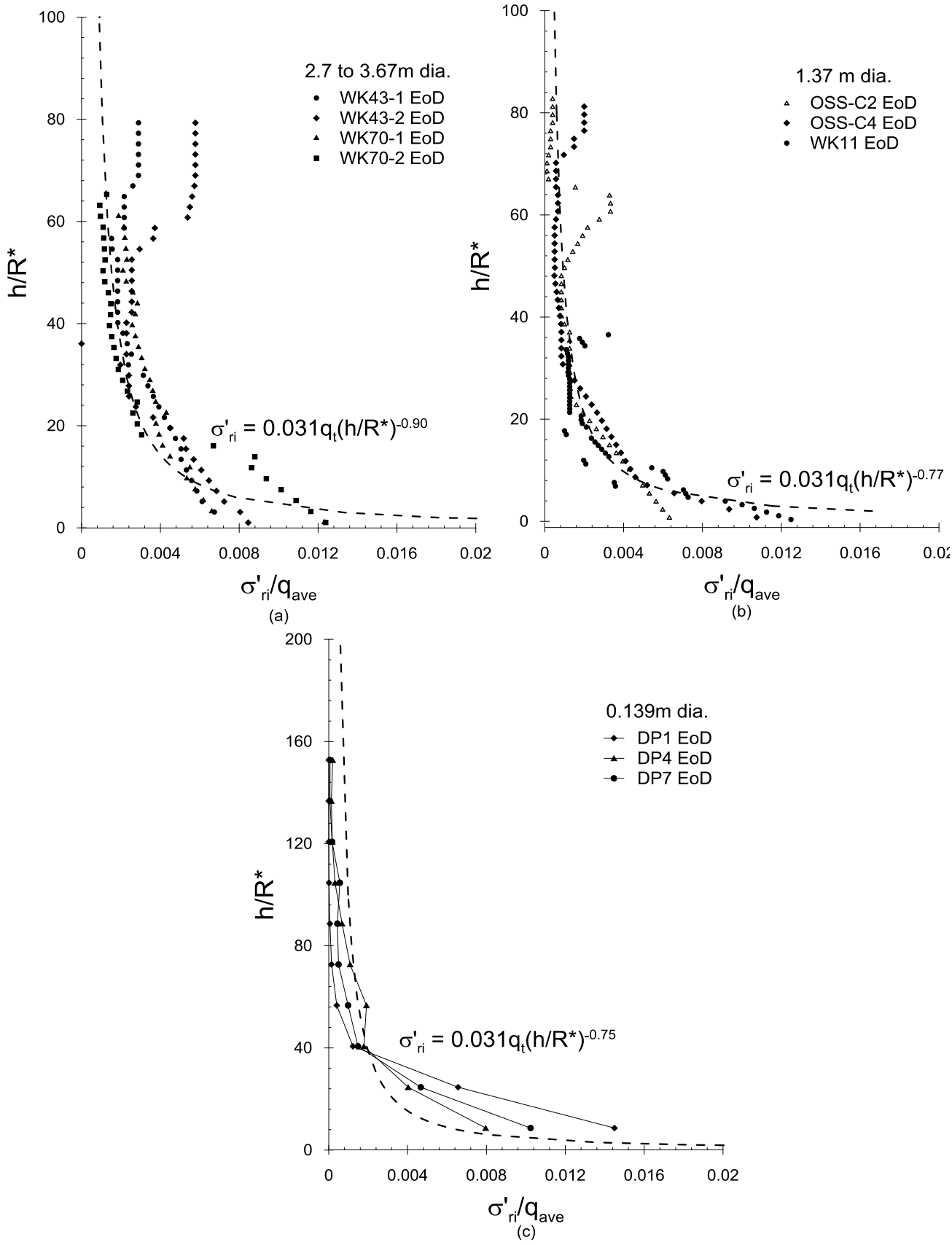


Figure 8-19: Normalised radial effective stresses versus h/R* at end of driving for (a) Wikinger 2.7 to 3.67m diameter piles (b) Wikinger 2.37m diameter piles (c) SNW 0.139m diameter piles

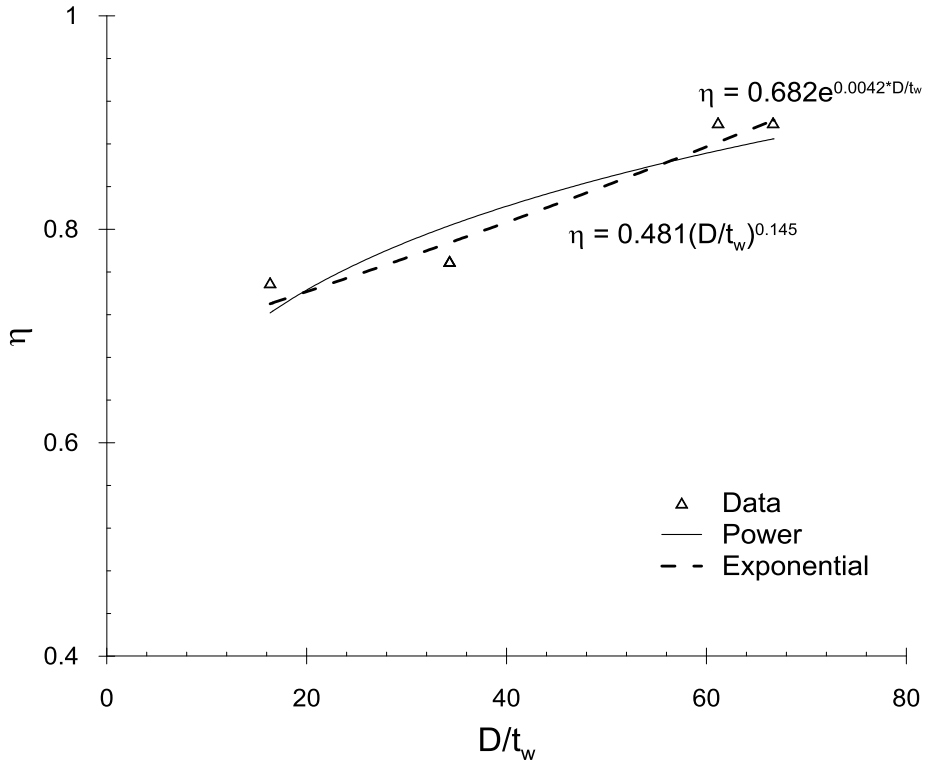


Figure 8-20: Relationship between parameter η and diameter to wall thickness ratio

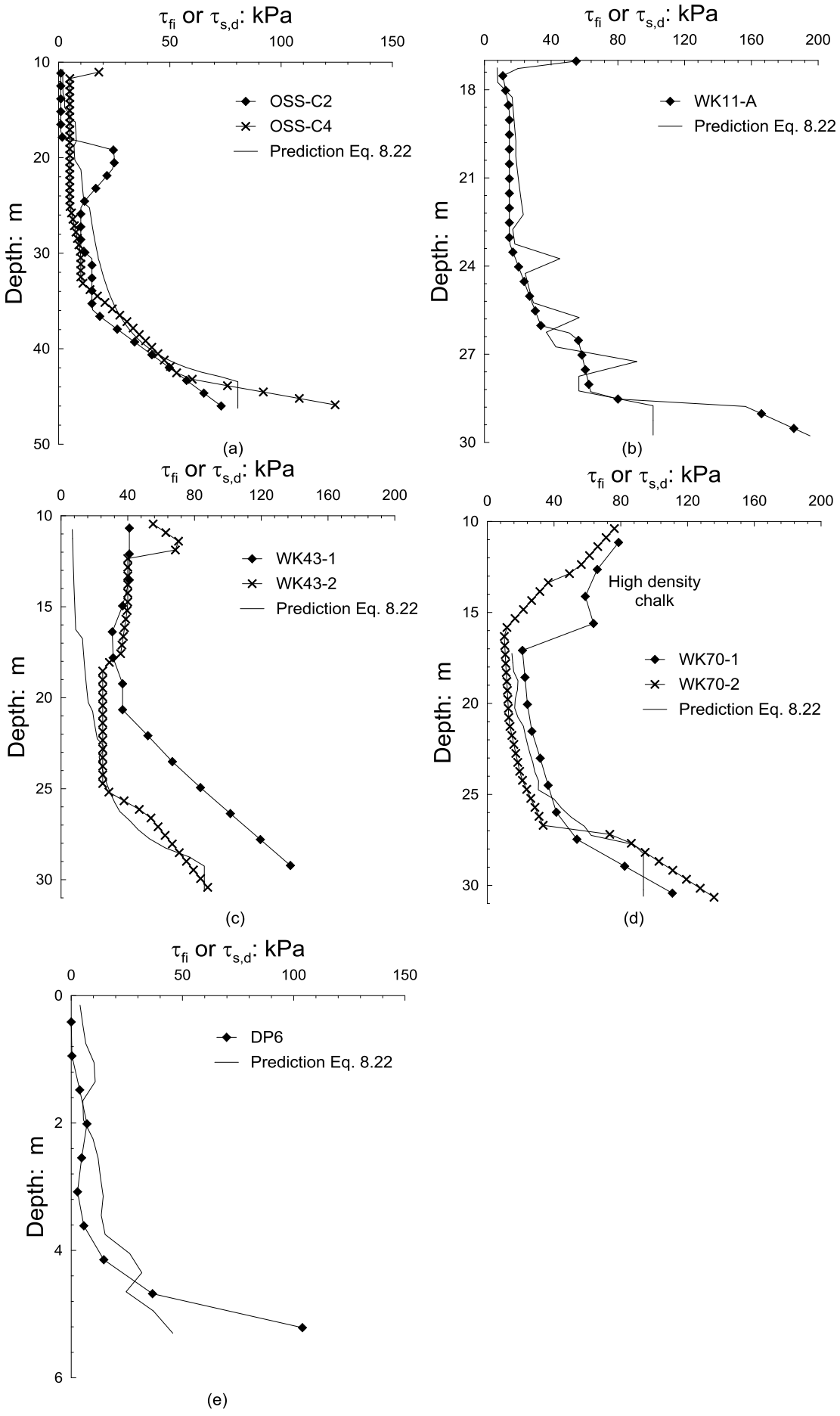


Figure 8-21: Measured and calculated profiles of shaft resistance at EoD (calculated using Eq. 8-22)

8.10 Equalised radial effective stress

Analysis of driving monitoring was employed in Section 8.9 to develop expressions for predicting the pile exterior shaft radial effective stress distribution applying during driving. This section applies a similar approach to examine the fully equalised shaft radial effective stress distributions from strain gauge measurements made during static tests and from the results of signal matching analysis of dynamic restrike tests on piles whose capacities had increased and at least partially stabilised over time after driving.

8.10.1 Choice of equalisation period

The offshore static and dynamic tests conducted at Wikinger on 1.37m diameter open-ended tubular steel piles were carried out at ages of between 77 and 108 days (or 2.5 and 3.5 months) after driving. The Author's static tests on similar 139mm diameter open-ended piles at the onshore St. Nicholas-at-Wade site were conducted on similarly separate, previously untested, piles at 10, 106 and 246 days after driving. The static tests reported at the same site by Ciavaglia *et al.* (2017a) on 762mm diameter piles were carried out at a maximum pile age of 119 days after several phases of prior testing (see Section 3.5.1). The long-term stabilised set-up trends with time from the three sets of pile tests were shown previously on Figure 8-18.

In order to develop a correlation for the radial effective stresses applying on the piles in the long-term, it is necessary to choose tests conducted at sufficient ages to allow set-up and ageing to have stabilised towards an equilibrium state. The ultimate set-up achieved by the Wikinger piles and the 139mm diameter piles in SNW were of similar magnitude, however the rates of capacity gain with time varied significantly between the two sets of tests (Section 8.8). The set-up observed at Wikinger in dynamic tests was, on average, 50% complete 29 minutes after the end of driving and apparently fully complete within the first day, taking the reference time, t_{ref} equal to zero, or the last driving blow. In contrast, the Author's tests at St. Nicholas-at-Wade on 139mm diameter driven piles reached 50% of their set-up 27 days after installation and the process appeared to be 83% complete after 100 days.

The static re-tests reported by Ciavaglia *et al.* (2017a) on 762mm diameter driven piles did not appear to reach a final equilibrium, with set-up still increasing between tests conducted 50 and 119 days after driving. However, the set-up trends observed in these tests are not fully comparable, since the reference point adopted to assess capacity was a restrike test conducted 2 hours after installation, which may itself have affected the piles' ageing behaviour. With the

exception of this test, set-up was thought to be at least 83% complete in the tests used to develop the correlations for long-term radial capacity, which are summarised in Table 8-1.

8.10.2 Preliminary correlations for equalised radial effective stresses

As argued in Section 8.6, consolidation occurred during pile driving leading to stress states on the denser side of critical (Figure 8-16) and therefore the long-term radial effective stresses will include a contribution from the constrained interface dilation mechanism to overall capacity. The dilation component, $\Delta\sigma'_{rd}$ must therefore be included as an additional radial effective stress component which will have a significant effect for small diameter piles only. The correlation for short-term static radial effective stresses will therefore take the form:

$$\tau_f = (\sigma'_{rc} + \Delta\sigma'_{rd})\tan\delta'_{ult} \quad 8\text{-}23$$

$$\Delta\sigma'_{rd} = \frac{4G\Delta r}{D} \quad 8\text{-}24$$

where σ'_{rc} is the radial effective stress applying after equalisation. Figure 8-22 shows the trends in σ'_{rc}/q_t against h/R* from strain gauge measurements on the 762mm diameter pile at St Nicholas-at-Wade (Test A_119) 119 days after driving and from signal matching of restrike tests at Wikinger (on 1.37m to 2.7m diameter piles) between 6 hours and 78 days after installation. As in Section 8.9, the signal matching of the Wikinger tests utilised the IMPACT software. The long-term radial effective stresses developed along the pile shaft can be seen to reduce with increasing pile tip depth. Power law trends with h/R*, of a similar form to Eq. 8-22, appear to apply. Comparison of Figure 8-19 and Figure 8-22 confirms that the radial effective shaft stresses applying after equalisation and ageing are significantly higher than in the short-term driving case, with average σ'_{rc}/q_t ratios amounting to five to six times the corresponding σ'_{ri}/q_t values.

In order to develop correlations for σ'_{rc}, two distinct approaches were investigated:

B1: Apply a set-up factor, Λ to the power law shown in Eq. 8-22 for the short-term radial effective stresses, σ'_{ri} applying after installation to obtain σ'_{rc}:

$$\sigma'_{rc} = \Lambda \text{ x } 0.031 q_t \left(\frac{h}{R^*}\right)^{-0.481\frac{D}{t_w}^{0.145}} \quad 8\text{-}25$$

Where the best fitting value of Λ for the Author's database is equal to 5.6.

B2: Fit a new power law of the form shown in Eq. 8-4 through the data from the four long-term tests. As shown on Figure 8-22, this approach leads to a relationship that has the

same form as Eq. 8-22, but with higher ζ value and a simpler (and lower) η parameter pair:

$$\sigma'_{rc} = 0.081 q_t \left(\frac{h}{R^*}\right)^{-0.52} \quad 8\text{-}26$$

No tendency for the rates of degradation of σ'_{rc}/q_t with h/R* to vary with D/t_w is apparent in the equalised radial effective stresses shown on Figure 8-22, which considers piles of between 762mm and 2.7m in diameter. As a result, Option B2 appears to be the most appropriate, which assumes that the diameter-to-wall thickness ratio is accounted for adequately through the use of R* to normalise h.

Both methods (B1 and B2) are used to calculate the capacity, using Eq. 8-23 integrated along the shaft, of the four available long-term static tests (diameters between 0.139 and 1.37m) and the results of three long-term dynamic tests (diameters between 1.37 and 2.7m) with the results summarised on Table 8-5. When integrated over the full shaft area via Eq. 8-15, Option B2 leads to a good prediction of the measured shaft capacity applying after equalisation for all four tests with a mean Q_c/Q_m of 1.0 and a standard deviation of 0.11 and therefore this appears, at this stage, to be the more appropriate formulation. The results reflect primarily tests on piles with diameters of 762mm or greater, where the contribution of dilation to overall capacity is less than 0.5%. A summary of the adopted correlations is provided in Table 8-6.

Table 8-5: Assessment of proposed correlation for aged shaft resistance for open-ended tubular steel piles

			B1	**B2**
Type	**Test site**	**Age (days)**	**Q_c/Q_m**	**Q_c/Q_m**
Static	WK43-2_SLT[1]	78	0.78	**0.82**
	WK70-2_SLT[2]	77	0.84	**0.97**
	1_A119	119	1.40	**1.02**
	DP6_T1	206	1.38	**1.08**
Dynamic	WK11-A_DPT	0.26	0.93	**1.15**
	WK43-1_DPT	78	0.88	**0.92**
	WK70-1_DPT	77	1.15	**1.06**
Mean			1.05	**1.00**
Std Dev			0.26	**0.11**

1. Includes an ICP clay calculation in the overlying glacial till
2. Includes an ICP clay calculation in the overlying glacial till and takes q_t = 50MPa in the high density chalk/Danian Limestone encountered between 10 and 15mbsb in WK70

Table 8-6: Summary of preliminary proposed correlations for shaft resistance of displacement piles in chalk

Shaft capacity	$Q_s = \pi D \int \tau_f dz$
Local shear stress	
During driving	$\tau_{fi} = \sigma'_{ri} \tan\delta'_{ult}$
Long-term static loading	$\tau_f = (\sigma'_{rc} + \Delta\sigma'_{rd}) \tan\delta'_{ult}$
Ultimate angle of interface friction (measured in interface shear tests at the appropriate roughness)	δ'_{ult}
Local radial effective stresses	
During driving	$\sigma'_r = \sigma'_{ri}$
q_t is averaged over 0.3m intervals (Power, 1982)	$\sigma'_{ri} = 0.031 q_t \left(\frac{h}{R}\right)^{-0.481\left(\frac{D}{t_w}\right)^{0.145}}$
Long-term[1] q_t is averaged over 0.3m intervals (Power, 1982)	$\sigma'_r = \sigma'_{rc}$ $\sigma'_{rc} = 0.081 q_t \left(\frac{h}{R}\right)^{-0.52}$
Increase in local radial effective stress during pile loading	$\Delta\sigma'_{rd} = \frac{G\Delta r}{D}$ Δr = 0.5 μm or ≈ $D_{50}/20$ $G = G_{max}$
Open-ended tubular piles	$R^* = \sqrt{R^2 - R_i^2}$ $R_i = R - t_w$

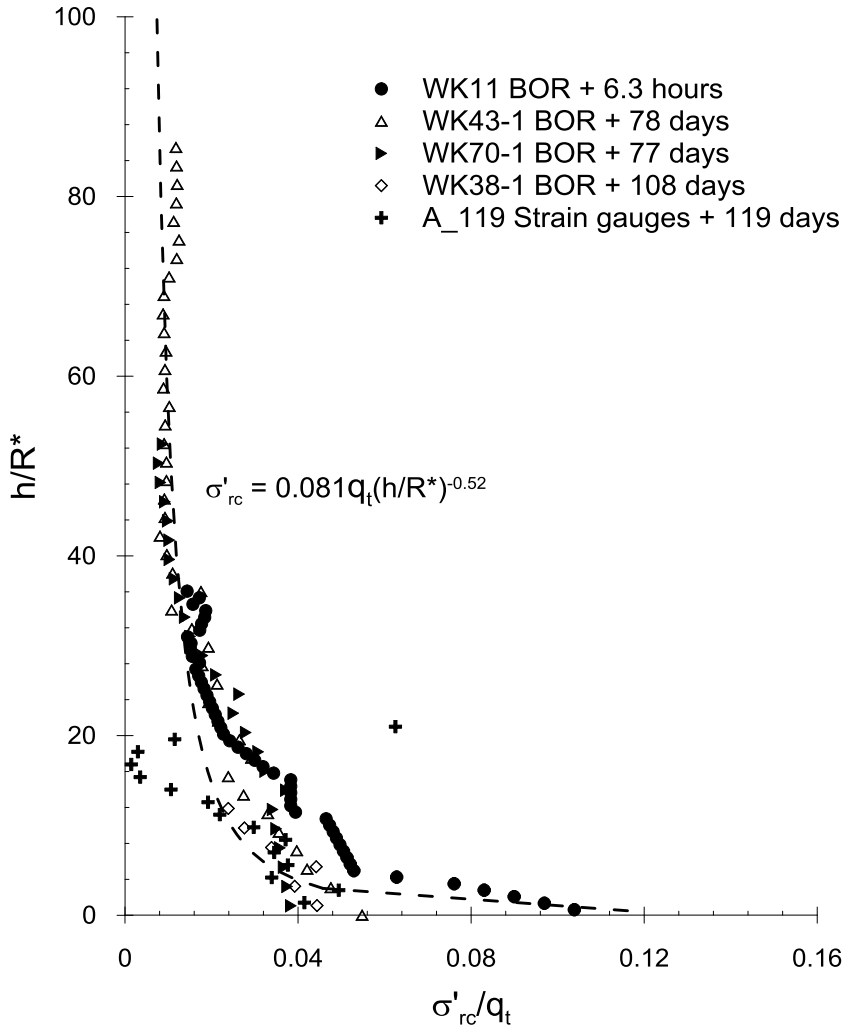


Figure 8-22: Normalised radial effective stresses versus h/R* at beginning of restrike from available dataset

8.11 Predictions of shaft capacity using existing methods

The advantage of applying the new correlations for shaft capacity over the current industry standard methods was assessed by comparison with both short and long-term measured shaft capacity. The two methods considered are the CIRIA PG6 *Piling in Chalk* guide (Hobbs and Healy, 1979) and the CIRIA C574 *Engineering in chalk* guidelines; Lord *et al.* (1994). The methods were discussed in detail in Chapter 3. The CIRIA PG6 method uses a traditional β-approach:

$$\tau_f = \sigma'_{vo} K \tan\delta \qquad 8\text{-}27$$

Hobbs and Healy (1979) recommend a K value of approximately 0.8 and a relatively low δ value of 20° giving $\tau_f \approx 0.291\sigma'_{vo}$.

The CIRIA C574 recommendations superseded the effective stress based PG6 approach and placed pile types into two classes based on the likelihood of penetration into chalk of different densities and grades. For small displacement (*Type PS*) piles, the authors recommended adopting an ultimate shaft resistance of 120kPa in high density Grade A chalk, and 20kPa in all other densities and grades, reducing to 10kPa if there is a possibility that the pile may "whip" during installation e.g. with flexible H piles. Neither of the CIRIA design methods distinguish between short-term and long-term, equalised capacity.

Both of the CIRIA methods were used to predict the end of driving, short-term capacity and the long-term equalised capacity of the available tests, as summarised on Table 8-7. The following points are noted in relation to the existing methods:

- The PG6 method is highly non-conservative when compared to the short-term capacity measured in the dynamic tests, with Q_c/Q_m ratios of 1.22 to 3.71 with a mean of 2.17;
- The C574 method is conservative when compared to the short-term capacity with Q_c/Q_m ratios of between 0.45 and 0.94 with a mean of 0.68. The method provides good short-term predictions for the longest piles in the set, where h/R* effects are most significant and reduce the τ_f values to low values that hardly increase with depth;
- Both the PG6 and C574 methods are highly conservative when compared to the long-term equalised capacity, with mean Q_c/Q_m ratios of 0.26 and 0.12 respectively. The PG6 method provides slightly less conservative predictions for long piles where τ_f increases in proportion to the effective overburden stresses and compensates to some degree for an under-prediction of τ_f.

8.12 Reliability of the new approach to estimate shaft capacity

8.12.1 Comparison with tests on open-ended piles

Table 8-7 summarises the results obtained for open-ended piles using the new correlations for shaft capacity, described in the previous sections and summarised in Table 8-6. The calculations for short and long-term capacity obtained using the new approach are the same as those summarised previously in Table 8-4 and Table 8-5. Where available, from either strain gauge measurements or dynamic pile tests, the predicted and measured long-term shaft stress profiles are summarised in Figure 8-23 and Figure 8-24.

The predicted long-term shaft resistance for the Wikinger static pile tests on 1.37m diameter piles shown on Figure 8-23 includes calculations for τ_f in the overlying glacial till using the static ICP-05 sand and clay methods (Jardine *et al.*, 2005a), described in Chapter 3. The ICP-05 clay method was used primarily in the glacial till, following the predictions described in Section 5.9.8, and detailed in Appendix A-1. The ICP calculation gave reasonable predictions of the long-term shaft stresses in the glacial till at two of the sites (WK38 and WK43), with mean Q_c/Q_m values of 0.96 and 1.04. The method over-predicted the capacity at WK70 with a Q_c/Q_m value of 1.66.

The predicted profiles, in the glacial till using the ICP-05 clay method and in the chalk using the new approach are shown on Figure 8-23. Figure 8-24 shows the prediction in the chalk only using the new approach, for the dynamic restrike test at WK11 and the static test on Pile 1 in SNW. ICP-05 clay calculations were not carried out for the till layers covering the restrike test case at WK11 as this test was only conducted 6 hours after driving, well before an any pore pressures could have equalised in the clay till.

Figure 8-23 and Figure 8-24 demonstrate that the proposed new correlation for radial effective stresses in chalk captures the shape of the shaft stress profiles developed along the pile length. Comparison with the predictions made using the CIRIA methods (Table 8-6) demonstrates that the new approach provides the best accuracy of the three methods in chalk with a mean of 0.97 and a standard deviation of 0.16 in the short-term (during driving) and a mean of 1.0 and a standard deviation of 0.11 in the long-term.

Table 8-7: Comparison of original approaches with proposed correlation for shaft resistance for open-ended tubular steel piles

		Short-term (driving) Q_c/Q_m[1]			Long-term Q_c/Q_m[1]		
Type	**Test site**	**PG6**	**C574**	**New IC**	**PG6**	**C574**	**New IC**
Static	WK43-2_SLT[1]	-	-	**-**	0.27	0.17	**0.82**
	WK70-2_SLT[1]	-	-	**-**	0.17	0.12	**0.97**
	1_A119	-	-	**-**	0.11	0.06	**1.02**
	DP6_T1	-	-	**-**	0.23	0.18	**1.08**
Dynamic	OSS-C2_DPT_EOD	3.71	0.92	**1.13**	-	-	-
	OSS-C4_DPT_EOD	3.78	0.94	**1.15**	-	-	-
	WK11-A_DPT_EOD	2.00	0.53	**0.93**	-	-	-
	WK43-1_DPT_EOD	1.98	0.45	**0.90**	-	-	-
	WK43-2_DPT_EOD	1.39	0.51	**0.63**	-	-	-
	WK70-1_DPT_EOD	1.56	0.67	**0.98**	-	-	-
	WK70-2_DPT_EOD	1.69	0.47	**1.01**	-	-	-
	DP6_DPT_EOD[2]	1.22	0.94	**1.02**	-	-	-
	WK11-A_DPT	-	-	**-**	0.35	0.09	**1.15**
	WK43-1_DPT	-	-	**-**	0.33	0.10	**0.92**
	WK70-1_DPT	-	-	**-**	0.33	0.11	**1.06**
Mean		2.17	0.68	**0.97**	0.26	0.12	**1.00**
Std Dev		1.01	0.22	**0.16**	0.09	0.04	**0.11**

1. Includes an ICP clay calculation in the overlying glacial till and sand

8.12.2 Comparison with tests on closed-ended piles

To provide independent evidence of the new correlations for long-term shaft capacity, the approach was also applied to two available high quality tests on closed-ended piles from Fleury-sur-Andelle (Bustamante *et al.*, 1980) as discussed in Chapter 3. The results of compression tests on two instrumented driven piles; one 400 x 400mm square section pre-cast concrete pile (P1) and one closed-ended 445mm diameter steel tube (P2) are considered here. All three piles were driven to penetrations of approximately 10.3m, with a total length of 7.5m in the chalk. The tests were conducted between 118 and 693 days after driving. The profiles of shaft stress interpreted from the strain gauge measurements at failure for the compression test on each pile type are shown on Figure 8-25 along with the measured stresses and stresses predicted using the new approach. The parameters adopted were summarised previously in Section 8.2. The shear modulus, for input into Eq. 3-23, is unknown for the site and for preliminary purposes was assumed equal to that at SNW.

The predicted and measured capacities for the closed-ended piles using the new IC predictions and the CIRIA C574 and PG6 methods are shown on Table 8-8. The new IC predictions show good agreement with the measured shaft shear stresses from the strain gauges on the concrete

pile and an over-prediction for the closed-ended tubular steel pile. While both of these tests were re-tests on piles failed previously on multiple occasions, the predictions provide encouraging preliminary support. However, it is self-evident that further tests are required to check and refine the new expressions for shaft radial effective stresses and base capacity.

Table 8-8: Comparison of original approaches with proposed correlation for aged shaft resistance for closed-ended steel piles

		Long-term Q_c/Q_m		
Type	**Test**	**PG6**	**C574**	**New IC**
Static	Fleury_P1	0.47	0.59	1.02
	Fleury_P2	0.56	2.55	1.77

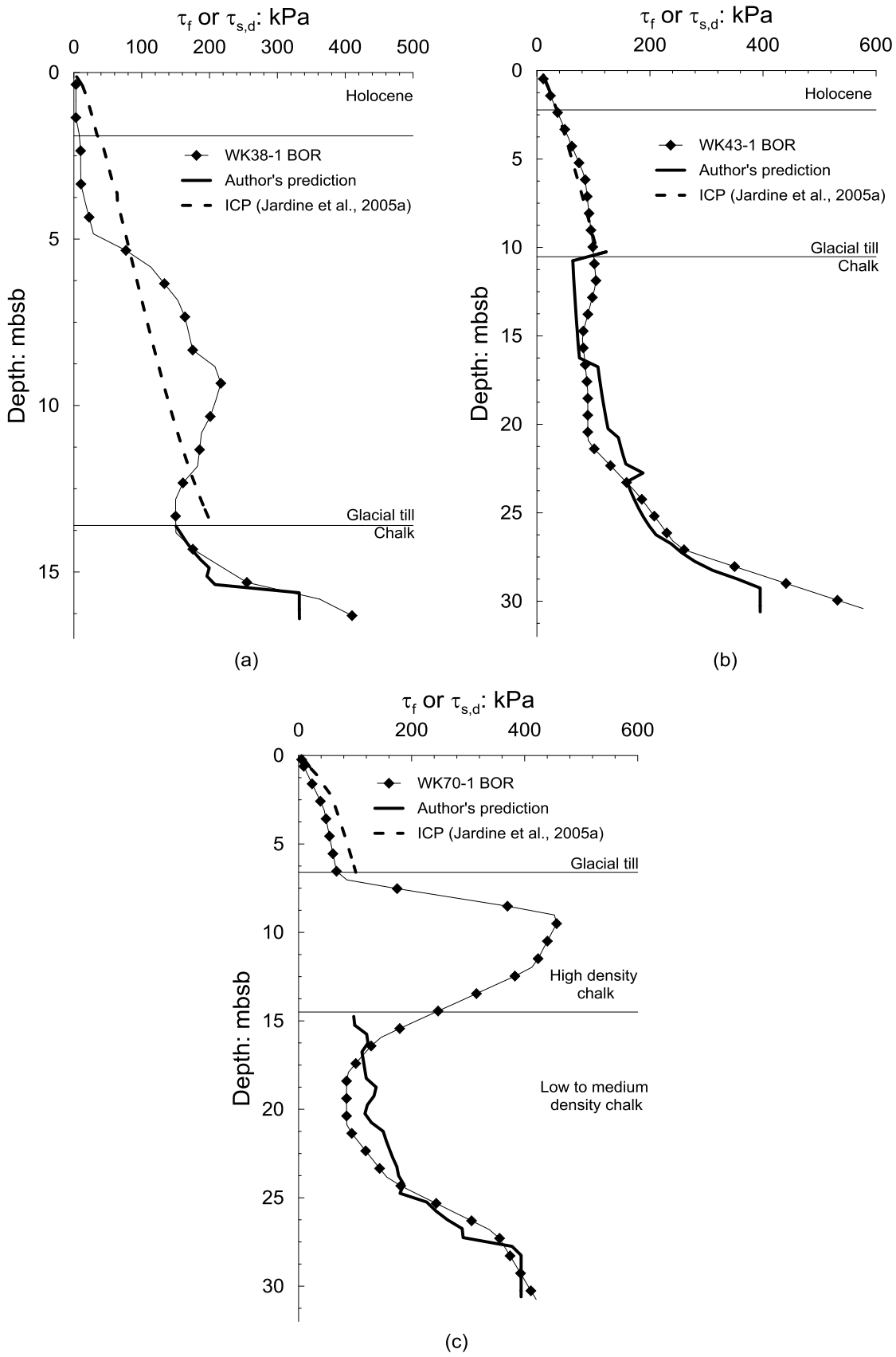


Figure 8-23: Profiles from dynamic tests and calculated profiles of aged shaft resistance on open-ended piles at Wikinger using ICP sand/clay and new chalk prediction (a) WK38 (b) WK43 (c) WK70

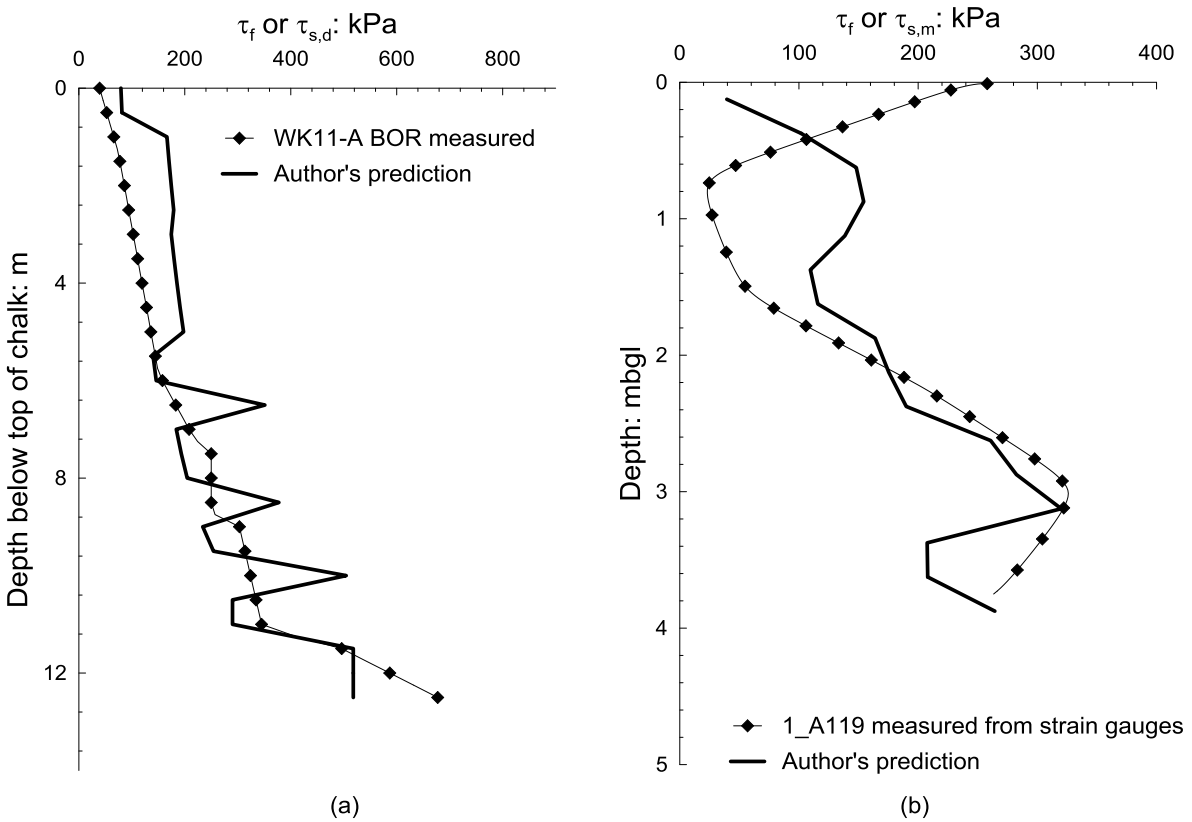


Figure 8-24: Profiles inferred from strain gauges during static tests and from dynamic tests and calculated profiles of aged shaft resistance on open-ended piles at Wikinger (a) WK11 (b) 1_A119

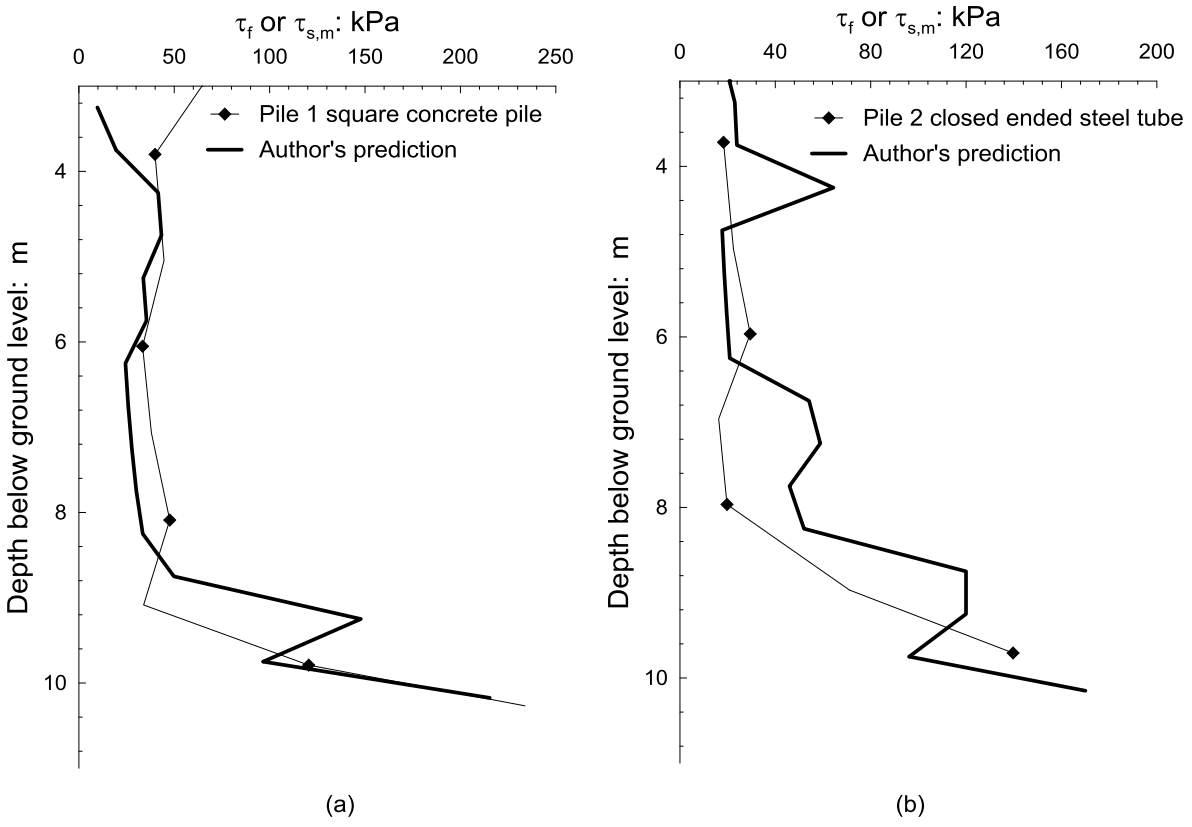


Figure 8-25: Profiles inferred from strain gauges during static tests and calculated profiles of aged shaft resistance on closed-ended piles at Fleury-sur-Andelle

8.13 Other design considerations

8.13.1 Axial cyclic loading

The Author's cyclic loading tests on 139mm diameter open-ended driven steel tubes discussed in Chapter 6 provided the first systematic study of the impact of axial cyclic loading on piles driven in chalk and the relationship between cyclic loading and aged axial pile capacity. The six tests' normalised Q_{mean} and Q_{cyc} loading components are shown on an axial cyclic interaction diagram (Karlsrud *et al.*, 1986, Poulos, 1988, Jardine and Standing, 2000, 2012) on Figure 8-26. The numbers of cycles imposed are also noted on this figure with the cyclic stability indicated in parentheses. The top-left to right-bottom diagonal in this diagram represents the static failure conditions, where the Utilisation (of tension shaft capacity) Ratio, $UR = Q_{max}/Q_{ref}$ is equal to 1. The line representing the minimum UR = 2/3 recommended by API/ISO guidance for extreme offshore environmental loading cases is also shown, along with an UR = 0.5 line.

A range of responses to axial cyclic testing (imposed around 250 days after driving) were observed in the Author's tests. One-way axial cycling that involved equivalent 'static' utilisation ratios (UR) greater than 0.70 led to clearly unstable behaviour with rapid accumulation of displacement, reductions in stiffness, failure in far less than 100 cycles and marked degradation in post-cyclic failure operational shaft capacity. One-way tests conducted with UR between 0.48 and 0.7 led to broadly stable capacities and cyclic stiffness remaining constant or growing as cycling continued but the associated accumulated displacement trends that did not stabilise within 1000 cycles, suggesting only meta-stability.

The supplementary tests available from the literature, as discussed in Chapter 3, are also plotted on Figure 8-26. All of the tests shown are on piles which had been failed previously, either in static tension or compression or by cyclic loading. The results of the test on Pile P04 at Henmoor (Lahrs and Kallias, 2013) appears to be consistent with the Author's results, reaching 1000 cycles without failure at a lower UR than the stable/metastable boundary identified above. The influence of the cyclic loading on operational capacity of this test is uncertain. The Luton box pile test (Burland and French, 1990) conducted at an age of 24 days failed after 20 cycles, exhibiting unstable behaviour, with a 60% reduction in post cyclic operational tension capacity. The latter test, also plotted on Figure 8-26, falls well below the lower bound to the unstable region identified by the Author's tests. The cyclic loading parameters for Pile 1 and Pile 4 tested cyclically at SNW by Iberdrola (2013) failed with

N<1000 at ages of between 692 and 695 days and their significant accumulation of permanent displacement indicated metastable/unstable behaviour from an earlier stage. These tests again fall well below the metastable/stable region identified by the Author's tests. A post failure cyclic test on Pile 4 indicated a 93% reduction in operational tension capacity, a further indication of unstable behaviour. However Pile 1 had been previously failed in static tension on three occasions and Pile 4 had been subjected to previously static and cyclic lateral loading (see Section 3.5.1).

The available evidence suggests that previous loading to failure has a significant deleterious effect on the ability of driven piles in chalk to withstand even relatively modest low-level cyclic loading. The Author's tests on small diameter driven piles suggest that under first time loading, low-level axial cyclic loading may reduce, but does not completely negate, the beneficial effects of time on capacity, as previously feared. Further investigation is required to explore the potential effects of pile scale and chalk density on the response of aged "virgin" piles to axial cyclic loading, as well as the cyclic response under a wider range of cyclic loading conditions. In particular, greater degradation can be expected at the same UR values under high-level two-way loading.

8.13.2 Effect of loading sense

Tension loading to failure in sands causes a general reduction in the stress field around the pile combined with elongation or compression of the pile during loading due to elastic Poisson effects (De Nicola and Randolph, 1993) and additional principal stress rotation effects (Lehane *et al.*, 1993). All of these factors may lead to a lower shaft capacities developing under tension than compression loading. The ICP-05 sand design methods for offshore piles (Jardine *et al.*, 2005b) and other CPT based axial design methods (e.g. Lehane *et al.*, 2005a) adopt reduced parameters or factors when calculating tension capacity in sands only. The ICP sand method recommends a 20% to 30% reduction in capacity on the calculated values when piles are loaded in tension, for closed-ended and open-ended conditions respectively (Jardine *et al.*, 2005a).

The correlations for shaft capacity of open and closed-ended piles developed in this chapter and summarised in Table 8-6 were developed primarily from compressive dynamic tests and instrumented static compression tests. For these preliminary correlations, it is assumed that tensile and compressive capacity are equal. A larger database of tests is required to determine whether changes in loading direction affect capacity in chalk.

8.13.3 Interactions with lateral loading

The offshore wind industry is inexorably moving towards larger structures and greater water depths that develop larger vertical, lateral and moment loads on offshore wind turbines. The predictions of long-term axial shaft capacity described in this chapter have not considered the practical effects of any lateral loading on axial capacity or vice versa. Multiple lateral loading tests conducted by Ciavaglia *et al.* (2017a) at the SNW test site were seen to have a significantly deleterious effect on the subsequent axial tension capacity of the piles, and may have significantly reduced the otherwise beneficial time effects on axial capacity. Further research is required to investigate the severity of any interactions of axial and lateral loading for piles driven in chalk. Consideration of how lateral cycling may affect axial capacity in clays and sands have been outlined by Merritt *et al.* (2012), Argiolas and Jardine (2017) and Hampson *et al.* (2017). The axial load-displacement behaviour also warrants further investigation, combined with the development of T-z curves based on the measured static test curves.

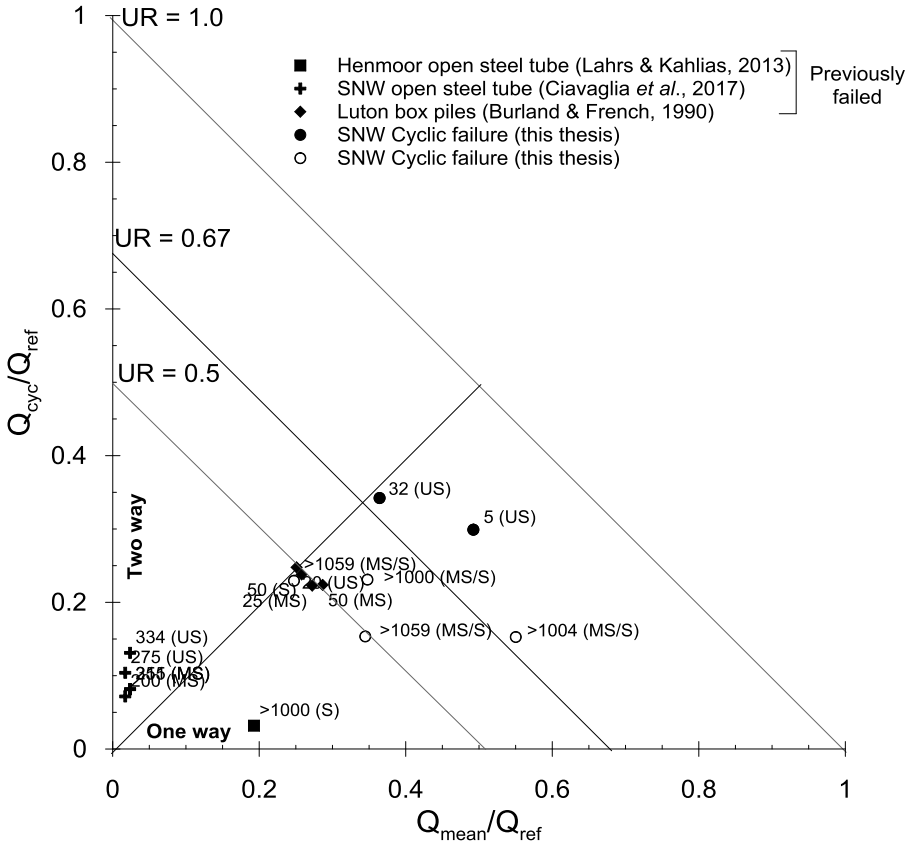


Figure 8-26: Cyclic stability diagram showing previous tests and the Author's test's described in Chapter 6

8.14 Summary and concluding remarks

This chapter has reviewed current understanding of the behaviour of displacement piles in chalk, including the advances made by the Author's experiments using driven and jacked piles, which were described in Chapters 5 to 7, and discussed the relevant design considerations for axial pile design in chalk. A preliminary new design approach to predict the radial effective stresses applying on the shaft of displacement piles in low-medium density chalk has been proposed. The following points are noted:

- The end bearing resistances mobilised on the annular area of open-ended steel piles during rapid penetration interpreted from dynamic load tests at the Author's test sites ranged from approximately 0.5 to 0.8 times the cone tip resistance. The base resistance applying during a static load test, and the proportion applying on the annular area and the plug base, are difficult to ascertain with the limited dataset;
- An approach similar to that adopted previously in sands has been developed to predict the radial effective stresses and thus the axial shaft capacity in chalk, which is based on CPT cone resistance, the relative distance of a given chalk horizon above the pile tip, h, and the interface shear characteristics;
- Preliminary correlations for radial effective stresses have been developed for both the during driving case and the long-term equalised case;
- The relationships for radial effective stresses were developed based on the results of dynamic pile tests and static compression tests on piles installed at the Wikinger and St. Nicholas-at-Wade sites described in Chapter 3, 5 and 6;
- When considering the long-term capacities, the dilational changes in radial effective stresses during loading were shown to have a relatively minor impact, even with small driven displacement piles (around 100mm in diameter), and to be negligible for large (1.37 to 3.7m) diameter offshore piles;
- The test results from static and dynamic tests on open-ended and closed-ended piles at three different sites were considered. The predictive reliability of the current industry guidelines were shown to vary between highly conservative and highly non-conservative in both the short and long-term;
- The new approach to estimate radial effective stresses and therefore shaft capacity was shown to (i) lead to far better predictions of both short-term and long-term capacity of open-ended piles and (ii) capture the variation in shaft resistance profiles with depth.

Reasonable agreement was also seen with the results of fully independent tests on closed-ended industrial driven piles. Further data is required to allow refinement of the equations and a possible reduction of the lower limit on h/R or h/R*.

The Author developed the preliminary correlations primarily from tests conducted at just two different sites with similar chalk grades and densities. They have been checked against one other independent site that was not included in the correlations. Further development and refinement of the method will be possible as the database of available static and high quality dynamic tests is expanded by adding test sites with both similar and differing chalk grades and densities.

In particular, instrumented static compression tests are required to further develop understanding and empirical correlations for end resistance and its relationship to *in-situ* test parameters and partial drainage. Compression and tension tests on piles of the same age and dimensions installed at the same site would also facilitate conclusions to be made on the effect of loading direction on ultimate capacity. The combined effects of lateral and axial loading must also be considered to facilitate more economical design.

CHAPTER 9

Conclusions and recommendations for future research

9.1 Introduction

This chapter summarises the primary conclusions from the thesis and recommendations for further work. The over-arching aim of the thesis was to advance the three primary research themes, set out below, which were explored through field experiments at two test sites. The tests were designed to investigate:

1. The reasons for the remarkably low axial resistances developed by piles driven in low-medium density chalk during and shortly after installation;
2. The degree to which the driven piles axial capacities increase with time after driving; and
3. The effects of axial cyclic loading on the behaviour of piles whose capacity has increased with time.

The Author's investigations included analysis of full-scale offshore static and dynamic pile tests on open-ended steel tubular piles founded in Weichsellian glacial till and Maastrichtian chalk, at the Wikinger site in the German Baltic Sea. These very costly tests were supplemented by further experiments on similar reduced-scale driven piles and jacked ICPs at an analogous onshore test site, located close to the village of St. Nicholas-at-Wade, Kent, Southern UK.

The onshore test site facilitated a systematic investigation of how ageing and cyclic loading affects driven steel piles over an eight month period. Two programmes of experiments were conducted. Firstly ICP pile experiments were planned to investigate the fundamental

effective stress behaviour of displacement piles in chalk. The ICP tests were supported by a secondary programme of tests on driven open-ended tubular steel piles, which delivered clear and significant results.

Additional database studies were conducted by the Author along with work with five MSc students into laboratory interface shear behaviour, the behaviour of remoulded or puttified chalk in the laboratory and pile driveability in chalk, added to the scope of the research. The primary conclusions from the Author's experimental programmes are summarised in the following sections, followed by a summary of the proposed approach to estimate shaft resistance for displacement piles in low-medium density chalk. The final section discusses recommendations for further research.

9.2 Primary experimental results

9.2.1 Offshore static and dynamic tests at the Wikinger offshore windfarm

1. Low average shaft resistances were observed in chalk during the driving of 1.37 to 3.7m diameter piles, which showed a clear trend to reduce with increasing relative tip depth (h/R*) into chalk;
2. The reductions in local shaft resistance with h/R* observed during pile driving are far more marked than is expected by representative current methods in sands or clays;
3. The shaft resistances in the glacial till at the end of driving observed also showed a tendency to reduce with increasing penetration or h/R*, although the trends were less marked than those seen in chalk;
4. Laboratory tests on samples of Wikinger chalk showed that compaction at natural moisture content causes marked de-structuration to a putty with very low undrained strength. Subsequent consolidation increases the shear strength and stiffness over time, but thixotropic effects were found to be less significant than has been suggested previously;
5. Static load tests conducted on 1.37m diameter piles at the predominantly chalk locations did not reach full failure due to the set-up capacities being far greater than the designer's predictions, highlighting the conservatism of all the methods considered by practitioners;

6. The static test conducted at the glacial till dominated site, which reached full failure, showed good agreement with the results of the dynamic restrike test conducted at the same time;
7. Shaft capacity changes over time were evaluated for the glacial till and chalk by comparing the aged and unaged static and dynamic tests. Capacity increases in the glacial till were significant, reaching factors of between two and three by the end of the programme. However, the capacity gains in chalk were still greater, reaching over 500%, and followed a hyperbolic trend that was 50% complete less than an hour after installation;
8. The application of multiple restrike blows to piles that had experienced long-term set-up was shown to reduce their capacities, starting from the first blow. Beneficial time effects observed during operational pauses were also shown to be degraded by further hammer blows or pile penetration. The advantages of concentrating only on first-time static or dynamic tests were clear;
9. The results of the static and dynamic testing programme represent a valuable dataset which set the agenda for further, lower cost, experiments on driven and jacked test piles at an analogous onshore test site.

9.2.2 Onshore static, dynamic and cyclic tests at St. Nicholas-at-Wade

The pile tests at St. Nicholas-at-Wade comprised both a driven pile programme and a set of ICP experiments. The primary conclusions from the testing programme on 139mmm diameter driven open ended steel tubes include:

1. Notably low shaft resistances applied along the piles' main shaft lengths during and immediately after driving;
2. There is a significant effect of installation rate on pile end bearing pressures, and installation was a partially drained event;
3. Dynamic analysis of driving data confirm the strong dependence of local shaft resistance on relative distance above the pile tip (h/R*) mirroring the trends seen in the PCPT at the test site and the behaviour seen at Wikinger;
4. Marginally lower average shaft driving resistances apply than suggested by the CIRIA static design guidance values;

5. Static tension capacities increase markedly after driving. Gains of more than 500% were interpreted after eight months, leading to average shaft stresses that exceeded the low-medium density CIRIA guidance value by a factor of 4.3;
6. A hyperbolic shaft capacity trend increase with time was observed that was 83% complete 100 days after installation. The set-up reached ultimate values similar to those seen at Wikinger, but took far longer to develop probably due to the nature of the fractures *in-situ*. Set-up appears to be fastest in cases where the fractures are closed tightly, as at Wikinger;
7. A single re-test conducted 8 months after one pile's first static failure showed a positive ageing trend, although its capacity fell well below that of the undisturbed piles;
8. Driving open-ended piles in chalk remoulds the material, creating a puttified zone and probably generated very high excess pore pressures near to the pile tip. Rapid excess pore water pressure dissipation during and after driving led to markedly lower water contents close to the shaft;
9. Evidence was presented, from field observations and laboratory tests, of changes in residual shear strength with time, for chalk-steel interfaces aged under load. Changes in interface shear properties can explain increases in local shear stress of approximately 10%, far below the observed long-term increases in shaft capacity of the driven piles;
10. Similarly, reconsolidation of chalk putty took place too rapidly to explain, on its own, the observed long-term increases in shaft capacity;
11. Other mechanisms are required to explain the observed long-term increases in shaft capacity. Consolidation of the chalk putty (contemporaneously with pile driving) followed by long-term creep and breakdown of arching allowed radial total stress re-growth providing possible explanations for the observed ageing trends, taken in combination with potential re-cementing and the redox chemical reactions that were noted to have occurred close to the pile shafts;
12. A range of responses was observed to axial cyclic loading imposed, with a range of loading combinations, around 250 days after driving. One-way axial cyclic loading that involved equivalent 'static' utilisation ratios (UR) > 0.70 led to clearly unstable behaviour with rapid accumulation of displacement, stiffness loss, failure in far less than 100 cycles and marked degradation in operational shaft capacity;
13. One-way tests conducted with 0.48 <UR< 0.70 led to broadly stable capacities and cyclic stiffness remaining constant or growing as cyclic loading continued. However, the piles' accumulated displacement trends did not stabilise within 1000 cycles,

suggesting only meta-stable behaviour. Greater degradation can be expected at the same UR values under high-level two-way loading;

14. The permanent displacement accumulation trends followed under the stable/metastable tests developed proportionally with N, raised to an exponent of ≈1/3 that appeared to be insensitive to the loading parameters within the limited range (one-way 0.48 < UR <0.70) considered. Higher exponents applied in the unstable range;
15. The experiments provide the first systematic study, of which the Author is aware, into the effects of undisturbed ageing and cyclic loading of previously unfailed piles driven in chalk. Overall, guidance based on driving monitoring and early age tests appear to be potentially highly conservative, while cyclic tests on aged piles showed responses that varied between stable and unstable, depending on the loading conditions.

9.2.3 Onshore jacked ICP tests at St. Nicholas-at-Wade

Parallel investigations were made into the governing effective stress processes with highly instrumented 101mm diameter Imperial College Piles at the St. Nicholas-at-Wade test site. The primary observations made include;

1. Base resistance varied directly with local cone resistance and depended on drainage conditions;
2. Shaft resistances are low during installation, with the jacked piles' average values exceeding those back analysed from open-ended piles driven at the same site;
3. Large excess pore water pressures are interpreted as having developed under the pile tip during penetration, similar to those seen in multiple PCPT tests, that dissipated rapidly as the tip advanced;
4. Low stationary radial effective stresses developed during installation that correlated directly with net cone resistance, showing ratios to q_t comparable to those in calcareous sands;
5. Strong total radial reductions in shaft radial effective stresses, σ'_{rs} developed immediately after the pile tip passes any given horizon, with more gentle additional degradation applying further along the shaft. Still more reductions in σ'_{rs} with relative tip depth (h/R*) apply to driven piles;
6. The effective stress paths recorded during static and cyclic loading tests show that shaft failure is controlled by a Coulomb law, with an interface shear angle similar to that

mobilised in laboratory interface ring shear tests. The radial effective stresses rise under static loading until interface dilation reaches its limit;

7. The degree of radial expansion experienced at the interface appears to be far smaller than with sands, due to the higher ratio between the pile roughness and the silt-sized crushed chalk grain size;
8. Long-term monitoring of the (slowly) jacked ICP piles showed total shaft radial stresses reducing with time after installation, falling by 11 to 34% after 23 and 80 days respectively. Tension load tests showed shaft capacity reducing by similar proportions over the weeks that followed installation, in marked contrast with the strong set-up shown by open-ended piles driven at the same site;
9. The piles were installed to the same depth at the same test site and tested after similar time periods using the same load and control equipment. Therefore, geometry and/or installation method must influence the ageing and subsequent loading behaviours and require further investigation.

The Author's test results indicate that the behaviour of displacement piles in chalk is similar in many respects to that seen in calcareous sands, mobilising relatively high base resistances during driving, with pore pressure equalisation occurring during and immediately after driving. Shaft radial effective and end bearing stresses follow the trends of CPT cone resistance and dilational changes in radial effective stresses are observed during static loading to failure.

9.3 Towards a new effective stress based design approach for displacement piles in chalk

The understanding drawn from the Author's tests, as well as from supplementary data from other sources was used to set out a route towards better rules for predicting the axial capacity of open-ended and closed-ended displacement piles in chalk. Capturing the radial effective stresses applying on pile shafts is the foundation of the proposed axial capacity design methodology. The thesis has proposed a new effective stress based design approach for displacement piles in chalk which is based on the key phenomena identified in earlier chapters. In summary:

1. An approach similar to that adopted previously in sands has been developed to predict the radial effective stresses and thus the axial shaft capacity in chalk, which uses the CPT cone resistance to allow for local variations in ground properties, recognises the

marked effect of the relative distance from the pile tip below any given chalk horizon being considered and addresses the chalk's interface effective stress shear failure characteristics;

2. Separate, preliminary correlations for radial effective stresses were developed for both the soil resistance to driving case and the long-term equalised case;
3. Relationships linking radial effective stresses to CPT cone resistance and h/R* were developed based on the results of dynamic pile tests and static compression tests on piles installed at the Wikinger and St. Nicholas-at-Wade sites described in Chapter 3, 5 and 6;
4. Dilation induced changes in radial effective stresses during loading are also considered for the long-term case and shown to be relatively minor in most circumstances;
5. The test results from static and dynamic tests on open-ended and closed-ended piles at three different sites were considered. The current industry guidelines were shown to be both highly conservative in some cases and highly non-conservative in others;
6. The new approach to estimate radial effective stresses and therefore shaft capacity was shown to lead to far better predictions of both short-term (during driving) and long-term shaft capacity of open-ended piles and to capture realistically the variation in shaft resistance profiles with depth;
7. During driving, the new shaft method offered a calculated to measured capacity ratio, Q_c/Q_m mean of 0.97 and a standard deviation of 0.16 (CoV = 0.16). For the long-term equalised case, the new method gave a mean Q_c/Q_m of 1.00 and a standard deviation of 0.11 (CoV = 0.11);
8. Reasonable agreement was also seen with the results of one set of fully independent tests on closed-ended industrial driven piles conducted in France in the 1970s. Further data would allow refinement of the equations and a possible reduction of the lower limit on h/R or h/R*.

9.4 Recommendations for future work

The Author's work has led to the primary conclusions outlined in the previous sections. Further research is recommended into the following primary areas;

1. *Base resistance:* instrumented static compression tests would help to further develop understanding of end resistance and facilitate empirical correlations with *in-situ* test parameters;

2. *Pile scale*: the Author's ageing investigations and axial cyclic tests demonstrated that axial cyclic loading of driven piles in chalk is not as onerous as previously thought, however this requires confirmation with tests on piles of different scale;
3. *Two-way axial cycling*: the axial cyclic loading tests conducted for this thesis were all conducted under one-way axial cyclic loading conditions. The effects of two-way axial cycling are expected to be more severe and require further characterisation;
4. *Lateral loading effects:* the effects of static and cyclic lateral loading have not been considered in the Author's tests and require further investigation, including into any possible interactions between axial and lateral capacity.

The research conducted for this thesis has helped set the agenda for the ALPACA (Axial-Lateral Chalk Analysis for Piles Applying multi-scale field and laboratory testing) project. The project, is in collaboration with the University of Oxford and funded by the Engineering and Physical Sciences Research Council (EPSRC) with support from over 10 industry partners. The project began in October 2017, with the primary testing programme planned for 2018, re-utilising the St. Nicholas-at-Wade test site. The primary aims of the research include:

1. Install a total of 21 open-ended industrial-scale steel piles (139mm and 508mm diameter) and investigate their dynamic driving behaviour and axial loading responses after ageing under both compression and tension;
2. Study both the one-way and two-way axial cyclic response of the piles after 8 months of ageing;
3. Utilising the 508mm diameter piles, investigate the static lateral loading response, the effects of lateral cyclic loading and the effect of lateral loading on axial capacity; and
4. Employ state-of-the-art field pile loading equipment and novel fibre-optic instruments to distinguish profiles of pile shaft axial and bending stresses under axial, lateral, static and cyclic loading.

The pile testing will be supplemented by additional experiments with a 36mm diameter mini-pile, adding pore pressure sensors to the highly instrumented device described by Jardine *et al.* (2009) as well as new investigations into the chalk's detailed mechanical behaviour, using high quality samples, *in-situ* testing, and advanced static and cyclic laboratory testing. The value of the new field and laboratory experiments and the scope of the analysis will be augmented by synthesising the pile test outcomes with data from other industrial project studies.

REFERENCES

Addis M. & Jones, M. (1990). Mechanical behaviour and strain rate dependance of high porosity chalk. *Proc. Intl. Chalk Symposium*, Brighton, UK: 239-244

Afshin A. & Rayhani, M. (2015). Evaluation of bearing capacity with time for small-scale piles driven into Leda clay. *Intl. J. Geotech. Eng.,* **9**, No. 3: 307-315

Al-Shafei K., Cox, W. & Helfrich, S. (1994). Pile load tests in dense sand: Analysis of static test results. *Offshore Technology Conference*, Houston, Texas: 83-103

Al-Tabbaa A. & Wood, D. M. (1989). An experimentally based "bubble" model for clay. *Proc. Intl. Symp. on Numerical Models in Geomechanics: NUMOG III*, Niagara Falls, Canada: 91-99

Alawneh A. S. & Malkawi, A. H. (2000). Estimation of post-driving residual stresses along driven piles in sand. *Geotech. Test. J,* **23**, No. 3: 313-326

Aldiss D., Bloomfield, J., Buckley, D., Doran, S., Evans, D., Hopson, P., Royse, K. & Woods, M. (2004). *A geological model of the chalk of East Kent,* British Geological Survey*,* Commissioned Report CR/04/092N

Allnamics (2015). *AllWavePDP User's reference manual,* Allnamics BV*,* Draft for review and comment

Alm T. & Hamre, L. (2002). Soil model for pile driveability predictions based on CPT interpretations. *Proc. 15th Intl. Conf. Soil Mech. Geotech. Eng.*, Istanbul, Turkey: 1297-1302

Altuhafi F. & Jardine, R. J. (2011). Effect of particle breakage and strain path reversal on the properties of sands located near to driven piles. *Proc. 5th Intl. Symp. Deformation Characteristics of Geomaterials*, Seoul, Korea: 388-395

Alves A. M., Lopes, F. R., Randolph, M. F. & Danziger, B. R. (2009). Investigations on the dynamic behavior of a small-diameter pile driven in soft clay. *Can. Geotech. J.,* **46**, No. 12: 1418-1430

Andersen K. H., Puech, A. & Jardine, R. J. (2013). Cyclic resistant geotechnical design and parameter selection for offshore engineering and other applications. *Proc. 18th Intl. Conf. Soil. Mech. Geotech. Eng: TC 209 Workshop - 'Design for cyclic loading: piles and other foundations'*, Paris, France: 9-44

Angemeer J., Carlson, E. G. & Klick, J. H. (1973). Techniques and results of offshore pile load testing in calcareous soils. *Offshore Technology Conference*, Houston, Texas: 677-693

API (2000). API RP 2A-WSD:Recommended practice for planning, designing and constructing fixed offshore platforms – working stress design, 21st Edition, American Petroleum Institute

API (2007). API RP 2A-WSD:Recommended practice for planning, designing and constructing fixed offshore platforms – working stress design, 21st Edition, Errata and Supplement 3, American Petroleum Institute

Argiolas R. & Jardine, R. J. (2017). An Integrated Pile Foundation Reassessment to Support Life Extension and 695 New Build Activities for a Mature North Sea Oil Field Project. *Proc. 8th Intl. Conf. Offshore Site Investigation and Geotechnics*, London, UK: 695-702

Åstedt B., Weiner, L. & Holm, G. (1992). Increase in bearing capacity with time for friction piles in silt and sand. *Proc. Nordic Geotech. Meeting*: 411-416

ASTM (2012). D5778: Standard Test Method for Electronic Friction Cone and Piezocone Penetration Testing of Soils, ASTM International

Augustesen A. H., Leth, C. T., Ostergaard, M. U., Moller, M., Dührkop, J. & Barbosa, P. (2015). Design methodology for cyclically and axially loaded piles in chalk for Wikinger OWF. *Proc. Frontiers in Offshore Geotechnics III*, Oslo, Norway: 509-514

Axelsson G. (2000). *Long-term set-up of driven piles in sand.* PhD Thesis, Royal Institute of Technology, Stockholm, Sweden

Baldi G., Belloti, R., Ghionna, V. N., Jamiolkowski, M. & Lo Presti, D. C. F. (1989). Modulus of sands from CPTs and DMTs. *Proc. 12th Intl. Conf. Soil Mech. Found. Eng.*: 165-170

Baligh M. M. (1985). Strain path method. *J. Geotech. Eng - ASCE,* **111**, No. 9: 1108-1136

Barbosa P., Geduhn, M., Jardine, R. J., Schroeder, F. C. & Horn, M. (2015). Offshore pile load tests in chalk. *Proc. 16th Eur. Conf. Soil Mech. Geotech. Eng.*, Edinburgh, Scotland: 2885-2890

Barbosa P., Geduhn, M., Jardine, R. J. & Schroeder, F. C. (2017). Large Scale Offshore Static Pile Tests - Practicality and Benefits. *Proc. 8th Intl. Conf. Offshore Site Investigation and Geotechnics*, London, UK: 515-520

Barmpopoulos I., Ho, T., Jardine, R. & Anh-Minh, N. (2010). The large displacement shear characteristics of granular media against concrete and steel interfaces. *Proc. Research Symp. on Characterisation and Behavior of Interfaces*, Atlanta, Georgia, USA: 16-23

Bea R. G., Jin, Z., Valle, C. & Ramos, R. (1999). Evaluation of reliability of platform pile foundations. *J. Geotech. Geoenviron. Eng. - ASCE,* **125**, No. 8: 696-704

Been K. & Jefferies, M. G. (1985). State Parameter for Sands. *Géotechnique,* **35**, No. 2: 99-112

Been K. & Jefferies, M. G. (1986). Discussion: A state parameter for sands. *Géotechnique,* **36**, No. 1: 123-132

Been K., Jefferies, M. G. & Hachey, J. (1991). The critical state of sands. *Géotechnique,* **41**, No. 3: 365-381

Been K. & Jefferies, M. G. (2006). *Soil Liquefaction: A Critical State Approach,* USA: Taylor & Francis.

Bell F. G., Culshaw, M. G. & Cripps, J. C. (1999). A review of selected engineering geological characteristics of English Chalk. *Engineering Geology,* **54**, No. 3: 237-269

Beringen F. L., Van Hooydonk, W. R. & Schaap, L. H. J. (1980). Dynamic pile testing: an aid in analyzing driving behaviour. *Proc. Intl. Seminar on the Application of Stress-Wave Theory to Piles*, Stockholm, Sweden: 77-97

BGS (2016a). Borehole log at Piers Road, Gillingham residential development. Accessed: 9th December 2016

BGS (2016b). Borehole log at King George V Dock - Norwest Holst Soil Engineering Ltd. Accessed: 6th December 2016

Bialowas G., Diambra, A. & Nash, D. (2016). Small strain stiffness evolution of reconstituted medium density chalk. *Proc. 1st IMEKO TC4 Intl. Workshop on Metrology for Geotechnics*, Benevento, Italy: 162-167

Bilfinger (2014). *Work Procedure Testing Operations on Test Piles (Phase III),* Bilfinger Construction GmbH, WIK-CIV-N-BIL-1044

Bilfinger (2015a). *Wikinger Offshore Windfarm - Offshore Pile Testing Investigation: Interim Pile test Report (Phase II),* Bilfinger Construction GmbH, WIK-CIV-C-BIL-0018

Bilfinger (2015b). *Wikinger Offshore Windfarm – Offshore Pile Testing Investigation: Final Factual Report Pile Test Campaign,* Bilfinger Construction GmbH, WIK-CIV-C-BIL-0023

Bishop A. W. (1966). The strength of soils as engineering materials. *Géotechnique,* **16**, No. 2: 91-130

Bishop A. W., Green, G., Garga, V. K., Andresen, A. & Brown, J. (1971). A new ring shear apparatus and its application to the measurement of residual strength. *Géotechnique,* **21**, No. 4: 273-328

Bloomfield J. P., Brewerton, L. J. & Allen, D. J. (1995). Regional trends in matrix porosity and dry density of the Chalk of England. *Q. J. Eng. Geol. Hydrogeol.,* **28**, No. S2: S131-S142

Bogard J. D. & Matlock, H. (1990). Application of model pile tests to axial pile design. *Offshore Technology Conference*, Houston, Texas: 271-278

Bond A. J. (1989). *Behaviour of displacement piles in overconsolidated clays.* PhD Thesis, Imperial College London (University of London), London, UK

Bond A. J., Jardine, R. J. & Dalton, J. C. P. (1991). Design and performance of the Imperial College instrumented pile. *Geotech. Test. J.,* **14**, No. 4: 413-424

Bond A. J. & Jardine, R. J. (1991). Effects of installing displacement piles in a high OCR clay. *Géotechnique,* **41**, No. 3: 341-363

Borges F. J. A. (2014). *The application of simple shear testing to evaluate the shaft resistance on piles driven in chalk.* MSc Thesis, University of Southampton, Southampton, UK

Boswell P. G. H. (1948). A preliminary examination of the thixotropy of some sedimentary rocks. *Q. J. Eng. Geol. Hydrogeol.,* **civ**, No. 4: 499-526

Boulon M. & Foray, P. (1986). Physical and numerical simulation of lateral shaft friction along offshore piles in sand. *Proc. 3rd Intl. Conf. on Numerical Methods in Offshore Piling*, Nantes, France: 127-147

Boulton G. & Deynoux, M. (1981). Sedimentation in glacial environments and the identification of tills and tillites in ancient sedimentary sequences. *Precambrian Research,* **15**, No. 3-4: 397-422

Bowden A. J., Spink, T. W. & Mortimore, R. N. (2002). The engineering description of chalk: its strength, hardness and density. *Q. J. Eng. Geol. Hydrogeol.,* **35**, No. 4: 355-361

Bracegirdle A., Mair, R. J. & Daynes, R. J. (1990). Construction problems associated with an excavation in chalk at Costessey, Norfolk. *Proc. Intl. Chalk Symposium*, Brighton, UK: 385-391

Briaud J. L. & Tucker, L. M. (1984). Residual stresses in piles and the wave equation. *Proc. ASCE Symp. Deep Foundations.*, San Francisco, California, USA: 119-137

Brinch Hansen J. (1963). Discussion: Hyperbolic Stress Strain Response: Cohesive Soils. *J. Soil Mech. Found. Div. - ASCE,* **89**, No. 4: 241-242

Bromley R. G. (1967). Some observations on burrows of thalassinidean Crustacea in chalk hardgrounds. *Q. J. Geol. Soc.,* **123**, No. 1-4: 157-177

Brown M. J. (2004). *The rapid load testing of piles in fine grained soils.* PhD Thesis, University of Sheffield, Sheffield, UK

Brucy F., Meunier, J. & Nauroy, J. F. (1991). Behavior of pile plug in sandy soils during and after driving. *Proc. Offshore Technology Conference*, Houston, Texas: 145-154

Brzezinski L. S. & Baba, H. U. (2012). Offshore Open End Steel Tubular Piles - A Case History. *Full-Scale Testing and Foundation Design: Honoring Bengt H. Fellenius*, Oakland, California: 568-589

BSH (2011). Guidance for use of the BSH standard “Design of Offshore Wind Turbines" Addendum 2011-02-02, Bundesamt für seeschifffahrt

BSI (1990a). BS 1377-7 Methods of test for soils for civil engineering purposes. Shear strength tests (total stress), British Standards Institution

BSI (1990b). British Standard 1377-2: 1990. Methods of test for soils for civil engineering purposes: Part 2: Classification tests, British Standards Institution

BSI (2015). BS 5930:1999 Code of practice for ground investigations, British Standards Institution

Buckley R. M. (2014). *Axial cyclic loading of piles in sand.* MSc Thesis, Imperial College London, London, UK

Buckley R. M., Jardine, R. J., Kontoe, S., Liu, T., Ushev, E., Lehane, B., Pine, T., Schroeder, F. C. & Barbosa, P. (2017a). Field investigations into the axial loading response of displacement piles in chalk. *Proc. 8th Int. Conf. on Offshore Site Investigation and Geotechnics*, London, UK:

Buckley R. M., Kontoe, S., Jardine, R. J., Maron, M., Schroeder, F. C. & Barbosa, P. (2017b). Common pitfalls of pile driving resistance analysis - A case study of the Wikinger offshore windfarm. *Proc. 8th Intl. Conf. Offshore Site Investigation and Geotechnics*, London, UK: 1246-1253

Buckley R. M., Jardine, R. J., Kontoe, S., Parker, D. & Schroeder, F. C. (2018a). Ageing and cyclic behaviour of axially loaded piles driven in chalk. *Géotechnique,* **68**, No. 2, *https://doi.org/10.1680/jgeot.17.P.012*: 146-161

Buckley R. M., Jardine, R. J., Kontoe, S. & Lehane, B. M. (2018b). Effective stress regime around a jacked steel pile during installation ageing and load testing in chalk. *Can. Geotech. J. doi: 10.1139/cgj-2017-0145,* **doi: 10.1139/cgj-2017-0145**, No.:

Bullock P. J., Schmertmann, J. H., McVay, M. C. & Townsend, F. C. (2005a). Side shear setup. I: Test piles driven in Florida. *J. Geotech. Geoenviron. Eng. - ASCE,* **131**, No. 3: 292-300

Bullock P. J., Schmertmann, J. H., McVay, M. C. & Townsend, F. C. (2005b). Side shear setup. II: Results from Florida test piles. *J. Geotech. Geoenviron. Eng. - ASCE,* **131**, No. 3: 301-310

Bundy S. P. S. (2013). *Geotechnical properties of chalk putties.* PhD Thesis, University of Portsmouth, Portsmouth, UK

Burland J. B. & French, D. J. (1990). Results of trials in weathered chalk of a novel piling system – the wedge pile. *Proc. Intl. Chalk Symposium*, Brighton, UK 375-383

Burland J. B. (1990). Preface. *Proc. Intl. Chalk Symposium*, Brighton, UK: 1-4

Bustamante M., Combarieu, O. & Gianeselli, L. (1980). Portance des pieux dans la craie altérée. *Annales de L'institut technique du Batiment et des Travaux Publics,* **388**, No. SOL FOND 174: 26-56

Bustamante M. & Gianeselli, L. (1982). Pile bearing capacity prediction by means of static penetrometer CPT. *Proc. 2nd Eur. Symp. on Penetration Testing*, Amsterdam, the Netherlands: 493-500

Butterfield R. & Johnston, I. W. (1973). The stresses acting on a continuously penetrating pile. *Proc. 8th Intl. Conf. Soil Mech. Found. Eng.*, Moscow, Russia: 39-45

Byrne B., McAdam, R., Burd, H., Houlsby, G., Martin, C., Beuckelaer, W., Zdravkovic, L., Taborda, D., Potts, D. & Jardine, R. (2017). PISA: new design methods for offshore wind turbine monopiles. *Proc. 8th Intl. Conf. Offshore Site Investigation and Geotechnics*, London UK: 142-161

Cambridge-Insitu (2013). *Wikinger Offshore Wind Farm Ground Investigation 2013 - Results of Pressuremeter tests* Cambridge Insitu Ltd*,* CIR1286/13

Carotenuto P., Meyer, V., Strøm, P. J., Cabarkapa, Z., St. John, H. & Jardine, R. J. (2018). Installation and axial capacity of the Sheringham Shoal offshore wind farm monopiles – a case history. *Proc. BGA Conf. Engineering in chalk (under review).*

Carrington T. M., Li, G. & Rattley, M. J. (2011). A new assessment of ultimate unit friction for driven piles in low to medium density chalk. *Proc. 15th Eur. Conf. Soil Mech. & Geotech. Eng.*, Amsterdam, The Netherlands: 825-830

Cassidy M. J. (2012). Experimental observations of the penetration of spudcan footings in silt. *Géotechnique,* **62**, No. 8: 727-732

Castelli R. J. & Hussein, M. (1998). Pile Foundation Construction for the Buckman Bridge Jacksonville, Florida. *Proc. 4th Intl. Conf. Case Histories in Geotechnical Engineering*, St. Louis, Missouri: 1079-1085

ChalkRock (2007). *Thanet Offshore Windfarm - St Nicholas Court Farm Chalk Pit Experimental Site - Chalk Core logging,* ChalkRock Ltd., Report 3

Chambers H. & Lehane, B. M. (2011). An assessment of the geotechnical strength reduction factors specified in the new Australian piling standard. *Australian Geomechanics,* **46**, No. 4: 71

Chan L. D. (2017). *Laboratory investigation of chalk-steel interface shearing.* MSc Thesis, Imperial College, London, UK

Cherrill H. E., Gammage, C. L. & Mitchell, J. M. (1992). Driven precast concrete piles in chalk and the use of bitumen slipcoating to reduce negative skin friction in chalk fill. *Proc. ICE Conf. Piling: European practice and worldwide trends*, London, UK: 322-329

Chin F. K. (1970). Estimation of the ultimate load of piles not carried to failure. *Proc. 2nd Southeast Asian Conf. on Soil Eng.*, Singapore: 81-92

Chin F. K. (1971). Discussion: Pile Tests—Arkansas River Project. *J. Soil Mech. Found. Div. - ASCE,* **97**, No. 6: 930-932

Chow F. C. (1997). *Investigations into Displacement Pile Behaviour for Offshore Foundations.* PhD Thesis, Imperial College London, London, UK

Chow F. C., Jardine, R. J., Brucy, F. & Nauroy, J. F. (1998). Effects of time on capacity of pipe piles in dense marine sand. *J. Geotech. Geoenviron. Eng. - ASCE,* **124**, No. 3: 254-264

Chung S. F., Randolph, M. F. & Schneider, J. A. (2006). Effect of penetration rate on penetrometer resistance in clay. *J. Geotech. Geoenviron. Eng. - ASCE,* **132**, No. 9: 1188-1196

Ciavaglia F., Carey, J. & Diambra, A. (2017a). Time-dependent uplift capacity of driven piles in low to medium density chalk. *Géotechnique Letters,* **7**, No. March: 1-7

Ciavaglia F., Carey, J. & Diambra, A. (2017b). Monotonic and cyclic lateral tests on driven piles in Chalk. *Proc. of the ICE Geotech. Eng.,* **170**, No. 4: 353-366

CIJV (2013). *Wikinger offshore windfarm: Geotechnical Site Survey Report based on main geotechnical campaign,* COWI/IMS Joint Venture, A031412-005-RP

CIJV (2014a). *Pile Load Test Concept Based on Geotechnical Main Campaign,* COWI/IMS Joint Venture, WIK-CIV-IB-0816

CIJV (2014b). *Wikinger offshore windfarm: soil and foundation expertise report based on main geotechnical campaign,* COWI/IMS Joint Venture, WIK-CIJV-IB-0488

CIJV (2016). *Wikinger Offshore Windfarm: Turbine location WK08 - Expert opinion about DLT results at WK08,* COWI/IMS Joint Venture, Ref: 301000021

Clarke B. G. (2017). *Engineering of Glacial Deposits,* UK: CRC Press.

Clausen C., Aas, P. & Karlsrud, K. (2005). Bearing capacity of driven piles in sand, the NGI approach. *Proc. Intl. Symp. Frontiers in Offshore Geotechnics*, Perth, Australia: 574-580

Clayton C. R. I. (1977). Some properties of remoulded chalk. *Proc. 9th Intl. Conf. Soil Mech. Found Eng.*, Tokyo, Japan: 65-68

Clayton C. R. I. (1983). The influence of diagenesis on some index properties of chalk in England. *Géotechnique,* **33**, No. 3: 225-241

Clayton C. R. I. & Matthews, M. C. (1987). Deformation, diagenesis and the mechanical behaviour of chalk. *Deformation of Sediments and Sedimentary Rocks, Geological Society Special Publication,* **29**, No. 1: 55-62

Clayton C. R. I. (1990). The mechanical properties of the Chalk. *Proc. Intl. Chalk Symposium*, Brighton, UK: 213-233

Clayton C. R. I., Gordon, M. A. & Matthews, M. C. (1994). Measurements of stiffness of soils and weak rocks using small strain laboratory tests and field geophysics. *Proc. Intl. Symp. on Pre-Failure Deformation Characteristics of Geomaterials*, Sapporo, Japan: 229-234

Clayton C. R. I. & Heymann, G. (2001). Stiffness of geomaterials at very small strains. *Géotechnique,* **51**, No. 3: 245-255

Clayton C. R. l. (1978). *Chalk as Fill.* PhD Thesis, University of Surrey, Surrey, UK

Clayton C. R. l., Matthews, M. C. & Heymann, G. (2002). The Chalk. *Proc. 1st Intl. Workshop on Characterisation and Engineering Properties of Natural Soils*, Singapore: 1403-1434

Collin F., Cui, Y. J., Schroeder, C. & Charlier, R. (2002). Mechanical behaviour of Lixhe chalk partly saturated by oil and water: experiment and modelling. *Intl. J. Numer. Anal. Methods Geomech.,* **26**, No. 9: 897-924

Coop M., Atkinson, J. & Taylor, R. (1995). Strength yielding and stiffness of structured and unstructured soils. *Proc. 11th Eur. Conf. Soil. Mech. Found. Eng.*, Copenhagen, Denmark: 55-62

Cotecchia F. & Chandler, R. (1997). The influence of structure on the pre-failure behaviour of a natural clay. *Géotechnique,* **47**, No. 3: 523-544

Coyle H. M. & Gibson, G. C. (1970). Empirical damping constants for sands and clays. *J. Soil Mech. Found. Div. - ASCE,* **96**, No. 3: 949-965

Coyle H. M., Bartoskewitz, R. E. & Berger, W. J. (1973). *Bearing capacity prediction by wave equation analysis - state of the art,* Texas transportation institute*,* Research report 125-8F

D'Alembert J. (1747). Recherches sur la courbe que forme une corde tendue mise en vibrations. *Histoire de l'Académie Royale des Sciences et Belles Lettres,* **3**, No.: 214-249

Danziger B. R., Lopes, F. R., Costa, A. M. & Pacheco, M. P. (1996). A Discussion on the Uniqueness of CAPWAP–type Analysis. *Proc. 5th Intl. Conf. on the Application of Stress-Wave Theory to Piles*, Orlando, Florida: 11-13

Davis E. H. (1968). Theories of plasticity and the failure of soil masses. *Soil Mechanics Selected Topics*. Butterworths: 341-380

Dayal U. & Allen, J. H. (1975). The effect of penetration rate on the strength of remolded clay and sand samples. *Can. Geotech. J.,* **12**, No. 3: 336-348

De Josselin de Jong G. (1956). Wat gebeurt er in de grond tijdens het heien. *De Ingenieur,* **68**, No.: B77-B88

De Josselin de Jong G. (1972). Discussion to session II *Proc. Roscoe Memorial Symp. on Predictive Soil Mechanics Stress strain behaviour of soils*, Cambridge, UK: 258-261

De Kuiter J. & Beringen, F. (1979). Pile foundations for large North Sea structures. *Marine Georesources & Geotechnology,* **3**, No. 3: 267-314

De Nicola A. & Randolph, M. F. (1993). Tensile and compressive shaft capacity of piles in sand. *J. Geotech. Eng. - ASCE,* **119**, No. 12: 1952-1973

de Raguenel A. (1973). Stabilite des ramblais crayeux de grande hauteur. *La craie: Bull. Liason Labo. P. de. Ch.*, No. Special V: 165-169

Decourt L. (1999). Behavior of foundations under working load conditions. *Proc. 11th Pan-American Conf. Soil Mech. and Geot. Eng.*, Foz do Iguassu, Brazil: 453-488

Deeks A. J. & Randolph, M. F. (1991). Evaluation of the inelastic response of an axisymmetric foundation to impact loading. *Proc. 7th Intl. Conf. on Computer Methods and Advances in Geomechanics*, Cairns, Australia: 735-740

Deeks A. J. & Randolph, M. F. (1995). A simple model for inelastic footing response to transient loading. *Int. J. Num. Meth. Geotech. Eng.,* **19**, No. 5: 307-329

DeJong J. T. & Westgate, Z. J. (2009). Role of initial state, material properties, and confinement condition on local and global soil-structure interface behavior. *J. Geotech. Geoenviron. Eng. - ASCE,* **135**, No. 11: 1646-1660

Delage P., Schroeder, C. & Cui, Y. J. (2008). *Proc. Conf. Prediction and performance on rock mechanics and rock engineering: EUROCK '96*, Torino, France: 1291-1298

Diambra A., Ciavaglia, F., Dimelow, C., Carey, J. & Nash, D. F. T. (2014). Performance of cyclic cone penetration tests in chalk. *Géotechnique Letters,* **4**, No. July–September: 230-237

Dietz M. S. (2000). *Developing an holistic understanding of interface friction using sand with direct shear apparatus.* PhD Thesis, University of Bristol, Bristol, UK

DIN (2005). DIN 4149:2005-04 Buildings in german earthquake areas - Design loads, analysis and structural design of buildings, DIN

DIN (2009). DIN-EN-1997-1: Eurocode 7: Geotechnical Design - Part 1: General rules; English version, DIN

DIN (2012). DIN-1054 Subsoil: Verification of the safety of earthworks and foundations, Supplementary rules to DIN EN 1997-1, DIN

Doherty P., Igoe, D., Murphy, G., Gavin, K., Preston, J., Mc Avoy, C., Byrne, B. W., McAdam, R., Burd, H. J., Houlsby, G. T., Martin, C. M., Zdravkovic, L., Taborda, D. M. G., Potts, D. M., Jardine, R. J., Sideri, M., Schroeder, F. C., Muir Wood, A., Kallehave, D. & Skov Gretlund, J. (2015). Field validation of fibre Bragg grating sensors for measuring strain on driven steel piles. *Géotechnique Letters,* **5**, No.: 74-79

Doughty L. (2016). *Laboratory testing of chalk.* MSc Thesis, Imperial College London, London, UK

Doughty L., Buckley, R. M. & Jardine, R. J. (2018). Laboratory testing of chalk. *Proc. BGA Conf. Engineering in chalk (under review).*

Dove J. E. & Jarrett, J. B. (2002). Behavior of dilative sand interfaces in a geotribology framework. *J. Geotech. Geoenviron. Eng. - ASCE,* **128**, No. 1: 25-37

Downing R. A. (1993). Groundwater resources, their development and management in the UK: an historical perspective. *Q. J. Eng. Geol. Hydrogeol.,* **26**, No. 4: 335-358

Dührkop J., Augustesen, A. H. & Barbosa, P. (2015). Cyclic pile load tests combined with laboratory results to design offshore wind turbine foundations in chalk. *Poc. 3rd Conf. Frontiers in Offshore Geotechnics*, Oslo, Norway: 533-538

Dührkop J., Maretzki, S. & Rieser, J. (2017). Re-evaluation of pile driveability in chalk. *Proc. 8th Intl. Conf. Offshore Site Investigation and Geotechnics* London, UK: 666-673

Dutt R. N., Doyle, E. H., Collins, J. T. & Ganguly, P. (1995). A simple model to predict soil resistance to driving for long piles in deepwater normally consolidated clays. *Offshore Technology Conference*, Houston, Texas: 257-269

EA-Pfähle (2014). *Recommendations on Piling: Piling Committee of the German Geotechnical Society (abbreviated as: EA Pfähle),* Germany: John Wiley & Sons.

Ebensperger I. (2017). *Back Analysis of Offshore Pile Driving Records in Chalk and Glacial Till.* MSc. Thesis, Imperial College London, London, UK

El Naggar M. H. & Novak, M. (1994). Non-linear model for dynamic axial pile response. *J. Geotech. Eng. - ASCE,* **120**, No. 2: 308-329

Esper S. (2017). *Back analysis of offshore pile driving records in chalk.* MSc Thesis, Imperial College London, London, UK

Fahey M. & Lee Goh, A. (1995). A comparison of pressuremeter and piezocone methods of determining the coefficient of consolidation. *Proc. 4th Intl. Symp. on the Pressuremeter and Its New Avenues*, Quebec, Canada: 153-60

Fellenius B. H. (1988). Variation of CAPWAP results as a function of the operator. *Proc. 3rd Intl. Conf. on the Application of Stress Wave Theory to Piles*, Ottawa, Canada: 814-825

Fellenius B. H., Edde, R. D. & Beriault, L. L. (1992). Dynamic and static testing for pile capacity in a fine-grained soil. *Proc. 4th Intl. Conf. on the Application of Stress-Wave Theory to Piles*, The Hague, Netherlands: 401-408

Fellenius B. H. (2002). Determining the Eesistance Distribution in Piles: Part 1: Notes on Shift of No-Load Reading and Residual Load. *Geotech. News Mag.,* **20**, No. 2: 35-38

Finnie I. M. S. & Randolph, M. F. (1994). Punch-through and liquefaction induced failure of shallow foundations on calcareous sediments. *Proc. Int. Conf. Behavior of Offshore Structures*, Boston, Massachusetts: 217-230

Fleming K., Weltman, A., Randolph, M. & Elson, K. (2008). *Piling engineering,* Taylor & Francis.

Focht J. A. & Vijayvergiya, V. N. (1972). A New Way to Predict Capacity of Piles in Clay. *Offshore Technology Conference*, Houston, Texas: 865-874

Foeken R. J. v., Daniels, B. J. & Middendorp, P. (1996). An improved method for the real time calculation of soil resistance during driving. *Proc. 5th Intl. Conf. on the Application of Stress-Wave Theory to Piles*, Orlando, Florida: 1132-1143

Foray P., Balachowski, L. & Rault, G. (1998). Scale effect in shaft friction due to the localisation of deformations. *Proc. Intl. Conf. Centrifuge 98*, Tokyo, Japan: 211-216

Fox E. N. (1932). Stress Phenomena Occurring in Pile Driving. *Engineering, 134.* 263-265

Frank R. (2009). Design of foundations in France with the use of Menard pressuremeter tests (MPM). *J. Soil Mech Found. Eng. - ASCE,* **46**, No. 6: 219-231

Fugro (2012a). *Laboratory testing report: Pile test site, chalk specific testing. St. Nicholas at Wade, UK,* Fugro Geoconsulting Ltd., D34001-2

Fugro (2012b). *Onshore geotechnical report: field data St. Nicholas at Wade UK,* Fugro Geoconsulting Ltd., D34001-1

Fugro (2013). *Wikinger Offshore Windfarm: Advanced Laboratory and Drivability Assessment,* Fugro Geoconsulting Ltd., J22026-1

Gavin K. & Lehane, B. M. (2007). Base load-displacement response of piles in sand. *Can. Geotech. J.,* **44**, No. 9: 1053-1063

Gavin K., Jardine, R. J., Karlsrud, K. & Lehane, B. M. (2015). The effects of pile ageing on the shaft capacity of offshore piles in sand. *Poc. 3rd Conf. Frontiers in Offshore Geotechnics*, Oslo, Norway: 129-151

Gens A. & Hight, D. (1979). The laboratory measurement of design parameters for a glacial till. *Proc. 7th Intl. Conf. Soil Mech. Found. Eng.*, Brighton, UK 57-66

Gens A. (1982). *Stress-strain and strength characteristics of a low plasticity clay.* PhD Thesis, Imperial College London (University of London), London, UK

Glanville W. H., Grime, G., Fox, E. N. & Davies, W. W. (1938). *An investigation of the stresses in reinforced concrete piles during driving,* British Building Research Station, Technical Paper No. 20

Goble G. G. & Rausche, F. (1970). *Pile load test by impact driving,* Paper sponsored by Committee on Construction Practices - Structures Presented at the 49th Annual Meeting

Goble G. G., Likins Jr, G. & Rausche, F. (1975). *Bearing capacity of piles from dynamic measurements,* Ohio Department of Transportation, OHIO-DOT005-75

Goble G. G. & Rausche, F. (1976). *Wave equation analysis of pile driving: WEAP program,* US Department of Transportation, Federal Highway Administration

Gommesen L. & Fabricius, I. L. (2001). Dynamic and static elastic moduli of North Sea and deep sea chalk. *Phys. Chem. Earth (A),* **26**, No. 1-2: 63-68

Haberman R. (2013). *Applied partial differential equations: with Fourier series and boundary value problems,* AMC.

Hampson K., Evans, T., Jardine, R. J., Moran, P., Mackenzie, B. & Rattley, M. (2017). BP Clair Ridge: Independent Foundation Assurance For The Capacity Of Driven Piles in

Very Hard Soils. *Proc. 8th Intl. Conf. Offshore Site Investigation and Geotechnics*, London, UK: 1299-1306
Hamre L. (2018). *RE: Typical monopile sizes.*
Hancock J. M. (1975). The petrology of the Chalk. *Proceedings of the Geologists' Association,* **86**, No. 4: 499-535
Hannigan P., Goble, G. G., Likins, G. & Rausche, F. (2006). *Design and Construction of Driven Pile Foundations,* FHWA, Report No. FHWA NHI-05-042
Hart M. (1987). Orbitally induced cycles in the chalk facies of the United Kingdom. *Cretaceous Research,* **8**, No. 4: 335-348
Hartley C. (2015). *RE: Preliminary pile test data background - Felixstowe South Reconfiguration Project.* Technical Note to Buckley, R. M.
Heerema E. P. (1978). Predicting pile driveability: heather as an illustration of the friction fatigue theory. *Proc. Eur. Offshore Petroleum Conf.*, London, UK: 413-422
Heerema E. P. (1979). Relationships between wall friction, displacement velocity and horizontal stress in clay and in sand, for pile driveability analysis. *Ground engineering,* **12**, No. 1: 55-61
Heymann G. (1998). *The stiffness of soils and weak rocks at very small strains*. PhD Thesis, University of Surrey, Surrey, UK
Hickman R. J. (2004). *Formulation and implementation of a constitutive model for soft rock.* PhD Thesis, Virginia Polytechnic Institute and State University, Virginia, USA
Ho T. Y. K., Jardine, R. J. & Anh-Minh, N. (2010). Large-displacement interface shear between steel and granular media. *Géotechnique,* **61**, No. 3: 221-234
Hobbs N. B. & Robins, P. (1976). Compression and tension tests on driven piles in chalk. *Géotechnique,* **26**, No. 1: 33-46
Hobbs N. B. (1976). Behaviour and design of piles in chalk. *Proc. Symp. on Piles in Weak Rock*, London, UK: 149-175
Hobbs N. B. (1977). Behaviour and design of piles in chalk - an introduction to the discussion of the papers on chalk. *Proc. Symp. on Piles in Weak Rock*, London, UK: 149-175
Hobbs N. B. & Healy, P. R. (1979). *Piling in Chalk* CIRIA, Report PG 6
Hobbs N. B. & Atkinson, M. S. (1993). Compression and tension tests on an open-ended tube pile in chalk. *Ground Engineering,* **26**, No. 3: 31-34
Hodges W. G. H. & Pink, S. (1971). The use of penetrometer soundings in the estimation of pile bearing capacity and settlement for driven piles in highly weathered chalk in Portsmouth areas as an alternative to site investigation by borehole sampling and laboratory testing. *Proc. Roscoe. Mem. Symp. : Stress strain behaviour of soils*, Cambridge University: 769-774
Holeyman A. (1985). Dynamic non-linear skin friction of piles. *Proc. Intl. Symp. on penetrability and driveability of piles - technical committee on penetrability and drivability of piles.*, San Franscisco, California: 173-176
Holeyman A., Legrand, C. & Van Rompaey, D. (1996). A method to predict the driveability of vibratory driven piles. *Proc. 3rd Intl. Conf. on the Application of Stress-Wave Theory to Piles*, Orlando, Florida: 1101-1112
Holloway-Strong M., Hughes, S. & Hellawell, E. (2007). Stress-Deformation Behavior of Chalk. *J. Geomechanics - ASCE,* **7**, No. 6: 403-409
Housel W. S. (1965). Michigan study of pile driving hammers. *J. Soil Mech. Found. Div. - ASCE,* **91** No. SM5: 37-64
Hunter A. & Davisson, M. (1969). Measurements of pile load transfer. *Performance of Deep Foundations ASTM STP 444*: 106-117
Hyde A. F., Higuchi, T. & Yasuhara, K. (2006). Liquefaction, cyclic mobility, and failure of silt. *J. Geotech. Geoenviron. Eng. - ASCE,* **132**, No. 6: 716-735

Iberdrola (2013). *Research project: onshore pile tests in chalk: two-way cyclic axial loading (Confidential Information),* Wind Support Ltd., C011/001TR

Isaacs D. V. (1931). Reinforced concrete pile formulae. *Journal of the Institution of Engineers Australia,* **3**, No. 9: 305-323

Ishihara K., Tatsuoka, F. & Yasuda, S. (1975). Undrained deformation and liquefaction of sand under cyclic stresses. *Soils Found.,* **15**, No. 1: 29-44

ISO (2007). 19902: 2008-07: Petroleum and natural gas industries–Fixed steel offshore structures. 1st Edition, International Standards Organisation

Iverson N. R., Hooyer, T. S. & Baker, R. W. (1998). Ring-shear studies of till deformation: Coulomb-plastic behavior and distributed strain in glacier beds. *Journal of Glaciology,* **44**, No. 148: 634-642

Jardine R., Lehane, B. & Everton, S. (1993). Friction coefficients for piles in sands and silts. *Proc. Conf. Offshore site investigation and foundation behaviour*, London, UK: 661-677

Jardine R. J., Symes, M. J. & Burland, J. B. (1984). The measurement of soil stiffness in the triaxial apparatus. *Géotechnique,* **34**, No. 3: 323-340

Jardine R. J., Brooks, N. J. & Smith, P. R. (1985). The use of electrolevel transducers for strain measurements in triaxial tests on weak rock. *Int. J. Rock Mech. Min. Sci. & Geomech. Abstr.,* **22**, No. 5: 331-337

Jardine R. J. (1985). *Investigations of pile-soil behaviour, with special reference to the foundations of offshore structures.* PhD Thesis, Imperial College London (University of London), London, UK

Jardine R. J. (1992). Some observations on the kinematic nature of soil stiffness. *Soils Found.,* **32**, No. 2: 111-124

Jardine R. J. & Standing, J. R. (2000). *Pile Load Testing Performed for HSE Cyclic Loading Study at Dunkirk, France Volume 1 & 2. ,* Health & Safety Executive, OTO2000 007

Jardine R. J., Chow, F. C., Overy, R. & Standing, J. R. (2005a). *ICP design methods for driven piles in sands and clays,* London: Thomas Telford.

Jardine R. J., Standing, J. R. & Kovacevic, N. (2005b). Lessons learned from full scale observations and the practical application of advanced testing and modeling. *Proc. 3rd Intl. Symp. on Deformation Characteristics of Geomaterials*, Lyon, France: 201-245

Jardine R. J., Standing, J. R. & Chow, F. C. (2006). Some observations of the effects of time on the capacity of piles driven in sand. *Géotechnique,* **56**, No. 4: 227-244

Jardine R. J. & Chow, F. C. (2007). Some recent developments in offshore pile design. *Proc. 6th Intl. Conf. Offshore Site investigation and Geotechnics*, London, UK: 303-332

Jardine R. J., Zhu, B., Foray, P. & Dalton, C. P. (2009). Experimental arrangements for investigation of soil stresses developed around a displacement pile. *Soils Found.,* **49**, No. 5: 661-673

Jardine R. J., Puech, A. & Andersen, K. H. (2012). Cyclic loading of offshore piles: potential effects and practical design. *Proc. 7th Intl. Conf. Offshore Site Investigation and Geotechnics*, London, UK: 59-97

Jardine R. J. & Standing, J. R. (2012). Field axial cyclic loading experiments on piles driven in sand. *Soils Found.,* **52**, No. 4: 723-736

Jardine R. J., Zhu, B. T., Foray, P. & Yang, Z. X. (2013a). Interpretation of stress measurements made around closed-ended displacement piles in sand. *Géotechnique,* **63**, No. 8: 613-627

Jardine R. J., Zhu, B. T., Foray, P. & Yang, Z. X. (2013b). Measurement of stresses around closed-ended displacement piles in sand. *Géotechnique,* **63**, No. 1: 1-17

Jardine R. J. (2014). Advanced laboratory testing in research and practice: the 2nd Bishop Lecture. *Geotechnical Research,* **1**, No. 1: 2-31

Jardine R. J., Thomsen, N. V., Mygind, M., Liingaard, M. A. & Le Blanc Thilsted, C. (2015). Axial capacity design practice for North European wind-turbine projects. *Proc. 3rd Intl. Symp. Frontiers in Offshore Geotechnics*, Oslo, Norway: 581-586

Johnston I. W. (1972). *Electro-Osmosis and Pore-Water Pressures: Their Effect on the Stresses Acting on Driven Piles.* PhD Thesis, University of Southampton, Southampton, UK

Jones D. L. & Morrison, M. (1990). Driven Piles in Chalk. *Proc. International Chalk Symposium*, Brighton, UK 359-364

Joseph T. M., Houlsby, G. T., Burd, H. J. & Taylor, P. (2017). Finite element analysis of soil plug behaviour within open-ended piles *Proc. 8th Intl. Conf. Offshore Site Investigation and Geotechnics* London, UK: 628-635

Kågeson-Loe N., Jones, M., Petley, D. & Leddra, M. (1993). Fabric evolution during the deformation of chalk. *Int. J. Rock Mech. Min. Sci. & Geomech. Abstr.,* **30**, No. 7: 739-745

Karlsrud K., Nadim, F. & Haugen, T. (1986). Piles in clay under cyclic axial loading - Field tests and computational modelling. *Proc. 3rd Intl. Conf. Numerical Methods in Offshore Piling*, Nantes, France: 165-190

Karlsrud K. & Haugen, T. (1986). Axial static capacity of steel model piles in overconsolidated clay. *Publikasjon-Norges Geotekniske Institutt*, No. 163: 1401-1406

Karlsrud K., Hansen, S., Dyvik, R. & Kalsnes, B. (1993a). NGI's pile tests at Tilbrook and Pentre—review of testing procedures and results. *Large-scale Pile Tests in Clay*, London, UK: 491-510

Karlsrud K., Kalsnes, B. & Nowacki, F. (1993b). Response of piles in soft clay and silt deposits to static and cyclic axial loading based on recent instrumented pile load tests. *Offshore Site Investigation and Foundation Behaviour*. Dordrecht: Springer: 549-583

Karlsrud K., Jensen, T. G., Lied, E. K. W., Nowacki, F. & Simonsen, A. S. (2014). Significant ageing effects for axially loaded piles in sand and clay verified by new field load tests. *Offshore Technology Conference*, Houston, Texas: 1-19

Kawabata N., Hayasni, M., Wakiya, Y., Kobayashi, Y. & Mishimura, S. (1994). Simultaneous loading tests of steel piles by dynamic and static methods *Proc. 5th Intl. Conf. & Exhibition on piling and deep foundations*, Bruges, Belgium: 35-40

Kessler T. C., Klint, K., Nilsson, B. & Bjerg, P. L. (2012). Characterization of sand lenses embedded in tills. *Quaternary Science Reviews,* **53**, No. 2012: 55-71

Kishida H. & Uesugi, M. (1987). Tests of the interface between sand and steel in the simple shear apparatus. *Géotechnique,* **37**, No. 1: 45-52

Kolk H. & der Velde, E. (1996). A reliable method to determine friction capacity of piles driven into clays. *Offshore Technology Conference*, Houston, Texas: 337-346

Kolk H. J., Baaijens, A. E. & Senders, M. (2005). Design criteria for pipe piles in silica sands. *Proc. 1st Intl. Symp. on Frontiers in Offshore Geotechnics*, Perth, Australia: 711-716

Komurka V. E., Wagner, A. B. & Edil, T. B. (2003). *Estimating soil/pile set-up* Wisconsin Department of Transportation*,* WHRP Report No. 03-05

Korsnes R., Wersland, E., Austad, T. & Madland, M. (2008). Anisotropy in chalk studied by rock mechanics. *J. Pet. Sci. Eng.,* **62**, No. 1: 28-35

Kraft L. M., Focht, J. A. & Amerasinghe, S. F. (1981). Friction capacity of piles driven into clay. *J. Geotech. Geoenviron. Eng. - ASCE,* **107**, No. 11: 1521-1541

Kuwano R. & Jardine, R. (1998). Stiffness measurements in a stress-path cell. *Pre-failure deformation behaviour of geomaterials*. London, UK: ICE: 391-94

Kuwano R. (1999). *The Stiffness and Yielding Anisotropy of Sand.* PhD Thesis, Imperial College London, London, UK

Kuwano R. & Jardine, R. (2007). A triaxial investigation of kinematic yielding in sand. *Géotechnique,* **57**, No. 7: 563-579

Lade P. V. & Overton, D. D. (1989). Cementation effects in frictional materials. *J. Geotech. Eng. - ASCE,* **115**, No. 10: 1373-1387
Lahrs T. & Kallias, A. (2013). Probebelastungen von Stahlrohren in Kreide für den Offshore-Windpark Baltic 2. *Proc. Pfahl Symposium*, Braunschweig, Germany: 451-466
Lake L. (1975). *Engineering Properties of Chalk with Special Reference to Foundation Design and Performance.* PhD Thesis, University of Surrey, Surrey, UK
Lambe T. W. & Whitman, R. V. (2008). *Soil mechanics: SI version,* John Wiley & Sons.
Lankelma (2016). S10-S15 Cone - CFI/CFIP Data sheet.
Le T. M. H., Eiksund, G. R. & Strøm, P. J. (2014). Characterisation of Residual Shear Strength at the Sheringham Shoal Offshore Wind Farm. *Proc. 33rd Intl. Conf. Ocean, Offshore and Arctic Eng.*, San Francisco, California: 1-9
Leddra M. J. & Jones, M. E. (1990). Steady-state flow during undrained loading of chalk. *Proc. Intl. Chalk Symposium*, Brighton, UK: 4-7
Leddra M. J., Jones, M. E. & Goldsmith, A. S. (1993). Compaction and shear deformation of a weakly-cemented, high porosity sedimentary rock. *The Engineering Geology of Weak Rock*, Leeds, UK 45-54
Lee S. L., Chow, Y. K., Karunaratne, G. P. & Wong, K. Y. (1988). Rational wave equation model for pile-driving analysis. *J. Geotech. Eng. - ASCE,* **114**, No. 3: 306-325
Lehane B. & Jardine, R. (1994a). Displacement-pile behaviour in a soft marine clay. *Can. Geotech. J.,* **31**, No. 2: 181-191
Lehane B. M. & Jardine, R. J. (1992a). The behavior of a displacement pile in glacial till. *Proc. 6th Int. Conf. Behavior of Offshore Structures*, Imperial College, UK: 555-566
Lehane B. M. & Jardine, R. J. (1992b). The behaviour of a displacement pile in Bothkennar clay. *Proc. Wroth Memorial Symp. on Predictive Soil Mechanics*, Oxford, UK: 421-435
Lehane B. M. (1992). *Experimental Investigations of Pile Behaviour using Instrumented Field Piles.* PhD Thesis, Imperial College London, London, UK
Lehane B. M., Jardine, R. J., Bond, A. J. & Frank, R. (1993). Mechanisms of shaft friction in sand from instrumented pile tests. *J. Geotech. Eng - ASCE,* **119**, No. 1: 19-35
Lehane B. M. & Jardine, R. J. (1994b). Displacement pile behaviour in glacial clay. *Can. Geotech. J.,* **31**, No. 1: 79-90
Lehane B. M., Schneider, J. A. & Xu, X. (2005a). The UWA-05 method for prediction of axial capacity of driven piles in sand. *Proc. 1st Intl. Symp. Frontiers in Offshore Geotechnics*, Perth, Australia: 683-689
Lehane B. M., Schneider, J. A. & Xu, X. (2005b). *A review of design methods for offshore driven piles in siliceous sand,* University of Western Australia*,* UWA Report 05358
Lehane B. M., Schneider, J. A. & Xu, X. (2007). Development of the UWA-05 design method for open and closed ended driven piles in siliceous sand. *Proc. GeoDenver 2007: Contemporary Issues In Deep Foundations*, Denver, Colarado, USA: 1-10
Lehane B. M., Schneider, J. A., Lim, J. K. & Mortara, G. (2012a). Shaft friction from instrumented displacement piles in an uncemented calcareous sand. *J. Geotech. Geoenviron. Eng. - ASCE,* **138**, No. 11: 1357-1368
Lehane B. M., Li, Y. & Williams, R. (2012b). Shaft capacity of displacement piles in clay using the cone penetration test. *J. Geotech. Geoenviron. Eng. - ASCE,* **139**, No. 2: 253-266
Lehane B. M., Lim, J. K., Carotenuto, P., Nadim, F., Lacasse, S., Jardine, R. J. & van Dijk, B. (2017). Characteristics of unified databases for driven piles. *Proc. 8th Intl. Conf. Offshore Site Investigation and Geotechnics*, London, UK: 162-194
Lemke W. (1998). Sedimentation und paläogeographische Entwicklung im westlichen Ostseeraum (Mecklenburger Bucht bis Arkonabecken) vom Ende der

Weichselvereisung bis zur Litorinatransgression. *Meereswissenschaftliche Berichte* **31**, No. 0: 1-156
Leroueil S. & Vaughan, P. R. (1990). The general and congruent effects of structure in natural soils and weak rocks. *Géotechnique,* **40**, No. 3: 467-488
Li X. S. & Wang, Y. (1998). Linear representation of steady-state line for sand. *J. Geotech. Geoenviron. Eng. - ASCE,* **124**, No. 12: 1215-1217
Liang R. Y. (2000). Correlative Study of Smith Damping Coefficient and SPT blow Count. *Proc. 6th Intl. Conf. on the Application of Stress-Wave Theory to Piles*, Rotterdam, The Netherlands: 461-467
Lim J. K. & Lehane, B. M. (2014). Characterisation of the effects of time on the shaft friction of displacement piles in sand. *Géotechnique,* **64**, No. 6: 476-485
Lim J. K. (2014). *Time and scale effects on the shaft friction of displacement piles in sand.* PhD Thesis, University of Western Australia, Crawley, Australia
Lim J. K. & Lehane, B. (2015a). Time effects on shaft capacity of jacked piles in sand. *Can. Geotech. J.,* **52**, No. 11: 1830-1838
Lim J. K. & Lehane, B. M. (2015b). Interpretation difficulties of pile setup in sand. *3rd Intl. Symp. Frontiers in Offshore Geotechnics*, Oslo, Norway: 605-611
Lings M. L. & Dietz, M. S. (2005). The peak strength of sand-steel interfaces and the role of dilation. *Soils Found.,* **45**, No. 6: 1-14
Litkouthi S. & Poskitt, T. J. (1980). Damping constants for pile driveability calculations. *Géotechnique,* **30**, No. 1: 77-86
Long M. & Menkiti, C. O. (2007). Geotechnical properties of Dublin boulder clay. *Géotechnique,* **57**, No. 7: 595-611
Lord J. (1976). A comparison of three types of driven cast in situ pile in chalk. *Géotechnique,* **26**, No. 1: 73-93
Lord J. A. & Davies, J. A. G. (1979). Lateral loading and tension tests on a driven cased pile in chalk. *Proc. ICE Conf. on Recent Developments in the Design and Construction of Piles*, London, UK: 113-120
Lord J. A., Twine, D. & Yeow, H. (1994). *Foundations in chalk Report,* CIRIA, PR11
Lord J. A., Clayton, C. R. l. & Mortimore, R. N. (2002). *Engineering in chalk,* CIRIA, C574
Loukidis D., Salgado, R. & Abou-Jaoude, G. (2008). *Assessment of Axially-Loaded Pile Dynamic Design Methods and Review of INDOT Axially-Loaded Design Procedure, Purdue University,* FHWA, FHWA/IN/JTRP-2008/6
Lunne T., Robertson, P. K. & Powell, J. J. M. (1997). *Cone penetration testing in Geotechnical Practice,* E & FN Spon.
Lysmer J. & Richart, F. E. (1966). Dynamic response of footings to vertical loading. *J. Eng. Mech. Div. - ASCE,* **92**, No. 1: 65-91
Mandolini A., Russo, G. & Viggiani, C. (2005). Pile foundations: Experimental investigations, analysis and design. *Proc. Intl. Conf. Soil Mech. Geotech. Eng.*, Osaka, Japan: 177-214
Manzari M. T. & Dafalias, Y. F. (1997). A critical state two-surface plasticity model for sands. *Géotechnique,* **47**, No. 2: 255-272
Marsland A. & Powell, J. (1985). Field and laboratory investigations of the clay tills at the Building Research Establishment test site at Cowden, Holderness. *Proc. Intl. Conf. Construction in Glacial Tills and Boulder Clays*, Edinburgh, UK: 147-168
Matlock H., Bogard, D., McClelland, F. & Chan, J. H. (1998). Technical Program - Tension Pile Study. *Offshore Technology Conference*, Houston, Texas: 407-413
Matsumoto T. & Takei, M. (1991). Effects of soil plug on behaviour of driven pipe piles. *Soils Found.,* **31**, No. 2: 14-34

Matthews M., Clayton, C. & Russell, C. (1993). Assessing the mass compressibility of chalk from visual description. *Proc. Conf. Engineering Geology of Weak Rocks*, Leeds, UK: 351-368

Matthews M. C. & Clayton, C. R. I. (1993). Influence of intact porosity on the engineering properties of a weak rock. *Intl. Symp. Geotechnical Engineering of Hard Soils and Soft Rocks*, Rotterdam, the Netherlands: 693-702

Matthews M. C. (1993). *The mass compressibility of fractured chalk.* PhD Thesis, University of Surrey, Surrey, UK

Matthews M. C., Clayton, C. R. I. & Own, Y. (2000). The use of field geophysical techniques to determine geotechnical stiffness parameters. *Proceedings of the ICE Geotech Eng,* **143**, No. 1: 31-42

Mayne P. W. & Kulhawy, F. H. (1982). Ko- OCR Relationships in Soil. *J. Soil Mech. Found. Div. - ASCE,* **108**, No. 6: 851-872

Mayne P. W. & Rix, G. J. (1993). G max-qc relationships for clays. *Geotech. Test. J,* **16**, No. 1: 54-60

McClelland B. (1974). Design of deep penetration piles for ocean structures. *J. Geotech. Eng. - ASCE,* **100**, No. GT7: 705-747

Meigh A. C. (1971). Some driving and loading tests on piles in gravel and chalk. *Proc. Conf. Behaviour of Piles*, London, UK: 9-16

Merritt A. S., Schroeder, F. C., Jardine, R. J., Stuyts, B., Cathie, D. & Cleverly, W. (2012). Development of a pile design methodology for an offshore wind farm in the North Sea. *Proc. 7th Intl. Conf. Offshore Site Investigation and Geotechnics*, London, UK: 439-447

Mesri G., Feng, T. W. & Benak, J. M. (1990). Post densification penetration resistance of clean sands. *J. Geotech. Eng. - ASCE,* **116**, No. 7: 1095-1115

Met-Office (2016). Daily and hourly ranfall datasets from weather station at Manston 30 September 2015 - 14 February 2016.

Michaelides O. D., Bouckovalas, G. & Gazetas, G. (1998). Non-linear soil properties and impedances for axially vibrating pile elements. *Soils Found.,* **38**, No. 3: 129-142

Middendorp P. (1987). *Numerical model for TNOWAVE,* TNO-IBBC*,* Report BI-86-75

Middendorp P. & Verbeek, G. E. H. (2006). 30 Years of Experience with the Wave Equation Solution Based on the Method of Characteristics. *Proc. GeoCongress 2006: Geotechnical Engineering in the Information Technology Age*, Atlanta, Georgia: 1-6

Middendorp P. (2015). *RE: Allwave-DLT signal match quality assessment - Personal Communication.*

Middendorp P. (2016). *RE: AllWave-PDP Buckley fatigue model instructions - Personal Communication.*

Mortimore R., Roberts, L. & Jones, D. (1990). Logging of chalk for engineering purposes. *Proc. Intl. Chalk Symposium*, Brighton, UK: 133-152

Mortimore R. (1996). *The geology of the Chalk along the route of the Channel Tunnel Rail Link with specific reference to the engineering geology of tunnels,* Union Railways Limited, Croydon*,* Review Report No. 4

Mortimore R. (2011). A chalk revolution: what have we done to the Chalk of England? *Proceedings of the Geologists' Association,* **122**, No. 2: 232-297

Mortimore R. N. & Fielding, P. M. (1990). The relationship between texture, density and strength of chalk. *Proc. Intl. Chalk Symposium*, Brighton, UK: 109-132

Mortimore R. N. (1990). Chalk or chalk. *Proc. Intl. Chalk Symposium*, Brighton, UK: 15-45

Mortimore R. N., Wood, C. J. & Gallois, R. W. (2001). The Upper Cretaceous rocks of the British Isles. *British upper Cretaceous stratigraphy, Geological Conservation Review Series, No. 23*. Joint Nature Conservation Committee: 1-26

Mortimore R. N., Stone, K. J., Lawrence, J. & Duperret, A. (2004). Chalk physical properties and cliff instability. *Coastal Chalk Cliff Instability, Geological Society, London, Engineering Geology Special Publications,* **20**, No. 1: 75-88

Mortimore R. N. (2012). The 11th Glossop Lecture: Making sense of Chalk: a total-rock approach to its Engineering Geology. *Q. J. Eng. Geol. Hydrogeol.,* **45**, No.: 252-334

Mortimore R. N. (2014a). The Engineering Geology of the Chalk. *Logging the Chalk - A one day workshop: Course Notes.*

Mortimore R. N. (2014b). *Logging the Chalk,* Scotland: Whittles publishing.

Moulds R. I. (2001). Pile Driving in Chalk. *Proc. Underground Construction Symposium*, London, UK: 425-438

Muir Wood A., Mackenzie, B., Burbury, D., Rattley, M., Clayton, C. R. I., Mygind, M., Wessel Andersen, K., Le Blanc Thilsted, C. & Albjerg Liingaard, M. (2015). Design of large diameter monopiles in chalk at Westermost Rough offshore wind farm. *Poc. 3rd Conf. Frontiers in Offshore Geotechnics*, Oslo, Norway: 723-728

Ng K. W. & Sritharan, S. (2013). Improving dynamic soil parameters and advancing the pile signal matching technique. *Computers and Geotechnics,* **54**, No.: 166-174

Nguyen T. T., Berggren, B. & Hansbo, S. (1988). A new soil model for pile driving and driveability analysis. *Proc. 3rd Intl. Conf. on Application of Stress-Wave Theory to Piles*, Vancouver, Canada: 353-367

Norrie C. (2015). *Pile driving performance in low to medium density chalk.* MSc Thesis, Imperial College London, London, UK

Novak M., Aboul-Ella, F. & Nogami, T. (1978). Dynamic soil reactions for plane strain case. *J. Eng. Mech. Div. - ASCE,* **104**, No. EM4: 953-959

Obst K., Nachtweide, C. & Müller, U. (2017). Late Saalian and Weichselian glaciations in the German Baltic Sea documented by Pleistocene successions at the southeastern margin of the Arkona Basin. *Boreas,* **46**, No. 1: 18-33

Orea Velazquez I. E. (2015). *Axial capacity of displacement piles in residual soil.* MEng Thesis, University of Western Australia, Crawley, Australia

Overy R. (2007). The use of ICP design methods for the foundations of nine platforms installed in the UK North Sea. *Proc. 6th Intl. Conf. Offshore Site investigation and Geotechnics*, London, UK: 359-366

Paikowsky S. G., Whitman, R. V. & Baligh, M. M. (1989). A new look at the phenomenon of offshore pile plugging. *Marine Georesources & Geotechnology,* **8**, No. 3: 213-230

Paikowsky S. G., Regan, J. E. & McDonnell, J. J. (1994). *A simplified field method for capacity evaluation of driven piles,* FHWA, FHWA-RD-94-042

Papamichos E., Brignoli, M. & Santarelli, F. (1997). An experimental and theoretical study of a partially saturated collapsible rock. *Mechanics of Cohesive-frictional Materials,* **2**, No. 3: 251-278

Pedersen S. H. & Rhett, D. W. (1998). A Parametric Study of Compressional and Shear Wave Velocities in Ekofisk Reservoir Chalk. *Proc. SPE/ISRM Rock Mechanics in Petroleum Engineering: EUROCK '98*, Trondheim, Norway: 1-8

Pellew A. L. (2002). *Field Investigations Into Pile Behaviour Clay.* PhD Thesis, Imperial College London, London, UK

Pestana J. M. & Whittle, A. (1995). Compression model for cohesionless soils. *Géotechnique,* **45**, No. 4: 611-632

Petley D., Jones, M. E., Fan, C., Stafford, C., Leddra, M. J. & Kageson-Loe, N. (1993). Deformation and fabric changes in weak fine-grained rocks during high pressure consolidation and shear. *Proc. 1st Intl. Symp. Geotech. Eng. of Hard Soils–Soft Rocks*, Athens, Greece: 737-743

Pile-Dynamics (2006). *CAPWAP - Case Pile Wave Analysis Program,* Pile Dynamics Inc., Background Report
Potyondy J. G. (1961). Skin friction between various soils and construction materials. *Géotechnique,* **11**, No. 4: 339-353
Poulos H. G. (1988). Cyclic stability diagram for axially loaded piles. *J. Geotech. Geoenviron. Eng. - ASCE,* **114**, No. 8: 877-895
Powell J. & Quarterman, R. (1994). *A reappraisal of CPT testing in chalk,* Building Research Establishment, G/GP/9412
Power P. (1982). The use of the electric static cone penetrometer in the determination of the engineering properties of chalk. *Proc. 2nd Eur. Symp. on Penetration Testing*, Amsterdam, The Netherlands: 769-774
Power P. T., Gillespie, A. C. & Thomas, S. (1990). Geotechnical investigation in the chalk at the Amethyst gas field, North Sea. *Proc. Intl. Chalk Symposium*, Brighton, UK: 403-412
Price M., Downing, R. A. & Edmunds, W. M. (1993). The Chalk as an aquifer. *The hydrogeology of the Chalk of north-west Europe*. Oxford University Press: 35-58
Randolph M. F. & Wroth, C. P. (1979). An analytical solution for the consolidation around a driven pile. *Intl. J. Numer. Anal. Methods Geomech.,* **3**, No. 3: 217-229
Randolph M. F. & Wroth, C. (1981). Application of the failure state in undrained simple shear to the shaft capacity of driven piles. *Géotechnique,* **31**, No. 1: 143-157
Randolph M. F. (1983). Design considerations for offshore piles. *Proc. Conf. Geotechnical Practice in Offshore Engineering*, Austin, Texas, USA: 422-439
Randolph M. F. & Murphy, B. S. (1985). Shaft capacity of driven piles in clay. *Offshore Technology Conference*, Houston Texas: 371-378
Randolph M. F. & Simons, H. A. (1986). An improved soil model for one-dimensional pile driving analysis. *Proc. 3rd Intl. Conf. Numerical Methods in Offshore Piling*, Nantes, France: 3-17
Randolph M. F. (1987). Modelling of the soil plug response during pile driving. *Proc. 9th South East Asian Conf. Soil Mech.*, Bangkok, Thailand: 6.1-6.14
Randolph M. F. (1990). Analysis of the dynamics of pile driving. *Developments in Soil Mechanics IV: Advanced Geotechnical Analyses*. Elsevier: 202-245
Randolph M. F. (1993). Analysis of stress-wave data from pile tests at Pentre and Tilbrook. *Large-scale pile tests in clay*, 1993 1993 London. pp.^
Randolph M. F., Dolwin, J. & Beck, R. (1994). Design of driven piles in sand. *Géotechnique,* **44**, No. 3: 427-48
Randolph M. F. (2003). Science and empiricism in pile foundation design. *Géotechnique,* **53**, No. 10: 847-875
Randolph M. F. (2004). Characterisation of soft sediments for offshore applications. *Proc. 2nd Intl. Conf. on Site Characterisation*, Porto, Portugal: 209-232
Randolph M. F. (2008). *IMPACT - Dynamic analysis of pile driving,* Manual
Randolph M. F. & Gourvenec, S. (2011). *Offshore geotechnical engineering,* CRC Press.
Rattley M., Costa, L., Jardine, R. J. & Cleverly, W. (2017). Laboratory Test Predictions of the Cyclic Axial Resistance of a Pile Driven in North Sea Soils. *Proc. 8th Intl. Conf. Offshore Site Investigation and Geotechnics*, London, UK: 636-643
Rausche F., Goble, G. G. & Likins Jr, G. E. (1985). Dynamic determination of pile capacity. *J. Geotech. Eng -ASCE,* **111**, No. 3: 367-383
Rausche F., Richardson, B. & Likins, G. (eds.) (1996). *Multiple blow Capwap analysis of pile dynamic records,* Orlando, Florida, USA: Balkema.

Rausche F., Robinson, B. & Liang, L. (2000). Automatic signal matching with CAPWAP. *Proc. 6th Intl. Conf. on the Application of Stress-Wave Theory to Piles*, Sao Paulo, Brazil: 53-58

Rausche F. & Hussein, M. (2000). Pile driving in calcareous sediments. *Proc. 2nd Intl. Conf. Engineering for Calcareous Sediments*, Bahrain: 345-359

Rausche F., Likins, G. & Hussein, M. (2008). Analysis of Post-installation Dynamic Load Test Data for Capacity Evaluation of Deep Foundations. *Proc. Geocongress 2008: From research to practice in geotechnical engineering*, No. 180: 312-330

Razoaki R. N. (2000). *Effect of ageing on mechanics of chalk slurries.* PhD Thesis, University of Portsmouth, Portsmouth, UK

Ridgway A. & Jardine, R. (2007). A re-evaluation of driven pile capacities for sites involving low plasticity, low OCR clays. *Proc. 6th Intl. Conf. Offshore Site Investigation and Geotechnics*, London, UK: 347-356

Riker R. & Fellenius, B. (1992). A comparison of static and dynamic pile test results. *Proc. 4th Intl. Conf. on the Application of Stress-Wave Theory to Piles*, The Hague, Netherlands: 143-152

Rimoy S. & Jardine, R. (2015). Analysis of an extended field test database regarding driven pile ageing in sands. *Proc. 16th Eur. Conf. Soil Mech. Geotech. Eng*, Edinburgh, Scotland 1157-1162

Rimoy S. P., Jardine, R. J. & Standing, J. R. (2013). Displacement response to axial cycling of piles driven in sand. *Proc. of the ICE Geotech. Eng.,* **166**, No. GE2: 131-146

Rimoy S. P., Silva, M., Jardine, R. J., Yang, Z. X., Zhu, B. T. & Tsuha, C. H. C. (2015). Field and model investigations into the influence of age on axial capacity of displacement piles in silica sands. *Géotechnique,* **65**, No. 7: 576-589

Risnes R., Kristensen, C. N. & Andersen, M. (1996). Triaxial tests on high porosity chalk with different saturating fluids. *Proc. 5th North Sea Chalk Symposium*, Reims, France: 1-13

Risnes R. & Flaageng, O. (1999). Mechanical properties of chalk with emphasis on chalk-fluid interactions and micromechanical aspects. *Oil & Gas Science and Technology – Rev. IFP,* **54 (1999)**, No. 6: 751-758

Risnes R. (2001). Deformation and yield in high porosity outcrop chalk. *Phys. Chem. Earth (A),* **26**, No. 1-2: 53-57

Roberts T. O. L. & Preene, M. (1990). Case studies of construction dewatering in chalk. *Proc. Intl. Chalk Symposium*, Brighton, UK: 571-575

Robertson P. K., Sully, J. P., Woeller, D. J. I., Lunne, T., Powell, J. J. M. & Gillespie, D. G. (1992). Estimating coefficient of consolidation from piezocone tests. *Can. Geotech. J.,* **29**, No. 4: 539-550

Røgen B., Fabricius, I. L., Japsen, P., Høier, C., Mavko, G. & Pedersen, J. M. (2005). Ultrasonic velocities of North Sea chalk samples: influence of porosity, fluid content and texture. *Geophysical Prospecting,* **53**, No. 4: 481-496

Roscoe K. H., Schofield, A. N. & Wroth, C. P. (1958). On the yielding of soils. *Géotechnique,* **8**, No. 1: 22-53

Saint-Venant A. J. C. B. d. (1856). *Mémoire sur la flexion des prismes: sur les glissements transversaux et longitudinaux qui l'accompagnent lorsqu'elle ne s' opère pas uniformément ou en arc de cercle, et sur la forme courbe affectée alors par leurs sections transversales primitivement planes,* Gauthier-Villars.

Saint-Venant A. J. C. B. d. (1867). Mémoire sur le choc longitudinal de deux barres élastiques de grosseurs et de matières semblables ou différentes, et sur la proportion de leur force vive qui est perdue pour la translation ultérieure; et généralement sur le mouvement longitudinal d'un système de deux ou plusieurs prismes élastiques. *Journal de Mathématiques Pures et Appliquées,* **12**, No.: 237-376

Salgado R., Lee, J. & Kim, K. (2002). *Load Tests on Pipe Piles for Development of CPT-Based Design Method,* FHWA, FHWA/IN/JTRP-2002/4
Salgado R., Loukidis, D., Abou-Jaoude, G. & Zhang, Y. (2015). The role of soil stiffness non-linearity in 1D pile driving simulations. *Géotechnique,* **65**, No. 3: 169-187
Schmertmann J. H. (1978). *Guidelines for cone penetration test (Performance and design),* FHWA, FHWA-TS-78-209
Schmertmann J. H. (1991). The mechanical aging of soils. *J. Geotech. Eng. - ASCE,* **117**, No. 9: 1288-1330
Schneider J. A., Xu, X. & Lehane, B. M. (2008). Database assessment of CPT-based design methods for axial capacity of driven piles in siliceous sands. *J. Geotech. Geoenviron. Eng. - ASCE,* **134**, No. 9: 1227-1244
Schneider J. A. (2008). *Analysis of piezocone data for displacement pile design.* PhD Thesis, University of Western Australia, Crawley, Australia
Schneider J. A. & Harmon, I. A. (2010). Analyzing Drivability of Open Ended Piles in Very Dense Sands. *DFI Journal,* **4**, No. 1: 32-44
Schofield A. & Wroth, P. (1968). *Critical state soil mechanics,* London: McGraw-Hill.
Scholle P. A. (1974). Diagenesis of Upper Cretaceous chalks from England, Northern Ireland and the North Sea. *Spec. Pub. int. Ass. Sediment,* **1**, No.: 177-210
Searle I. W. (1979). The interpretation of Begemann friction jacket cone results to give soil types and design parameters. *Proc. 7th Eur. Conf. Soil Mech. Found. Eng.*, Brighton, UK: 265-270
Seng S. & Tanaka, H. (2012). Properties of very soft clays: A study of thixotropic hardening and behavior under low consolidation pressure. *Soils Found.,* **52**, No. 2: 335-345
SETech (2007). *Trial site investigation - Thanet offshore wind farm trial site,* SEtech (Geotechnical Engineers) Ltd., 8564/1
Simons H. A. & Randolph, M. F. (1985). A new approach to one dimensional pile driving analysis. *Intl. Conf. on Numerical Methods in Geomechanics*, Nagoya, Japan: 1457-1464
Simons H. A. (1985). *A theoretical study of pile driving.* PhD Thesis, University of Cambridge, Cambridge, UK
Skempton A. (1951). The bearing capacity of clays. *Building Research Congress Division 1, Part 3*, London, UK: 180-189
Skempton A. (1986). Standard penetration test procedures and the effects in sands of overburden pressure, relative density, particle size, ageing and overconsolidation. *Géotechnique,* **36**, No. 3: 425-447
Skov R. & Denver, H. (1988). Time-dependence of bearing capacity of piles. *Proc. 3rd Int. Conf. on the Application of Stress-Wave Theory to Piles*, Ottowa, Canada: 879-888
Šliaupa S. & Hoth, P. (2011). Geological evolution and resources of the Baltic Sea area from the Precambrian to the Quaternary. *The Baltic Sea Basin*. Springer: 13-51
Smith A. K. C. (2001). Interpretation of cone penetration tests in chalk. *Ground Engineering,* **34**, No. 9: 30-35
Smith E. A. L. (1962). Pile-driving analysis by the wave equation. *J. Soil Mech Found. Eng. - ASCE,* **4**, No. 86: 35-61
Spink T. W. (2002). The CIRIA Chalk description and classification scheme. *Q. J. Eng. Geol. Hydrogeol.,* **35**, No. 4: 363-369
Stallebrass S. & Taylor, R. (1997). The development and evaluation of a constitutive model for the prediction of ground movements in overconsolidated clay. *Géotechnique,* **47**, No. 2: 235-253
Suzuki Y. (2014). *Investigation and interpretation of cone penetration rate effects.* PhD Thesis, The University of Western Australia, Crawley, Australia

Svinkin M. (1996). Soil damping in wave equation analysis of pile capacity. *Proc. 5th Intl. Conf. Application of Stress-Wave Theory to Piles*, Orlando, Florida, USA: 128-143

Svinkin M. R., Morgano, C. M. & Morvant, M. (1994). Pile capacity as a function of time in clayey and sandy soils. *Proc. 5th Intl. Conf. and Exhibition on Piling and Deep Foundations*, Bruges, Belgium: 1.1-1.11

Svinkin M. R. (2004). Some uncertainties in high-strain dynamic pile testing. *Proc. GeoTrans 2004: Geotechnical Engineering for Transportation Projects* Los Angeles, California: 705-714

Taborda D. M. G., Zdravković, L., Kontoe, S. & Potts, D. M. (2014). Computational study on the modification of a bounding surface plasticity model for sands. *Computers and Geotechnics,* **59**, No. 2014: 145-160

Talesnick M. L. & Brafman, M. (1998). Small strain deformation characteristics of two chalks subjected to varying stress conditions. *Q. J. Eng. Geol. Hydrogeol.,* **31**, No. 3: 161-174

Talesnick M. L., Hatzor, Y. H. & Tsesarsky, M. (2001). The elastic deformability and strength of a high porosity, anisotropic chalk. *Int. J. Rock Mech. Min. Sci. & Geomech. Abstr.,* **38**, No. 4: 543-555

Tan S. L., Cuthbertson, J. & Kimmerling, R. E. (2004). Prediction of pile set-up in non-cohesive soils. *Current practices and future trends in deep foundations: Contributions in Honor of George G. Gobel*, Los Angeles, California, USA: 50-65

Tchepak S. (1992). Dynamic and sonic pile integrity testing - a contractors experience. . *Proc. 4th Intl. Conf. on the Application of Stress-Wave Theory to Piles*, The Hague, Netherlands: 339-350

Teh C. I. & Houlsby, G. T. (1991). An analytical study of the cone penetration test in clay. *Géotechnique,* **41**, No. 1: 17-34

Thomas J., van den Berg, M., Chow, F. & Maas, N. (2010). Behaviour of driven tubular steel piles in calcarenite for a marine jetty in Fujairah, United Arab Emirates. *Proc. 2nd Intl. Symp. Frontiers in Offshore Geotechnics.*, Perth, Australia: 549-554

Tomlinson M. J. (1957). The adhesion of piles driven in clay soils. *Proc. 4th Intl. Conf. Soil Mech. Found. Eng.*, London, UK: 66-71

Trenter N. A. (1999). *Engineering in glacial tills,* CIRIA, C504

Tsuha C. H. C., Foray, P. Y., Jardine, R. J., Yang, Z. X., Silva, M. & Rimoy, S. (2012). Behaviour of displacement piles in sand under cyclic axial loading. *Soils Found.,* **52**, No. 3: 393-410

Uesugi M. & Kishida, H. (1986). Frictional resistance at yield between dry sand and mild steel. *Soils Found.,* **26**, No. 4: 139-149

Urmos J. & Wilkens, R. H. (1993). In situ velocities in pelagic carbonates: New insights from ocean drilling program leg 130, Ontong Java Plateau. *Journal of Geophysical Research: Solid Earth,* **98**, No. B5: 7903-7920

Ushev E. (2018). *Laboratory investigation of the mechanical properties of cowden till under static and cyclic conditions.* PhD Thesis, London, UK

Vesic A. S. (1977). *Design of pile foundations,* National cooperative highway research program No. 42

Vijayvergiya V. (1977). Load-movement characteristics of piles. *Proc. 4th Annual Symp. ASCE Waterway, Port, Coastal and Ocean Division*, Long Beach, California, USA: 269-284

Vijayvergiya V. N., Cheng, A. P. & Kolk, H. J. (1977). Design and installation of piles in chalk. *Offshore Technology Conference*, Houston, Texas: 459-464

Voitus van Hamme G., Jansz, J. W., Bomer, H. & Arentsen, D. (1974). Hydroblock and improved pile driving analysis. *De Ingenieur,* **86**, No. 18: 344-353

Wakeling T. (1970). A comparison of the results of standard site investigations methods against the results of a detailed geotechnical investigationin middle chalk at Mundford, Norfolk *Proc. Conf. In situ Investigations in Soils and Rocks*, London, UK: 17-22

Ward W. H., Burland, J. B. & Gallois, R. W. (1968). Geotechnical assessment of a site at Mundford, Norfolk, for a large proton accelerator. *Géotechnique,* **18**, No. 4: 399-431

White D. J. & Bolton, M. D. (2005). Comparing CPT and pile base resistance in sand. *Proceedings of the ICE Geotech Eng,* **158**, No.: 3-14

White J. (2014). *Dynamic Pile Driving Analysis for Assessment of Axial Pile Capacity.* MSc. Thesis, Imperial College London, London, UK

Whittle R. W. (1999). Using non-linear elasticity to obtain the engineering properties of clay - A new solution for the self boring pressuremeter test. *Ground engineering,* **32**, No. 5: 30-34

Whittle R. W., Palix, E. & Donaghy, D. (2017). The Influence of Insertion Process on Determining the Stiffness Characteristics of Chalk, using Pre-Bored, Self-Bored and Pushed Pressuremeters. *Proc. 8th Intl. Conf. Offshore Site Investigation and Geotechnics*, London, UK: 308-315

Wind-Support (2012). *Research Project: Onshore Pile Tests in Chalk - Final Report,* Wind Support Ltd C010/004TR

Xu X., Liu, H. & Lehane, B. M. (2006). Pipe pile installation effects in soft clay. *Proc. of the ICE Geotech. Eng.,* **159**, No. 4: 285-296

Yang Z. X., Jardine, R. J., Zhu, B. T., Foray, P. & Tsuha, C. H. C. (2010). Sand grain crushing and interface shearing during displacement pile installation in sand. *Géotechnique,* **60**, No. 6: 469-482

Yang Z. X., Guo, W. B., Jardine, R. J. & Chow, F. C. (2016). Design method reliability assessment from an extended database of axial load tests on piles driven in sand. *Can. Geotech. J.,* **54**, No. 1: 59-74

Zhang C., Yang, Z., Nguyen, G., Jardine, R. & Einav, I. (2014). Theoretical breakage mechanics and experimental assessment of stresses surrounding piles penetrating into dense silica sand. *Géotechnique Letters,* **4**, No. 1: 11-16

Ziogos A., Brown, M., Ivanovic, A. & Morgan, N. (2016). Chalk-steel interface testing for marine energy foundations. *Proc. of the ICE Geotech. Eng,* **170**, No. 3: 285-298

LIST OF FIGURES

Figure 1-1 The extent of the Chalk in north west Europe (Mortimore, 2012) 4
Figure 2-1 Distribution of Upper Cretaceous chalk lithologies in England (Mortimore, 2011) . 11
Figure 2-2 Coccolithic chalk with foraminifera from Grimes Graves, Norfolk (Lord *et al.*, 2002) 14
Figure 2-3 Geographical variation in intact dry density for a study in English chalk by Clayton (1983) 19
Figure 2-4: Grain sizes for a range of crushed chalks by wet sieving (Clayton, 1978, Lord et al., 2002)..... 19
Figure 2-5 Moisture contents of natural occurring chalks from cliffs and quarry faces and Intact Dry Density – saturated moisture content line (Mortimore and Fielding, 1990, Mortimore *et al.*, 2004)..... 20
Figure 2-6 Variation of UCS strength with IDD and porosity (Matthews and Clayton, 1993) .. 20
Figure 2-7 CIRIA chalk grading scheme proposed by Lord *et al.* (1994), Lord *et al.* (2002) 24
Figure 2-8 Typical cone penetration test profile in chalk at the Mundford site (Power, 1982) .. 29
Figure 2-9 Classification of chalk grade using CPT tests from results available in the literature (data from Power, 1982, Powell and Quarterman, 1994, Smith, 2001)..... 29
Figure 2-10 Relationship between ultrasonic velocity and porosity (adapted from Røgen *et al.*, 2005)..... 30
Figure 2-11: Comparison of initial shear modulus measured in surface geophysics and laboratory tests (adapted from Clayton *et al.*, 1994, Clayton *et al.*, 2002)..... 30
Figure 2-12 Scheme for multiple yielding surface framework (Kuwano and Jardine, 2007) 35
Figure 2-13 One dimensional compression for cohesionless soils showing the Limiting Compression Curve (Pestana and Whittle, 1995)..... 36
Figure 2-14 Definition of the state parameter 36
Figure 2-15 Comparison of behaviour of sand as a function of relative density and the state parameter (Been and Jefferies, 2006) 37
Figure 2-16 De-structured and structured oedometer compression curves and structure permitted space (Leroueil and Vaughan, 1990)..... 37
Figure 2-17 One dimensional K_0 compression tests on four different structured materials (a) schematic stress paths (b) sensitive Canadian clay (c) unweathered Keuper Marl (Mercia Mudstone) (d) artificially bonded soil (e) chalk (Leroueil and Vaughan, 1990)..... 38
Figure 2-18 Stiffness of chalk during undrained shearing in triaxial and surface wave from field testing methods (E=3G assumed for geophysical data) (Heymann, 1998)..... 43
Figure 2-19 Stress-strain curves for low, intermediate and high density chalks in uniaxial compression (Matthews and Clayton, 1993) 43

Figure 2-20 Undrained triaxial tests adapted from Kågeson-Loe et al. (1993) on high porosity Butser Hill chalk consolidated to different mean effective stresses a) stress-strain behaviour b) stress paths Note: numbers indicate initial confining stress in MPa 44
Figure 2-21 Compression of chalk slurry in the oedometer test (Clayton and Matthews, 1987) 50
Figure 2-22 Compression paths for aged and unaged chalk slurry (Razoaki, 2000)..... 50
Figure 2-23 Undrained triaxial compression tests on chalk slurry (Razoaki, 2000) 51
Figure 2-24 Undrained triaxial compression stress paths showing the effect of ageing on undrained stress path for chalk slurry (Razoaki, 2000) 52
Figure 2-25 Change in effective stress at constant water content for remoulded white chalk (Figure taken from Lord et al., 2002) 52
Figure 3-1: (a) A pile in sand under compression load (installation process) (b) residual stresses at the end of the compression test (c) variation of residual load with depth (Alawneh and Malkawi, 2000)..... 61
Figure 3-2: Shaft capacity components in open-ended piles (a) unplugged or fully coring mode (b) plugged mode (adapted from Chow, 1997) 61
Figure 3-3: Schematic illustration of the definitions of Q_{mean} and Q_{cyc} (adapted from Jardine and Standing, 2012)..... 62
Figure 3-4: Interaction diagram showing the influence of number of cycles N and normalised loading parameters on cyclic response along with tentative stability zones (adapted from Jardine and Standing, 2012) Note: Q_{ref} taken as tension shaft capacity 62
Figure 3-5: Dependence of radial effective stresses after installation on relative tip depth (a) definition of relative tip depth (Jardine and Chow, 2007) (b) Installation radial effective stresses measured at instruments along the pile shaft with different h/R values in a soft marine clay (Lehane and Jardine, 1994a)..... 75
Figure 3-6: Stationary radial effective stresses measured in dense sand at Dunkirk at different instrumentation levels reflecting the importance of h/R (Chow, 1997) 76
Figure 3-7: Variation in stationary radial stationary effective stresses (σ'_{rs}/q_b) normalised by base resistance with h/R during installation of piles in sand (Chow, 1997)..... 76
Figure 3-8: Average shaft resistance from CIRIA PR11/C574 database (a) versus average vertical effective stress (b) versus penetration of pile into chalk (adapted from Lord *et al.*, 2002)..... 85
Figure 3-9: Ultimate base resistance versus SPT N value from CIRIA PR11/C574 test database (adapted from Lord *et al.*, 2002)..... 86
Figure 3-10: Piles and *in-situ* locations tests at Fleury-sur-Andelle; adapted from Bustamante *et al.* (1980) 106
Figure 3-11: Pile tests Fleury-sur-Andelle (a) cone penetration profiles (b) shear stress from strain gauges at static failure during compression tests; adapted from Bustamante *et al.* (1980) 106

Figure 3-12: Load displacement behaviour of expanded and unexpanded box piles (Burland and French, 1990)..... 107
Figure 3-13: Results of signal matching at end of driving (EoD) and beginning of restrike (BoR) at a) Humber International Terminal and b) Humber Sea terminal (adapted from Moulds, 2001)..... 108
Figure 3-14: Dynamic and static set-up factors obtained from tests on four piles in Hemmoor Germany. (adapted from Lahrs and Kallias, 2013) 109
Figure 3-15: Staged axial static tension tests at various ages at St. Nicholas at Wade on Pile 1 (adapted from Ciavaglia *et al.*, 2017a) 109
Figure 3-16: Normalised shaft load versus time after driving for static tension tests on Pile 1 and Pile 4 at St. Nicholas at Wade (Wind-Support, 2012, Ciavaglia *et al.*, 2017a, b)..... 110
Figure 3-17: Staged axial static tension tests at various ages at St. Nicholas at Wade on Pile 2 (adapted from Ciavaglia *et al.*, 2017a) 110
Figure 3-18: Pile global axial stiffness versus pile head displacement for static tension tests on a) Pile 1 b) Pile 2 (after Ciavaglia *et al.*, 2017a, Wind-Support, 2012)..... 111
Figure 3-19: Load distribution along the pile length at tension failure for a) 2_A7, b) 2_A122 and c)1_A119 (Ciavaglia *et al.*, 2017a)..... 112
Figure 3-20: Applied load versus time for cyclic and static tests on Pile 1 during Phase 2 (Iberdrola, 2013)..... 113
Figure 3-21: Permanent accumulated cyclic displacement normalised by pile diameter for cyclic tests on Pile 1 (Iberdrola, 2013)..... 114
Figure 3-22: Cyclic loading and unloading stiffnesses for cyclic tests on Pile 1 (Iberdrola, 2013) 114
Figure 3-23: Applied load versus time for cyclic and static tests on Pile 4 during Phase 2 (Iberdrola, 2013)..... 115
Figure 3-24: Permanent accumulated cyclic displacement normalised by pile diameter for cyclic tests on Pile 4 (Iberdrola, 2013)..... 116
Figure 3-25: Cyclic loading and unloading stiffnesses for cyclic tests on Pile 4 (Iberdrola, 2013) 116
Figure 3-26: Local shaft resistance from dynamic and static pile tests at Port of Felixstowe; adapted from data provided by Hartley (2015) 117
Figure 3-27: Cone resistance and base capacity from pile tests (after Hodges and Pink, 1971) 117
Figure 3-28: Set-up factor against time after driving for tests on pre-cast concrete piles driven at Nykøbing Falster; after Skov and Denver (1988)..... 118
Figure 3-29: Additional test results on Type PS piles along with CIRIA database Type PS tests shown on Figure 3-8..... 124

Figure 3-30: Set-up factors with time for tests in the database (a) low-medium density chalk (b) high density chalk 125
Figure 3-31: Ratio of calculated to measured shaft resistance during static tests of open-ended piles using CIRIA PG6 (Hobbs and Healy, 1979) and CIRIA C574 (Lord *et al.*, 2002) methods versus (a) diameter or equivalent diameter (b) length of penetration into chalk (c) pile age 126
Figure 3-32: Comparison of current methods to predict shaft capacity in chalk with measured data 127
Figure 3-33: Cyclic loading tests in the database shown on a cyclic loading interaction diagram along with MS/S/US boundaries for sand after Jardine and Standing (2012) 128
Figure 4-1: Schematic illustration of method of characteristics and waves affected by soil resistance; adapted from Middendorp and Verbeek (2006) 139
Figure 4-2: Strain gauges and accelerometers near the pile head (a) installation/cable handling (b) sealed and fixed sensors (Bilfinger, 2015a) 139
Figure 4-3: Dynamic mechanisms at a) the shaft and b) the base (Loukidis *et al.*, 2008) 145
Figure 4-4: Traditional soil resistance models (a) model configuration adapted from Smith (1962) (b) elasto-plastic behaviour at a shaft node 145
Figure 4-5: Rational soil resistance models adopted at the shaft and at the base; adapted from Randolph and Simons (1986) and Deeks and Randolph (1991) 154
Figure 4-6: Variation of normalised stiffness coefficients Sω1 and Sω2 with frequency 154
Figure 4-7: Effect of soil modulus on spring and radiation dashpot at a pile element for an easy driving case (a) spring b) radiation dashpot (c) total response Note: spring and dashpot shown in active and inactive cases 155
Figure 4-8: Illustration of condition for re-joining of pile and soil at a pile node for an easy driving case (a) $\tau_{s,p}$ versus pile displacement (b) $\tau_{s,p}$ versus time 155
Figure 4-9: Displacements at a pile element during a hammer blow for an easy driving case (a) soil displacements (b) pile displacements 156
Figure 4-10: Effect of soil modulus on spring and radiation dashpot at a pile element for a hard driving case (a) spring b) radiation dashpot (c) total response 156
Figure 4-11: Illustration of condition for re-joining of pile and soil at a pile node for a hard driving case (a) $\tau_{s,p}$ pile displacement (b) time 157
Figure 4-12: Displacements at a pile element during a hammer blow for a hard driving case (a) soil displacements (b) soil displacements 157
Figure 4-13: Viscosity parameters considered and the effect τ_{inter}/τ_{stat} (a) vary β (b) vary α 157
Figure 4-14: Evolution of τinter/τstat with pile displacement (a) vary β (b) vary α 158
Figure 4-15: Effect of (a) varying β on upward travelling wave (b) varying β on pile head displacement (c) varying α on upward travelling wave (d) varying α on pile head displacement 158

Figure 4-16: Comparison of upward travelling waves with different numerical methods 161
Figure 4-17: Upward travelling wave and schematic of stress waves in a pile; adapted from Randolph (2008) - data from Wikinger dataset 170
Figure 4-18: Example of operator dependency for (a) a BoR (hard driving) blow (b) an EoD (easy driving) blow 174
Figure 5-1: Static tension capacity-time trends from first time tests on steel pipe piles driven in sand at 3 sand sites, normalised by ICP-05 tension capacities (adapted from Rimoy *et al.*, 2015) 180
Figure 5-2: Depth from seabed to top of glacial till at the Wikinger OWF (data from CIJV, 2013) 183
Figure 5-3: Depth from seabed to top of chalk at the Wikinger OWF (data from CIJV, 2013) 183
Figure 5-4: Envelopes of PCPT results in fluvioglacial and glacial till 190
Figure 5-5: Secant shear stiffness from pressuremeter tests as interpreted by Cambridge-Insitu (2013) in glacial till, also showing G_{vh} from PCPT correlation at the same depths 190
Figure 5-6: Grading curves in till from hydrometer tests carried out at the 8 test sites 191
Figure 5-7: Undrained shear strength profiles in glacial till at three test sites based on PCPT correlation (Nkt = 22.5), CAU tests and UU tests 191
Figure 5-8: CAU triaxial tests on samples of glacial till from the test sites (a) effective stress paths (b) q/p' versus axial strain 192
Figure 5-9: Oedometer tests on intact samples of glacial till 193
Figure 5-10: Yield stress ratio with depth in glacial till interpreted from oedometer and triaxial test results 193
Figure 5-11: Bishop ring shear apparatus (a) simplified principles of operation (Bishop *et al.*, 1971) (b) photo of apparatus (Chan, 2017) 194
Figure 5-12: Ring shear tests on samples of glacial till conducted at Imperial College (a) interface friction angle versus displacement (b) change in sample thickness versus displacement 195
Figure 5-13: Effect of averaging PCPT parameters over 300mm for tests conducted from the seabed (a) cone resistance (b) sleeve friction (c) penetration pore pressures 204
Figure 5-14: Effect of averaging PCPT parameters over 300mm for tests conducted by down-hole wireline (a) cone resistance (b) sleeve friction (c) penetration pore pressures 204
Figure 5-15: Correlation between cone resistance and cone resistance in chalk developed from the results at eight sites 205
Figure 5-16: Envelopes of PCPT results in Grade A1/A2 chalk (a) cone resistance (b) sleeve friction (c) penetration pore pressures 206
Figure 5-17: Intact dry density at the test sites with depth 206
Figure 5-18: Intact dry density relationship with natural moisture content 207
Figure 5-19: Relationship between unconfined compressive strength and IDD in chalk 207

Figure 5-20: Triaxial tests on samples of intact structured and structureless Wikinger chalk (a) effective stress paths (b) deviator stress versus axial strain 208
Figure 5-21: Shear modulus, G_{vh} in chalk from suspension P-S logging at the test sites 209
Figure 5-22: Oedometer tests on samples of intact chalk 209
Figure 5-23: Putty chalk preparation in the laboratory using a 2.5kg Proctor compactor 210
Figure 5-24: Consolidation and undrained shearing on chalk putty samples from Wikinger (Doughty, 2016, Doughty *et al.*, 2018)..... 210
Figure 5-25: Undrained triaxial tests on chalk putty samples - stress paths and interpreted bounding surfaces (Doughty, 2016, Doughty *et al.*, 2018) 211
Figure 5-26: Secant stiffness normalised by initial mean effective stress for aged and unaged triaxial tests on chalk putty (Doughty, 2016, Doughty *et al.*, 2018) 211
Figure 5-27 Undrained triaxial tests on chalk putty samples – stress – strain behaviour during shearing (Doughty, 2016, Doughty et al., 2018) 212
Figure 5-28: Ring shear tests on chalk samples using mild steel interfaces (Fugro, 2013) 213
Figure 5-29: Pile installation at Wikinger (a) schematic of sensor positions around the test piles (b) Triplex template used to guide installation of test piles (Bilfinger, 2015a)..... 220
Figure 5-30: Recorded blow counts during installation of PC test piles including pauses during installation detailed in Table 5-5 (a) WK38 (b) WK43 (c) WK70..... 221
Figure 5-31: Offshore tensile load test system at Wikinger (a) test pile configuration and spreader beam (b) displacement monitoring system (Bilfinger, 2014) 222
Figure 5-32: Static test loading procedure for offshore tests at Wikinger for loading up to 15MN (adapted from Bilfinger, 2014)..... 223
Figure 5-33: Jacket foundations at Wikinger (a) Isometric 3D view of the jacket foundation (b) jacket plan view from top to bottom showing pile locations (CIJV, 2016)..... 223
Figure 5-34: Blow counts recorded during installation of production piling DPTs at Wikinger 224
Figure 5-35: End of driving shaft resistance of pre-construction piles from back analysis of dynamic measurements 240
Figure 5-36: Example signal match from blow WK38-2_DPT_EOD: measured and calculated (a) force and velocity times impedance (b) upward travelling force (c) displacement 240
Figure 5-37: Trend of normalised radial effective stress reduction with normalised distance from the pile tip for 15 driving blows in chalk..... 241
Figure 5-38: Load – displacement behaviour during static axial tension test WK38-2_SLT_108 241
Figure 5-39: Extrapolation of creep rates to failure (a) Wk38-2 (b) WK43-2 (c) WK70-2..... 242
Figure 5-40: Average shaft resistance against time mobilised during WK38-2_CYC_108 243
Figure 5-41: WK38-2_CYC_108 (a) permanent cyclic displacements normalised by pile diameter (b) cyclic loading and unloading stiffness..... 243

Figure 5-42: Load – displacement behaviour during static axial tension test on WK43-2 244
Figure 5-43: Load – displacement behaviour during static axial tension test on WK70-2 245
Figure 5-44: Stiffness evolution during SLT tests on WK38-2, WK43-2 and WK70-2 246
Figure 5-45: Demonstration of change in F and Zv traces with time at WK70-1 (a) at End of Driving (b) at Beginning of Restrike 77 days after driving 246
Figure 5-46: Demonstration of change in F_{up} traces with time over a pause in installation..... 247
Figure 5-47: Shaft resistance profiles at EOD and BOR from pre-construction test campaign 247
Figure 5-48: Effect of multiple restrike blows on pile set-up factor (a) in chalk (b) in glacial. 248
Figure 5-49: Change in shaft resistance immediately following a driving pause and with subsequent driving – location WK70-2 248
Figure 5-50: Set-up trends in glacial till from dynamic restrike tests and from blows following driving pauses with logarithmic capacity increase trend 249
Figure 5-51: (a) Set-up trends in chalk from dynamic restrike tests and from blows following driving pauses (b) with interpreted trend 250
Figure 6-1: (a) St Nicholas-at-Wade test site location (UK Grid: TR 25419 66879) (b) overall site plan showing IC test site and previous JIP 255
Figure 6-2: (a) Piles and site investigation at the previous JIP site (Ciavaglia *et al.*, 2017a, b) (b) piles and site investigation at the IC test site 256
Figure 6-3: Correlation of stratigraphy encountered at the test site with the closest onshore section located at North Foreland and offshore borehole No. 7 at the Thanet Offshore Windfarm as carried out by Prof. Rory Mortimore (adapted and simplified from ChalkRock, 2007) 266
Figure 6-4: Typical profiles of cone resistance, q_t, sleeve friction, f_s, pore pressure at the sleeve position, u_2 and pore pressure at the u_1 position measured at the Imperial College test site 267
Figure 6-5: Section A-A cone resistance with depth across the Imperial College test site 268
Figure 6-6: Envelopes of CPT test parameter profiles at the Imperial College test site compared to those at the previous JIP site 269
Figure 6-7: Measurement of PCPT load during installation (a) total load measured in the CPT truck compared with load on the tip (b) average shaft stress during penetration on CPT rods, τ_{cpt} compared with sleeve friction measurements, f_s (c) τ_{cpt}/q_t versus length of penetration normalised by diameter 270
Figure 6-8: Effect of variable penetration rate on cone resistance at PCPT08. Adjacent PCPT06 also shown where penetration was at a rate of 2cm/s (b) cone resistance during variable penetration versus normalised velocity 271
Figure 6-9: Shear wave velocity and shear modulus crosshole, P-S suspension logging and SCPT 272
Figure 6-10: Shear wave velocity versus IDD at the site compared with other sites 272

Figure 6-11: (a) Bulk density and dry density profiles (b) moisture content and saturated moisture content at the previous JIP site (data from Fugro, 2012a, SETech, 2007) 273
Figure 6-12: Grading curve from samples of crushed chalk at the test site (Bialowas *et al.*, 2016) 273
Figure 6-13: One dimensional compression and swelling curves from oedometer tests on intact and remoulded samples (data from Fugro, 2012a) 274
Figure 6-14: Peak failure envelopes interpreted from Consolidated Drained (CD) and Consolidated Undrained (CU) triaxial tests on intact and remoulded samples (data from Fugro, 2012a) 274
Figure 6-15: (a) Undrained triaxial tests on remoulded samples (a) stress paths in q-p′ space (b) q-ε_{ax} (data from Fugro, 2012a) 275
Figure 6-16: Drained triaxial tests on intact samples (data from Fugro, 2012a) 275
Figure 6-17: Shear modulus from triaxial stress path tests and multi stage resonant column tests on remoulded samples (data from Fugro, 2012a) 276
Figure 6-18: Example of pre-test roughness measurement of ring shear interface using Talysurf (MSt-RGH-200kPa) 276
Figure 6-19: (a) effect of relative roughness on δ normalised by the soil-soil friction angle ϕ (b) change in sample height versus relative roughness (c) ultimate interface friction angle versus stress level (data from Chan, 2017) 277
Figure 6-20: Comparison between aged and unaged large strain interface ring shear tests at IC in the Bishop apparatus on samples from the St Nicholas-at-Wade test site (a) interface friction angle versus displacement (b) change in sample height (data from Chan, 2017) 278
Figure 6-21: Blow counts/250mm penetration during installation of 139mm diameter test piles 283
Figure 6-22: Example of a signal match found with IMPACT for pile DP7 (a) force and velocity times impedance (b) pile head displacement 283
Figure 6-23: Profiles of overall resistance at EoD from analysis of dynamic pile test 284
Figure 6-24: Schematic of conditions in chalk surrounding 139mm diameter test piles 284
Figure 6-25: Radial water content profiles with radial distance from the pile centre normalised by pile outside radius R (a) near and far field (b) near field 285
Figure 6-26: Schematic of load test system used in the axial static and cyclic investigation ... 289
Figure 6-27: Pile head piece and displacement monitoring system 289
Figure 6-28: (a) overview of load testing system (b) including cyclic loading system 290
Figure 6-29: Schematic of cyclic load test system 291
Figure 6-30: Schematic illustration of cyclic loading conventions and cyclic loading control parameters 291
Figure 6-31: Average shaft resistance versus pile head displacement for first time tension tests to failure on DP2, DP3 and DP6 294

Figure 6-32: Global stiffness versus average shaft resistance for first time tension tests to failure on DP2, DP3 and DP6 and retest on DP2 294
Figure 6-33: (a) Shaft capacity growth with time for first time tension tests on pile DP2, DP3, and DP6 and re-test on DP2 (b) trend from (a) compared with trend from re-tests on 762mm diameter piles reported by Ciavaglia *et al.* (2017a) 295
Figure 6-34: Definitions of cyclic displacement and stiffness; adapted from Rimoy *et al.* (2013) 299
Figure 6-35: Average shaft resistance versus time during cyclic load tests DP5-CY1 and DP5-CY2 300
Figure 6-36: Permanent accumulated cyclic displacement normalised by pile diameter for unfailed tests (a) DP1-CY1 (b) DP4-CY1 (c) DP5-CY1 (d) DP7-CY1 and (e) re-test DP4-CY2 301
Figure 6-37: Permanent accumulated cyclic displacement normalised by pile diameter for failed tests DP1-CY2 and DP5-CY2 302
Figure 6-38: Cyclic loading interaction diagram with number of cycles either to failure or to the end of test if unfailed 302
Figure 6-39: Global axial loading stiffness for (a) unfailed tests (b) failed tests 303
Figure 6-40: Global axial unloading stiffness for (a) unfailed tests (b) failed tests 303
Figure 6-41: Permanent accumulated displacement with cycles for meta-stable/stable tests on natural scale with power law fits and parameters shown 304
Figure 6-42: Cyclic interaction charts showing accumulated displacements (normalised by pile diameter) at (a) N=3, (b) N=10, (c) N=20 (d) N=100 (e) N=300 and (f) N=600 305
Figure 6-43: 3D plot showing variation of s_{acc}/D with N, Q_{cyc}/Q_{ref} and Q_{mean}/Q_{ref} for s_{acc}/D of a) 0.2% b) 0.5% and c) 2.0% 306
Figure 7-1 ICP configuration used during tests in chalk a) ICP01 b) ICP02 319
Figure 7-2 The combined axial load cell and pore pressure unit (Bond, 1989) 320
Figure 7-3 The pore pressure probe (Bond, 1989) 320
Figure 7-4 The surface stress transducer (Bond, 1989) 321
Figure 7-5 Calibration of axial load cells at a) ALC1 (leading cluster) and b) ALC2 (following cluster) 321
Figure 7-6 Calibration of radial and shear stress circuits in the surface stress transducers in a dead weight bi-axial calibration jig 322
Figure 7-7 Calibration of surface stress transducers using purpose built bi-axial calibration jig for a) radial circuit SST1 b) radial circuit SST2 c) shear circuit SST1 and d) shear circuit SST2 323
Figure 7-8 Pile jacking rate measured during installation of ICP01 and ICP02 327
Figure 7-9 ICP head piece used for tension load test 327
Figure 7-10 *In-situ* tests used in the analysis of jacked pile test results 328

Figure 7-11 Force at the pile head during installation (Q_{tot}) force at the pile base (Q_b), average shear stress over the pile length ($\tau_{install}$) and envelope of q_t measurements 343
Figure 7-12 Pore pressures measured during penetration at both the leading and following instruments 344
Figure 7-13 Variation in excess pore water pressure with normalised distance from the tip during PCPT and jacked pile penetration. Note: initial pre-installation pore pressures are small or negative..... 344
Figure 7-14 CPT measurement positions for IC CPTs after Lankelma (2016) and ASTM (2012) 345
Figure 7-15 Variation in ratio q_b/q_t with normalised velocity for the jacked pile 345
Figure 7-16 Profiles of SST measurements at the leading instrument during pauses in jacking a) stationary local radial effective stresses b) stationary local shear stresses 346
Figure 7-17 Illustration of stationary (minima) and moving (maxima) radial, shear and base stresses at the end of an installation push and at the end of a jacking pause 346
Figure 7-18 Relationship between cone resistance and radial effective stress at the leading instrument 347
Figure 7-19 Normalised stationary radial effective stresses along the pile shaft during installation compared to historical measurements 347
Figure 7-20 Normalised stationary and moving radial effective stresses from SST measurements, CPT f_s readings and back analysis of dynamic test data on driven piles . 348
Figure 7-21 Typical short-term changes in local radial effective stress, local shear stress and pore water pressures 348
Figure 7-22 Variations with time over entire equalisation period of (a) local effective shaft radial stresses (b) local effective shaft shear stresses (c) pore water pressures 349
Figure 7-23 Long-term pore pressures with time compared with daily rainfall measurements taken at Manston airport (Met-Office, 2016) 350
Figure 7-24 Average shaft resistance mobilised versus displacement during static tension and one way cyclic loading on ICP01 and ICP02 350
Figure 7-25 Variation in axial load and shear stress interpolated between the load cells along the pile length at the point of tension failure 351
Figure 7-26 Evolution of radial stress and shear stress with pile head displacement during a static load test 351
Figure 7-27 Effective stress paths during static tension loading at a) the leading SST1 and b) the following SST2..... 352
Figure 7-28 Comparison of set-up factors observed during static testing of jacked piles following equalisation periods with driven piles..... 353

Figure 7-29 Two depths at which the effective stress states are considered during ICP penetration with (a) the final level of the following instrument (b) the final level of the leading instrument 354
Figure 7-30 Schematic diagram of soil element at the ICP shaft and below the pile tip 355
Figure 7-31 Mohr's circles for different assumed failure modes in simple shear (a) planes parallel to direction of shear are planes of maximum stress obliquity (b) co-axial plasticity at critical state (c) planes normal to direction of shear are planes of maximum stress obliquity..... 355
Figure 7-32 Illustration of stress state changes during ICP pile installation and equalisation .. 356
Figure 7-33 Evolution of permanent pile head displacement with number of cycles 356
Figure 7-34 Example radial and shear stresses changes during cycling at the leading and following instruments during the test on ICP02 357
Figure 7-35 Effective stress paths during one way cyclic loading at a) leading SST1 during ICP01 b) following SST2 during ICP01 c) leading SST1 during ICP02 d) following SST2 during ICP02 358
Figure 7-36 Changes in pore pressure with cycling at both instrument levels during (a) ICP01 and (b) ICP02 359
Figure 8-1: Comparison of average shaft stresses, τ_{avg}, for open-ended piles, from the CIRIA database, tests identified by the Author and the Author's tests 364
Figure 8-2: Cone resistance profiles from case studies at Wikinger (a) OSS (b) WK11 (c) WK43 (d) WK70..... 370
Figure 8-3: Cone resistance profiles from case studies at St. Nicholas-at-Wade (a) Imperial College site (b) Previous JIP site..... 371
Figure 8-4: Cone resistance profiles from case study at Fleury-sur-Andelle (note uncorrected q_c as no information on pore pressures at the site) 371
Figure 8-5: Comparison between index properties at the three sites (a) water content versus intact dry density relationship (b) Unconfined compressive strength versus IDD 372
Figure 8-6: (a) schematic illustration of non-dilative interface (b) conceptual model of dilatancy and friction (c) idealised dilative interface system (Dove and Jarrett, 2002) 381
Figure 8-7: Interface sliding angle, θ, as a function of particle size/normalised roughness (Uesugi and Kishida, 1986)..... 381
Figure 8-8: Concept of interface friction and normalised roughness (Kishida and Uesugi, 1987) 382
Figure 8-9: Typical stress paths measured by ICP instruments during static testing..... 382
Figure 8-10: Variation in particle size distributions of crushed chalk 383
Figure 8-11: Predictions of $\Delta\sigma'_{rd}$ during loading of jacked ICP piles at St. Nicholas-at-Wade 383
Figure 8-12: Predictions magnitudes of $\Delta\sigma'_{rd}$ for piles of different diameter in the case studies. 384

Figure 8-13: Typical effective stress paths from undrained triaxial tests to failure on remoulded chalk putty at 0 and 7 days (Doughty, 2016) 389
Figure 8-14 Illustration of stress states during driven pile penetration at a depth z 389
Figure 8-15 Schematic diagram of soil element at the shaft and below the steel annulus 390
Figure 8-16: Illustration of stress states during installation, equalisation and ageing of driven piles 390
Figure 8-17: Set-up factors versus time since end of driving for three sets of tests 402
Figure 8-18: Illustration of variation in CPT cone resistance with radial effective stress (SST1 ICP02) 402
Figure 8-19: Normalised radial effective stresses versus h/R* at end of driving for (a) Wikinger 2.7 to 403
Figure 8-20: Relationship between parameter η and diameter to wall thickness ratio 404
Figure 8-21: Measured and calculated profiles of shaft resistance at EoD (calculated using Eq. 8-22) 405
Figure 8-22: Normalised radial effective stresses versus h/R* at beginning of restrike from available dataset 410
Figure 8-23: Profiles from dynamic tests and calculated profiles of aged shaft resistance on open-ended piles at Wikinger using ICP sand/clay and new chalk prediction (a) WK38 (b) WK43 (c) WK70 415
Figure 8-24: Profiles inferred from strain gauges during static tests and from dynamic tests and calculated profiles of aged shaft resistance on open-ended piles at Wikinger (a) WK11 (b) 1_A119 416
Figure 8-25: Profiles inferred from strain gauges during static tests and calculated profiles of aged shaft resistance on closed-ended piles at Fleury-sur-Andelle 416
Figure 8-26: Cyclic stability diagram showing previous tests and the Author's test's described in Chapter 6 419

LIST OF TABLES

Table 2-1: Typical range of index properties for chalk (Lord *et al.*, 2002) 16
Table 2-2: Classification of chalk at the Mundford site (Ward *et al.*, 1968, Wakeling, 1970, Power, 1982)..... 22
Table 2-3: Intact dry density scales of chalk; Mortimore *et al.* (1990), Matthews *et al.* (1993). 22
Table 2-4: Structured chalk grading and comparison between Mundford and CIRIA grading schemes (Spink, 2002)..... 23
Table 3-1: Summary of pile categories and likelihood of pile penetration in chalk of different grade and density (Lord *et al.*, 1994, Lord *et al.*, 2002)..... 80
Table 3-2: Summary of piles in the chalk test database 87
Table 3-3: Summary of compression tests at Fleury-sur-Andelle (Bustamante *et al.*, 1980) 89
Table 3-4: Static axial tension and one way cyclic tests using at Luton (Burland and French, 1990)..... 91
Table 3-5: Dynamic & static shaft resistances (after Lahrs & Kahlias, 2013)..... 94
Table 3-6: Summary of pile details and CAPWAP results for relevant historical tests at St. Nicholas at Wade (Wind-Support, 2012) 96
Table 3-7: Axial tension testing programme on Pile 1 and Pile 2 during Phase 1 tests at St. Nicholas at Wade (Wind-Support, 2012, Ciavaglia *et al.*, 2017a, b) 96
Table 3-8: Two way axial cyclic and compression tests on Pile 1 during second phase of testing at St Nicholas at Wade by Iberdrola (2013) 98
Table 3-9: Two way axial cyclic and compression tests on Pile 4 during second phase of testing at St Nicholas at Wade by Iberdrola (2013) 100
Table 3-10: Summary of static tests on closed-ended piles where ultimate shaft resistance is known 121
Table 3-11: Summary of static tests on open-ended piles where ultimate shaft resistance is known 122
Table 4-1: Viscosity parameters for clay based on research studies 144
Table 4-2: Summary of equations and parameters using Simons and Randolph (1985) and Deeks and Randolph (1995) models in IMPACT 149
Table 4-3: Capabilities of the signal matching codes used in the research 159
Table 4-4: Summary of parameters used in comparison of numerical methods 161
Table 4-5: Summary of unknowns in typical commercial codes 163
Table 4-6: Summary of equations, parameters and source using IMPACT 164
Table 4-7: Driving resistance recommendations after Dührkop *et al.* (2015)..... 167
Table 4-8: Match quality intervals; after Middendorp (2015)..... 169
Table 5-1: Details of the test sites and pile penetrations at Wikinger included in the study..... 182
Table 5-2: Index properties from the 8 test sites in glacial till and fluvioglacial till..... 185

Table 5-3: Index properties from the 8 test sites in structureless and structured chalk 199
Table 5-4: Summary of test pile installation 215
Table 5-5: Significant pauses (>5 min) during test pile installation 215
Table 5-6: Summary of pile test codes and test histories during test campaigns 218
Table 5-7: Summary of equations and adopted parameters using models in IMPACT 226
Table 5-8: Pile capacities at the end of driving for all twelve EoD tests 229
Table 5-9: Static tension failure loads for offshore pile tests at Wikinger 233
Table 5-10: Summary of pile capacity predictions in glacial till for the static tension test on WK38-2 conducted 108 days after driving 239
Table 6-1: Classification and index tests from 0 to 7m depth (SETech, 2007, Fugro, 2012a) 261
Table 6-2: Summary of ring shear tests on samples from the site (after Chan, 2017) 264
Table 6-3: Summary of pile test codes and test histories for ageing trends 286
Table 6-4: Summary of pile test codes and test histories for cyclic loading effects 286
Table 6-5: Post ageing and end of driving capacities of virgin piles in the static capacity study 292
Table 6-6: Summary of cyclic loading test outcomes 296
Table 7-1: Calibration coefficients for the pore pressure transducers used in this study 314
Table 7-2 Direct and cross sensitivity factors for the radial and shear stress transducers 317
Table 7-3: Summary of 102mm diameter ICP test programme 326
Table 8-1: Summary of open-ended tubular piles and relevant static and dynamic tests included in the study 367
Table 8-2: Summary of closed ended steel piles and H-piles at Fleury-sur-Andelle included in the study 368
Table 8-3: Quake and damping parameters used in the drivability analysis (Alm and Hamre, 2002) 397
Table 8-4: Assessment of proposed correlation for end of driving shaft resistance for open-ended tubular steel piles 401
Table 8-5: Assessment of proposed correlation for aged shaft resistance for open-ended tubular steel piles 408
Table 8-6: Summary of preliminary proposed correlations for shaft resistance of displacement piles in chalk 409
Table 8-7: Comparison of original approaches with proposed correlation for shaft resistance for open-ended tubular steel piles 413
Table 8-8: Comparison of original approaches with proposed correlation for aged shaft resistance for closed-ended steel piles 414

APPENDIX A-1

Supplementary Pile test data

A-1.1. Fleury-sur-Andelle

FICHE TECHNIQUE DU PIEU

N°28

SITE : FLEURY/ANDELLE

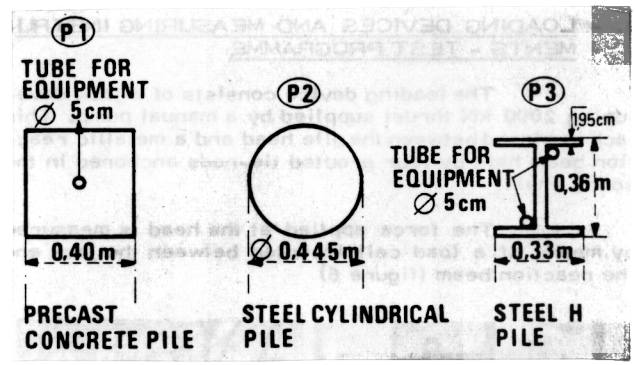
① Mode de mise en place.

☐ forage ☒ battage ☐ vérinage

Les trois pieux ont été battus à l'aide d'un mouton DELMAG D 12.

La fiche des trois pieux d'essais est de 10,20 par rapport au terrain naturel.

② Géométrie.



③ Equipement.

a) de la tête : 4 comparateurs au 1/100ème de mm pour mesure des déplacements verticaux.

b) du fût : Extensomètres amovibles Ø 50 pour les pieux B.A. et H.
Tripodes pour le pieu tubulaire.

④ Massif de réaction :

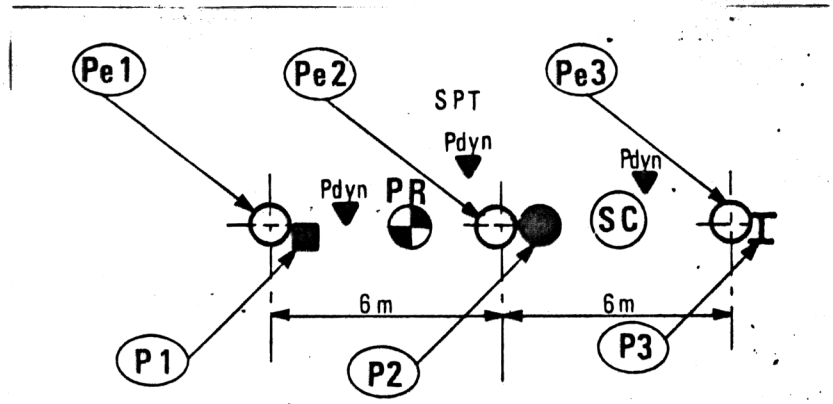
Poutre de réaction des L.P.C. maintenue par 4 tirants.
Réaction maxi. : 5000 KN.

⑤ Observations :

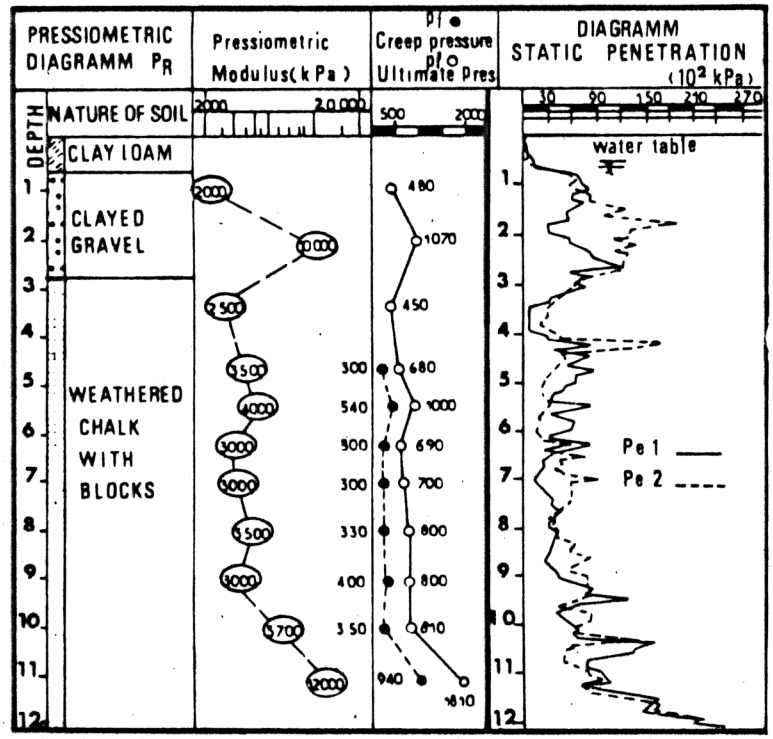
FICHE GEOTECHNIQUE N° 28

SITE : FLEURY/ANDELLE

① Schéma d'implantation des essais et du pieu :



② Coupe et essais en place :



③ Essais de laboratoire :

BORE HOLE	Percent of sampling	GEOLOGIE DESCRIPTION	TRIAXIAL TESTS W%	γ h	γ d	Cuu	φ′	C′
AUGER BORING Ø 17cm		CLAY LOAM COMPACT CLAYED GRAVEL (water table)						
PERCUSSION BORING Ø 12.5cm DIAMOND CORE BORING Ø 13.1cm	90 0 90 90 100 100 70 80 90 100	WLEARED CHALK WITH BLOCKS OF FIRE STONE AND HARD CHALK COMPACT CHALK	25,3 30.9 30.5 26.8 25.5 26	1.880 1,875 1.94 1.95 1.87 1.905	1.505 1.430 1.485 1.54 1.495 1.51	40 21 110 20 82 150	28	110

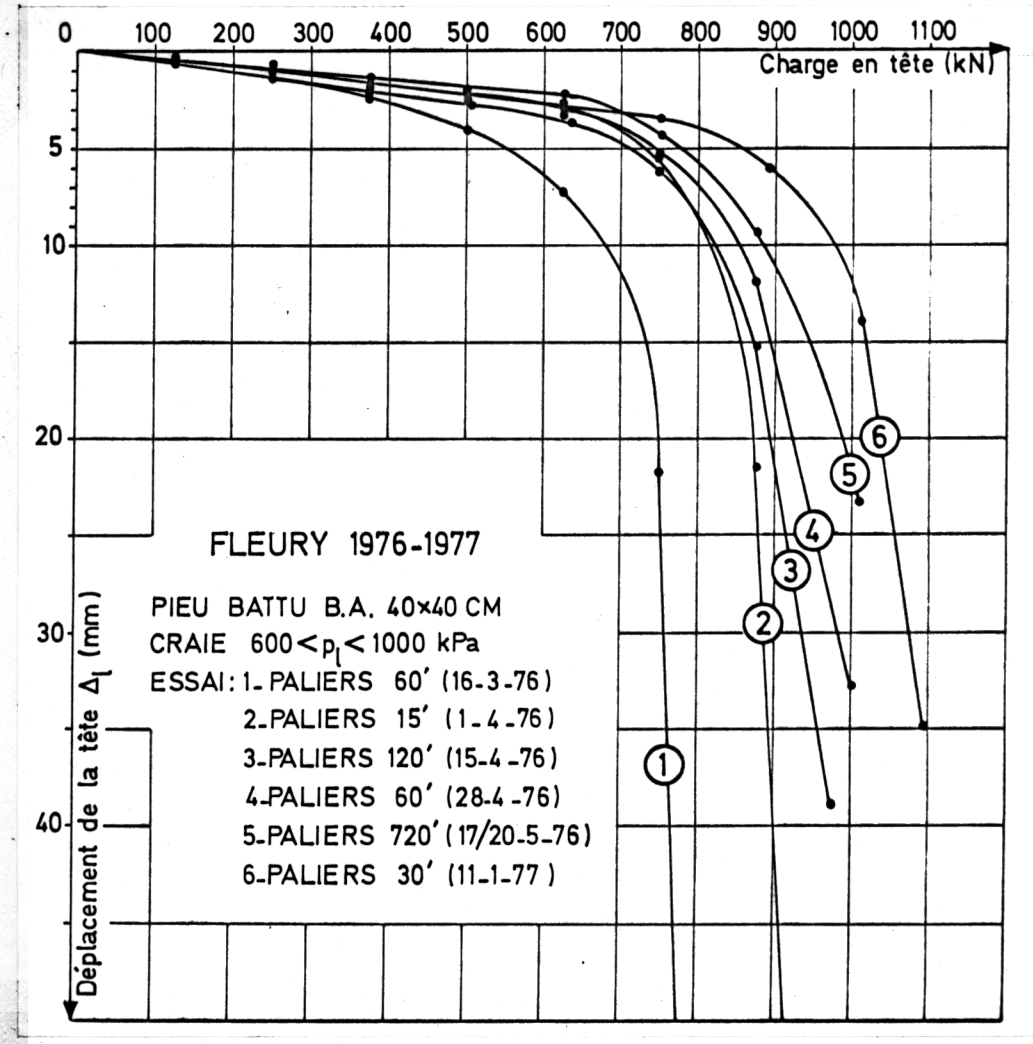
④ Observations :

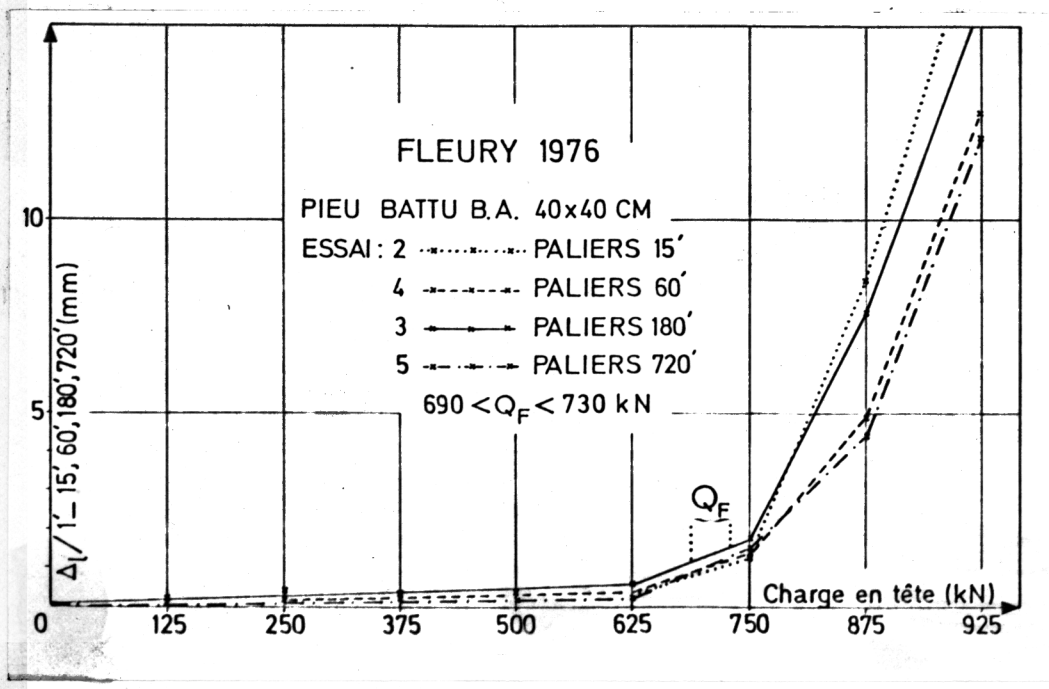
FICHE D'INTERPRETATION

N°28

SITE : FLEURY / ANDELLE. PIEU BATTU B.A

① Courbes enfoncement - charge en tête.



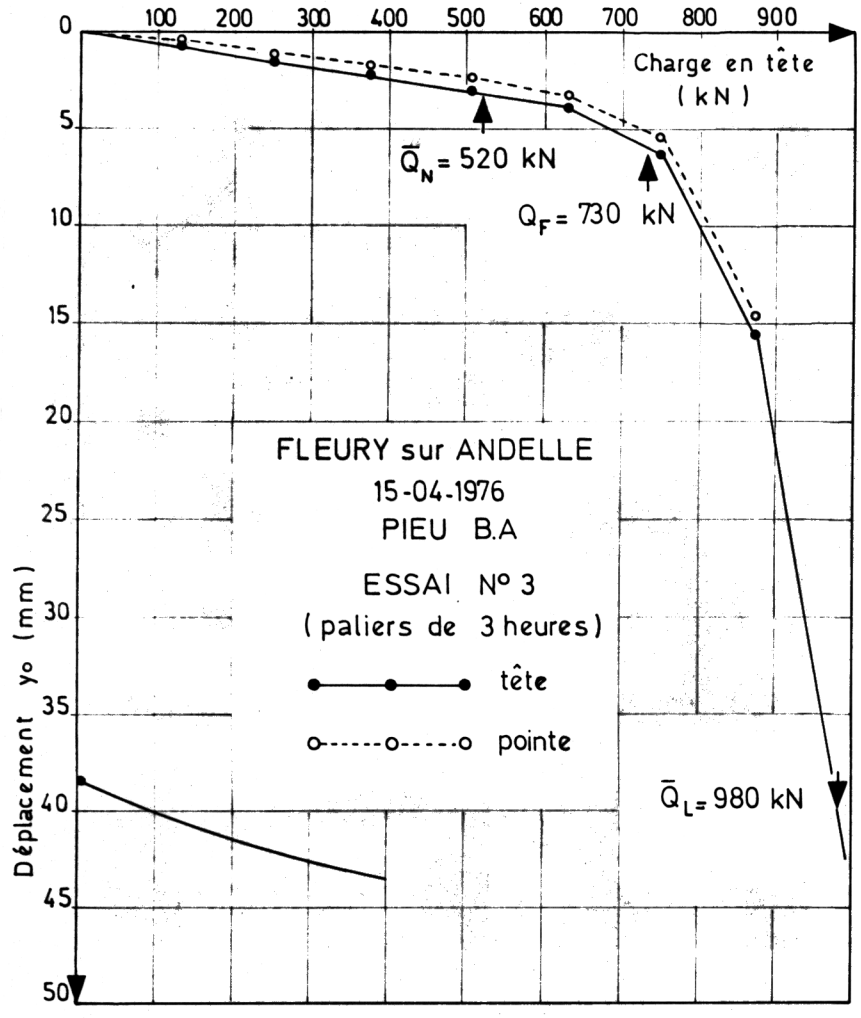


FICHE D'INTERPRETATION

N°28

SITE : FLEURY / ANDELLE PIEU BATTU B.A. *suite...*

① Courbes enfoncement - charge en tête.

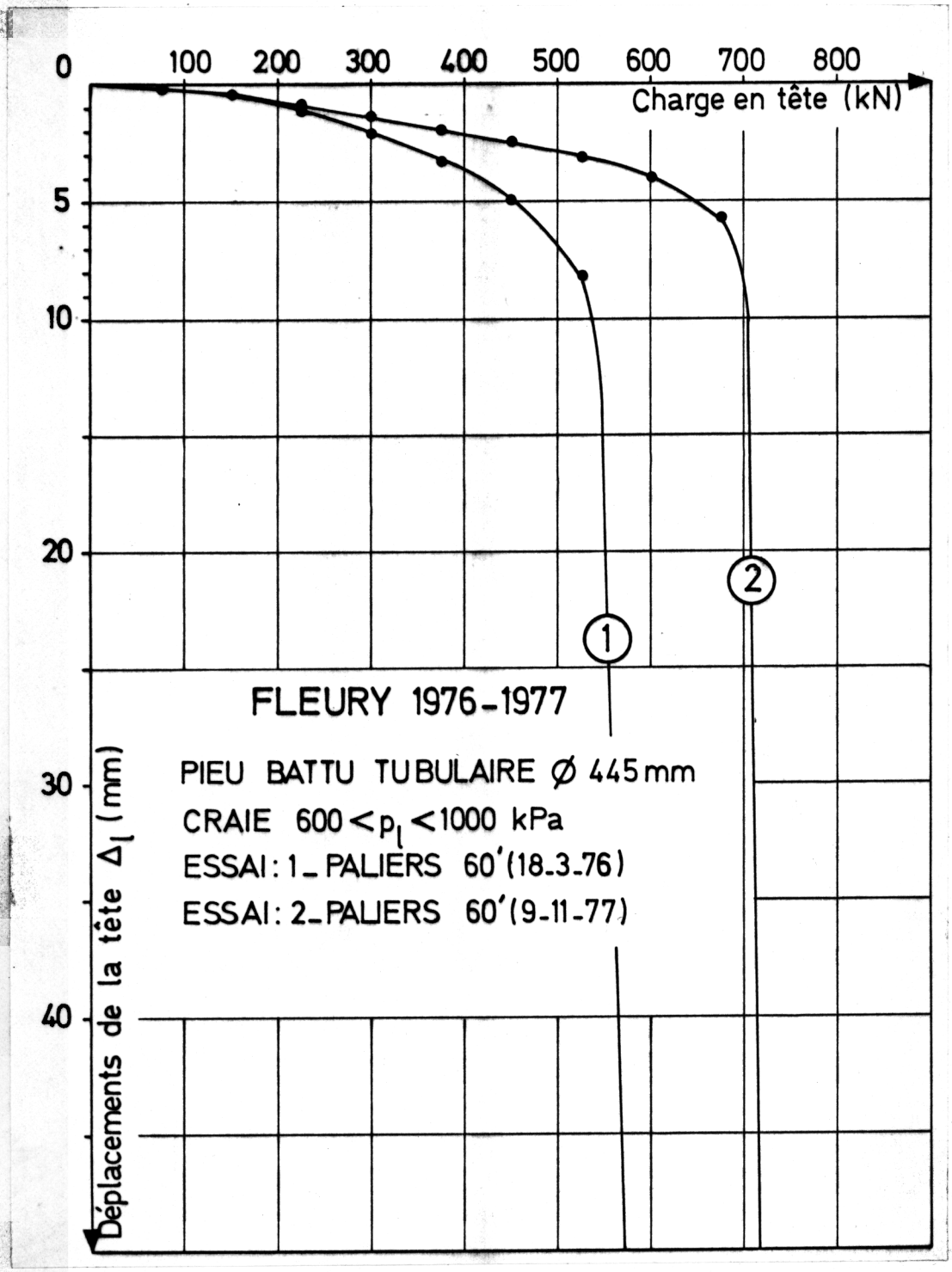


FICHE D'INTERPRETATION

N° 28

SITE : FLEURY / ANDELLE. PIEU TUBULAIRE BATTU

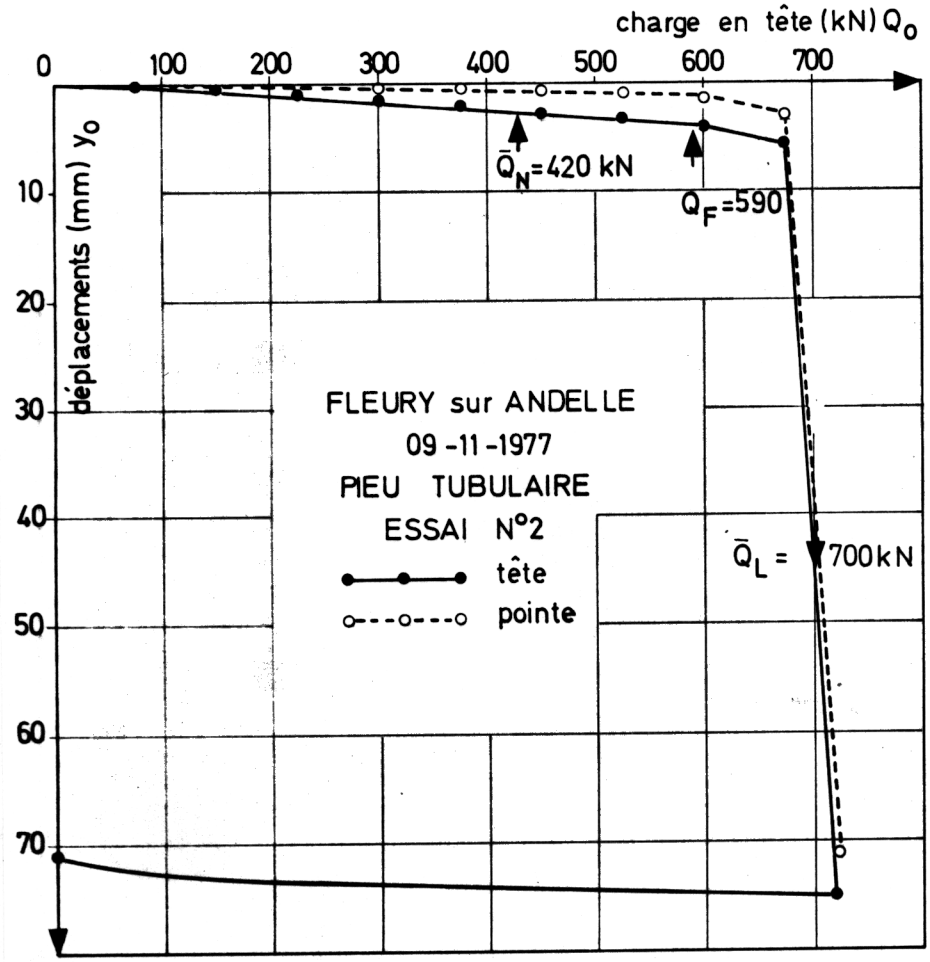
① Courbes enfoncement - charge en tête.



FICHE D'INTERPRETATION N°28

SITE : FLEURY / ANDELLE PIEU TUBULAIRE BATTU *suite...*

① Courbes enfoncement - charge en tête.

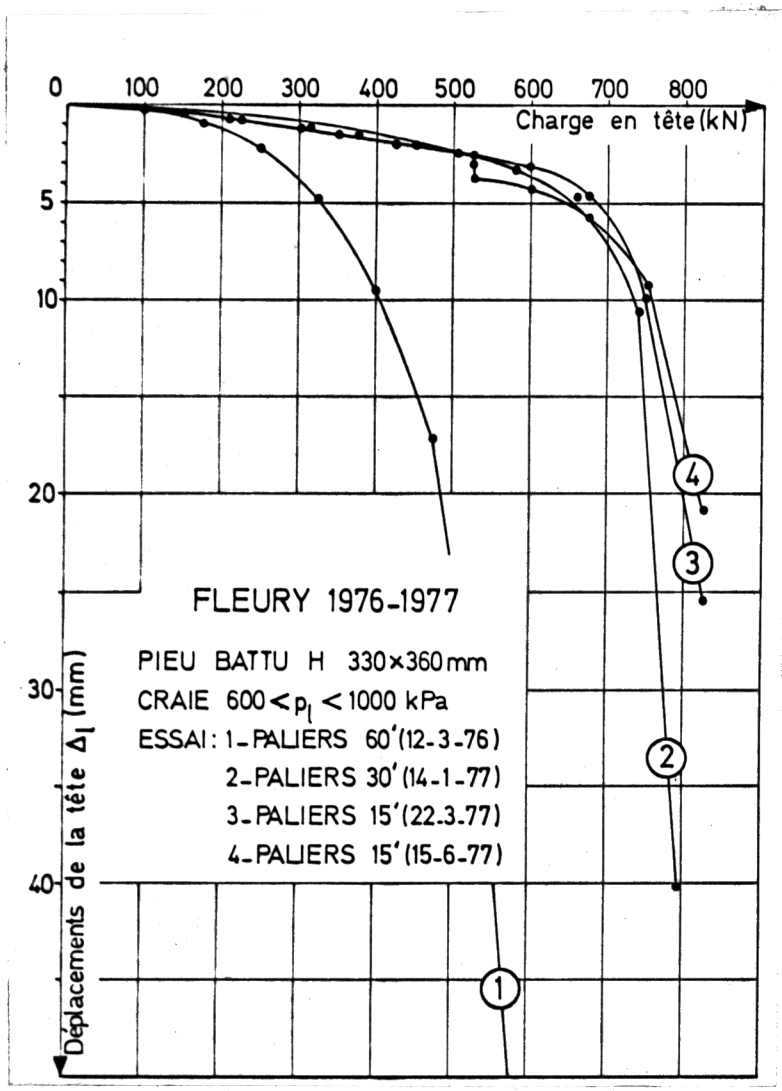


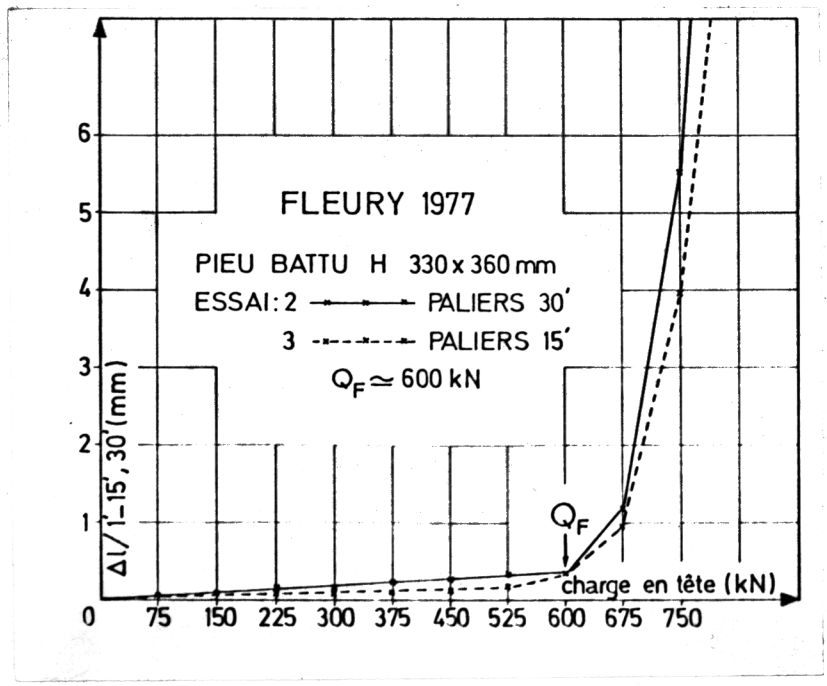
FICHE D'INTERPRETATION

N° 28

SITE : FLEURY / ANDELLE. PIEU BATTU H

① Courbes enfoncement - charge en tête.

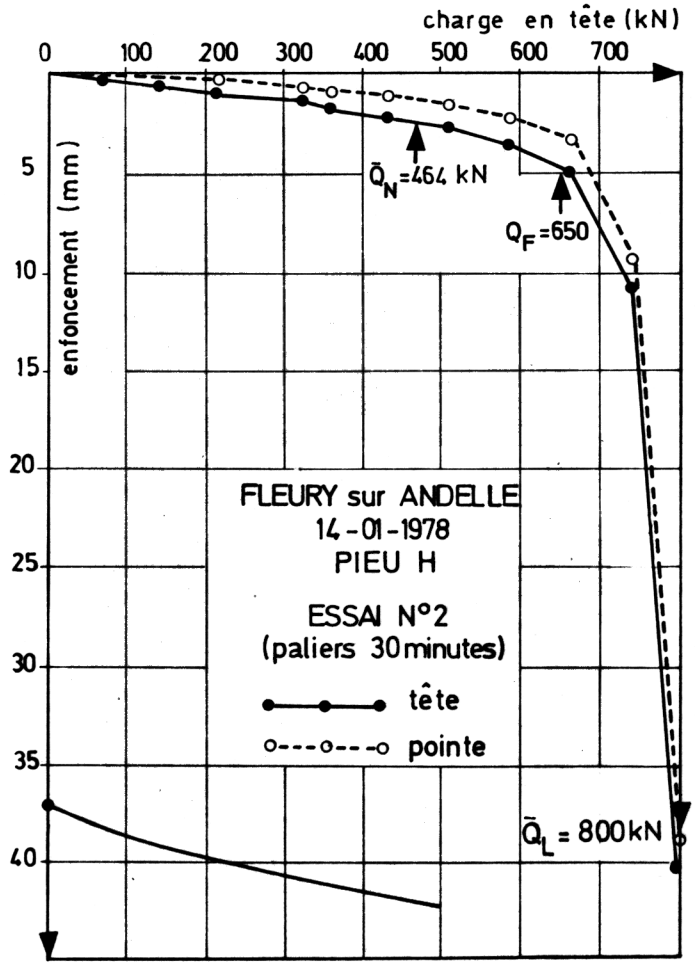




FICHE D'INTERPRETATION N° 28

SITE : FLEURY / ANDELLE *suite...*

① Courbes enfoncement - charge en tête.



FICHE D'INTERPRETATION

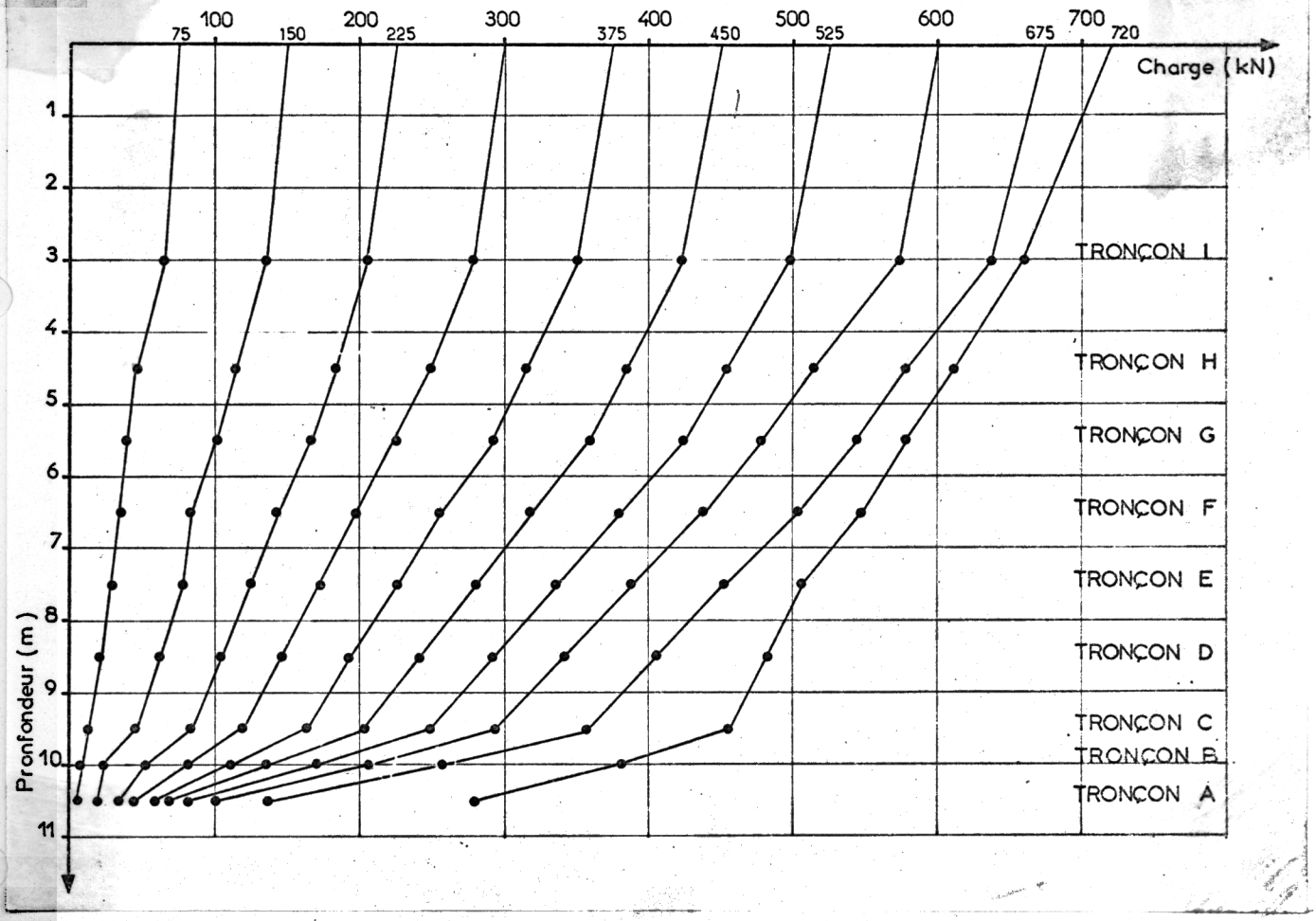
N° 28

SITE : FLEURY / ANDELLE.

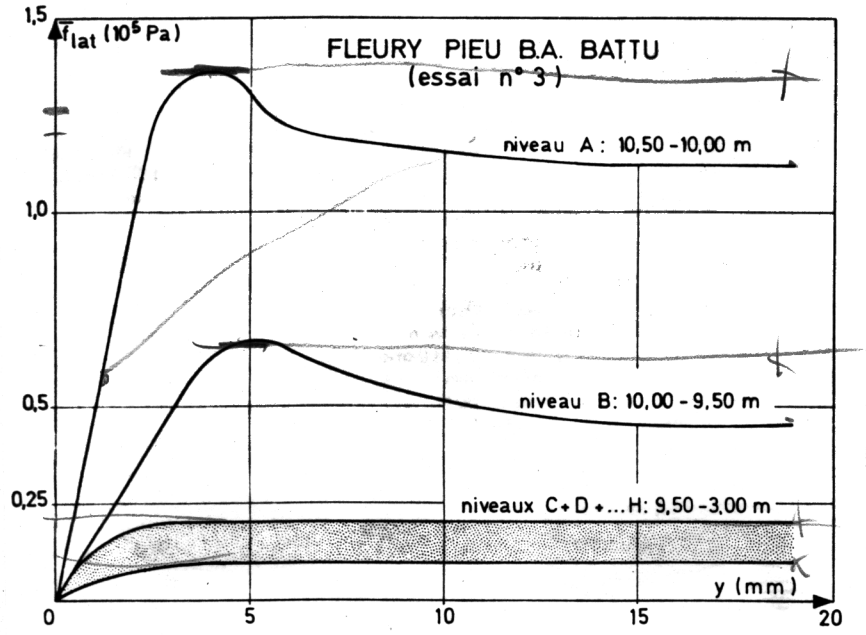
suite...

② Répartition des efforts le long du fût.

- PIEU TUBULAIRE - ESSAI des 9 et 10 Nov. 1977 -



③ Mobilisation du frottement latéral.

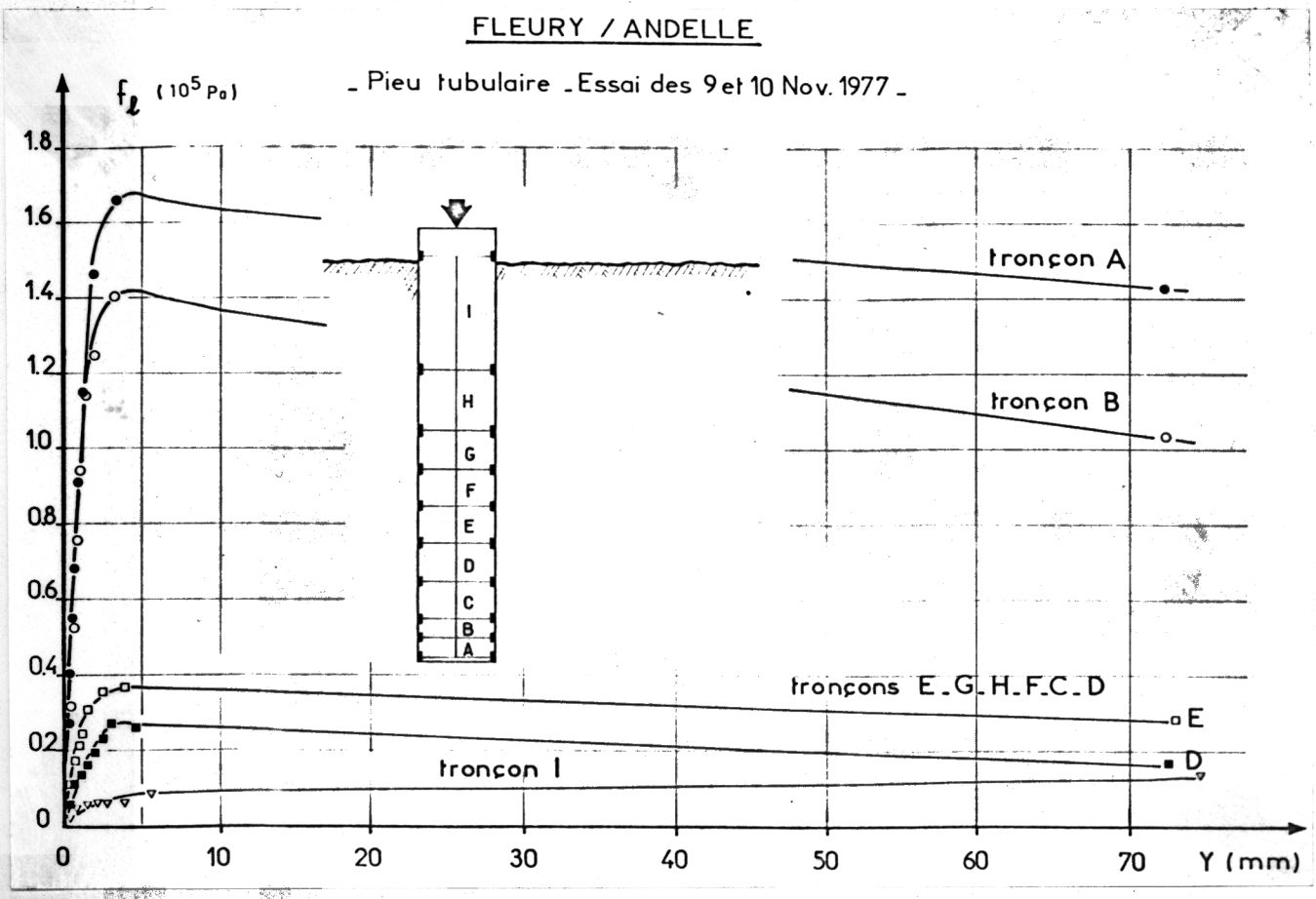


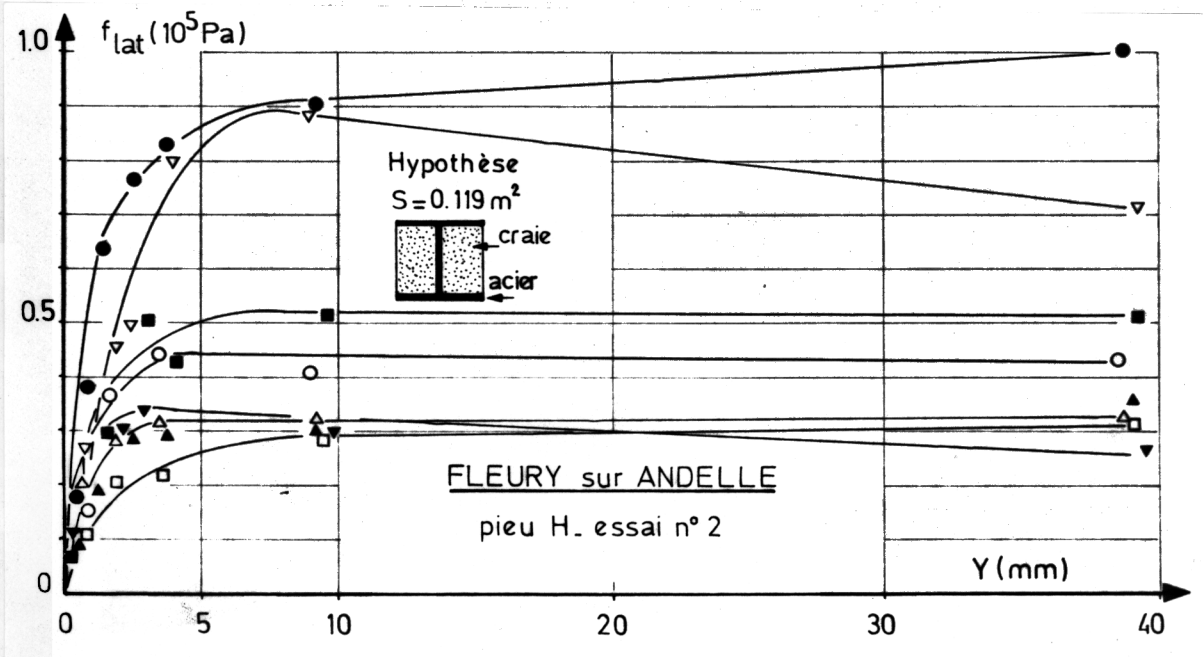
FICHE D'INTERPRETATION

N° 28

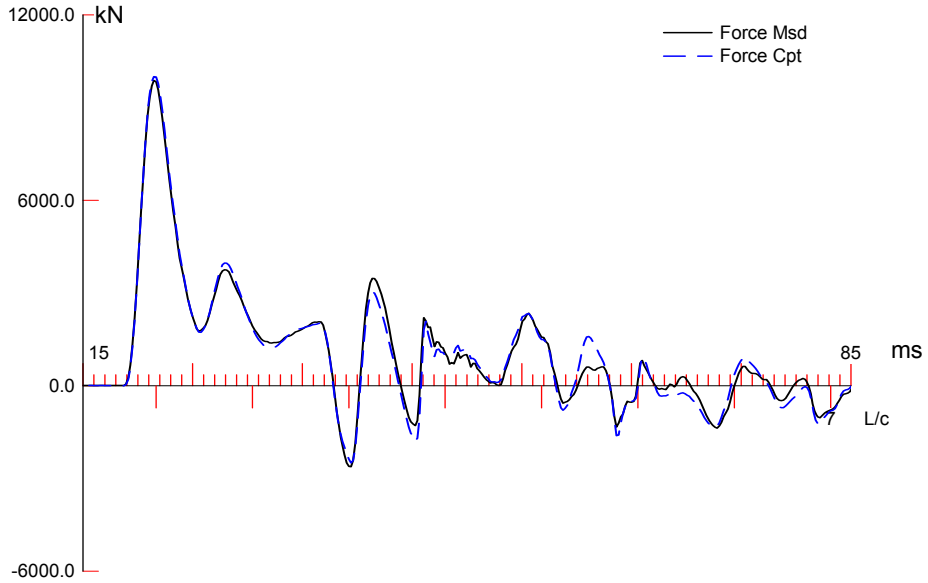
suite...

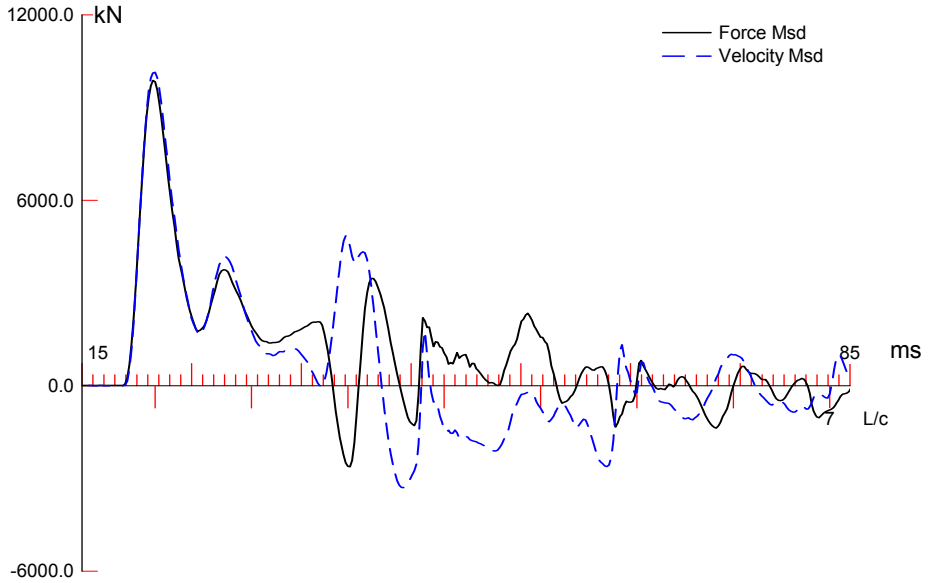
SITE : FLEURY / ANDELLE .

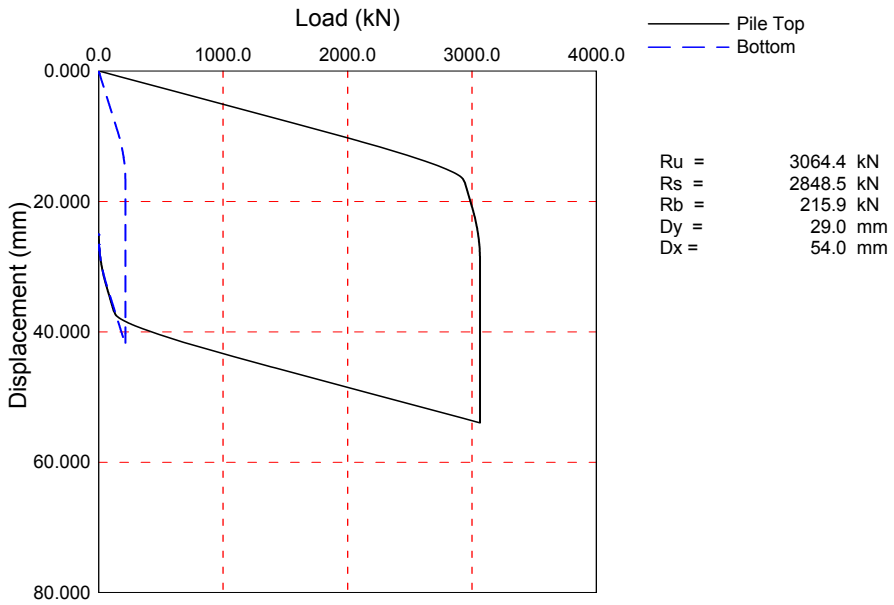




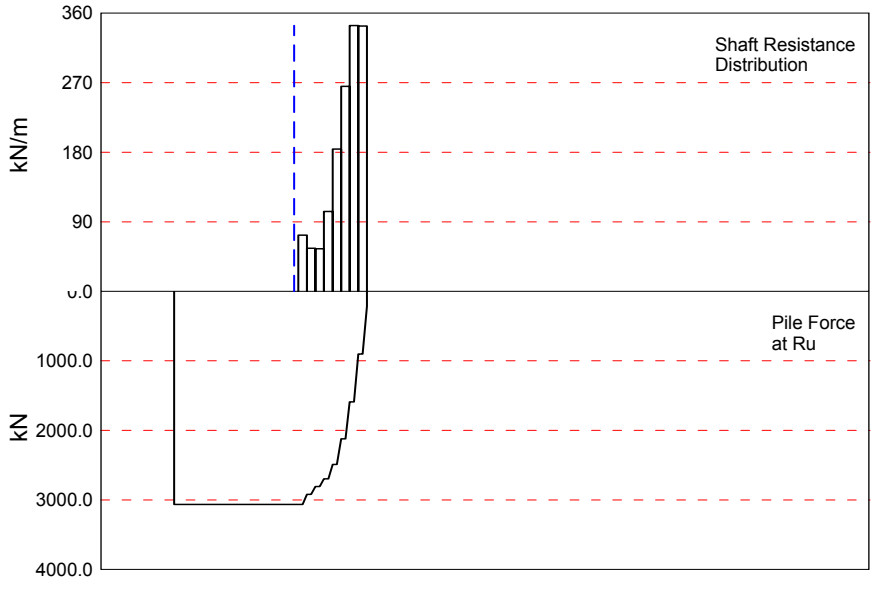
A-1.2. Port of Felixstowe



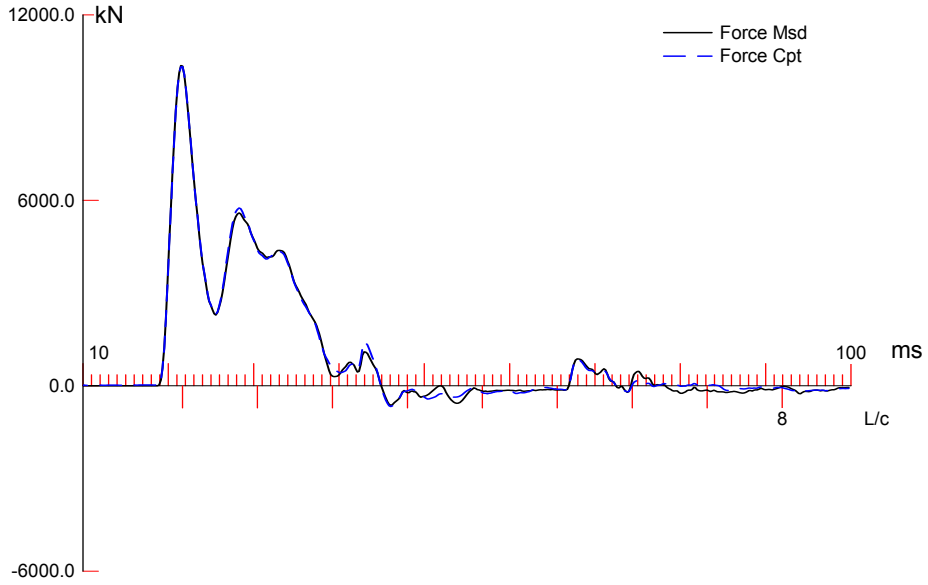


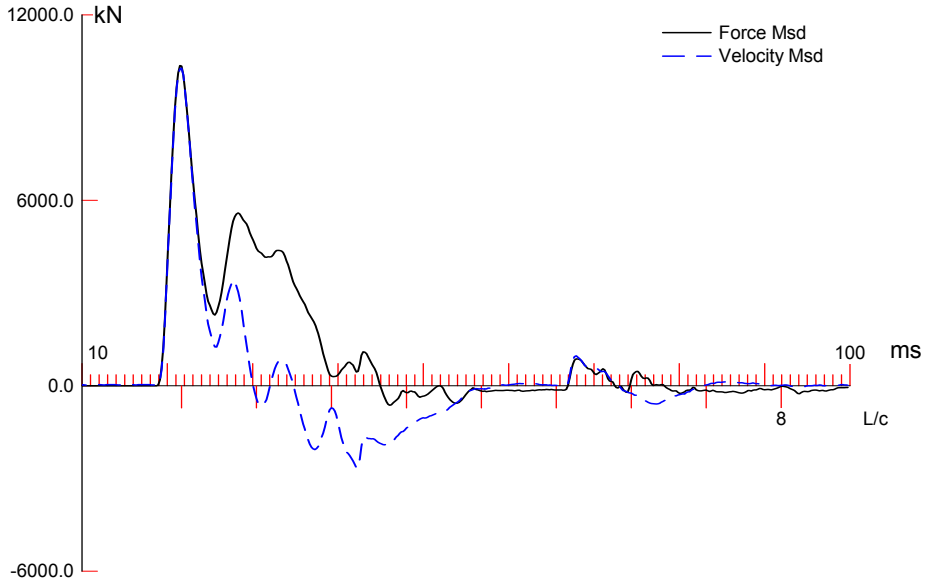


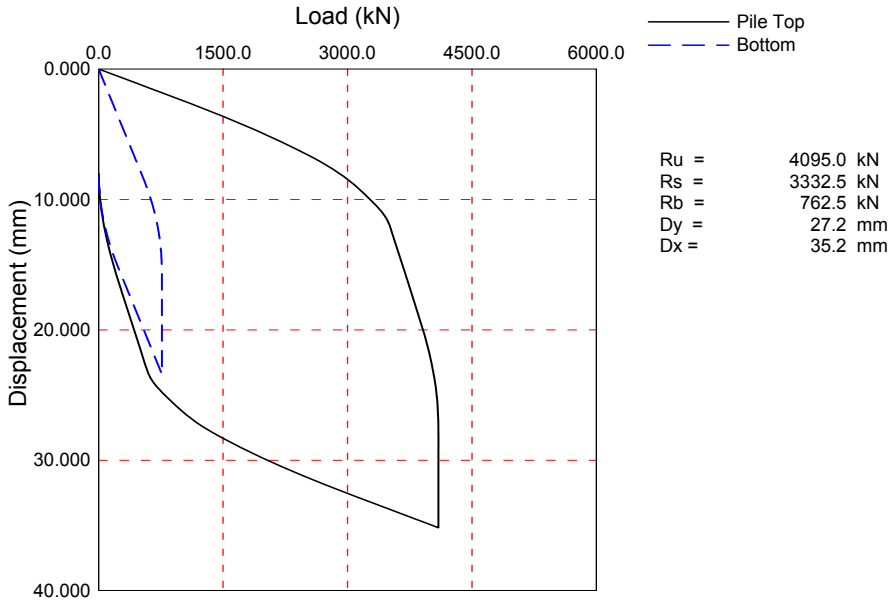
Ru = 3064.4 kN
Rs = 2848.5 kN
Rb = 215.9 kN
Dy = 29.0 mm
Dx = 54.0 mm

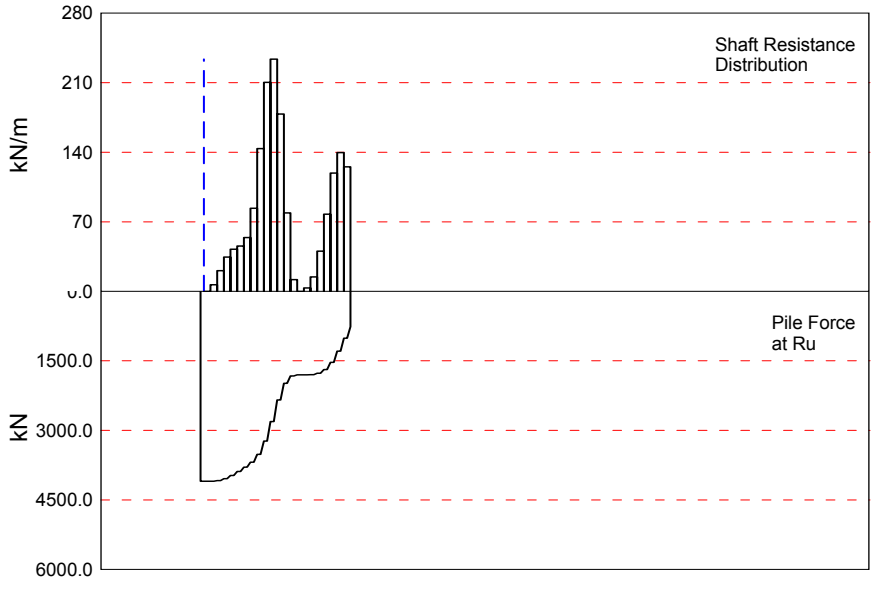


CAPWAP(R) 2006 Licensed to Precision Monitoring & Control Ltd.







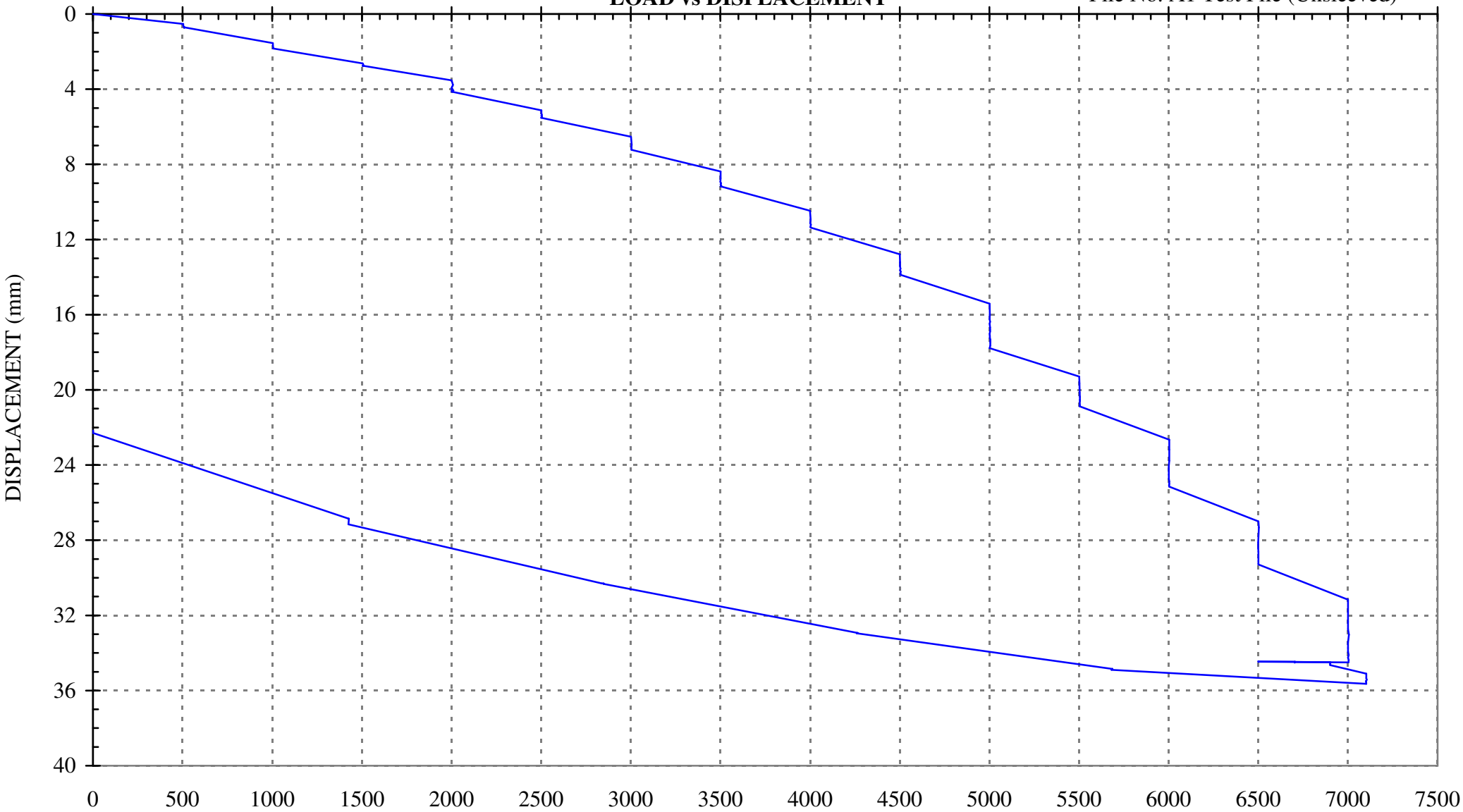


CAPWAP(R) 2006 Licensed to Precision Monitoring & Control Ltd.

PRECISION MONITORING & CONTROL LTD.

LOAD vs DISPLACEMENT

Pile No. A1 Test Pile (Unsleeved)



SW Curlew House
Port of Felixstowe
09 to 10 September 2008

COSTAIN LTD

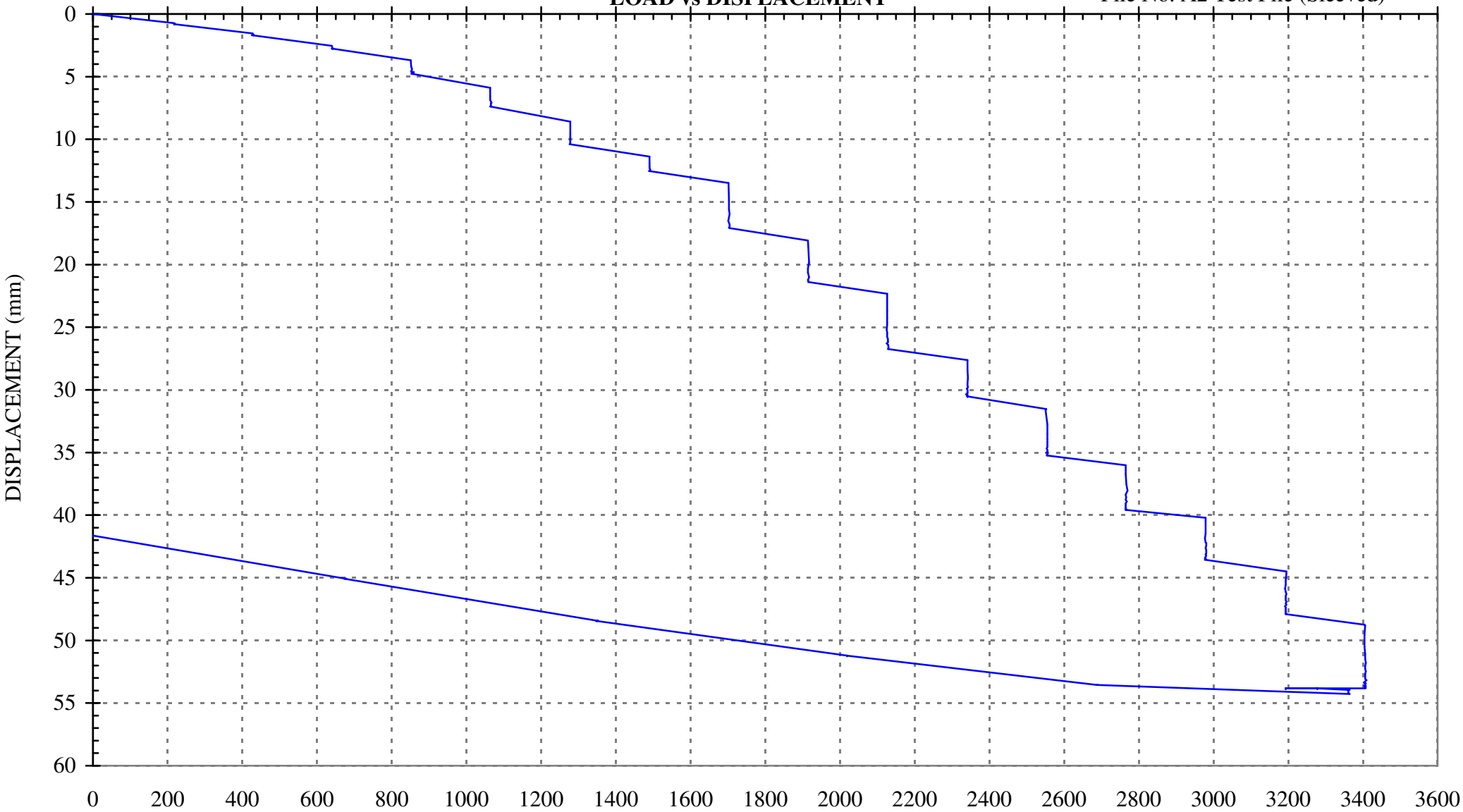
Maximum Displacement = 35.65mm

Residual Displacement = 22.17mm

PRECISION MONITORING & CONTROL LTD.

LOAD vs DISPLACEMENT

Pile No. A2 Test Pile (Sleeved)

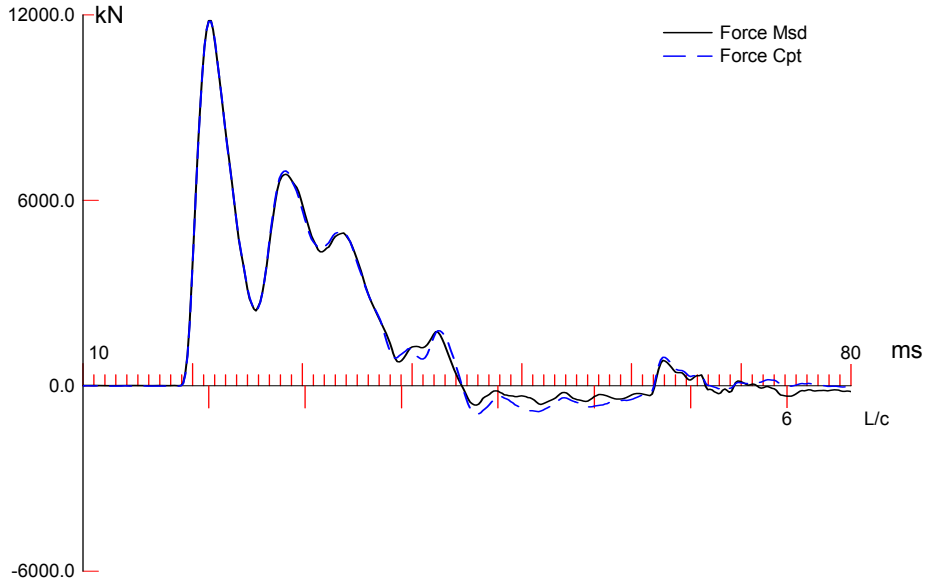


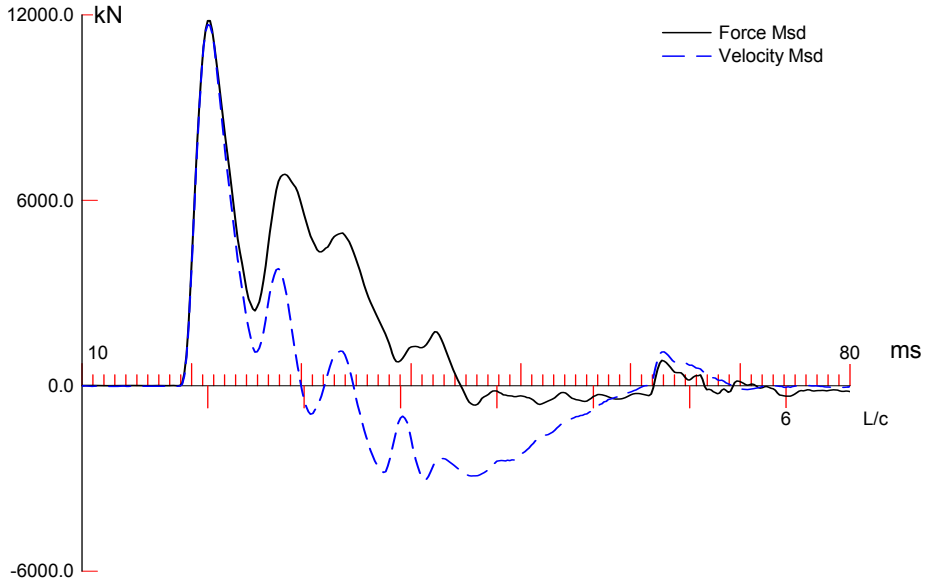
SW Curlew House
Port of Felixstowe
11 to 12 September 2008

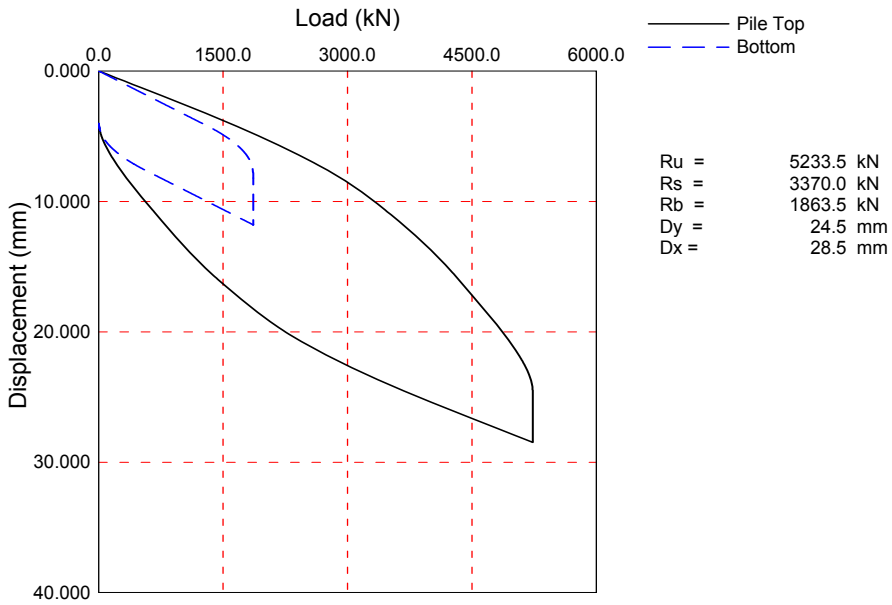
COSTAIN LTD

Maximum Displacement = 54.27mm

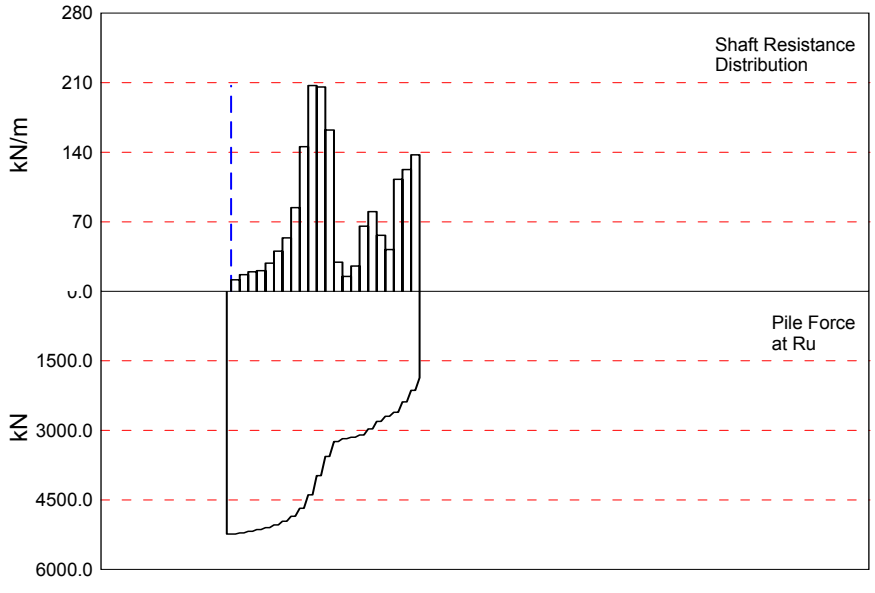
Residual Displacement = 41.63mm



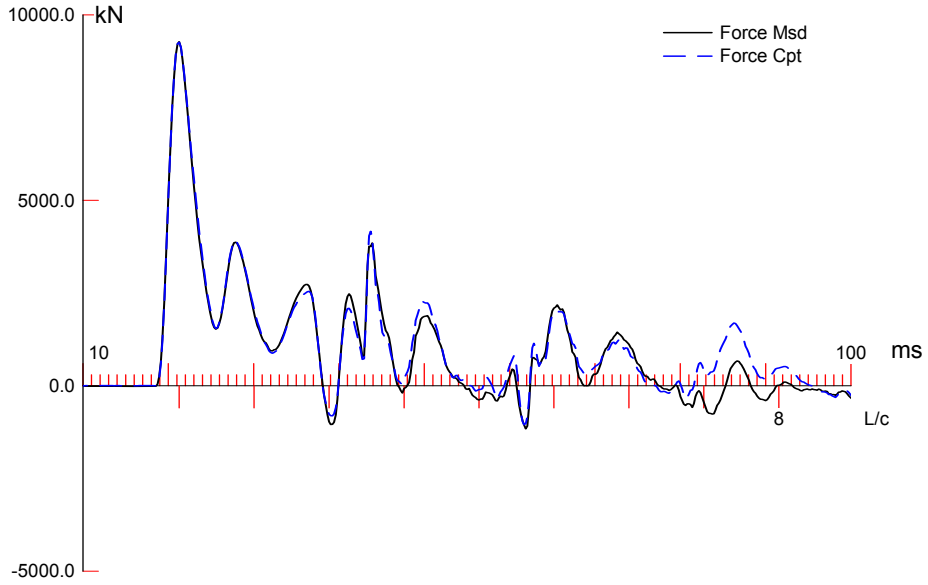


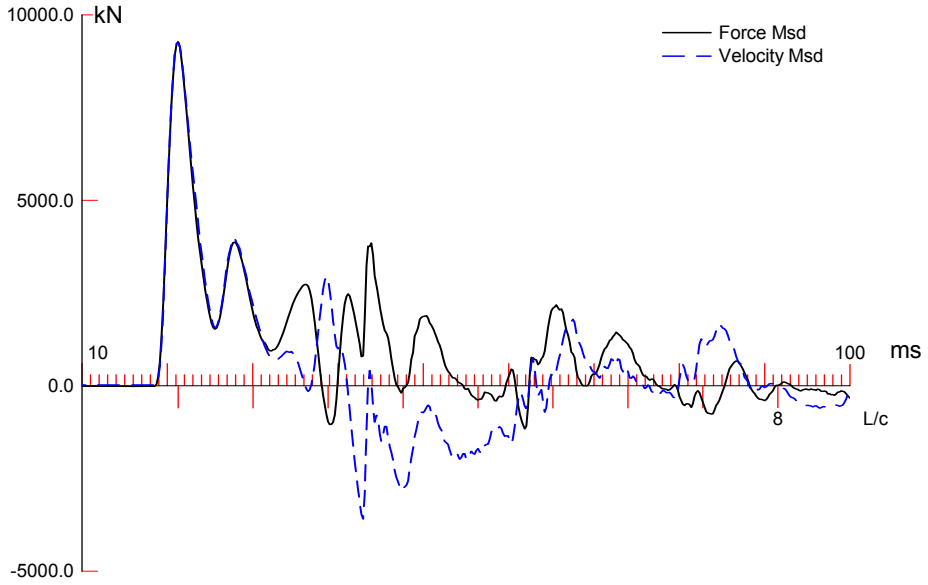


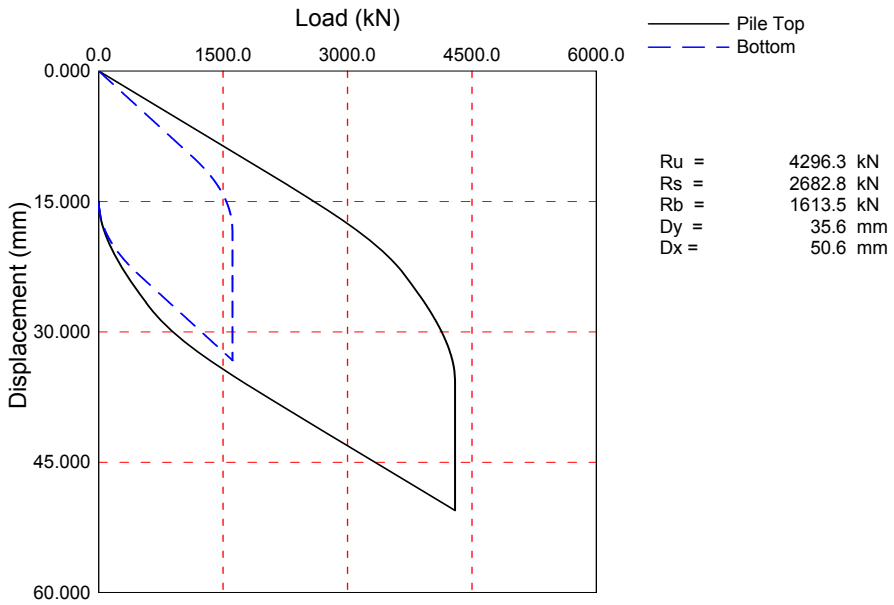
Ru = 5233.5 kN
Rs = 3370.0 kN
Rb = 1863.5 kN
Dy = 24.5 mm
Dx = 28.5 mm



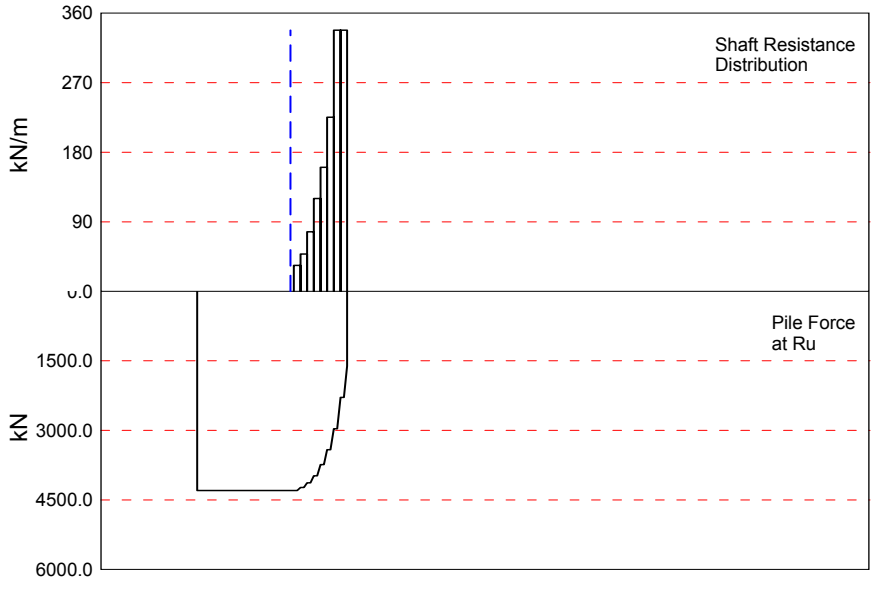
CAPWAP(R) 2006 Licensed to Precision Monitoring & Control Ltd.



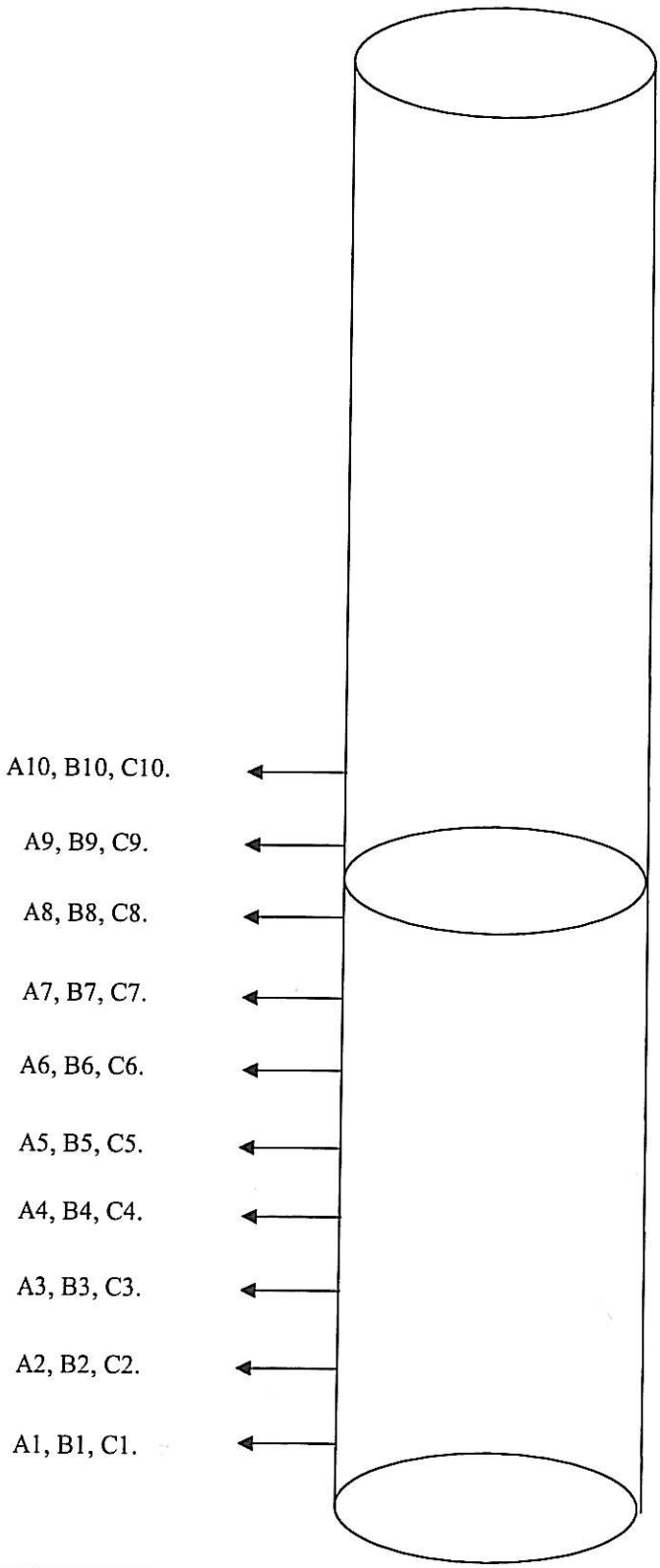




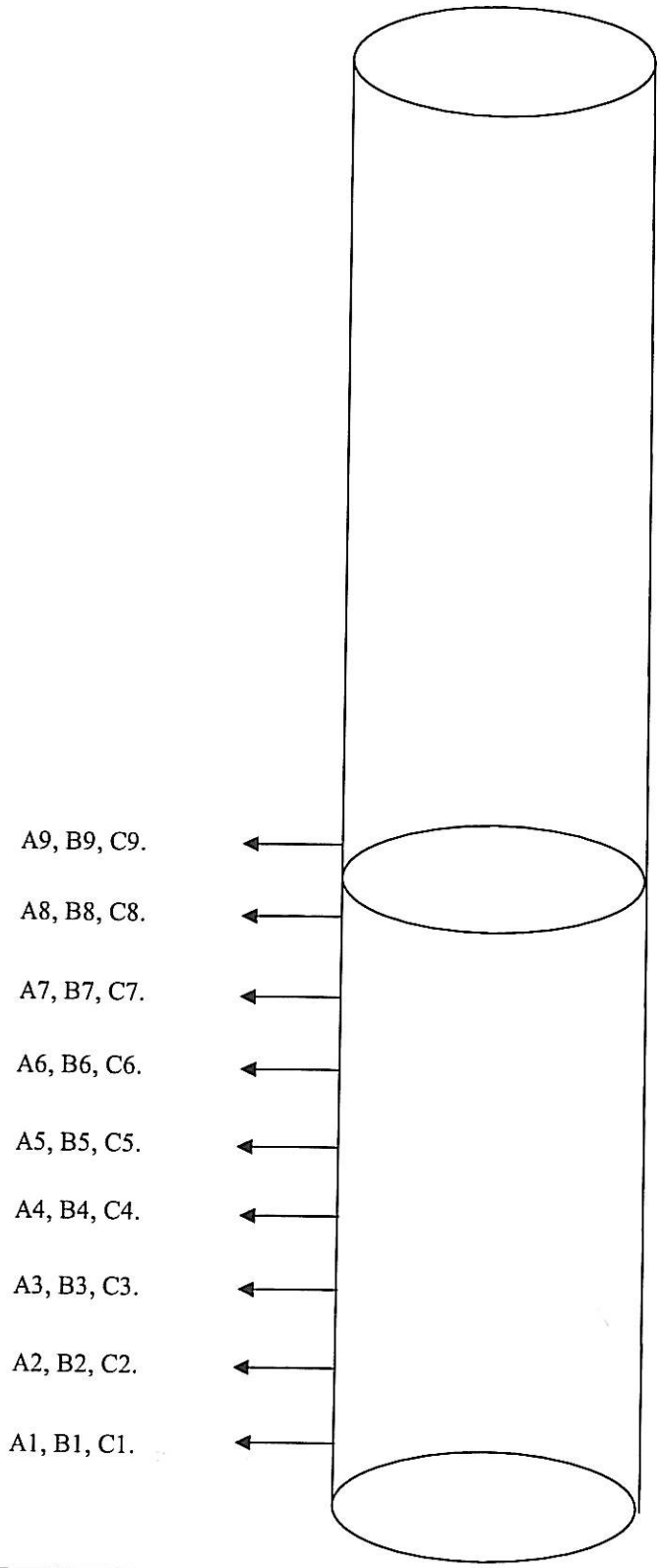
Ru = 4296.3 kN
Rs = 2682.8 kN
Rb = 1613.5 kN
Dy = 35.6 mm
Dx = 50.6 mm



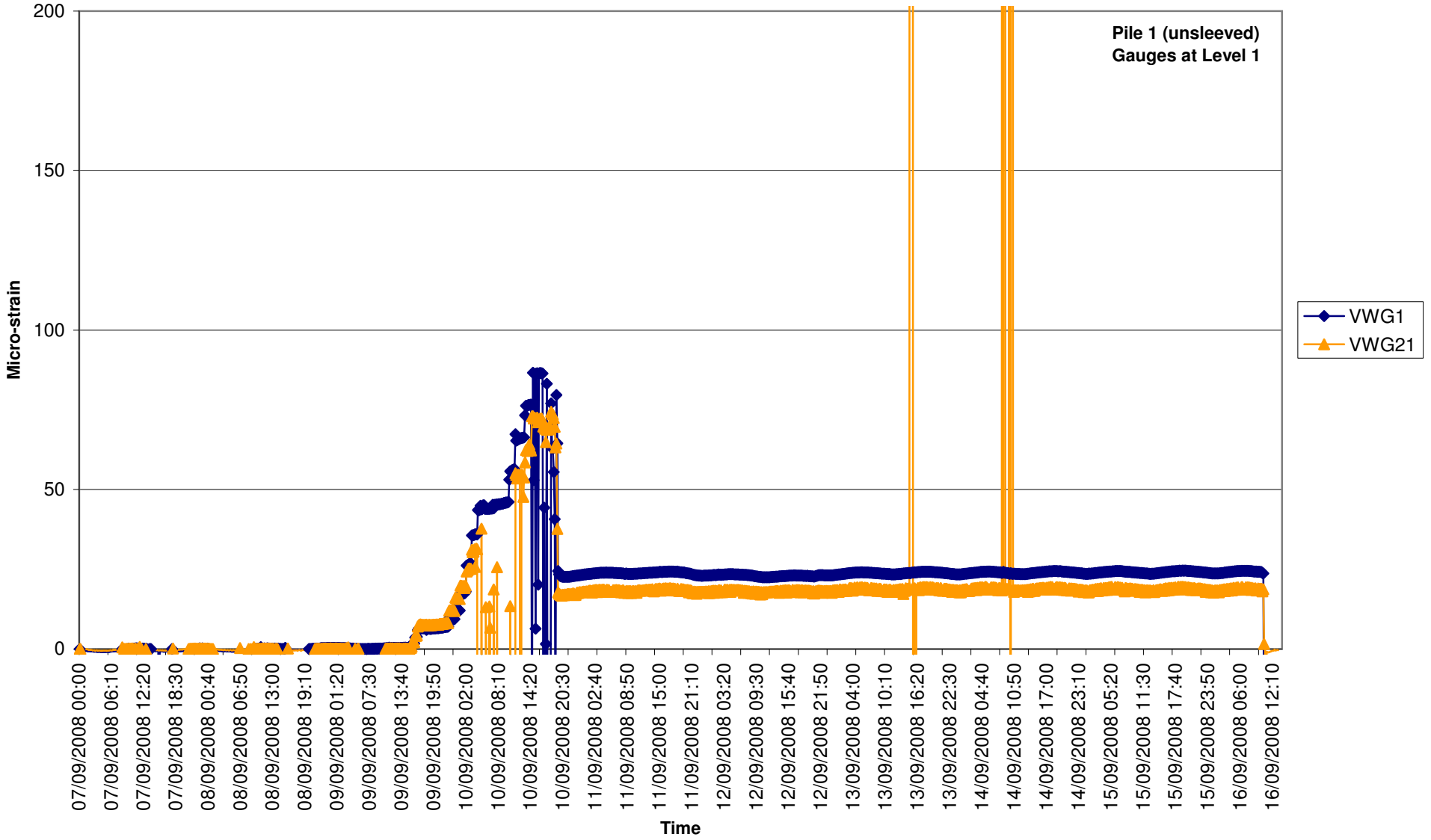
CAPWAP(R) 2006 Licensed to Precision Monitoring & Control Ltd.

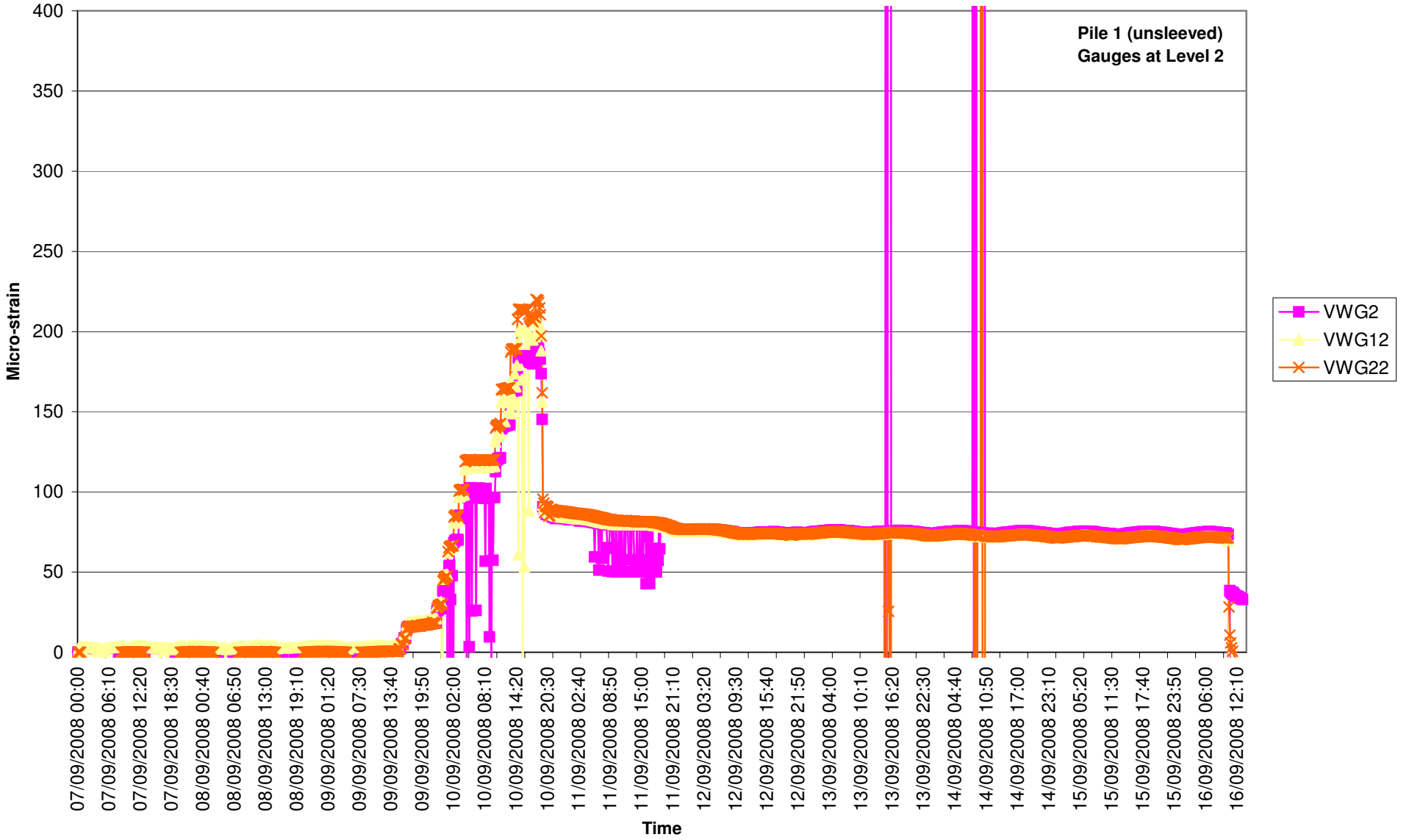


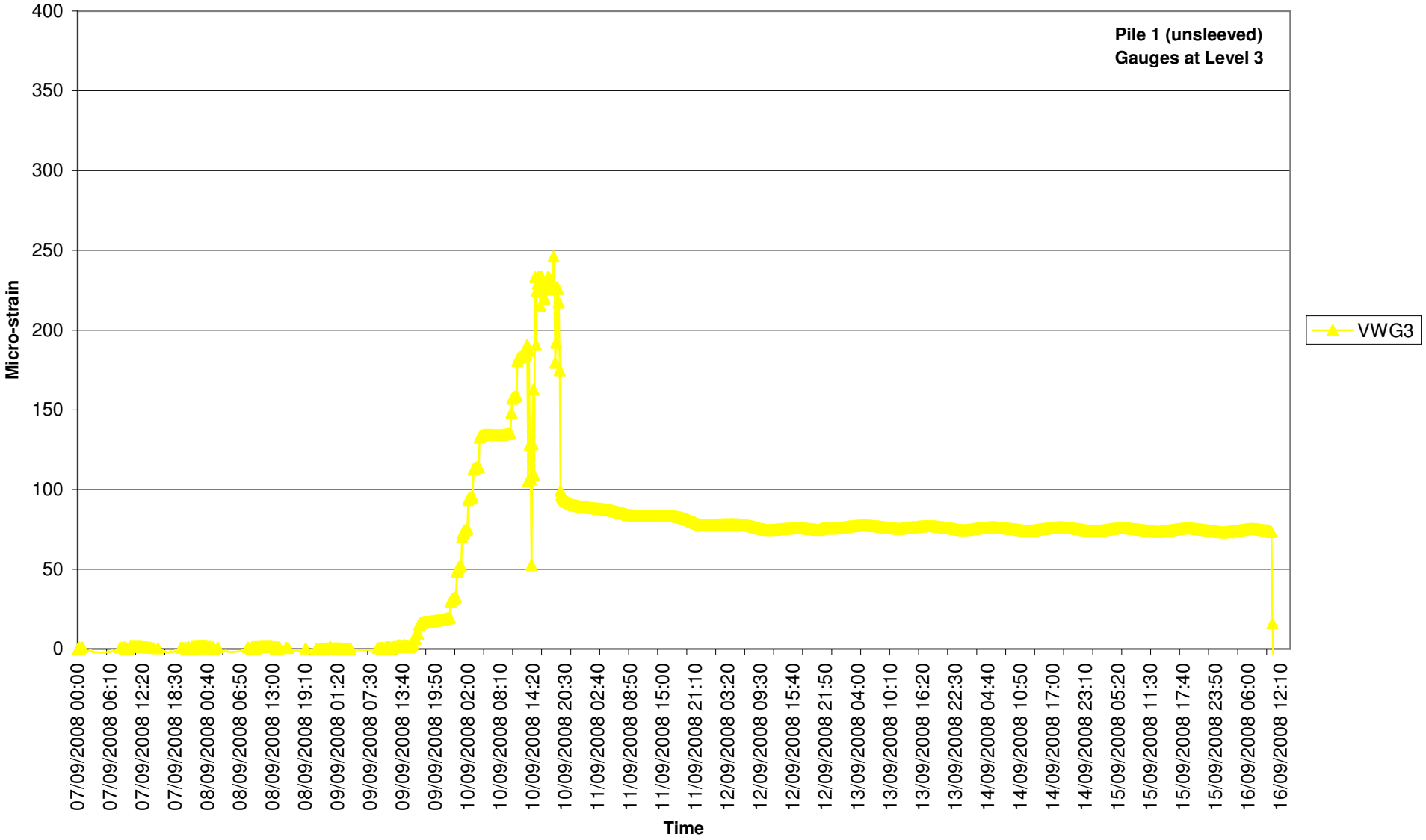
Drawn by:	Scale:	Contract.:	
	N.T.S.	Felixstowe South Reconfiguration	Sol Data
	Date:	Drawing.:	
		Gauge locations on PILE 1 of 2	

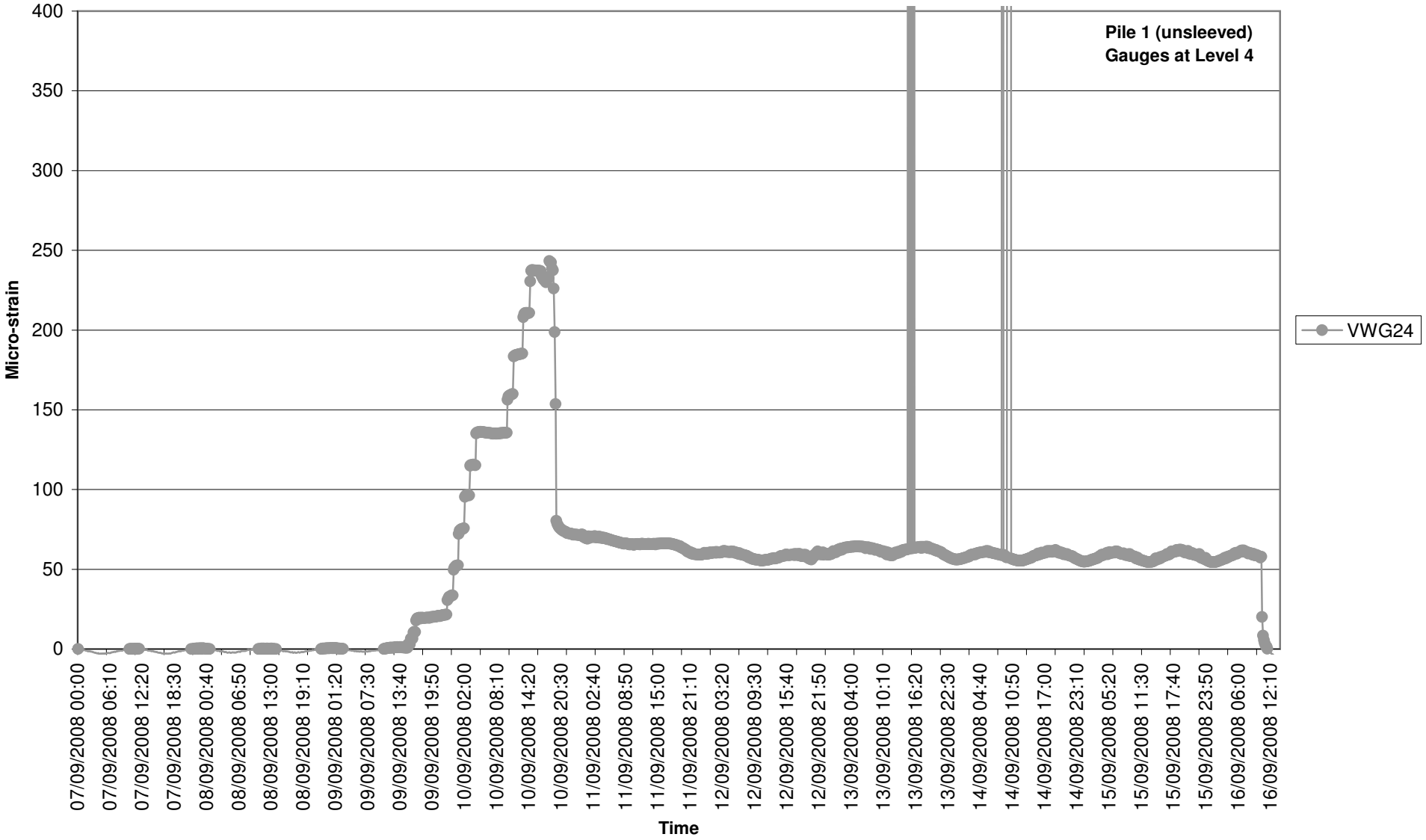


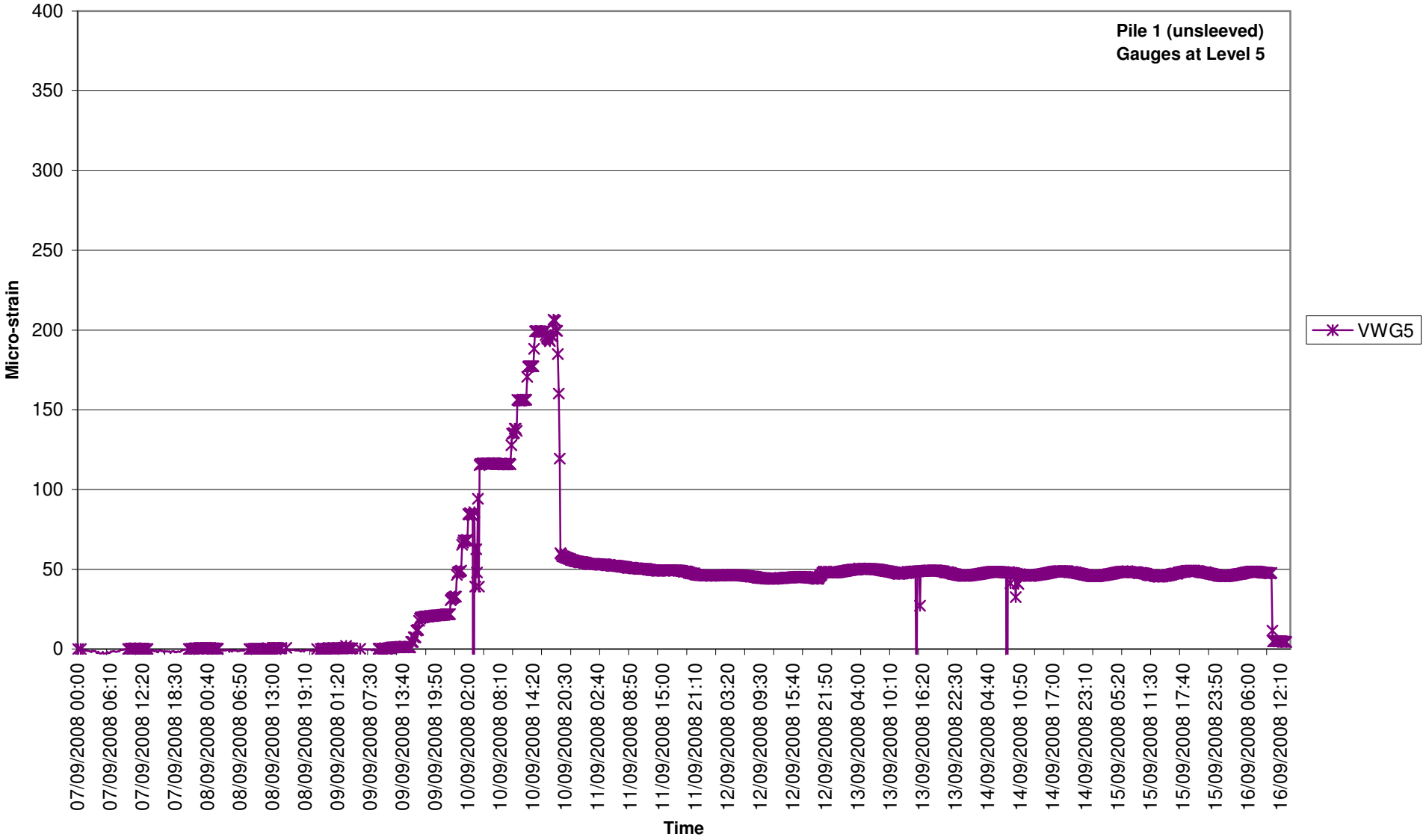
Drawn by:	Scale:	Contract.:	
	N.T.S.	Felixstowe South Reconfiguration	Sol Data
	Date:	Drawing.:	
		Gauge locations on PILE 2 of 2	

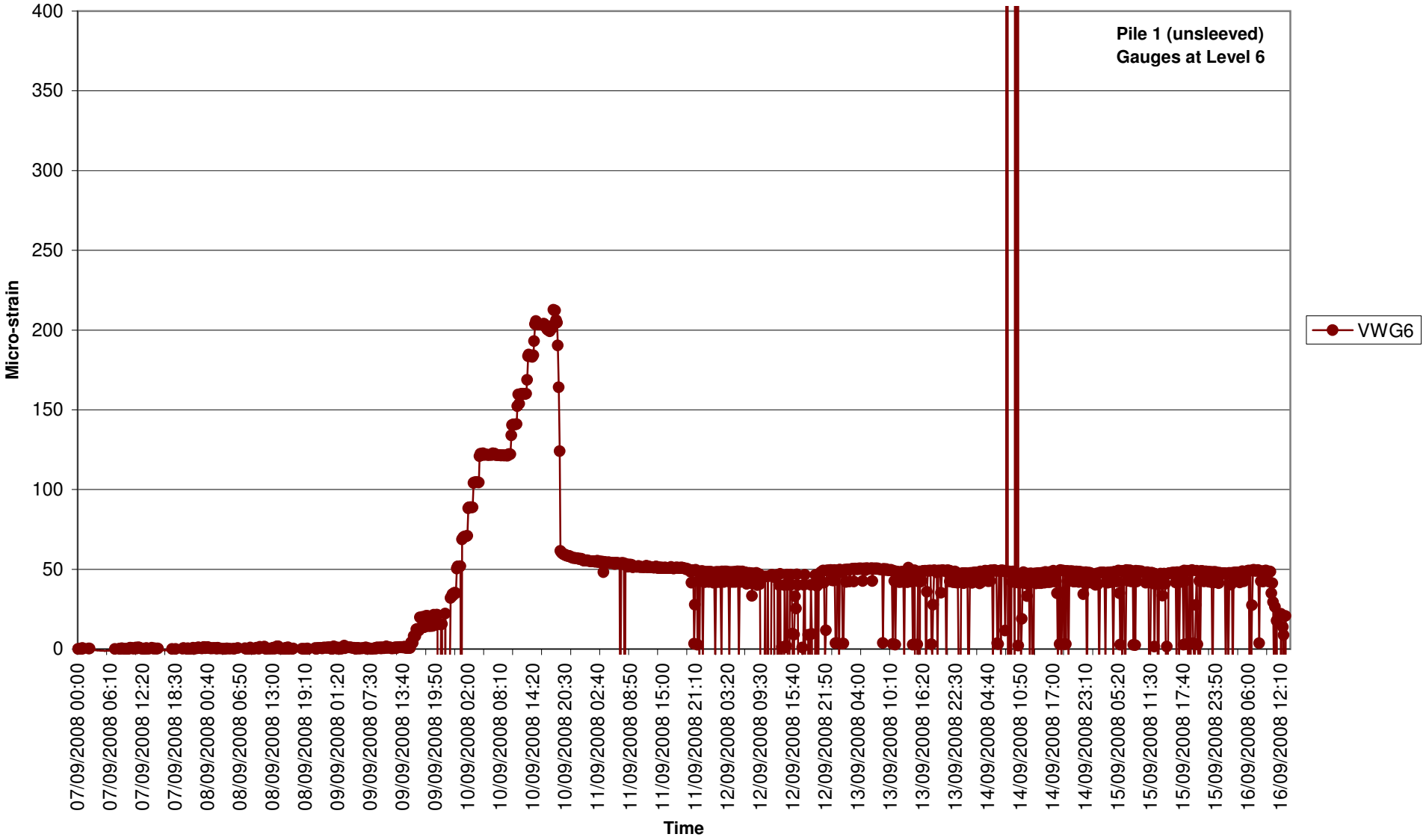

Pile 1 (unsleeved)
Gauges at Level 1
Micro-strain
200
150
100
50
0
Time
07/09/2008 00:00
07/09/2008 06:10
07/09/2008 12:20
07/09/2008 18:30
08/09/2008 00:40
08/09/2008 06:50
08/09/2008 13:00
08/09/2008 19:10
09/09/2008 01:20
09/09/2008 07:30
09/09/2008 13:40
09/09/2008 19:50
10/09/2008 02:00
10/09/2008 08:10
10/09/2008 14:20
10/09/2008 20:30
11/09/2008 02:40
11/09/2008 08:50
11/09/2008 15:00
11/09/2008 21:10
12/09/2008 03:20
12/09/2008 09:30
12/09/2008 15:40
12/09/2008 21:50
13/09/2008 04:00
13/09/2008 10:10
13/09/2008 16:20
13/09/2008 22:30
14/09/2008 04:40
14/09/2008 10:50
14/09/2008 17:00
14/09/2008 23:10
15/09/2008 05:20
15/09/2008 11:30
15/09/2008 17:40
15/09/2008 23:50
16/09/2008 06:00
16/09/2008 12:10
VWG1
VWG21

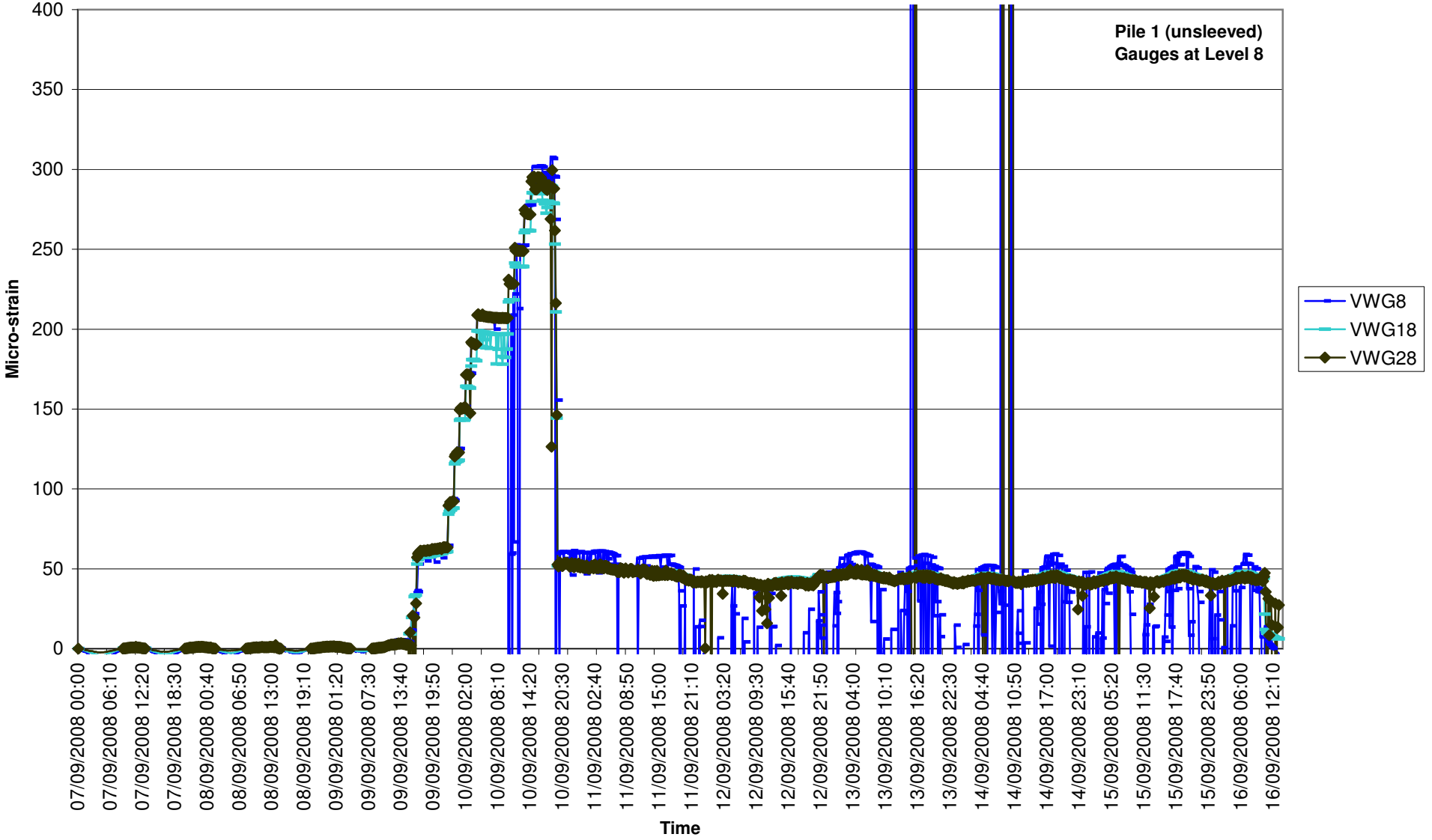

Pile 1 (unsleeved)
Gauges at Level 2
Micro-strain
400
350
300
250
200
150
100
50
0
Time
07/09/2008 00:00
07/09/2008 06:10
07/09/2008 12:20
07/09/2008 18:30
08/09/2008 00:40
08/09/2008 06:50
08/09/2008 13:00
08/09/2008 19:10
09/09/2008 01:20
09/09/2008 07:30
09/09/2008 13:40
09/09/2008 19:50
10/09/2008 02:00
10/09/2008 08:10
10/09/2008 14:20
10/09/2008 20:30
11/09/2008 02:40
11/09/2008 08:50
11/09/2008 15:00
11/09/2008 21:10
12/09/2008 03:20
12/09/2008 09:30
12/09/2008 15:40
12/09/2008 21:50
13/09/2008 04:00
13/09/2008 10:10
13/09/2008 16:20
13/09/2008 22:30
14/09/2008 04:40
14/09/2008 10:50
14/09/2008 17:00
14/09/2008 23:10
15/09/2008 05:20
15/09/2008 11:30
15/09/2008 17:40
15/09/2008 23:50
16/09/2008 06:00
16/09/2008 12:10
VWG2
VWG12
VWG22

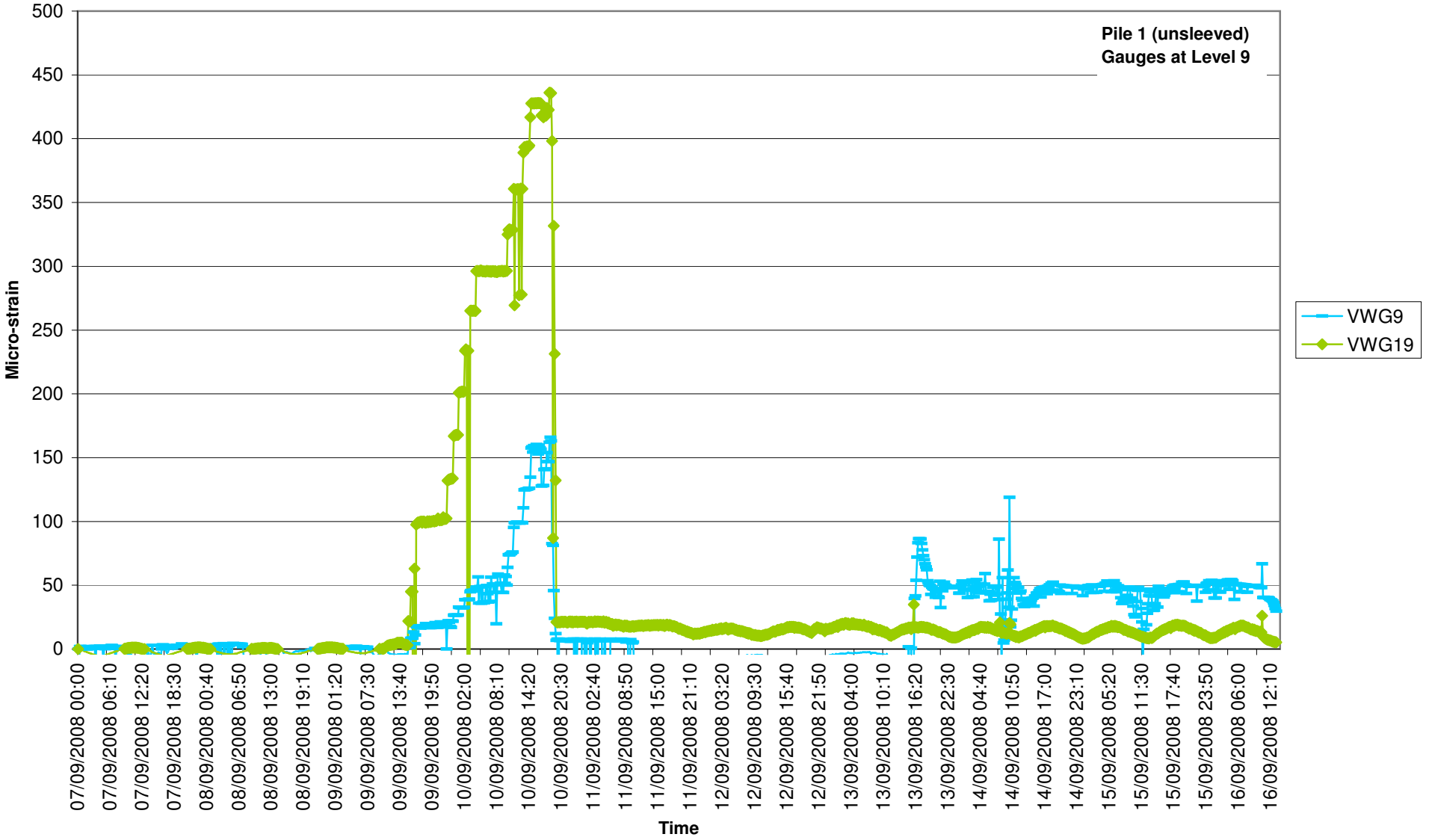

Pile 1 (unsleeved)
Gauges at Level 3
Micro-strain
400
350
300
250
200
150
100
50
0
Time
07/09/2008 00:00
07/09/2008 06:10
07/09/2008 12:20
07/09/2008 18:30
08/09/2008 00:40
08/09/2008 06:50
08/09/2008 13:00
08/09/2008 19:10
09/09/2008 01:20
09/09/2008 07:30
09/09/2008 13:40
09/09/2008 19:50
10/09/2008 02:00
10/09/2008 08:10
10/09/2008 14:20
10/09/2008 20:30
11/09/2008 02:40
11/09/2008 08:50
11/09/2008 15:00
11/09/2008 21:10
12/09/2008 03:20
12/09/2008 09:30
12/09/2008 15:40
12/09/2008 21:50
13/09/2008 04:00
13/09/2008 10:10
13/09/2008 16:20
13/09/2008 22:30
14/09/2008 04:40
14/09/2008 10:50
14/09/2008 17:00
14/09/2008 23:10
15/09/2008 05:20
15/09/2008 11:30
15/09/2008 17:40
15/09/2008 23:50
16/09/2008 06:00
16/09/2008 12:10
VWG3

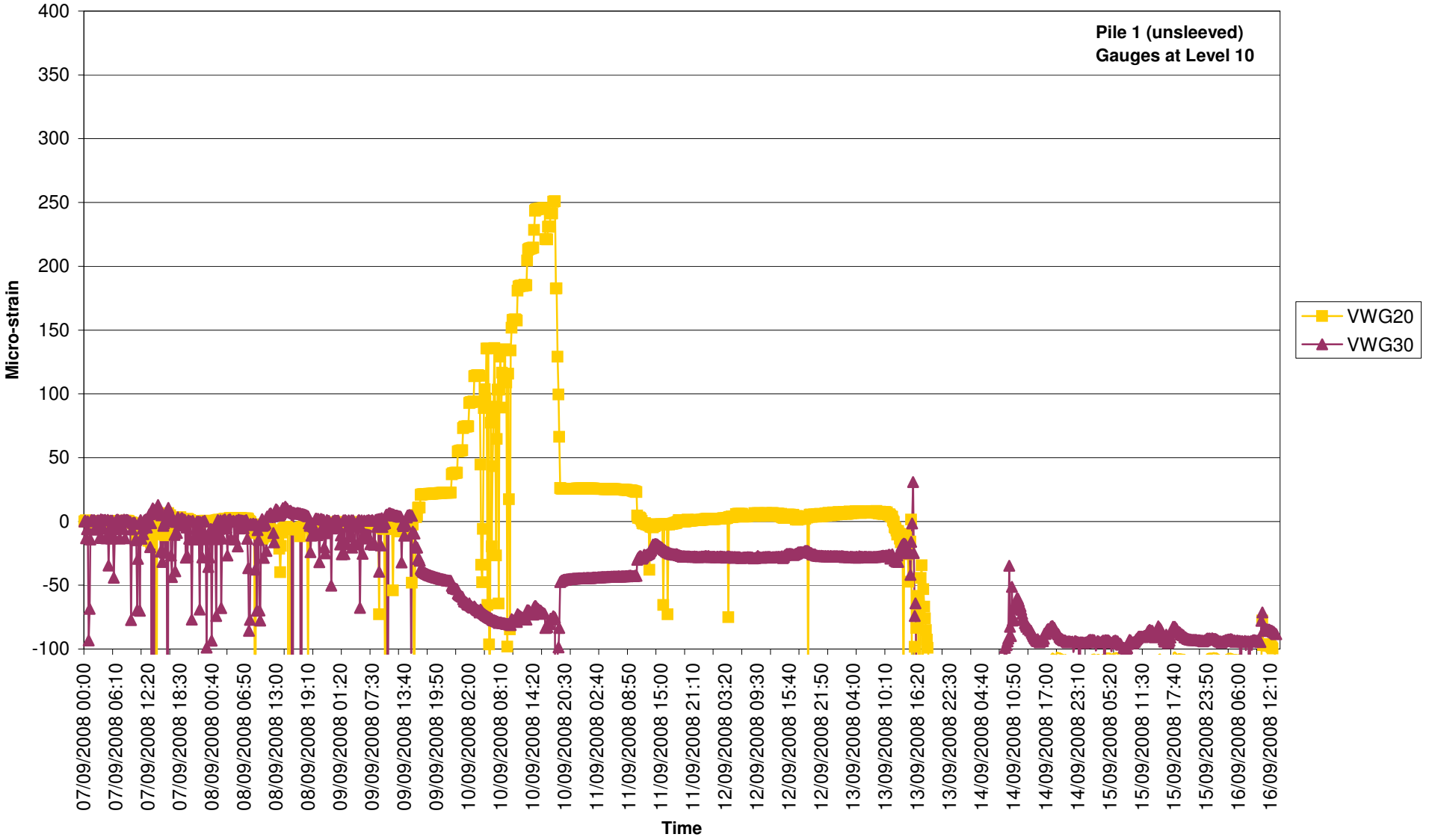

Pile 1 (unsleeved)
Gauges at Level 4
Micro-strain
400
350
300
250
200
150
100
50
0
Time
07/09/2008 00:00
07/09/2008 06:10
07/09/2008 12:20
07/09/2008 18:30
08/09/2008 00:40
08/09/2008 06:50
08/09/2008 13:00
08/09/2008 19:10
09/09/2008 01:20
09/09/2008 07:30
09/09/2008 13:40
09/09/2008 19:50
10/09/2008 02:00
10/09/2008 08:10
10/09/2008 14:20
10/09/2008 20:30
11/09/2008 02:40
11/09/2008 08:50
11/09/2008 15:00
11/09/2008 21:10
12/09/2008 03:20
12/09/2008 09:30
12/09/2008 15:40
12/09/2008 21:50
13/09/2008 04:00
13/09/2008 10:10
13/09/2008 16:20
13/09/2008 22:30
14/09/2008 04:40
14/09/2008 10:50
14/09/2008 17:00
14/09/2008 23:10
15/09/2008 05:20
15/09/2008 11:30
15/09/2008 17:40
15/09/2008 23:50
16/09/2008 06:00
16/09/2008 12:10
VWG24

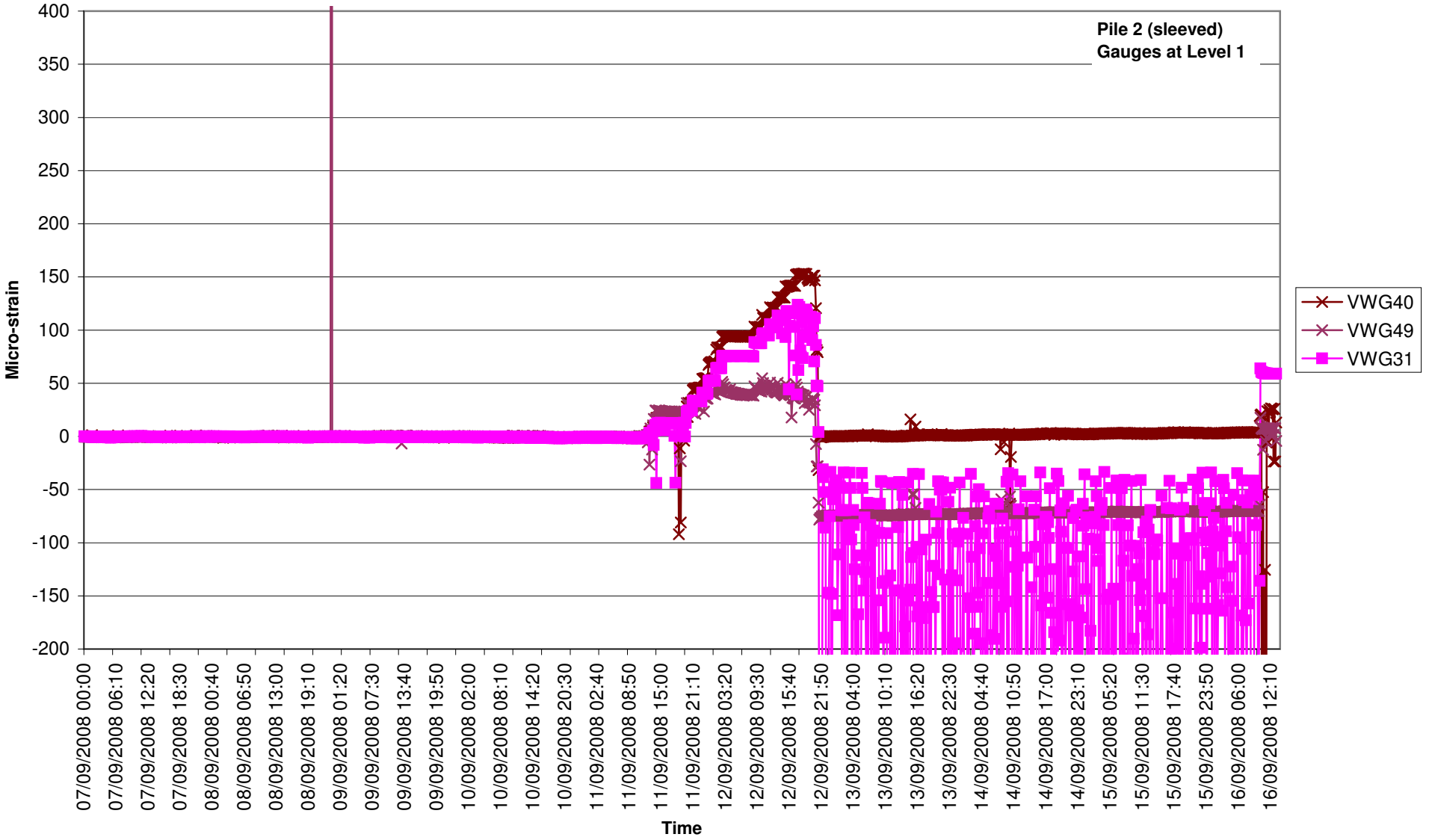

Pile 1 (unsleeved)
Gauges at Level 5
Micro-strain
400
350
300
250
200
150
100
50
0
Time
07/09/2008 00:00
07/09/2008 06:10
07/09/2008 12:20
07/09/2008 18:30
08/09/2008 00:40
08/09/2008 06:50
08/09/2008 13:00
08/09/2008 19:10
09/09/2008 01:20
09/09/2008 07:30
09/09/2008 13:40
09/09/2008 19:50
10/09/2008 02:00
10/09/2008 08:10
10/09/2008 14:20
10/09/2008 20:30
11/09/2008 02:40
11/09/2008 08:50
11/09/2008 15:00
11/09/2008 21:10
12/09/2008 03:20
12/09/2008 09:30
12/09/2008 15:40
12/09/2008 21:50
13/09/2008 04:00
13/09/2008 10:10
13/09/2008 16:20
13/09/2008 22:30
14/09/2008 04:40
14/09/2008 10:50
14/09/2008 17:00
14/09/2008 23:10
15/09/2008 05:20
15/09/2008 11:30
15/09/2008 17:40
15/09/2008 23:50
16/09/2008 06:00
16/09/2008 12:10
VWG5

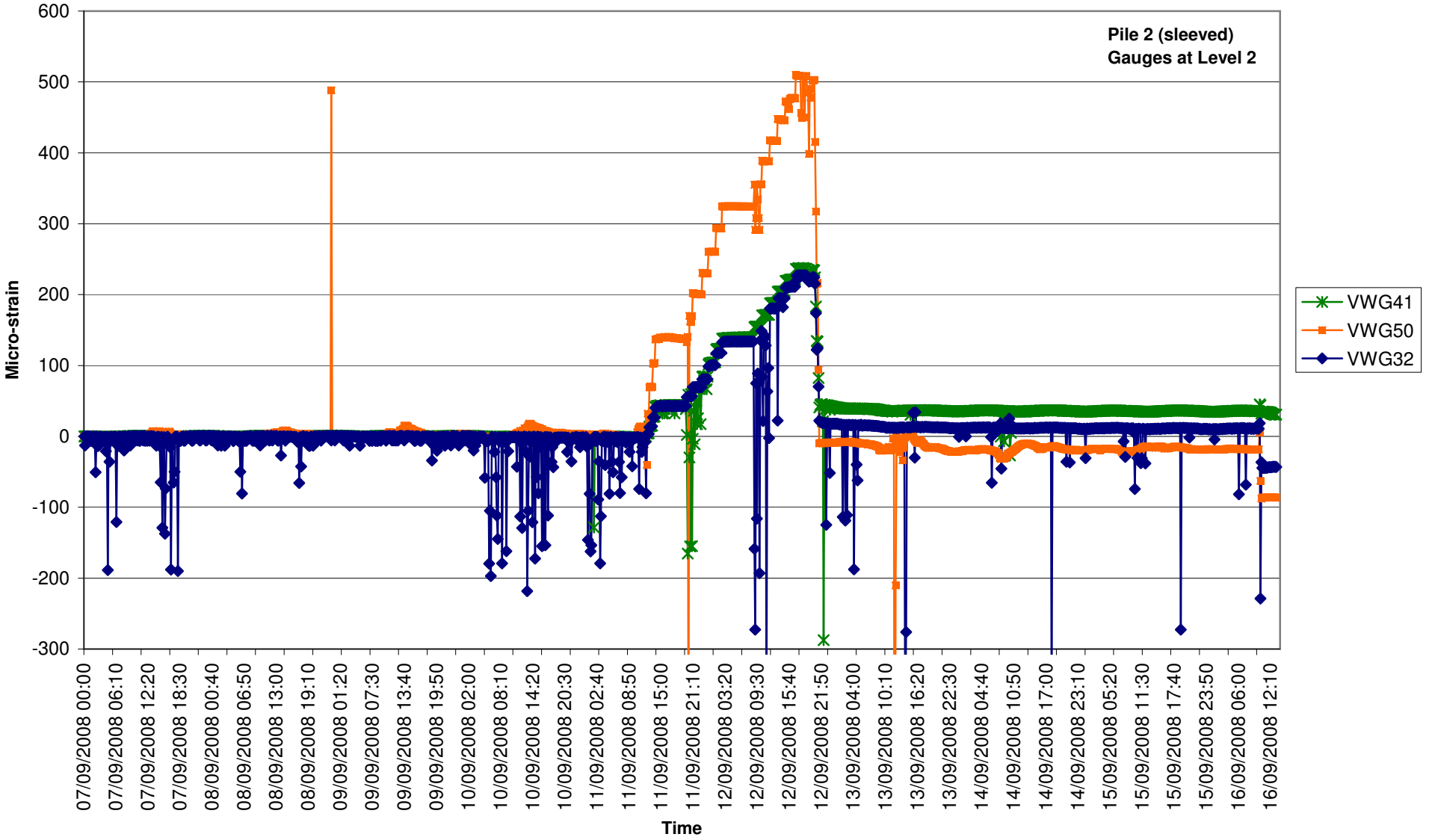

Pile 1 (unsleeved)
Gauges at Level 6
Micro-strain
400
350
300
250
200
150
100
50
0
Time
07/09/2008 00:00
07/09/2008 06:10
07/09/2008 12:20
07/09/2008 18:30
08/09/2008 00:40
08/09/2008 06:50
08/09/2008 13:00
08/09/2008 19:10
09/09/2008 01:20
09/09/2008 07:30
09/09/2008 13:40
09/09/2008 19:50
10/09/2008 02:00
10/09/2008 08:10
10/09/2008 14:20
10/09/2008 20:30
11/09/2008 02:40
11/09/2008 08:50
11/09/2008 15:00
11/09/2008 21:10
12/09/2008 03:20
12/09/2008 09:30
12/09/2008 15:40
12/09/2008 21:50
13/09/2008 04:00
13/09/2008 10:10
13/09/2008 16:20
13/09/2008 22:30
14/09/2008 04:40
14/09/2008 10:50
14/09/2008 17:00
14/09/2008 23:10
15/09/2008 05:20
15/09/2008 11:30
15/09/2008 17:40
15/09/2008 23:50
16/09/2008 06:00
16/09/2008 12:10
VWG6

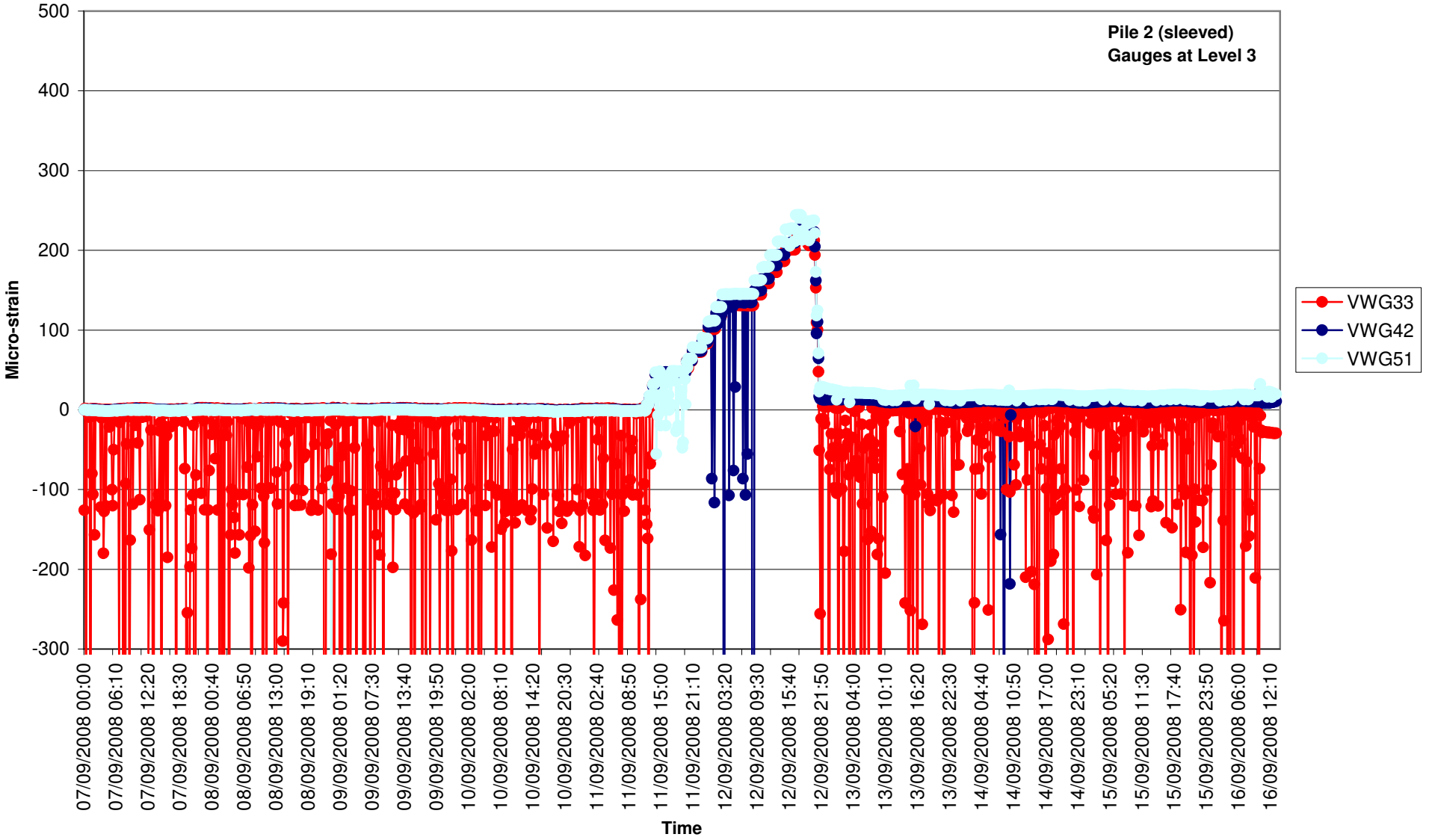

Pile 1 (unsleeved)
Gauges at Level 8
Micro-strain
400
350
300
250
200
150
100
50
0
Time
07/09/2008 00:00
07/09/2008 06:10
07/09/2008 12:20
07/09/2008 18:30
08/09/2008 00:40
08/09/2008 06:50
08/09/2008 13:00
08/09/2008 19:10
09/09/2008 01:20
09/09/2008 07:30
09/09/2008 13:40
09/09/2008 19:50
10/09/2008 02:00
10/09/2008 08:10
10/09/2008 14:20
10/09/2008 20:30
11/09/2008 02:40
11/09/2008 08:50
11/09/2008 15:00
11/09/2008 21:10
12/09/2008 03:20
12/09/2008 09:30
12/09/2008 15:40
12/09/2008 21:50
13/09/2008 04:00
13/09/2008 10:10
13/09/2008 16:20
13/09/2008 22:30
14/09/2008 04:40
14/09/2008 10:50
14/09/2008 17:00
14/09/2008 23:10
15/09/2008 05:20
15/09/2008 11:30
15/09/2008 17:40
15/09/2008 23:50
16/09/2008 06:00
16/09/2008 12:10
VWG8
VWG18
VWG28

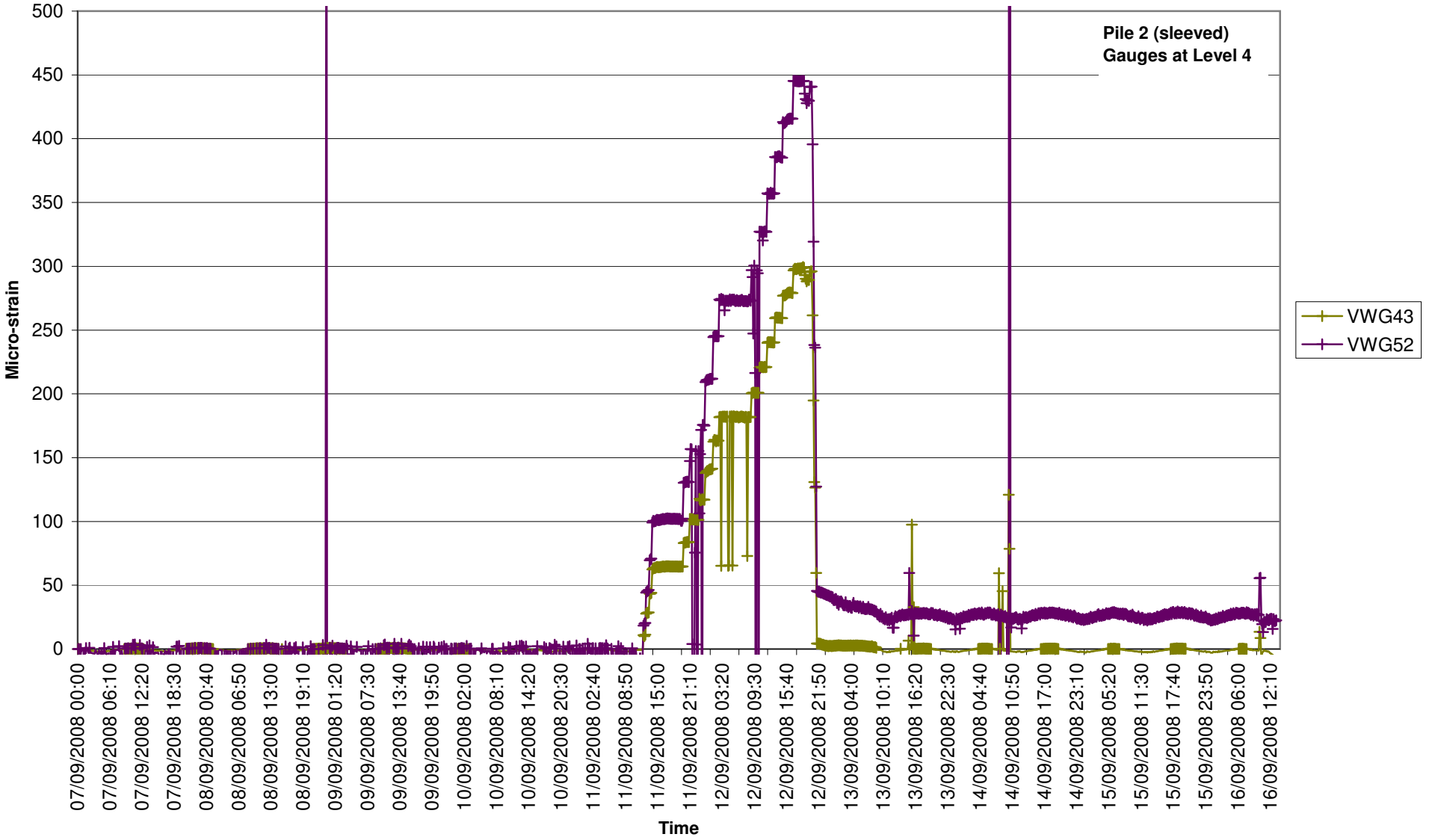

Pile 1 (unsleeved)
Gauges at Level 9
Micro-strain
500
450
400
350
300
250
200
150
100
50
0
VWG9
VWG19
07/09/2008 00:00
07/09/2008 06:10
07/09/2008 12:20
07/09/2008 18:30
08/09/2008 00:40
08/09/2008 06:50
08/09/2008 13:00
08/09/2008 19:10
09/09/2008 01:20
09/09/2008 07:30
09/09/2008 13:40
09/09/2008 19:50
10/09/2008 02:00
10/09/2008 08:10
10/09/2008 14:20
10/09/2008 20:30
11/09/2008 02:40
11/09/2008 08:50
11/09/2008 15:00
11/09/2008 21:10
12/09/2008 03:20
12/09/2008 09:30
12/09/2008 15:40
12/09/2008 21:50
13/09/2008 04:00
13/09/2008 10:10
13/09/2008 16:20
13/09/2008 22:30
14/09/2008 04:40
14/09/2008 10:50
14/09/2008 17:00
14/09/2008 23:10
15/09/2008 05:20
15/09/2008 11:30
15/09/2008 17:40
15/09/2008 23:50
16/09/2008 06:00
16/09/2008 12:10
Time

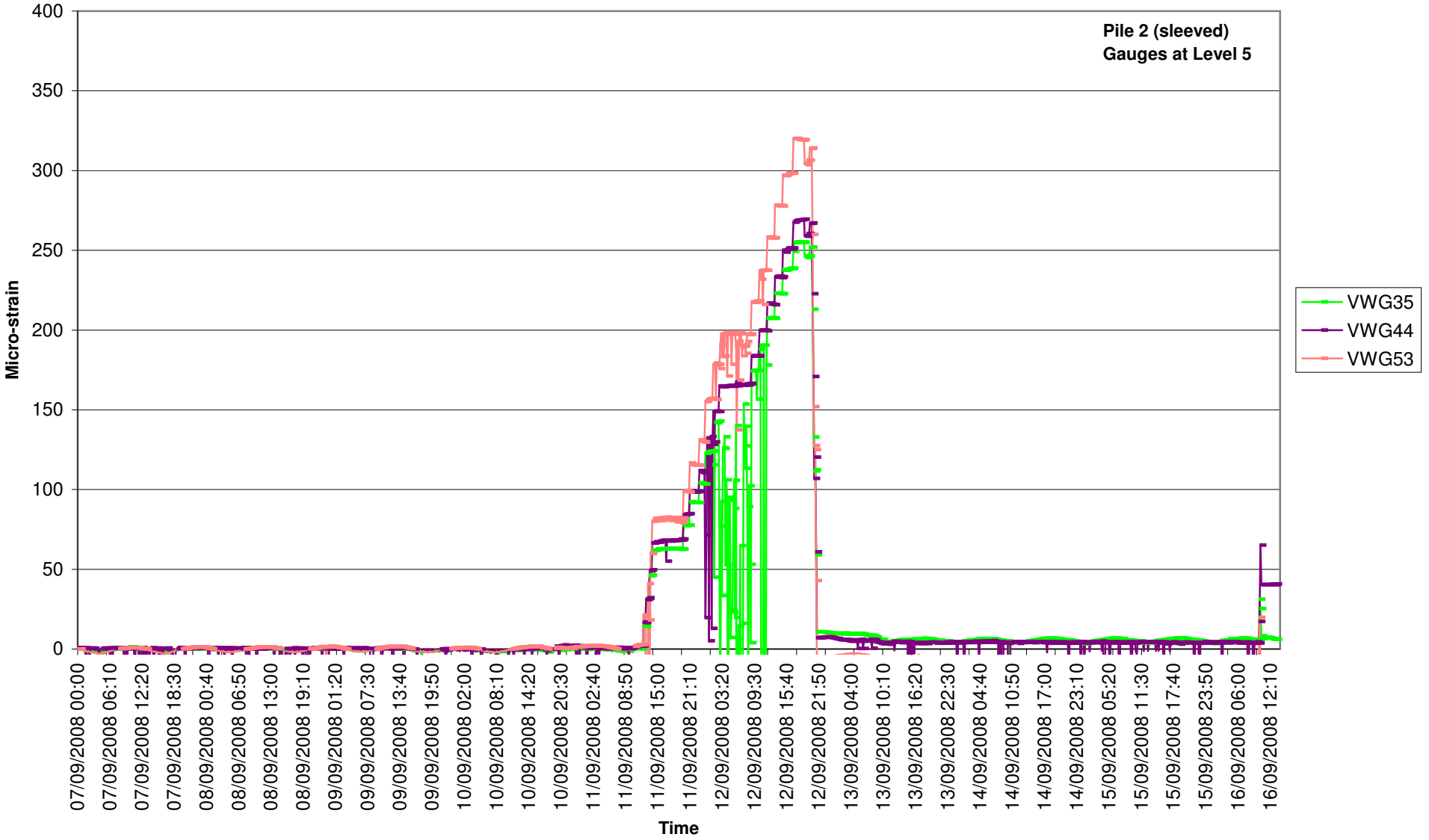

Pile 1 (unsleeved)
Gauges at Level 10
Micro-strain
400
350
300
250
200
150
100
50
0
-50
-100
VWG20
VWG30
Time
07/09/2008 00:00
07/09/2008 06:10
07/09/2008 12:20
07/09/2008 18:30
08/09/2008 00:40
08/09/2008 06:50
08/09/2008 13:00
08/09/2008 19:10
09/09/2008 01:20
09/09/2008 07:30
09/09/2008 13:40
09/09/2008 19:50
10/09/2008 02:00
10/09/2008 08:10
10/09/2008 14:20
10/09/2008 20:30
11/09/2008 02:40
11/09/2008 08:50
11/09/2008 15:00
11/09/2008 21:10
12/09/2008 03:20
12/09/2008 09:30
12/09/2008 15:40
12/09/2008 21:50
13/09/2008 04:00
13/09/2008 10:10
13/09/2008 16:20
13/09/2008 22:30
14/09/2008 04:40
14/09/2008 10:50
14/09/2008 17:00
14/09/2008 23:10
15/09/2008 05:20
15/09/2008 11:30
15/09/2008 17:40
15/09/2008 23:50
16/09/2008 06:00
16/09/2008 12:10

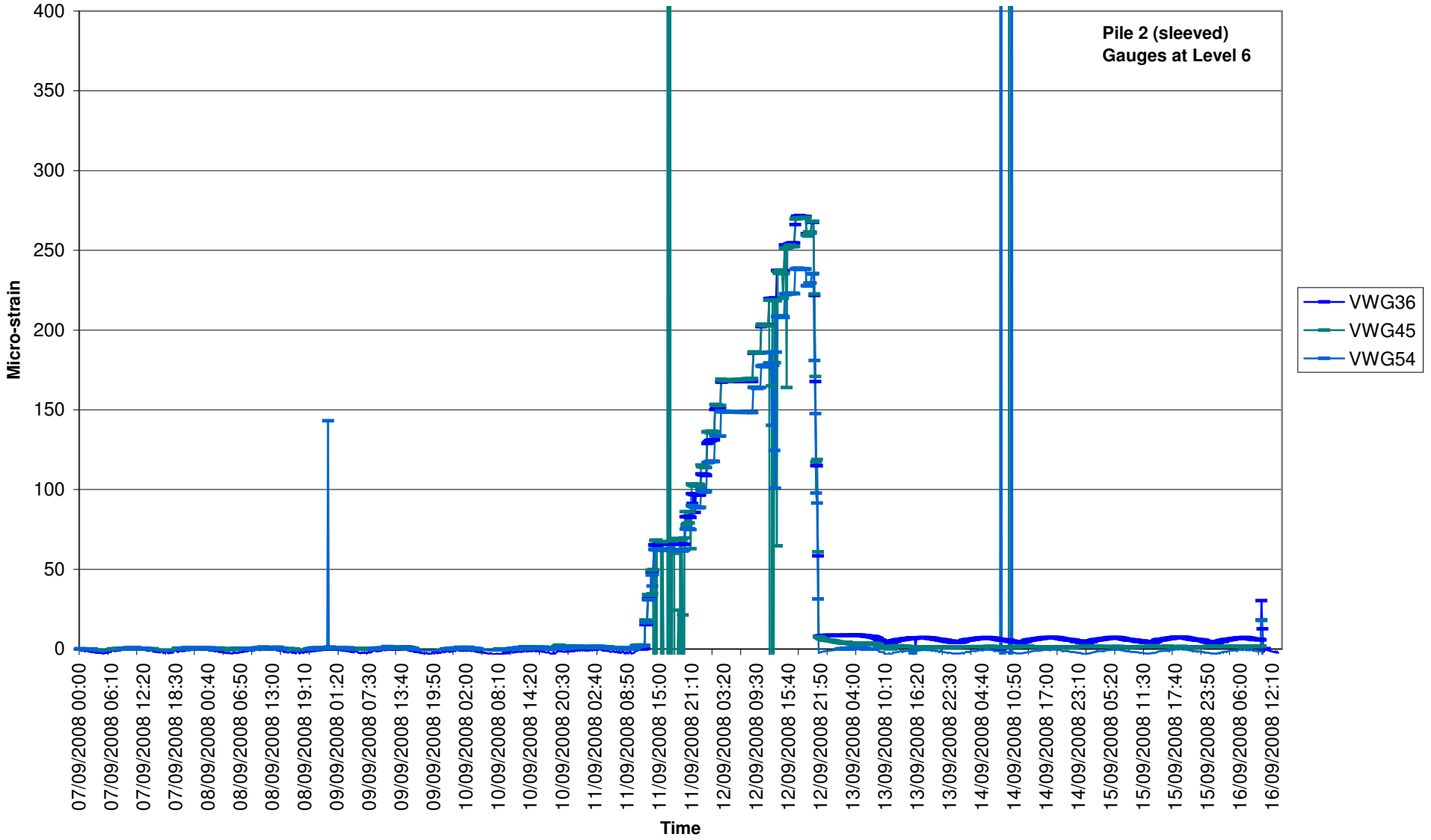

Pile 2 (sleeved)
Gauges at Level 1
Micro-strain
400
350
300
250
200
150
100
50
0
-50
-100
-150
-200
07/09/2008 00:00
07/09/2008 06:10
07/09/2008 12:20
07/09/2008 18:30
08/09/2008 00:40
08/09/2008 06:50
08/09/2008 13:00
08/09/2008 19:10
09/09/2008 01:20
09/09/2008 07:30
09/09/2008 13:40
09/09/2008 19:50
10/09/2008 02:00
10/09/2008 08:10
10/09/2008 14:20
10/09/2008 20:30
11/09/2008 02:40
11/09/2008 08:50
11/09/2008 15:00
11/09/2008 21:10
12/09/2008 03:20
12/09/2008 09:30
12/09/2008 15:40
12/09/2008 21:50
13/09/2008 04:00
13/09/2008 10:10
13/09/2008 16:20
13/09/2008 22:30
14/09/2008 04:40
14/09/2008 10:50
14/09/2008 17:00
14/09/2008 23:10
15/09/2008 05:20
15/09/2008 11:30
15/09/2008 17:40
15/09/2008 23:50
16/09/2008 06:00
16/09/2008 12:10
Time
VWG40
VWG49
VWG31

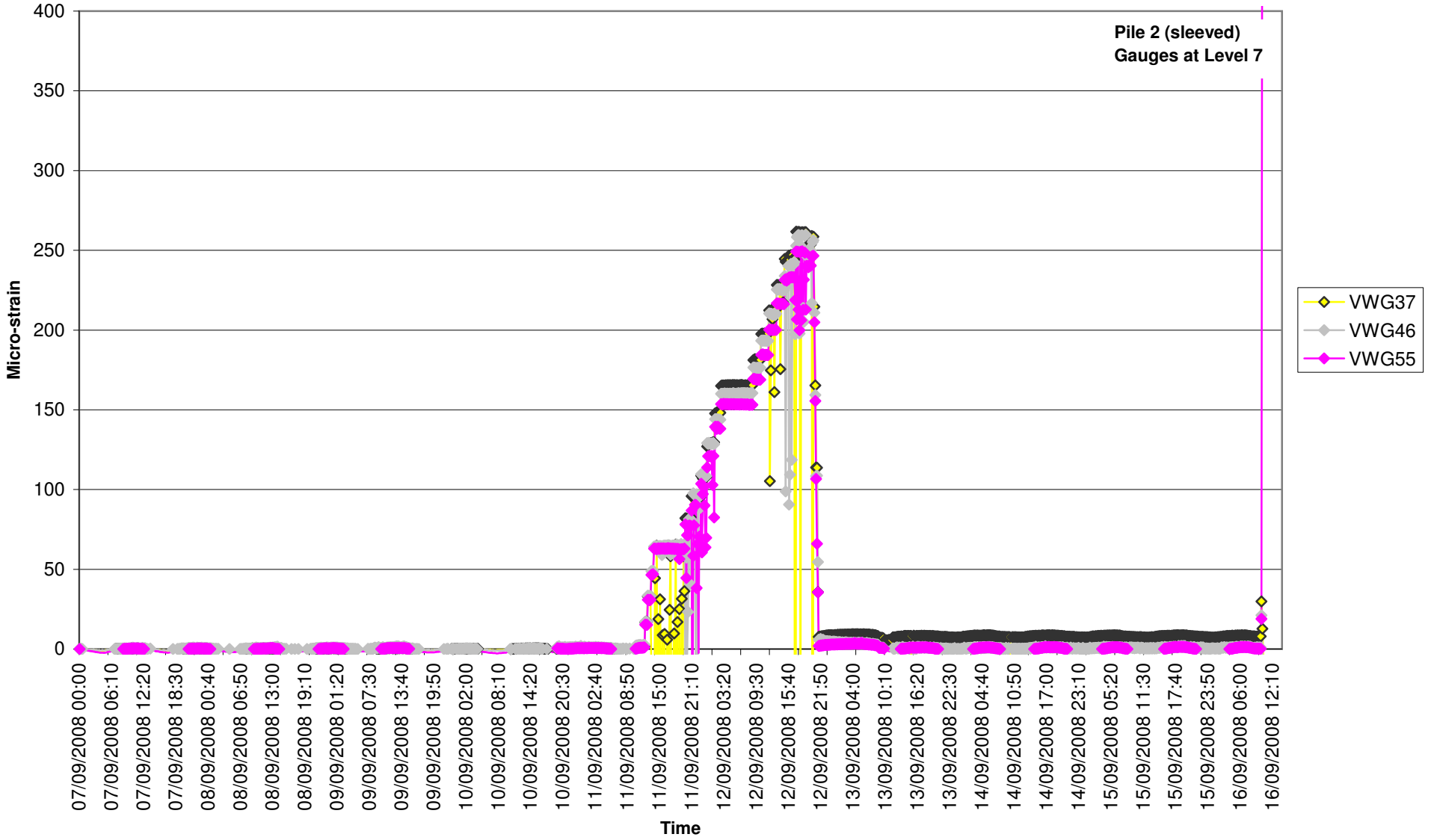

Pile 2 (sleeved)
Gauges at Level 2
Micro-strain
600
500
400
300
200
100
0
-100
-200
-300
VWG41
VWG50
VWG32
07/09/2008 00:00
07/09/2008 06:10
07/09/2008 12:20
07/09/2008 18:30
08/09/2008 00:40
08/09/2008 06:50
08/09/2008 13:00
08/09/2008 19:10
09/09/2008 01:20
09/09/2008 07:30
09/09/2008 13:40
09/09/2008 19:50
10/09/2008 02:00
10/09/2008 08:10
10/09/2008 14:20
10/09/2008 20:30
11/09/2008 02:40
11/09/2008 08:50
11/09/2008 15:00
11/09/2008 21:10
12/09/2008 03:20
12/09/2008 09:30
12/09/2008 15:40
12/09/2008 21:50
13/09/2008 04:00
13/09/2008 10:10
13/09/2008 16:20
13/09/2008 22:30
14/09/2008 04:40
14/09/2008 10:50
14/09/2008 17:00
14/09/2008 23:10
15/09/2008 05:20
15/09/2008 11:30
15/09/2008 17:40
15/09/2008 23:50
16/09/2008 06:00
16/09/2008 12:10
Time

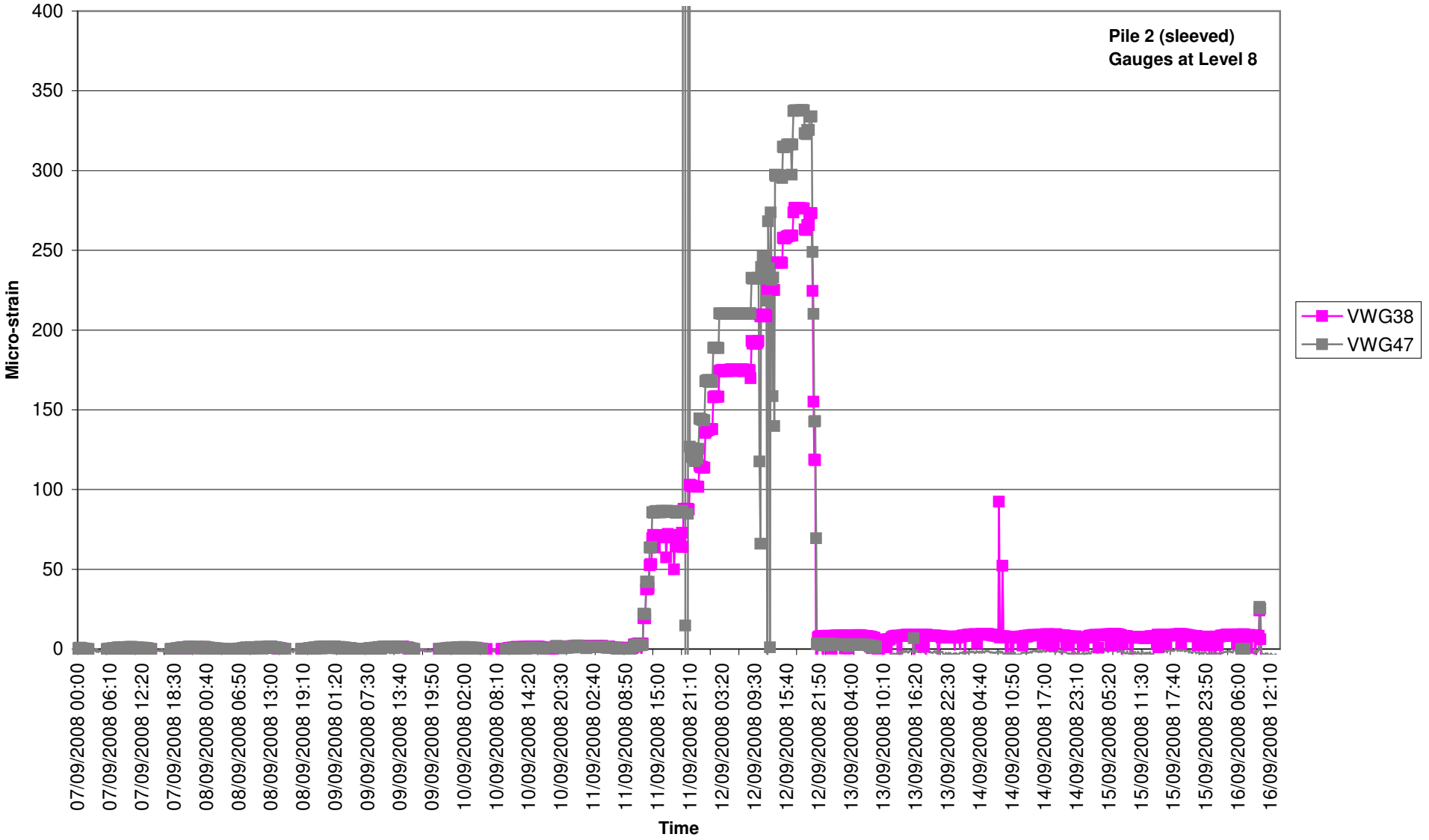

Pile 2 (sleeved)
Gauges at Level 3
Micro-strain
500
400
300
200
100
0
-100
-200
-300
VWG33
VWG42
VWG51
Time
07/09/2008 00:00
07/09/2008 06:10
07/09/2008 12:20
07/09/2008 18:30
08/09/2008 00:40
08/09/2008 06:50
08/09/2008 13:00
08/09/2008 19:10
09/09/2008 01:20
09/09/2008 07:30
09/09/2008 13:40
09/09/2008 19:50
10/09/2008 02:00
10/09/2008 08:10
10/09/2008 14:20
10/09/2008 20:30
11/09/2008 02:40
11/09/2008 08:50
11/09/2008 15:00
11/09/2008 21:10
12/09/2008 03:20
12/09/2008 09:30
12/09/2008 15:40
12/09/2008 21:50
13/09/2008 04:00
13/09/2008 10:10
13/09/2008 16:20
13/09/2008 22:30
14/09/2008 04:40
14/09/2008 10:50
14/09/2008 17:00
14/09/2008 23:10
15/09/2008 05:20
15/09/2008 11:30
15/09/2008 17:40
15/09/2008 23:50
16/09/2008 06:00
16/09/2008 12:10

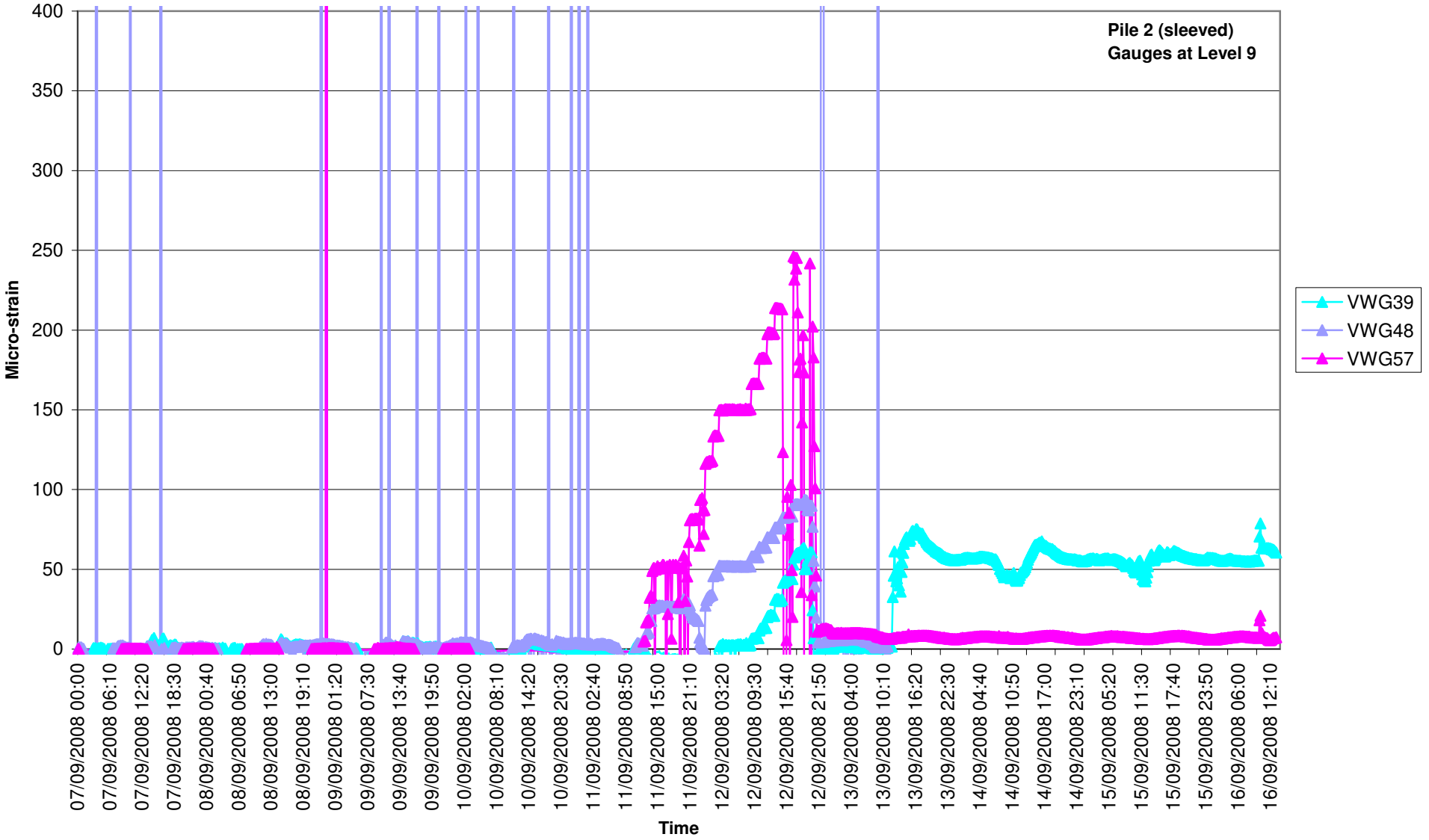

Pile 2 (sleeved)
Gauges at Level 4
Micro-strain
500
450
400
350
300
250
200
150
100
50
0
VWG43
VWG52
Time
07/09/2008 00:00
07/09/2008 06:10
07/09/2008 12:20
07/09/2008 18:30
08/09/2008 00:40
08/09/2008 06:50
08/09/2008 13:00
08/09/2008 19:10
09/09/2008 01:20
09/09/2008 07:30
09/09/2008 13:40
09/09/2008 19:50
10/09/2008 02:00
10/09/2008 08:10
10/09/2008 14:20
10/09/2008 20:30
11/09/2008 02:40
11/09/2008 08:50
11/09/2008 15:00
11/09/2008 21:10
12/09/2008 03:20
12/09/2008 09:30
12/09/2008 15:40
12/09/2008 21:50
13/09/2008 04:00
13/09/2008 10:10
13/09/2008 16:20
13/09/2008 22:30
14/09/2008 04:40
14/09/2008 10:50
14/09/2008 17:00
14/09/2008 23:10
15/09/2008 05:20
15/09/2008 11:30
15/09/2008 17:40
15/09/2008 23:50
16/09/2008 06:00
16/09/2008 12:10


Pile 2 (sleeved)
Gauges at Level 5
Micro-strain
400
350
300
250
200
150
100
50
0
Time
07/09/2008 00:00
07/09/2008 06:10
07/09/2008 12:20
07/09/2008 18:30
08/09/2008 00:40
08/09/2008 06:50
08/09/2008 13:00
08/09/2008 19:10
09/09/2008 01:20
09/09/2008 07:30
09/09/2008 13:40
09/09/2008 19:50
10/09/2008 02:00
10/09/2008 08:10
10/09/2008 14:20
10/09/2008 20:30
11/09/2008 02:40
11/09/2008 08:50
11/09/2008 15:00
11/09/2008 21:10
12/09/2008 03:20
12/09/2008 09:30
12/09/2008 15:40
12/09/2008 21:50
13/09/2008 04:00
13/09/2008 10:10
13/09/2008 16:20
13/09/2008 22:30
14/09/2008 04:40
14/09/2008 10:50
14/09/2008 17:00
14/09/2008 23:10
15/09/2008 05:20
15/09/2008 11:30
15/09/2008 17:40
15/09/2008 23:50
16/09/2008 06:00
16/09/2008 12:10
VWG35
VWG44
VWG53


Pile 2 (sleeved)
Gauges at Level 6
Micro-strain
400
350
300
250
200
150
100
50
0
VWG36
VWG45
VWG54
Time
07/09/2008 00:00
07/09/2008 06:10
07/09/2008 12:20
07/09/2008 18:30
08/09/2008 00:40
08/09/2008 06:50
08/09/2008 13:00
08/09/2008 19:10
09/09/2008 01:20
09/09/2008 07:30
09/09/2008 13:40
09/09/2008 19:50
10/09/2008 02:00
10/09/2008 08:10
10/09/2008 14:20
10/09/2008 20:30
11/09/2008 02:40
11/09/2008 08:50
11/09/2008 15:00
11/09/2008 21:10
12/09/2008 03:20
12/09/2008 09:30
12/09/2008 15:40
12/09/2008 21:50
13/09/2008 04:00
13/09/2008 10:10
13/09/2008 16:20
13/09/2008 22:30
14/09/2008 04:40
14/09/2008 10:50
14/09/2008 17:00
14/09/2008 23:10
15/09/2008 05:20
15/09/2008 11:30
15/09/2008 17:40
15/09/2008 23:50
16/09/2008 06:00
16/09/2008 12:10


Pile 2 (sleeved)
Gauges at Level 7
Micro-strain
400
350
300
250
200
150
100
50
0
Time
07/09/2008 00:00
07/09/2008 06:10
07/09/2008 12:20
07/09/2008 18:30
08/09/2008 00:40
08/09/2008 06:50
08/09/2008 13:00
08/09/2008 19:10
09/09/2008 01:20
09/09/2008 07:30
09/09/2008 13:40
09/09/2008 19:50
10/09/2008 02:00
10/09/2008 08:10
10/09/2008 14:20
10/09/2008 20:30
11/09/2008 02:40
11/09/2008 08:50
11/09/2008 15:00
11/09/2008 21:10
12/09/2008 03:20
12/09/2008 09:30
12/09/2008 15:40
12/09/2008 21:50
13/09/2008 04:00
13/09/2008 10:10
13/09/2008 16:20
13/09/2008 22:30
14/09/2008 04:40
14/09/2008 10:50
14/09/2008 17:00
14/09/2008 23:10
15/09/2008 05:20
15/09/2008 11:30
15/09/2008 17:40
15/09/2008 23:50
16/09/2008 06:00
16/09/2008 12:10
VWG37
VWG46
VWG55

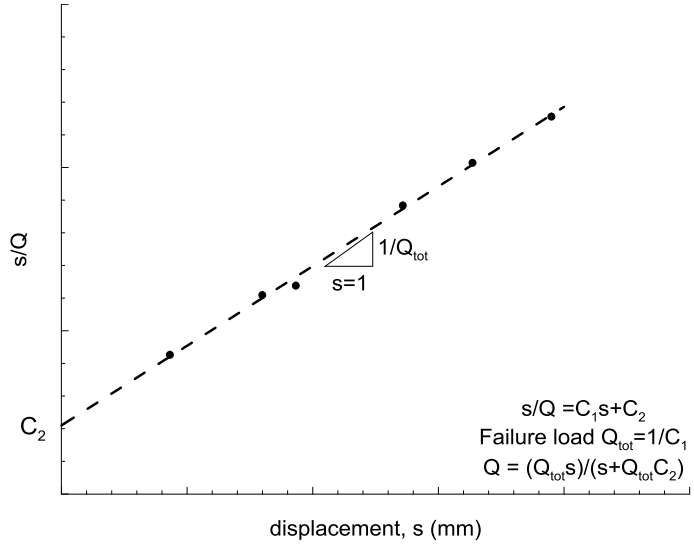

Pile 2 (sleeved)
Gauges at Level 8
Micro-strain
400
350
300
250
200
150
100
50
0
Time
07/09/2008 00:00
07/09/2008 06:10
07/09/2008 12:20
07/09/2008 18:30
08/09/2008 00:40
08/09/2008 06:50
08/09/2008 13:00
08/09/2008 19:10
09/09/2008 01:20
09/09/2008 07:30
09/09/2008 13:40
09/09/2008 19:50
10/09/2008 02:00
10/09/2008 08:10
10/09/2008 14:20
10/09/2008 20:30
11/09/2008 02:40
11/09/2008 08:50
11/09/2008 15:00
11/09/2008 21:10
12/09/2008 03:20
12/09/2008 09:30
12/09/2008 15:40
12/09/2008 21:50
13/09/2008 04:00
13/09/2008 10:10
13/09/2008 16:20
13/09/2008 22:30
14/09/2008 04:40
14/09/2008 10:50
14/09/2008 17:00
14/09/2008 23:10
15/09/2008 05:20
15/09/2008 11:30
15/09/2008 17:40
15/09/2008 23:50
16/09/2008 06:00
16/09/2008 12:10
VWG38
VWG47


Pile 2 (sleeved)
Gauges at Level 9
Micro-strain
400
350
300
250
200
150
100
50
0
VWG39
VWG48
VWG57
Time
07/09/2008 00:00
07/09/2008 06:10
07/09/2008 12:20
07/09/2008 18:30
08/09/2008 00:40
08/09/2008 06:50
08/09/2008 13:00
08/09/2008 19:10
09/09/2008 01:20
09/09/2008 07:30
09/09/2008 13:40
09/09/2008 19:50
10/09/2008 02:00
10/09/2008 08:10
10/09/2008 14:20
10/09/2008 20:30
11/09/2008 02:40
11/09/2008 08:50
11/09/2008 15:00
11/09/2008 21:10
12/09/2008 03:20
12/09/2008 09:30
12/09/2008 15:40
12/09/2008 21:50
13/09/2008 04:00
13/09/2008 10:10
13/09/2008 16:20
13/09/2008 22:30
14/09/2008 04:40
14/09/2008 10:50
14/09/2008 17:00
14/09/2008 23:10
15/09/2008 05:20
15/09/2008 11:30
15/09/2008 17:40
15/09/2008 23:50
16/09/2008 06:00
16/09/2008 12:10

APPENDIX A-2

Pile test extrapolation methods

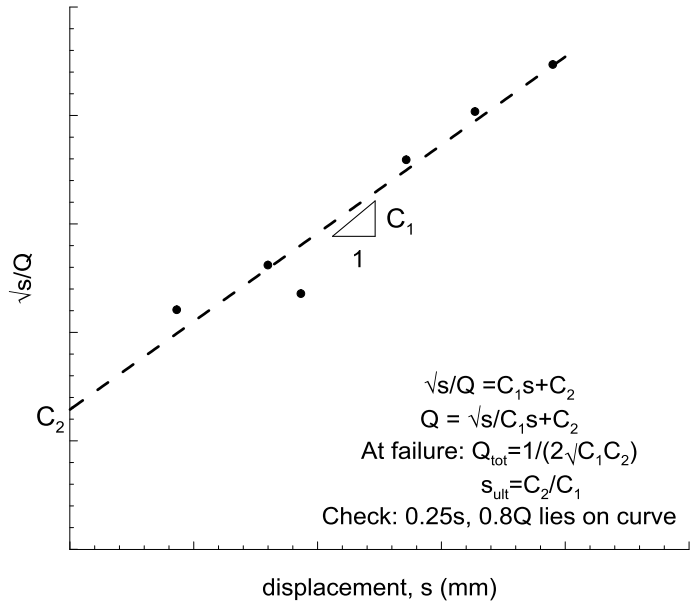
Graphical Procedure	Method



Chin (1971, 1970)

Assumes load displacement relationship is approximately hyperbolic. Plot s/Q versus s, where s is pile head displacement and Q is the corresponding load.

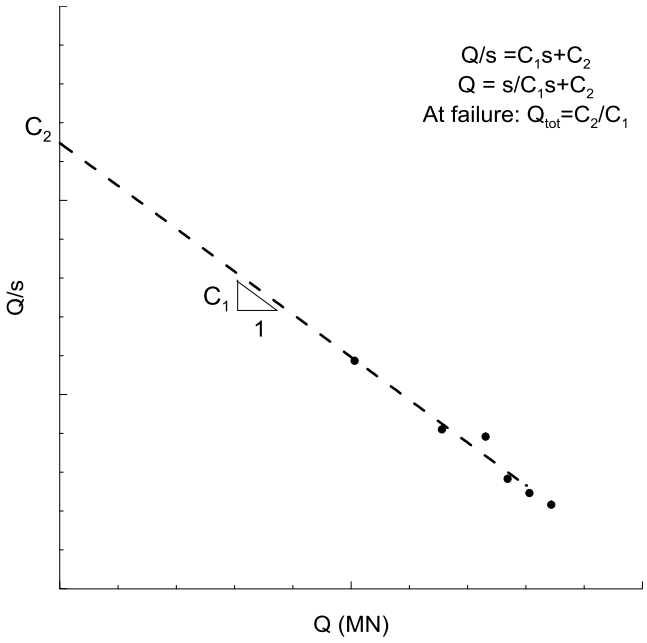
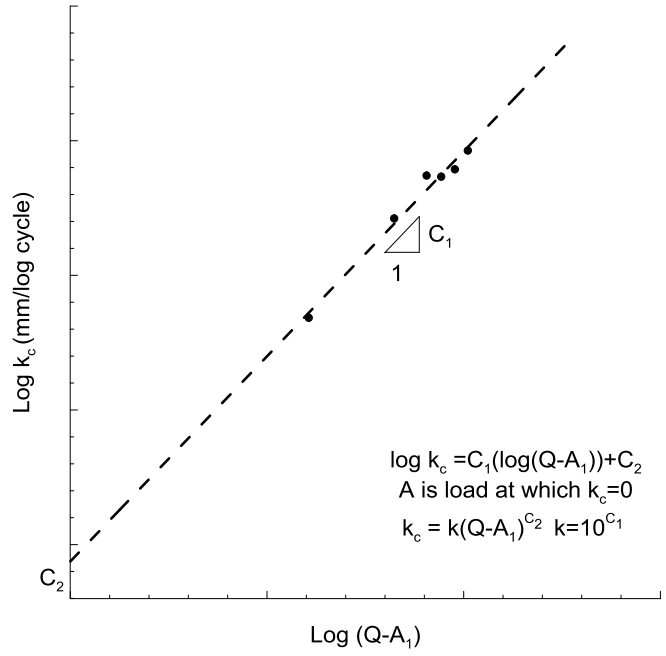
An ideal curve of load ver displacement is then determined us the slope and intercept of this line. T ultimate pile load, Q_{tot} and the ultim pile head displacement, s_{ult} can determined.



Brinch Hansen (1963)

Assumes load displacement relatio is approximately parabolic:

Plot √s/Q versus s and an ideal curve of load versus displacement is then determined using the slope and inverse of this line. The ultimate pile load, Q_{tot} and the ultimate pile head displacement, s_{ult} are a function of the slope and intercept of this line. The point (0.25s, 0.8Q) must lie on the obtained idealised curve.

Graphical Procedure	Method
	Decourt (1999) Assumes load displacement relationship is hyperbolic. Plot Q/s versus Q. An ideal curve of load versus displacement is then determined using the slope and inverse of this line. The ultimate pile load, Q_{tot} and the ultimate pile head displacement, s_{ult} are a function of the slope and intercept of this line.
	Extrapolation of creep rates Plot log k_c versus log Q-A_1, where k_c is the creep rate measured over the monitoring period and A_1 is the load at which k_c=0. A power law relationship for k_c as a function of Q-A_1 can then be plotted. Extrapolation of this curve to the creep rate criterion for failure gives the failure load.

APPENDIX A-3

Consultant's original pile design

A-3.1 Introduction

The consultant's original pile design (CIJV, 2014b) for the Wikinger OWF is reviewed here to provide background on the pile capacities which were expected during the pre-construction pile test campaign, described in Chapter 5.

A-3.2 Shaft resistance in glacial till

Shaft resistance in the glacial till, τ_f was derived using either (i) a total stress α approach or (i) a site specific effective stress β approach.

A-3.2.1 Total stress (α) approach

For the α-approach, τ_f is given as a function of s_u and an adhesion factor, α:

$$\tau_f = \alpha s_u \quad \text{A3-1}$$

The correlation, originally proposed by Randolph and Murphy (1985) between α and s_u incorporated into the American Petroleum Institute (API) guidelines (API, 2007) was adopted:

$$\alpha = \left(\frac{s_u}{\sigma'_{vo}}\right)^{0.5}_{NC}\left(\frac{s_u}{\sigma'_{vo}}\right)^{-0.5} \text{ for } \frac{s_u}{\sigma'_{vo}} < 1.0 \quad \text{A3-2}$$

$$\alpha = \left(\frac{s_u}{\sigma'_{vo}}\right)^{0.5}_{NC}\left(\frac{s_u}{\sigma'_{vo}}\right)^{-0.25} \text{ for } \frac{s_u}{\sigma'_{vo}} > 1.0 \quad \text{A3-3}$$

A-3.2.1 Effective stress (β) approach

An effective stress β approach was also suggested, with:

$$\tau_f = c' + K_0 \sigma'_{vo} \tan \delta_f \quad \text{A3-4}$$

K_0 was determined from the oedometer tests discussed in Section 5.5.5. The results of constant normal stiffness direct shear box (CNS-DS) tests on samples were used to determine c' (with a lower bound 15kPa adopted) and δ'_f (equal to 32°). The latter was determined by reducing the φ' value obtained from the soil-soil tests by an adhesion factor (0.7).

A-3.2 Shaft resistance in chalk

In the chalk, τ_f was derived using the results of CNS-DS soil-soil tests. The samples were remoulded to replicate the conditions next to the shaft and consolidated to an *in situ* horizontal stress calculated using an assumed K_0 value of 0.4. The obtained shear stress at failure was plotted against the σ'_{vo} to establish a trend with depth, which had a slope β:

$$\tau_f = \beta \sigma'_{vo} \leq 100\text{kPa} \quad \text{A3-5}$$

$$\beta = K_o \tan \delta_{ult} \quad \text{A3-6}$$

An adhesion factor was used to reduce the values obtained from the soil-soil CNS tests to account for soil-steel conditions in the real (soil-steel) case resulting in δ'_{ult} of 32°. Characteristic and lower bound shaft resistance were recommended for all chalk types as β = 0.21. Upper bound values of β were given for structureless (0.25), low density structured (0.29) and medium density structured chalk (0.33). The characteristic β=0.21 equates to a K_0=0.33, while the UB value for medium density structured gives K_0=0.53. An arbitrary limit of 100kPa was imposed on τ_f which limits the UB trend for structured chalk at σ'_{vo} values of between 300 and 345kPa and the characteristic trend at σ'_{vo} values greater than 475kPa.

A-3.2 Assessment of cyclic loading effects

Static and cyclic triaxial tests combined with CNL-DS and CNS-DS tests were used to assess susceptibility to cyclic loading. The results suggested that while the glacial till and the intact chalk show a low sensitivity of strength and stiffness to cycling, a significant impact of cyclic loading on strength due to contraction is apparent for the remoulded chalk (Augustesen

et al., 2015). A cyclic model was developed using load transfer curves (t-z), employing the RATZ computer program calibrated using the cyclic laboratory results, which gave a per cycle degradation of strength. The validity of this approach was tested by applying the model to the axial cyclic test results at Kent described in Chapter 2 (Dührkop *et al.*, 2015). A detailed analysis at each WTG was not carried out. The WTGs were divided into groups based on the length of penetration of the pile into chalk and a degradation profile was established for each group. The degradation in local peak shaft friction in the chalk varies from 25-40% for the various groups, while a constant degradation value of 15% was given for the till.

A-3.3 Estimated tensile failure loads for the pre-construction test piles

An estimate of the failure loads required to induce failure during the pre-construction tension pile test programme was made by CIJV (2014a). The characteristic tensile capacity, $R_{t,c}$ was calculated using the methods developed to estimate τ_f discussed in the previous two sections, with the following modifications:

- A factor of 0.8 was applied to account for loading in tension.
- Inner shaft resistance was taken as 70% of the outer τ_f;
- Cyclic degradation was taken as 15% in glacial till and 30% in chalk.

The characteristic axial load in tension, $R_{t,c}$ at the bottom of the grouted connection for the 2.67m diameter production piles was 5.015MN. The value of $R_{t,c}$ was reduced by 50% for the pre-construction test piles to 2.58MN. Upper bound tensile shaft capacity, $R_{t,ub}$ was calculated using a lower cone factor (N_{kt} = 10) in the glacial till, and an increase in the UB τ_f in chalk from 100 to 160kPa. In both materials, no cyclic degradation was accounted for, tension capacity was assumed equal to compression capacity, and the inner shaft resistance was assumed equal to the outer. The characteristic and UB resistances determined by the designer are summarised in Table A-3.1. The required pull-out load for the tension SLT was set at 15MN based on the highest UB estimate for shaft capacity, at the till dominated WK38.

Table A3-1: Predicted tensile loads for pre-construction SLT (CIJV, 2014a)

				Characteristic		Upper bound	
Pile	**Conditions**	**D (m)**	**L_p (m)**	**$R_{t,c}$ (MN)**	**τ_{avg} (kPa)**	**$R_{t,ub}$ (MN)**	**τ_{avg} (kPa)**
WK38-2	Glacial till dominated representative conditions	1.37	16.8	5.8	80	15.0	207
WK43-2	Chalk dominated most adverse conditions	1.37	30.7	4.9	37	12.2	92
WK70-2	Chalk dominated most adverse conditions	1.37	31.0	4.9	37	12.6	94

APPENDIX A-4

Shaft capacity predictions

A-4.1 Introduction

This Appendix outlines the shaft capacity calculations in the glacial till using the ICP-05 clay method (Jardine *et al.*, 2005a), the UWA-13 expressions suggested by Lehane *et al.* (2012b) and the API (2007). Section 3.3.2 provided an overview of current axial capacity design methods for displacement piles in clay, developed following reviews of predictions with the API method which showed significant biases and skews in predictions with respect to pile length (or L_p/D) and yield stress ratio (YSR) or apparent OCR; e.g. Chow (1997), Jardine *et al.* (2005a). As discussed in Chapter 3, Lehane *et al.* (2017), as part of a JIP, assessed the performance of the ICP-05 clay method using a newly assembled database of pile tests. The latter method did not appear to perform as well, overall, as previously reported. It was recognised that this was related, at least partly, to the very small number of sites for which the necessary site investigation information existed and the exclusion of all of the ICP tests because of their small diameter and jacked installations. Several other critical cases were also excluded, while retaining in the greatly reduced database of a large proportion of tests from low OCR silty clay sites, including Lierstranda in Norway, where very low axial capacities had been measured showing remarkably low net cone resistance values. Potential problems had been raised by Chow (1997) and Jardine *et al.* (2005a) with several of the tests. Ridgway and Jardine (2007)set out how such sites such as Lierstranda might be recognised and recommended that the ICP should not be applied in such conditions.

A-4.2 Shaft capacity predictions in glacial till

Lehane *et al.* (2017) report that a CPT based method, suggested by Lehane *et al.* (2012b) following a similar database study and termed "UWA-13", provided generally good

predictions for shaft resistance in the larger database of tests for which reliable CPT data existed. The method relates shaft resistance to net cone resistance, q_t in the clay retaining the ICP-05 h/R* term (Eq. 3-15) and reducing the lower limit on h/R* to 1. Two expressions were proposed, with and without inclusion of the pile shaft clay interface friction angle and effective overburden pressure (shown previously as Eq. 3-19 and 3-20).

The performance of the ICP-05 clay method in predicting shaft capacity for the clay glacial tills at Wikinger is assessed further along with the UWA-13 method and the API method using the results of the static test conducted at the glacial till dominated site. This test, conducted 108 days after driving, showed a net tensile failure load of 8.8MN. The dynamic restrike test conducted at the same time on an adjacent pile showed a shaft capacity in close correspondence (11% higher see Section 5.9.5) with the static tension test to failure. The signal matching showed that 69% of the capacity is attributable to the glacial till, indicating that 6.07MN was mobilised in the glacial till during the static test. In order to predict this capacity, five different methods were considered:

1. The ICP-05 clay methodology (Jardine *et al.*, 2005a) described in Section 3.3.2 with parameters (YSR, S_t and δ') as set out in Section 5.2 applied to the full glacial till thickness;
2. As above but with the ICP-05 sand methodology (Section 3.3.4) applied in the dense sand layers that comprised approximately 20% of the section and were indicated by high cone resistance. The adopted cone resistance profile is shown in Figure A4-1, and the parameters set out in Section 5.2;
3. The UWA-13 expression suggested by Lehane *et al.* (2012b) which includes the interface friction angle and overburden pressure in the formulation (i.e. Eq. 3-19) applied to the full glacial till thickness;
4. As above but with the UWA-13 expression which does not include the interface friction angle or the overburden pressure (i.e. Eq. 3-20);
5. The API alpha approach, described in Section 3.3.2 using a site specific N_{kt} factor of 22.5 (Figure A4-2), the undrained strength profile shown in Figure A4-3,, and assuming only external shaft resistance during a static tension test.

Table A4-1 summarises the ratios of calculated to measured shaft capacity (Q_c/Q_m) where Q_m is that measured during the static test. Overall, both the API method and the UWA-13 method (both formulations) tended to over-predict the capacity, assessed 108 days after

driving, showing Q_c/Q_m ratios of 1.55 and approximately 3.2, respectively. The use of the ICP-05 clay method plus the ICP_05 in the assessed sand layers under-predicted the capacity by approximately 12%. The ICP-05 clay method, applied to the glacial till layer, provided the closest match to the capacity measured 108 days after driving, under predicting the result by just 4% in this case.

However the set-up trend in the glacial till, shown on Figure 5-50, suggests that the increases in capacity with time had not stabilised fully when the testing was carried out. Noting that the methods are intended to predict capacity after full equalisation has occurred, the Q_c/Q_m ratios calculated using all five methods should further reduce over time. This may lead to an improvement in the UWA-13 prediction with time and to the ICP-05 methods becoming more conservative. However, it seems inadvisable to adopt the UWA-13 method for high YSR insensitive glacial tills such as those encountered at Wikinger.

Table A4-1: Summary of pile capacity predictions in glacial till for the static test at WK38-2 conducted 108 days after driving

Test code	**Q_c (MN)**	**Q_m (MN)**	**Q_c/Q_m (MN)**
ICP-05 clay	5.85	6.07	0.96
ICP-05 clay + ICP-05 sand	5.37	6.07	0.88
UWA-13 (Eq. A6-1)	20.02	6.07	3.30
UWA-13 (Eq. A6-2)	19.51	6.07	3.21
API alpha method	9.43	6.07	1.55

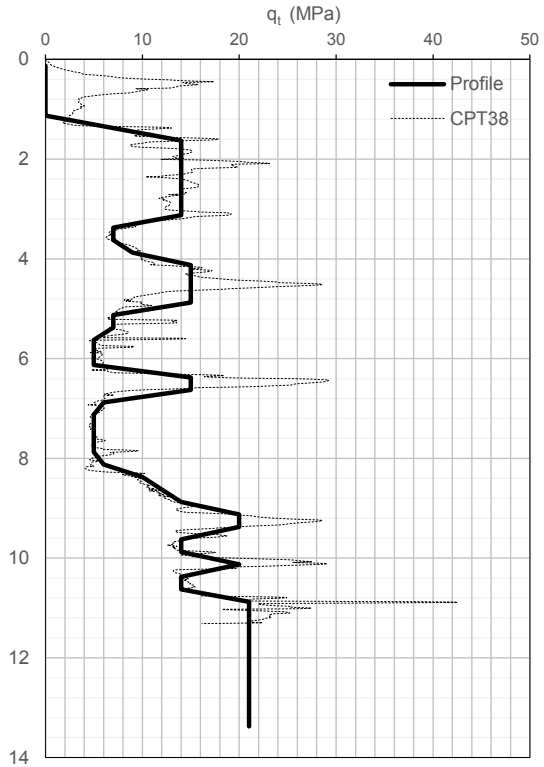


Figure A4-1: Cone resistance and adopted profile at glacial till dominated test site (WK38-1)

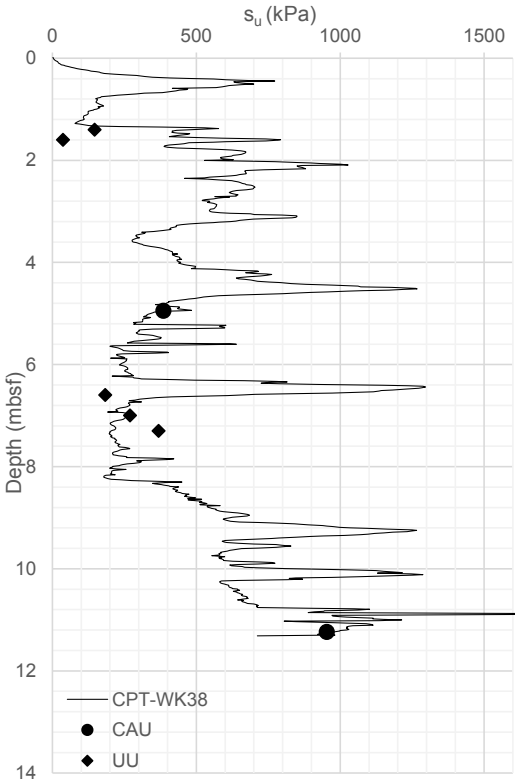


Figure A4-2: Cone resistance converted to undrained shear strength using N_{kt} = 22.5

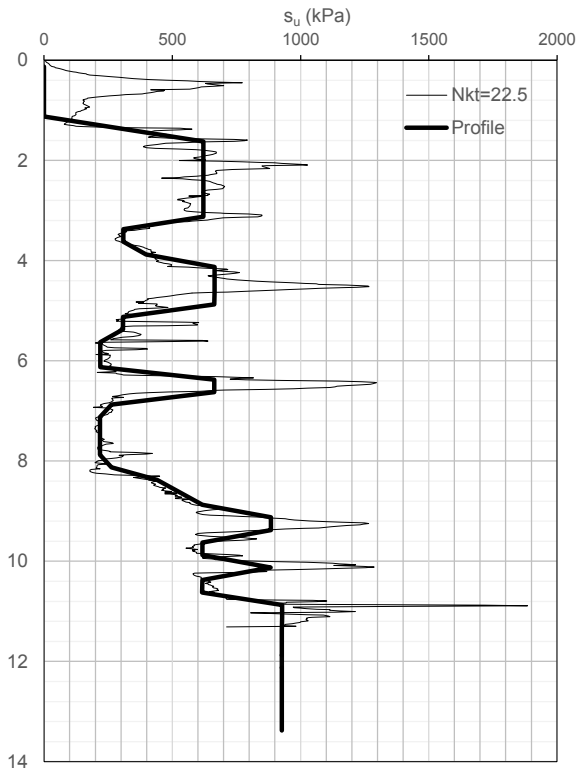


Figure A4-3: Adopted undrained shear strength profile from CPT WK-38 using N_{kt} = 22.5

Pile	WK38
Blow	BoR

ICP-05 CLAY

t (m)	40
t (mm)	0.04
R (m)	0.6858
R* (m)	0.231
Pile tip depth (m)	16.8
Embedment length (m)	16.8
A_{base} (m^2)	1.48
A_{steel} (m^2)	0.17

Holocene	Dry density	20.11	kN/m^3
	Bouy. density	10.31	kN/m^3
	Soil type	Glacial Till	
Glacial till	Dry density	21.41	kN/m^3
	Bouy. density	11.61	kN/m^3

								Sand inputs			Clay Inputs					Sand Calculation					Clay calculation				
Layer no.	**Top of layer (m)**	**Bottom of layer (m)**	**dz (m)**	**Unit weight kN/m^3**	**σ'_v (kPa)**	**h/R***	**δ (°)**	**η**	**G (Mpa)**	**σ'_{rd} (kPa)**	**YSR**	**ΔI_{vy}**	**Kc (ΔIvy)**	**ΔI_{v0}**	**K_c (ΔI_{v0})**	**σ'_{rc} (kPa)**	**σ'_{rf} (kPa)**	**T_f (kPa)**	**T_f x dz (kN/m)**	**σ'_{rc} (kPa)**	**σ'_{rf} (kPa)**	**T_f (kPa)**	**T_f x dz (kN/m)**	**T_f (kPa)**	**Q_s kN**
1	0	0.25	0.25	10.31	1.3	72.3	28	0	0	0	60	0	7.5			0	0	0.0	0.00	10	8	4.11	1.0	4	4
2	0.25	0.5	0.25	10.31	3.9	71.2	28	0	0	0	60	0	7.5			0	0	0.0	0.00	29	23	12.36	3.1	12	13
3	0.5	0.75	0.25	10.31	6.4	70.1	28	0	0	0	45	0	6.2			0	0	0.0	0.00	40	32	17.02	4.3	17	18
4	0.75	1	0.25	10.31	9.0	69.0	28	0	0	0	37	0	5.4			0	0	0.0	0.00	49	39	20.87	5.2	21	22
5	1	1.25	0.25	10.31	11.6	67.9	28	0	0	0	32	0	5.0			0	0	0.0	0.00	57	46	24.44	6.1	24	26
6	1.25	1.5	0.25	10.31	14.2	66.8	28	0	0	0	28	0	4.6			0	0	0.0	0.00	65	52	27.83	7.0	28	30
7	1.5	1.75	0.25	10.31	16.8	65.8	28	0	0	0	25	0	4.4			0	0	0.0	0.00	73	58	31.07	7.8	31	33
8	1.75	2	0.25	10.31	19.3	64.7	28	0	0	0	23	0	4.2			0	0	0.0	0.00	80	64	34.19	8.5	34	37
9	2	2.25	0.25	11.61	24.7	63.6	28	0	0	0	21	0	4.0			0	0	0.0	0.00	99	79	41.93	10.5	42	45
10	2.25	2.5	0.25	11.61	27.6	62.5	28	0	0	0	20	0	3.9			0	0	0.0	0.00	106	85	45.28	11.3	45	49
11	2.5	2.75	0.25	11.61	30.5	61.4	28	0	0	0	19	0	3.7			0	0	0.0	0.00	114	91	48.55	12.1	49	52
12	2.75	3	0.25	11.61	33.4	60.3	28	0	0	0	18	0	3.6			0	0	0.0	0.00	122	97	51.78	12.9	52	56
13	3	3.25	0.25	11.61	36.3	59.3	28	0	0	0	17	0	3.6			0	0	0.0	0.00	129	103	54.95	13.7	55	59
14	3.25	3.5	0.25	11.61	39.2	58.2	28	0	0	0	16	0	3.5			0	0	0.0	0.00	137	109	58.09	14.5	58	63
15	3.5	3.75	0.25	11.61	42.1	57.1	29	0	0	0	15	0	3.4			0	0	0.0	0.00	144	115	63.80	16.0	64	69
16	3.75	4	0.25	11.61	45.0	56.0	28	0	0	0	15	0	3.4			0	0	0.0	0.00	151	121	64.28	16.1	64	69
17	4	4.25	0.25	11.61	47.9	54.9	28	0	0	0	14	0	3.3			0	0	0.0	0.00	158	127	67.34	16.8	67	73
18	4.25	4.5	0.25	11.61	50.8	53.8	28	0	0	0	14	0	3.3			0	0	0.0	0.00	165	132	70.38	17.6	70	76
19	4.5	4.75	0.25	11.61	53.7	52.8	28	0	0	0	13	0	3.2			0	0	0.0	0.00	173	138	73.41	18.4	73	79
20	4.75	5	0.25	11.61	56.6	51.7	28	0	0	0	13	0	3.2			0	0	0.0	0.00	180	144	76.43	19.1	76	82
21	5	5.25	0.25	11.61	59.5	50.6	28	0	0	0	12	0	3.1			0	0	0.0	0.00	187	149	79.44	19.9	79	86
22	5.25	5.5	0.25	11.61	62.4	49.5	28	0	0	0	12	0	3.1			0	0	0.0	0.00	194	155	82.44	20.6	82	89
23	5.5	5.75	0.25	11.61	65.3	48.4	28	0	0	0	12	0	3.1			0	0	0.0	0.00	201	161	85.45	21.4	85	92
24	5.75	6	0.25	11.61	68.2	47.3	28	0	0	0	11	0	3.0			0	0	0.0	0.00	208	166	88.46	22.1	88	95
25	6	6.25	0.25	11.61	71.1	46.3	28	0	0	0	11	0	3.0			0	0	0.0	0.00	215	172	91.47	22.9	91	99
26	6.25	6.5	0.25	11.61	74.0	45.2	28	0	0	0	11	0	3.0			0	0	0.0	0.00	222	178	94.50	23.6	94	102
27	6.5	6.75	0.25	11.61	76.9	44.1	28	0	0	0	10	0	3.0			0	0	0.0	0.00	229	183	97.53	24.4	98	105
28	6.75	7	0.25	11.61	79.8	43.0	28	0	0	0	10	0	3.0			0	0	0.0	0.00	236	189	100.58	25.1	101	108
29	7	7.25	0.25	11.61	82.7	41.9	28	0	0	0	10	0	2.9			0	0	0.0	0.00	244	195	103.64	25.9	104	112
30	7.25	7.5	0.25	11.61	85.6	40.8	28	0	0	0	10	0	2.9			0	0	0.0	0.00	251	201	106.72	26.7	107	115
31	7.5	7.75	0.25	11.61	88.5	39.8	28	0	0	0	10	0	2.9			0	0	0.0	0.00	258	207	109.83	27.5	110	118
32	7.75	8	0.25	11.61	91.4	38.7	28	0	0	0	9	0	2.9			0	0	0.0	0.00	266	212	112.95	28.2	113	122
33	8	8.25	0.25	11.61	94.3	37.6	28	0	0	0	9	0	2.9			0	0	0.0	0.00	273	218	116.11	29.0	116	125
34	8.25	8.5	0.25	11.61	97.2	36.5	28	0	0	0	9	0	2.9			0	0	0.0	0.00	280	224	119.30	29.8	119	129
35	8.5	8.75	0.25	11.61	100.1	35.4	28	0	0	0	9	0	2.9			0	0	0.0	0.00	288	230	122.52	30.6	123	132
36	8.75	9	0.25	11.61	103.0	34.3	28	0	0	0	9	0	2.9			0	0	0.0	0.00	296	237	125.78	31.4	126	136
37	9	9.25	0.25	11.61	105.9	33.3	28	0	0	0	9	0	2.9			0	0	0.0	0.00	303	243	129.09	32.3	129	139
38	9.25	9.5	0.25	11.61	108.8	32.2	28	0	0	0	8	0	2.9			0	0	0.0	0.00	311	249	132.44	33.1	132	143
39	9.5	9.75	0.25	11.61	111.7	31.1	28	0	0	0	8	0	2.9			0	0	0.0	0.00	319	255	135.84	34.0	136	146
40	9.75	10	0.25	11.61	114.6	30.0	28	0	0	0	8	0	2.9			0	0	0.0	0.00	327	262	139.30	34.8	139	150
41	10	10.25	0.25	11.61	117.6	28.9	28	0	0	0	8	0	2.9			0	0	0.0	0.00	336	269	142.83	35.7	143	154
42	10.25	10.5	0.25	11.61	120.5	27.8	28	0	0	0	8	0	2.9			0	0	0.0	0.00	344	275	146.42	36.6	146	158
43	10.5	10.75	0.25	11.61	123.4	26.8	28	0	0	0	8	0	2.9			0	0	0.0	0.00	353	282	150.09	37.5	150	162
44	10.75	11	0.25	11.61	126.3	25.7	28	0	0	0	8	0	2.9			0	0	0.0	0.00	362	289	153.84	38.5	154	166
45	11	11.25	0.25	11.61	129.2	24.6	28	0	0	0	8	0	2.9			0	0	0.0	0.00	371	297	157.69	39.4	158	170
46	11.25	11.5	0.25	11.61	132.1	23.5	28	0	0	0	8	0	2.9			0	0	0.0	0.00	380	304	161.64	40.4	162	174
47	11.5	11.75	0.25	11.61	135.0	22.4	28	0	0	0	7	0	2.9			0	0	0.0	0.00	390	312	165.70	41.4	166	178
48	11.75	12	0.25	11.61	137.9	21.3	28	0	0	0	7	0	2.9			0	0	0.0	0.00	399	320	169.89	42.5	170	183
49	12	12.25	0.25	11.61	140.8	20.3	28	0	0	0	7	0	2.9			0	0	0.0	0.00	410	328	174.22	43.6	174	188
50	12.25	12.5	0.25	11.61	143.7	19.2	28	0	0	0	7	0	2.9			0	0	0.0	0.00	420	336	178.71	44.7	179	193
51	12.5	12.75	0.25	11.61	146.6	18.1	28	0	0	0	7	0	2.9			0	0	0.0	0.00	431	345	183.39	45.8	183	198
52	12.75	13	0.25	11.61	149.5	17.0	28	0	0	0	7	0	3.0			0	0	0.0	0.00	443	354	188.27	47.1	188	203
53	13	13.25	0.25	11.61	152.4	15.9	28	0	0	0	7	0	3.0			0	0	0.0	0.00	455	364	193.38	48.3	193	208
54	13.25	13.5	0.25	11.61	155.3	14.8	28	0	0	0	7	0	3.0			0	0	0.0	0.00	467	374	198.77	49.7	199	214
																							Q_s(MN)		5.85
																							Q_c/Q_m		0.96

Pile	WK38
Blow	BoR

ICP-05 CLAY + SAND

t (m)	40
t (mm)	0.04
R (m)	0.6858
R* (m)	0.231
Pile tip depth (m)	16.8
Embedment length (m)	16.8
A_{base} (m^2)	1.48
A_{steel} (m^2)	0.17

Holocene	Dry density		20.11	kN/m³
	Bouy. density		10.31	kN/m³
	Soil type		Glacial Till	
Glacial till	Dry density		21.41	kN/m³
	Bouy. density		11.61	kN/m³
	Soil type		Chalk	
	Dry density		19.1	kN/m³
	Bouy. density		9.3	kN/m³

									Sand inputs			Clay Inputs				Sand Calculation					Clay calculation				
Layer no.	Top of layer (m)	Bottom of layer (m)	dz (m)	Unit weight kN/m³	σ'_v (kPa)	q_c (Mpa)	h/R*	δ (°)	η	G (Mpa)	σ'_{rd} (kPa)	YSR	ΔI_{vy}	Kc (ΔIvy)	ΔI_{v0}	K_c (ΔI_{v0})	σ'_{rc} (kPa)	σ'_{rf} (kPa)	T_f (kPa)	T_f x dz (kN/m)	σ'_{rc} (kPa)	σ'_{rf} (kPa)	T_f (kPa)	T_f x dz (kN/m)	T_f (kPa)	Q_s kN
1	0	0.25	0.25	10.31	1.3	0	72.3	28	0	0.0	0.0		0.00	0.0			0.0	0	0.0	0.00	0	0	0.00	0.0	0	0
2	0.25	0.5	0.25	10.31	3.9	0	71.2	28	0	0.0	0.0		0.00	0.0			0.0	0	0.0	0.00	0	0	0.00	0.0	0	0
3	0.5	0.75	0.25	10.31	6.4	0	70.1	28	0	0.0	0.0		0.00	0.0			0.0	0	0.0	0.00	0	0	0.00	0.0	0	0
4	0.75	1	0.25	10.31	9.0	0	69.0	28	0	0.0	0.0		0.00	0.0			0.0	0	0.0	0.00	0	0	0.00	0.0	0	0
5	1	1.25	0.25	10.31	11.6	0	67.9	28	0	0.0	0.0		0.00	0.0			0.0	0	0.0	0.00	0	0	0.00	0.0	0	0
6	1.25	1.5	0.25	10.31	14.2	7	66.8	28	186	33.2	1.9		0.00	0.0			31.9	34	18.0	4.50	0	0	0.00	0.0	18	19
7	1.5	1.75	0.25	10.31	16.8	14	65.8	28	342	45.8	2.7		0.00	0.0			65.6	68	36.3	9.07	0	0	0.00	0.0	36	39
8	1.75	2	0.25	10.31	19.3	14	64.7	28	318	47.5	2.8		0.00	0.0			67.2	70	37.2	9.31	0	0	0.00	0.0	37	40
9	2	2.25	0.25	11.61	24.7		63.6	28	0	0.0	0.0	21	0.00	4.0			0	0	0.0	0.00	99	79	41.93	10.5	42	45
10	2.25	2.5	0.25	11.61	27.6		62.5	28	0	0.0	0.0	20	0.00	3.9			0	0	0.0	0.00	106	85	45.28	11.3	45	49
11	2.5	2.75	0.25	11.61	30.5		61.4	28	0	0.0	0.0	19	0.00	3.7			0	0	0.0	0.00	114	91	48.55	12.1	49	52
12	2.75	3	0.25	11.61	33.4		60.3	28	0	0.0	0.0	18	0.00	3.6			0	0	0.0	0.00	122	97	51.78	12.9	52	56
13	3	3.25	0.25	11.61	36.3		59.3	28	0	0.0	0.0	17	0.00	3.6			0	0	0.0	0.00	129	103	54.95	13.7	55	59
14	3.25	3.5	0.25	11.61	39.2		58.2	28	0	0.0	0.0	16	0.00	3.5			0	0	0.0	0.00	137	109	58.09	14.5	58	63
15	3.5	3.75	0.25	11.61	42.1		57.1	29	0	0.0	0.0	15	0.00	3.4			0	0	0.0	0.00	144	115	63.80	16.0	64	69
16	3.75	4	0.25	11.61	45.0	9	56.0	28	134	54.2	3.2		0.00	0.0			51	54	28.8	7.19	0	0	0.00	0.0	29	31
17	4	4.25	0.25	11.61	47.9	15	54.9	28	217	64.1	3.7		0.00	0.0			86	90	47.9	11.96	0	0	0.00	0.0	48	52
18	4.25	4.5	0.25	11.61	50.8	15	53.8	28	210	65.4	3.8		0.00	0.0			88	91	48.6	12.15	0	0	0.00	0.0	49	52
19	4.5	4.75	0.25	11.61	53.7	15	52.8	28	205	66.6	3.9		0.00	0.0			89	93	49.3	12.33	0	0	0.00	0.0	49	53
20	4.75	5	0.25	11.61	56.6	15	51.7	28	199	67.8	4.0		0.00	0.0			90	94	50.1	12.52	0	0	0.00	0.0	50	54
21	5	5.25	0.25	11.61	59.5		50.6	28	0	0.0	0.0	12	0.00	3.1			0	0	0.0	0.00	187	149	79.44	19.9	79	86
22	5.25	5.5	0.25	11.61	62.4		49.5	28	0	0.0	0.0	12	0.00	3.1			0	0	0.0	0.00	194	155	82.44	20.6	82	89
23	5.5	5.75	0.25	11.61	65.3		48.4	28	0	0.0	0.0	12	0.00	3.1			0	0	0.0	0.00	201	161	85.45	21.4	85	92
24	5.75	6	0.25	11.61	68.2		47.3	28	0	0.0	0.0	11	0.00	3.0			0	0	0.0	0.00	208	166	88.46	22.1	88	95
25	6	6.25	0.25	11.61	71.1	5	46.3	28	59	55.5	3.2		0.00	0.0			32	36	18.9	4.73	0	0	0.00	0.0	19	20
26	6.25	6.5	0.25	11.61	74.0	15	45.2	28	174	74.5	4.3		0.00	0.0			98	103	54.6	13.65	0	0	0.00	0.0	55	59
27	6.5	6.75	0.25	11.61	76.9	15	44.1	28	171	75.6	4.4		0.00	0.0			100	104	55.4	13.84	0	0	0.00	0.0	55	60
28	6.75	7	0.25	11.61	79.8	6	43.0	28	67	60.8	3.5		0.00	0.0			40	44	23.4	5.85	0	0	0.00	0.0	23	25
29	7	7.25	0.25	11.61	82.7		41.9	28	0	0.0	0.0	10	0.00	2.9			0	0	0.0	0.00	244	195	103.64	25.9	104	112
30	7.25	7.5	0.25	11.61	85.6		40.8	28	0	0.0	0.0	10	0.00	2.9			0	0	0.0	0.00	251	201	106.72	26.7	107	115
31	7.5	7.75	0.25	11.61	88.5		39.8	28	0	0.0	0.0	10	0.00	2.9			0	0	0.0	0.00	258	207	109.83	27.5	110	118
32	7.75	8	0.25	11.61	91.4		38.7	28	0	0.0	0.0	9	0.00	2.9			0	0	0.0	0.00	266	212	112.95	28.2	113	122
33	8	8.25	0.25	11.61	94.3		37.6	28	0	0.0	0.0	9	0.00	2.9			0	0	0.0	0.00	273	218	116.11	29.0	116	125
34	8.25	8.5	0.25	11.61	97.2		36.5	28	0	0.0	0.0	9	0.00	2.9			0	0	0.0	0.00	280	224	119.30	29.8	119	129
35	8.5	8.75	0.25	11.61	100.1		35.4	28	0	0.0	0.0	9	0.00	2.9			0	0	0.0	0.00	288	230	122.52	30.6	123	132
36	8.75	9	0.25	11.61	103.0		34.3	28	0	0.0	0.0	9	0.00	2.9			0	0	0.0	0.00	296	237	125.78	31.4	126	136
37	9	9.25	0.25	11.61	105.9		33.3	28	0	0.0	0.0	9	0.00	2.9			0	0	0.0	0.00	303	243	129.09	32.3	129	139
38	9.25	9.5	0.25	11.61	108.8		32.2	28	0	0.0	0.0	8	0.00	2.9			0	0	0.0	0.00	311	249	132.44	33.1	132	143
39	9.5	9.75	0.25	11.61	111.7		31.1	28	0	0.0	0.0	8	0.00	2.9			0	0	0.0	0.00	319	255	135.84	34.0	136	146
40	9.75	10	0.25	11.61	114.6		30.0	28	0	0.0	0.0	8	0.00	2.9			0	0	0.0	0.00	327	262	139.30	34.8	139	150
41	10	10.25	0.25	11.61	117.6		28.9	28	0	0.0	0.0	8	0.00	2.9			0	0	0.0	0.00	336	269	142.83	35.7	143	154
42	10.25	10.5	0.25	11.61	120.5		27.8	28	0	0.0	0.0	8	0.00	2.9			0	0	0.0	0.00	344	275	146.42	36.6	146	158
43	10.5	10.75	0.25	11.61	123.4		26.8	28	0	0.0	0.0	8	0.00	2.9			0	0	0.0	0.00	353	282	150.09	37.5	150	162
44	10.75	11	0.25	11.61	126.3		25.7	28	0	0.0	0.0	8	0.00	2.9			0	0	0.0	0.00	362	289	153.84	38.5	154	166
45	11	11.25	0.25	11.61	129.2		24.6	28	0	0.0	0.0	8	0.00	2.9			0	0	0.0	0.00	371	297	157.69	39.4	158	170
46	11.25	11.5	0.25	11.61	132.1		23.5	28	0	0.0	0.0	8	0.00	2.9			0	0	0.0	0.00	380	304	161.64	40.4	162	174
47	11.5	11.75	0.25	11.61	135.0		22.4	28	0	0.0	0.0	7	0.00	2.9			0	0	0.0	0.00	390	312	165.70	41.4	166	178
48	11.75	12	0.25	11.61	137.9		21.3	28	0	0.0	0.0	7	0.00	2.9			0	0	0.0	0.00	399	320	169.89	42.5	170	183
49	12	12.25	0.25	11.61	140.8		20.3	28	0	0.0	0.0	7	0.00	2.9			0	0	0.0	0.00	410	328	174.22	43.6	174	188
50	12.25	12.5	0.25	11.61	143.7		19.2	28	0	0.0	0.0	7	0.00	2.9			0	0	0.0	0.00	420	336	178.71	44.7	179	193
51	12.5	12.75	0.25	11.61	146.6		18.1	28	0	0.0	0.0	7	0.00	2.9			0	0	0.0	0.00	431	345	183.39	45.8	183	198
52	12.75	13	0.25	11.61	149.5		17.0	28	0	0.0	0.0	7	0.00	3.0			0	0	0.0	0.00	443	354	188.27	47.1	188	203
53	13	13.25	0.25	11.61	152.4		15.9	28	0	0.0	0.0	7	0.00	3.0			0	0	0.0	0.00	455	364	193.38	48.3	193	208
54	13.25	13.5	0.25	11.61	155.3		14.8	28	0	0.0	0.0	7	0.00	3.0			0	0	0.0	0.00	467	374	198.77	49.7	199	214
																								Q_s(MN)		5.37
																								Q_c/Q_m		0.88

Pile	WK38
Blow	BoR

UWA-13

t (m)	40
t (mm)	0.04
R (m)	0.6858
R* (m)	0.231
Pile tip depth (m)	16.8
Embedment length (m)	16.8
A_{base} (m^2)	1.48
A_{steel} (m^2)	0.17

Holocene	Dry density		20.11	kN/m^3
	Bouy. density		10.31	kN/m^3
	Soil type		Glacial Till	
Glacial till	Dry density		21.41	kN/m^3
	Bouy. density		11.61	kN/m^3

Layer no.	Top of layer (m)	Bottom of layer (m)	dz (m)	Unit weight kN/m^3	σ'_v (kPa)	qt (Mpa)	h/R*	δ (°)
1	0	0.25	0.25	10.31	1.3	0	72.3	28
2	0.25	0.5	0.25	10.31	3.9	0	71.2	28
3	0.5	0.75	0.25	10.31	6.4	0	70.1	28
4	0.75	1	0.25	10.31	9.0	0	69.0	28
5	1	1.25	0.25	10.31	11.6	0	67.9	28
6	1.25	1.5	0.25	10.31	14.2	7	66.8	28
7	1.5	1.75	0.25	10.31	16.8	14	65.8	28
8	1.75	2	0.25	10.31	19.3	14	64.7	28
9	2	2.25	0.25	11.61	24.7	14	63.6	28
10	2.25	2.5	0.25	11.61	27.6	14	62.5	28
11	2.5	2.75	0.25	11.61	30.5	14	61.4	28
12	2.75	3	0.25	11.61	33.4	14	60.3	28
13	3	3.25	0.25	11.61	36.3	14	59.3	28
14	3.25	3.5	0.25	11.61	39.2	7	58.2	28
15	3.5	3.75	0.25	11.61	42.1	7	57.1	29
16	3.75	4	0.25	11.61	45.0	9	56.0	28
17	4	4.25	0.25	11.61	47.9	15	54.9	28
18	4.25	4.5	0.25	11.61	50.8	15	53.8	28
19	4.5	4.75	0.25	11.61	53.7	15	52.8	28
20	4.75	5	0.25	11.61	56.6	15	51.7	28
21	5	5.25	0.25	11.61	59.5	7	50.6	28
22	5.25	5.5	0.25	11.61	62.4	7	49.5	28
23	5.5	5.75	0.25	11.61	65.3	5	48.4	28
24	5.75	6	0.25	11.61	68.2	5	47.3	28
25	6	6.25	0.25	11.61	71.1	5	46.3	28
26	6.25	6.5	0.25	11.61	74.0	15	45.2	28
27	6.5	6.75	0.25	11.61	76.9	15	44.1	28
28	6.75	7	0.25	11.61	79.8	6	43.0	28
29	7	7.25	0.25	11.61	82.7	5	41.9	28
30	7.25	7.5	0.25	11.61	85.6	5	40.8	28
31	7.5	7.75	0.25	11.61	88.5	5	39.8	28
32	7.75	8	0.25	11.61	91.4	5	38.7	28
33	8	8.25	0.25	11.61	94.3	6	37.6	28
34	8.25	8.5	0.25	11.61	97.2	10	36.5	28
35	8.5	8.75	0.25	11.61	100.1	12	35.4	28
36	8.75	9	0.25	11.61	103.0	14	34.3	28
37	9	9.25	0.25	11.61	105.9	20	33.3	28
38	9.25	9.5	0.25	11.61	108.8	20	32.2	28
39	9.5	9.75	0.25	11.61	111.7	14	31.1	28
40	9.75	10	0.25	11.61	114.6	14	30.0	28
41	10	10.25	0.25	11.61	117.6	20	28.9	28
42	10.25	10.5	0.25	11.61	120.5	14	27.8	28
43	10.5	10.75	0.25	11.61	123.4	14	26.8	28
44	10.75	11	0.25	11.61	126.3	21	25.7	28
45	11	11.25	0.25	11.61	129.2	21	24.6	28
46	11.25	11.5	0.25	11.61	132.1	21	23.5	28
47	11.5	11.75	0.25	11.61	135.0	21	22.4	28
48	11.75	12	0.25	11.61	137.9	21	21.3	28
49	12	12.25	0.25	11.61	140.8	21	20.3	28
50	12.25	12.5	0.25	11.61	143.7	21	19.2	28
51	12.5	12.75	0.25	11.61	146.6	21	18.1	28
52	12.75	13	0.25	11.61	149.5	21	17.0	28
53	13	13.25	0.25	11.61	152.4	21	15.9	28
54	13.25	13.5	0.25	11.61	155.3	21	14.8	28

	UWA-13	UWA-13	UWA-13	UWA-13
	Eq. 3-21	Eq. 3-22	Eq. 3-21	Eq. 3-22
qt (Mpa)	T_f (kPa)	T_f (kPa)	Qs (kN)	Qs (kN)
0	0	0	0	0
0	0	0	0	0
0	0	0	0	0
0	0	0	0	0
0	0	0	0	0
7	146	166	157	179
14	270	333	291	359
14	277	334	298	360
14	288	336	311	362
14	294	337	317	363
14	300	338	323	364
14	305	339	328	365
14	310	340	334	367
7	174	171	188	184
7	185	171	199	185
9	222	221	239	238
15	348	370	375	399
15	352	372	379	400
15	357	373	384	402
15	361	375	389	404
7	191	176	206	189
7	193	176	208	190
5	147	127	158	136
5	148	127	160	137
5	150	128	162	138
15	386	385	416	415
15	390	387	420	417
6	181	156	195	168
5	157	130	169	140
5	158	131	170	141
5	160	132	172	142
5	162	132	174	143
6	191	160	205	172
10	297	268	320	289
12	351	323	378	348
14	404	380	435	409
20	553	546	596	588
20	559	549	602	592
14	417	387	449	417
14	422	390	454	420
20	578	561	622	605
14	431	396	465	426
14	436	399	470	430
21	623	604	671	650
21	631	609	679	656
21	639	614	688	662
21	647	620	697	668
21	655	626	706	675
21	664	633	715	682
21	674	640	726	689
21	683	647	736	697
21	694	655	748	706
21	705	664	760	715
21	717	673	773	725
Q_s(MN)			20.02	19.51
		Q_c/Q_m	3.30	3.21

Pile	WK38
Blow	BoR

API (2007)

t (m)	40
t (mm)	0.04
R (m)	0.6858
R* (m)	0.231
Pile tip depth (m)	16.8
Embedment length (m)	16.8
A_{base} (m^2)	1.48
A_{steel} (m^2)	0.17

Dry density	20.11	kN/m^3
Bouy. density	10.31	kN/m^3
Soil type	Glacial Till	
Dry density	21.41	kN/m^3
Bouy. density	11.61	kN/m^3

Nkt	22.5

Layer no.	Top of layer (m)	Bottom of layer (m)	dz (m)	Unit weight kN/m^3	σ'_v (kPa)	s_u (kPa)	s_u/σ'_v	Alpha	Unit T_f (kPa)	Qs (ext) (kN)
1	0	0.25	0.25	10.31	1.3	0	0	0.00	0	0
2	0.25	0.5	0.25	10.31	3.9	0	0	0.00	0	0
3	0.5	0.75	0.25	10.31	6.4	0	0	0.00	0	0
4	0.75	1	0.25	10.31	9.0	0	0	0.00	0	0
5	1	1.25	0.25	10.31	11.6	-1	0	0.00	0	0
6	1.25	1.5	0.25	10.31	14.2	310	22	0.23	72	77
7	1.5	1.75	0.25	10.31	16.8	621	37	0.20	126	136
8	1.75	2	0.25	10.31	19.3	621	32	0.21	130	141
9	2	2.25	0.25	11.61	24.7	621	25	0.22	139	149
10	2.25	2.5	0.25	11.61	27.6	621	23	0.23	143	154
11	2.5	2.75	0.25	11.61	30.5	621	20	0.24	146	157
12	2.75	3	0.25	11.61	33.4	621	19	0.24	149	161
13	3	3.25	0.25	11.61	36.3	621	17	0.25	153	164
14	3.25	3.5	0.25	11.61	39.2	309	8	0.30	92	99
15	3.5	3.75	0.25	11.61	42.1	309	7	0.30	94	101
16	3.75	4	0.25	11.61	45.0	398	9	0.29	115	124
17	4	4.25	0.25	11.61	47.9	665	14	0.26	172	185
18	4.25	4.5	0.25	11.61	50.8	664	13	0.26	175	188
19	4.5	4.75	0.25	11.61	53.7	664	12	0.27	177	191
20	4.75	5	0.25	11.61	56.6	664	12	0.27	179	193
21	5	5.25	0.25	11.61	59.5	308	5	0.33	102	110
22	5.25	5.5	0.25	11.61	62.4	308	5	0.34	103	111
23	5.5	5.75	0.25	11.61	65.3	219	3	0.37	81	87
24	5.75	6	0.25	11.61	68.2	219	3	0.37	82	88
25	6	6.25	0.25	11.61	71.1	219	3	0.38	83	89
26	6.25	6.5	0.25	11.61	74.0	663	9	0.29	192	207
27	6.5	6.75	0.25	11.61	76.9	663	9	0.29	194	208
28	6.75	7	0.25	11.61	79.8	263	3	0.37	98	105
29	7	7.25	0.25	11.61	82.7	219	3	0.39	86	92
30	7.25	7.5	0.25	11.61	85.6	218	3	0.40	86	93
31	7.5	7.75	0.25	11.61	88.5	218	2	0.40	87	94
32	7.75	8	0.25	11.61	91.4	218	2	0.40	88	95
33	8	8.25	0.25	11.61	94.3	262	3	0.39	102	109
34	8.25	8.5	0.25	11.61	97.2	440	5	0.34	151	163
35	8.5	8.75	0.25	11.61	100.1	529	5	0.33	174	188
36	8.75	9	0.25	11.61	103.0	618	6	0.32	197	213
37	9	9.25	0.25	11.61	105.9	884	8	0.29	260	280
38	9.25	9.5	0.25	11.61	108.8	884	8	0.30	262	282
39	9.5	9.75	0.25	11.61	111.7	617	6	0.33	201	217
40	9.75	10	0.25	11.61	114.6	617	5	0.33	203	218
41	10	10.25	0.25	11.61	117.6	884	8	0.30	267	287
42	10.25	10.5	0.25	11.61	120.5	617	5	0.33	205	221
43	10.5	10.75	0.25	11.61	123.4	617	5	0.33	206	222
44	10.75	11	0.25	11.61	126.3	928	7	0.30	282	304
45	11	11.25	0.25	11.61	129.2	928	7	0.31	283	305
46	11.25	11.5	0.25	11.61	132.1	927	7	0.31	285	307
47	11.5	11.75	0.25	11.61	135.0	927	7	0.31	286	309
48	11.75	12	0.25	11.61	137.9	927	7	0.31	288	310
49	12	12.25	0.25	11.61	140.8	927	7	0.31	289	312
50	12.25	12.5	0.25	11.61	143.7	927	6	0.31	291	313
51	12.5	12.75	0.25	11.61	146.6	927	6	0.32	292	315
52	12.75	13	0.25	11.61	149.5	927	6	0.32	294	316
53	13	13.25	0.25	11.61	152.4	927	6	0.32	295	318
54	13.25	13.5	0.25	11.61	155.3	926	6	0.32	296	319

Q_s(MN)	9.43
Q_c/Q_m	1.55

APPENDIX A-5

Pile exhumation inspections



Zone A:
0-14mm from pile wall
Oxidised surface approximately 1-2mm thick mottled brown with remoulded Chalk, no evidence of shear surface or aligned particles. 2-14mm zone consists of remoulded Chalk (previously puttified Chalk) with no distinct features. Very soft, finger nails easily pushed into sample. Adheres to the surface of the pile. No evidence of recent shearing associated with pile movement.

Zone B:
14-50mm from pile wall
Intact chalk with gritty fragments, crumbles between fingers into dice sized blocks. Evidence of recent clean fracturing with no staining. Fractures closed or open to <3mm. No clear evidence of shear surfaces except recent fracturing.

Zone C:
Intact chalk: breaks into bigger blocks approximately 40 x 30mm size. Fractures are iron and manganese stained (old) and covered with vegetation in places. Fractures open to <1mm.

Figure A5-1: DP1 at 0.5mbgl – typical condition



DP1

From 0 – 0.6m

Conditions similar to Figure 1

Zone A:

i.e. Oxidised surface approximately 1-2mm thick mottled brown with remoulded Chalk, no evidence of shear surface or aligned particles. 2-14mm zone consists of remoulded Chalk (previously puttified Chalk) with no distinct features. Adheres to the surface of the pile. No evidence of recent shearing associated with pile movement.

Zone B:

14-50mm from pile wall

Intact chalk with gritty fragments, crumbles between fingers into dice sized blocks. Evidence of recent clean fracturing with no staining. Fractures closed or open to <0.5mm.

Zone C:

Intact chalk: breaks into bigger blocks approximately 40 x 30mm size. Fractures are iron and manganese stained (old) and covred with vegetation in places. Fractures open to <1mm. No clear evidence of shear surfaces except recent fracturing.

From 0.8 – 1.1m

Remoulded zone <5mm thick and difficult to distinguish from intact Chalk potentially due to issues with access to the pit. Slight change in strength from finger nail pressure. Changes in physcial propoerties not visible. Fractures terminate close to the pile wall indicating a lower thickness of remoulded material.

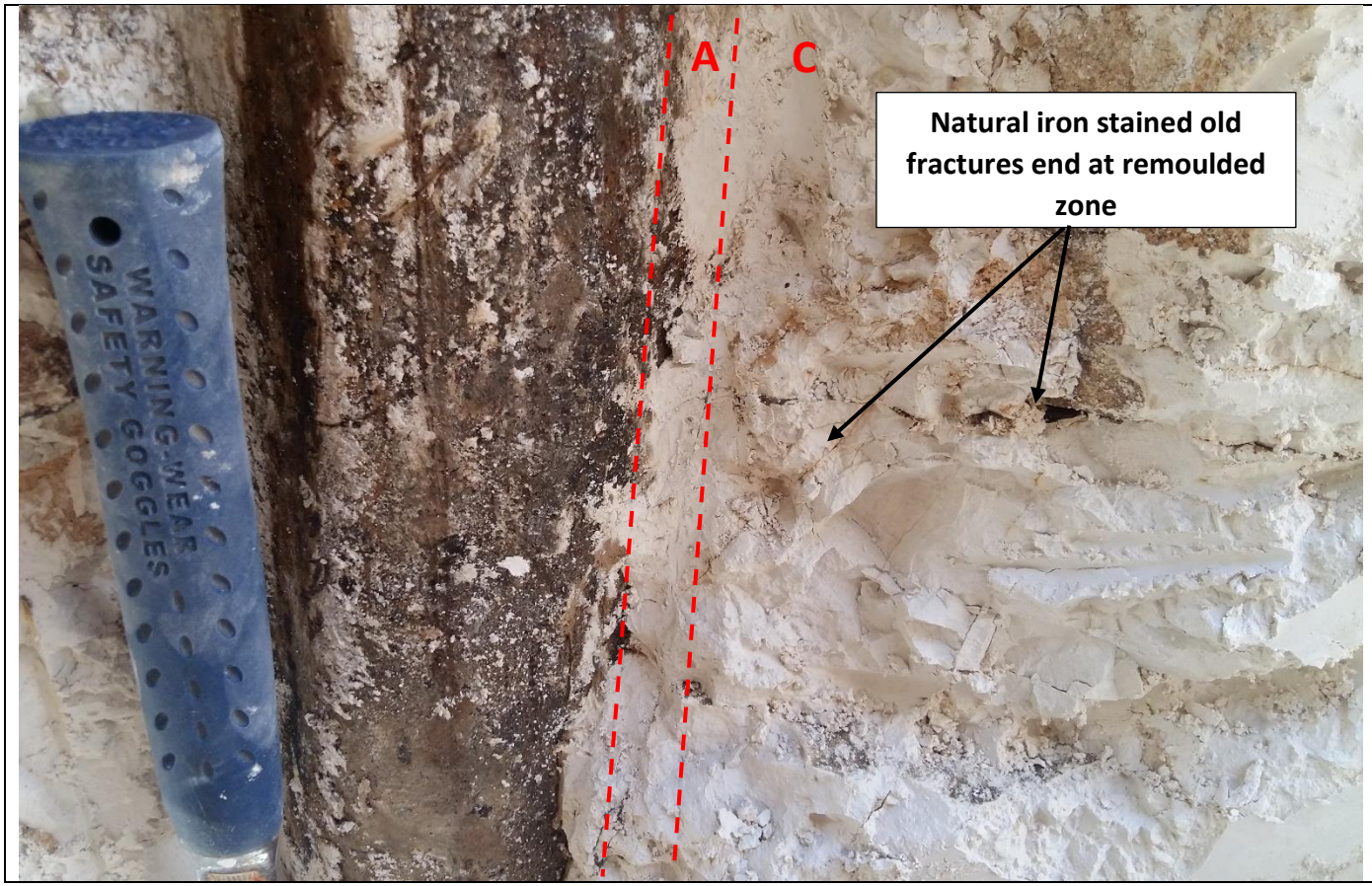
Figure A5-2: DP1– change in conditions below 0.8m depth





Zone A
Material from oxidised surface immediately adjacent to the pile. Brown and mottled black in places. Thickness of 1-2mm constant along the pile length and seen in all excavations and at all depths. No evidence of polished surfaces however material smears more easily than the rest of the remoulded zone or the intact Chalk.

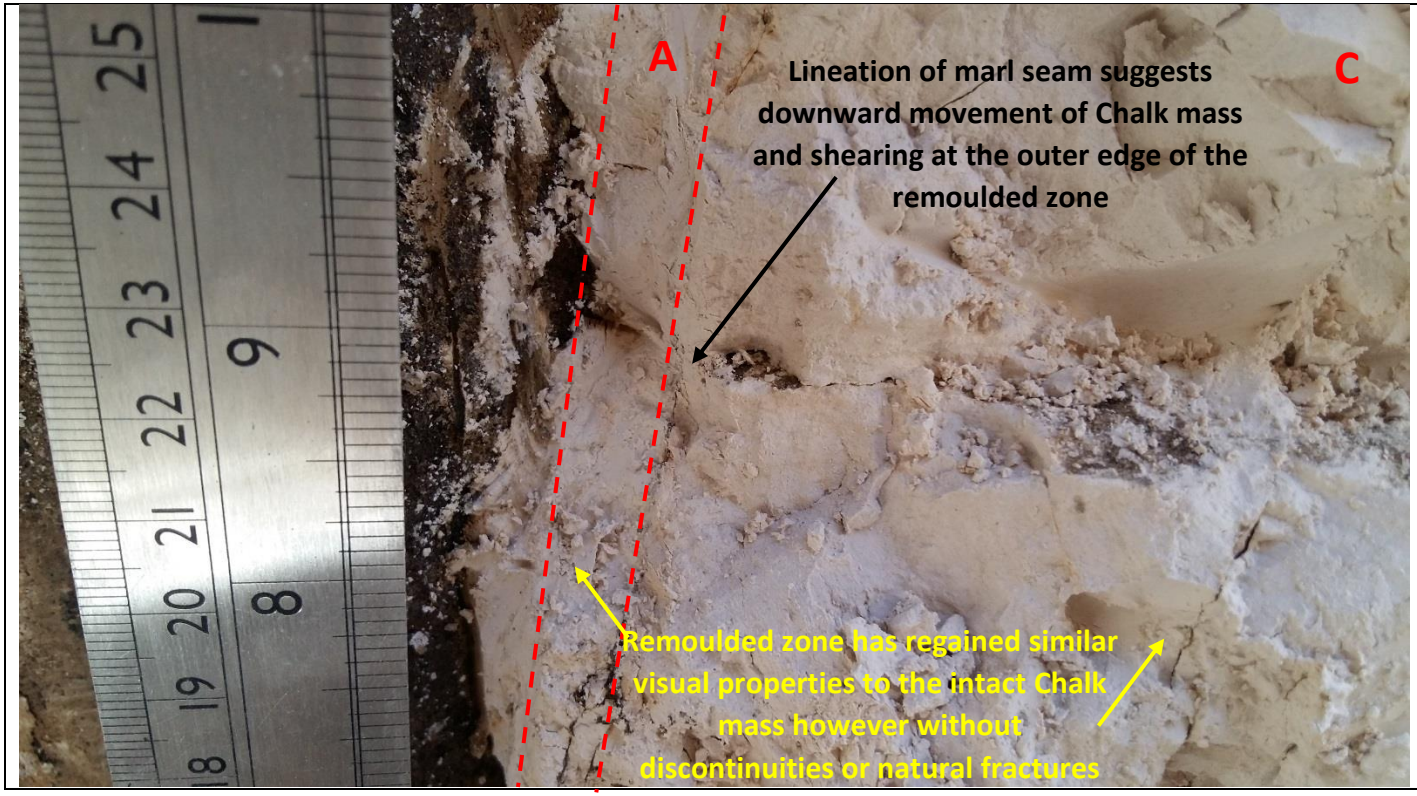
Figure A5-3: DP1 at 0.8mbgl – close up of oxidised surface immediately adjacent to the pile



Zone A:
0-15mm from pile wall
Oxidised surface approximately 1-2mm thick mottled brown with remoulded Chalk, no evidence of shear surface or aligned particles. 2-15mm zone consists of remoulded Chalk (previously puttified Chalk) with no distinct features. Adheres to the surface of the pile.

Zone C:
Intact chalk: breaks into bigger blocks. Fractures are iron and manganese stained (old). Fractures open to <1mm. Fracture (apparent dip = 52º L>70mm) terminates at remoulded zone. Marl seam also terminates at the outer edge of the previously puttified zone and appears to lineate downwards indicating movement of adjacent soil mass during pile driving and shearing at the outer edge of the remoulded zone.

Figure A5-4: DP7 at 0.6mbgl - Shear surface and remoulded (previously puttified Chalk zone



As Figure A5-4

Figure A5-5: DP7 at 0.6mbgl – Close of up of Fig A5-4

APPENDIX A-6
ICP instrument performance

A-6.1 Introduction

The performance of the instruments deployed on the Imperial College Pile are described within this Appendix. In general, the instruments performed adequately during the tests, with the majority of the measurements proving reliable and consistent after cross checking. However, water ingress into the pile during long-term monitoring caused some erroneous results in ICP01, in addition to under-registration of SST stresses during installation. Supplementary information on general performance, instrument drifts over time and under-registration of stresses is therefore provided in this Appendix.

A-6.2 General instrument performance

A-6.2.1 Pore pressure probes & axial load cells

The performance of the PPTs is summarised in Table A-6.1, where PPTa/b are the sensors at the leading instrument and PPTc/d are those at the following instrument. One of the pore pressure probes in ICP01 at the *following* position was lost during installation due to cable breakage. During the installation of ICP02, one of the *leading* probes and one of the *following* probes gave erroneous results, which have not been used in the interpretation of the installation data. As a result, there were three working pore pressure probes during installation of ICP01, and two during the installation of ICP02; these data are sufficient to calculate the radial effective stresses at each instrument level in both tests. The ALCs functioned well during both tests.

Table A-6.1: Axial load cell and pore pressure performance during the test programme

Test		Sensor Performance
ICP01	PPTa	Performed well during installation
	PPTb	Performed well during installation, drifted during equalisation
	PPTc	Performed well
	PPTd	Cable damaged beyond repair during installation
	ALC1	Performed well during installation, drifted during equal.
	ALC2	Performed well
ICP02	PPTa	Performed well
	PPTb	Used during load testing only
	PPTc	Performed well
	PPTd	Erroneous readings during installation. Equalisation and load testing only.
	ALC1	Performed well
	ALC2	Performed well

A-6.2.2 Surface stress transducers

Table A-6.2 summarises the SST's performance during both the ICP01 and ICP02 tests. Water ingress into the pile during long-term monitoring of ICP01 caused some erroneous results in the SST measurements. It was also noticed for both SSTs that the incremental outputs from the twin radial circuits in each SST were not changing equally under load for both SSTs. While the R1 (top) circuit was generally consistent and stable in terms of incremental changes and also read reasonable values for the duration of both tests, less stable and consistent readings were encountered with the second radial sensor R2 (bottom) in both SSTs that could lead to erroneous measurements, particularly during long-term monitoring. As a result the test interpretation relied on R1 alone to measure radial stress.

During installation, the local shear stresses, τ_{rz} were measured by the *leading* and *following* SSTs, while the pile was both moving and stationary. The average shear stresses on the pile casings at the same point can be calculated from the ALC measurements, by linear interpolation of force between the sensors and provide vital checks on the reliability of the local readings. The SSTs can be affected by cell action effects and their asymmetric design makes them susceptible to bending under high axial loads. Measurements of average shear stress have

the advantage of being free of such effects, due to the simple axially-symmetric design of the ALCs. Chow (1997) reported substantial differences between the local and average shear stress measurements in dense sand at Dunkirk during *installation* and *compression* load testing, with the measured τ_{rz} up to 70kPa lower than the average shaft stress values interpolated from the ALCs. The problem was considered prior to the tests at Dunkirk and it was assessed that the solution, of increasing the pile diameter to allow inclusion of symmetrical SSTs, was overly expensive. The under-registration was thought to be caused by compression bending of the asymmetric load cell under high loads; the axial loads at Dunkirk were almost three times higher than those measured at previous ICP test sites. Chow argued that axial load induced bending causes the platen on the SST to deflect inwards (Figure A-6.1) causing a change in the calibration coefficients for the shear and radial stresses, or a reduction in the pressure between the soil and the platen and a subsequent reduction in measured local stresses.

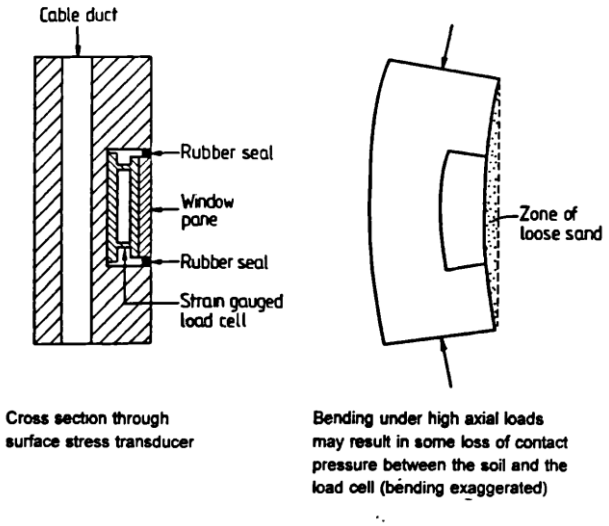


Figure A-6.1: The effect of bending on the SSTs (Chow, 1997)

The average axial loads experienced by the ALCs on installation at this site were similar to the maximum of 270kN seen at Dunkirk and a similar under-registration of compressive installation stresses was observed. No static compression load tests were carried out during this testing programme. The uncorrected local shear stress measurements recorded during installation suggest unfeasibly low interface angles of friction, δ'_f under compressive installation loading. In contrast, under static load tension testing where the axial loads were low, the interface friction angle at failure was close to the value of δ'_{ult} measured at failure in interface ring shear tests (Chapter 7). These apparently low anomalous installation shear

stresses were assessed after making corrections for the effect of axial load on the radial and shear stresses indicated by the laboratory and "in air" field calibrations as set out in Chapter 7. However the latter only account for the changes in the "zero" point of the radial and shear sensors, that develop as load is applied to the free cell, and do not include secondary effects of high axial loads on the soil-cell interactions, which include reducing the contact pressure between the window pane and the chalk as indicated in Figure A-6.1. The radial stress and shear stress under-registration has a limited impact on the tests in this study, since:

1. High axial loads were only developed during penetration;
2. The axial load cells functioned well during installation, so allowing cross checking of the penetration shear stress measurements and identification of under-registration;
3. Pauses during installation, and between installation and load testing were subject to zero axial load and therefore free of any bending effects.
4. Only static tension tests were carried out, where the sensors were free of bending effects due to the low negative axial loads induced.

The data from the chalk tests showed a similar general trend of increasing error with axial load to the Dunkirk tests; a maximum of 44kPa under-registration was recorded at the *following* (h/R=32) instrument in ICP01.The radial stresses under-registered by a lesser degree than the shear stresses; σ'_r was underestimated by up to 31kPa at the *following* instrument in ICP01. Elastic analyses of the susceptibility of the SSTs to cell action effects suggest that under-registration of radial stresses is likely to be approximately half that of the shear stress under-registration (Jardine, 1985, Bond, 1989).

The asymmetry of the SSTs was understood as an unavoidable potential weakness by Bond (1989). Although the large corrections required for the jacking data reduce the reliability of the penetration stage measurements, it is important to note that no correction was required for the radial and shear stresses during zero load jacking pauses, over the equalisation periods or during the tension load tests, where the axial loads were comparatively low. Overall, approximately 75% of the SST data recorded required no correction for the effects of axial load induced bending.

Table A-6.2: SST instrument performance and drift during the test programme (negative numbers denote a reduction in measured quantity with time)

Test	Sensor	Performance
ICP01	1R1	Performed well during pauses. Under-predicted during penetration stages due to axial load induced bending. Drifted significantly during equalisation due to water ingress. Not used during load testing.
	1R2	Performed well during jacking pauses and in tension testing. Under-predicted during penetration stages due to axial load induced bending. Drifted significantly during equalisation due to water ingress.
	1S	Performed well during jacking pauses and in tension testing. Under-predicted during penetration stages due to axial load induced bending. Drifted significantly during equalisation due to water ingress.
ICP02	1R1	Performed well during jacking pauses and in tension testing. Under-predicted penetration stages due to axial load induced bending.
	1R2	Not used as R1 more consistent with shear profile. Erroneous results observed during equalisation. Not used.
	1S	Performed well during jacking pauses and in tension testing. Under-predicted due to axial load induced bending
ICP01	2R1	Performed well during jacking pauses and in tension testing. Under-predicted penetration stages due to axial load induced bending.
	2R2	Performed well during jacking pauses. Under-predicted penetration stages due to axial load induced bending. Not used during equalisation or load testing,
	2S	Performed well during jacking pauses and in tension testing. Under-predicted penetration stages due to axial load induced bending.
ICP02	2R1	Performed well during jacking pauses and in tension testing. Under-predicted penetration stages due to axial load induced bending.
	2R2	Not used as R1 more consistent with shear profile and significant drift observed during equalisation.
	2S	Performed well during jacking pauses and in tension testing. Under-predicted penetration stages due to axial load induced bending

A-6.3 Instrument drifts

The Author's ICP tests were extended and monitored for far longer periods than any earlier ICP test campaign. The experiments were conducted in damp and cold site conditions which were expected to have led to some potential drift in the strain gauged instruments' voltage outputs under zero load. The magnitude of this potential drift was checked by comparing the instrument "zero values" established immediately following extraction of each particular instrument, when the pile was "hanging" in the borehole, with those recorded immediately prior to installation. These measurements can be used to identify and correct for, any long-term measurement drift. The resulting instrument drifts are shown in Table A-6.3 and in Table A-6.4 for the axial load/pore pressure sensors and surface stress transducers respectively.

Some relatively minor drift appears to have developed in ALC1 during the long-term monitoring of ICP01 and in ALC2 during the long-term monitoring on ICP02. The measurements from the *leading* SST in test ICP01 show significant drift, due to water ingress which is thought to have taken place through a joint in the ICP sections. These have been sealed in earlier tests with a "Hylomar" liquid gasket product, but this step was not considered feasible during the tests in this study. Soon after installation the leaking radial, shear and axial load sensors began to drift significantly. This may have been exacerbated by a power outage that occurred two days after installation and allowed the instruments to cool down. The radial sensor drift was 5.6 kPa per day or 129.6kPa over the entire period. An "earth leak" test was carried out 18 days after installation which confirmed the presence of water in the instruments. At this time the *leading* instrument cluster was unplugged to prevent further damage, and only re-energised prior to the final load test.

In order to correct the equalisation results for the effects of drift in the instrument zeroes, it has been assumed that drift began immediately following installation and developed linearly over time until the load test, after which new zero values were established on pile extraction. While it is accepted that a significant sudden drift may have occurred at any time during the equalisation period, monitoring of the cells under bench testing following the pile tests suggests that drift continued in a steady, approximately linear, fashion and corrections have been made accordingly. The data obtained in the final loading tests could be corrected on the basis of 'zero-value' checks undertaken when the piles were extracted shortly after completing the load tests.

Table A-6.3: Instrument drifts in pore pressure and axial load sensors during the test programme (negative numbers denote a reduction in measured quantity with time)

Test	Sensor	Drift (kPa)	Drift (kPa/day)
ICP01	PPTa	0.9	0.04
	PPTb	6.1	0.30
	PPTc	1.4	0.06
	PPTd	-	-
	ALC1	- 6.7	-0.29
	ALC2	-0.8	-0.04
ICP02	PPTa	-5.0*	-0.07
	PPTb	8.88	0.13
	PPTc	12.9	0.18
	PPTd	23.8	0.34
	ALC1	1.47	0.02
	ALC2	-10.5	-0.15

Table A-6.4: Instrument drifts in surface stress transducer sensors during the test programme (negative numbers denote a reduction in measured quantity with time)

Test	Sensor	Drift (kPa)	Drift (kPa/day)
ICP01	1R1	- 129.6	- 5.6[1]
	1R2	- 132.5	- 5.8
	1S	-33.1	- 1.4
ICP02	1R1	-13.3	-0.19
	1R2	14.2	0.2
	1S	-0.7	-0.01
ICP01	2R1	-5.0	-0.22
	2R2	-2.0	-0.09
	2S	-1.4	-0.06
ICP02	2R1	9.0	0.13
	2R2	-47.9	-0.68
	2S	2.7	0.04

1. Associated with water ingress into the pile – not used in interpretation of equalisation data